DOE-ER-0313/62
Distribution
Categories
UC-423, -424

FUSION MATERIALS
SEMIANNUAL PROGRESS REPORT
FOR THE PERIOD ENDING

June 30, 2017

Prepared for
DOE Office of Fusion Energy Sciences
(AT 60 20 10 0)

DATE PUBLISHED: October 2017

Prepared by
OAK RIDGE NATIONAL LABORATORY
Oak Ridge, Tennessee 37831
Managed by
UT-Battelle, LLC
For the
U.S. DEPARTMENT OF ENERGY

FOREWORD

This is the sixty-second in a series of semiannual technical progress reports on fusion materials science activity supported by the Fusion Energy Sciences Program of the U.S. Department of Energy. It covers the period ending June 30, 2017. This report focuses on research addressing the effects on materials properties and performance of exposure to the neutronic, thermal and chemical environments anticipated in the chambers of fusion experiments and energy systems. This research is a major element of the national effort to establish the materials knowledge base for an economically and environmentally attractive fusion energy source. Research activities on issues related to the interaction of materials with plasmas are reported separately.

The results reported are the products of a national effort involving a number of national laboratories and universities. A large fraction of this work, particularly in relation to fission reactor irradiations, is carried out collaboratively with partners in Japan, Russia, and the European Union. The purpose of this series of reports is to provide a working technical record for the use of program participants, and to provide a means of communicating the efforts of fusion materials scientists to the broader fusion community, both nationally and worldwide.

This report has been compiled under the guidance of F. W. (Bill) Wiffen and Stephanie Melton, Oak Ridge National Laboratory. Their efforts, and the efforts of the many persons who made technical contributions, are gratefully acknowledged.

Daniel Clark
Research Division
Office of Fusion Energy Sciences

TABLE OF CONTENTS

1 FERRITIC/MARTENSITIC STEEL DEVELOPMENT

1.1 **DEVELOPMENT OF CASTABLE NANOSTRUCTURED ALLOYS AS ADVANCED RAFM STEELS**—L. Tan, C.M. Parish (Oak Ridge National Laboratory) 1

1.2 **IRRADIATION HARDENING BEHAVIOR OF F82H IN JP28 AND 29**—H. Sakasegawa, M. Ando, H. Tanigawa, T. Hirose (National Institutes for Quantum and Radiological Science and Technology, Japan), and X. Chen, J.W. Geringer, Y. Katoh (Oak Ridge National Laboratory) 3

1.3 **EFFECTS OF HIGH DOSE NEUTRON IRRADIATION ON REDUCED-ACTIVATION FERRITIC/MARTENSITIC STEEL F82H**—T. Hirose, H. Tanigawa, H. Sakasegawa, M. Ando (National Institutes for Quantum and Radiological Science and Technology, Japan), Y. Katoh, K.G. Field, B.K. Kim, D.T. Hoelzer, L. Tan, R.E. Stoller (Oak Ridge National Laboratory), and L.L. Snead (Stony Brook University) 8

1.4 **FATIGUE PRECRACKING M4CVN TYPE STEEL SPECIMENS FOR THE EUROfusion PROJECT**—X. Chen, R.L. Swain, E.T. Manneschmidt, K.D. Linton (Oak Ridge National Laboratory) 14

2 ODS AND NANOCOMPOSITED ALLOY DEVELOPMENT

2.1 **EFFECT OF DEFORMATION PROCESSING ON THE MICROSTRUCTURE AND TEXTURE OF 14YWT NFA-1**—S. Pal, M. E. Alam, G. R. Odette (University of California, Santa Barbara), S. A. Maloy (Los Alamos National Laboratory), D. T. Hoelzer (Oak Ridge National Laboratory), and J. J. Lewandowski (Case Western Reserve University) 28

2.2 **ANNEALING TREATMENTS TO HEAL MICROCRACKS IN 14YWT NFA-1 AND THEIR EFFECTS ON MICROSTRUCTURAL AND MECHANICAL BEHAVIOR**—M.E. Alam, S. Pal, D. Gragg, K. Fields, N. J. Cunningham, G. R. Odette (University of California, Santa Barbara), D. T. Hoelzer (Oak Ridge National Laboratory) and S. A. Maloy (Los Alamos National Laboratory) 45

2.3 **APT AND TEM CHARACTERIZATION OF α-PHASE FORMATION IN NEUTRON IRRADIATED 14YW AND 14YWT ODS STEELS USING STEM AND 3D-APT**—Karen Kruska, Danny Edwards, Richard J. Kurtz (Pacific Northwest National Laboratory) 61

3 CERAMIC COMPOSITE STRUCTURAL MATERIAL DEVELOPMENT

3.1 **LOW ACTIVATION JOINING OF SiC/SiC COMPOSITES FOR FUSION APPLICATIONS: A DUAL-PHASE MICROSTRUCTURAL APPROACH TO MODEL THERMAL AND IRRADIATION-INDUCED SWELLING EFFECTS ON INTEGRITY OF Ti_3SiC_2/SiC JOINTS**—B.N. Nguyen, C.H. Henager, Jr., R.J. Kurtz; (Pacific Northwest National Laboratory) 73

3.2 **IRRADIATION-INDUCED β TO α SiC TRANSFORMATION AT LOW TEMPERATURE**—C.M. Parish, T. Koyanagi, Y. Katoh (Oak Ridge National Laboratory) and S. Kondo (Kyoto University) 79

TABLE OF CONTENTS

3.3 **MICROSTRUCTURAL EVOLUTION OF NEUTRON IRRADIATED 3C-SiC**—D.J. Sprouster, E. Dooryhee, S.K. Ghose, L.E. Ecker (Brookhaven National Laboratory) and Y. Katoh, T. Koyanagi (Oak Ridge National Laboratory) **80**

3.4 **EQUILIBRIUM SHAPES AND SURFACE SELECTION OF NANOSTRUCTURES IN 6H-SiC**—S. Kondo (Kyoto University) and C.M. Parish, T. Koyanagi, Y. Katoh (Oak Ridge National Laboratory) **81**

4 HIGH HEAT FLUX MATERIALS AND COMPONENT TESTING

4.1 **PROPERTIES AND CHARACTERIZATION OF NOVEL COPPER ALLOYS FOR FUSION ENERGY APPLICATIONS**—Ying Yang (Oak Ridge National Laboratory), Ling Wang (University of Tennessee at Knoxville), Steven J. Zinkle (University of Tennessee at Knoxville and Oak Ridge National Lab), and Lance Snead (Stony Brook University) **82**

4.2 **FABRICATION OF ROLL BONDED FUNCTIONALLY GRADED TUNGSTEN-STEEL LAMINATE**—L. M. Garrison, J. Mettler, J. Moon (Oak Ridge National Laboratory) **93**

4.3 **FABRICATION OF ULTRASONIC WELDED FUNCTIONALLY GRADED TUNGSTEN-STEEL LAMINATE**—L. M. Garrison, D. Leonard (Oak Ridge National Laboratory) and M. Norfolk, J. Wenning (Fabrisonic LLC.) **102**

4.4 **4.4 TUNGSTEN/SiC AND TUNGSTEN/GRAPHITE JOINING**—L.M. Garrison, Y. Katoh, E. Proehl, P. Menchhofer (Oak Ridge National Laboratory) **108**

4.5 **PREPARATION OF TUNGSTEN SURFACES FOR PLASMA-MATERIAL INTERACTION STUDIES**—L.M. Garrison, M. Bannister, F. Meyer, D. Leonard (Oak Ridge National Laboratory) **109**

4.6 **MICROSTRUCTURE AND MECHANICAL PROPERTIES OF IRRADIATED PHENIX PROGRAM TUNGSTEN**—L.M. Garrison, Y. Katoh, N. Reid, E. Proehl, (Oak Ridge National Laboratory) and M. Fukuda (Tohoku University) **112**

4.7 **CHARACTERIZATION OF SELF-ION IRRADIATED TUNGSTEN**—Weilin Jiang, Danny Edwards, Giridhar Nandipati, Wahyu Setyawan, Charles H. Henager Jr., Richard J. Kurtz (Pacific Northwest National Laboratory) and Aaron French, Xuemei Wang, Lin Shao (Texas A&M University) **125**

4.8 **MORPHOLOGIES OF TUNGSTEN NANOTENDRILS GROWN UNDER HELIUM EXPOSURE**—Amith Darbal, Robert Stroud (AppFive, Tempe, AZ), Kun Wang, F. W. Meyer, M. E. Bannister, Chad M. Parish (Oak Ridge National Laboratory), and R. P. Doerner, M. J. Baldwin (University of California-San Diego) **131**

4.9 **PRECIPITATION OF TRANSMUTANT ELEMENTS IN NEUTRON IRRADIATED TUNGSTEN**—X. Hu, C. Parish, K. Wang, Y. Katoh (Oak Ridge National Laboratory) **132**

TABLE OF CONTENTS

4.10 **NEUTRON IRRADIATION EFFECTS IN TUNGSTEN**—L.M. Garrison, Y. Katoh, M. McAlister, T. Koyanagi (Oak Ridge National Laboratory), L. L. Snead (Stony Brook University), T. S. Byun (Pacific Northwest National Laboratory), and T. Hwang, M. Fukuda (Tohoku University, Japan **145**

5 **MAGNETIC AND DIAGNOSTIC SYSTEM MATERIALS**
No contributions this reporting period.

6 **FUSION CORROSION AND COMPATIBILITY SCIENCE**
No contributions this reporting period.

7 **MECHANISMS AND ANALYSIS**

7.1 **VIEWPOINT: NANOSCALE CHEMISTRY AND CRYSTALLOGRAPHY ARE BOTH THE OBSTACLE AND PATHWAY TO ADVANCED RADIATION-TOLERANT MATERIALS**—Chad M. Parish, Kun Wang, Philip D. Edmondson (Oak Ridge National Laboratory) **148**

7.2 **EXPLORATION OF THE RADIATION RESISTANCE OF HIGH ENTROPY ALLOYS**—C. Li, S.J. Zinkle (University of Tennessee), and X. Hu, J. Qiu (Oak Ridge National Laboratory) **149**

7.3 **EFFECTS OF IRRADIATION AND ANNEALING ON THE MICROSTRUCTURE AND MECHANICAL PROPERTIES OF BULK METALLIC GLASS ALLOYS**—L. Mora, Y. Zhang, H. Bei, J. Neuefeind, W. Dmowski, T. Egami, S. J. Zinkle (Oak Ridge National Laboratory) and J. Brechtl, M. L. Crespillo, T. Yang, H. Wang, J. Salasin, I. Gussev, M. Lang (University of Tennessee **158**

7.4 **MICROSTRUCTURE-BASED VISCOPLASTICITY MODEL OF TUNGSTEN IN PLASMA TRANSIENTS**—David Rivera, Giacomo Po, Yue Haung, Nasr M. Ghoniem (University of California, Los Angeles **179**

7.5 **CONTROLLING STRAIN BURSTS AND AVALANCHES AT THE NANO-TO-MICRO SCALE**—Y.N. Cui, G. Po, N.M. Ghoniem (University of California, Los Angeles **202**

8 **MODELING PROCESSES IN FUSION SYSTEM MATERIALS**

8.1 **DEVELOPMENT OF INTERATOMIC POTENTIALS IN TUNGSTEN-RHENIUM SYSTEMS**—W. Setyawan and R. J. Kurtz (Pacific Northwest National Laboratory), and N. Gao (Institute of Modern Physics, Chinese Academy of Science, China) **206**

8.2 **CONFIGURATIONAL MULTIPLICITY OF GRAIN BOUNDARY PHASES IN BCC METALS**—Timofey Frolov, R. E. Rudd (Lawrence Livermore National Laboratory), W. Setyawan, R. J. Kurtz (Pacific Northwest National Laboratory), J. Marian (University of California Los Angeles), A. R. Oganov (Stony Brook University), and Q. Zhu (University of Nevada Las Vegas) **213**

8.3 **EFFECT OF SIA TRAPPING AND DETRAPPING ON DEFECT ACCUMULATION IN TUNGSTEN DUE TO RADIATION CORRESPONDING TO 14-MeV-NEUTRON AND HFIR PKA SPECTRA**—Giridhar Nandipati, Wahyu Setyawan, Kenneth J. Roche, Richard J. Kurtz (Pacific Northwest National Laboratory), Brian D. Wirth (University of Tennessee) **214**

TABLE OF CONTENTS

8.4 **SIMULATING IRRADIATION HARDENING IN TUNGSTEN UNDER FAST NEUTRON IRRADIATION INCLUDING TRANSMUTATION RHENIUM PRODUCTION**—Chen-Hsi Huang, Jaime Marian (Department of Materials Science and Engineering, University of California Los Angeles), and Mark R. Gilbert (Culham Science Centre, Abingdon, UK) **215**

8.5 **MODELING DUCTILE-PHASE TOUGHENED TUNGSTEN FOR PLASMA-FACING MATERIALS: PROGRESS IN DAMAGE FINITE ELEMENT ANALYSIS OF TUNGSTEN-COPPER BEND TESTS**—B. N. Nguyen, C. H. Henager, Jr., R. J. Kurtz (Pacific Northwest National Laboratory) **232**

9 **FUSION SYSTEM DESIGN**

No contributions this reporting period.

10 **IRRADIATION METHODS, EXPERIMENTS AND SCHEDULES**

10.1 **MINIATURE MECHANICAL TEST DEVELOPMENT FOR TUNGSTEN-BASED MATERIALS**—L. M. Garrison, Emily Proehl, Frank Chen (Oak Ridge National Laboratory) **239**

10.2 **HFIR IRRADIATION EXPERIMENTS**—J.P. Robertson (Oak Ridge National Laboratory) **241**

TABLE OF CONTENTS

1 FERRITIC/MARTENSITIC STEEL DEVELOPMENT

1.1 **DEVELOPMENT OF CASTABLE NANOSTRUCTURED ALLOYS AS ADVANCED RAFM STEELS**—L. Tan, C.M. Parish (Oak Ridge National Laboratory) 1

A new CNA heat #2905 was used to explore TMT effects on microstructure evolution. Following a warm-rolling (WR) TMT, samples were prepared for microstructural characterization. The #2905-WR was characterized to produce a dual-phase structure, consisting of tempered martensite and a network of fine ferrite grains. Unlike tempered martensite having a high density of lath boundaries and dislocations, the ferrite grains are “free” of dislocation. However, some nano-sized Cr-rich carbides, together with many unresolved ultrafine particles, were revealed in the ferrite grains. Further studies will attempt to identify the rod-shaped carbon-rich particles and Laves-structured particles.

1.2 **IRRADIATION HARDENING BEHAVIOR OF F82H IN JP28 AND 29**—H. Sakasegawa, M. Ando, H. Tanigawa, T. Hirose (National Institutes for Quantum and Radiological Science and Technology, Japan), and X. Chen, J.W. Geringer, Y. Katoh (Oak Ridge National Laboratory) 3

The result of thermometry analysis was supported by the irradiation hardening behavior observed in this work, because F82H mod3 heat showed comparable hardness at the designed temperatures of 673 and 773 K. From the summary of dose dependence of irradiation hardening including the result of JP26 and 27, significant increase in hardness was not observed in the result of JP28 at 673 K. Since any decrease in irradiation temperature generally promotes irradiation hardening, it can be assumed that the decrease in actual irradiation temperature in the 673 K specimen holder did not largely affect the irradiation behavior of F82H. However, further investigations are indispensable in future work.

1.3 **EFFECTS OF HIGH DOSE NEUTRON IRRADIATION ON REDUCED-ACTIVATION FERRITIC/MARTENSITIC STEEL F82H**—T. Hirose, H. Tanigawa, H. Sakasegawa, M. Ando (National Institutes for Quantum and Radiological Science and Technology, Japan), Y. Katoh, K.G. Field, B.K. Kim, D.T. Hoelzer, L. Tan, R.E. Stoller (Oak Ridge National Laboratory), and L.L. Snead (Stony Brook University) 8

Post irradiation tensile tests were conducted on F82H irradiated up to 87 dpa at 573, 673 and 773 K in the HFIR, and the following was found;

- Irradiation hardening and loss of ductility were observed even at 673 and 773 K.
- Specimens irradiated in the FFTF demonstrated softening at these temperatures.
- Differences between FFTF and HFIR should be investigated including transmutation effects.
- Lower irradiation temperatures resulting from deformation of capsule material is possible.
- Hardening was significant in the specimen irradiated at 573 K. The increment gradually decreased with irradiation dose, but the strength was obviously larger than in previous work.
- Ductility after irradiation exhibited a minimum at 673 K, and did not saturate up to 87dpa.
- F82H + Ni-58, which produced 920 atomic ppm of helium, demonstrated significant hardening at 573 K. However, the hardening increment diminished at 673 and 773 K.

TABLE OF CONTENTS

1.4 FATIGUE PRECRACKING M4CVN TYPE STEEL SPECIMENS FOR THE EUROfusion PROJECT—X. Chen, R.L. Swain, E.T. Manneschmidt, K.D. Linton (Oak Ridge National Laboratory) **14**

We performed fatigue pre-cracking of M4CVN specimens for the EUROfusion project. The test materials include different variants of reduced activation ferritic and martensitic (RAFM) steels from both Europe and US for the EUROfusion project. Additional fatigue pre-cracking will be performed on M4CVN specimens machined from Eurofer 97 baseline material.

2 ODS AND NANOCOMPOSITED ALLOY DEVELOPMENT

2.1 EFFECT OF DEFORMATION PROCESSING ON THE MICROSTRUCTURE AND TEXTURE OF 14YWT NFA-1—S. Pal, M. E. Alam, G. R. Odette (University of California, Santa Barbara), S. A. Maloy (Los Alamos National Laboratory), D. T. Hoelzer (Oak Ridge National Laboratory), and J. J. Lewandowski (Case Western Reserve University) **28**

Hot extrusion of as milled NFA-1 powder produces an inhomogeneous microstructure with strong bimodal grain size distribution with <110> α-fiber texture along the extrusion direction (ED) and a mix of <111> and <100> texture in the normal directions (ND). Hot cross-rolling completely transforms <111> texture to <100> ND texture and strengthens α-fiber in the extrusion direction. This introduces a high volume fraction of low toughness {001}<110> brittle cleavage systems. Dislocation reactions and pile ups at sessile low angle grain boundaries forming {001} planes in combination with residual stress produces microcracks running parallel to the plate. Shear dominated hydrostatic extrusion heals microcracks and transforms the ND texture to <111> from <100>. Effect of processing routes on the volume fraction of different texture components, dislocation density, and grain boundary misorientation angle-axis distribution are presented.

2.2 ANNEALING TREATMENTS TO HEAL MICROCRACKS IN 14YWT NFA-1 AND THEIR EFFECTS ON MICROSTRUCTURAL AND MECHANICAL BEHAVIOR—M.E. Alam, S. Pal, D. Gragg, K. Fields, N. J. Cunningham, G. R. Odette (University of California, Santa Barbara), D. T. Hoelzer (Oak Ridge National Laboratory) and S. A. Maloy (Los Alamos National Laboratory) **45**

The FCRD NFA-1 is a larger heat of 14YWT nanostructured ferritic alloy (NFA) produced by ball milling FeO with argon atomized Fe-14Cr-3W-0.35Ti-0.25Y powders, followed by hot extrusion (850 ºC), annealing and cross-rolling, both at 1000 ºC to form ≈ 10 mm thick plate. As-fabricated NFA-1 exhibits unusually good in-plane isotropic properties with a near-record strength-toughness combination at lower temperatures, due to pre-existing micro cracks that form multiple delaminations upon deformation. However, tensile testing in short thickness direction (S) results in elastic regime, with a flat, faceted fracture surface, due to the micro cracks that run normal to its loading direction. A series of high temperature anneals from 1100 to 1300 ºC, each for 1 and 5 h have been carried out to understand their effect on microstructure and mechanical properties, both in- and out-of-plane orientations.

TABLE OF CONTENTS

2.3 **APT AND TEM CHARACTERIZATION OF α-PHASE FORMATION IN NEUTRON IRRADIATED 14YW AND 14YWT ODS STEELS USING STEM AND 3D-APT**—Karen Kruska, Danny Edwards, Richard J. Kurtz (Pacific Northwest National Laboratory) 61

Both scanning transmission electron microscopy (STEM) elemental mapping and 3D-atom probe tomography (APT) were used to explore the α'-phase particles that formed in irradiated 14YWT and 14YW. The STEM EDS maps were obtained on an aberration corrected JEOL ARM200CF equipped with a large collection angle SDD detector. High count maps with sub-nanometer probes yielded clear evidence of α'-phase particle formation in each alloy, from which size distributions and densities could be determined over an area larger than available in a typical APT sample. In each case, the average α'-phase particles were smaller than in the APT analysis, likely due to STEM elemental mapping being unable to detect particles less than ~3 nm in diameter. The STEM elemental mapping combined with 3D-APT provides a more detailed global view of the α'-phase particle distributions. Correlative STEM/APT work will be pursued in the future to better document the α'-phase particle relationships to oxide particles and cavities.

3 CERAMIC COMPOSITE STRUCTURAL MATERIAL DEVELOPMENT

3.1 **LOW ACTIVATION JOINING OF SiC/SiC COMPOSITES FOR FUSION APPLICATIONS: A DUAL-PHASE MICROSTRUCTURAL APPROACH TO MODEL THERMAL AND IRRADIATION-INDUCED SWELLING EFFECTS ON INTEGRITY OF Ti_3SiC_2/SiC JOINTS**—B.N. Nguyen, C.H. Henager, Jr., R.J. Kurtz; (Pacific Northwest National Laboratory) 73

We investigated a MAX phase composite joint,Ti_3SiC_2/SiC, irradiated in HFIR at 800°C to 5 dpa. Before irradiation, SEM examination indicated no transverse cracks or micro cracks in the bonding layer or at the interfaces. After irradiation, limited crack propagation along the interface between the bonding layer and the CVD substrate was observed, and micro cracks were also found in the Ti_3SiC_2/SiC joint layer. The purpose of our work is to understand the micro cracking mechanisms and their chronology in the irradiated joint. Irradiation material degradation affecting mechanical properties is not modeled, but the developed modeling approach accounts for the *irradiation-induced swelling* that can cause subsequent damage if the material is constrained. This report expands the methods discussed in other reports [1-4] to model and predict cracking due to residual stresses caused by the mismatch of thermo-elastic properties in combination with the swelling-induced mismatch between the joint and joint materials.

3.2 **IRRADIATION-INDUCED β TO α SiC TRANSFORMATION AT LOW TEMPERATURE**—C.M. Parish, T. Koyanagi, Y. Katoh (Oak Ridge National Laboratory) and S. Kondo (Kyoto University) 79

Abstract of a manuscript published in Scientific Reports 7 *(2017) 1198 | DOI:10.1038/s41598-017-01395-y*.

3.3 **MICROSTRUCTURAL EVOLUTION OF NEUTRON IRRADIATED 3C-SiC**—D.J. Sprouster, E. Dooryhee, S.K. Ghose, L.E. Ecker (Brookhaven National Laboratory) and Y. Katoh, T. Koyanagi (Oak Ridge National Laboratory) 80

Abstract of a manuscript published in Scripta Materialia 137 (2017) 132–136.

TABLE OF CONTENTS

3.4 **EQUILIBRIUM SHAPES AND SURFACE SELECTION OF NANOSTRUCTURES IN 6H-SiC**—S. Kondo (Kyoto University) and C.M. Parish, T. Koyanagi, Y. Katoh (Oak Ridge National Laboratory) **81**

Abstract of a manuscript published in Applied Physics Letters 110 (2017) 142106; doi: 10.1063/1.4979550.

4 **HIGH HEAT FLUX MATERIALS AND COMPONENT TESTING**

4.1 **PROPERTIES AND CHARACTERIZATION OF NOVEL COPPER ALLOYS FOR FUSION ENERGY APPLICATIONS**—Ying Yang (Oak Ridge National Laboratory), Ling Wang (University of Tennessee at Knoxville), Steven J. Zinkle (University of Tennessee at Knoxville and Oak Ridge National Lab), and Lance Snead (Stony Brook University) **82**

Thermal-mechanical treatment was completed on newly developed Cu-Cr-Nb-Zr and Cu-Cr-Ta-Zr alloys. Optical microscopy and hardness measurements were carried out on these new alloys. Tensile properties were evaluated between room temperature and 500°C at three strain rates ($2x10^{-4}$ to 0.056 s^{-1}) for several of the recently developed Cu-Cr-Nb-Zr alloys, and initial TEM characterization was performed on one of developed Cu-Cr-Nb-Zr alloys.

4.2 **FABRICATION OF ROLL BONDED FUNCTIONALLY GRADED TUNGSTEN-STEEL LAMINATE**—L. M. Garrison, J. Mettler, J. Moon (Oak Ridge National Laboratory) **93**

Two roll-bonded tungsten-steel composites have been fabricated. Shear punch tests of the individual tungsten and steel foils showed the tungsten foil mechanical properties are closely tied to the grain orientation texture. Tensile tests of the generation 1 composite were completed and showed increasing strength and decreasing ductility with increasing W content. The composite has improved ductility at room temperature compared to tungsten foil or tungsten plate.

4.3 **FABRICATION OF ULTRASONIC WELDED FUNCTIONALLY GRADED TUNGSTEN-STEEL LAMINATE**—L. M. Garrison, D. Leonard (Oak Ridge National Laboratory) and M. Norfolk, J. Wenning (Fabrisonic LLC.) **102**

A feasibility study for ultrasonic welding tungsten to steel was completed. The 34 trials varied the parameters of foil thickness, interlayer material, welding force, vibration amplitude, and other welding parameters. Promising results were obtained for joining tungsten directly to steel and tungsten to steel with an aluminum interlayer.

4.4 **4.4 TUNGSTEN/SiC AND TUNGSTEN/GRAPHITE JOINING**—L.M. Garrison, Y. Katoh, E. Proehl, P. Menchhofer (Oak Ridge National Laboratory) **108**

Thin tungsten foils, 25 µm thick, were joined to graphite and SiC using hot pressing. Initial results showed that the W-graphite bond was weak but the W-SiC bonding was successful. Despite the good bond, SEM cross sectional analysis did not show a noticeable reaction layer between the W and SiC. Next, 6 mm disc samples will be machined to determine if the layers remain bonded after machining.

TABLE OF CONTENTS

4.5 PREPARATION OF TUNGSTEN SURFACES FOR PLASMA-MATERIAL INTERACTION STUDIES—L.M. Garrison, M. Bannister, F. Meyer, D. Leonard (Oak Ridge National Laboratory) **109**

The cutting and polishing methods used on tungsten can change the characteristics of the near-surface region, which is important for the type of morphology that develops during ion implantation to simulate use as a plasma-facing component. Electrical discharge machining, slow speed sawing and water jet cutting were compared in terms of surface damage and contamination. Tungsten that has been mechanically polished has a damaged surface layer that is not representative of the bulk and can undergo further morphological changes at temperatures below tungsten's recrystallization temperature. Initial ion implantation results suggest that different polishes can result in different morphologies after ion implantation.

4.6 MICROSTRUCTURE AND MECHANICAL PROPERTIES OF IRRADIATED PHENIX PROGRAM TUNGSTEN—L.M. Garrison, Y. Katoh, N. Reid, E. Proehl, (Oak Ridge National Laboratory) and M. Fukuda (Tohoku University) **112**

Hardness tests, room temperature tensile tests, and microstructural analysis have been completed on the unirradiated control materials from the PHENIX RB*19J irradiation campaign. Almost all the varieties of polycrystalline tungsten have higher hardness and higher fracture strength than the single crystal tungsten. Grain size distributions have been calculated from SEM images of the unirradiated microstructures.

4.7 CHARACTERIZATION OF SELF-ION IRRADIATED TUNGSTEN—Weilin Jiang, Danny Edwards, Giridhar Nandipati, Wahyu Setyawan, Charles H. Henager Jr., Richard J. Kurtz (Pacific Northwest National Laboratory) and Aaron French, Xuemei Wang, Lin Shao (Texas A&M University) **125**

This progress report presents our preliminary results on self-ion irradiation in monocrystalline and polycrystalline tungsten at 300 and 900 K, characterized by in-situ Rutherford backscattering spectrometry in ion-channeling conditions (RBS/C) and ex-situ transmission electron microscopy (TEM). The RBS/C data suggest that the self-interstitials are extremely mobile during irradiation even at 300 K, leading to fast diffusion and annihilation of the interstitials probably through recombination with vacancies and surface sinks. Defect recovery is observed during 20 min isochronal annealing of 300 K irradiated tungsten. The TEM results also do not provide any evidence for formation of a damage band in irradiated tungsten, which is consistent with the RBS/C data. Edge-on ⟨100⟩{100} dislocation loops are not observed, but ½⟨111⟩{111} loops are likely present in the irradiated tungsten.

4.8 MORPHOLOGIES OF TUNGSTEN NANOTENDRILS GROWN UNDER HELIUM EXPOSURE—Amith Darbal, Robert Stroud (AppFive, Tempe, AZ), Kun Wang, F. W. Meyer, M. E. Bannister, Chad M. Parish (Oak Ridge National Laboratory), and R. P. Doerner, M. J. Baldwin (University of California-San Diego) **131**

Abstract of an article in Scientific Reports 7 (2017) 42315.

TABLE OF CONTENTS

4.9 PRECIPITATION OF TRANSMUTANT ELEMENTS IN NEUTRON IRRADIATED TUNGSTEN—X. Hu, C. Parish, K. Wang, Y. Katoh (Oak Ridge National Laboratory) **132**

In this study, we have used advanced electron microscope methods to explore the response of tungsten to high dose neutron irradiation in the High Flux Isotope Reactor, focusing on the detailed characterization of irradiation-induced W-Re-Os precipitates in polycrystalline tungsten through TEM, X-ray mapping in STEM, and multivariate statistical analysis data-mining of the X-ray data. The association of voids and precipitates, the chemical compositions, crystal structures and phases of precipitates along the grain boundary and within the grains were identified. The results showed that the intragranular precipitates are $(Re,Os)_2W$ Laves phase and strong association of voids and precipitates are observed. More work is needed to validate the crystalline structures of the intergranular and intragranular precipitates.

4.10 NEUTRON IRRADIATION EFFECTS IN TUNGSTEN—L.M. Garrison, Y. Katoh, M. McAlister, T. Koyanagi (Oak Ridge National Laboratory), L. L. Snead (Stony Brook University), T. S. Byun (Pacific Northwest National Laboratory), and T. Hwang, M. Fukuda (Tohoku University, Japan) **145**

The aim of this work is to evaluate tungsten and tungsten-based composites for potential use as part of a plasma-facing component for future fusion reactors. Tungsten foils are considered as an option for fabricating tungsten composites, so their mechanical properties were evaluated before and after neutron irradiation in the TITAN irradiation campaign.

5 MAGNETIC AND DIAGNOSTIC SYSTEM MATERIALS
No contributions this reporting period.

6 FUSION CORROSION AND COMPATIBILITY SCIENCE
No contributions this reporting period.

7 MECHANISMS AND ANALYSIS

7.1 VIEWPOINT: NANOSCALE CHEMISTRY AND CRYSTALLOGRAPHY ARE BOTH THE OBSTACLE AND PATHWAY TO ADVANCED RADIATION-TOLERANT MATERIALS—Chad M. Parish, Kun Wang, Philip D. Edmondson (Oak Ridge National Laboratory) **148**

Abstract of an invited review paper, in press at Scripta Materialia.

7.2 EXPLORATION OF THE RADIATION RESISTANCE OF HIGH ENTROPY ALLOYS—C. Li, S.J. Zinkle (University of Tennessee), and X. Hu, J. Qiu (Oak Ridge National Laboratory) **149**

This report summarizes the experimental characterization of neutron and ion irradiated 27%Fe-27%Mn-28%Ni-18%Cr high entropy alloy (HEA). Samples have been neutron irradiated at ~70˚C from 0.1 dpa to 1 dpa. Post-irradiation isochronal annealing was conducted from 100 to 600˚C. Following each anneal, positron annihilation spectroscopy (PAS), micro-hardness and electrical resistivity were measured at room temperature. PAS indicated a major vacancy annealing process occurs at ~400˚C, and no sizable change of defects up to 600˚C. Micro-hardness measurement showed different trend in the annealing of hardness for 0.1 and 1dpa samples. A large change in electrical resistivity is observed after annealing, which may be related to the strong chemical disordering intrinsic to HEA.

TABLE OF CONTENTS

7.3 **EFFECTS OF IRRADIATION AND ANNEALING ON THE MICROSTRUCTURE AND MECHANICAL PROPERTIES OF BULK METALLIC GLASS ALLOYS**—L. Mora, Y. Zhang, H. Bei, J. Neuefeind, W. Dmowski, T. Egami, S. J. Zinkle (Oak Ridge National Laboratory) and J. Brechtl, M. L. Crespillo, T. Yang, H. Wang, J. Salasin, I. Gussev, M. Lang (University of Tennessee) **158**

Bulk metallic glasses (BMGs), which are advanced potentially irradiation-resistant materials, are composed of a topologically disordered structure which prohibits the creation of Frenkel pair defects. For this study, microstructural analysis and nano-indentation tests were performed on $Zr_{52.5}Cu_{17.9}Ni_{14.6}Al_{10}Ti_5$ (BAM-11) and $Cu_{60}Zr_{20}Hf_{10}Ti_{10}$ bulk metallic glass (BMG) alloys. Here samples were irradiated at 25-360°C with 5 MeV C^+ or 9 MeV Ni^{3+} ions (midrange doses of 0.5 and 10 dpa). The BAM-11 BMG was also irradiated with fission neutrons to 0.1 dpa at ~90°C. Neutron diffraction results indicate that the BAM-11 samples underwent disordering during neutron irradiation. At an indentation depth of ~450 nm, the alloys experienced an increase in the nano-indentation hardness of 16% and 24% respectively from the as-cast to the irradiated condition of 9 MeV Ni^{3+} 10 dpa 360°C. At the same depth, the Young's Modulus was found to increase 10% and 24% respectively for the BAM-11 and Cu BMGs under the same irradiation conditions.

7.4 **MICROSTRUCTURE-BASED VISCOPLASTICITY MODEL OF TUNGSTEN IN PLASMA TRANSIENTS**—David Rivera, Giacomo Po, Yue Haung, Nasr M. Ghoniem (University of California, Los Angeles) **179**

Materials developed with special surface architecture are shown here to be more resilient to the transient thermomechanical environments imposed by intermittent exposures to high heat flux thermal loading typical of long-pulse plasma transients. In Part 1 of this article, we present experimental results that show the relaxation of residual thermal stresses in micro-engineered W surfaces. A dislocation-based model is extended within the framework of large deformation crystal plasticity. The model is applied to the deformation of single crystals, polycrystals, and micro-engineered surfaces composed of a uniform density of micro-pillars. The model is utilized to design tapered surface micro-pillar architecture, composed of a Re core and W coatings. Residual stresses generated by cyclic thermomechanical loading of these architectures show that the surface can be in a compressive stress state, following a short shakedown plasma exposure, thus mitigating surface fracture.

7.5 **CONTROLLING STRAIN BURSTS AND AVALANCHES AT THE NANO-TO-MICRO SCALE**—Y.N. Cui, G. Po, N.M. Ghoniem (University of California, Los Angeles) **202**

We demonstrate, through 3-dimensional discrete dislocation dynamics simulations, that the complex dynamical response of nano and micro crystals to external constraints can be tuned. Under load rate control, strain bursts are shown to exhibit scale-free avalanche statistics, similar to critical phenomena in many physical systems. For the other extreme of displacement rate control, strain burst response transitions to quasi-periodic oscillations, similar to stick-slip earthquakes. External load mode control is shown to enable a qualitative transition in the complex collective dynamics of dislocations from self-organized criticality to quasi-periodic oscillations. It opens new possibilities for novel experiments with a faster response rate than currently obtainable, which can be designed to explore this regime.

TABLE OF CONTENTS

8 MODELING PROCESSES IN FUSION SYSTEM MATERIALS

8.1 **DEVELOPMENT OF INTERATOMIC POTENTIALS IN TUNGSTEN-RHENIUM SYSTEMS**—W. Setyawan and R. J. Kurtz (Pacific Northwest National Laboratory), and N. Gao (Institute of Modern Physics, Chinese Academy of Science, China) **206**

New reference data are generated using ab initio methods corresponding to interstitial configurations in bcc W and hcp Re. Initial fits of EAM potentials for pure W and Re systems are presented. Several parametrizations are explored. For W, the order of stability among bcc, fcc, and hcp can be reproduced. However, the potentials typically predict the <100> dumbbell to be the most stable interstitial configuration. For Re, the order of stability among hcp, fcc, and bcc is also reproduced. Notably, the Re potential labeled as Re_eam_1/set22 predicts the correct ground state for the interstitial configuration, namely configuration C, consistent with DFT, however its formation energy is 8.07 eV compared to DFT value of 6.52 eV.

8.2 **CONFIGURATIONAL MULTIPLICITY OF GRAIN BOUNDARY PHASES IN BCC METALS**—Timofey Frolov, R. E. Rudd (Lawrence Livermore National Laboratory), W. Setyawan, R. J. Kurtz (Pacific Northwest National Laboratory), J. Marian (University of California Los Angeles), A. R. Oganov (Stony Brook University), and Q. Zhu (University of Nevada Las Vegas) **213**

Extended abstract of a paper submitted to Physical Review Letters.

8.3 **EFFECT OF SIA TRAPPING AND DETRAPPING ON DEFECT ACCUMULATION IN TUNGSTEN DUE TO RADIATION CORRESPONDING TO 14-MeV-NEUTRON AND HFIR PKA SPECTRA**—Giridhar Nandipati, Wahyu Setyawan, Kenneth J. Roche, Richard J. Kurtz (Pacific Northwest National Laboratory), Brian D. Wirth (University of Tennessee) **214**

This is an Extended Abstract for a paper in preparation for journal submission.

8.4 **SIMULATING IRRADIATION HARDENING IN TUNGSTEN UNDER FAST NEUTRON IRRADIATION INCLUDING TRANSMUTATION RHENIUM PRODUCTION**—Chen-Hsi Huang, Jaime Marian (Department of Materials Science and Engineering, University of California Los Angeles), and Mark R. Gilbert (Culham Science Centre, Abingdon, UK) **215**

Simulations of neutron damage under fusion energy conditions must capture the effects of transmutation, both in terms of accurate chemical inventory calculations as well as the physics of the interactions between transmutation elements and irradiation defect clusters. In this work, we integrate neutronics, primary damage calculations, molecular dynamics results, rhenium transmutation calculations, and stochastic cluster dynamics simulations in order to study neutron damage in single-crystal tungsten to mimic divertor materials. We use established correlations to translate damage accumulation into hardening increases and compare our results to the experimental measurements. We find hardening increases in excess of 5000 MPa in all cases, which casts doubts about the integrity of W-based materials under long-term fusion exposure.

TABLE OF CONTENTS

8.5 MODELING DUCTILE-PHASE TOUGHENED TUNGSTEN FOR PLASMA-FACING MATERIALS: PROGRESS IN DAMAGE FINITE ELEMENT ANALYSIS OF TUNGSTEN-COPPER BEND TESTS—B. N. Nguyen, C. H. Henager, Jr., R. J. Kurtz (Pacific Northwest National Laboratory) **232**

A promising approach to increasing fracture toughness and decreasing the ductile-brittle transition temperature (DBTT) of a W-alloy is by ductile-phase toughening (DPT) [1-3]. In this method, a ductile phase is included in a brittle matrix to prevent fracture propagation by crack bridging or crack deflection. Liquid-phase sintered W-Ni-Fe alloys and hot-pressed and sintered W-Cu composites are two examples of such materials that PNNL and the University of California at Santa Barbara are investigating. However, there is a need for improved mechanical property models of such composite systems in order to begin to optimize these structural materials with regard to strength and fracture toughness. This report describes a dual-phase microstructural model that has recently been developed at PNNL. The model predictions have been validated against the experimental results for W-Cu bend bar tests.

9 FUSION SYSTEM DESIGN

No contributions this reporting period.

10 IRRADIATION METHODS, EXPERIMENTS AND SCHEDULES

10.1 MINIATURE MECHANICAL TEST DEVELOPMENT FOR TUNGSTEN-BASED MATERIALS—L. M. Garrison, Emily Proehl, Frank Chen (Oak Ridge National Laboratory) **239**

Because of activation concerns after irradiation, miniaturized, non-standard tungsten sample geometries are often used. Additionally, many tungsten based composites employ tungsten foils or tungsten fibers which also cannot use standard size mechanical test fixtures. A miniaturized, non-standard fracture toughness test is being developed for tungsten samples with dimensions 10×4×2 mm^3. This geometry of fracture toughness tungsten samples was included in the PHENIX RB*19J irradiation capsule. Initial tests on the unirradiated control samples from the RB*19J materials are underway in preparation for future tests with the irradiated tungsten samples.

10.2 HFIR IRRADIATION EXPERIMENTS—J.P. Robertson (Oak Ridge National Laboratory) **241**

HFIR completed 3.7 cycles during the first half of 2017. Cycle 470 began on January 3, 2017 and ended on January 28, 2017, accumulating 2160.04 MWD, Cycle 471 began on February 14, 2017 and ended on March 11, 2017 (2180.37 MWD), Cycle 472 began on May 3, 2017 and ended on May 27, 2017 (2074.94 MWD), and Cycle 473 began on June 13 and is expected to end on July 8.

1. FERRITIC/MARTENSITIC STEEL DEVELOPMENT

1.1 DEVELOPMENT OF CASTABLE NANOSTRUCTURED ALLOYS AS ADVANCED RAFM STEELS

L. Tan, C.M. Parish (Oak Ridge National Laboratory)

OBJECTIVE

Castable nanostructured alloys (CNAs) are being developed at Oak Ridge National Laboratory to favor the formation of a larger amount of ultrafine stable precipitates in reduced-activation ferritic-martensitic steels using conventional, affordable steelmaking methods. The high density of fine precipitates is expected to improve high temperature strength and radiation resistance of the alloys. This work is to examine the microstructure of a CNA heat #2905 after a special thermomechanical treatment (TMT).

SUMMARY

A new CNA heat #2905 was used to explore TMT effects on microstructure evolution. Following a warm-rolling (WR) TMT, samples were prepared for microstructural characterization. The #2905-WR was characterized to produce a dual-phase structure, consisting of tempered martensite and a network of fine ferrite grains. Unlike tempered martensite having a high density of lath boundaries and dislocations, the ferrite grains are “free” of dislocation. However, some nano-sized Cr-rich carbides, together with many unresolved ultrafine particles, were revealed in the ferrite grains. Further studies will attempt to identify the rod-shaped carbon-rich particles and Laves-structured particles.

PROGRESS AND STATUS

Introduction

Tempered martensite microstructures suffer noticeable recovery of dislocations and lath structures during deformation at high temperatures, above ~600°C. To retain long-term high-temperature strength and microstructural stability, a dual-phase structure of mixed ferrite and tempered martensite may be a route. The stable ferrite grains strengthened by precipitates are expected to balance or compensate for the recovery of tempered martensite.

Experimental Procedure

CNA heat #2905 was used in this study. A TMT of warm rolling the re-normalized material at 700°C was followed by a conventional tempering heat treatment to achieve some tempered martensite and relieve some internal stress. Scanning electron microscopy (SEM), together with electron backscatter diffraction (EBSD), conventional/scanning transmission electron microscopy (CTEM or STEM) and energy dispersive x-ray spectroscopy (EDS), was used to characterize the material. Conventional metallography sample preparation was used for SEM and EBSD characterization, and focused-ion beam was used to prepare electron transparent lamellae for TEM characterization.

Results

Figure 1a shows a backscattered electron image (BEIs) of heat #2905-WR, illustrating a dual-phase structure of tempered martensite and a network of ferrite grains. The image quality (IQ) and kernel average misorientation (KAM) images of EBSD in Fig. 1b and c, respectively, from a small area in Fig. 1a reveal dense lath structures with high strain in the tempered martensite, but low strain in the fine-grained ferrite. Similar to the EBSD-KAM image, STEM characterization in high angular annular dark field (HAADF) mode in Fig. 2a shows a high density of dislocations in the tempered martensite but “free” dislocations in the ferrite grains. The bright-field (BF) STEM image in Fig. 2b and EDS maps of Cr and C in Fig. 2c and d indicate that ferrite grains contain Cr-rich carbides at nanometer scale, together with many ultrafine particles that were not able to be resolved in the EDS scan. It should be noted here that the EDS used the high efficient Super-X four SDD-EDS system on the FEI Talos F200X S/TEM, which provides superfast high quantitative characterization compared to conventional EDS system.

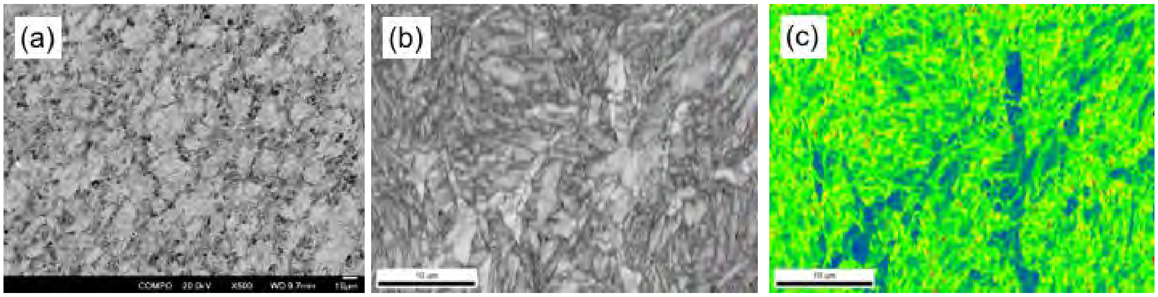

Figure 1. (a) BEI, (b) EBSD-IQ, and (c) EBSD-KAM (blue-to-red indicating minimum-to-maximum) of CNA heat #2905-WR.

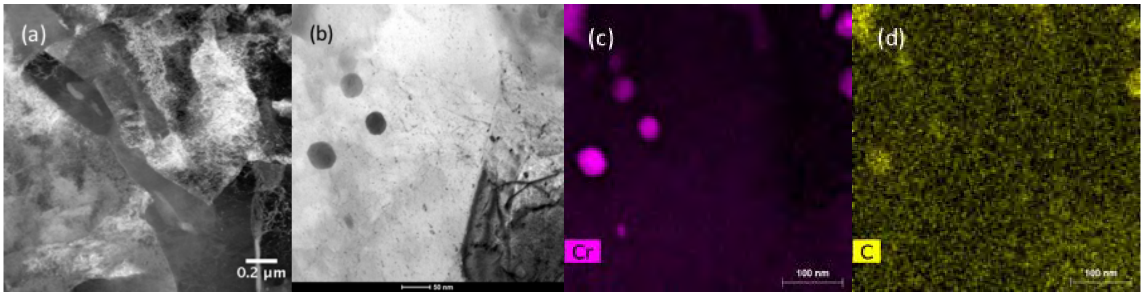

Figure 2. (a) HAADF of CNA heat #2095-WR and (b) STEM-BF and corresponding EDS maps of (c) Cr and (d) C at a ferrite grain.

In addition to the unresolved ultrafine particles, some rod-shaped particles were observed with only carbon-enrichment as shown in Fig. 3a (annular dark field – ADF) and 3b. Selected area electron diffraction is required to identify their microstructure as graphite (hexagonal), carbon (amorphous), or other structures. Additionally, dark-field image by CTEM revealed some Laves phase particles as shown in Fig. 3c, which had an orientation relationship with the matrix as $[-171]_{\text{Laves}}//[-1-31]_{\text{matrix}}$. However, the Laves phase was not yet characterized by STEM-EDS. It is important to determine the consumed elements (W, Ta, or Ti) by the Laves phase, which help understand the predictable amount of Ta/Ti-rich MX precipitates in the CNAs.

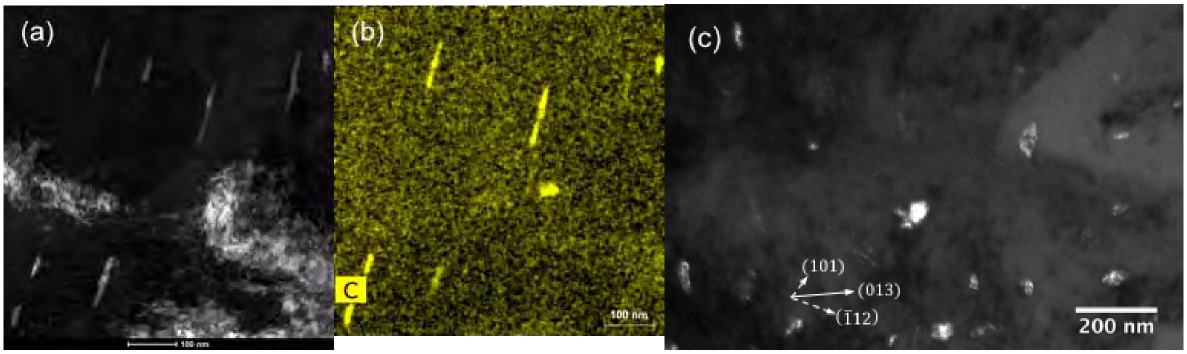

Figure 3. (a) STEM-ADF and (b) corresponding EDS carbon map of some unknown particles, together with (c) CTEM-DF of Laves phase in CNA heat #2905-WR.

1.2 IRRADIATION HARDENING BEHAVIOR OF F82H IN JP28 AND 29

H. Sakasegawa, M. Ando, H. Tanigawa, T. Hirose (National Institutes for Quantum and Radiological Science and Technology, Japan), and X. Chen, J.W. Geringer, Y. Katoh (Oak Ridge National Laboratory)

OBJECTIVE

The analysis on the thermometry of JP28 demonstrated a possibility of irradiation temperatures lower than designed for the specimen holders at 673 and 773 K. In this work, we investigated this possible lower temperature irradiation, studying the irradiation hardening behavior of F82H IEA and mod3 heats. This work is part of the U.S. Department of Energy – National Institutes for Quantum and Radiological Science and Technology fusion materials collaboration.

SUMMARY

The result of thermometry analysis was supported by the irradiation hardening behavior observed in this work, because F82H mod3 heat showed comparable hardness at the designed temperatures of 673 and 773 K. From the summary of dose dependence of irradiation hardening including the result of JP26 and 27, significant increase in hardness was not observed in the result of JP28 at 673 K. Since any decrease in irradiation temperature generally promotes irradiation hardening, it can be assumed that the decrease in actual irradiation temperature in the 673 K specimen holder did not largely affect the irradiation behavior of F82H. However, further investigations are indispensable in future work.

PROGRESS AND STATUS

Introduction

The reduced activation ferritic/martensitic steel, F82H, will be used as the structural material of ITER test blanket and DEMO blanket modules. It is important to study the high dose neutron irradiation effect on mechanical and physical properties as well as microstructures for the fabrication of blanket module. In the companion report by T. Hirose, et al., high temperature tensile tests were conducted on F82H in a pair of HFIR irradiation capsules JP28 and 29 up to the maximum dose of 87 dpa, which has not previously been attained. New findings were reported, but there remained an issue about the actual irradiation temperature [1]. The result of thermometry analysis indicated that the irradiation at the designed temperatures of 673 and 773 K were possibly conducted at lower temperatures, though no significant difference was observed between the designed and analyzed temperatures for the irradiation of JP29 at 573 K. It is necessary to study and confirm the irradiation temperatures of JP28. In this work, we investigated the possible lower irradiation temperatures by studying irradiation hardening behavior.

Experimental Procedure

The materials studied were F82H IEA heat and mod3 heat with a higher tantalum content [1, 2]. F82H with nickel isotopes were also irradiated in JP 28 and 29 to investigate the effect of transmutation helium, but we studied IEA and mod3 only to focus on the fundamental irradiation hardening behavior for the investigation of possible lower irradiation temperature. F82H IEA and mod3 heats were irradiated in HFIR for a period longer than eight years (~ 70 kh) up to 87 dpa maximum at the designed temperatures of 573, 673 and 773 K. Table 1 shows the irradiation conditions, together with conditions for capsules JP26 and 27. In JP26 and 27, the common specimen holders were employed and dose dependence of irradiation hardening can be obtained from the comparison between JP26, 27, 28 and 29. As reported in the previous work [2], designed temperatures have been successfully achieved in JP26 and 27 through the validation of irradiation temperature using silicon carbide passive thermometry. However, the thermometry analysis result for JP28 demonstrated the possibility of irradiation temperatures lower than designed for 673 and 773 K, as shown in Table 2 [1]. Post-irradiation hardness tests were carried out on SS-J3 tensile specimens from JP26, 27, 28 and 29, and PCCVN fracture toughness specimens from JP 26 and 27 in the Irradiated Materials Examination and Testing (IMET) hot cell facility to measure irradiation hardening.

Results

Figure 1 shows the Vickers hardness test result for F82H IEA and mod3 heats irradiated in JP28 and 29. In the figure, the shown temperatures are the design temperatures. For the IEA heat, hardness decreased with increasing irradiation temperature, but mod3 heat showed no significant difference in hardness at 673 and 773 K. This unexpected irradiation hardening behavior of mod3 supports the possible lower irradiation temperatures for the 673 and 773 K specimen holders, which was indicated by the thermometry analysis.

Figure 2 shows the dose dependence of Vickers hardness summarized from the results of JP26, 27, 28 and 29. In this figure, the shown temperatures are also the design temperatures. As for the result of 573 K in Figure 2 (a), hardness increased with increasing dose, though post-irradiation tensile and hardness test results in the past report indicated that irradiation hardening was saturated by 9 dpa [3]. The reason that saturation of irradiation hardening was observed in this past work could be caused by the limited test results. Except for the saturation behavior, the irradiation hardening behavior shown in this figure was comparable to that given in the past report and no significant difference in irradiation hardening behavior was observed between IEA and mod3 heats.

For the result at 673 K in Figure 2 (b), no significant change was found from ~22 dpa (JP27) to ~86 dpa (JP28). The thermometry analysis indicated that the actual irradiation temperature was lower than the designed temperature by about 80 K, as given in Table 2. In general, a decrease in irradiation temperature tends to enhance irradiation hardening and to increase hardness. No significant change in hardness means that the decrease in actual irradiation temperature did not largely affect the irradiation behavior of F82H in the 673 K specimen holder. Attention needs to be paid to the possibility of softening during irradiation, since such softening can compensate for the hardening due to a temperature decrease. However, in the case of aged IEA heat, no significant softening was reported for up to 100 kh at temperatures lower than 823 K [4] and FFTF irradiation at 673 K for better controlled temperature operation showed irradiation hardening rather than softening from 40 to 60 dpa, as shown in the companion report by T. Hirose, et al. Consequently, softening during irradiation can hardly be expected, but further works should be done such as microstructural observation for confirmation.

As for the result of 773 K irradiation in Figure 2 (c), although the obtained data were limited compared to the other irradiation temperature results, the hardness showed no significant change up to ~8.6 dpa (JP26) but increased after ~86 dpa irradiation (JP28). As given in Table 2, the thermometry analysis indicated that the actual irradiation temperature was lower than the designed temperature by about 155 K. The result of mod3 heat given in Figure 1 supports that irradiation hardening was possibly promoted due to the decrease in irradiation temperature, because the hardness at 773 K was comparable to that at 673 K.

In future work, microstructural observations of irradiated F82H will be performed and dimensional changes in specimen holders will be additionally investigated. This is because one of the possible reasons is considered to be the creep deformation of specimen holder during irradiation which gives simultaneous improved cooling condition and decrease irradiation temperature. It will also be helpful to perform thermometry analyses for other specimen holders which have not yet been performed.

Table 1. Irradiation conditions for HFIR target capsules

Capsules	Dose (dpa)	Designed temperature (K)
JP26	~8.6	573/673/773
JP27	~22	573/673
JP28 & 29	~87	573/673/773

Table 2. Dilatometry analysis result of HFIR capsule passive temperature monitors [1]

Designed temperature (K)	Specimen ID	Analyzed median temperature (K)	Difference (K)
573	JP29TM0704	591.6	18.6
	JP29TM0708	557.3	-15.7
673	JP28TM0702	593.5	-79.5
	JP28TM0704	587.7	-85.3
773	JP28TM0902	620.2	-152.8
	JP28TM0904	612.3	-160.7

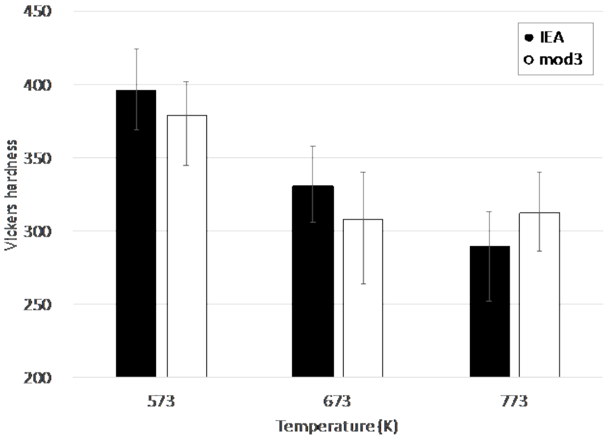

Figure 1. Vickers hardness test result for F82H irradiated in JP28 and 29.

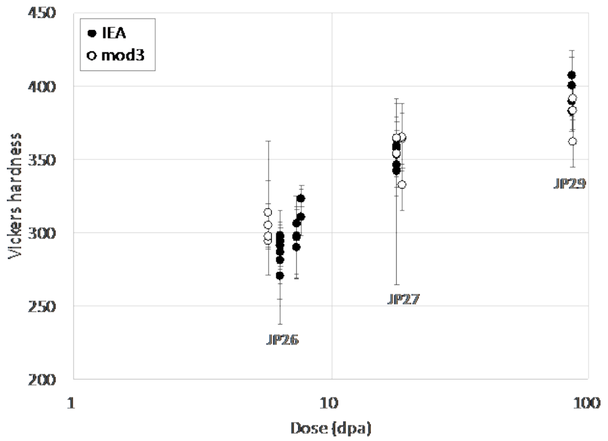

(a) 573 K

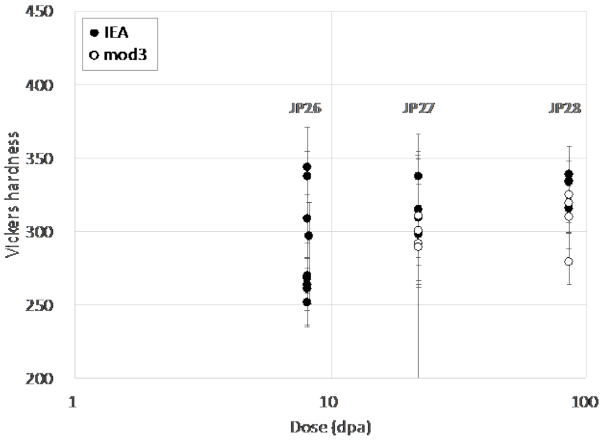

(b) 673 K

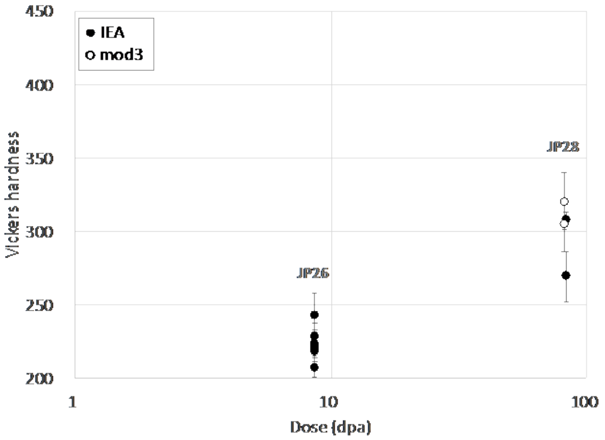

(c) 773 K

Figure 2. Dose dependence of Vickers hardness for F82H irradiated in JP28 and 29.

Acknowledgements

This research was sponsored by the National Institutes for Quantum and Radiological Science and Technology (Japan Atomic Energy Research Institute) and the Office of Fusion Energy Sciences, U.S. Department of Energy, under contracts NFE-10-02779 and DE-AC05-00OR22725, respectively, with UT-Battelle, LLC.

References

[1] H. Sakasegawa, H. Tanigawa, T. Hirose, M. Ando, Y. Katoh, C.O. Stevens, M.R. McAlister, “TENSILE FRACTURE MECHANISM OF HFIR-HEAVILY-IRRADIATED F82Hs”, DOE/ER-0313 Semi-Annual Progress Reports, 59 (2015) 22-25.

[2] T. Hirose, N. Okubo, H. Tanigawa, Y. Katoh, A.M. Clark, J.L. McDuffee, D.W. Heatherly, R.E. Stoller, “IRRADIATION TEMPERATURE DETERMINATION OF HFIR TARGET CAPSULES USING DILATOMETRIC ANALYSIS OF SILICON CARBIDE MONITORS”, DOE/ER-0313 Semi-Annual Progress Reports, 49 (2010) 94-99.

[3] T. Hirose, N. Okubo, H. Tanigawa, M. Ando, M.A. Sokolov, R.E. Stoller, G.R. Odette, “IRRADIATION HARDENING IN F82H IRRADIATED AT 573 K IN THE HFIR”, Journal of Nuclear Materials, 417 (2011) 108-111.

[4] Takuya Nagasaka, Yoshimitsu Hishinuma, Takeo Muroga, Yanfen Li, Hideo Watanabe, Hiroyasu Tanigawa, Hideo Sakasegawa, Masami Ando, “EXTRACTION RESIDUE ANALYSIS ON F82H-BA07 HEAT AND OTHER REDUCED ACTIVATION FERRITIC/MARTENSITIC STEELS”, Fusion Engineering and Design, 86 (2011) 2581-2584.

1.3 EFFECTS OF HIGH DOSE NEUTRON IRRADIATION ON REDUCED-ACTIVATION FERRITIC/MARTENSITIC STEEL F82H

—T. Hirose, H. Tanigawa, H. Sakasegawa, M. Ando (National Institutes for Quantum and Radiological Science and Technology, Japan), Y. Katoh, K.G. Field, B.K. Kim, D.T. Hoelzer, L. Tan, R.E. Stoller (Oak Ridge National Laboratory), and L.L. Snead (Stony Brook University)

OBJECTIVE

Reduced activation ferritic martensitic steel F82H was irradiated up to 87 dpa in the High Flux Isotope Reactor (HFIR) at Oak Ridge National Laboratory. Tensile tests of the irradiated miniature dog bone specimen, SS-J3, were conducted at nominal irradiation temperatures of, 573, 673 and 773 K to study the effects of high dose neutron irradiation on tensile properties and dose-dependent evolution. This work is part of the U.S. Department of Energy – National Institutes for Quantum and Radiological Science and Technology fusion materials collaboration.

SUMMARY

Post irradiation tensile tests were conducted on F82H irradiated up to 87 dpa at 573, 673 and 773 K in the HFIR, and the following was found;

- Irradiation hardening and loss of ductility were observed even at 673 and 773 K.
- Specimens irradiated in the FFTF demonstrated softening at these temperatures.
- Differences between FFTF and HFIR should be investigated including transmutation effects.
- Lower irradiation temperatures resulting from deformation of capsule material is possible.
- Hardening was significant in the specimen irradiated at 573 K. The increment gradually decreased with irradiation dose, but the strength was obviously larger than in previous work.
- Ductility after irradiation exhibited a minimum at 673 K, and did not saturate up to 87dpa.
- F82H + Ni-58, which produced 920 atomic ppm of helium, demonstrated significant hardening at 573 K. However, the hardening increment diminished at 673 and 773 K.

PROGRESS AND STATUS

Introduction

Reduced activation ferritic/martensitic (RAFM) steels are assumed as structural material in the majority of the ongoing blanket design activities including ITER Test Blanket Modules (TBM), DEMO, and advanced power reactor concepts. Determining the effects of high dose neutron irradiation on mechanical and physical properties and microstructures is essential for the RAFM steels, not only to qualify their use in fusion blankets beyond ITER but also to help shape future efforts in developing materials with improved radiation tolerance. For fusion applications, not only irradiation hardening but also transmutation effects on hardening and embrittlement behavior is quite important to forecast service limits of the structural materials. Isotope tailoring and injection of gaseous atom using ion accelerator or fission reactors have been employed to evaluate transmutation gas effects [1, 2, 3]. It is necessary to evaluate effects of neutron irradiation itself for clear understanding of the transmutation effects. Neutron irradiation effects on RAFM steels have been investigated for more than 20 years in the Japan-US collaboration. In phase V of this program, six non instrumented HFIR capsules with the common specimen holder design have been prepared to investigate the dose dependence of the irradiation response of RAFM steels [4, 5, 6, 7]. As a part of this experiment, a pair of irradiation capsules JP-28 and -29, containing specimens of various RAFMs, were irradiated in HFIR, achieving a maximum dose of 87 dpa. In this work, the dose-dependent evolution of the tensile properties of RAFMs are discussed based on initial results from the post-irradiation tensile tests.

Experimental

The materials examined in this work are reduced activation ferritic/martensitic steel, F82H (0.1C -8Cr-2W-0.2V-0.04Ta) and F82H with additional tantalum for toughness improvement, F82H-mod3 (0.1C-8Cr-2W-0.2V-0.09Ta) [8, 9]. In order to investigate effects of transmutation helium, F82H with nickel isotopes (0.07C-8Cr-2W-0.3V-0.02Ta-1.4Ni) was also used [10]. Since the irradiation response of RAFM is strongly affected by the additional nickel itself, two types of nickel isotopes were employed

[11]. The steel with Ni-58 produces transmutation helium with approximately 10 atomic ppm / dpa transmutation rate. On the contrary, the steel with Ni-60 does not produce transmutation helium and these two steels were compared to clarify the effects of helium.

Six full-length flux trap capsules containing specimens of RAFM steels including F82H-IEA and F82H-mod3 were irradiated in HFIR at ORNL over a period of more than 8 years, achieving a maximum dose of 87 dpa. Irradiation conditions for these capsules are summarized in Table 1. These capsules employed the common specimen holders with previous capsules JP-26 (8.6 dpa) and JP-27 (22 dpa), and the irradiation temperature was validated using silicon carbide passive thermometry. As reported in the previous work, designed temperatures have been successfully achieved in JP-26 and JP-27 experiments [12]. Preliminary analysis on the thermometry from JP-28 and JP-29 demonstrated the possibility of lower temperature irradiation than design temperature, especially for specimen holders for 673 and 773 K [13]. However, distribution of surface oxides on the specimen from these holders exhibited similar features to the previous experiments [14]. The irradiation temperatures for these holders are to be investigated using microstructural analysis, and design validity of the holder design for high dose irradiation is to be confirmed with the following similar JP-30 and JP-31 experiments [15].

Post-irradiation tensile tests were carried out on the SS-J3 sheet tensile specimens, which has gauge section of 5 x 0.76 x 1.2 mm, at irradiation temperature in vacuum with a strain rate of 1.6×10^{-3} s^{-1}. All tests were conducted in the Irradiated Materials Examination and Testing (IMET) hot cell facility at ORNL.

Results

Tensile properties of F82H irradiated up to 87 dpa

The results of post irradiation tensile tests are summarized in Table 2, and engineering stress-strain curves are presented in Figure 1. All specimen demonstrated hardening and loss of elongation. Hardening was significant at lower temperatures. Tensile properties of F82H-mod3 is comparable with F82H-IEA. Although Ni-doped steels demonstrated the highest strength, it drastically decreased with irradiation and test temperatures. It is noted that the all specimen demonstrated hardening even above 673 K where no significant hardening was observed in the previous work [16]. The minimum elongation was found at 673 K, where unirradiated F82H shows the minimum elongation. Most specimens demonstrated poor elongation of less than 10 % at this temperature except for F82H-1.4%Ni-60. As for helium effects, 920 appm of transmutation helium was produced in F82H-1.4%Ni-58 and it demonstrated greater hardening and less ductility than F82H-1.4%Ni-60. It is noted that the difference steeply decreased with irradiation and test temperature. It cannot be denied the post-irradiation mechanical properties in this work was affected by the unexpected irradiation temperatures. However, the previous work up to 22 dpa achieved the designed irradiation temperature [12]. The cause of the unexpected irradiation temperature is considered to be dimensional changes in specimen holders due to high dpa irradiation and simultaneous improved cooling conditions. Therefore, it is considered that the irradiation temperature gradually decreased above 22 dpa irradiation. The companion paper by H. Sakasegawa, et al. discusses the unexpected irradiation temperature basing on the latest hardness test results.

Dose dependence of tensile properties

The dose dependence of hardening in 0.2% proof stress and total elongation are presented in Figure 2 and Figure 3, respectively. These figures include previous results for material irradiated in the Fast Breeder Reactors (FBRs) such as Fast Flux Test Facility (FFTF) and BOR-60 [16, 17]. Irradiation hardening at 573 K asymptotically increases to 500 MPa, and seems consistent with the previous work using FBRs. On the contrary, the hardening gradually increased with dose in the HFIR at temperature above 663 K where softening was observed in FBRs experiments. It is noted that F82H irradiated in the FFTF demonstrated a tendency of hardening from 40 to 60 dpa. Therefore, hardening at higher temperatures might have an incubation dose for hardening.

As shown in Figure 3, the dose dependence of ductility seems to be strongly affected by specimen geometry. Specimen with lower aspect ratio demonstrated of tendency of saturation of total elongation around 7% [12]. On the contrary, modified specimens with larger aspect ratio, SS-J3 successfully evaluated gradual decrease of total elongation. It is noted that no obvious tendency of saturation in loss of ductility was observed in this work.

Table 3 summarizes irradiation conditions of HFIR and FFTF experiments [18, 19]. As shown in this table, the difference in damage rate normalized to megawatt days (MWD) is within a factor of 2. Moreover, the irradiation periods are too short to demonstrate mechanical property change due to thermal aging [20]. Therefore, these facts imply hardening behavior is affected by the difference in the irradiation conditions.

It is reported that HFIR introduces 30 times greater transmutation of tungsten than FFTF [21]. It is due to the three orders of difference between neutron flux around 20 eV neutron energy where tungsten has a giant resonance [22]. Although it is reported that osmium and rhenium have no significant effects in martensitic steel, precipitates such as laves phase including these elements has a strong impact on the mechanical properties [23]. Although the hardening at 673 and 773 K would avoid a decrease of the design allowable stress at this temperature range, the ductility loss and embrittlement should be monitored since these properties might limit the use of these steels.

As for transmutation helium effects, Ni-58 doped steel demonstrated enhanced hardening and ductility loss compared with Ni-60 doped steel. However, hardening and ductility loss seem to be suppressed compared with F82H. Since Ni doped steels demonstrated lower Ac1, recovery might take place at temperature above 673 K. Microstructural analyses is required to characterize this behavior.

Table 1. Irradiation conditions for the HFIR target capsules

Capsules	Dose (dpa)	Helium in F82H-1.4%Ni58 (appm)	Irradiation temperature (K)
JP-26	~8.6	Not available	573/673/773
JP-27	~22	240	573/673
JP-28 & 29	~87	920	573/673/773
JP-30 & 31	50	Not available	573/673/893

Table 2. Results of tensile tests of F82H irradiated in HFIR over 80 dpa

Material	Dose	Irr. Temp., T_{irr}	Test Temp., T_{test}	0.2% Proof stress, $\sigma_{0.2}$	Ultimate tensile strength, σ_u	Uniform elongation, ε_u	Total elongation, ε_t
	(dpa)	(K)	(K)	(MPa)	(MPa)	(%)	(%)
F82H-IEA	87	573	576	961	964	0.29	8.5
	85	673	675	714	715	0.22	7.5
	83	773	773	510	510	0.20	11.0
F82H-mod3	87	573	575	883	892	0.03	8.8
	85	673	670	790	791	0.14	8.9
	83	773	772	472	473	0.41	14.3
F82H-1.4%Ni58	87	573	576	1024	1024	0.19	7.6
	85	673	676	659	659	0.17	8.7
	83	773	775	466	471	0.41	7.1
F82H-1.4%Ni60	87	573	574	836	837	0.18	11.1
	85	673	672	584	598	0.55	11.6
	83	773	774	413	417	0.44	12.9

Table 3. Irradiation parameters for HFIR and FFTF irradiation [18, 19]

Irradiation vehicles	Dose (dpa)	dpa/MWD	Irradiation period (h)
FFTF/MOTA 2B	20	4E-04	5E+03
HFIR JP-27	22	9E-04	8E+03
FFTF/MOTA 2A	39	5E-04	8E+03
HFIR JP-14	34	9E-04	2E+04
FFTF/MOTA 2A+2B	59	4E-04	1E+04
HFIR JP-28 & 29	87	1E-03	2E+04

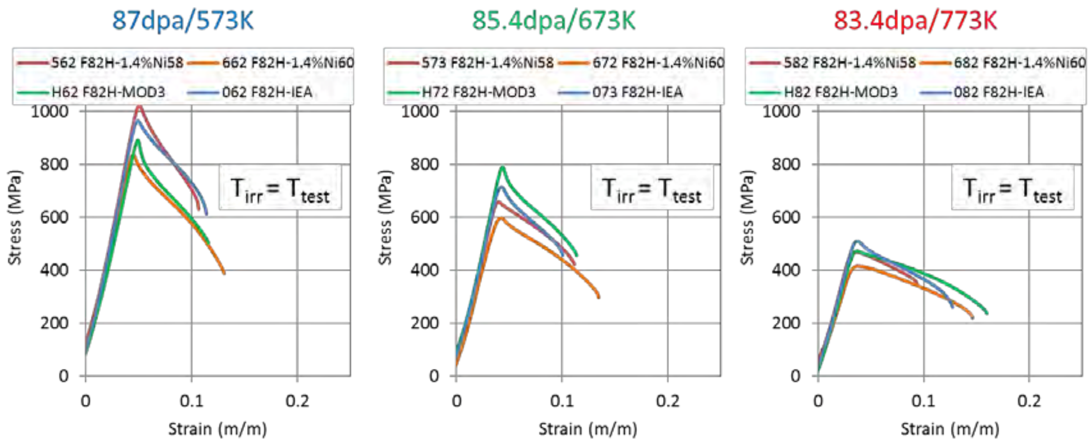

Figure 1. Stress strain curves of F82H irradiated in HFIR over 80 dpa and tested at the irradiation temperature.

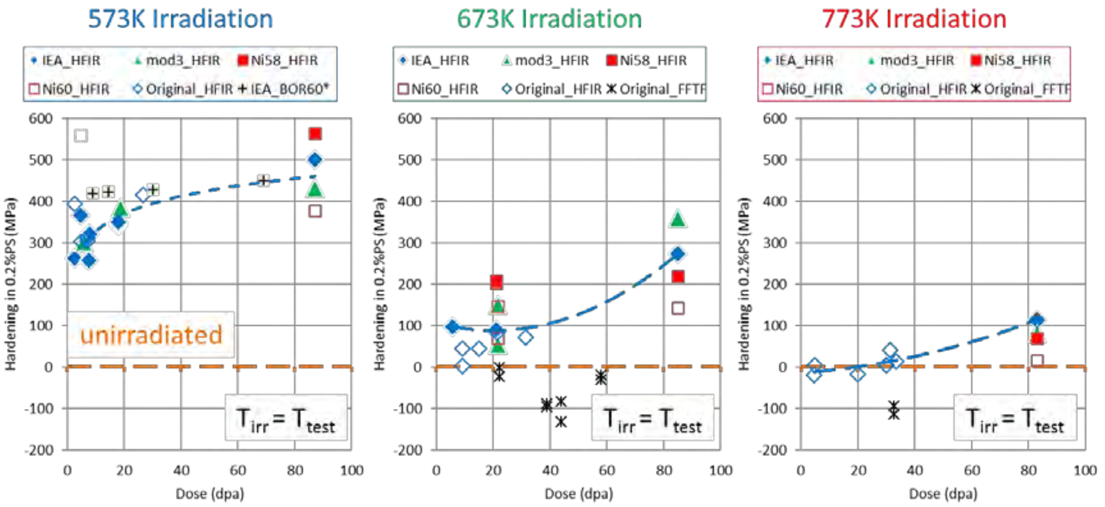

Figure 2. Dose dependence of irradiation hardening in F82H.

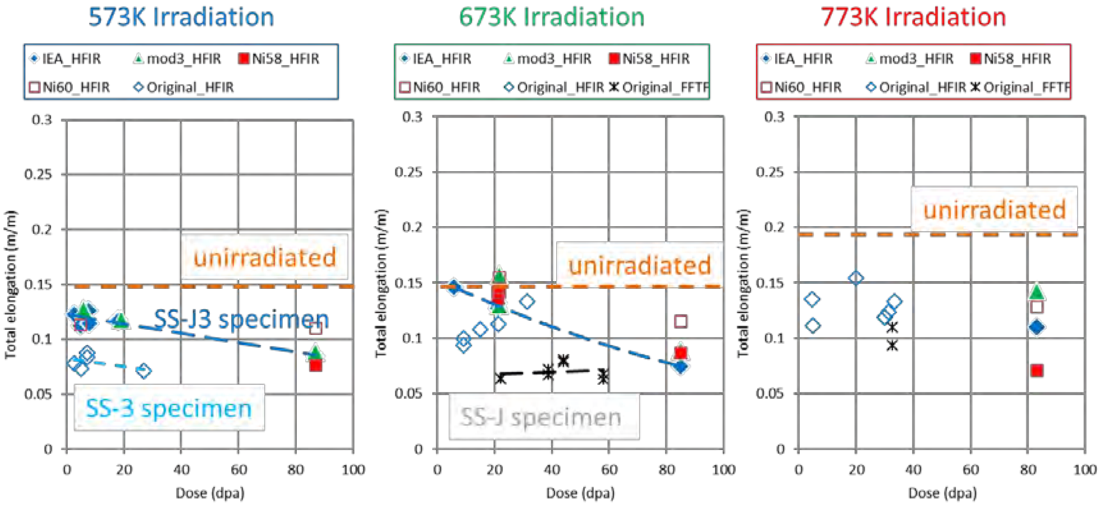

Figure 3. Dose dependence of irradiation induced ductility loss in F82H.

Acknowledgements

This research was sponsored by the National Institutes for Quantum and Radiological Science and Technology (Japan Atomic Energy Research Institute) and the Office of Fusion Energy Sciences, U.S. Department of Energy, under contracts NFE-10-02779 and DE-AC05-00OR22725, respectively, with UT-Battelle, LLC.

References

[1] D.S. Gelles, M.L. Hamilton, B.M. Oliver, L.R. Greenwood, S. Ohnuki, K. Shiba, Y. Kohno, A. Kohyama, J.P. Robertson, “Recent results for the ferritics isotopic tailoring (FIST) experiment,” Journal of Nuclear Materials, 307–311, (2002) 212-216.

[2] M Ando, E Wakai, T Sawai, H Tanigawa, K Furuya, S Jitsukawa, H Takeuchi, K Oka, S Ohnuki, A Kohyama, “Synergistic effect of displacement damage and helium atoms on radiation hardening in F82H at TIARA facility,” Journal of Nuclear Materials, 329–333 (2004) 1137-1141.

[3] T. Yamamoto, G.R. Odette, P. Miao, D.T. Hoelzer, J. Bentley, N. Hashimoto, H. Tanigawa, R.J. Kurtz, “The transport and fate of helium in nanostructured ferritic alloys at fusion relevant He/dpa ratios and dpa rates,” Journal of Nuclear Materials, 367–370 (2007) 399-410.

[4] K. R. Thoms, D. W. Heatherly, S. H. Kim, R. G. Sitterson, R. E. Stoller, and H. Tanigawa, “Assembly of the US-Japan JP-26 experiment and start of irradiation in the HFIR,” Fusion Materials Semiannual Progress Report, DOE/ER-0313/35 (2003) 250-263.

[5] D.K. Felde, K.R. Thoms, D.W. Heatherly, S.H. Kim, R.G. Sitterson, R.E. Stoller, H. Tanigawa, “Assembly of the US–Japan JP-27 experiment and start of irradiation in the HFIR,” Fusion Materials Semiannual Progress Report, DOE/ER-0313/36 (2004) 124.

[6] D. K. Felde, D. W. Heatherly, S. H. Kim, R. G. Sitterson, R. E. Stoller, and C. Wang, M. Ando and H. Tanigawa, “Assembly of the US-Japan JP-28 and JP-29 experiments and start of irradiation in the HFIR,” DOE/ER-0313, Semi-Annual Progress Reports, 38 (2005) 164-182.

[7] T. Nozawa, T. Hirose, H. Tanigawa, M. Ando, J.L. McDuffee, D.W. Heatherly, R.G. Sitterson, M.A. Sokolov, L. Tan, D.T. Hoelzer, R.E. Stoller, L.L. Snead and T. Yamamoto, “Assembly of the US-Japan JP-30 and JP-31 HFIR Target Irradiation Experiments,” DOE/ER-0313/51, Semi-Annual Progress Reports (2011) 131-144.

[8] K. Shiba, A. Hishinuma, A. Tohyama, K. Masamura, JAERI-Tech 97-038, 1997.

[9] K. Shiba, H. Tanigawa, T. Hirose, T. Nakata, “Development of the Toughness Improved Reduced Activation F82H Steel for DEMO Reactor,” Fusion Science and Technology, 62 (2012) 145-149.

[10]T. Sawai, M. Ando, E. Wakai, K. Shiba, S. Jitsukawa, “Ni-Doped F82H to investigate He effects in HFIR irradiation” Fusion Science and Technology, 44, 1 (2003) 201-205.

[11]R. Kasada, A. Kimura, H. Matsui, M. Narui, “Enhancement of irradiation hardening by nickel addition in the reduced-activation 9Cr–2W martensitic steel” Journal of nuclear materials, 258 (1998) 1199-1203.

[12]T. Hirose, N. Okubo, H. Tanigawa, Y. Katoh, A.M. Clark, J.L. McDuffee, D.W. Heatherly, R.E. Stoller, “Irradiation Temperature Determination of HFIR Target Capsules Using Dilatometric Analysis of Silicon Carbide Monitors,” DOE/ER-0313/49 Semi-Annual Progress Reports (2010) 94-99.

[13]H. Sakasegawa, H. Tanigawa, T. Hirose, M. Ando, Y. Katoh, C.O. Stevens, M.R. McAlister, “TENSILE FRACTURE MECHANISM OF HFIR-HEAVILY-IRRADIATED F82Hs,” DOE/ER-0313 Semi-Annual Progress Reports, 59 (2015) 22-25.

[14]M. Ando, D. Hamaguchi and H. Tanigawa, R. G. Bowman, G. C. Morris, J. P. Robertson and Y. Katoh, “Disassembly of HFIR JP28&29 Tensile Holders and Vickers Hardness Results on F82H Irradiated at 573 K,” DOE/ER-0313 “Semi-Annual Progress Reports,” 56 (2014) 15-18.

[15]T. Nozawa, T. Hirose, H. Tanigawa, M. Ando, J.L. McDuffee, D.W. Heatherly, R.G. Sitterson, M.A. Sokolov, L. Tan, D.T. Hoelzer, R.E. Stoller, L.L. Snead and T. Yamamoto, “Assembly of the US-Japan JP-30 and JP-31 HFIR Target Irradiation Experiments,” DOE/ER-0313 “Semi-Annual Progress Reports,” 51 (2011) 131-144.

[16]Y. Kohno, A. Kohyama, T. Hirose, M.L. Hamilton, M. Narui, “Mechanical property changes of low activation ferritic/martensitic steels after neutron irradiation,” Journal of Nuclear Materials 271&272 (1999) 145-150.

[17]E. Gaganidze, J. Aktaa, “Assessment of neutron irradiation effects on RAFM steels” Fusion Engineering and Design, 88 (2013) 118-128.

[18]A. M. Ermi, L. R. Greenwood and H. L. Heinisch, “1.4 Irradiation Parameters for the FFTF Materials Open Test Assemblies from 1983 through 1992,” DOE/ER-0313/18 Semi-Annual Progress Reports (1995) 27-62.

[19]J.P. Robertson, K.E. Lenox, I. Ioka, and E. Wakai, “Status of DOE/JAERI Collaborative Program Phase II and Phase III Capsules,” DOE/ER-0313/21 Semiannual Progress Reports (1996) 249-252.

[20] K. Shiba, H. Tanigawa, T. Hirose, H. Sakasegawa, S. Jitsukawa, “Long-term properties of reduced activation ferritic/martensitic steels for fusion reactor blanket system,” Fusion Engineering and Design, 86 (2011) 2895-2899.

[21]L.R. Greenwood and F.A. Garner, “Transmutation of Mo, Re, W, Hf and V in various irradiation facilities and STARFIRE,” Journal of Nuclear Materials, 212-215 (1994) 635-639.

[22]R.E. Stoller and L.R. Greenwood, “Subcascade formation in displacement cascade simulations: Implications for fusion reactor materials,” Journal of Nuclear Materials, 271-272 (1999) 57-62.

[23]R.L. Klueh, D.J. Alexander, M.A. Sokolov, “Effect of rhenium and osmium on mechanical properties of a 9Cr–2W–0.25V–0.07Ta–0.1C steel,” Journal of Nuclear Materials 279 (2000) 91-99.

1.4 FATIGUE PRECRACKING M4CVN TYPE STEEL SPECIMENS FOR THE EUROfusion PROJECT—X. Chen, R.L. Swain, E.T. Manneschmidt, K.D. Linton (Oak Ridge National Laboratory)

OBJECTIVE

The aim of this task is to perform fatigue pre-cracking of multi-notch bend type specimens (referred to as M4CVN specimens) for the EUROfusion project. Fatigue pre-cracking results in a sharp initial crack in the specimen, necessary for fracture toughness testing.

SUMMARY

We performed fatigue pre-cracking of M4CVN specimens for the EUROfusion project. The test materials include different variants of reduced activation ferritic and martensitic (RAFM) steels from both Europe and US for the EUROfusion project. Additional fatigue pre-cracking will be performed on M4CVN specimens machined from Eurofer 97 baseline material.

PROGRESS AND STATUS

Introduction

In the EUROfusion project, the irradiation effects on transition fracture toughness of Eurofer 97 RAFM steel is one of the core required properties. To fully utilize limited irradiation volume in High Flux Isotope Reactor (HFIR) at Oak Ridge National Laboratory, a M4CVN specimen, which enables four fracture toughness tests in one single specimen, is used. The prerequisite of transition fracture toughness testing is to create a sharp starting crack in the specimen which is realized by high frequency fatigue pre-cracking. The aim of this task is to perform fatigue pre-cracking on M4CVN specimens for the project.

Experimental Procedure

<u>Materials</u>

A wide variety of RAFM steels from both Europe and US were selected to machine M4CVN specimens. Table 1 summarizes different material variants. Eurofer 97 baseline material was provided from the EUROfusion project sponsor to use in machine M4CVN specimens.

Table 1. Summary of variants of RAFM steels included in this study

Material	Number of M4CVN specimens
US augment (CNA-54, E97-23, E97-54)	44
EUROFusion task #7 (10 material variants)	80
Eurofer 97 baseline	38

The M4CVN specimen dimensions as well as ID markings for the specimen are shown in Fig. 1. The specimen has a thickness B of 1.65 mm, width W of 3.3 mm, and machined notch depth of 0.50 mm. Each individual notch of the specimen is uniquely marked from left to right as L, LM, RM, and R.

<u>Test setup and procedures</u>

We performed fatigue pre-cracking on M4CVN specimens using a 3-point bend type test fixture mounted on a 44.5 kN capacity servo-hydraulic frame as shown in Fig. 2. The ratio of distance between the sample contact points at the bottom sample holder (aka. span distance) to the sample width W was

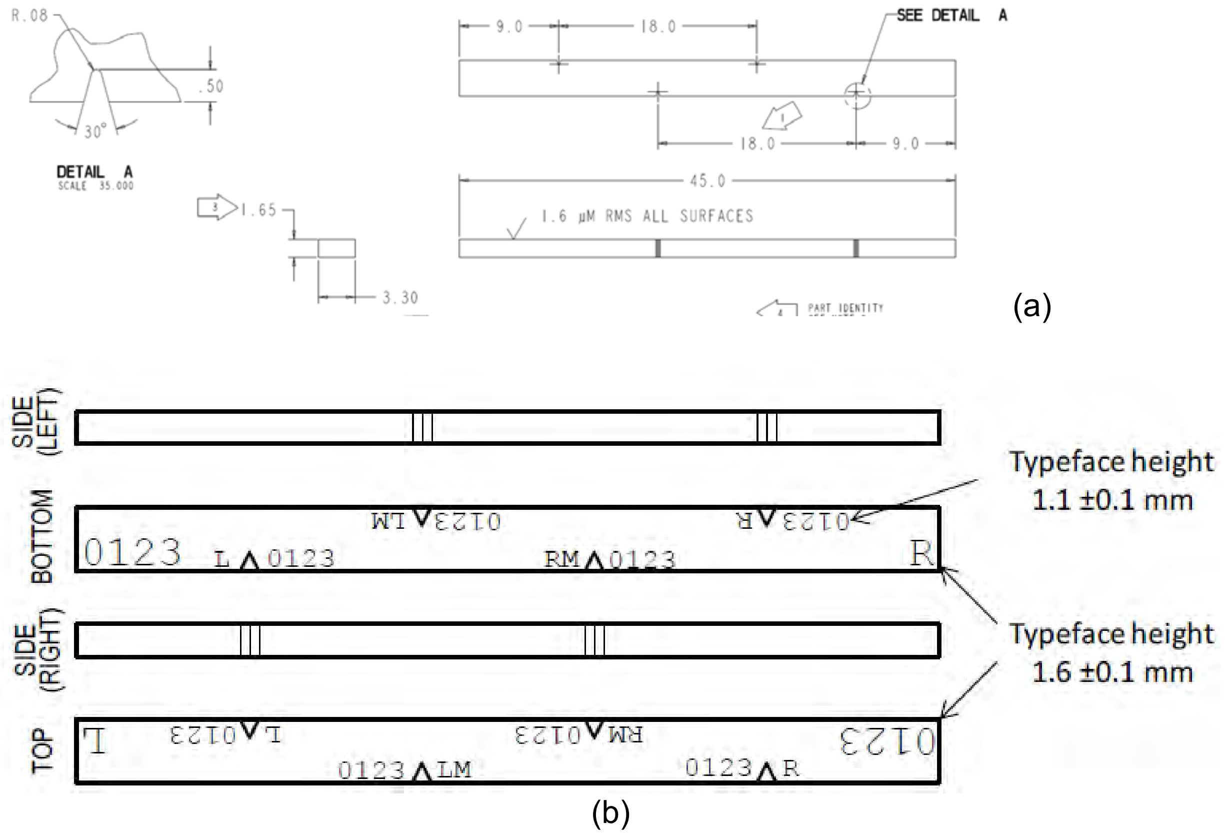

Figure 1. M4CVN specimen dimension in (a) and ID markings in (b).

kept constant at 4. During the fatigue pre-cracking process, the compliance at the machined notch of the specimen was measured by a deflection gauge which yields the real-time crack length using the equation [1]:

$$a/W = 1.0005 - 4.1527U + 9.7477U^2 - 214.2U^3 + 1604.3U^4 - 4633.4U^5$$
$$U = 1/\{[dE(BB_n)^{1/2}/P]^{1/2} + 1\} \tag{1}$$

where a is the sample crack length, d/P is the measured compliance, E is material Young's modulus, and B_n is the sample net thickness which equals the sample thickness B for non-sidegrooved specimens.

We applied the fatigue pre-cracking procedure in accordance with ASTM E1921 Standard Test Method for Determination of Reference Temperature, T_0, for Ferritic Steels in the Transition Range [2]. The standard sets limitations on both the maximum fatigue force (P_m) as well as the allowable maximum stress intensity factor (K_{max}) during the fatigue pre-cracking process. P_m for the M4CVN specimen used in this study is defined in the equation:

$$P_m = \frac{0.5Bb_0^{\,2}\sigma_Y}{S} \tag{2}$$

where b_0 is the length for the initial uncracked ligament, σ_Y is the average of material yield and tensile strengths, and S is the span distance. After substituting the specimen dimensions and typical Eurofer 97 yield strength (560 MPa) and tensile strength (670 MPa) into Eq. (2), P_m for the M4CVN specimen is approximately 302.5 N (68 lbs). The allowable K_{max} per ASTM E1921 is more complex to explain. However, to fulfill the requirement on P_m, the applied stress intensity was already well below the allowable K_{max}, hence satisfying the K_{max} requirement in ASTEM E1921. During fatigue pre-cracking, we applied a constant stress intensity in the range of 11.9-12.3 MPa√m. The fatigue pre-cracking frequency was between 40-45 Hz and the minimum to maximum fatigue force ratio (aka. R-ratio) was 0.1.

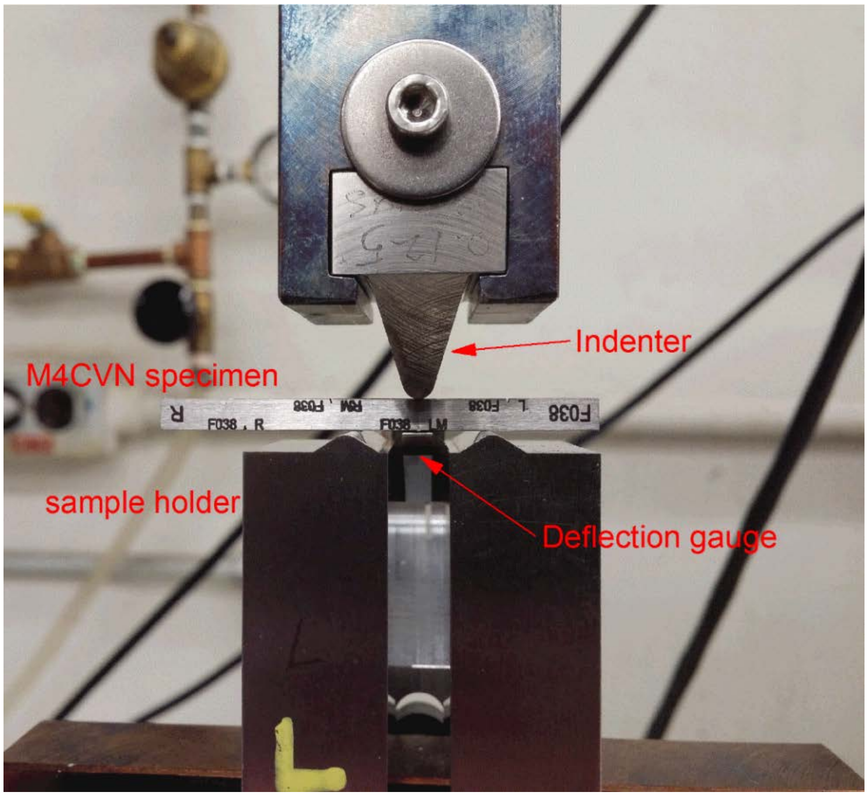

Figure 2. Fatigue pre-cracking test fixture for a M4CVN specimen.

Results

The detailed fatigue pre-cracking records for all tested M4CVN specimens are listed in Table 2. For the majority of tests, the final fatigue pre-crack length for each notch was approximately 1.452-1.485 mm (0.0572-0.0585 inch) corresponding to a crack length to specimen width ratio (a/W) of 0.44-0.45.

Table 2. Fatigue pre-cracking record for M4CVN steel specimens

Material group	Specimen ID	Notch location	Stress intensity (MPa√m)	Peak load (N)	a/W ratio	Fatigue cycles
US augment E97-54	B954-14	L	12.3	290	0.450	367,310
		LM	12.3	281	0.451	359,469
		RM	12.3	289	0.450	365,401
		R	12.3	271	0.451	373,138
US augment E97-54	B954-6	L	12.3	284	0.451	341,775
		LM	12.3	290	0.451	357,482
		RM	12.3	289	0.450	315,896
		R	12.3	301	0.450	338,033

Table 2. Fatigue pre-cracking record for M4CVN steel specimens (Continued)

Material group	Specimen ID	Notch location	Stress intensity (MPa√m)	Peak load (N)	a/W ratio	Fatigue cycles
US augment E97-54	B954-1	L	12.3	273	0.450	371,248
		LM	12.3	297	0.450	329.821
		RM	12.3	281	0.451	325,696
		R	12.3	297	0.450	377,291
US augment E97-54	B954-9	L	12.3	289	0.450	367,977
		LM	12.3	287	0.451	386,224
		RM	12.3	285	0.451	352,205
		R	12.3	285	0.451	343,291
US augment E97-54	B954-16	L	12.3	297	0.450	345,342
		LM	12.3	294	0.450	375,289
		RM	12.3	280	0.450	369,517
		R	12.3	294	0.450	404,309
US augment E97-54	B954-4	L	12.3	285	0.451	386,704
		LM	12.3	276	0.450	385,545
		RM	12.3	276	0.450	394,618
		R	12.3	287	0.450	399,210
US augment E97-54	B954-15	L	12.3	285	0.451	360,673
		LM	12.3	280	0.451	394,180
		RM	12.3	289	0.450	365,461
		R	12.3	291	0.451	399,079
US augment E97-54	B954-12	L	12.3	280	0.450	383,925
		LM	12.3	298	0.450	354,323
		RM	12.3	286	0.450	370,252
		R	12.3	302	0.450	403,358
US augment E97-54	B954-2	L	12.3	290	0.450	397,479
		LM	12.3	289	0.450	353,598
		RM	12.3	289	0.450	375,443
		R	12.3	294	0.450	385,197
US augment E97-54	B954-11	L	12.3	284	0.450	468,902
		LM	12.3	289	0.450	332,714
		RM	12.3	289	0.450	393,118
		R	12.3	283	0.450	348,208
US augment E97-54	B954-3	L	12.3	285	0.450	370,950
		LM	12.3	293	0.450	352,733
		RM	12.3	271	0.451	359,780
		R	12.3	294	0.450	342,408
US augment E97-54	B954-7	L	12.3	282	0.450	363,518
		LM	12.3	287	0.451	385,038
		RM	12.3	291	0.450	365,264
		R	12.3	286	0.450	439,920
US augment E97-54	B954-5	L	12.3	286	0.450	403,303
		LM	12.3	294	0.451	388,783
		RM	12.3	281	0.450	374,419
		R	12.3	302	0.450	362,924

Table 2. Fatigue pre-cracking record for M4CVN steel specimens (Continued)

Material group	Specimen ID	Notch location	Stress intensity (MPa√m)	Peak load (N)	a/W ratio	Fatigue cycles
US augment E97-54	B954-13	L	12.3	290	0.450	405,979
		LM	12.3	278	0.450	423,828
		RM	12.3	300	0.451	363,441
		R	12.3	287	0.450	364,790
US augment E97-54	B954-10	L	12.3	282	0.450	338,361
		LM	12.3	301	0.450	344,581
		RM	12.3	282	0.450	351,160
		R	12.3	277	0.450	377,765
US augment E97-54	B954-8	L	11.9	289	0.450	369,509
		LM	12.1	283	0.450	383,139
		RM	12.3	286	0.450	367,262
		R	12.3	290	0.450	359,840
US augment E97-23	A923-4	L	12.1	263	0.450	487,737
		LM	12.1	267	0.450	361,964
		RM	12.1	267	0.450	419,882
		R	12.1	268	0.450	379,174
US augment E97-23	A923-12	L	12.1	268	0.450	397,984
		LM	12.1	298	0.451	376,120
		RM	12.1	271	0.450	411,002
		R	12.1	274	0.450	380,117
US augment E97-23	A923-1	L	12.1	261	0.450	358,819
		LM	12.1	280	0.450	282,121
		RM	12.1	258	0.450	344,485
		R	12.1	262	0.450	330,553
US augment E97-23	A923-14	L	12.1	280	0.451	350,302
		LM	12.1	262	0.450	331,764
		RM	12.1	276	0.451	378,292
		R	12.1	271	0.450	316,291
US augment E97-23	A923-6	L	12.1	245	0.450	366,168
		LM	12.1	254	0.451	365,147
		RM	12.1	253	0.450	337,537
		R	12.1	249	0.450	333,709
US augment E97-23	A923-8	L	12.1	245	0.450	409,212
		LM	12.1	258	0.450	338,436
		RM	12.1	249	0.450	320,701
		R	12.1	262	0.450	364,102
US augment E97-23	A923-13	L	11.9	258	0.450	369,823
		LM	11.9	258	0.451	373,364
		RM	11.9	268	0.451	332,084
		R	11.9	270	0.450	343,243
US augment E97-23	A923-3	L	11.9	276	0.450	380,110
		LM	11.9	276	0.450	379,129
		RM	11.9	267	0.450	492,160
		R	11.9	277	0.451	423,977

Table 2. Fatigue pre-cracking record for M4CVN steel specimens (Continued)

Material group	Specimen ID	Notch location	Stress intensity (MPa√m)	Peak load (N)	a/W ratio	Fatigue cycles
US augment E97-23	A923-9	L	11.9	250	0.450	424,587
		LM	11.9	247	0.450	337,188
		RM	11.9	247	0.451	363,475
		R	11.9	246	0.451	384,948
US augment E97-23	A923-7	L	11.9	263	0.450	343,379
		LM	11.9	262	0.450	335,767
		RM	11.9	262	0.450	338,371
		R	11.9	254	0.450	427,168
US augment E97-23	A923-11	L	11.9	241	0.451	366,385
		LM	11.9	245	0.450	400,957
		RM	11.9	240	0.450	361,968
		R	11.9	248	0.450	377,762
US augment E97-23	A923-10	L	11.9	329	0.451	321,818
		LM	11.9	300	0.450	330,338
		RM	11.9	287	0.450	371,790
		R	11.9	292	0.450	361,957
US augment E97-23	A923-2	L	11.9	275	0.450	358,989
		LM	11.9	285	0.450	367,776
		RM	11.9	286	0.451	352,620
		R	11.9	294	0.450	333,652
US augment E97-23	A923-5	L	11.9	276	0.450	282,589
		LM	11.9	267	0.450	301,598
		RM	11.9	276	0.450	321,633
		R	11.9	270	0.450	314,984
US augment CNA-54	C54-14	L	12.3	282	0.450	347,059
		LM	12.3	285	0.450	386,056
		RM	12.3	272	0.450	394,235
		R	12.3	286	0.450	383,864
US augment CNA-54	C54-6	L	12.3	283	0.450	352,571
		LM	12.3	306	0.450	290,330
		RM	12.3	289	0.450	338,167
		R	12.3	299	0.450	353,242
US augment CNA-54	C54-2	L	12.3	286	0.450	370,183
		LM	12.3	285	0.450	371,389
		RM	12.3	282	0.450	347,453
		R	12.3	282	0.451	327,091
US augment CNA-54	C54-3	L	12.3	289	0.450	327,051
		LM	12.3	289	0.451	356,218
		RM	12.3	297	0.450	358,339
		R	12.3	299	0.450	316,852
US augment CNA-54	C54-5	L	12.3	290	0.450	325,619
		LM	12.3	278	0.450	367,186
		RM	12.3	283	0.450	357,514
		R	12.3	283	0.451	357,081

Table 2. Fatigue pre-cracking record for M4CVN steel specimens (Continued)

Material group	Specimen ID	Notch location	Stress intensity (MPa√m)	Peak load (N)	a/W ratio	Fatigue cycles
US augment CNA-54	C54-4	L	12.3	290	0.450	331,614
		LM	12.3	297	0.450	377,384
		RM	12.3	289	0.450	359,530
		R	12.3	302	0.450	354,907
US augment CNA-54	C54-13	L	12.3	285	0.450	339,877
		LM	12.3	300	0.450	335,594
		RM	12.3	294	0.450	339,188
		R	12.3	307	0.450	307,442
US augment CNA-54	C54-8	L	12.3	298	0.451	364,449
		LM	12.3	291	0.450	334,986
		RM	12.3	305	0.450	364,112
		R	12.3	294	0.450	337,623
US augment CNA-54	C54-10	L	12.3	296	0.450	319,689
		LM	12.3	298	0.450	335,164
		RM	12.3	300	0.450	370,203
		R	12.3	304	0.450	318,961
US augment CNA-54	C54-1	L	12.3	291	0.450	368,741
		LM	12.3	296	0.450	355,075
		RM	12.3	308	0.451	328,937
		R	12.3	300	0.450	385,546
US augment CNA-54	C54-12	L	12.3	285	0.450	344,305
		LM	12.3	294	0.450	356,566
		RM	12.3	301	0.451	329,937
		R	12.3	290	0.450	351,528
US augment CNA-54	C54-7	L	12.1	290	0.500	441,575
		LM	12.3	299	0.450	309,836
		RM	12.3	306	0.450	318,168
		R	12.3	284	0.450	375,784
US augment CNA-54	C54-9	L	12.3	280	0.450	335,987
		LM	12.3	290	0.450	360,610
		RM	12.3	285	0.450	316,607
		R	12.3	289	0.450	320,811
US augment CNA-54	C54-11	L	12.3	294	0.451	326,610
		LM	12.3	297	0.450	327,650
		RM	12.3	277	0.451	385,476
		R	12.3	292	0.450	332,314
EUROFusion task #7 material H	H000	L	12.1	281	0.441	275,383
		LM	12.1	293	0.440	263,062
		RM	12.1	285	0.441	271,732
		R	12.1	278	0.440	280,470
EUROFusion task #7 material H	H001	L	12.1	283	0.441	253,487
		LM	12.1	294	0.440	242,683
		RM	12.1	290	0.440	247,826
		R	12.1	294	0.440	247,647

Table 2. Fatigue pre-cracking record for M4CVN steel specimens (Continued)

Material group	Specimen ID	Notch location	Stress intensity (MPa√m)	Peak load (N)	a/W ratio	Fatigue cycles
EUROFusion task #7 material H	H002	L	12.1	288	0.440	279,173
		LM	12.1	289	0.440	254,156
		RM	12.1	288	0.441	259,719
		R	12.1	294	0.440	257,737
EUROFusion task #7 material H	H003	L	12.1	282	0.441	258,159
		LM	12.1	289	0.440	245,707
		RM	12.1	294	0.440	253,291
		R	12.1	289	0.441	263,788
EUROFusion task #7 material H	H004	L	12.1	285	0.440	258,989
		LM	12.1	292	0.440	232,072
		RM	12.1	299	0.440	246,313
		R	12.1	284	0.440	272,671
EUROFusion task #7 material H	H005	L	12.1	286	0.440	267,488
		LM	12.1	285	0.441	263,032
		RM	12.1	276	0.440	277,873
		R	12.1	289	0.440	262,384
EUROFusion task #7 material H	H006	L	12.1	285	0.440	257,344
		LM	12.1	289	0.441	250,174
		RM	12.1	298	0.440	249,280
		R	12.1	286	0.440	278,902
EUROFusion task #7 material H	H007	L	12.1	268	0.441	326,330
		LM	12.1	289	0.441	258,571
		RM	12.1	286	0.440	277,778
		R	12.1	290	0.440	273,286
EUROFusion task #7 material I	I000	L	12.1	290	0.441	252,695
		LM	12.1	294	0.440	243,634
		RM	12.1	289	0.440	248,782
		R	12.1	285	0.440	286,738
EUROFusion task #7 material I	I001	L	12.1	294	0.440	267,235
		LM	12.1	294	0.441	261,440
		RM	12.1	294	0.440	263,620
		R	12.1	290	0.440	267,955
EUROFusion task #7 material I	I002	L	12.1	281	0.440	282,532
		LM	12.1	290	0.440	252,459
		RM	12.1	289	0.441	253,765
		R	12.1	285	0.440	264,181
EUROFusion task #7 material I	I003	L	12.1	246	0.440	527,541
		LM	12.1	245	0.440	499,086
		RM	12.1	249	0.440	518,373
		R	12.3	274	0.440	393,232
EUROFusion task #7 material I	I004	L	12.1	257	0.440	451,089
		LM	12.1	262	0.440	373,240
		RM	12.3	262	0.440	433,662
		R	12.3	258	0.440	416,538

Table 2. Fatigue pre-cracking record for M4CVN steel specimens (Continued)

Material group	Specimen ID	Notch location	Stress intensity (MPa√m)	Peak load (N)	a/W ratio	Fatigue cycles
EUROFusion task #7 material I	I005	L	12.3	272	0.440	388,510
		LM	12.3	269	0.440	385,597
		RM	12.3	267	0.440	403,788
		R	12.3	267	0.440	400,542
EUROFusion task #7 material I	I006	L	12.3	269	0.440	375,385
		LM	12.3	267	0.440	384,611
		RM	12.3	267	0.440	367,136
		R	12.3	270	0.441	360,205
EUROFusion task #7 material I	I007	L	12.3	267	0.441	453,194
		LM	12.3	267	0.440	392,170
		RM	12.3	272	0.440	388,630
		R	12.3	262	0.440	376,880
EUROFusion task #7 material P	P000	L	12.1	285	0.440	302,292
		LM	12.1	285	0.440	272,322
		RM	12.1	289	0.440	255,754
		R	12.1	287	0.441	293,433
EUROFusion task #7 material P	P001	L	12.1	284	0.440	276,452
		LM	12.1	291	0.441	266,090
		RM	12.1	280	0.441	297,076
		R	12.1	267	0.440	358,946
EUROFusion task #7 material P	P002	L	12.1	290	0.440	297,132
		LM	12.1	288	0.441	296,962
		RM	12.1	289	0.440	289,875
		R	12.1	290	0.440	296,031
EUROFusion task #7 material P	P003	L	12.1	258	0.440	376,163
		LM	12.1	290	0.440	283,407
		RM	12.1	291	0.441	256,555
		R	12.1	294	0.441	266,273
EUROFusion task #7 material P	P004	L	12.1	292	0.440	282,233
		LM	12.1	288	0.441	305,128
		RM	12.1	290	0.441	292,981
		R	12.1	280	0.440	288,164
EUROFusion task #7 material P	P005	L	12.1	286	0.441	289,875
		LM	12.1	285	0.440	269,907
		RM	12.1	287	0.440	274,291
		R	12.1	289	0.440	259,763
EUROFusion task #7 material P	P006	L	12.1	286	0.440	280,814
		LM	12.1	289	0.441	263,233
		RM	12.1	286	0.440	268,556
		R	12.1	284	0.440	270,717
EUROFusion task #7 material P	P007	L	12.1	287	0.440	269,684
		LM	12.1	291	0.440	259,371
		RM	12.1	298	0.440	244,592
		R	12.1	296	0.440	259,662

Table 2. Fatigue pre-cracking record for M4CVN steel specimens (Continued)

Material group	Specimen ID	Notch location	Stress intensity (MPa√m)	Peak load (N)	a/W ratio	Fatigue cycles
EUROFusion task #7 material L	L000	L*	12.1	264	0.441	491,584
		LM	12.1	266	0.440	308,135
		RM	12.1	267	0.440	316,006
		R	12.1	267	0.440	297.684
EUROFusion task #7 material L	L001	L	12.1	268	0.440	378,211
		LM	12.1	271	0.440	270,228
		RM	12.1	262	0.440	345,927
		R	12.1	270	0.440	317,800
EUROFusion task #7 material L	L002	L	12.1	274	0.440	302,588
		LM	12.1	275	0.440	293,812
		RM	12.1	279	0.440	275,184
		R	12.1	262	0.440	312,101
EUROFusion task #7 material L	L003	L	12.1	268	0.441	366,220
		LM	12.1	265	0.440	297,435
		RM	12.1	277	0.440	342,971
		R	12.1	262	0.440	347,868
EUROFusion task #7 material L	L004	L	12.1	281	0.450	473,408
		LM	12.1	254	0.440	494,069
		RM	12.1	276	0.440	411,331
		R	12.1	258	0.440	437,159
EUROFusion task #7 material L	L005	L	12.1	302	0.440	569,046
		LM	12.1	302	0.440	310,883
		RM	12.1	320	0.440	293,572
		R	12.1	311	0.440	295,442
EUROFusion task #7 material L	L006	L	12.1	316	0.440	308,577
		LM	12.1	279	0.441	314,235
		RM	12.1	285	0.440	291,777
		R	12.1	280	0.440	305,903
EUROFusion task #7 material L	L007	L	12.1	277	0.440	370,940
		LM	12.1	272	0.440	359,904
		RM	12.1	271	0.441	412,056
		R	12.1	267	0.440	430,516
EUROFusion task #7 material J	J000	L	12.1	285	0.440	426,474
		LM	12.1	276	0.440	552,999
		RM	12.1	281	0.441	259,592
		R	12.1	285	0.441	244,803
EUROFusion task #7 material J	J001	L	12.1	286	0.441	311,999
		LM	12.1	283	0.441	349,939
		RM	12.1	309	0.440	282,510
		R	12.1	291	0.441	309,931
EUROFusion task #7 material J	J002	L	12.1	296	0.440	280,552
		LM	12.1	276	0.440	334,555
		RM	12.1	294	0.441	315,767
		R	12.1	288	0.440	298,655

Table 2. Fatigue pre-cracking record for M4CVN steel specimens (Continued)

Material group	Specimen ID	Notch location	Stress intensity (MPa√m)	Peak load (N)	a/W ratio	Fatigue cycles
EUROFusion task #7 material J	J003	L	12.1	296	0.440	326,730
		LM	12.1	276	0.440	356,046
		RM	12.1	286	0.440	332,299
		R	12.1	294	0.440	292,958
EUROFusion task #7 material J	J004	L	12.1	285	0.440	235,983
		LM	12.1	286	0.441	262,148
		RM	12.1	294	0.441	216,603
		R	12.1	276	0.440	270,790
EUROFusion task #7 material J	J005	L	12.1	276	0.440	291,820
		LM	12.1	292	0.440	281,506
		RM	12.1	281	0.440	293,078
		R	12.1	284	0.440	305,745
EUROFusion task #7 material J	J006	L	12.1	303	0.440	271,941
		LM	12.1	294	0.441	306,568
		RM	12.1	298	0.440	250,829
		R	12.1	224	0.440	371,424
EUROFusion task #7 material J	J007	L	12.1	289	0.440	243,888
		LM	12.1	298	0.440	211,651
		RM	12.1	298	0.441	217,894
		R	12.1	280	0.440	256,042
EUROFusion task #7 material K	K000	L	11.9	285	0.440	428,127
		LM	12.1	285	0.440	448,261
		RM	12.1	302	0.440	413,292
		R	12.1	303	0.440	357,274
EUROFusion task #7 material K	K001	L	12.1	279	0.440	333,298
		LM	12.1	294	0.441	299,363
		RM	12.1	307	0.441	259,156
		R	12.1	298	0.440	300,934
EUROFusion task #7 material K	K002	L	12.1	285	0.440	442,022
		LM	12.1	294	0.441	426,114
		RM	12.1	306	0.440	399,452
		R	11.9	289	0.440	467,969
EUROFusion task #7 material K	K003	L	12.1	291	0.440	293,378
		LM	12.1	289	0.440	318,594
		RM	12.1	285	0.440	293,208
		R	12.1	280	0.440	320,813
EUROFusion task #7 material K	K004	L	12.1	298	0.441	432,660
		LM	12.1	285	0.440	482,149
		RM	12.1	280	0.440	468,418
		R	12.1	290	0.440	544,097
EUROFusion task #7 material K	K005	L	12.1	280	0.441	465,197
		LM	11.9	287	0.440	460,449
		RM	12.1	285	0.440	459,371
		R	12.1	289	0.440	451,789

Table 2. Fatigue pre-cracking record for M4CVN steel specimens (Continued)

Material group	Specimen ID	Notch location	Stress intensity (MPa√m)	Peak load (N)	a/W ratio	Fatigue cycles
EUROFusion task #7 material K	K006	L	12.1	293	0.440	422,628
		LM	12.1	298	0.441	411,944
		RM	12.1	294	0.440	452,372
		R	12.1	288	0.440	474,235
EUROFusion task #7 material K	K007	L	12.1	285	0.440	334,403
		LM	12.1	302	0.440	283,555
		RM	12.1	304	0.440	295,937
		R	12.1	284	0.441	318,137
EUROFusion task #7 material M	M000	L	12.3	267	0.440	387,695
		LM	12.3	275	0.440	347,914
		RM	12.3	268	0.440	398,847
		R	12.3	272	0.440	386,287
EUROFusion task #7 material M	M001	L	12.3	294	0.440	365,829
		LM	12.3	287	0.440	378,405
		RM	12.3	256	0.441	495,140
		R	12.3	280	0.440	325,067
EUROFusion task #7 material M	M002	L	12.3	273	0.440	433,761
		LM	12.3	277	0.440	426,833
		RM	12.3	271	0.440	420,437
		R	12.3	285	0.441	378,423
EUROFusion task #7 material M	M003	L	12.3	278	0.440	383,969
		LM	12.3	275	0.440	416,653
		RM	12.3	275	0.440	394,567
		R	12.3	280	0.440	386,484
EUROFusion task #7 material M	M004	L	12.3	276	0.440	401,165
		LM	12.3	282	0.441	370,634
		RM	12.3	276	0.440	396,523
		R	12.3	262	0.440	433,924
EUROFusion task #7 material M	M005	L	12.3	274	0.440	401,968
		LM	12.3	280	0.440	358,890
		RM	12.3	270	0.440	459,679
		R	12.3	281	0.440	316,625
EUROFusion task #7 material M	M006	L	12.3	258	0.440	408,911
		LM	12.3	282	0.440	343,957
		RM	12.3	266	0.440	484,357
		R	12.3	269	0.440	404,882
EUROFusion task #7 material M	M007	L	12.3	285	0.440	404,896
		LM	12.3	286	0.440	365,739
		RM	12.3	271	0.440	441,498
		R	12.3	282	0.440	384,961
EUROFusion task #7 material N	N000	L	12.3	280	0.440	437,704
		LM	12.3	286	0.440	410,684
		RM	12.3	285	0.440	446,359
		R	12.3	293	0.440	410,302

Table 2. Fatigue pre-cracking record for M4CVN steel specimens (Continued)

Material group	Specimen ID	Notch location	Stress intensity (MPa√m)	Peak load (N)	a/W ratio	Fatigue cycles
EUROFusion task #7 material N	N001	L	12.3	258	0.441	484,817
		LM	12.3	309	0.440	386,535
		RM	12.3	246	0.441	442,105
		R	12.3	242	0.440	560,813
EUROFusion task #7 material N	N002	L	12.3	294	0.441	396,810
		LM	12.3	270	0.440	486.743
		RM	12.3	293	0.440	407,906
		R	12.3	271	0.440	464,367
EUROFusion task #7 material N	N003	L	12.3	307	0.440	424.807
		LM	12.3	247	0.440	910,181
		RM	12.3	285	0.441	315,573
		R	12.3	262	0.440	418,319
EUROFusion task #7 material N	N004	L	12.3	307	0.440	363,640
		LM	12.3	262	0.440	547,552
		RM	12.3	311	0.440	305,884
		R	12.3	267	0.440	620,443
EUROFusion task #7 material N	N005	L	12.3	270	0.440	476,337
		LM	12.3	299	0.441	359,692
		RM	12.3	271	0.440	492,802
		R	12.3	299	0.440	322,214
EUROFusion task #7 material N	N006	L	12.3	290	0.440	398,874
		LM	12.3	285	0.440	408,504
		RM	12.3	286	0.440	409,440
		R	12.3	285	0.440	409,800
EUROFusion task #7 material N	N007	L	12.3	281	0.440	455,718
		LM	12.3	278	0.440	438,441
		RM	12.3	303	0.441	335,379
		R	12.3	279	0.441	422,622
EUROFusion task #7 material O	O000	L	12.3	277	0.440	382,592
		LM	12.3	264	0.440	520,455
		RM	12.3	259	0.440	434,840
		R	12.3	233	0.440	735,247
EUROFusion task #7 material O	O001	L	12.3	259	0.440	574,417
		LM	12.3	286	0.440	442,750
		RM	12.3	262	0.440	533,575
		R	12.3	269	0.440	484,654
EUROFusion task #7 material O	O002	L	12.3	227	0.440	1,026,995
		LM	12.3	264	0.440	416,697
		RM	12.3	231	0.440	648,584
		R	12.3	251	0.441	512,448
EUROFusion task #7 material O	O003	L	12.3	272	0.440	475,108
		LM	12.3	266	0.440	497,630
		RM	12.3	270	0.441	525,899
		R	12.3	288	0.440	458,129

Table 2. Fatigue pre-cracking record for M4CVN steel specimens (Continued)

Material group	Specimen ID	Notch location	Stress intensity (MPa√m)	Peak load (N)	a/W ratio	Fatigue cycles
EUROFusion task #7 material O	O004	L	12.3	279	0.440	463,120
		LM	12.3	278	0.441	509,036
		RM	12.3	285	0.440	432,801
		R	12.3	272	0.440	453,334
EUROFusion task #7 material O	O005	L	12.3	285	0.441	413,820
		LM	12.3	265	0.440	513,114
		RM	12.3	289	0..440	376,213
		R	12.3	290	0.440	390,729
EUROFusion task #7 material O	O006	L	12.3	289	0.440	430,876
		LM	12.3	280	0.440	431,138
		RM	12.3	286	0.440	426,476
		R	12.3	278	0.440	480,166
EUROFusion task #7 material O	O007	L	12.3	286	0.440	419,986
		LM	12.3	284	0.440	434,564
		RM	12.3	286	0.440	NA**
		R	12.3	270	0.441	482,672

*Notched overloaded to 378 N during the sample installation

**The test was interrupted due to a fuse failure for the servo-hydraulic pump. We had to reboot the test computer to resume the test, but lost the record for the total fatigue cycles

References

[1] J. Underwood et al., ASTM STP 1114 (1991) 197.

[2] ASTM E1921-17a: Standard Test Method for Determination of Reference Temperature, T_0, for Ferritic Steels in the Transition Range, ASTM International, West Conshohocken, PA, 2017.

2. ODS AND NANOCOMPOSITED ALLOY DEVELOPMENT

2.1 EFFECT OF DEFORMATION PROCESSING ON THE MICROSTRUCTURE AND TEXTURE OF 14YWT NFA-1

—S. Pal, M. E. Alam, G. R. Odette (University of California, Santa Barbara), S. A. Maloy (Los Alamos National Laboratory), D. T. Hoelzer (Oak Ridge National Laboratory), and J. J. Lewandowski (Case Western Reserve University)

OBJECTIVE

The objective of this research is to characterize and compare texture and microstructure development of 14YWT NFA-1 for different deformation processing routes.

SUMMARY

Hot extrusion of as milled NFA-1 powder produces an inhomogeneous microstructure with strong bimodal grain size distribution with <110> α-fiber texture along the extrusion direction (ED) and a mix of <111> and <100> texture in the normal directions (ND). Hot cross-rolling completely transforms <111> texture to <100> ND texture and strengthens α-fiber in the extrusion direction. This introduces a high volume fraction of low toughness {001}<110> brittle cleavage systems. Dislocation reactions and pile ups at sessile low angle grain boundaries forming {001} planes in combination with residual stress produces microcracks running parallel to the plate. Shear dominated hydrostatic extrusion heals microcracks and transforms the ND texture to <111> from <100>. Effect of processing routes on the volume fraction of different texture components, dislocation density, and grain boundary misorientation angle-axis distribution are presented.

PROGRESS AND STATUS

Introduction

The promise of nanostructure ferritic alloys (NFAs) for fusion applications has been fully demonstrated [1]. While we know how to make great NFAs, deformation processing of them to make defect free components remains a challenge [1,2]. Recently, UCSB, LANL and ONRL collaborated to develop a larger best practice heat of a prototype 14YWT NFA, called FCRD NFA-1. The alloy has a nominal composition of Fe-14Cr-3W-0.4Ti-0.3Y. The as processed alloy, in the form of an extruded and cross-rolled plate, shows a near record strength-toughness combination, with a very low BDTT (≈ -175ºC) [2]. Unfortunately, the cross- rolled plate, contains a large population of microcracks lying normal to the plate surfaces. The microcracks make further deformation processing to produce delicate and defect free components, such as thin-walled tubing, extremely difficult. Our previous characterization studies elucidated the micromechanism leading to this microcrack formation [3]. During hot cross rolling of the as extruded billet a high volume fraction of {001}<110> texture component, the most brittle cleavage system in bcc-Fe with a toughness of 4-5 MPa$\sqrt{m}$, develops in the short thickness direction. During plastic deformation at high temperature, sessile low angle sub boundary form on {001} planes by dislocation reactions and act as a barrier site for pile ups producing stress concentration, which finally lead to crack tip opening. Propagation of the crack is driven by residual stress developed during the deformation and available low toughness brittle cleavage system. The crack propagation path follows the low angle sub grain boundary trajectory and runs in the deformation directions.

Therefore, it is critically important to characterize the texture and microstructure development of the as-processed plate after each deformation step to identify the optimal processing path. Here, we report a details characterization studies on microstructure, texture, and grain boundary characterization for different orientations of a hot extruded billet bar, an annealed-hot cross-rolled plate and a thin wall tube produced by hydrostatic extrusion from the hot cross-rolled plate. Quantification of different texture components was carried out and microstructure development of the alloy is assessed based on the stress state and strain path developed during the deformation processing.

Experimental Procedure

Details of all the three processing paths for FCRD NFA-1 have been reported elsewhere [2-6]. Hot extrusion produced a square billet bar (deformation step 1), which was hot cross-rolled to produce a plate (deformation step 2). A gun drilled mother tube was extracted from the plate and hydrostatically extruded to produce a thin wall tube. Note, while the as extruded billed is in the form of a square bar, the characterization was carried out on a tube gun drilled from the bar, with the tube axis parallel to the extrusion direction. Small test coupons were extracted from different section orientations for the three deformation steps. Figure 1 shows the sample section orientations. Note the view planes are labeled based on their normal direction.

An EBSD, SEM/FIB and TEM were used for texture and microstructure characterization, respectively. A FIB was used to prepare thin lamella for TEM observation. Orientation imaging microscopy (OIM) was performed using EBSD scan. The texture characterization included orientation maps (OM), inverse pole figures (IPF), pole figures (PF), orientation distribution functions (ODF), grain boundary misorientation angle and misorientation axis distributions. The different texture component were quatified using MTEX code [7]. Two-beam BF imaging and SAD patterns were used to measure the dislocation density. TEM foil thickness was measured using the CBED technique.

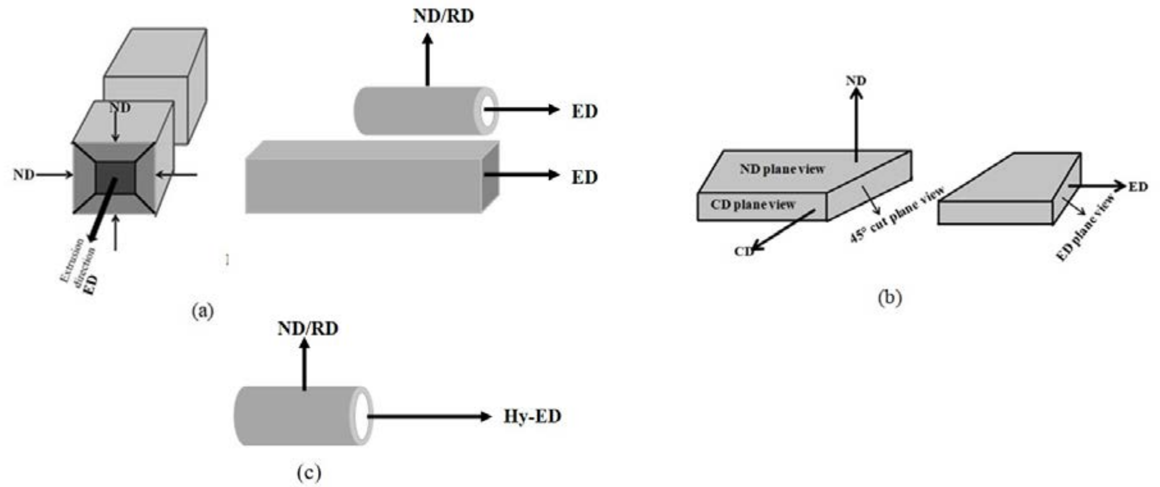

Figure 1. Schematic illustrations of the: a) extruded billet bar and gun drilled tube made from the billet bar; b) cross-rolled plate; and, c) hydrostatically extruded tube. The extrusion direction is the same in all three deformation conditions.

Results

The Hot Extruded Billet Bar

Grain and Texture Characterization: Microstructure and texture characterization of the hot extruded billet bar were carried on a gun-milled tube, of with a long axis parallel to the extrusion direction. The different orientation and viewing plane sections for the tube are shown in Figure 1a. Figures 2a and b show the FIB-SEM microstructure of the RD/ND and ED sections of the extruded tube, respectively. The OIM map is not only helped to characterize the texture of the as processed tube, it also provides detail information regarding the microstructure's length scale and grain boundary character.

The average diameter of the small grain is ≈ 0.6 ± 0.17 μm in the ED section view and the same 0.54 ± 0.16 μm in the RD section view. The small grains are equiaxed in the ED and have an average GAR of 1.65 ± 0.3 in the RD. While the small grains are numerically dominant, a strongly bi-modal grain size distribution is clearly evident. Detailed statistics of microstructure characterization using SEM is reported elsewhere [4]. Here, we focus on texture and grain boundary characterization from OIM data. Figures 3a and b shows the orientation map, measured on the RD and ED section views.

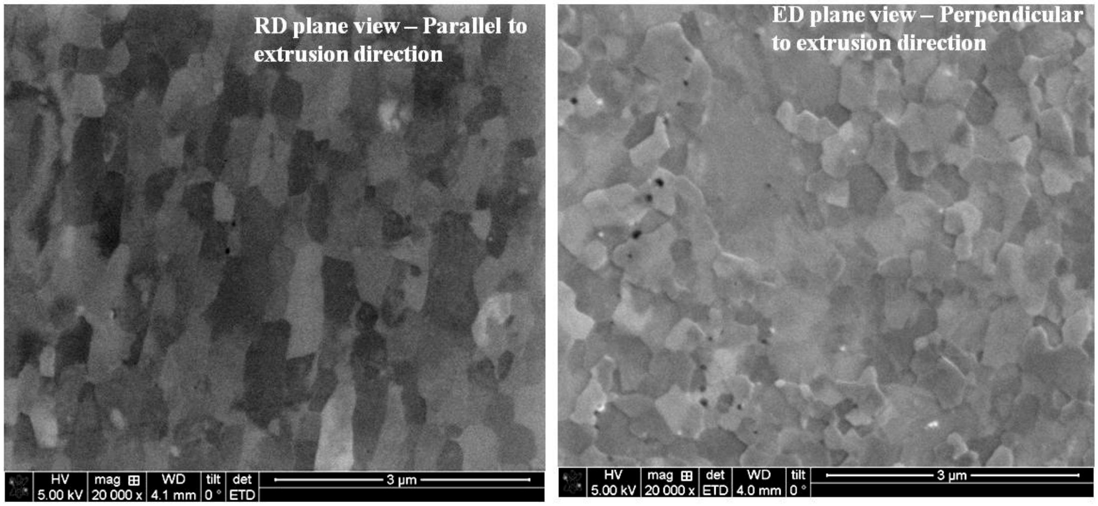

(a) (b)

Figure 2. FIB-SEM micrographs of extruded tube: a) the RD section view; and b) the ED section view. The orientation of the extruded tube directions are shown in Figure 1a.

The OIM not only useful to characterize texture, since it also provides detail information regarding the microstructure’s length scale and grain boundary character. The OM in Figure 3 shows that texture along the extrusion direction is <110>, while a mix of <111> and <100> texture is produced in the RD/ND direction of the tube. This observation is further corroborated by the inverse pole figure (IPF) plot of the OIM scan for the ED section view shown in Figure 4.

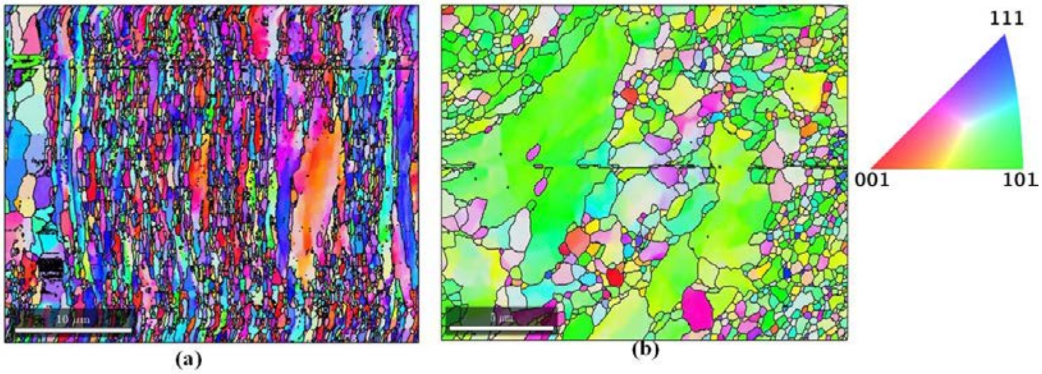

(a) (b)

Figure 3. Orientation map of the gun drilled extruded tube: a) RD section view and b) ED section view. Plane sections are defined by their normal direction as indicated in Figure 1a. The insert color codes the different crystallographic orientations.

The PF plot of the ED view section in Figure 5 shows clustering of the {011} poles at the center of the stereogram (the ED direction) surrounded by a circular distribution of the {011} fiber poles. The texture intensity of {011} poles is much higher than the {001} and {111} poles. Thus, a significant <110> fiber texture develops in the extrusion direction of the as consolidated bar. A more quantitative texture description is shown in the 2D section plots of orientation distribution function (ODF) in Figure 6 for $\Phi_2 = 0$ and 45° sections, derived from the OIM scan. Figures 6a and b show the ODF plot for the RD and Figures 6c and d, are for the ED section view.

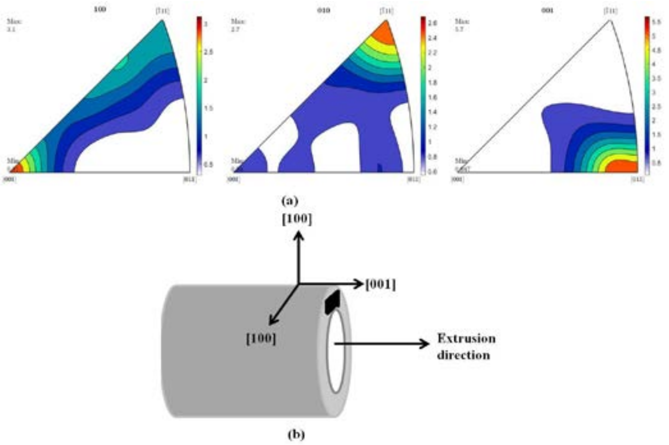

Figure 4. a) IPF plots of the ED section view of the extruded tube; and, b) a schematic showing the location of the OIM scan.

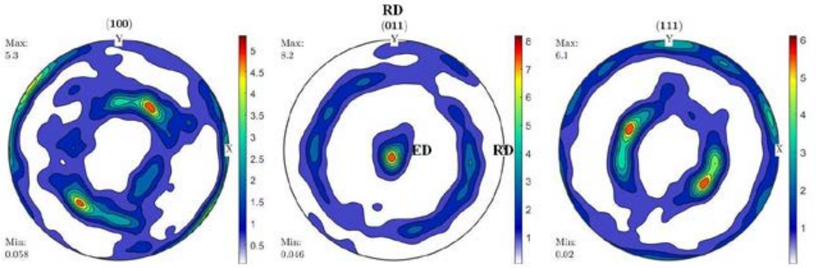

Figure 5. Pole figures (PF) for of the ED section view.

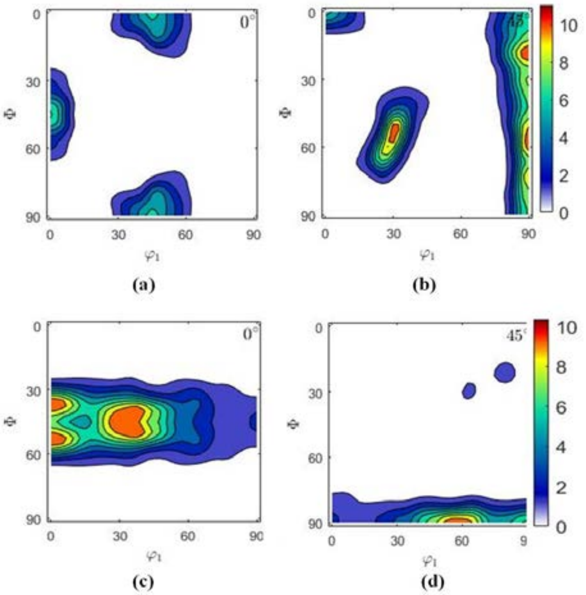

Figure 6. ODF plots of: a, and b) Φ_2 = 0 and $\Phi_2 = 45^{\circ}$ sections for the RD of the extruded tube; c) and d) Φ_2 = 0 and 45° sections for the ED of the extruded tube.

Comparing the ODF plots of Figure 6 with ideal Φ_2 = 0 and 45° sections for bcc Fe, in Figure 7, demonstrates that primary texture components in the RD section view of the tube are {011}<110>, {112}<111>, {111}<112> and {011}<110>; the strongest textures are {112}<111> and {111}<112>. The primary texture components observed in the ED section view are {011}<100>, {011}<211>, {011}<111> and {011}<111>; the dominant ED texture components are {011}<100> and {011}<111>. The volume fractions of the different texture components calculated from the ODF plots are shown in Table. 1.

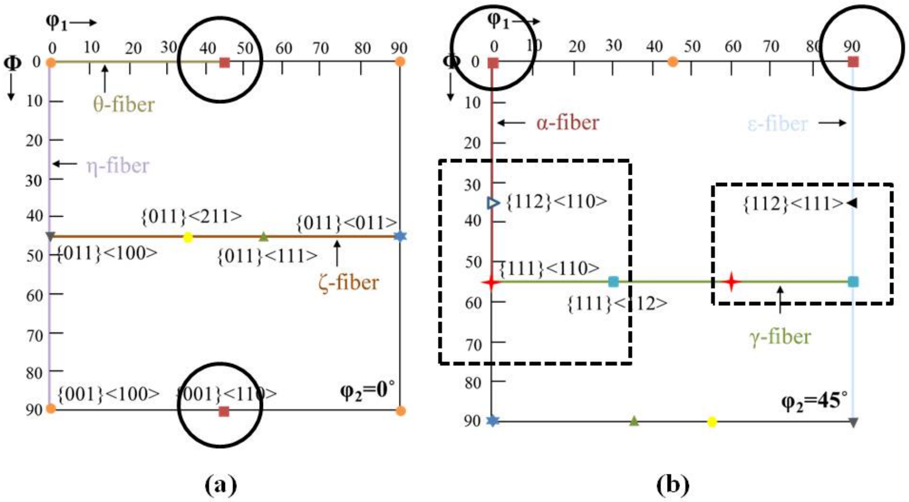

Figure 7. Ideal ODF plots of bcc Fe, a) Φ_2= 0 and b) 90° sections of the plot. Important texture components are also labeled.

Microstructure and grain boundary and misorientation angle and axis distribution characterization: In order to completely describe a grain boundary, we need to identify at least the misorientation between two neighboring grains and the axis of misorientation. Both the parameter has been calculated from the OIM data using the MTEX package. A high angle grain boundary is defined on the basis of a minimum misorientation value of 15°; a minimum misorientation value of 1° applies to low angle grain boundaries. Both the parameter has been calculated from the OIM data using MTEX package. The results are shown in Figures 8 and 9. A high population of low angle grain boundaries are observed for both the ED and RD view section. The high angle grain boundary distributions are random (see Figures 8c and d). The misorientation axis distribution of grain boundaries for both ED and RD section views has the highest intensity around the <111> crystallographic axis. Hence, our texture characterization reveals that after hot extrusion a moderate <110> fiber texture develops along the extrusion direction with a mix of <111> and <100> in the RD/ND direction of the tube.

The dislocation substructure and grain boundaries were characterized by TEM. Figure 10a shows BF-TEM image of the plane perpendicular to extrusion direction. A mix of equiaxed and elongated grains are observed. The grains are stretched in the 45° direction of the image plane. Rotation of the grains towards the 45° in the plane perpendicular to the extrusion occurs because this results in easy deformation in the highest resolved sheer stress direction under axi-symmetric compression.

The Hot Cross-Rolled Plate

Grain and Texture Characterization: Figures 11a and b show 3D FIB-SEM and OIM map of annealed and hot cross-rolled plate, constructed from the 2D micrographs obtained for the different plane sections. FIB-SEM micrographs clearly reveal that equiaxed grains with an average size of ≈0.5 µm on plate surface (the ND section), whereas elongated pancake shaped grains with an average size of ≈ 0.5 µm and GAR of ≈ 2.2 ± 0.9 are observed in ED and CD section views. Notably, microcracks, ranging from 1-100 µm long, are also observed in the short thickness side and front sections of the plate. Cracks run in planes perpendicular to the short plate dimension. A detailed analysis of the grain and microcracks in the cross-rolled plate is reported elsewhere [2]. The 3D-OIM map shows that the <111> and <100> ND texture of the hot extruded billet completely transforms to <100> ND texture upon hot cross rolling. The details texture analysis was reported previously [3, 5]. Hot cross-rolling strengthens the ED <110>α-fiber, initially produced during hot extrusion, and develops a broken/partial <110>α-fiber in the cross-rolling direction (see in Figure 11b). Moreover, hot cross rolling produces and stabilizes a high volume fraction of the {001}<111> texture component of α-fiber in the through thickness ND directions of the plate. This observation is further corroborated in the OIM map of the 45° cut section (with respect to the extrusion direction of the plate) seen in Figure 11b, as well as by the 2D section plot of ODF of the OIM results for the ND plane and 45° cut sections of the cross-rolled plate, see Figure 12.

Table. 1. Volume fractions of different texture components present in the as extruded tube along different orientation. An angular tolerance limit of 20° was chosen for the calculation.

Sample Orientation	**Texture components**	**Volume fractions (%)**
RD section view	{001}<110>	0.82
	{112}<111>	**15.97**
	{111}<112>	**15.84**
	{011}<100>	4.0
ED section view	**{011}<100>**	**17.79**
	{011}<211>	10.93
	{011}<111>	**19.76**
	{011}<011>	7.33

The dislocation density (ρ) of the as extruded tube was determined by tilting a grain in two-beam condition. Details of the method are reported elsewhere [9]. Figure 10b shows typical image of high dislocation density in grain along a <111> zone axis, for a {211} types diffraction spot (Figure 10c.) The estimated dislocation density for the extruded tube is in the range ≈ $0.8 \pm 0.2 \times 10^{15}$ m/m^3.

Comparison of the ODF plots in Figure 12 with the ideal ODF plots for bcc material clearly demonstrate that in the ND section view a high volume fraction of {001}<110> texture component of α-fiber family has developed during cross rolling. Moreover, alignment of {001} planes in the through thickness directions were further confirmed by the ODF plots of 45° section, seen in Figure 12b. The respective volume fractions of different texture components present in the ND section view and 45° cut section of the hot cross-rolled plate, calculated from the ODF plots, are given in Table 2.

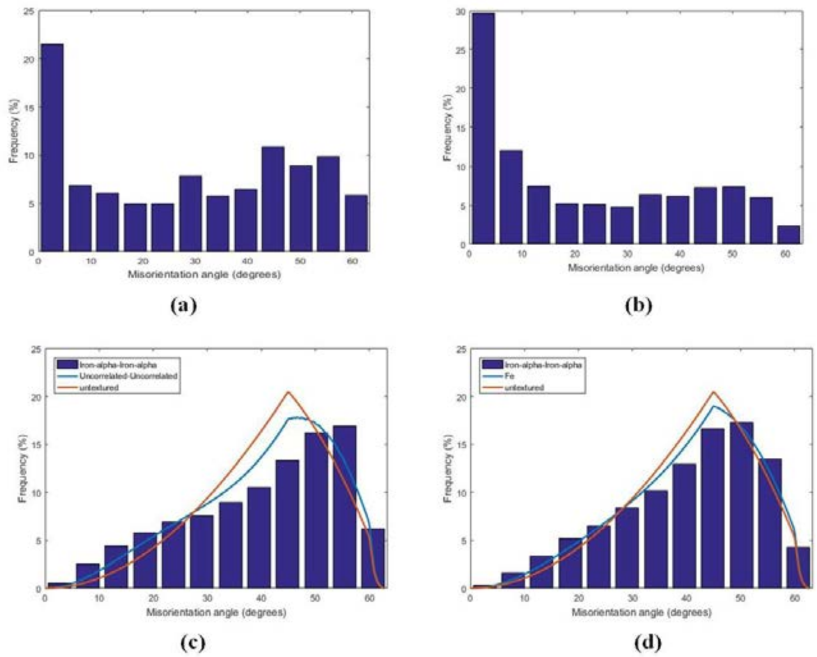

(a) (b)

(c) (d)

Figure 8. The correlated misorientation angle distribution extracted from the OIM data for the: a) RD section view; and, b) ED section view. Figures 8c) and d) show ideal random and non-texture (ideal) misorientation distribution plots for the RD and ED plane view sections, respectively.

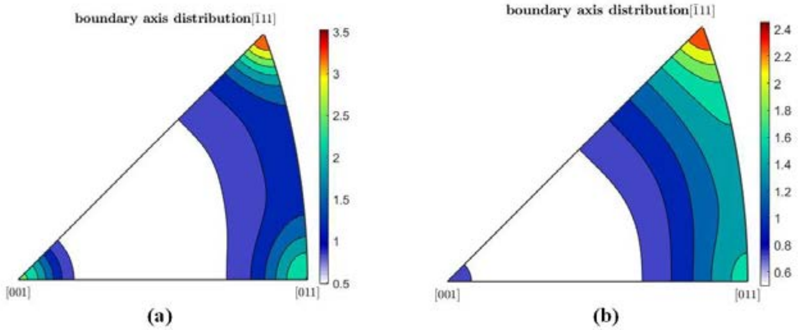

(a) (b)

Figure 9. The misorientation axis distribution of neighboring grains calculated from the OIM scan: a) The RD/ND section view; and, b) ED section view.

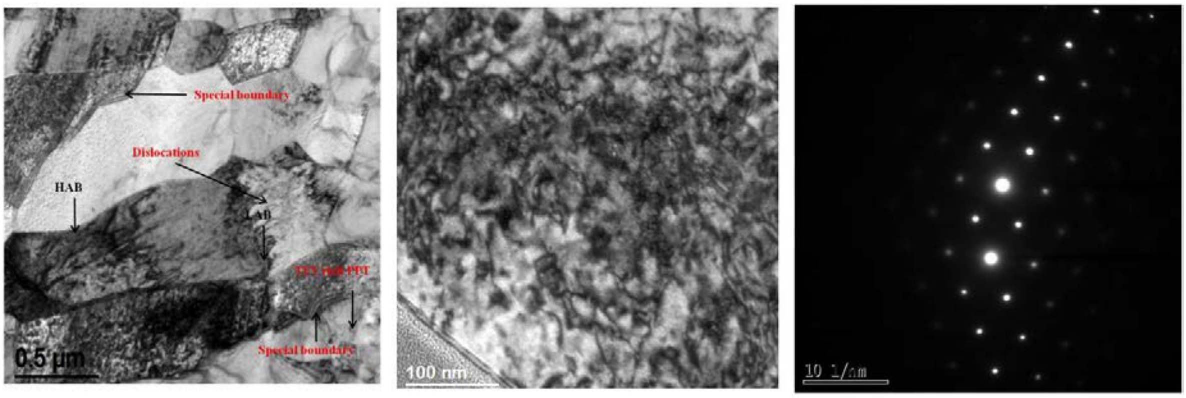

(a) (b) (c)

Figure 10. a) BF-TEM image of the plane perpendicular to ED direction. b) high mag BF-TEM image of dislocation substructure c) orientation of the image b, two beam condition at <111> zone axis orientation and {211} spot is highlighted.

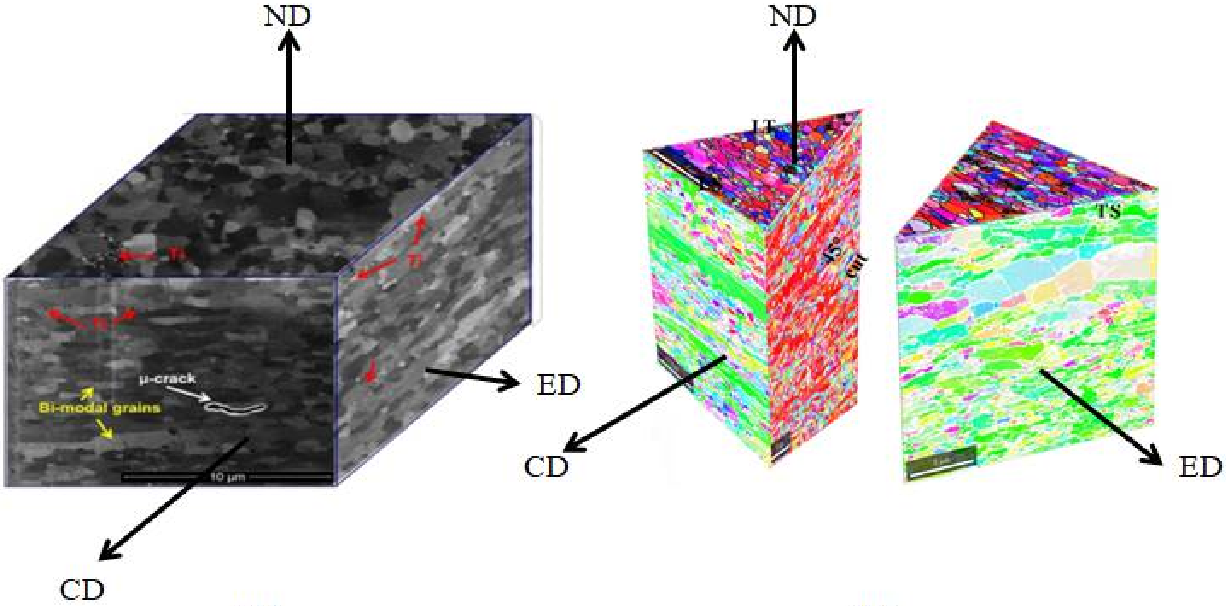

(a) (b)

Figure 11. a) shows the FIB-SEM 3D micrographs of the cross-rolled plate where the sample orientations are clearly marked. b) 3D-OIM maps of the sample cross-rolled plate.

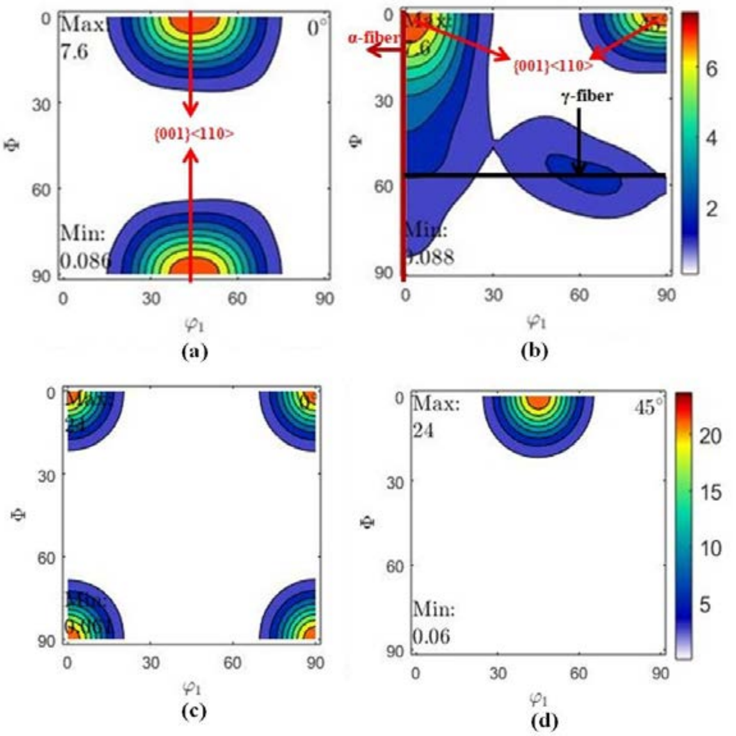

Figure 12. ODF plots of a) $\Phi_2 = 0$ and b) $\Phi_2 = 45^{\circ}$ sections of the ND section view of the cross-rolled plate; c) and d) are the same $\Phi_2 = 0$ and 45° sections of the 45° cut section view of the plate.

Microstructure and grain boundary and misorientation angle and axis distribution characterization: Hot cross-rolling of the extruded billet also has a substantial impact on the microstructure of the as-processed NFA-1 alloy. Grain boundary characterizations also reveals that there is strong preference for the 30° misorientation for both the ND and 45° cut sections, as see in Figure 13. The contribution of low angle boundary formation is less in the ND plane section of the cross-rolled plate. Moreover, the misorientation axis shows highest intensity of ≈ 20% around <111>.

Table 2. Volume fractions of different texture components present in the ND and 45° cut section view of the hot cross-rolled plate. An angular tolerance limit of 20° was chosen for the calculation.

Sample orientation	Texture component	Volume fraction (%)
ND plane view	**{001}<110>**	**34.57**
	{112}<110>	10.90
	{111}<110>	9.54
	{111}<112>	5.51
45° cut view	**{001}<100>**	**54.76**

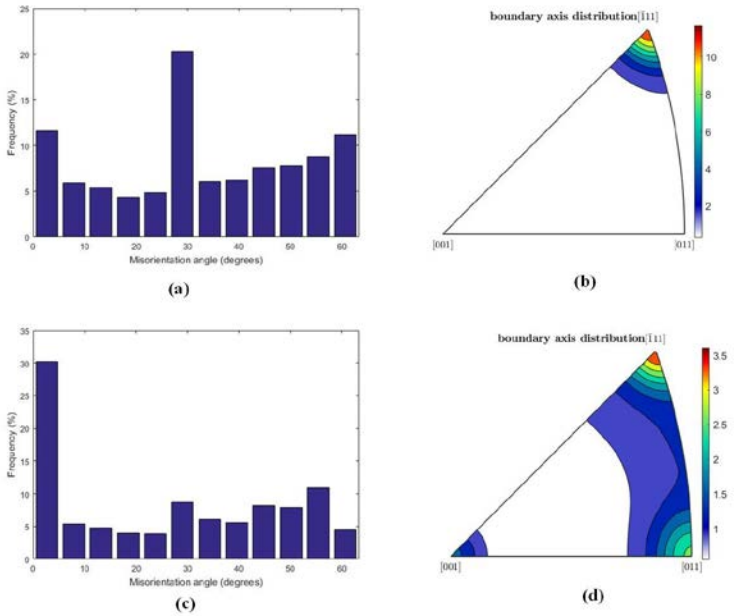

Figure 13. a) and b) misorientation angle and axis distribution for ND section view of the hot cross-rolled plate, respectively. Similarly, c) and d) shows the misorientation angle and axis distribution for 45° cut view section.

The microstructure and texture characterization clearly reveals that hot cross-rolling makes the thickness direction of the as-processed alloy brittle, by the formation of high volume fraction of {001}<110> and {001}<100> (observed in the 45°cut section view, shown in Figures 12c and d) texture components, leading to microcrack formation,. We previously reported the microcracking mechanism occurs by producing low angle sessile boundaries composed of a<100> dislocations stack-ups formed by reactions of a/2<111> type of dislocations. Further deformation leads to pile-ups at the low angle boundary, ultimately opens up a nanocrack, as originally proposed by Cottrell [10]. Residual stresses developed during the deformation processing drives the propagation of the nanocracks upon cooling below BDTT. The high volume fraction of brittle {001}<110> and {001}<100> texture components represent the most brittle cleavage systems in bcc Fe, with toughness of around 3-5 MPa√m [11,12]. These processes are illustrated in Figure 14. A detailed discussion of these results can be found in [6]. The ρ in the hot cross-rolled plate is ≈ 0.4±0.15x10^{15} m^{-2}. Notably, the microcrack propagates in a transgranular manner along the subgrain boundary formed on {001}<110> cleavage system.

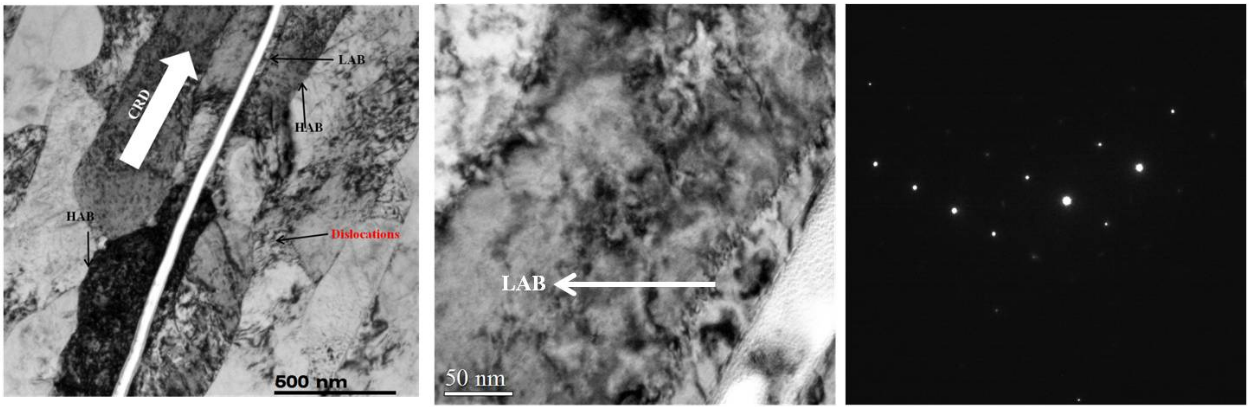

Figure 14. a) BF-TEM image of the microcrack formed in the hot-cross-rolled plate; b) High mag. BF-TEM image showing low angle boundary parallel to the crack; c) SAD pattern showing two beam condition. The highlighted spot is (1-12) and the zone axis is <110>.

The Hydrostatically Extruded Tube

Grain and Texture Characterization: FIB-SEM micrographs of RD and HyED sections of hydrostatically extruded tube are shown in Figures 15a and b, respectively. Hydrostatic extrusion produce more or less uniform microstructure compared to the other two deformation processing routes. On average, ≈ 0.46 ± 0.16 μm equiaxed grains cover ≈ 83% of the area of the ED section. The grains are elongated, with an average size of ≈ 0.6 ± 0.12, with a GAR of 1.98 ± 0.6, and area coverage of 92%. Most notably, tube produced by hydrostatic extrusion is completely free from the microcracks which formed during hot cross-rolling.

Figures 16a and b show an OM of the RD and HyED sections of hydrostatically extruded tube which are similar to the SEM observations. Hydrostatic extrusion produces more or less homogeneous microstructure. Effect of hydrostatic extrusion on the hot-cross-rolled plate is substantial. In the previous subsection, we found that hot cross-rolling forms and stabilizes <100> ND texture components and strengthens the <110> α fiber texture along the extrusion direction of the hot cross-rolled plate. However, hydrostatic extrusion again changes <100> ND texture to <111> ND (RD) texture as well as weakening the <110> α fiber texture, as clearly seen in the IPF in Figure 17.

Further quantitative texture description was carried out by plotting orientation distribution function, by analyzing the EBSD data with the MTEX package, in a 2D Euler space for $\Phi_2 = 0$ and 45° sections. The dominant texture components, clearly seen in Figure 10, are {011}<111> in the RD section and {112}<111> and {111}<110> in HyED section.

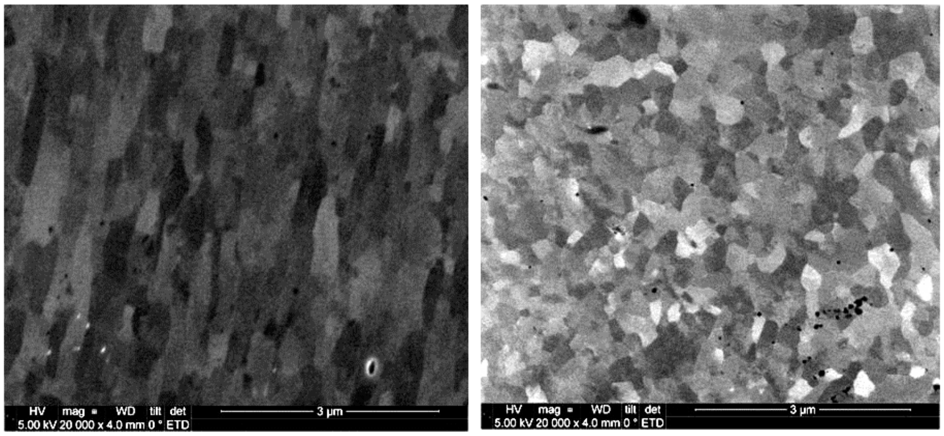

(a) (b)

Figure 15. FIB-SEM micrographs of extruded tube: a) the RD section view; and b) the Hy-ED section view. The orientation of the extruded tube is shown in Figure 1c.

.

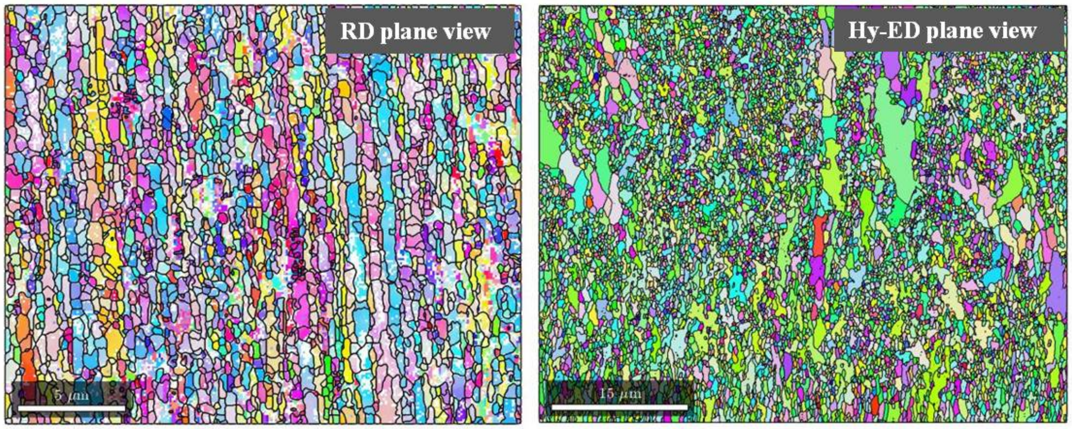

(a) (b)

Figure 16. Orientation maps generated from the EBSD scan of hydrostatically extruded tube: a) the RD section view; and, b) the Hy-ED section view. The orientation of the extruded tube is shown in Figure 1a.

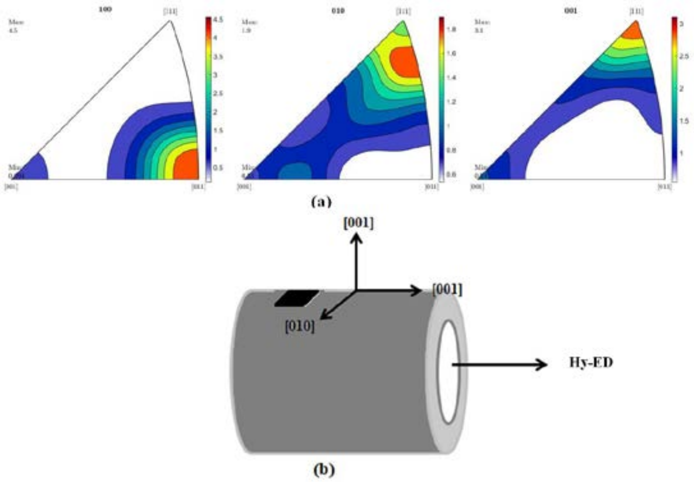

Figure 17. a) IPF plot of the EBSD data collected from the RD section view of hydrostatically extruded tube; b) schematic of the tube. Location of the EBSD scan on the RD section view is marked in Figure 9b.

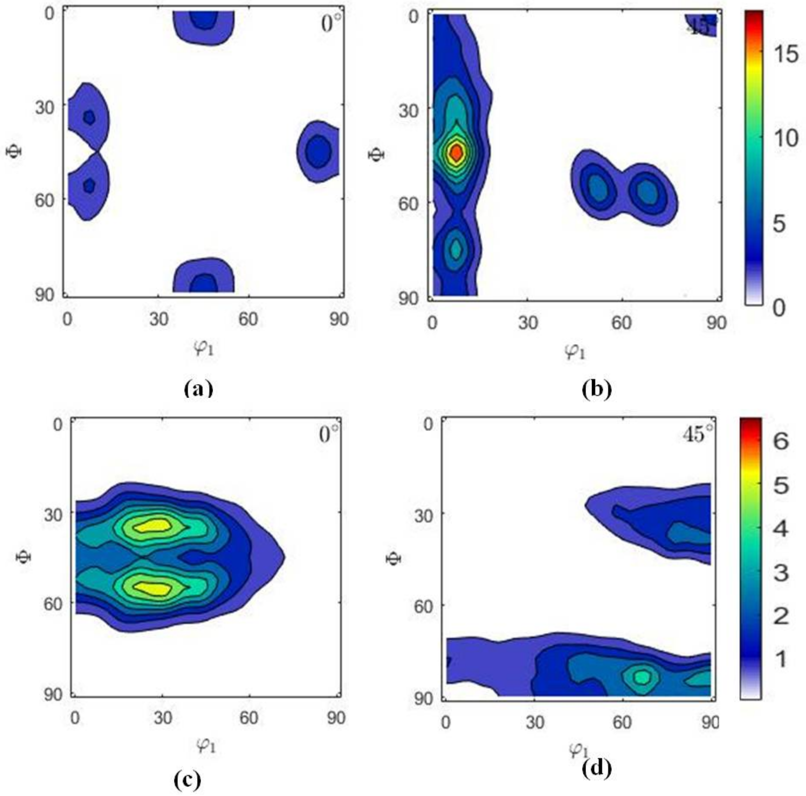

Figure 18. 2D ODF plot for $\Phi_2 = 45^{\circ}$ section of hydrostatically extruded tube for a) RD section view; b) Hy-ED section view.

A <110> α-fiber texture along the ED persists, however, the dominant Goss shear texture component {011}<110>, and {112}<110>, {111}<110> and {011}<100> texture components also develop. The same texture components were also observed by Aydogan et. al. for the same hydrostatically extruded NFA-1 tube [6]. Volume fraction of different texture components are calculated from the ODF data using MTEX package and are shown in Table 3.

The highest volume fraction is observed for the {011}<110> texture components for the both RD and Hy-ED sections. In the radial direction, 6.23 % of {001}<110> still persist. Misorientation angle and axis distribution along the neighboring grain boundaries are also calculated from the OIM map and shown in Figure 19.

Microstructure and grain boundary and misorientation angle and axis distribution characterization: Both OIM map and FIB-SEM micrographs show that grains are elongated along the extrusion direction. Notably, in the RD section view, a high frequency of 30 and 45^0 misorientation angles along the high angle grain boundaries are observed. Whereas, misorientation across high angle boundaries of Hy-ED section view do not follow any special relationship, similar to the non-textured material. In case of RD section view, misorientation axis distribution across grain boundaries shows strong preference along the <111> and <100>. For Hy-ED plane view section, <110> is the preferred misorientation axis. However, a high volume fraction of low angle grain boundaries (misorientation angle less than 15°) is observed for the hydrostatically extruded tube, also reported by Aydogan et.al [6].

TEM observations confirm to our SEM and OIM data, see Figure 20. Grains along the extrusion directions are elongated, while equiaxed grains are observed in the plane perpendicular to the extrusion direction. High populations of low angle grain boundaries along with dislocation substructure are clearly visible in the TEM micrographs. Typically dislocation density calculated from the two beam condition BF-TEM image, see Figure 20b, are in the range of ≈ 0.9 ± 0.42 X 10^{15} /m^2. Grain boundary misorientation angle distribution calculated from the OIM scans also show high population of low angle grain boundaries.

Table 3. Volume fractions of different texture components present in the as extruded tube along different orientation. An angular tolerance limit of 20° was chosen for the calculation.

Sample Orientation	**Texture components**	**Volume fractions (%)**
RD section view	{001}<110>	6.23
	{112}<110>	**9.33**
	{111}<110>	**9.41**
	{011}<110>	**14.39**
ED section view	**{011}<110>**	**14.39**
	{011}<211>	0.72
	{011}<111>	0.80
	{011}<100>	**5.78**

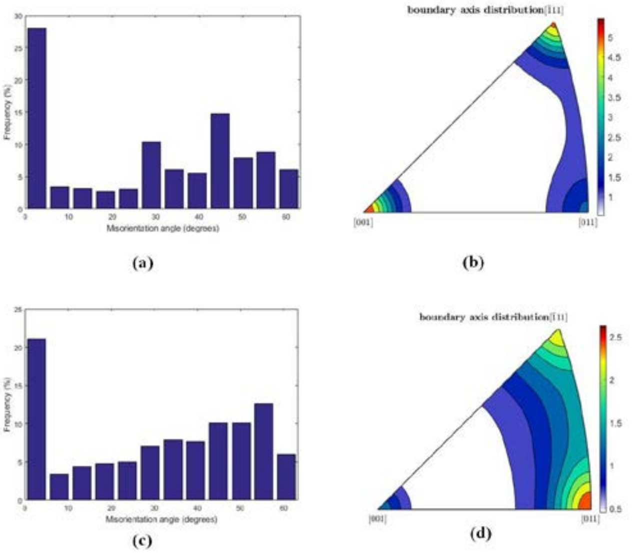

Figure 19. a) and b) misorientation angle and axis distribution for RD section view of the hydrostatically extruded tube; and, c) and d) the misorientation angle and axis distribution for Hy-ED section view.

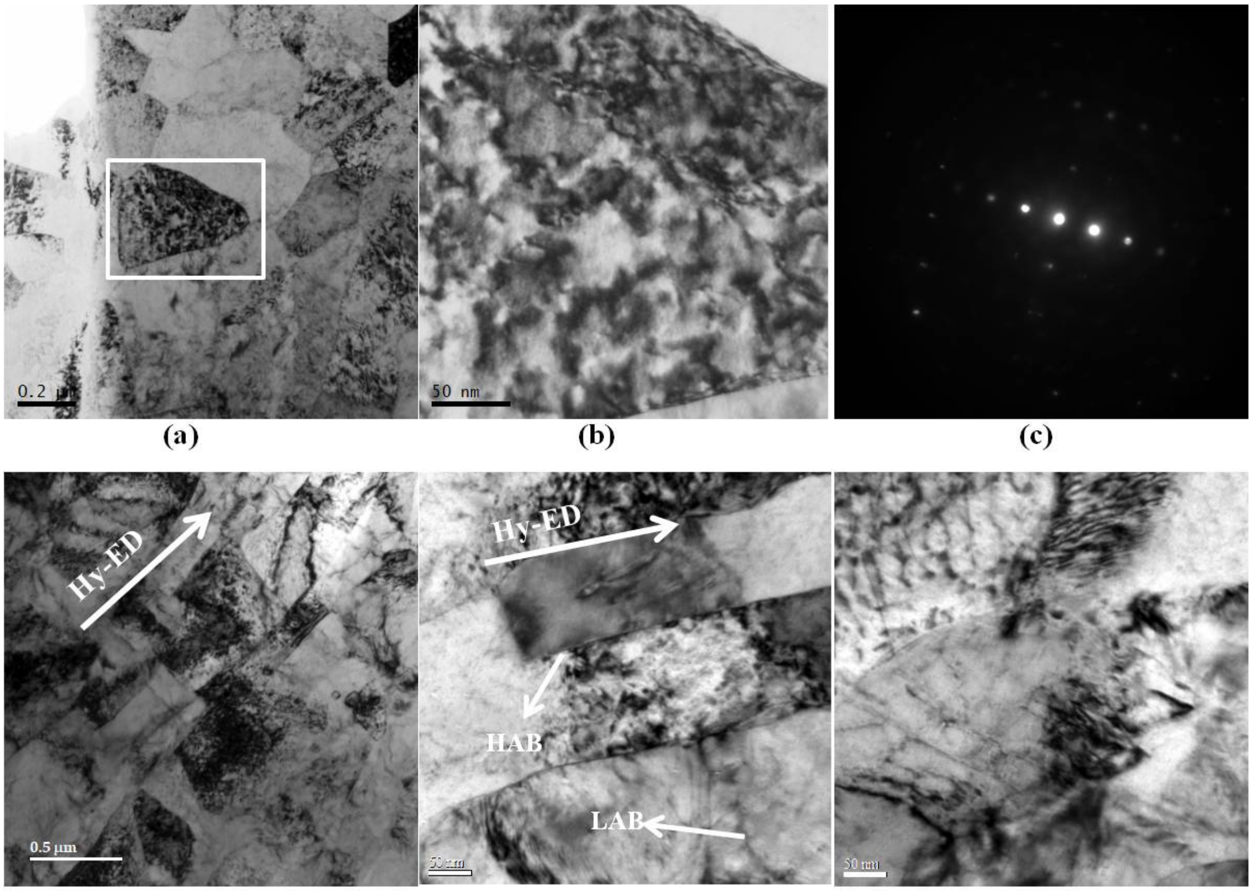

(a) (b) (c)

(d) (e) (f)

Figure 20. a) Two-beam BF-TEM image of the hydrostatically extruded tube, extrusion direction is normal to the image plane; b) high magnification image of the marked region of Figure a showing a high dislocation density; c) two-beam SAD pattern along <100> zone axis, showing orientation of the grain marked in Figures a; d), e) and f) BF-TEM images of the plane parallel to the Hy-ED. The Hy-ED direction and grain boundaries are marked in Figure 20e. Figure 20f shows the dislocation substructure.

Discussion

Present study shows that the microstructural and crystallographic texture developments during deformation processing of NFA-1 depend very strongly on the stain path and stress state. Axisymmetric extrusion process imposes a radial compressive strain on the billet perpendicular to the extrusion direction as material starts to flow though the die. The high shear stress result in formation of shear texture components of {110}<111> and {110}<001> in the ND and a modest <110> α-fiber texture in the ED. In contrast, during cross rolling, the interior of the plate interior deforms under a nearly plane strain stress state. The plane strain deformation produces and stabilizes {001}<110>-texture components by relaxing the local shear strain components [13]. The <100> ND texture produced during deformation, along with the a strengthened <110> α-fiber texture results in a high volume fraction of low toughness {001}<110> planes with normals parallel to the plate thickness direction. The formation of brittle cleavage system leads to a large population of microcracks. Hydrostatic extrusion, which is a shear dominated deformation process, of mother tubes extracted from the microcracked plate to fabricate thin wall tubes not only alters texture in the ND/RD direction but also eliminates microcracks Overall texture intensity of hydrostatically extruded tube is lower than for the other deformation conditions. In a comprehensive review on effect of hydrostatic pressure on the mechanical behavior and deformation processing of materials, Lewandowski et.al showed that flow stress of bcc Fe decreases with increasing superimposed hydrostatic pressure even at lower homologous temperature due to introduction of mobile dislocations [14]. The lower internal stresses partly lead to higher fracture strains. Notably, hydrostatic extrusion removes the pre-existing microcracks through plastic flow and crack face bonding. Hydrostatic extrusion produces shear dominated texture components in the radial direction of the tube, rather than the extremely brittle {001}<111> texture components formed during hot-cross rolling. TEM and OIM show higher population of dislocations as well as tough (not cleavage prone) low angle boundaries in hydrostatically extruded tube. These results suggest that fabrication of delicate components from an intrinsically brittle material is possible, perhaps even at lower temperature.

Summaries

- Extrusion produces an inhomogeneous microstructure along with elongated grains slightly elongated in the extrusion direction.
- Extrusion produces a mix of <111> and <100> in the ND direction and a moderate intensity of <110> α-fiber in the extrusion direction. The dominant texture components in ND are {110}<111> and {110}<001>.
- Hot–cross-rolling produces a grain structure that appears equiaxed on the surface ND section views of the plate and elongated in both the hot-cross-rolling (CR) and extrusion (ED) directions. The pancake shaped grains are accompanied by numerous microcracks.
- Hot cross-rolling completely transforms <111> and <100> ND texture to <100> ND texture, in addition increases strength of the α-fibers along the extrusion direction and produce a broken α-fiber in the cross-rolling direction.
- The intrinsic brittleness of the hot-cross-rolled plated is originated due to the presence of high volume fraction of {001}<110> brittle texture components and microcracks that nucleate and propagate at the sessile low angle {001} sub boundaries.
- The top surface of the hot-cross-rolled plate exhibits a low population of low angle grain boundaries and high population of Σ13b (27.96 ° misorientation angle- <111> misorientation axis) boundaries.
- Hydrostatic extrusion eliminates microcracks by providing a shear dominated deformation in the through thickness direction of the tube. The texture in the radial direction of the tube transforms to <111> from <100> ND texture of the hot cross-rolled plate, with shear texture components of {110}<111> and {110}<001>.

Acknowledgments

We thankfully acknowledge the support provided by U.S. Department of Energy through the Office of Fusion Energy Sciences (DE-FG03-94ER54275) and the Fuel Cycle Research and Development Program via a subcontract from Los Alamos National Laboratory (LANL8-442550-59434). The U.S. National Science Foundation supported California Nanoscience Institute provided facilities critical the success of this research.

References

[1] G. R. Odette, "Recent Progress in Developing and Qualifying Nanostructured Ferritic Alloys for Advanced Fission and Fusion Applications," *JOM,* vol. 66, no. 12, pp. 2427-2441, 2014.

[2] M.E.Alam, S.Pal, K.Fields, S.A.Maloy, D.T.Hoelzer, G.R.Odette, “Tensile deformation and fracture properties of a 14YWT nanostructured ferritic alloy”, *Mater. Sci. Engg. A*, vol. 675, pp. 437- 448, 2016.

[3] S. Pal, M.E. Alam, G. R. Odette, D. T. Hoelzer and S. A. Maloy (LANL) ”Characterization of the Microstructure and Texture of NFA-1 for Two Deformation Processing Routes”, *Fusion Reactor Materials Program*, DOE/ER-0313/58, pp. 66-82, 30 June 2015.

[4] S. Pal, M.E. Alam, G. R. Odette,” Texture Evolution and Microcracking Mechanisms in As Extruded and Cross Rolled Conditions in a 14YWT Nanostructured Ferritic Alloy”, Manuscripts under preparation.

[5] S. Pal, M. E. Alam, G. R. Odette, S. A. Maloy, D. T. Hoelzer, J.J. Lewandowski “Microstructure, Texture and Mechanical Properties of the 14YWT Nanostructured Ferritic Alloy” 10.1007/978-3-319-51097-2_4. In book: *Mechanical and Creep Behavior of Advanced Materials*, Edited by I.Charit, pp.43-54, 2017..

[6] E. Aydogan, S. Pal, O. Anderoglu, S. A. Maloy, S. C. Vogel, G. R. Odette, J. J. Lewandaski, D. T. Hoelzer, I. E. Anderson and J. R. Rieken, "Effect of tube processing methods on the texture and grain boundary characteristics of 14YWT nanostructured ferritic alloys," Materials Science and Engineering: A, vol. 661, pp. 222-232, 2016.

[7] F. Bachmann, R. Hielscher, H. Schaeben, “Texture analysis with MTEX-Free and open source toolbox” Solid Phenomena, vol. 160, pp. 63-68, 2010.

[8] J.K. Mackenzie, “Second Paper on Statistics Associated with the Random Disorientation of Cubes”. Biometrika, vol. 45, pp. 229, 1958.

[9] J.R. Yang , H.K.D.H. Bhadeshia, "Dislocation density determination in acicular ferrite steel welds " Welding Research Supplement, pp. 305S–307S, 2014.

[10] A. H. Cottrell, "Theory of brittle facture in steel and similar metals.," *Trans. Metallurgical Soc. AIME,* vol. 212, pp. 192-203, 1958.

[11] M. L. Hribernik, G. R. Odetter and M. Y. He, "On the intrinsic initiation and arrest cleavage fracture toughness of ferrite," *DOE- Fusion Semianual Report,* vol. 40, pp. 74-79, 30 June 2006.

[12] G. R. Odette, H. J. Rathbun, M. Hribernick, T. Yamamoto and M. He, “A multiscale approach to measuring and modeling cleavage fracture in structural steels”, in *Materials Issues for Generation IV Systems*, pp. 203-226, 2008.

[13] J. L. RAPHANEL’ and I. Van-Houte, "Simulation of the rolling texture of BCC metals by means of relaxed Taylor theory," Acta Materialla, vol. 33, no. 8, pp. 1481-1488, 1985.

[14] J.J. Lewandowski & P. Lowhaphandu, “Effects of hydrostatic pressure on mechanical behaviour and deformation processing of materials," International Materials Reviews, vol. 43, no. 4, pp. 145-187, 1998.

2.2 ANNEALING TREATMENTS TO HEAL MICROCRACKS IN 14YWT NFA-1 AND THEIR EFFECTS ON MICROSTRUCTURAL AND MECHANICAL BEHAVIOR

—M.E. Alam, S. Pal, D. Gragg, K. Fields, N. J. Cunningham, G. R. Odette (University of California, Santa Barbara), D. T. Hoelzer (Oak Ridge National Laboratory) and S. A. Maloy (Los Alamos National Laboratory)

OBJECTIVE

The objective of this study is to understand the effect of annealing at varying times and temperatures on micro crack healing and the corresponding effects on microstructural and mechanical properties of a 14YWT nanostructured ferritic alloy.

SUMMARY

The FCRD NFA-1 is a larger heat of 14YWT nanostructured ferritic alloy (NFA) produced by ball milling FeO with argon atomized Fe-14Cr-3W-0.35Ti-0.25Y powders, followed by hot extrusion (850 ºC), annealing and cross-rolling, both at 1000 ºC to form ≈ 10 mm thick plate. As-fabricated NFA-1 exhibits unusually good in-plane isotropic properties with a near-record strength-toughness combination at lower temperatures, due to pre-existing micro cracks that form multiple delaminations upon deformation. However, tensile testing in short thickness direction (S) results in elastic regime, with a flat, faceted fracture surface, due to the micro cracks that run normal to its loading direction. A series of high temperature anneals from 1100 to 1300 ºC, each for 1 and 5 h have been carried out to understand their effect on microstructure and mechanical properties, both in- and out-of-plane orientations.

PROGRESS AND STATUS

Introduction

The nanostructured ferritic alloys (NFAs), a variant of oxide dispersion strengthened (ODS) steels, are a promising candidate alloy class for the advanced nuclear fission and future fusion reactor applications in extremely hostile, chemically aggressive environment due to their high tensile, fatigue and creep strengths over a wide range of temperature, as well as unique irradiation tolerance and outstanding thermal stability up to 900 ºC, thanks to the presence of ultrahigh number density ($\approx 10^{23}/m^3$) of 2-5 nm nano-oxides (NOs), submicron grains (≈ 500 nm) and high dislocation density ($\approx 10^{15}/m^2$) [1-3]. Recently, a 14YWT nanostructured ferritic alloy, dubbed as FCRD NFA-1, has been developed in collaboration between University of California Santa Barbara (UCSB), Oak Ridge National Laboratory (ORNL), and Los Alamos National Laboratory (LANL), and a complete set of microstructural and mechanical properties of as-fabricated NFA-1 has been conducted that can be found elsewhere [3-7]. In summary, the NFA-1 plate contains a bimodal distribution of highly textured, submicron pancake-shaped grains along with a large population of micro cracks lying in planes normal to the plate thickness direction. The micro cracks form on {001} planes and propagate in <110> directions along low angle subgrain boundaries formed during high-temperature deformation [3, 7]. In-plane (parallel to the extrusion, L or cross-rolling, T, see Figure 1) tensile tests manifest isotropic properties with high strength (0.2% yield strength up to $s_y \approx 1550$ MPa) and good ductility (≈17%) over a wide range of temperatures (-196 ºC to 800 ºC) [3, 5].

In contrast, the S-orientation (short plate thickness direction) room temperature loading exhibits much lower tensile fracture strength ($s_f \approx 700$ MPa) with a flat, cleavage facet fracture surfaces and ≈ 0% ductility [7]. Lower strength elastic fracture in the S orientation is due to the propagation of the pre-existing micro cracks by brittle cleavage. Notably, the pre-existing micro cracks act as a source of delaminations at lower temperatures that help to improve fracture toughness (K_{Jc}), either by relaxing triaxial stress in thin delaminated ligaments near the tip, or crack deflection, depending on the specimen orientation. Thus NFA-1 exhibits a near-record strength-toughness combination for iron-based alloys [3]. Nevertheless, the extensive micro crack population and texturing in the as-fabricated NFA-1 plates complicate fabrication of defect-free components, such as thin-walled cladding tubes for nuclear reactor application.

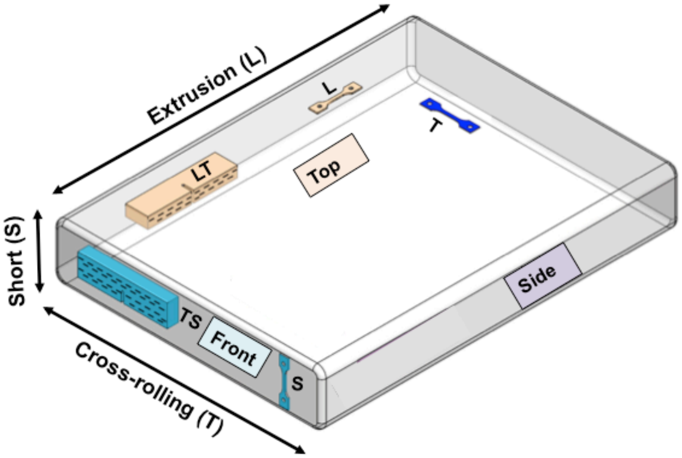

Figure 1. The specimen orientations and definition of the section views with respect to the extrusion, cross-rolling and plate thickness directions.

Cracking is generally viewed an irreversible phenomenon [8]. However, some recent studies reported that smaller cracks could be healed, at least partially, by various techniques like heat-treatment [9,10], electro pulsing [11], or thermal cycling [12]. A variety of healing mechanisms have been proposed, especially for ceramics [12-16]. However, we found very few studies (<10) that reported crack healing in metals and alloys. Proposed mechanisms include and their mentioned mechanisms crack filling by surface diffusion and, grain growth and recrystallization [9-11, 17-19]. None of these studies report on the effect of crack healing on mechanical properties, which motivate us to perform high temperature annealing for as-fabricated cracked body NFA-1. Therefore, we have carried out a series of high temperature annealing treatments from 1100 to 1300°C for times of 1 and 5h to investigate their effect on microstructure and mechanical properties.

Experimental Procedure

Details of processing of NFA-1 can be found elsewhere [4,5]. Subsized tensile and 3PB specimens from the as-fabricated plate were wrapped in a molybdenum getter foil and annealed in vacuum at 1100, 1200 and 1300 °C for 1h and 5h. Microstructural (i.e. grain size and morphology, precipitates, micro cracks, texture) and mechanical (i.e. micro hardness, tensile and fracture toughness at room and -150 ºC) characterizations were also performed on the as-fabricated and annealed specimens and details of sample preparation and characterization techniques can be found elsewhere [3-5]. Note 101, 111, 135 notations are used in some cases to represent as-fabricated or annealing condition. Here first two digits represent the annealing temperature in hundreds of ºC, and last digit represents annealing time in hours. For example 101 and 135 notations have been used for as-fabricated (1000 ºC/1h) and annealed at 1300 ºC/5h conditions, respectively.

Results

Microstructure

Figure 1 shows the section views and specimen orientations of this study. Here we use the notation of L, T and S for the extrusion (L), transverse cross rolling (T) and thickness (S) directions, respectively. The corresponding plane section directions are defining L, T and S: the extrusion section view (TS), the cross-rolling section (LS) and the thickness section (LT). Figure 2 shows SEM/FIB images of the grain structure of as-fabricated and annealed NFA-1 at different plane section views. Corresponding grain statistics are also shown in Figures 3a and b and Table 1. The as-fabricated microstructural features (including grain morphology, precipitates and crack statistics) of front (TS) and side (LS) views are nearly isotropic [3, 5]. Therefore, microstructural features in these sections are not reported individually. The average grain size was taken as d= (l+s)/2, and grain aspect ratio (GAR) as r = l/s, where l and s represent longest and shortest length of a grain, respectively. The plate face LT section is composed of nearly uniform, equiaxed and ultrafine grain morphology with bimodal distribution in all conditions. The average grain size is almost same or minimally increases (~700 nm) up to 1300 ºC/1h, and only modestly increases (~850 nm) in the 1300 ºC/5h condition. While, the average grains are still in submicron size at all conditions, some (~20%) are over the range of 1-10µm. The front TS and side LS sections are pancake-shaped and elongated in the extrusion and cross-rolling directions. GAR decreases at longer annealing time and higher temperature, and the grains are almost equiaxed in 1300 ºC/5h condition. While the average grain size does not vary significantly, the 5h anneals produce slightly larger grains than 1h at their corresponding counterpart.

Due to the large annealing matrix, nano scale Y-Ti-O nano oxides (NO, mostly $Y_2Ti_2O_7$ pyrochlore) and the coarser scale Ti/Y-rich oxinitrides were characterized, by APT, and SEM +TEM respectively, only in the 1300 ºC/1h specimens. The results are shown in Table 2, along with the corresponding as fabricated condition [4, 20]. APT shows that the average diameter of NO increases from ≈ 2.0 nm to ≈ 3.1 nm with annealing, while both the number density and volume fraction decreases (Table 2 and Figure 3c). The average particle size of Ti/Y-rich coarse precipitates also increases from ≈ 60 nm to ≈ 100 nm. As seen in Figure 3d, the entire histogram shifts towards larger sizes, with an expected decrease in number density by ≈ a factor of 2 (Table 2). These inclusions are predominantly located at, or near, grain and prior powder boundaries, in the form of stringers aligned parallel to the extrusion and cross-rolling directions (Figure 2). EELS and EDS measurements identify the inclusions as Ti-rich (Ti-N-O: darker) oxynitrides with fewer Y-rich (Y-O: gray) oxides [3, 21]. Table 2 also shows that the maximum inclusion size increases from ≈ 260 nm to ≈ 400 nm in the1300 ºC/1h condition. Post-test SEM fractographs coarser precipitates are located in ductile of dimples acting as a source of microvoid nucleation sites.

The as-fabricated NFA-1 contains a large number of micro cracks running parallel to the cross-rolling and extrusion directions and plate surfaces. As-fabricated crack statistics and micro mechanism of crack formation is reported elsewhere [3, 6-7]. In summary, extrusion followed by cross-rolling creates {100}<110> plane-direction combinations, which are a brittle cleavage system in bcc Fe. The {001}<110>-cleavage system is generated by reactions between glissile a/2<111> dislocations to form sessile a<100> dislocation stack-ups that constitute a {100} subgrain boundary. The micro cracks nucleate at dislocation pile-ups at the subgrain boundary and the leading dislocations form a nano crack opening displacement, following the theory of Cottrell [22]. Both local pile-ups and residual stresses then drive formation of µm-scale cracks at temperatures below the Fe-Cr ferrite {001}<110> cleavage system brittle to ductile transition temperature (BDTT). The number density of observed micro cracks noticeably decreases with higher annealing temperatures and longer times (see Figure 3e). For example, the 1100 ºC/1h annealing reduces the number density of observed micro cracks by a factor of ten while micro cracks are not observed following annealing at 1300 ºC at 1 and 5h. The cracks heal by vacancy migration from higher energy small radius (r) tips, due to the Gibbs Thomson 2□/r effect, where □is the surface energy, to lower energy locations along the flat sides of the cracks (r = ∞). The vacancy fluxes are exactly balanced by atom fluxes in the opposite direction. The overall healing process takes place in two steps: (a) the cracks are filled by surface and bulk or boundary diffusion leaving a large number of small micro voids; the micro voids anneal by bulk diffusion or boundary diffusion [9, 10, 19].

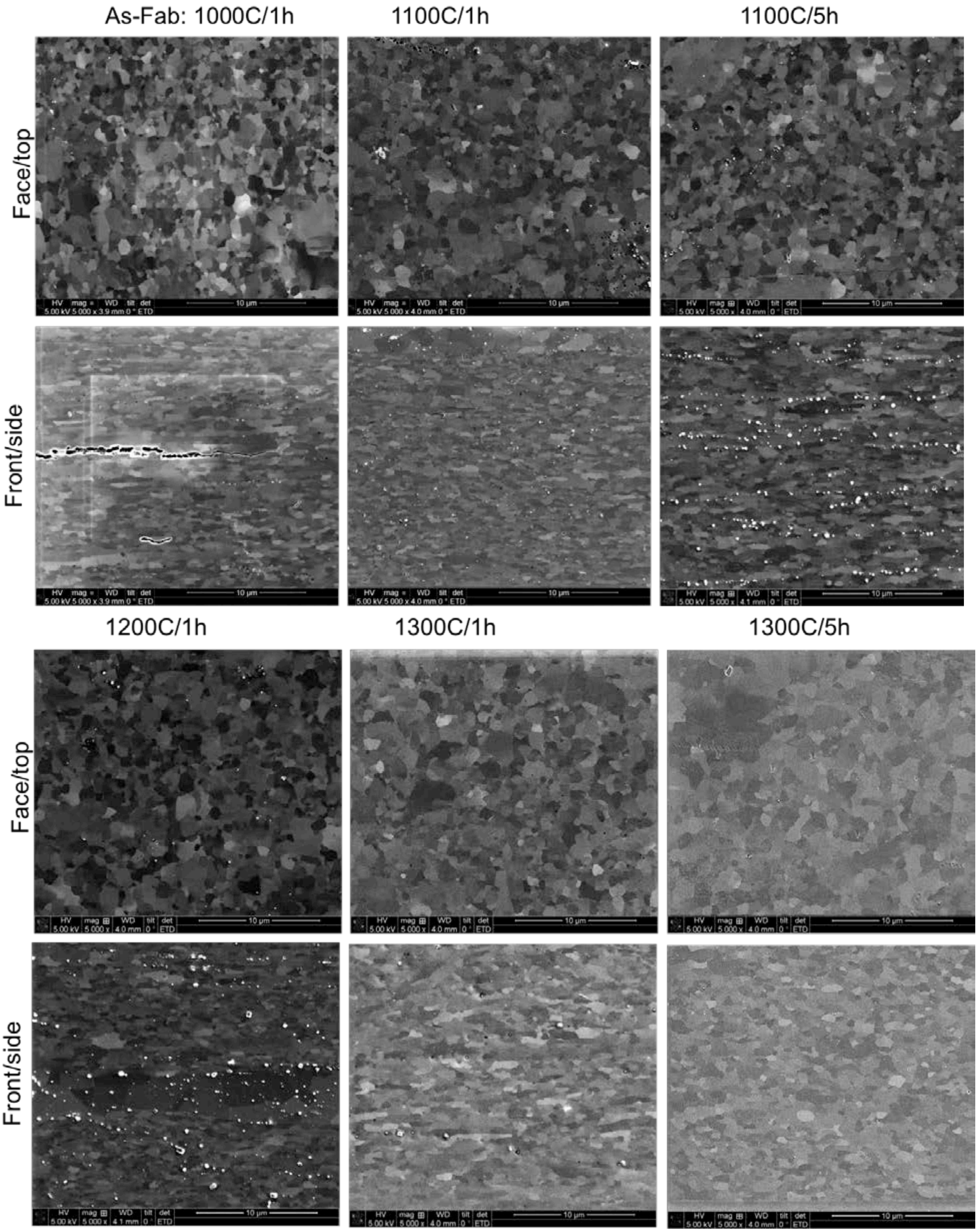

Figure 2. Different section views of the as-fabricated and annealed NFA-1

Gao et al [9] observed by in-situ TEM on BCC-Fe that as expected, the smaller and narrower cracks heal faster and at lower temperature than the wider and longer cracks, consistent with our observations. Molecular Dynamics simulation by Wei et al [17] found the crack healed by pinching off in the middle (a Raleigh-Taylor type instability), leaving pores at both initial crack tips. The simplest concept is that the healing kinetics are governed by a rate controlling diffusion coefficient D of Fe and 2□/r driving forces. Healing time scales with the crack length (l) as l^2/D. Thus smaller cracks (<10µ) heal at 1100ºC, while longer cracks only partially heal. Higher annealing temperature might further promote healing by recrystallization and grain boundary migration [9, 23]. While residual pores are present, no micro cracks were observed following the 1300 ºC anneals. However, we cannot rule-out the possibility that micro cracks still exist, even after 1300 ºC/5h anneal that are below the resolution limit of the characterization techniques that we used. Notably, EBSD IPF maps show that annealing does not alter the main texture components, although their intensity is slightly reduced at higher annealing temperatures (see Figure 4).

Table 1. Grain morphology and hardness of NFA-1

Annealing condition[*]	Long, l (µm)	Short, s (µm)	Avg, d= (l+s)/2 (µm)	Aspect ratio l/s	Microhardness, HV, (Kg/mm^2)
LT101	0.767 ± 0.566	0.517 ± 0.355	0.642 ± 0.450	1.5 ± 0.4	376 ± 18
TS101	0.799 ± 0.833	0.296 ± 0.180	0.548 ± 0.482	2.7 ± 1.3	352 ± 39
LT111	0.740 ± 0.479	0.574 ± 0.318	0.657 ± 0.385	1.4 ± 0.3	343 ± 6
TS111	0.757 ± 0.451	0.289 ± 0.171	0.523 ± 0.295	2.6 ± 1.1	364 ± 19
LT115	0.760 ± 0.433	0.639 ± 0.338	0.700± 0.361	1.3 ± 0.3	348 ± 14
TS115	0.770 ± 0.492	0.318 ± 0.149	0.544 ± 0.299	2.4 ± 1.0	348 ± 21
LT121	0.744 ± 0.547	0.593 ± 0.467	0.669 ± 0.495	1.4 ± 0.4	349 ± 13
TS121	0.765 ± 0.696	0.326 ± 0.210	0.545 ± 0.440	2.3 ± 0.8	344 ± 13
LT125	0.828± 0.516	0.623 ± 0.386	0.725 ± 0.436	1.4 ± 0.3	324 ±16
TS125	0.801 ± 0.650	0.378 ± 0.291	0.589 ± 0.450	2.2 ± 0.9	312 ± 18
LT131	0.842 ± 0.493	0.547 ± 0.285	0.695 ± 0.367	1.6 ± 0.4	294 ± 13
TS131	0.849 ± 0.544	0.354 ± 0.144	0.602 ± 0.320	2.4 ± 1.3	304 ± 17
LT135	0.979 ± 0.481	0.694 ± 0.325	0.837 ± 0.390	1.4 ± 0.4	252 ± 7
TS135	0.963 ± 0.371	0.537 ± 0.197	0.750 ± 0.266	1.8 ± 0.5	247 ± 13

[*] LT101: **10**00ºC/**1**h (As-fabricated), LT111: Annealed at **1100 º**C for **1**h, LT115: Annealed at **1100 º**C for **5**h etc.

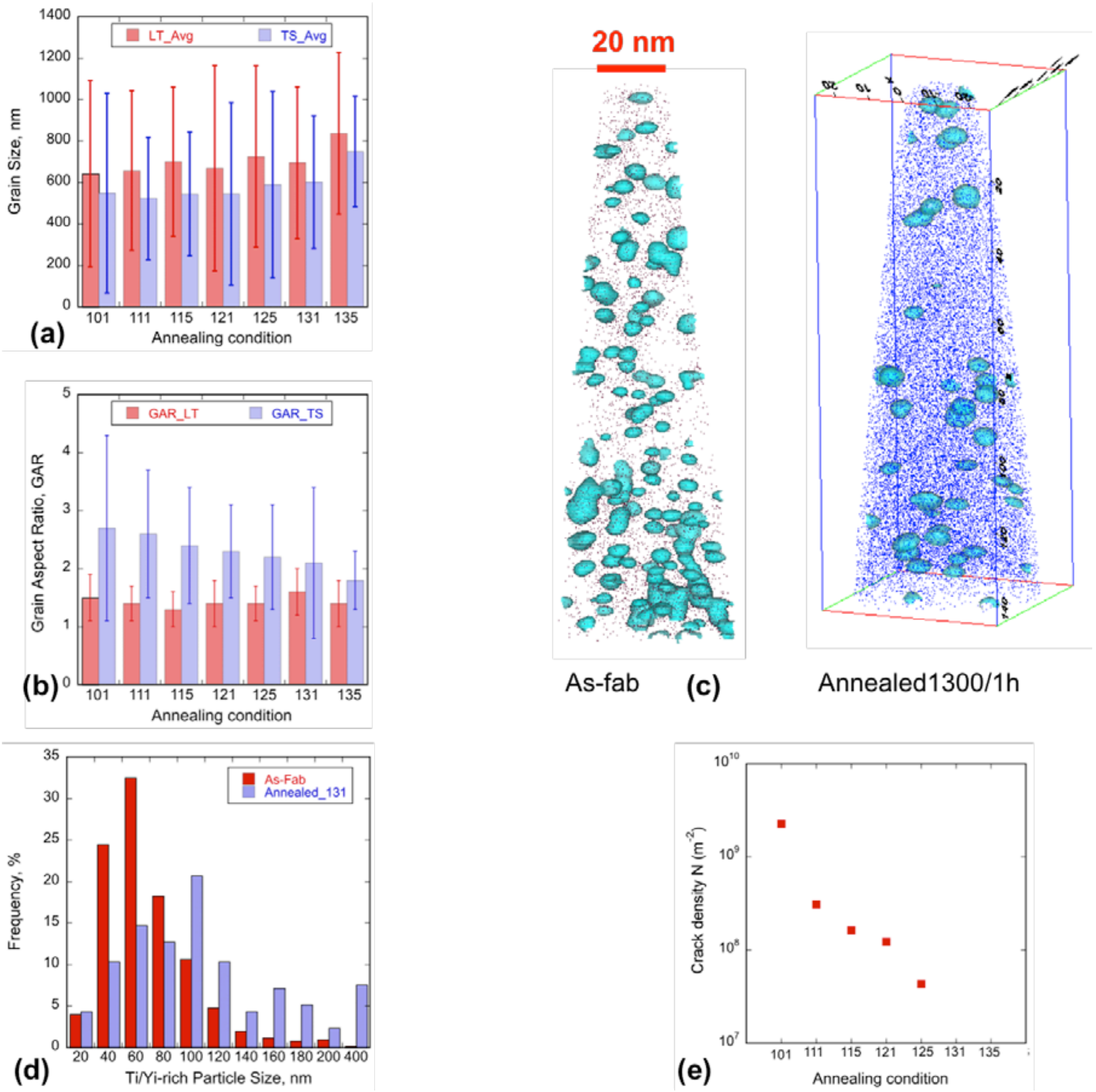

Figure 3. Images showing: (a) the average grain size, (b) the grain aspect ratio, (c) APT reconstructions for NO's, (d) the coarser Ti/Yi-rich precipitate distribution, and (e) crack density for as-fabricated and annealed conditions.

Table 2. Nano-oxide (NO) and Ti/Y rich precipitates of NFA-1

Condition	NO's dia (nm)	Number density (m^{-3})	Volume fraction (%)	Ti/Y rich particle size (nm)	Density (m/m^{-3})
As-Fab	2.0	6.9 x 10^{23}	0.74	Dia: 57 ± 33 Range: 10-262	9.8 x 10^{11}
Annealed (1300 ºC/1h)	3.1	2.2 x 10^{23}	0.38	Dia: 98 ± 63 Range: 11-405	4.4 x 10^{11}

Microhardness

Vicker's microhardness (H_v) data for the as-fabricated and annealed NFA-1 are summarized in Tables 1 and Figure 5a. H_v averages 376 ± 18 (kg/mm^2) and 352 ± 39 (kg/mm^2) on the face and side sections, respectively, and can be considered nearly the same. Hardness remains almost unchanged up to 1200 ºC/1h and then starts to decrease, dropping ≈ 30% following the 1300 ºC/5h anneal. Softening is due to coarsening of the NOs and the grains (Tables 1 and 2). The hardness variation among different sections is negligible for the annealed conditions.

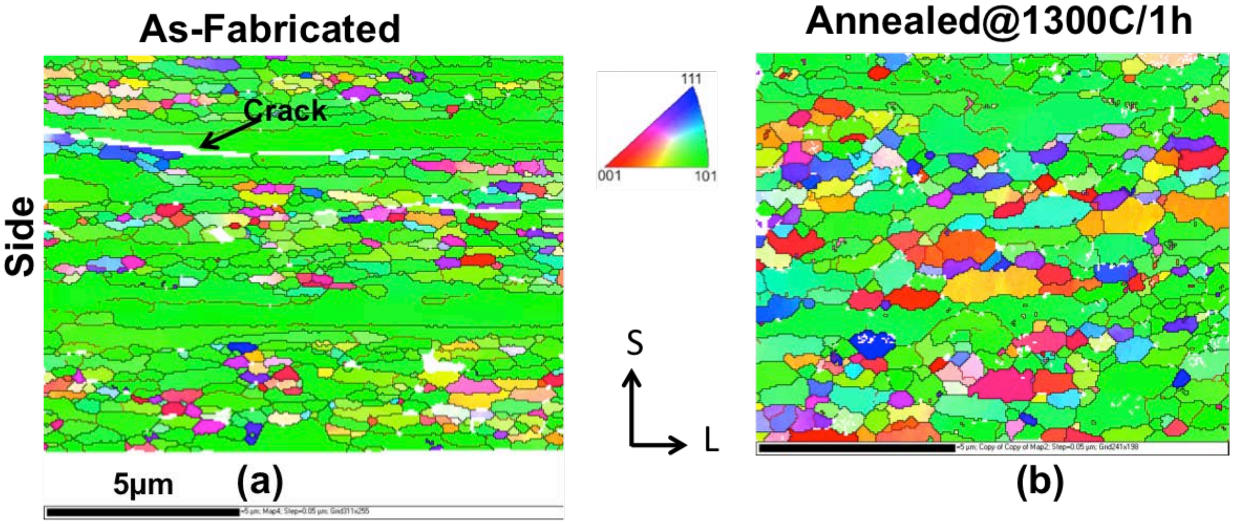

Figure 4. EBSD inverse pole figure (IPF) maps showing strong <110> texture along the extrusion direction for (a) as-fabricated, and (b) annealed 1300 ºC/1h conditions. Note, the annealed condition shows more random textures.

Tensile Properties

Figure 6 shows engineering stress-strain s(e) curves for as-fabricated and annealed in-plane (L) and out-of-plane (S) tensile specimens tested at room temperature and -150 ºC. The 0.2% yield stress (s_y), ultimate tensile (or fracture) stress ($s_{u/f}$), and total elongation (e_t) values are plotted in Figures 5b, c and d, respectively, and summarized in Table 3, along with the uniform elongation (e_u) and reduction of area (RA). The room temperature strength properties for the L-orientation decrease only slightly for anneals for up to 1200 ºC/1h (s_u ≈ 1133 - 1071 MPa). Significant softening begins at 1200 ºC/5h and is largest for the 1300ºC/5h condition (s_u ≈ 884 MPa). These results correlate with the corresponding microhardness trends. The various measures of ductility for the L-orientation are largely unaffected by annealing (Tables 1 and 3).

In contrast, annealing does have a large effect of the strength properties for the S-orientation room temperature tests. However the s_y is significantly lower (600 - 720 MPa) compared to the L-orientation (1042 - 770 MPa). However, even the lowest temperature and shortest time anneal (111) increases the total elongation relative to the as-fabricated condition (101). Note some specimens yielded earlier, with a lower s_y/s_u ratio, and fractured by shear. The S-orientation tests also show very scattered results in some cases. The S-orientation ultimate stress, s_u, of annealed varies between ≈ 750 and 920 MPa, which is slightly higher compared to as-fabricated condition (≈ 730 MPa). The total ductility, e_t, increases from ≈ 0% (elastic fracture, E) to ≈ 4% following 1200ºC/5h annealing and then jumps to ≈ 18% and 21% for 1300ºC/1h and 5h, respectively (Table 3 and Figures 5d and 6b). The L and S-orientation s_y and s_u are comparable to L-loading after the 1300ºC anneals. Although annealing partially heals micro cracks, some larger micro cracks (>40 μm) are still also observed up to the 1200ºC/5h anneal, and are likely the cause of the lower ductility. In contrast no micro cracks were found for the 1300 ºC/1 and 5h anneals, resulting in high room temperature S-orientation ductility.

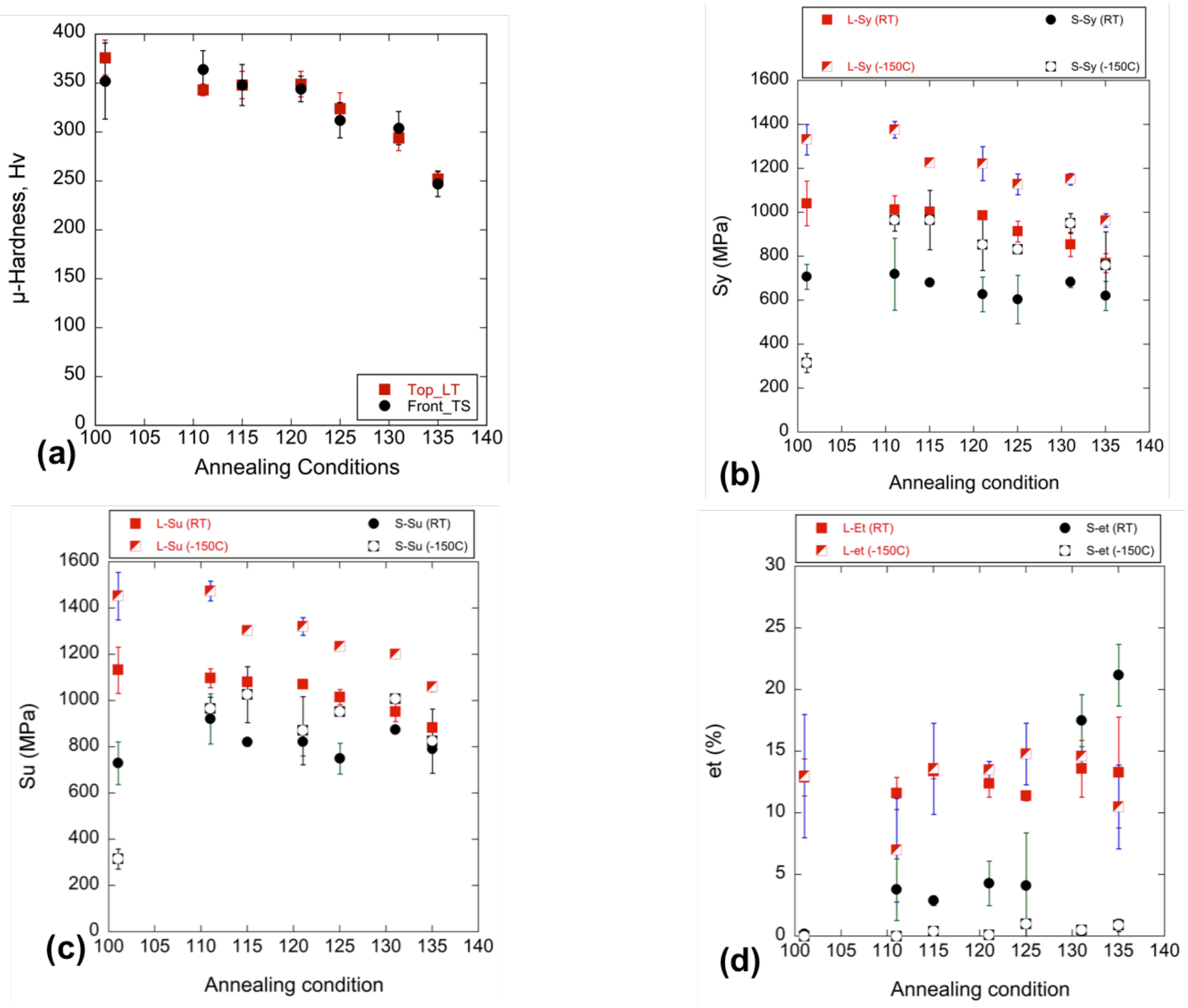

Figure 5. Data trends as a function of specimen L vs. S orientation, test temperature, and annealing condition: a) microhardness; and tensile test results; for b) the 0.2% yield stress, s_y; c) the ultimate tensile stress, s_u; and, (d) the total elongation, e_t.

Low temperature (-150 ºC) L-orientation tests show a very large increase in s_y and s_u between the as-fabricated and lowest time and temperature anneal. However, following this initial improvement in properties, both s_y and s_u decrease with annealing time and temperature, roughly following the pattern in the RT S-orientation and all L-orientation tests. However, as expected, the -150ºC strength properties increase by ≈ 22 - 36% compared to RT tests. Surprisingly, the average e_t = 10.5 - 14.8% is also generally larger or equal to the respective room temperature values (except 1100 ºC/1h, e_t = 7 ± 4%). The reduction of area (RA) remains ≈ 50 ± 10 % for all annealing conditions and test temperatures. In sharp contrast, as-fabricated S-tensile loading at -150ºC shows much lower strength than its room temperature counterpart (s_u ≈ 316 vs 730 MPa). All the annealing treatments increase then S-orientation -150ºC strength significantly compared to the as-fabricated condition, although the fracture remains elastic in all cases, with total elongations ≤1%. Annealing increases the s_y by ≈ 150 - 200%, and the increment for s_u is even larger (up to ≈ 230%). The tensile strength, s_u is ≈ 850 -1000 MPa up to the 1300ºC/1h anneal. The lowest -150 °C S-orientation strength is in the 1300 ºC/5h annealed condition (s_y ≈ 760 MPa, s_u ≈ 825

MPa). These complex trends at -150°C can be readily qualitatively understood in terms of the competition between the softening and crack healing which increases the cleavage fracture strength.

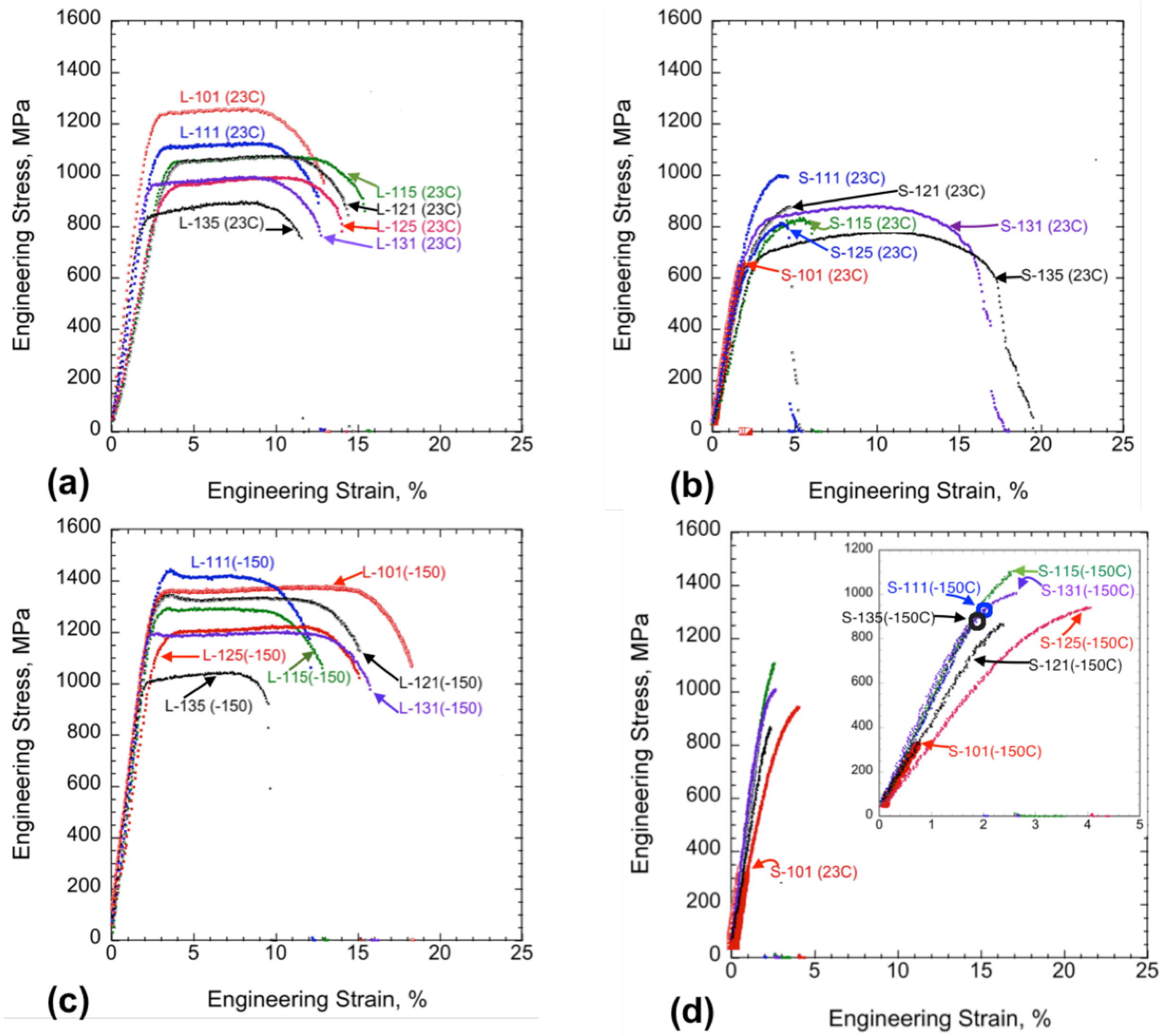

Figure 6. Engineering stress-strain curves for different annealing conditions: a, and b) L and S-orientations at RT; c and d) L and S-orientations at -150 ºC.

Table 3. Room and -150 ºC temperature tensile test results of NFA-1 specimens at different annealing conditions

Annealing Condition	**Test Condition**		**s_y (MPa)**	**s_u (MPa)**	**e_u (%)**	**e_t (%)**	**RA (%)**
1000 ºC/1h	23C	L	1042± 102	1133±100	3.8±3.7	12.9±1.5	56 ± 8
		S	708± 57	730± 92	0.2 ±0.3	0.2±0.3	4 ± 2
	-150C	L	1332 ± 69	1453 ± 103	6 ±6.5	13 ±5	50 ± 4
		S	316 ± 43	316 ± 43	0	0 (E)	0
1100 ºC/1h	23C	L	1013±64	1098±41	6.1 ± 0.8	11.6 ± 1.3	56 ± 8
		S	720 ± 164	922 ± 108	3.8 ± 2.5	3.8 ± 2.5	7 ± 1
	-150C	L	1377 ± 38	1475 ± 43	0.9 ± 0	7 ± 4.2	42 ± 11
		S	966 ± 50	966 ± 50	0	0	0
1100 ºC/5h	23C	L	1004 ± 5	1081± 8	6.8±0.2	13.4±0.6	48
		S	682 ±18	821± 17	1.9± 0.5	2.9±0.4	16 ±1
	-150C	L	1227 ±1	1304±13	5.1 ±3	13.6 ±3.7	47 ±0.3
		S	966±135	1027 ±121	0.4 ± 0.1	0.4 ± 0.1	4 ± 1
1200 ºC/1h	23C	L	987 ± 15	1071±8	7.1±1.1	12.4±1.1	51
		S	628 ± 79	823 ± 61	2.4 ± 1.7	4.3 ± 1.8	9
	-150C	L	1223±77	1322±38	3.7±3.8	13.5±0.7	48±4
		S	853 ± 116	871 ± 147	0.1 ± 0.2	0.1 ± 0.2	4
1200 ºC/5h	23C	L	914 ± 47	1016± 33	7.2 ±1.1	11.4±0.4	48
		S	605 ± 110	750 ± 67	2.1 ± 1.4	4.1 ± 4.3	23
	-150C	L	1129 ± 47	1234 ±9	8.1±0.1	14.8±2.5	46±2
		S	833 ± 21	953 ± 15	1 ±0.1	1±0.1	7
1300 ºC/1h	23C	L	855 ± 55	953 ± 43	7.5 ± 1.5	13.6 ± 2.3	55 ± 5
		S	683 ±24	874 ±8	8.1 ±1.3	17.5 ±2.1	54 ± 1
	-150C	L	1152 ± 26	1201 ± 4	8.4 ± 0.3	14.6 ± 0.8	48 ± 0
		S	951 ± 45	1008 ± 1	0.5 ± 0.4	0.5 ± 0.4	7 ± 1
1300 ºC/5h	23C	L	770 ± 43	884 ± 19	8.1 ± 3	13.3 ± 4.5	51 ± 9
		S	621 ± 66	791 ± 16	10.7 ± 4.0	21.2 ± 2.5	58 ± 6
	-150C	L	964 ± 30	1060 ± 20	7.5 ± 3.3	10.5 ± 3.4	44 ± 9
		S	760 ± 153	826 ± 139	0.9 ± 0.5	0.9 ± 0.5	6 ± 1

Figure 7 shows low magnification SEM fractographs for the as fabricated and all annealed conditions for tests at RT and -150 ºC for both the L- and S-orientations. Higher magnification SEM fractographs are shown in Figure 8 for the as-fabricated and 1300 ºC/1h annealed conditions. The fracture surfaces for the L orientation show less delamination and a shift to more uniform in-plane microvoid coalescence dimple fracture with increasing annealing time and temperature. Crater-like features are also observed in the fractographs. The size of these craters increases with higher time-temperature annealing as they nucleate on coarsened Ti/Y-rich inclusions. The S tensile specimen tested at RT that fails in a complete brittle elastic manner, with almost no ductility, shows very flat, shiny cleavage fracture surface (see Figures 7 and 8). Upon loading, the pre-existing micro cracks that run perpendicular to the loading direction propagate by brittle cleavage. Annealing improves S-orientation RT ductility, marked by increasing amounts of dimple features. The very high ductility for the 1300 ºC annealed condition is associated with fully ductile dimple fracture (see Figures 7 and 8). Another distinguished observation of annealing effect can be seen on the side-surfaces of room temperature S-orientation post-test shown in Figure 8 (bottom-left for as-fabricated and bottom-middle for 1300 ºC/1h). In both cases, loading direction is horizontal. The red arrows show large side surface cracks normal to the loading direction, while no side cracks observed in the annealed specimen. In contrast, the -150 °C fracture surfaces S tensile fractographs in that far right micrographs are relatively featureless, as all of them failed ≤1% by predominantly cleavage fracture. Only a small amount of dimpling is observed for higher temperature annealing (see bottom-right of Figure 8).

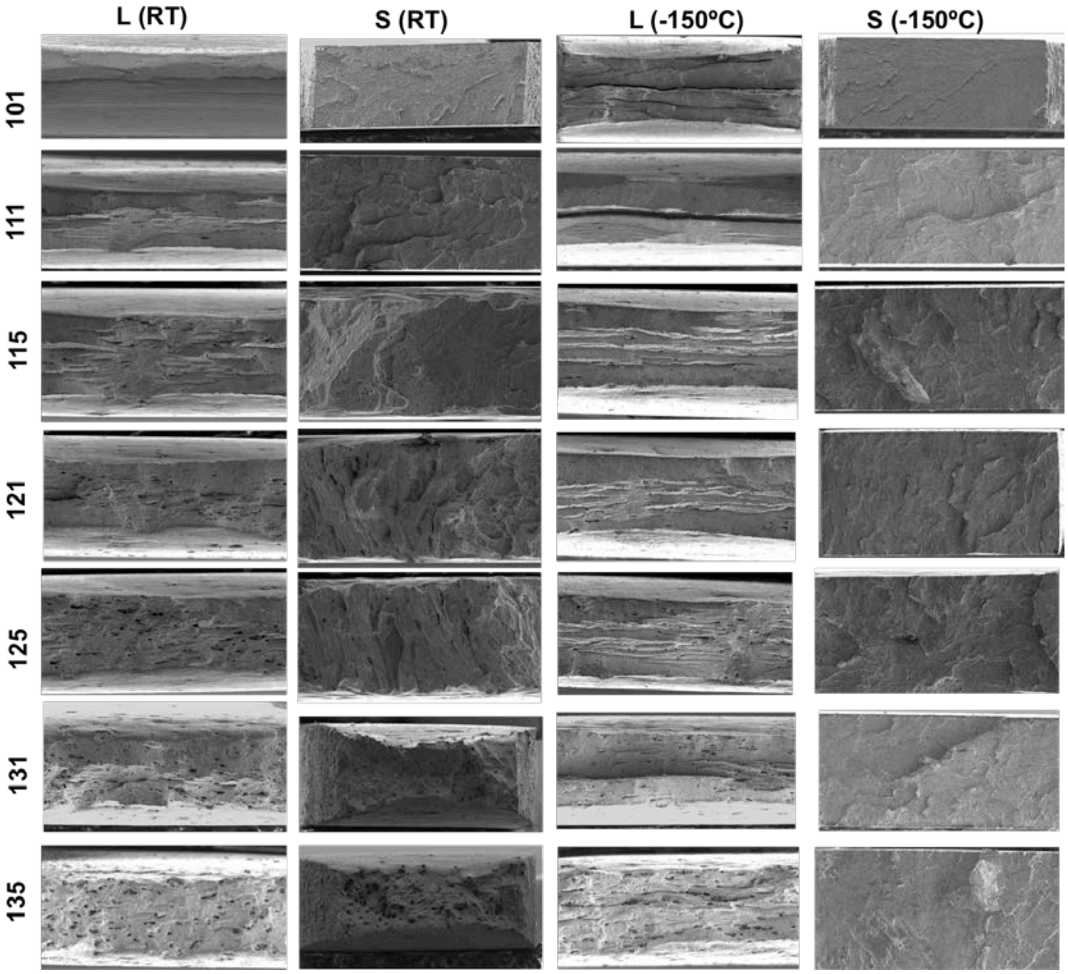

Figure 7. Low magnification SEM images of the L and S-orientation tensile fracture surfaces for different annealing conditions. Codes 101= 1000 ºC/1h (as-fab), 111= 1100 ºC/1h, 115= 1100 ºC/5h etc.

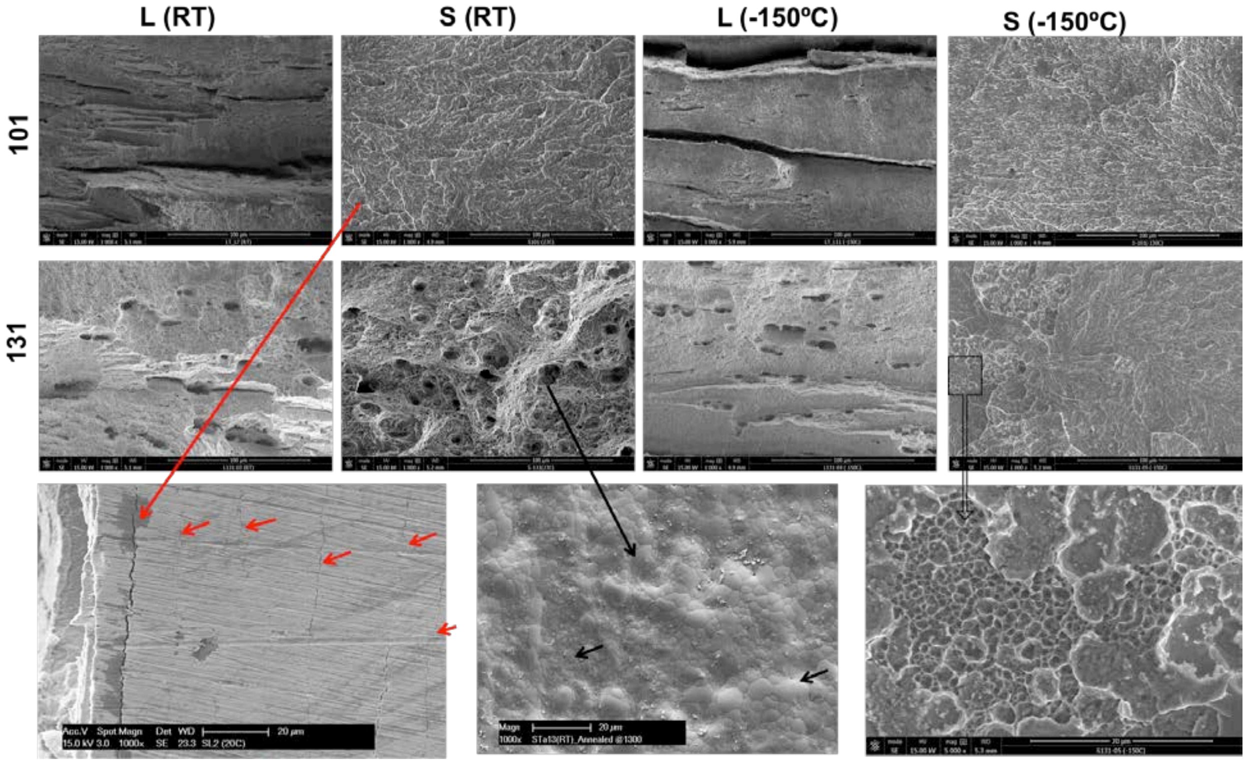

Figure 8. SEM fractographs of as-fabricated (101) and annealed at 1300ºC/1h (131) tensile specimens tested at room temperature and -150 ºC for L and S orientations.

Fracture toughness

The RT fracture toughness tests were conducted on in-plane (L-T) and out-of-plane (T-S) oriented as-fabricated and for all of the annealed conditions. Corresponding low temperature (-150 ºC) toughness tests were only conducted for the as-fabricated and 1300 ºC/1h annealed conditions. Note, L-T and T-S notations have been used to represent 3PB specimens, whereas LT and TS notations are used to represent planes. Representative load-displacement (P-Δ) curves that are normalized to a/W=0.5, for better intercomparisons, are shown in Figure 9. The maximum load fracture toughness, K_{Jc}, is summarized in Table 4 and also plotted in Figure 10a. Corresponding low magnification SEM fractographs are shown in Figure 10b. The P-Δ curves show a series of pop-ins especially for the T-S orientation, where they are larger. Otherwise the load drops with increasing Δ, following the maximum load (P_{max}) that marks the initiation of stable crack growth with strong resistance curve behaviour. The T-S-orientation is significantly tougher (K_{Jc} ≈ 123-168 MPa√m) than the L-T-orientation (70-115 MPa√m) both for the as-fabricated and annealing conditions at RT, except perhaps for 1300 ºC/5h that have similar toughness (≈ 82-88 MPa√m). in both orientations. The higher toughness T-S specimens are due to crack deflections ~ 90º from its initial direction by a delamination, analogous to mode II crack propagation (Figure 10b). Further details of the crack deflection mechanism can be found elsewhere [3].

Figure 10b shows that the delamination frequency decreases with increasing annealing time and temperature for both the L-T and T-S orientations at RT. Delamination's are rare or do not occur for the L-T orientation above 1250 ºC and 1 h (T-S) and 5 h (L-T). However considering the large scatter annealing does not appear to have a significant and systematic effect on K_{Jc} in either orientation at RT. Annealing partly or fully heals micro cracks. Hence the modest effect on toughness is a bit surprising. However, this may be due to a competition between a decrease in delamination toughening mitigated by a corresponding increase due to the lower strength of the annealed. Further since the texture does not change, and the brittle {100}<110> plane-direction cleavage system remains, the observed toughness require micro cracks in the absence of delaminations. Note, the crack deflection mechanism for similar ODS alloys, has been reported in cases that did not mention pre-existing micro cracks [24-26]. Note the L-T and T-S K_{Jc} is similar for 1300 ºC/5h annealed condition (Figure 10b). The corresponding SEM fractographs do not show any delamination for the L-T and minimal to no crack deflection for the T-S orientations. This suggests nearly complete crack recovery. The smooth P-Δ curve for 1300 ºC/5h also support this conclusion.

The low temperature -150 °C toughness tests result in delamination's in both the as-fabricated and 1300 ºC/1h annealed conditions, although they are fewer in the latter case. Again there is not an apparent strong effect of annealing on K_{Jc}.

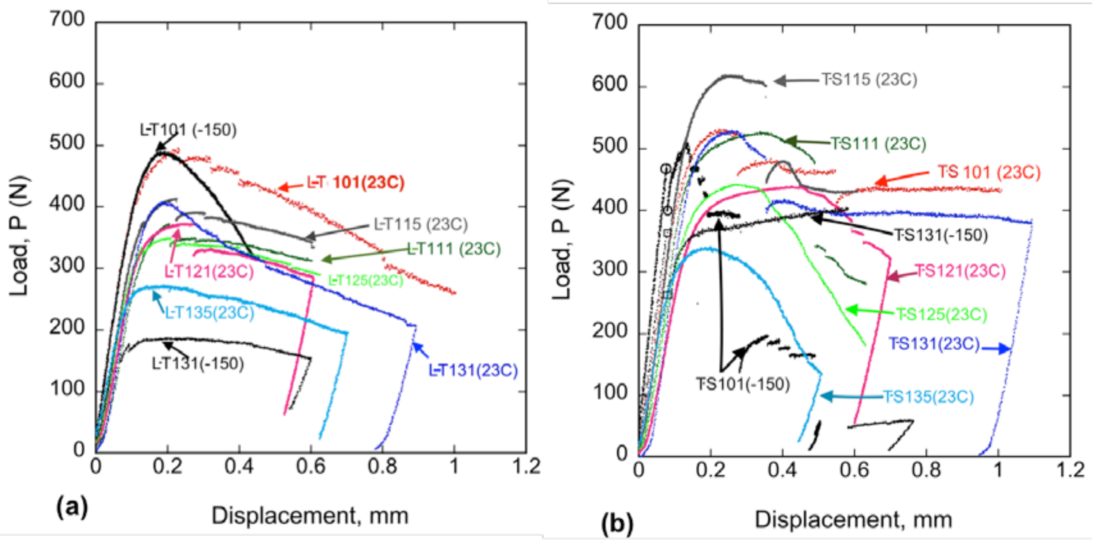

Figure 9. Normalized (a/W=0.5) P-Δ curves for 3PB toughness tests for the various annealing conditions: a) L-T and b) T-S orientations.

Table 4. Fracture toughness (K_{Jc}) of NFA-1 for different annealing conditions

Annealing Condition	**Test Temperature (ºC)**	**L-T: K_{Jc} (MPa√m)**	**T-S: K_{Jc} (MPa√m)**
1000 ºC/1h	23	88 ± 12	140 ± 21
	-150	79 ± 23	82 ± 10
1100 ºC/1h	23	79 ± 10	126 ± 31
1100 ºC/5h	23	98 ± 7	121 ± 8
1200 ºC/1h	23	115 ± 12	168 ± 1
1200 ºC/5h	23	74 ± 24	123 ± 1
1300 ºC/1h	23	70 ± 1	143 ± 52
	-150	69 ± 57	128 ± 81
1300 ºC/5h	23	82 ± 11	88 ± 14

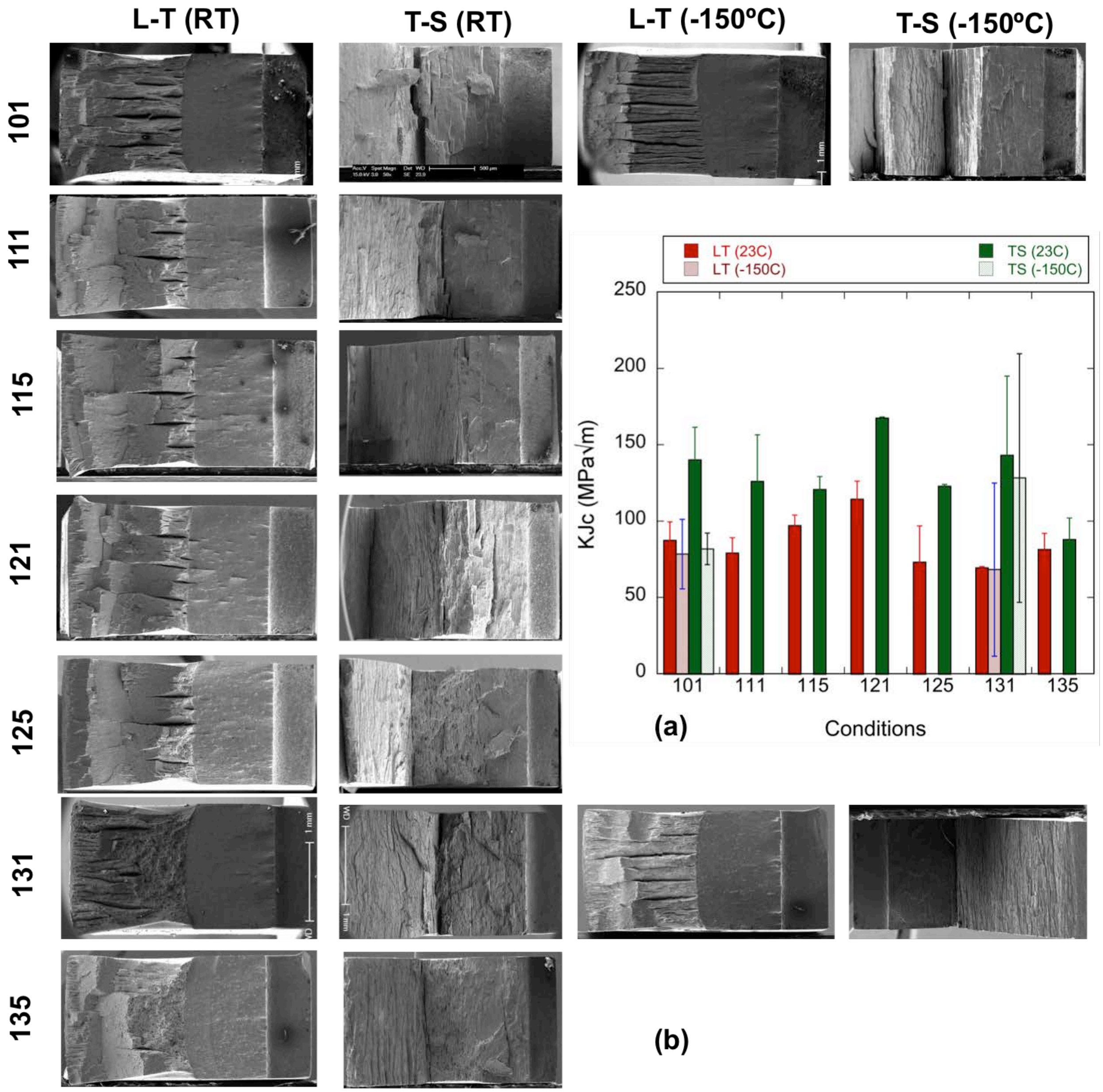

Figure 10. 3PB toughness tests: a) maximum load toughness, K_{Jc}, for different annealing conditions; and, b) corresponding representative SEM fractographs.

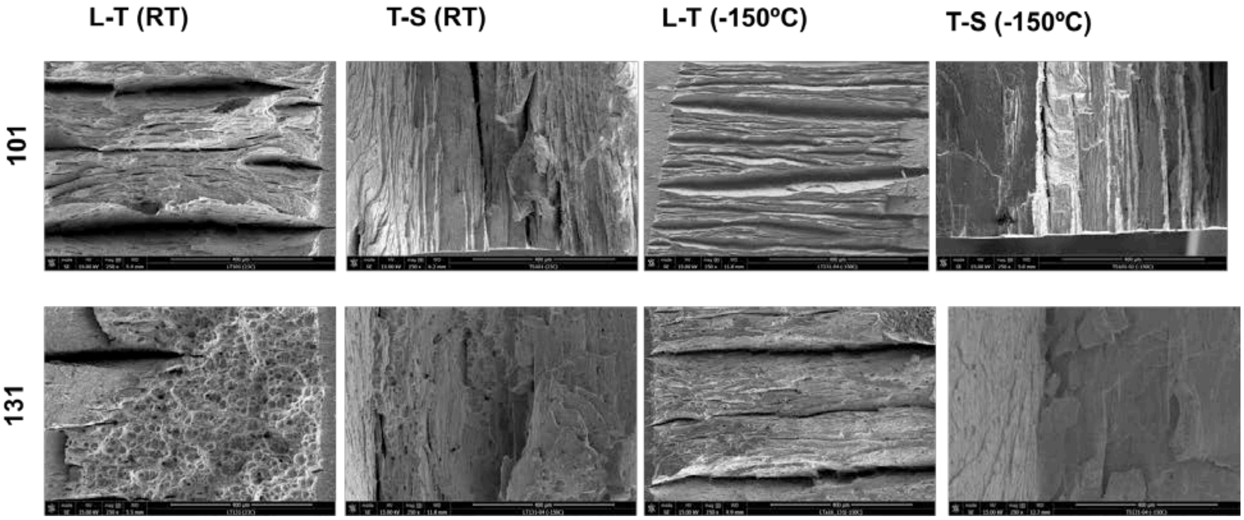

Figure 11. Selected high magnification SEM fractographs of as-fabricated (101) and 1300 ºC/1h (131) annealed 3PB toughness specimens tested at room temperature and -150 ºC for the L-T and T-S orientations.

Conclusions and Future Works

Time-temperature annealing studies show that micro crack healing begins for anneals at 1100 °C/1h, increasing with time and temperature, until near completion at 1300 ºC/5h. The grain sizes do not change much up to 1200 ºC but increase slightly beginning at 1300 ºC. The NO's and coarser Ti/Y-rich precipitate follow similar coarsening trends. Microhardness decreases noticeably at 1200 ºC/5h and above, and is lowest for the 1300 ºC/5h anneal. The tensile strength properties for the L-orientation decrease with annealing time and temperature, without a significant change in ductility. In contrast, annealing improves tensile strength properties for the S orientation at room temperature, and especially at a low temperature of -150 °C with strength up to ≈ 230%. The RT temperature tensile ductility for the S-orientation also increases from ≈ 0% for as-fabricated condition to ≈18-21% for 1300ºC-annealed condition. Deformation mechanisms also evolve from delamination dominated towards classical microvoid coalescence ductile dimple formation with higher annealing temperatures and longer times. Microstructural and mechanical results are more isotropic at 1300 ºC condition. Future work will include creep studies to help determine optimal annealing conditions.

Acknowledgments

We thank our UCSB colleagues Takuya Yamamoto, and Yuan Wu, for their important contributions to this work. We also acknowledge the support provided by U.S. Department of Energy through the Office of Fusion Energy Sciences (DE-FG03-94ER54275) and the Fuel Cycle Research and Development Program via a subcontract from Los Alamos National Laboratory (LANL8-442550-59434). The U.S. National Science Foundation supported California Nanoscience Institute provided facilities critical to the success of this research.

References

[1] G.R. Odette, "Recent progress in developing and qualifying nanostructured ferritic alloys for advanced fission and fusion applications," JOM. 66 (2014) 2427.
[2] S.J. Zinkle, G.S. Was, "Materials challenges in nuclear energy", Acta Materialia, 61 (2013) 735-758.
[3] M.E. Alam, S. Pal, S.A. Maloy, G.R. Odette, "On delamination toughening of a 14YWT nanostructured ferritic alloy", Acta Materialia, 136 (2017) 61-73.

[4] N.J. Cunningham, Y. Wu, G.R. Odette, D.T. Hoelzer, S.A. Maloy, " Characterization of a larger best practice heat of 14YWT in annealed powder, HIP consolidated and extruded forms", Fusion Materials Semiannual Progress Report for Period Ending June 30, 2013, DOE/ER-0313/54, U. S. Department of Energy, 15.

[5] M.E. Alam, S. Pal, K. Fields, S.A. Maloy, D.T. Hoelzer, G.R. Odette, "Tensile deformation and fracture properties of a 14YWT nanostructured ferritic alloy" Materials Science & Engineering A 675 (2016) 437–448.

[6] S. Pal, M. E. Alam, G. R. Odette, D. Hoelzer and S. Maloy, " Microstructure, texturing, microcracking and delamination behavior of NFA-1", DOE/ER-0313/58 (2015), DOE Fusion Reactor Materials Program Semiannual Progress Report, 58 (2015) 66-82.

[7] S. Pal, M.E. Alam, G.R. Odette, S.A. Maloy, D.T. Hoelzer, J. Lewandowski, "Microstructure, texture and mechanical properties of the 14YWT nanostructured ferritic alloy NFA-1", in: I. Charit, et al. (Eds.), Mechanical and Creep Behavior of Advanced Materials Ch 4, Springer, (2017) 43-54.

[8] A. Griffith, Phenomena of rupture and flow in solids, Philos. Trans. R. Soc. Lond. Ser. A 221 (4) (1920) 163–198.

[9] K.W. Gao, L.J. Qiao, and W. Y. Chu, "In situ TEM observation of crack healing in □α-Fe", Scripta Materialia, 44 (2001) 1055-1059.

[10] D. Wei, J. Han, Z.Y. Jiang, C. Lua, A.K. Tieu, "A study on crack healing in 1045 steel", Journal of Materials Processing Technology 177 (2006) 233–237.

[11] Y. Zhou, J. Guo, M. Gao, G. He, "Crack healing in a steel by using electropulsing technique", Materials Letters 58 (2004) 1732–1736.

[12] R.U. Vaidya, A.K. Zurek, A. Wolfenden, M.W. Cantu, "Strength and Modulus of a Molybdenum-Coated Ti-25Al-10Nb-3V-1Mo Intermetallic", Journal of Materials Engineering and Performance, JMEPEG 6 (1997) 46-50.

[13] T.K. Gupta J. Am. Ceram. Soc., 59 (1976), 259.

[14] B.A. Wilson, K.Y. Lee, E.D. Case, Mater. Res. Bull., 32 (1997), 1607.

[15] A.M. Thompson, H.M. Chan, M.P. Harmer, R. E. Cook. "Crack healing and stress relaxation in Al_2O_3 SiC "nanocomposites", Journal of the American Ceramic Society 78, no. 3 (1995) 567-571.

[16] G. M. Song, Y.T. Pei, W.G. Sloof, S.B. Li, J.T.M De Hosson, S. Van der Zwaag, "Oxidation-induced crack healing in Ti_3AlC_2 ceramics", Scripta Materialia, 58(1) (2008) 13-16.

[17] D. Wei, J. Han, A. K. Tieu, Z. Jiang, "Simulation of crack healing in BCC steel', Scripta Materialia 51 (2004) 583–587.

[18] E Shapiro, G.E. Deiter, "High temperature-high strain rate fracture of Inconel 600", Metallurgical Transactions 1 (1970) 1712-1719.

[19] J. Han, Z. Gang, C. Qixiang, "Internal crack recovery of 20MnMo steel", Sci China 40 (1997)164-169.

[20] Y. Wu, J. Ciston, S. Kräemer, N. Bailey, G.R. Odette and P. Hosemann, The crystal structure, orientation relationships and interfaces of the nanoscale oxides in nanostructured ferritic alloys, Acta Mater. 111 (2016) 108–115.

[21] S. Pal, M. E. Alam, G. R. Odette, S.A. Maloy, D. Hoelzer, "Characterization of processing induced impurity phase precipitates in the as-processed FCRD-NFA-1" Fusion Materials Semiannual Progress Report for Period Ending December 31, 2015, DOE/ER-0313/59, U. S. Department of Energy, 59 (2015) 26-34.

[22] A.H. Cottrell, Theory of brittle fracture in steel and similar metals, Transactions of the metallurgical society of AIME, 212 (1958) 192-203.

[23] G. Xu, M. J. Demokowicz, "Crack healing in nanocrystalline palladium", Extreme Mechanics Letters, 8 (2016) 208-212.

[24] S. Ukai, W. Izawa, N. Oono, S. Hayashi, Y. Kohno, S. Ohtsuka and T. Kaito, Charpy impact property related to {100} cleavage fracture in 15Cr ODS steel, Materials Science and Technology, 30 (2014) 1709-1714.

[25] Y. Kimura, T. Inoue, F. Yin, K. Tsuzaki, Delamination toughening of ultrafine grain structure steels processed through tempforming at elevated temperature, ISIJ International, 50 (2010) 152-161.

[26] A.G. Junceda, M.H. Mayoral, M. Serrano, Influence of the microstructure on the tensile and impact properties of a 14Cr ODS steel bar, Materials Science and Engineering A, 556 (2012) 696-703.

2.3 APT AND TEM CHARACTERIZATION OF α-PHASE FORMATION IN NEUTRON IRRADIATED 14YW AND 14YWT ODS STEELS USING STEM AND 3D-APT

Karen Kruska, Danny Edwards, Richard J. Kurtz (Pacific Northwest National Laboratory)

OBJECTIVE

The objective is to compare the characteristics of the α'-phase formation of nanostructured ferritic 14YWT versus the oxide dispersion strengthened 14YW after irradiation at 500°C in the HFIR.

SUMMARY

Both scanning transmission electron microscopy (STEM) elemental mapping and 3D-atom probe tomography (APT) were used to explore the α'-phase particles that formed in irradiated 14YWT and 14YW. The STEM EDS maps were obtained on an aberration corrected JEOL ARM200CF equipped with a large collection angle SDD detector. High count maps with sub-nanometer probes yielded clear evidence of α'-phase particle formation in each alloy, from which size distributions and densities could be determined over an area larger than available in a typical APT sample. In each case, the average α'-phase particles were smaller than in the APT analysis, likely due to STEM elemental mapping being unable to detect particles less than ~3 nm in diameter. The STEM elemental mapping combined with 3D-APT provides a more detailed global view of the α'-phase particle distributions. Correlative STEM/APT work will be pursued in the future to better document the α'-phase particle relationships to oxide particles and cavities.

PROGRESS AND STATUS

Introduction

The ODS ferritic alloys are candidate materials for first-wall and plasma facing materials in fusion reactors due to their high temperature mechanical properties with high swelling resistance. However, these properties are strongly dependent upon the thermomechanical processing and the resulting size, spatial distribution and type of oxide particles that are formed during processing. As discussed in recent reviews [1-3], it is now recognized that ferritic alloys are susceptible to enhanced swelling in the presence of large levels (1000 to 3000 appm) of helium such as will be generated during service in a fusion environment. This occurs due to the formation of helium bubbles that can transition to unstably growing voids once the pressurized bubbles reach a size of ~3 nm. Efforts are being explored to help control the helium inventory in a manner which keeps the helium dispersed at such a fine scale as to minimize or prevent the transition from helium bubbles to unstably growing voids. At present, the best approach appears to be the incorporation of nano-oxide particles in the size range of 2 nm or less at a density approaching 10^{24} particles/m^3. Helium is attracted to the particle/matrix, allowing small bubbles to nucleate at each particle. The high trapping efficiency slows bubble growth and lengthens the time it takes for the bubbles to reach the critical size.

These alloys are not single phase, however, and additional changes such as alpha prime formation occur during neutron irradiation, which can lead to embrittlement of the alloy. The interplay between the α'-phase particle formation and the presence of large levels of helium has not been thoroughly explored. In addition, the interplay between the oxide particle distributions, helium bubbles and voids, and α'-phase particle has not been thoroughly explored.

The following work describes recent work on two ferritic ODS alloys aimed at exploring the distribution of the alpha prime via 3D-APT in conjunction with aberration corrected STEM analysis. The recent improvements realized by the coupling the intense electron probes formed in a probe corrected STEM with the higher detection efficiency of large area silicon drift detector energy dispersive detectors now enables the exploration of α'-phase formation over a larger area (or volume) than obtained by a single 3D-APT needle. The use of both techniques can be used to more thoroughly explore the spatial distribution of alpha prime, while also providing correlative information on the distribution of helium bubbles and oxide particles.

Experimental Procedure

The 3D-APT and STEM analysis were performed on two alloys, 14YWT and 14YW, the compositions of which are listed in Table 1. Both 14YWT and 14YW are powder metallurgy products hot isostatically pressed at 1150°C. The 14YW is generally considered to be a non-optimal alloy due to a coarse distribution of oxide particles, whereas the 14YWT possesses a much higher density of small particles that help to improve its mechanical properties and swelling resistance. TEM discs of each alloy were neutron irradiated to a dose of 21.2 dpa at 500°C in the High Flux Isotope Reactor at Oak Ridge National Laboratory. A 4 µm NiAl coating used for the ISHI was applied to one side of a 3-mm TEM disc, [4-6] which allows FIB lamella to be extracted from either side of the TEM discs to explore the impact of neutron irradiation with or without concurrent helium injection. The NiAl coating produces a He concentration of about 1230 appm in the ferritic matrix extending uniformly over a depth of ~6 µm below the coating. Cross-sectional TEM samples, prepared by a FIB (FEI Quanta 3D), were finalized with low-energy surface cleaning (2 keV Ga^+ ion) at ±2° tilt angles. The TEM lamella were extracted from each side of the TEM disc, yielding samples that were either neutron irradiated only (NIO) from the non-coated side, or that had helium injection (ISHI side).

Table 1. Composition of 14YWT and 14YW alloys after HFIR irradiation

Alloy	Composition (wt.%) with Fe balance											
	Al	**Si**	**Ti**	**Cr**	**Mn**	**Fe**	**Ni**	**Y**	**Mo**	**W**	**Re**	**Os**
14YW	1.61	0.79	0.00	13.70	1.88	78.97	0.09	0.05	0.04	1.97	0.08	0.51
14YWT	0.82	0.22	0.41	13.76	2.16	79.25	0.09	0.13	0.07	2.04	0.21	0.54

The analytical TEM characterization was performed using a Cs-corrected JEOL ARM 200CF microscope equipped with a Centurio silicon drift detector (SDD) for energy dispersive X-ray spectroscopy (EDS), a Gatan Quantum 965 Dual electron energy loss spectrometer (EELS) system, and high angle annular dark field (HAADF) and bright field (BF) STEM detectors. For elemental mapping in STEM mode, a sub-nanometer probe of 0.18 nm with a probe current of ~2 nA was used with a convergence angle of 48 mrad. Sample thickness was determined through EELS. APT analysis was conducted in a Cameca LEAP 4000HR with a laser wavelength of 255 nm (UV) with a pulse energy of 60 pJ and a frequency of 125 – 250 kHz at a set temperature of 40 K.

Results

SEM analysis

Electro-polishing of the specimen surface revealed the grain structure in each alloy as shown in Figure 1. The SEM imaging was performed to select suitable regions for TEM and APT sample removal. The grain structure is bimodal with large grains of ~5-10 µm diameter surrounded by small grains (<1 µm). Figure 2 shows the cross sections revealed during TEM sample preparation. Only a few large intergranular precipitates are present in the large grains, while their density is higher at the grain boundaries of the nanocrystalline regions. The APT samples were extracted from the large grained regions, while the TEM samples included a mix of grain sizes.

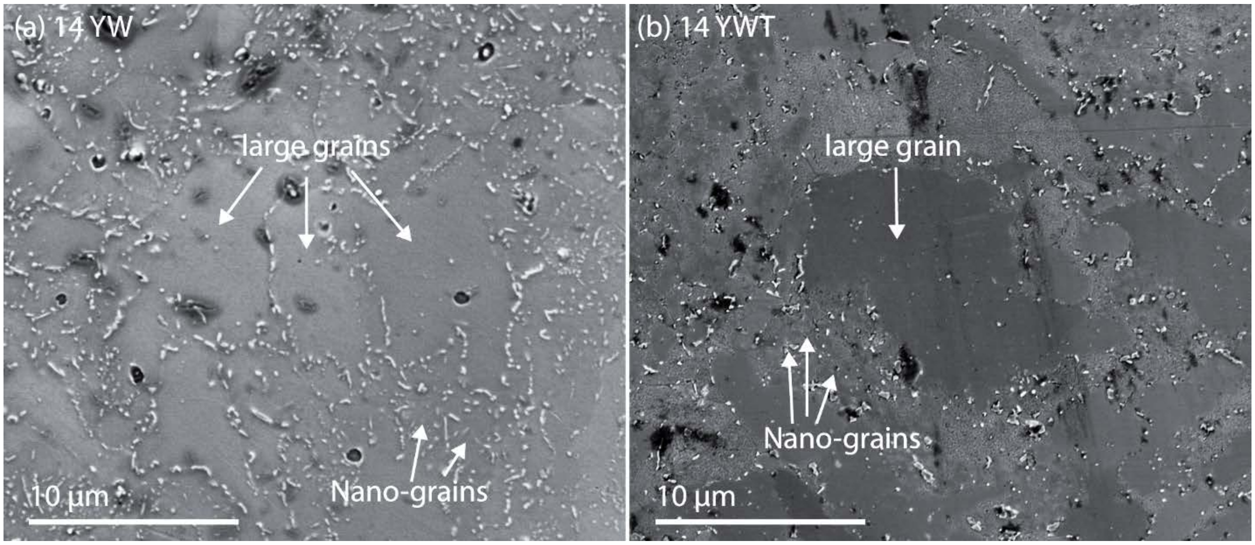

Figure 1. (a) SEM SE image showing the grain structure in neutron irradiated 14YW. (b) SEM SE image showing the grain structure in neutron irradiated 14YWT.

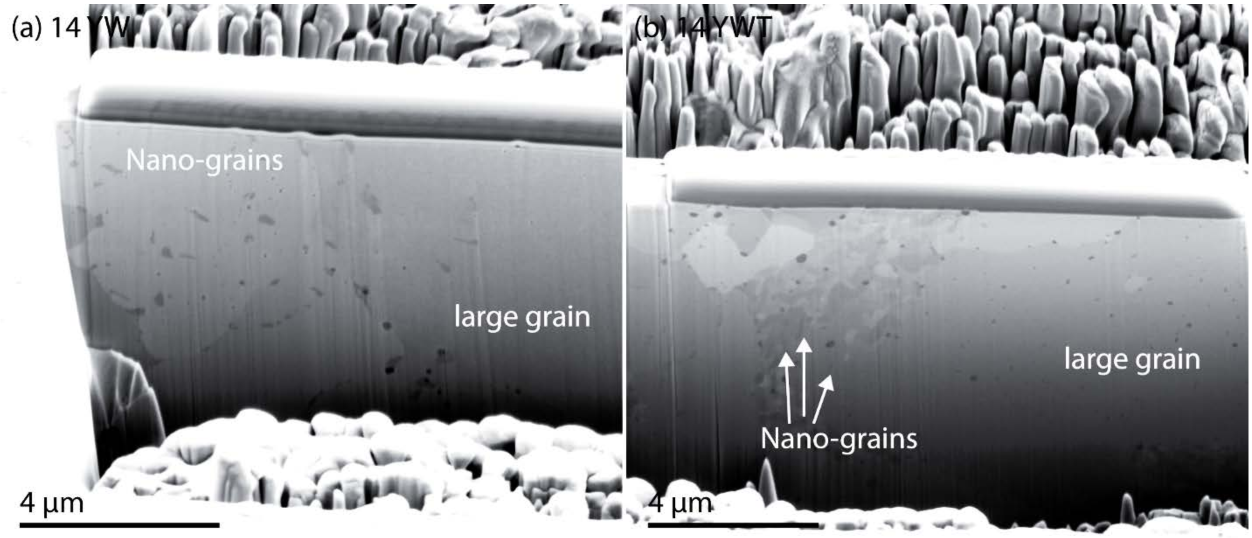

Figure 2. (a) SEM SE image showing the grain structure in neutron irradiated 14YW. (b) SEM SE image showing the grain structure in neutron irradiated 14YWT.

TEM and STEM analysis

The STEM images in Figure 3 confirm the distinct regions of small grains (300-1000 nm) and the large grains of several µm diameters. TiN precipitates are present in both regions, and complex Cr-rich particles are present on the grain boundaries. Due to the similar masses of Fe and Cr, STEM HAADF imaging reveals little about the α’-phase, and TEM images don’t reveal more than a mottled contrast in most cases due to the small or non-existent strain field. While the α’-phase can’t be imaged directly and reliably, elemental mapping with the aberration-corrected probe and large collection angle of the Centurio detector allowed high resolution maps to be obtained in <15 minutes that revealed the Cr enrichment assigned to the α’-phase. An example of the elemental maps obtained from the NIO side of the irradiated 14YWT is shown in Figure 4 along with the accompanying HAADF image. The elemental mapping revealed a high density of α’-phase throughout the region of interest near a large TiN particle.

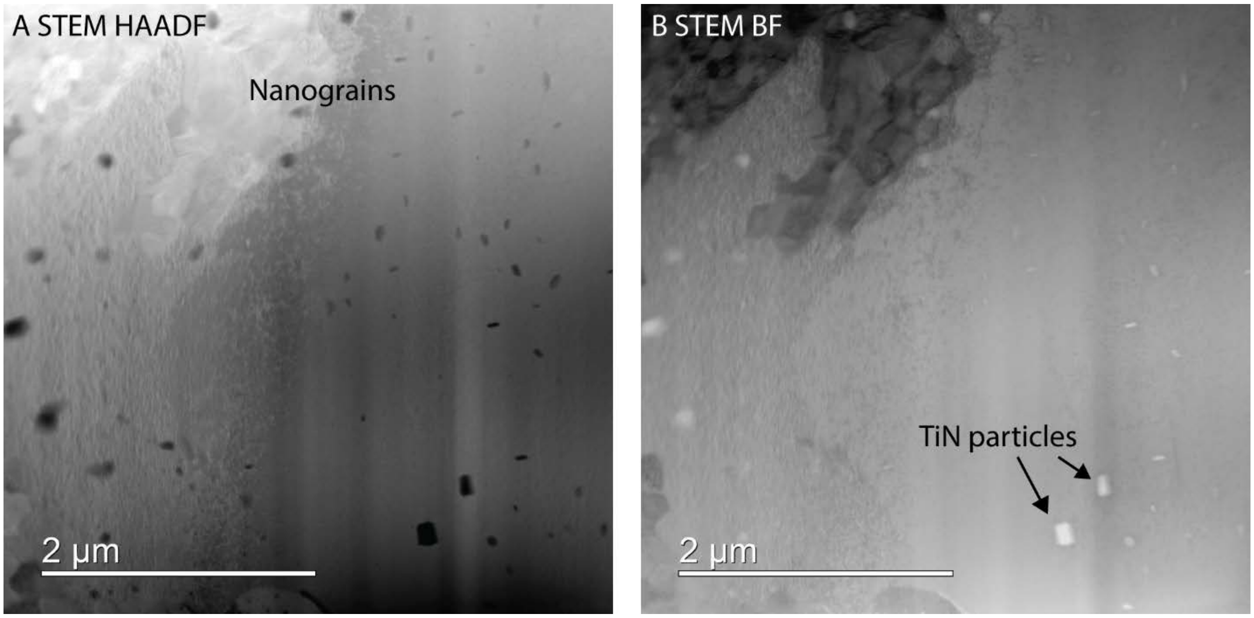

Figure 3. STEM images showing the general microstructure of 14 YWT after neutron irradiation. A) STEM HAADF. B) STEM BF.

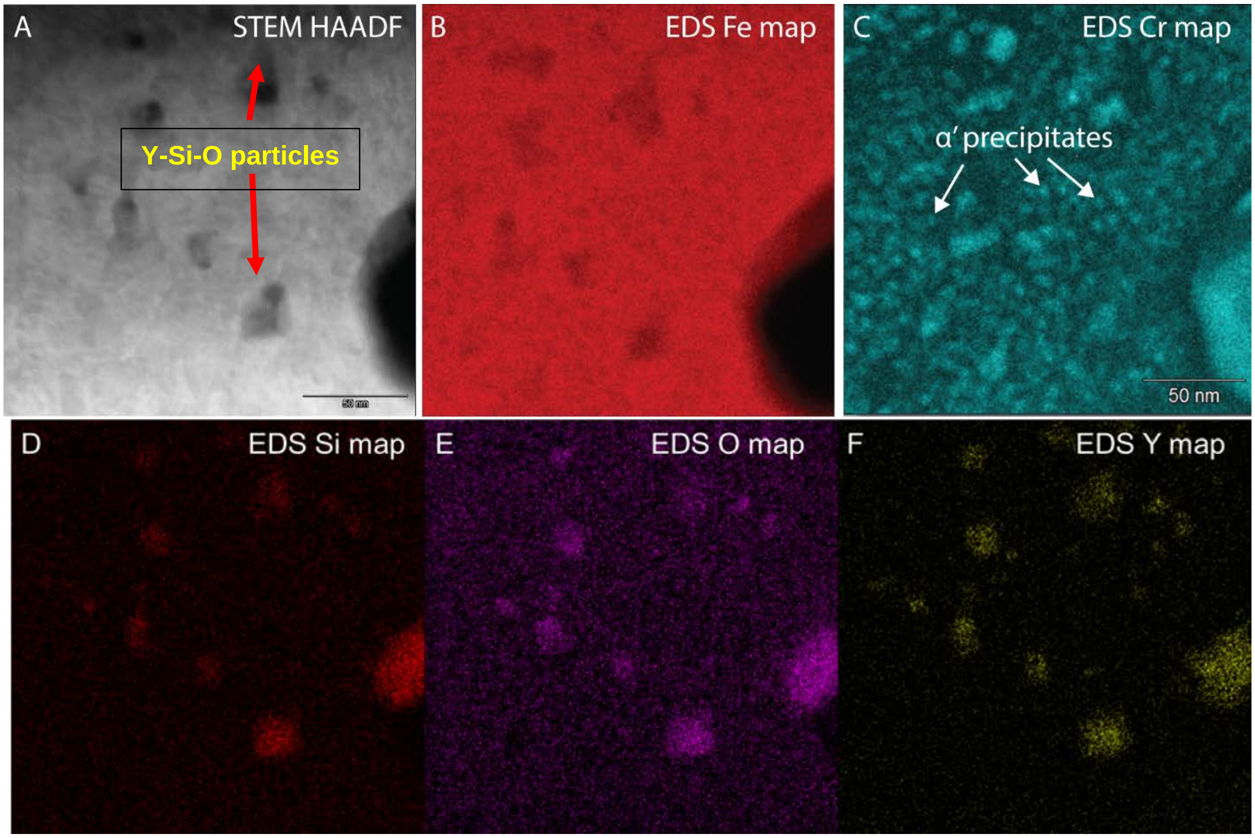

Figure 4. A) STEM HAADF image of NIO 14YWT. B) EDS net counts map for Fe. C) EDS net counts map for Cr. The large dark particle on the right side is a TiN particle with some other particles mixed in. D-F) EDS net counts maps for Si, O, and Y, respectively.

While the local depletion in Fe doesn't reveal much about the α'-phase, the local Cr concentration in the α'-phase is high enough to reveal discrete particles. The red arrows indicate discrete Y-Si-O particles scattered at random near the TiN particle. The particles are visible both in the HAADF image and the elemental maps. The analysis of the size distributions and densities of the α'-phase in the 14YW was measured from the EDS maps as shown in Figure 4, plus those obtained from the ISHI side of the 14YW alloy. Figure 5B shows the size distribution of the α' precipitates measured from the maps in Figure 4C. A comparison of the size distributions shows that the precipitates exhibit a narrower size range in the case of the 14YW than in the 14YWT. The size of the precipitates was 6 ±2.7 nm for the 14YWT sample and 7.1 ±1.6 nm in 14YW. The volume of the sample was calculated with the respective thickness maps and the number density was determined to be 2.1×10^{23} m^{-3} in the 14YWT and 1.3×10^{23} m^{-3} in the 14YW. Given the heterogeneity of the samples, the data is fairly limited in the sense that additional work is needed to explore different regions of the sample, in particular the differences in fine grain areas versus large grained areas, Elemental maps taken near the Cr-rich inclusions on the grain boundaries indicate substantial denuding of α'-phase exists, another issue to explore in these alloys.

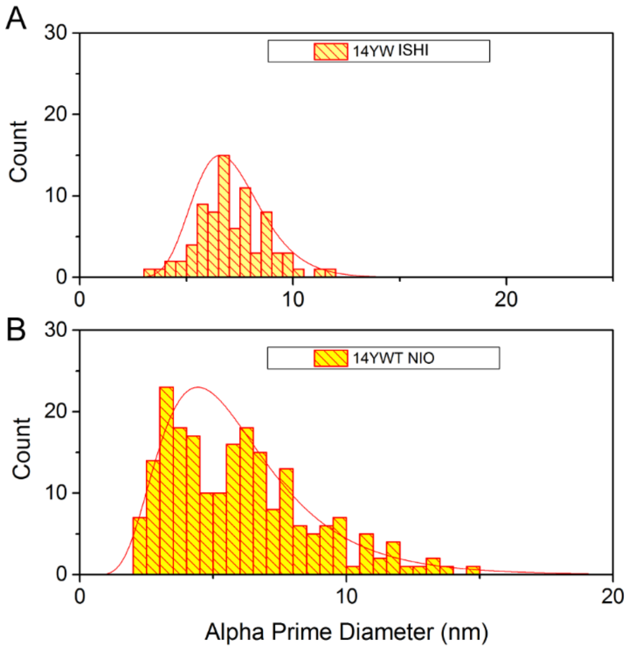

Figure 5. Size distribution of the α'prime precipitates as measured in EDS compositional maps. A) 14YW from the ISHI side. B) 14YWT from the NIO side of the TEM disc.

APT analysis

Three APT tips were extracted from each of the two irradiated alloys (14YW ISHI side and 14YWT NIO). Due to the high Cr concentration in the ODS steels (~14 at%), analysis of the α' phase was conducted using 27 at% Cr iso-surfaces. A novel cluster search algorithm developed at PNNL (OPTICS) was used for the analysis of oxide clusters [7].

14YW

The Cr-rich α'-prime phase consists of small (~10 nm) precipitates that are randomly distributed in the grain interior. A look at the ion maps in Figure 6 shows immediately that the local precipitate density has some variation over the length of the APT needle, with the upper half of the needle in Figure 6b exhibiting a much lower cluster density than the lower half.

Table **1** shows that the precipitate density varies by a factor of 2 between data sets (a) and (b). The mean precipitate density across the data sets was 5.0 ±1.8 × 10^{23} m^{-3}. The size distribution of all 385 precipitates is illustrated in Figure 7. The mean was calculated 5.4 ±2.0 nm. The Cr concentration in the center of the precipitates was analyzed with proximity- histograms (proxigrams).

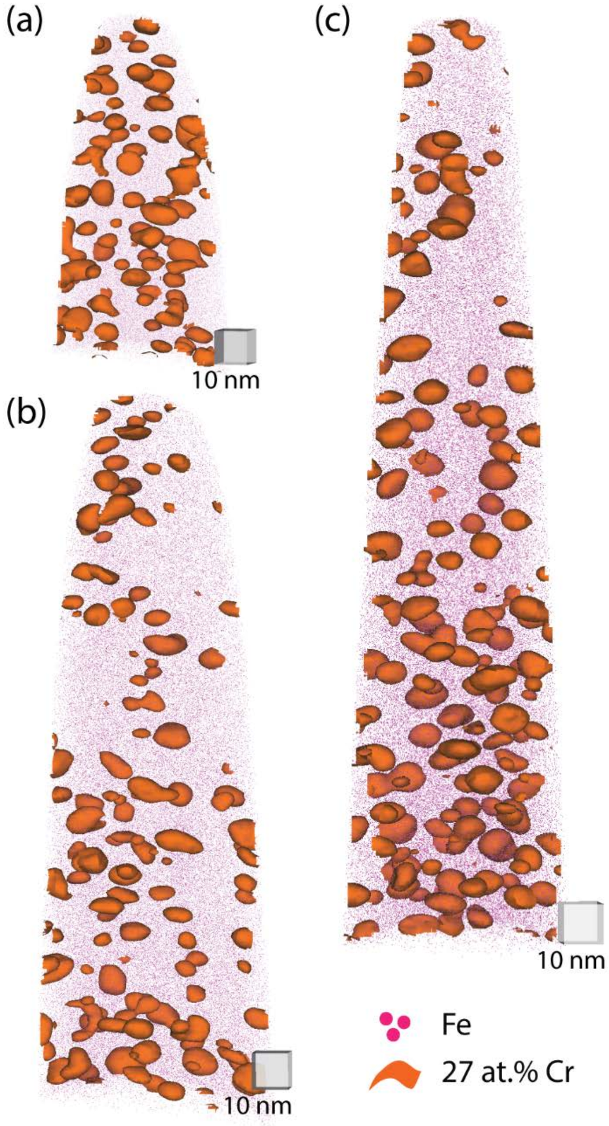

Figure 6. 3D ion maps showing the distribution of Cr-rich α’-phase particles in 3 APT datasets of neutron irradiated 14YW taken from the ISHI side.

Table 1. α’-phase particle density distribution in the 3 data sets shown in Figure 6

Data set	Volume of data set (nm^3)	α’-phase particles	Density (x 10^{23} m^{-3})
(a)	132,000	89	6.7
(b)	406,000	130	3.2
(c)	323,000	166	5.1

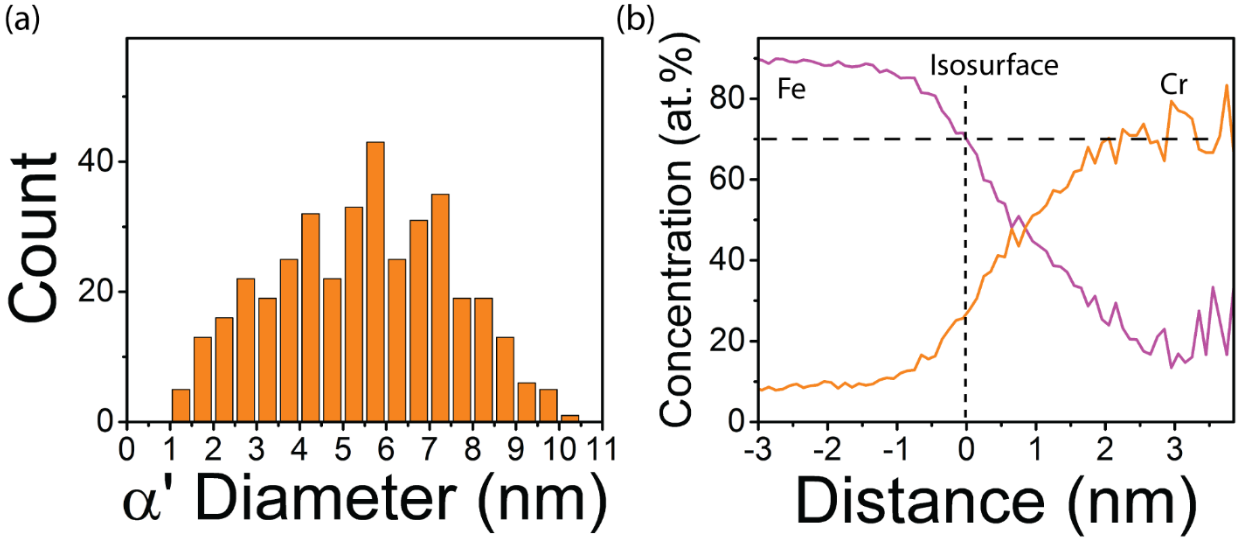

Figure 7. (a) Histogram showing the size distribution of the Cr-rich α'-phase particle in 14YW. (b) Typical proximity-histogram showing the composition inside one of the larger Cr-rich clusters.

Table 2. Y-oxide cluster analysis

Data set	Volume of data set (nm^3)	# of clusters	Diameter (nm)	Density (x 10^{23} m^{-3})
(a)	132000	6	5.5±0.99	0.4
(b)	406000	17	5.2±1.9	0.42
(c)	323000	2	5.8±2.3	0.062

The maximum Cr concentration varied between ~60 and 80 at.% Cr where higher Cr concentrations were found in larger precipitates. Cluster search for Y oxide clusters was performed in using Y ions only. The results are summarized in Table 2. Ion maps frequently showed evaporation of CrO ions from Y oxide cluster regions suggesting a mixed Y-Cr oxide is present. The cluster search for Y-rich precipitates did not return a large number of clusters and the distribution was not very homogeneous. In data set (b) it appeared that Y-rich oxide clusters were denser in regions relatively free from α' precipitates, but with the small number of total clusters observed no definitive conclusions about the correlation between Y-Cr-O clusters and α' precipitates can be drawn. The low number density of Y-oxide clusters observed in the 3D-APT results matches the TEM results, which shows a particle density of ~5x10^{21} per m^3 with particles ranging from 5 to 15 nm in size. The 3D-APT dataset showed no evidence of the larger Y-Si-O particles observed in the elemental maps.

14YWT

As in the case of the 14YW, the α'-phase consists of small precipitates that are randomly distributed in the grain interior. Figure 8 shows that the local precipitate density again has some variation over the length scale of an APT data set. The needle in Figure 5b has a much lower cluster density than that shown in Figure 8a. Table 3 shows that the α' precipitate density varies almost by a factor of 2 between data sets (a) and (b). The mean α' precipitate density across all data sets was 5.2 ± 4.1 × 10^{23}, which is comparable to the precipitate density in 14YW.

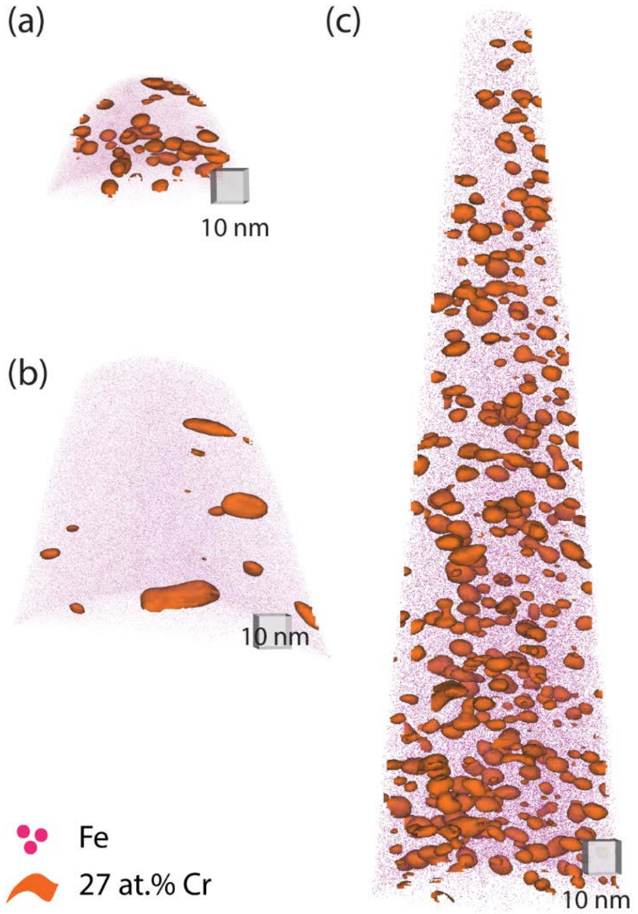

Figure 8. 3D ion maps showing the distribution of Cr-rich α’-phase particles in 3 APT datasets of 14YWT taken from the NIO side.

Table 3. α’-phase particle density distribution in the 3 data sets shown in Figure 8

Data set	Volume of data set (nm^3)	# of precipitates	Density (x 10^{23} m^{-3})
(a)	42,000	33	7.9
(b)	269,000	12	4.5
(c)	505,000	367	7.3

The size distribution of all 412 α’-phase particles is provided in Figure 9a. The mean was calculated 4.2 ±1.9 nm. The Cr concentration in the center of a typical larger Cr-rich precipitate is shown in the proxigram in Figure 9b. The maximum Cr concentration varied between ~60 and 80 at.% Cr where higher Cr concentrations were found in larger precipitates.

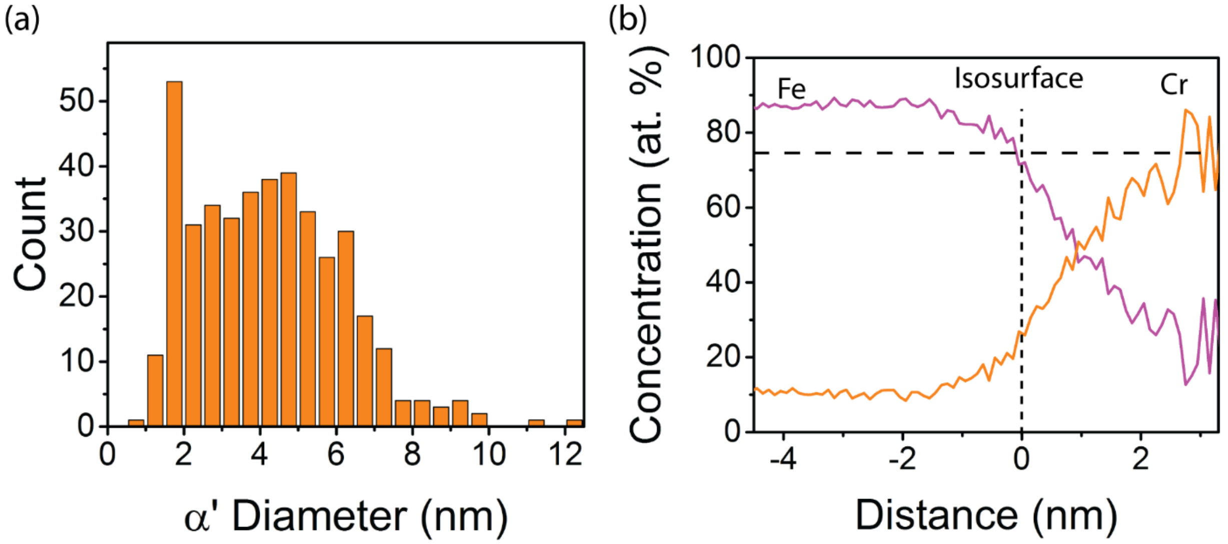

Figure 9. (a) Histogram showing the size distribution of the Cr-rich precipitates. (b) Typical proximity-histogram showing the composition inside one of the larger Cr-rich clusters.

Visual analysis of the ion maps showed the presence of small clusters containing Y, TiO and CrO ions. These regions were distinctly different from the Cr-rich clusters analyzed previously. All Y, TiO and CrO ions were used for the cluster search. Figure 10 shows the distribution of the oxide clusters (purple) as well as Cr-rich precipitates (orange). A 1 at.% isoconcentration surface for Y ions was used to show the location of the clusters. However, counting and size measurement were performed with the OPTICS cluster search algorithm. It is immediately obvious that the Y-Ti-Cr-oxide clusters are smaller and have a higher density compared to the Y-Cr-oxide clusters in the 14YW. The count statistics for each data set are shown in Table 4. A histogram showing the size distribution for 371 clusters is shown in Figure 11a. Figure 11b shows the proxigram for one of the larger clusters from dataset (c). No “typical composition” was found however, the metal-metal ratio varied in each cluster. It appeared that all clusters contain some amount of Ti, while not all clusters contained both Y and Cr. The mean was calculated 4.1 ± 0.93 nm. The mean precipitate density across the data sets was 4.5 ±3 $\times 10^{23}$ m^{-3}. Oxide clusters of all compositions appeared to have a similar size distribution.

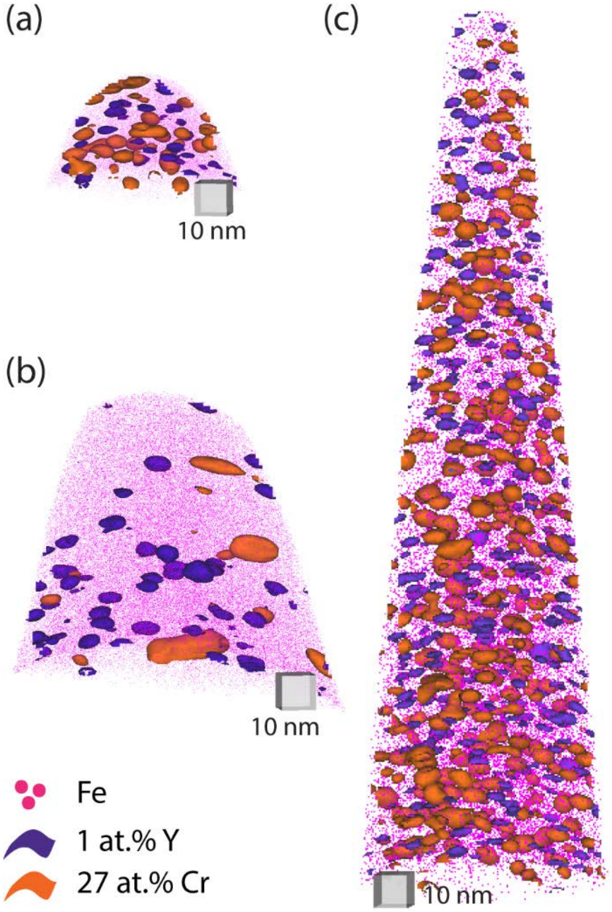

Figure 10. 3D ion maps showing the distribution of Y-Ti-Cr-oxide clusters in correlation with Cr-rich α’-phase particles in 3 different APT datasets of 14YWT taken from the NIO side.

Table 4. Y-TiO-CrO cluster analysis (OPTICS)

Data set	Volume of data set (nm^3)	# of precipitates	Diameter (nm)	Density (x 10^{23} m^{-3})
(a)	42,000	33	3.7 ±1.4	7.8
(b)	269,000	52	4.4 ±0.93	1.9
(c)	506,000	286	4.1 ±0.86	3.7

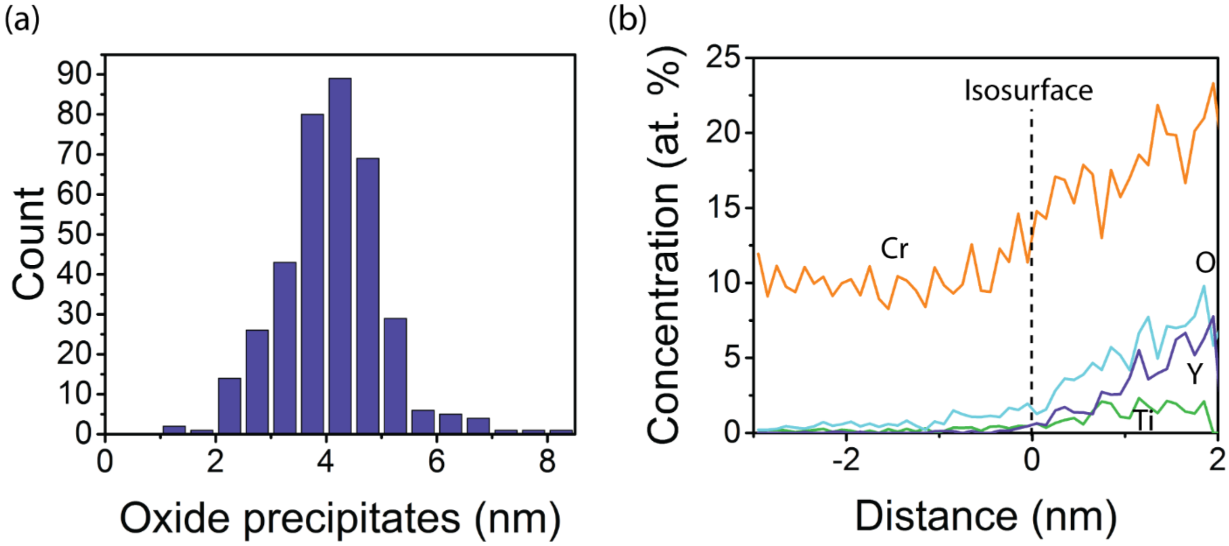

Figure 11. (a) Histogram showing the size distribution of the Y-Ti-Cr-oxide precipitates. (b) Typical proximity-histogram showing the composition inside one of the larger oxide clusters.

Summaries

The focus of this report is to compare the effectiveness of STEM elemental mapping versus 3D-APT for characterizing alpha prime particles in irradiated 14YW and 14YWT. The STEM and APT analysis are generally in good agreement; however, the STEM elemental mapping didn't capture particles less than ~3 nm in diameter. The volume analyzed via STEM mapping is not significantly larger than each 3D-APT needle when performed at resolutions required to capture the α'-phase particles. Still, if the α'-phase particles have coarsened to the extent they can be seen by STEM elemental mapping, mapping over multiple regions can be done quickly enough to obtain a better sense of the α'-phase particle distributions over a broader scale that supplements the more sensitive 3D-APT technique. This could be potentially useful to understand the α'-phase particle distributions near sinks such as grain boundaries or large Cr-rich particles on the grain boundaries. This is turn can help to direct the location from which the APT needles are chosen, since any highly localized inhomogeneity could affect the APT results. The results in this study demonstrate the potential of the newer aberration-corrected STEM instruments to achieve sensitivity levels approaching 3D-APT for certain elements, but caution is needed to thoroughly explore the limits of each technique for a given microstructural condition.

Future Work

1) Complete the matrix of experiments by conducting STEM analysis of NIO 14YW, ISHI 14YWT.
2) Explore the relationship between oxide and alpha prime distributions in regions of different gain sizes, perform a correlative STEM analysis in the same region from which 3D-APT dataset are extracted.
3) Conduct TEM imaging/STEM elemental mapping on each APT needle before it is run in the atom probe to develop a correlative analysis of the distribution of cavities, particles and α'-phase particles.
4) Comparison with the archive material for each alloy following the same sampling guidelines with respect to grain size.
5) Confirm the distribution of α'-phase particles near the vicinity of the Cr-rich particles on the grain boundaries.

Acknowledgements

This research was supported by Office of Fusion Energy Sciences, U.S. Department of Energy (DOE) under Contract DE-AC05-76RL01830. A portion of the research was performed using EMSL, a national

scientific user facility sponsored by the DOE's Office of Biological and Environmental Research and located at PNNL.

References

[1] R.L. Klueh, P.J. Maziasz, I.S. Kim, L. Heatherly, D.T. Hoelzer, N. Hashimoto, E.A. Kenik, K. Miyahara, J. Nucl. Mater. 307-311 (2002) 773.
[2] Y. Dai, G.R. Odette, T. Yamamoto, Comprehensive Nuclear Materials, Elsevier, Atlanta, GA, 2012.
[3] G.R. Odette, JOM 66 (No. 12) (2014).
[4] T. Yamamoto, G.R. Odette, L.R. Greenwood, Fusion Materials Semiannual Report 1/1 to 6/30/2005 DOE/ER-313/38, 2005, p. 95.
[5] [27] T. Yamamoto, G.R. Odette, P. Miao, D.T. Hoelzer, J. Bentley, N. Hashimoto,
[6] H. Tanigawa, R.J. Kurtz, J. Nucl. Mater. 367-370 (2007) 399.[28] R.J. Kurtz, G.R. Odette, T. Yamamoto, D.S. Gelles, P. Miao, B.M. Oliver, J. Nucl. Mater 367-370 (2007) 417.
[7] J. Wang, N. Bailey, P. Hosemann, D.K. Schreiber, J. Liu, M.B. Toloczko, Cluster Analysis in Atom Probe Tomography Data: a New Method Based on The OPTICS Algorithm, presented at Atom Probe Tomography User Meeting 2017, Madison, WI, USA.

3. CERAMIC COMPOSITE STRUCTURAL MATERIAL DEVELOPMENT

3.1 LOW ACTIVATION JOINING OF SiC/SiC COMPOSITES FOR FUSION APPLICATIONS: A DUAL-PHASE MICROSTRUCTURAL APPROACH TO MODEL THERMAL AND IRRADIATION-INDUCED SWELLING EFFECTS ON INTEGRITY OF Ti_3SiC_2/SiC JOINTS

B.N. Nguyen, C.H. Henager, Jr., R.J. Kurtz; (Pacific Northwest National Laboratory)

OBJECTIVE

The objective of this effort is to investigate in detail the micro cracking mechanisms responsible for Ti_3SiC_2/SiC joint damage and fracture observed at the macroscopic scale after irradiation experiments. A dual-phase microstructural approach to damage and fracture of Ti_3SiC_2/SiC joints was developed that uses a dual-phase finely discretized domain based on a digital image of an actual microstructure involving embedded Ti_3SiC_2 and SiC phases. The behaviors of SiC and Ti_3SiC_2 in the domain were described by the continuum damage mechanics (CDM) model reported in [1]. The dual-phase microstructural model was applied to predict micro cracking mechanisms occurring in a typical Ti_3SiC_2/SiC joint subjected to heating to 800°C followed by irradiation-induced swelling at this temperature and cooling to room temperature after the applied swelling had reached the maximum swelling levels observed in the experiments for SiC and Ti_3SiC_2.

SUMMARY

We investigated a MAX phase composite joint,Ti_3SiC_2/SiC, irradiated in HFIR at 800°C to 5 dpa. Before irradiation, SEM examination indicated no transverse cracks or micro cracks in the bonding layer or at the interfaces. After irradiation, limited crack propagation along the interface between the bonding layer and the CVD substrate was observed, and micro cracks were also found in the Ti_3SiC_2/SiC joint layer. The purpose of our work is to understand the micro cracking mechanisms and their chronology in the irradiated joint. Irradiation material degradation affecting mechanical properties is not modeled, but the developed modeling approach accounts for the *irradiation-induced swelling* that can cause subsequent damage if the material is constrained. This report expands the methods discussed in other reports [1-4] to model and predict cracking due to residual stresses caused by the mismatch of thermo-elastic properties in combination with the swelling-induced mismatch between the joint and joint materials.

PROGRESS AND STATUS

Introduction

As discussed Ref. [2], joining SiC to itself or to other materials is a critical technological need that has not been resolved. There are two key issues central to this problem [1]. The first issue is the poor irradiation stability that was observed through limited data available on the irradiation of joints and joining materials. The second issue is the lack of a widely accepted standard test method for joining of SiC. In addition to the above issues, there is a general lack of predictive modeling tools that can either assist in designing a ceramic joint to resist irradiation-induced damage, or provide guidance to develop a joining method for SiC and its composites. This work attempts to address the lack of modeling tools by applying a continuum damage mechanics (CDM) model at the microstructural scale to elucidate the origin of cracking observed in ceramic joints subjected to heating followed by neutron irradiations at elevated temperatures (up to 800°C). The model relies on CDM for the constitutive relations and uses a dual-phase microstructural domain in which the embedded phases (SiC and Ti_3SiC_2) are finely discretized to capture in detail the deformation and micro cracking mechanisms.

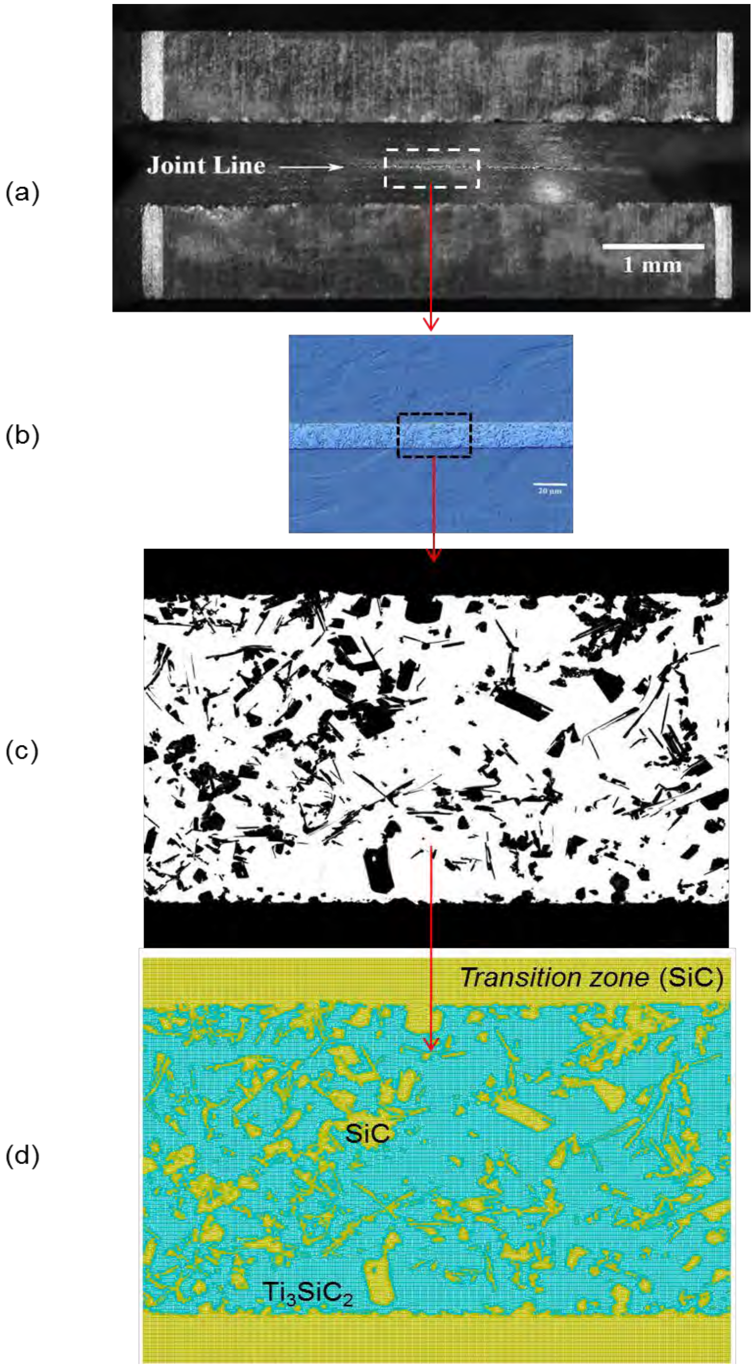

Figure 1. Schematic of the dual-phase microstructural approach: (a) An as-formed THG specimen, (b) A micrograph taken from this specimen, (c) the digital image of the Ti_3SiC_2/SiC joint microstructure obtained from this micrograph, and (d) the finite element mesh built from the digital image using the NIST's OOF2 software.

We considered the MAX-phase joining in which a composite made of SiC and Ti_3SiC_2 is produced using a displacement reaction between SiC and TiC [6]: $3TiC + 2Si \rightarrow Ti_3SiC_2 + SiC$. Pacific Northwest National Laboratory (PNNL) has developed a tape casting process to join ceramics using this reaction [7].

Previous modeling work using CDM for the unirradiated Ti_3SiC_2/SiC joint and joining SiC subjected to torsion was reported in [3].

Model Development

Figure 1 presents a schematic of the dual-phase microstructural approach developed to predict micro cracking mechanisms occurring at the microstructural scale and that are responsible for the Ti_3SiC_2/SiC joint damage observed in experiments. Starting from the as-formed THG specimen illustrated in Figure 1(a), a micrograph of the joint area including the SiC transition zone was taken as shown in Figure 1(b). Next, a digital image of the Ti_3SiC_2/SiC microstructure including the SiC transition zones was created (Figure 1(c)) to build the two-dimensional (2D) FE mesh of this microstructure (Figure 1(d)) using the OOF2[1] public domain software. Figure 1(d) shows a very fine 2D FE mesh containing 251,055 elements over a 23-μm x 17-μm domain. Particularly, very fine discretizations were achieved along the boundaries between the Ti_3SiC_2 and SiC phases as illustrated in Figure 2 that shows the detailed mesh in a local snapshot.

This dual-phase microstructural approach uses the Nguyen *et al*. damage model for brittle ceramics [1,4] to describe the occurrence and evolution of micro cracking damage in the constituent SiC and Ti_3SiC_2 phases. We have explored the observed size effect on the material strength to establish the stress-strain responses of the micron-scale SiC and Ti_3SiC_2 allowing the application of this damage model at the microstructural scale where the size of the phases correspond to the particle size. Continuum finite elements are used to discretize the individual phases, but the dual-phase model does not explicitly discretize the interfaces between different phases using, e.g., cohesive finite elements. However, by very finely discretizing the interface regions, local stress concentrations along all the boundaries can be captured more accurately for damage and fracture analyses. If micro cracking damage and fracture are predicted to develop in the elements along the interfaces, then debonding between the individual phases sharing those interfaces occurs. Due to the lack of knowledge about the interface properties for a complete description of interface debonding, an approach using cohesive finite elements would introduce more uncertainties into the model than the dual-phase continuum approach used in this work.

Results

We have applied the CDM model implemented in ABAQUS® to analyze the dual-phase Ti_3SiC_2/SiC microstructural domain subjected to similar experimental conditions as the THG specimen with the Ti_3SiC_2/SiC bonding joint experienced. Figure 3a shows the damage distribution in the dual-phase domain at the end of heating to 800°C. Damage occurred mainly in the SiC phase regions under local tensile/shear stress states. A few *transgranular* micro cracks have been observed in some SiC phase regions indicated by the damage indicator equal to 1. The Ti_3SiC_2 regions undergoing compressive stresses appear to be practically intact after heating to 800°C as indicated on Figure 3a that shows zero or very small values of the damage indicator. The non-zero but very small values of the damage indicator have been observed mainly in the Ti_3SiC_2 regions along the boundaries between SiC and Ti_3SiC_2. Shearing along the boundaries between the tensile SiC and compressive Ti_3SiC_2 resulting from mismatches of thermo-elastic properties have caused some damage in these interface regions, but damage is predicted to be negligible and no debonding has been found after heating to 800°C.

Once the dual-phase microstructure was brought to 800˚C, it was then subjected to irradiation-induced swelling at this temperature up to the respective maximum levels (0.8% for SiC [8] and 1.47% for Ti_3SiC_2 [9]) (Figure 3b). Important damage development has been found during swelling (Figure 3c) due to more pronounced concentrations of tensile stresses in the SiC phase because the much higher swelling of Ti_3SiC_2 is constrained by the lower swelling SiC. Thus, the irradiation-induced swelling effect has added to the preceding thermal expansion effect causing significantly more damage to the dual-phase domain. Figure 3c clearly shows four types of micro cracking mechanisms: (i) *transgranular micro cracking* in SiC, (ii) *intergranular micro cracking* along the SiC and Ti_3SiC_2 boundaries, (iii) *debonding* along the interfaces between the bonding joint and the SiC transition zones, and (iv) *transverse micro cracking* of the SiC

---

[1] Software developed at the National Institute of Standards and Technology

transition zone. Increased tensile stresses in SiC during irradiation-induced swelling have caused transgranular micro cracking in SiC as this mechanism was already predicted after heating to 800°C but to a much lesser extent. High tensile stresses in the upper SiC transition zone also caused the transverse micro cracking of this zone. Intergranular micro cracking along SiC and Ti_3SiC_2 boundaries was caused by significant shear stresses that increased during swelling. The shear stresses were also responsible for the debonding predicted along the interfaces between the bonding joint and the SiC transition zones.

After irradiation swelling, the dual-phase domain model was uniformly cooled to room temperature. The damage and fracture development at the end of cooling is presented in Figure 3d, which clearly shows the same types of micro cracking mechanisms predicted at the end of irradiation swelling. During cooling, thermal contraction of the cracked microstructure combined with irreversible swelling strains has caused more damage and fracture for SiC and along many boundaries between SiC and Ti_3SiC_2. The prediction of these mechanisms due combined thermal and irradiation-induced swelling effects appears to globally agree with the experimental observation about the presence of micro cracks in the joint after the irradiation experiment of the THG specimen at 800°C [2].

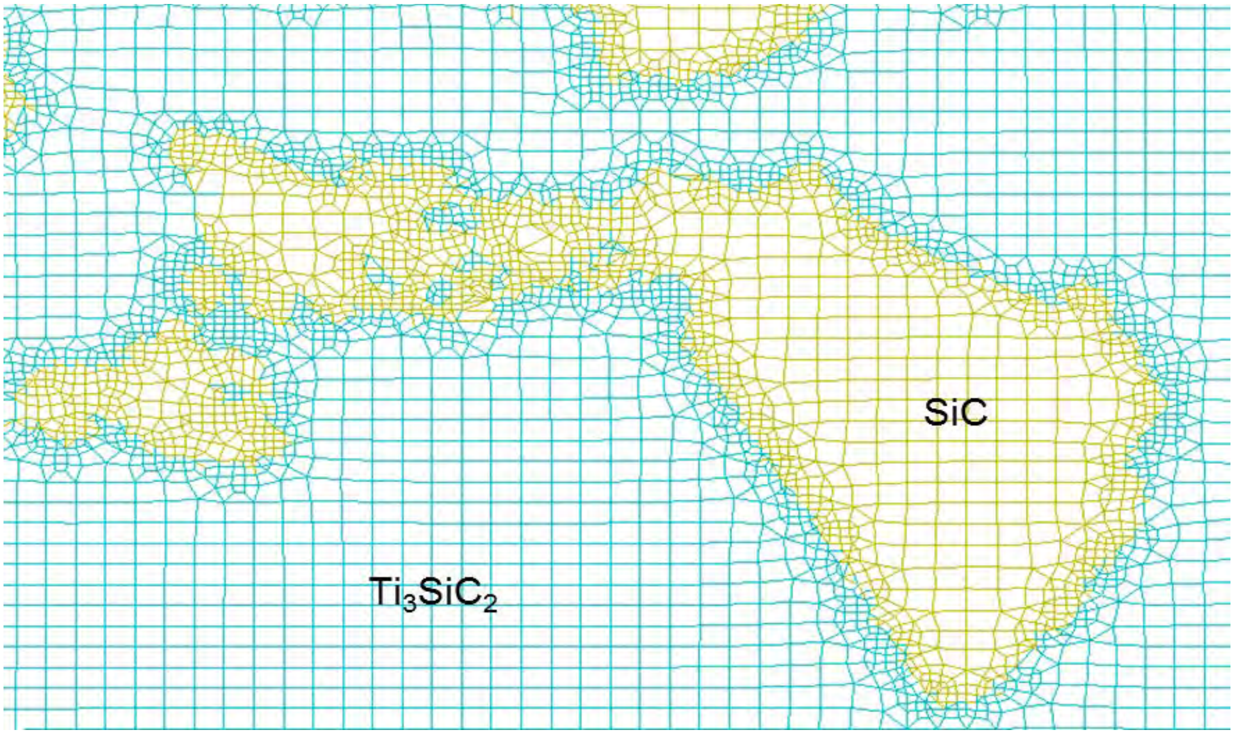

Figure 2. A local snapshot showing the high-resolution mesh along the Ti_3SiC_2 and SiC boundaries.

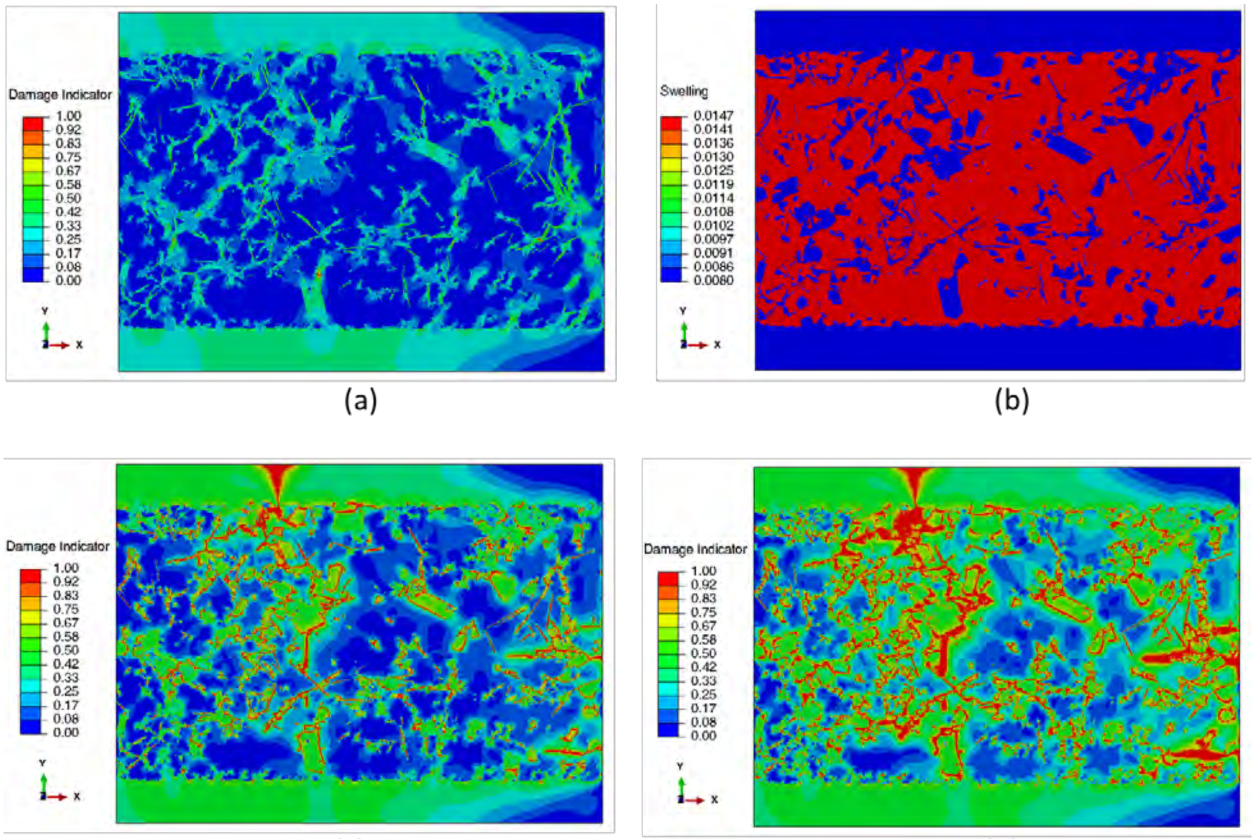

(a) (b)

(c) (d)

Figure 3. (a) Predicted damage distribution at the end of heating to 800°C, (b) Simulated irradiation-induced swelling at 800°C, Predicted damage and fracture developments (c) after irradiation-induced swelling at 800˚C, and (d) after cooling to room temperature.

Results

The dual-phase microstructural approach developed in this work depends on the local microstructure that statistically varies from location to location. In addition, the strength of ceramics at the micron scale can vary significantly and are not very well known. Therefore, damage and fracture predictions based on a typical microstructure with the assumed mechanical behaviors for the constituent phases could over-predict or under-predict the actual damage and fracture states observed after irradiation experiments. Also, the modeling performed at the microstructural scale alone can help describe the deformation and damage mechanisms but cannot produce the actual constraints a macroscopic specimen experiences. Amid these uncertainties and limitations, the dual-phase microstructural approach developed here appears to reasonably capture the micro cracking mechanisms and their occurrence chronology observed in limited experiments. This approach has been demonstrated to be effective and robust, and can be readily extended to involve more phases that exist in an actual microstructure of a ceramic composite joint. It can be used to optimize composite microstructure through phase distributions, operating conditions or limits in terms of temperature range and dose to minimize damage to support the neutron-irradiation based design of joined ceramics and composites in conjunction with structural analyses of components and in-reactor testing.

References

[1] Nguyen BN, CH Henager, Jr, RJ Kurtz, M Ferraris, and Y Katoh. 2017. "Low Activation Joining of SiC/SiC Composites for Fusion Applications: Modeling Thermal and Irradiation-induced Swelling Effects on Integrity of Ti3SiC2/SiC Joint." Chapter 3.2 in Fusion Materials Semiannual Progress Report For Period Ending December 31, 2016, vol. 61; /DOE/ER-0313/61, ed. FW Wiffen and S Melton, pp. 58-65. Oak Ridge National Laboratory, Oak Ridge, TN.

[2] Katoh Y, LL Snead, T Cheng, C Shih, WD Lewis, T Koyanagi, T Hinoki, CH Henager Jr, and M Ferraris, J. Nucl. Mater., 2014. 448(1-3): p. 497-511.

[3] Henager Jr. CH, BN Nguyen, RJ Kurtz, TJ Roosendaal, BA Borlaug, M Ferraris, A Ventrella, Y Katoh, J. Nucl. Mater., 466 (2015) 253–268.

[4] Nguyen BN, CH Henager Jr., and RJ Kurtz, "Modeling Thermal and Irradiation-induced Swelling Effects on Integrity of Ti3SiC2/SiC Joint, 2017, *Submitted*.

[5] Nguyen BN, CH Henager Jr., and RJ Kurtz, " A Dual-Phase Microstructural Approach to Damage and Fracture of Ti3SiC2/SiC Joints," 2017, *In preparation*.

[6] Radhakrishnan R, CH Henager, JL Brimhall, and SB Bhaduri, Script. Mater., 34 (1996) 1809–1814.

[7] Henager Jr. CH and R.J. Kurtz, J. Nucl. Mater., 417 (2011) 375–378.

[8] Snead LL, T Nozawa, Y Katoh, B Thak-Sang, S Kondo, and DA Petti, J. Nucl. Mater., 2007. 371(1-3): p. 329-77.

[9] Ang C, S Zinkle, C Shih, C Silva, N Cetiner, and Y Katoh, J. of Nucl. Mater., 483 (2017) 44-53.

3.2 IRRADIATION-INDUCED β TO α SiC TRANSFORMATION AT LOW TEMPERATURE—C.M. Parish, T. Koyanagi, Y. Katoh (Oak Ridge National Laboratory) and S. Kondo (Kyoto University)

Abstract of a manuscript published in Scientific Reports 7 *(2017) 1198* |
DOI:10.1038/s41598-017-01395-y.

We observed that β-SiC, neutron irradiated to 9 dpa (displacements per atom) at ≈1440 °C, began transforming to α-SiC, with radiation-induced Frank dislocation loops serving as the apparent nucleation sites. 1440 °C is a far lower temperature than usual β → α phase transformations in SiC. SiC is considered for applications in advanced nuclear systems, as well as for electronic or spintronic applications requiring ion irradiation processing. β-SiC, preferred for nuclear applications, is metastable and undergoes a phase transformation at high temperatures (typically 2000 °C and above). Nuclear reactor concepts are not expected to reach the very high temperatures for thermal transformation. However, our results indicate incipient β → α phase transformation, in the form of small (~5–10 nm) pockets of α-SiC forming in the β matrix. In service transformation could degrade structural stability and fuel integrity for SiC-based materials operated in this regime. However, engineering this transformation deliberately using ion irradiation could enable new electronic applications.

3.3 MICROSTRUCTURAL EVOLUTION OF NEUTRON IRRADIATED 3C-SiC—D.J. Sprouster, E. Dooryhee, S.K. Ghose, L.E. Ecker (Brookhaven National Laboratory) and Y. Katoh, T. Koyanagi (Oak Ridge National Laboratory)

Abstract of a manuscript published in Scripta Materialia 137 (2017) 132–136.

The microstructural response of neutron irradiated 3C-SiC has been investigated over a wide irradiation temperature and fluence range via qualitative and quantitative synchrotron-based X-ray diffraction characterization. We identify several neutron fluence- and irradiation temperature-dependent changes in the microstructure, and directly highlight the specific defects introduced through the course of irradiation. By quantifying the microstructure, we aim to develop a more detailed understanding of the radiation response of SiC. Such studies are important to build mechanistic models of material performance and to understand the susceptibility of various microstructures to radiation damage for advanced energy applications.

3.4 EQUILIBRIUM SHAPES AND SURFACE SELECTION OF NANOSTRUCTURES IN 6H-SiC—S. Kondo (Kyoto University) and C.M. Parish, T. Koyanagi, Y. Katoh (Oak Ridge National Laboratory)

Abstract of a manuscript published in Applied Physics Letters 110 (2017) 142106;
doi: 10.1063/1.4979550.

The equilibrium shape of 6H-SiC nanostructures and their surfaces were studied by analyzing nano-void (~10 nm) shapes, which were introduced in monocrystalline 6H-SiC by high temperature neutron irradiation, using transmission electron microscopy. The nano-voids were determined to be irregular icosahedrons truncated with six {-1100}, twelve {-1103}, one smaller top-basal, and one larger bottom-basal planes, which suggests that {-1100} and {-1103} are the next stable surface class after the basal planes. The relatively frequent absence of the {-1100} surface in the nano-voids indicated that the (-110-3) surface type is energetically rather stable. These non-basal surfaces were found not to be atomically flat due to the creation of nanofacets with half unit-cell height in the c-axis. The {-1100} and {-1103} surfaces were classified as two and four face types according to their possible nanofacets and surface termination, respectively. We also discuss the surface energy difference between the (-110-3) and (-1103) face types in relation to the energy balance within the equilibrium, but irregular, polyhedron, in which the (-1103) surface had double the surface energy of the (-110-3) surface (~3900 erg/cm2).

4. HIGH HEAT FLUX MATERIALS AND COMPONENT TESTING

4.1 PROPERTIES AND CHARACTERIZATION OF NOVEL COPPER ALLOYS FOR FUSION ENERGY APPLICATIONS

—Ying Yang (Oak Ridge National Laboratory), Ling Wang (University of Tennessee at Knoxville), Steven J. Zinkle (University of Tennessee at Knoxville and Oak Ridge National Lab), and Lance Snead (Stony Brook University*)*

OBJECTIVE

This study aims at developing high strength, high conductivity Cu alloys with improved thermal creep strength for long pulse fusion high heat flux structures, through an accelerated approach of computational thermodynamics guided alloy design.

SUMMARY

Thermal-mechanical treatment was completed on newly developed Cu-Cr-Nb-Zr and Cu-Cr-Ta-Zr alloys. Optical microscopy and hardness measurements were carried out on these new alloys. Tensile properties were evaluated between room temperature and 500°C at three strain rates ($2x10^{-4}$ to $0.056\ s^{-1}$) for several of the recently developed Cu-Cr-Nb-Zr alloys, and initial TEM characterization was performed on one of developed Cu-Cr-Nb-Zr alloys.

PROGRESS AND STATUS

Materials design and fabrication

Work performed during this reporting period built upon recently reported [1,2] efforts to design, fabricate and characterize new high strength, high conductivity Cu alloys designed to simultaneously suppress dislocation power law creep (high density of matrix precipitates) and grain boundary sliding (grain boundary precipitates) while also providing good radiation resistance via the matrix precipitates. Based on recent thermodynamic calculation results [2], three new alloys have been fabricated. Two are Cu-Cr-Ta-Zr alloys (1CCTZ and 2CCTZ) and one is a Cu-Cr-Nb-Zr (4CCNZ) alloy. The design criteria for microstructure is briefly described here: the first Cu-Cr-Ta-Zr alloy has Cr_2Ta-C15 serving as GB precipitates and the **Bcc-Cr**, Cu_5Zr and $Cu_{51}Zr_{14}$ as the matrix precipitates, and the second Cu-Cr-Ta-Zr alloy has the same Cr_2Ta-C15 serving as GB precipitates but with **Bcc-Ta** and CuZr intermetallics as the matrix precipitates. The newly designed Cu-Cr-Nb-Zr alloy has the Cr_2Nb-C15 as the GB precipitates, with **Bcc-Nb** and CuZr intermetallics as the matrix precipitates. The novelty of these new alloys compared to the previously developed [1] Cu-Cr-Nb-Zr alloys is twofold; to explore Ta as a potential alloying element replacing Nb to reach lower long-lived radioactivity after fusion neutron irradiation, and secondly to explore the strengthening role of the Bcc-Ta and Bcc-Nb phase as matrix precipitates. These three new alloys were fabricated through traditional (inexpensive) arc melting and drop casting techniques. The Cr and Ta (or Cr and Nb) had to be pre-alloyed to avoid vaporization of Cu. The as cast alloy had dimensions of 0.5×0.5×4in. It was then cold rolled to 70%-reduction in thickness. The as-rolled alloys were then solutionized at 970°C for 20 mins followed by water quench and then aging at 475°C for 3h. The compositions of newly designed alloys along with prior alloys are listed in Table 1.

Table 1. The compositions of developed Cu alloys

	Cu,wt%	Cr,wt%	Nb,wt%	Zr,wt%	Ta,wt%	GB and Disl. ppts	Matrix PPts
1CCNZ	Bal.	2	1.35	0.15		Cr_2Nb	Cr, Cr_5Zr
2CCNZ	Bal.	2.25	1.35	0.3		Cr_2Nb	Cr, Cr_5Zr
3CCNZ	Bal.	2.25	1.35	0.15		Cr_2Nb	Cr,Cr_5Zr
4CCNZ	Bal.	1.25	2	0.15		Cr_2Nb	Nb
1CCTZ	Bal.	2		0.15	2.5	Cr_2Ta	Cr,Cr_5Zr
2CCTZ	Bal.	1.25		0.15	4	Cr_2Ta	Ta

Optical microscopy and hardness measurement

The optical images of 1CCTZ are shown in Figure 1. There are two heat treatment conditions: solutioning state at 970°C for 20 min. followed by water quench, and aging state of the solutionized samples at 475°C for 3 h. The top row is low magnification images and the bottom row is high magnification images. In both states, we can see numerous precipitates with size less than 1 um distributed along the grain boundaries, dislocations and stacking faults. These precipitates, according to thermodynamic calculation, correspond to the Cr_2Ta_Laves phase. Another feature is that the microstructure of aged samples shows better recrystallized grain structure and more stacking faults. The hardness measurement shows Vickers hardness of aged samples at 116±4, almost twice that of the solutionized samples at 60 ±1.3. The increase of hardness, as suggested by thermodynamic calculation, is mainly due to the formation of Cr matrix precipitates, which could not be observed in the optical image due to their anticipated small size (<10 nm diameter). TEM characterization of these alloys is currently ongoing.

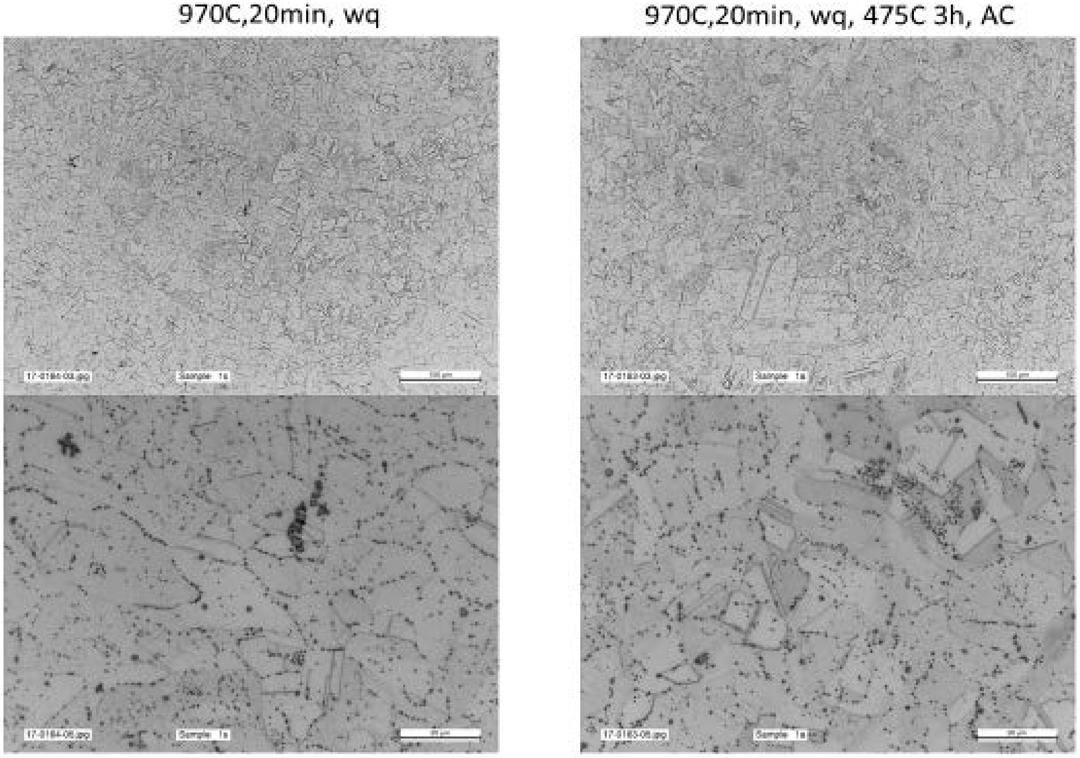

Figure 1. Optical images of 1CCTZ under two heat treatment conditions (left) solutioning state, (right) aging state and two magnifications (top) low mag. (bottom) high mag.

The optical images of 2CCTZ are shown in Figure 2. They followed the same fabrication, cold rolling and heat treatments conditions as the first alloy. Compared to the 1CCTZ alloy, this alloy shows few grain boundary precipitates. This alloy was designed to have Cr_2Ta-Laves GB precipitates and Ta matrix precipitates. What we observed here suggested most Ta, instead of forming the Cr_2Ta-Laves phase, was mainly used to form the Ta matrix precipitate, which however could not be observed under the optical imaging. In addition, the grain size is larger than that of 1CCTZ, probably due to less pinning from the GB precipitates. The hardness of aged samples is 104±2, compared to of the solutionized samples at 55±4.6, supporting our assumption that most of the Ta solute is forming Ta matrix precipitates for the heat treatment conditions used for the alloy fabrication.

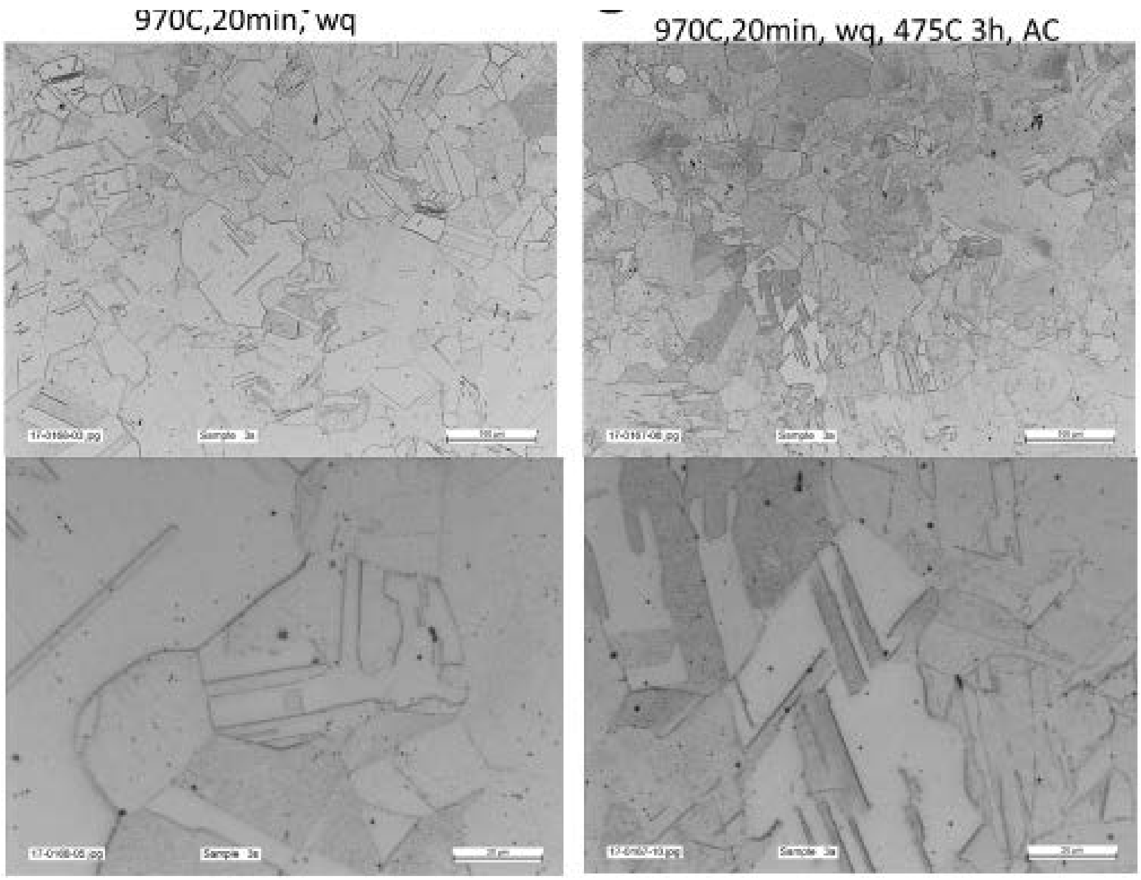

Figure 2. Optical images of 2CCTZ under two heat treatment conditions (left) solutioning state, (right) aging state and two magnifications (top) low mag. (bottom) high mag.

The optical images of 4CCNZ are shown in Figure 3. This alloy was designed to have Cr_2Nb-Laves GB precipitates and Nb matrix precipitates. This alloy shows less GB precipitates than 1CCNZ, 2CCNZ and 3CCNZ, which can also be due to formation of Nb matrix precipitates. In contrast to the CCTZ alloys, this alloy shows clustered regions of the larger-size second phase as a result of solidification segregation. The contrast suggests Nb has a stronger tendency to form solidification segregation than Ta. The hardness of aged samples is 117±3, compared to the solutionized samples at 67±7, supporting our assumption that most Nb is used to form Nb matrix precipitates.

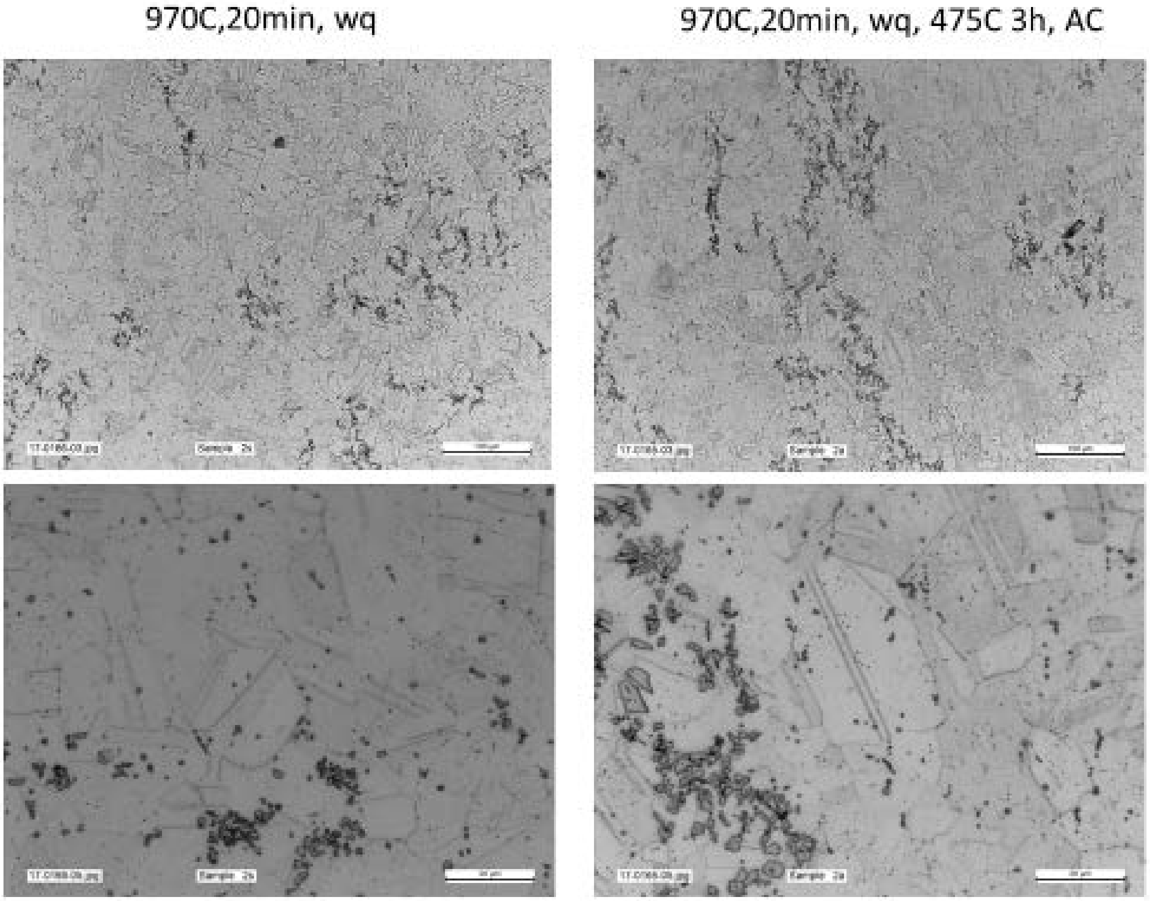

Figure 3. Optical images of 4CCNZ alloy under two heat treatment conditions (left) solutioning state, (right) aging state and two magnifications (top) low mag. (bottom) high mag.

Electrical and tensile properties

Type SSJ3 miniature sheet tensile specimens were machined from the cold-worked, solutionized and aged 1CCNZ, 2CCNZ and 3CCNZ thermomechanically treated Cu alloys. Following measurement of the room temperature electrical resistivity on the tensile samples, they were tensile tested at temperatures between 23 and 500°C. Most of the tensile tests were performed at a strain rate of $2.2\text{x}10^{-3}$ s^{-1}. A few tests at 300 and 500°C were performed at lower and higher strain rates ($2.2\text{x}10^{-4}$ or 0.056 s^{-1}). The room temperature tests were in air, whereas the elevated temperature tests were performed in inert gas. Table 2 summarizes the room temperature hardness, electrical resistivity and tensile properties of these three alloys. The electrical conductivity values were low compared to standard high strength, high conductivity alloys such as Cu-Cr-Zr [3], but still represents relatively high conductivity for a high strength Cu alloy. All of the alloys exhibited good work hardening capacity and good ductility at room temperature.

Table 2. Summary of room temperature properties of Cu-Cr-Nb-Zr alloys. All alloys were cast, cold-rolled 50% (70% for 1CCNZ-T alloy series), then solutionized at 970°C for 20 minutes, quenched and aged at 475°C for 3 h (SAA treatment).

Alloy and TMT	Hardness (VHN)	Electrical conductivity (%IACS)	Yield strength (MPa)	Ultimate strength (MPa)	Uniform elongation (%)	Total elongation (%)
1CCNZ-F (50%CW+SAA)	124.7	55.8	230	336	12.2	21
1CCNZ-T (70%CW+SAA)	124.7	56.7	255	385	20.2	29
3CCNZ-X (50%CW+SAA)	124.0	56.5	232	302	7.2	13
2CCNZ-Y (50%CW+SAA)	106.5	57.8	239	383	19	28

Figures 4 and 5 summarize the temperature-dependent yield strength and ultimate tensile strength, respectively for the four tensile-tested Cu-Cr-Nb-Zr alloys. Whereas the room temperature yield strengths are comparable for the four tested alloy conditions, at 500°C the 3CCNZ alloy exhibited significantly lower yield strength. This alloy also exhibited the lowest ultimate tensile strength at both room temperature and 500°C. The other three tested alloys exhibited similar high temperature yield strengths, with the 1CCNZ alloy subjected to 70% cold work prior to solution annealing and aging having slightly higher yield strength and the 2CCNZ alloy exhibiting slightly higher ultimate tensile strength. All of the alloys exhibited satisfactory uniform elongations over the entire range of tested temperatures, with observed values in the range of 7 to 19%.

The temperature dependence of the yield strength of the 1CCNZ-F series alloy is compared with several other copper alloys in Figure 6. Overall, the decrease in strength with increasing temperature for the Cu-Cr-Nb-Zr alloys was somewhat less pronounced than that observed [3] in traditional high strength, high conductivity copper alloys such as GlidCop Al25 or CuCrZr, and was comparable to that of Cu-8%Cr-4%Nb (GrCop84) [4] produced by relatively expensive powder metallurgy/ rapid solidification techniques.

To provide further insight on the thermal creep behavior of the CuCrNbZr alloys, the yield strength (σ_y) versus strain rate (de/dt) behavior is plotted at 300 and 500°C and compared with that of several other Cu alloys [3] in Figure 7. At relatively low temperatures, the strain rate sensitivity parameter m, defined by $m_y=C(de/dt)^m$ where C is a constant, is small indicating a weak dependence on strain rate. As the test temperature increases into regimes relevant for thermal creep deformation processes, the strain rate sensitivity parameter increases. For the case of CuCrNbZr, the strain rate parameter remains small (m~0.06) for test temperatures up to 500°C.

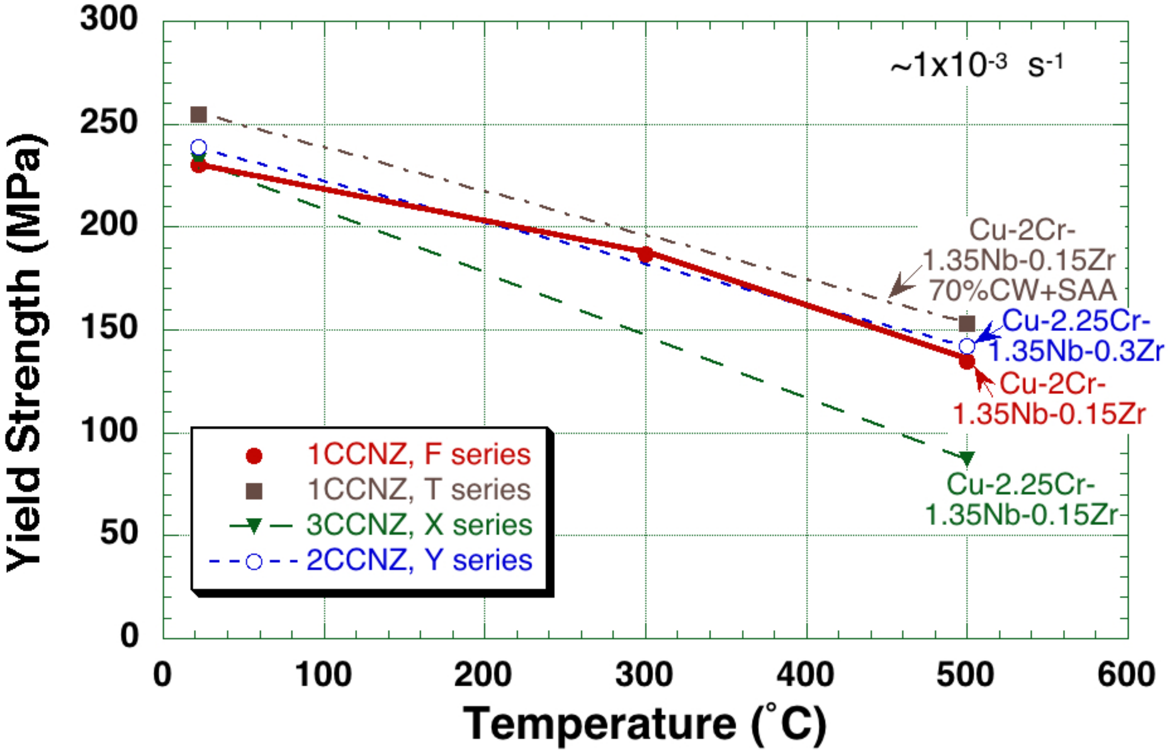

Figure 4. Temperature dependence of CuCrNbZr alloy yield strength.

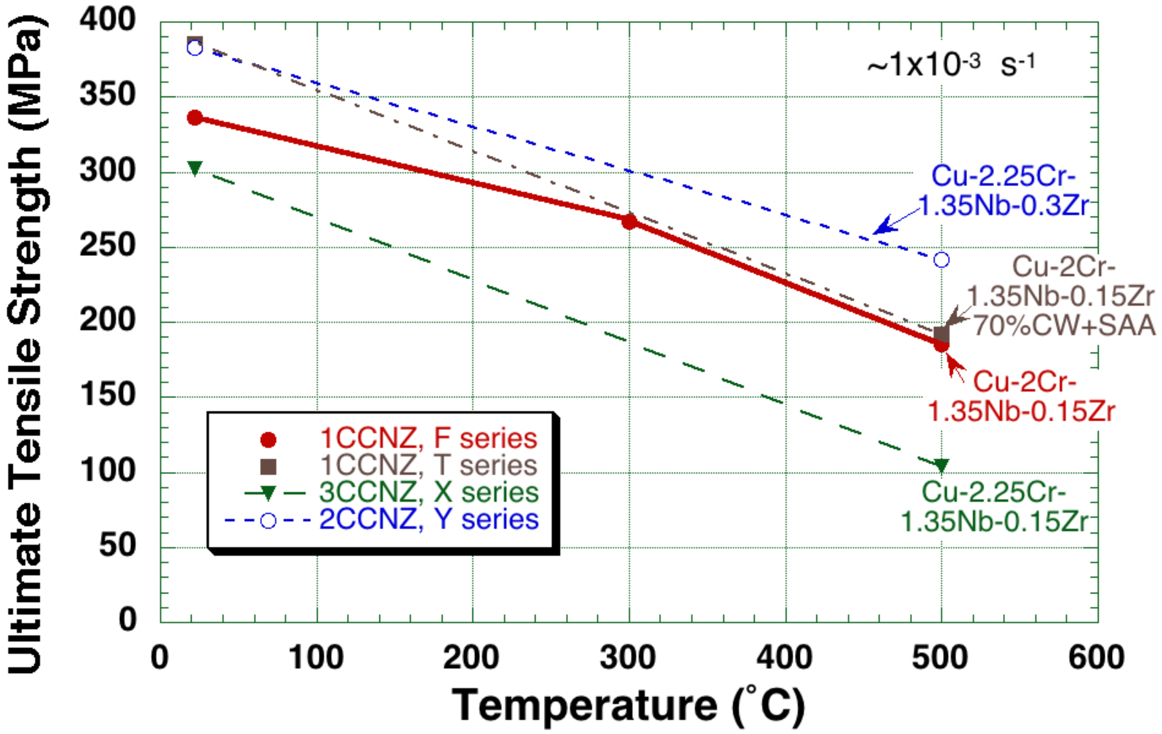

Figure 5. Temperature dependence of CuCrNbZr alloy ultimate tensile strength.

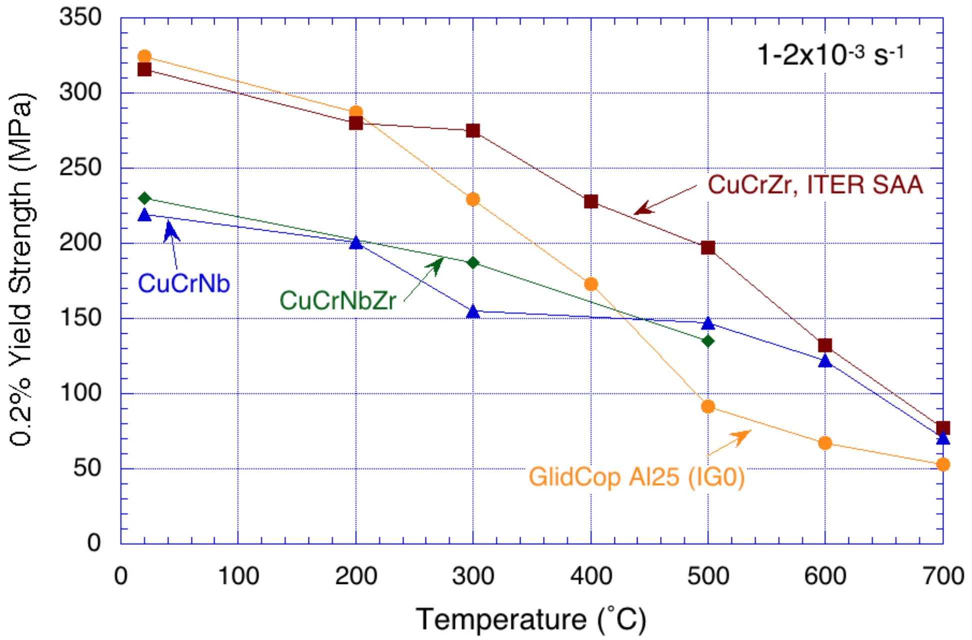

Figure 6. Comparison of the temperature-dependent yield strength of 1CCNZ (F-series) with several other Cu alloys.

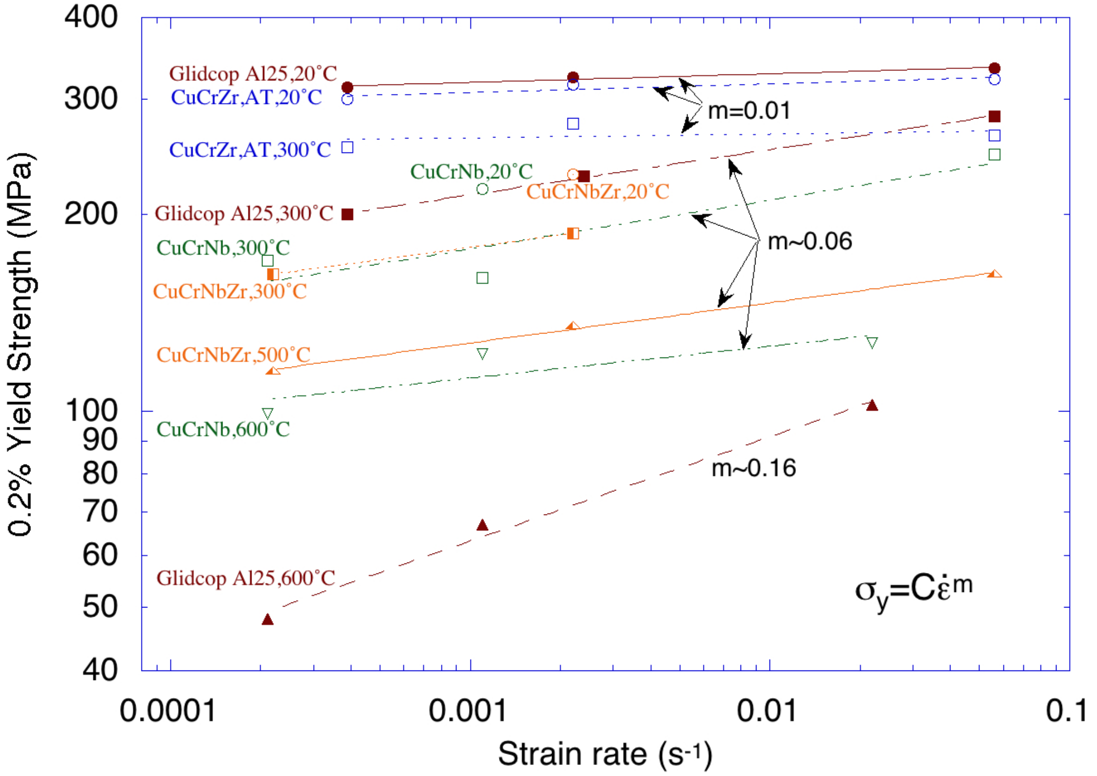

Figure 7. Effect of strain rate on the yield strength of 1CCNZ (F series) and several other Cu alloys at various temperatures.

TEM characterization

Microstructural characterization by TEM has been performed on the aged 1CCNZ and 3CCNZ alloy. These two alloys were cold rolled to a thickness of 3.75 or 6.26 mm (70% and 50% CW, respectively) then annealed at 970°C for 20 minutes followed by water quench and then aged at 475°C for 3h followed by air cooling. The TEM sample was prepared using Quanta focused ion beam milling. For the 3CCNZ alloy, Figure 8 (a) shows four precipitates located on grain boundaries, with diameters between 150 nm and 350 nm, that are considered to be Cr_2Nb Laves phases according to the heat treatment. The insert diffraction pattern is from the dark grain on the left. Figure 8(b) is a STEM mode BF image showing the distribution of those Cr precipitates. The denuded width around grain boundaries is 150 nm as showed in Figure 8(c) when the TEM sample was tilted at 0 degree. Figure 8(d) is selected from the area in this dark grain with a magnified image in Figure 8(e) showing a uniform distribution and nearly spherical shape of Cr precipitates with a size range from 5 nm to 10 nm. Many of the precipitates are coherent with the matrix, judging from the BF image under two beam conditions when the so-called no contrast line appears in normal direction to the ***g*** vector. The density of Cr precipitates is approximately $1.3\times10^{22}/m^3$.

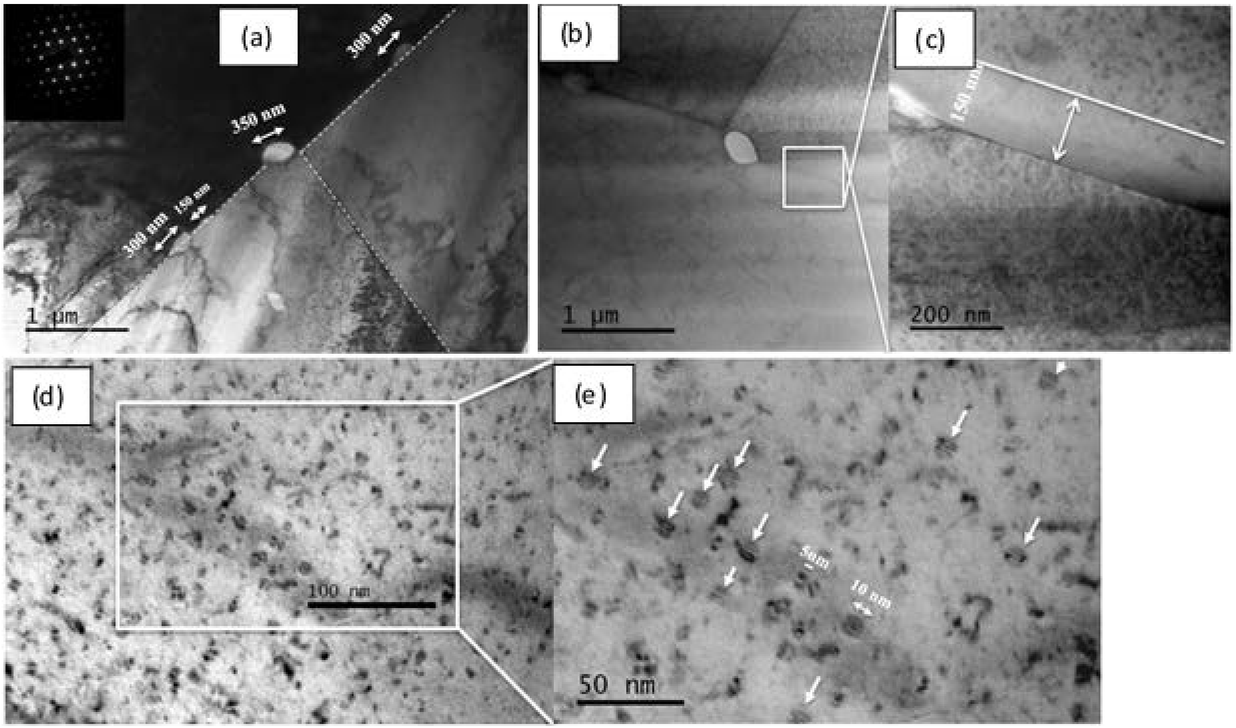

Figure 8. (a) TEM image of the 3CCNZ alloy with precipitates on the grain boundary, the insert image is the diffraction pattern for dark grain. (b) a STEM mode BF image showing the distribution of Cr and Cr_2Nb precipitates. (c) the denuded area around 150 nm away from the grain boundary. (d). Bright Field image selected from the area in dark grain in Figure 8. (a). (e)the zoom-in image showing the coherent relationship between Cr precipitates and Cu matrix. White arrows indicate the so-called no-contrast line appears in normal direction to the ***g*** vector.

For 1CCNZ alloy, Figure 9(a) is a STEM mode BF image showing matrix precipitates are on each side of the grain boundaries; two precipitates are located on the grain boundary with the size of 85 nm and 43 nm as shown in Figure 9(b). The density of those precipitates calculated from Figure 9(c) is approximately

$1.2x10^{22}/m^3$ with average precipitate size of 10 nm and sample thickness of 120 nm as shown in Figure (d).

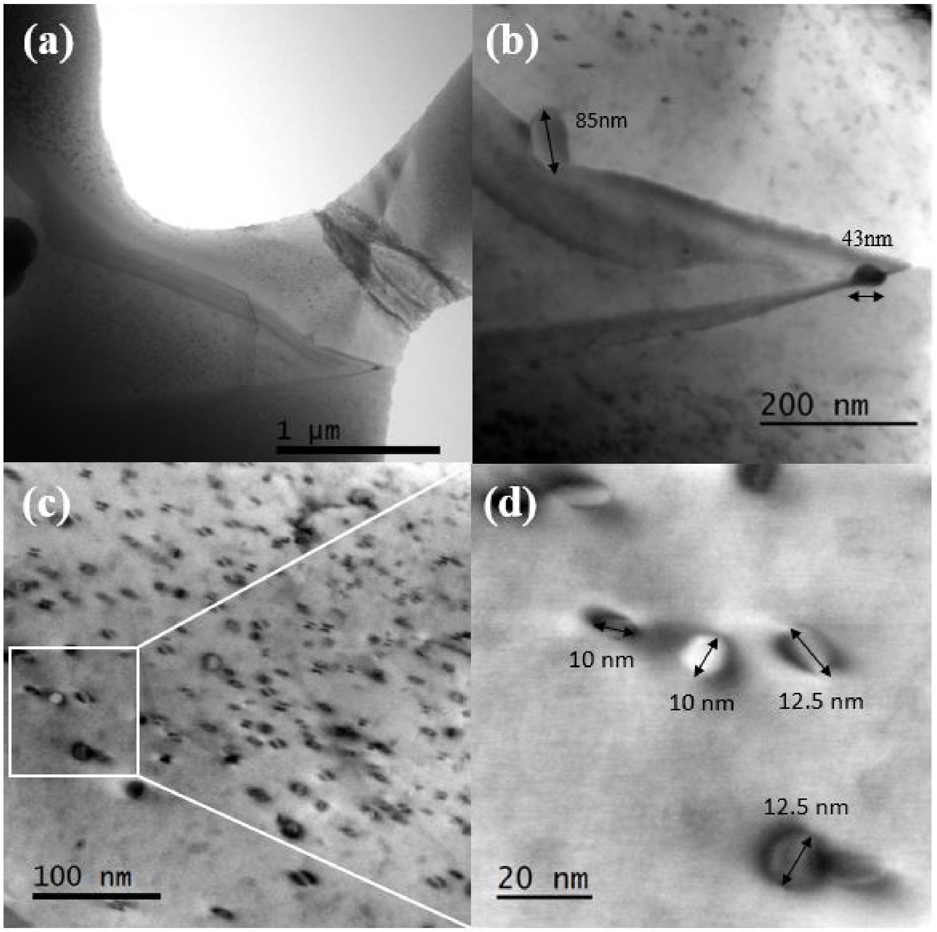

Figure 9. (a), (b), (c) and (d) are all STEM mode BF images of the 1CCNZ alloy; (a) the distribution of matrix precipitates is on each side of the grain boundary; (b) two precipitates located on the grain boundary with size of 85 nm and 43 nm diameter; (c) a magnified image allowing the density of those matrix precipitates to be estimated as around $1.2x10^{22}/m^3$ (d) the average precipitate size near 10 nm is indicated with black arrows in Figure 9(d).

The comparison between the TEM images of the 3CCNZ and 1CCNZ alloys suggested several similarities and differences. First, the number density of Cr precipitates in 3CCNZ is $1.3x10^{22}$ $/m^3$, nearly identical to that in the 1CCNZ alloy ($1.2x10^{22}$ $/m^3$). Second, the Cr precipitates in 3CCNZ didn't show greater coarsening than those in 1CCNZ (5~10nm in 3CCNZ vs. 10~12.5nm in CCNZ_A). Third, the GB precipitates in 3CCNZ alloy are much larger and lower density than those in the 1CCNZ alloy (150~350nm in 3CCNZ vs 43~85nm in 1CCNZ). Therefore, we can hypothesize that the high Cr content did not significantly enhance the formation of Cr matrix precipitates but did lead to significantly coarsened Cr_2Nb GB precipitates. Because the formation of Cr_2Nb GB precipitates happened at high temperature, it has fast kinetics and therefore can grow into large sizes. The larger size and lower number density of GB precipitate in 3CCNZ is less effective at pinning the grain boundary; therefore, some abnormal grain growth occurred. This finding may correlate the weaker tensile properties of the 3CCNZ alloy to the larger size and lower number density of GB Cr_2Nb precipitates. If the TEM study of the 2CCNZ alloy also shows smaller size and higher number density of GB precipitates, that would confirm this hypothesis.

Future work

1) Continue TEM characterization of additional CCNZ and CCTZ alloys, and identify fine and ultrafine precipitates.
2) Continue tensile tests and thermal physical properties of CCTZ and 4CCNZ alloys.
3) Perform thermodynamic calculations of the Cu-Cr-X-Y system to explore other potential Cu alloys for high heat flux structures.

References

[1]. Y. Yang and S.J. Zinkle, "Design and development of novel Cu alloys for fusion energy applications", Fusion Materials Semiannual Progress Report for Period ending June 30, 2016, DOE/ER-0313/60, pp. 83-88.

[2]. Y. Yang, S.J. Zinkle and L.L. Snead, "Design and development of novel Cu alloys for fusion energy applications", Fusion Materials Semiannual Progress Report for Period ending Dec. 31, 2016, DOE/ER-0313/61, pp. 69-72.

[3] S.J. Zinkle, "Tensile properties of high-strength, high-conductivity copper alloys at high temperatures", Fusion Materials Semiannual Progress Report for Period ending June 30, 2000, DOE/ER-0313/28, Oak Ridge National Lab, 2000, pp. 171-175.

[4] H.C. deGroh, D.L. Ellis, W.S. Loewenthal, Comparison of GRCop-84 to other Cu alloys with high thermal conductivities, J. Mater. Eng. Perf. 17 (2008) 594-606.

4.2 FABRICATION OF ROLL BONDED FUNCTIONALLY GRADED TUNGSTEN-STEEL LAMINATE—L. M. Garrison, J. Mettler, J. Moon (Oak Ridge National Laboratory)

OBJECTIVE

The objective of this project is to create a functionally graded tungsten to steel laminate composite for use in plasma facing components in fusion reactors.

SUMMARY

Two roll-bonded tungsten-steel composites have been fabricated. Shear punch tests of the individual tungsten and steel foils showed the tungsten foil mechanical properties are closely tied to the grain orientation texture. Tensile tests of the generation 1 composite were completed and showed increasing strength and decreasing ductility with increasing W content. The composite has improved ductility at room temperature compared to tungsten foil or tungsten plate.

PROGRESS AND STATUS

Foil Properties

Understanding the properties of the composite requires understanding the properties of the individual foils. Shear punch, three point bend, and tensile tests have been carried out at room temperature on tungsten and steel foils of different thicknesses. The steel foils all have some ductility in shear punch tests, but for the tungsten foils the ductility is strongly influenced by the crystallographic texture and degree of deformation (Figure 1). Additionally, tungsten foil with the same thickness, but produced by different manufacturers (ESPI or PLANSEE) show different behavior in shear punch tests.

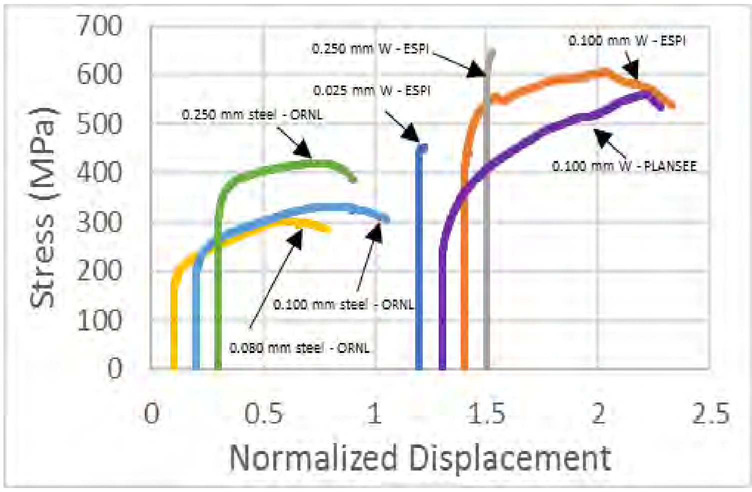

Figure 1. Room temperature shear punch stress versus normalized displacement for tungsten and steel foils.

Roll-bonding

The roll-bonded composites were fabricated by alternately stacking W and steel foils inside a stainless steel box, which was vacuum welded closed before forging and rolling to prevent oxidation of the composite. In the generation 1 composite, the thicknesses of W and steel foils were varied throughout the thickness of the composite to attempt to create a functionally graded composition (Figure 2). The bonding of the foils was accomplished by forging and rolling the outer stainless steel shell at 1000°C to

80% total thickness reduction. Tensile bars were machined from the generation 1 composite such that the tensile direction was parallel to the rolling direction of the foils and composite.

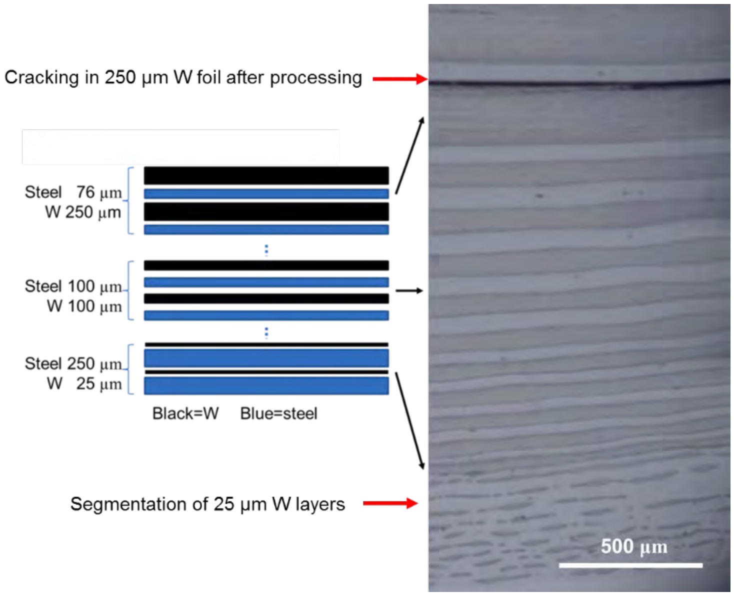

Figure 2. Diagram of tungsten and steel foil stacking sequence before processing with corresponding cross section image of composite after processing. In the image on the right, tungsten layers have darker contrast than steel layers.

Tungsten-steel composites of the three different geometries shown in Figure 1, with either 250, 100, or 25 µm thick initial W foils, were tensile tested at room temperature with a crosshead speed of 0.5 mm/sec. All the samples tested were of SSJ 2 geometry. The samples are identified according to the thickness of the tungsten foil used to produce the sample, with W250-1, for example, representing the first sample tested which was produced using 250 µm thick tungsten foil (the top section in Figure 2). The composite was produced from alternating layers of cold rolled tungsten and steel, so the actual layer thicknesses in each tensile sample is less than the thickness of the foil used to produce the sample. The results of tensile testing are shown in Figure 3. Five samples of each type were tested and tests which ended in a brittle fracture are excluded from Figure 3. The results are plotted excluding elastic strain due to the lack of an extensometer.

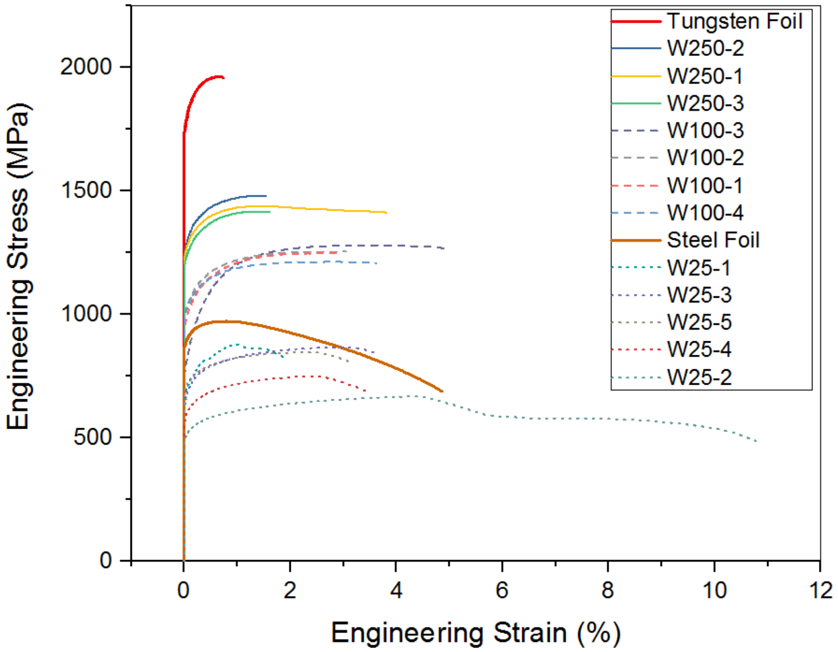

Figure 3. Stress-strain relationship in various tungsten-steel composites tested at room temperature. The elastic strain has been removed from the data, so only the plastic strain is shown and the initial part of the curve is represented as a vertical line.

Samples consisting primarily of tungsten exhibit a greater ultimate tensile strength than those with a larger fraction of steel, as expected. A much larger variability was observed in the samples consisting of mostly steel, likely a result of the fact that the tungsten layers in these samples became fragmented during production and no longer formed contiguous layers, as seen in the lower region of Figure 2. This resulted in uneven, tearing fractures rather than clean breaks as was observed in other sample types. It should also be noted that samples consisting of a larger amount of tungsten were more likely to undergo brittle fracture before reaching the plastic deformation region. Two samples of the W250 type and one of the W100 type showed brittle failure, whereas none of the W25 type underwent brittle failure.

The two lines depicting “Steel Foil” and “Tungsten Foil” in Figure 3 represent the results of testing the 250 µm steel and tungsten foils individually. The results indicate that the steel foil exhibited a higher UTS than any of the composites produced using 25 µm tungsten foil. This is likely a result of a combination of factors, such as the fact that the grain geometry was elongated during the cold rolling process and that the samples were thick enough to no longer exhibit the same flexibility demonstrated in foils. Considering the W100 and W250 composite samples, as tungsten thickness increases the UTS also increases, deviating further from steel and instead approaching the behavior exhibited by the tungsten foil.

Figure 4 depicts three examples of fracture surfaces after tensile testing. Figure 4a demonstrates the typical fracture surface observed in samples from the W25 group. These fractures tended to be more ductile, producing rugged fracture surfaces, compared to the more cleavage-like fractures seen in W100 and W250 samples. This may be a result of the discontinuous nature of the tungsten layers in the W25 samples. The rugged surfaces observed in the W25 samples made them more difficult to image, and resulted in low contrast between the tungsten and steel layers, making it difficult to identify and measure layer thicknesses. Polishing will be necessary to determine layer thickness in these samples. Figures 4b and 4c by comparison clearly depict the alternating tungsten and steel layers. Measurements of one representative interior layer for each sample were taken based on the digital images and the results are recorded in Table 1. Further details of the fracture surface images can be found in the appendix at the end of this section. It should be noted that some samples showed a greater variability in layer thickness than others. This is reflective of inconsistencies produced during cold rolling and further contributes to the variability seen in the tensile results of Figure 3. Further work will be necessary to examine the effect of these variations on the results obtained.

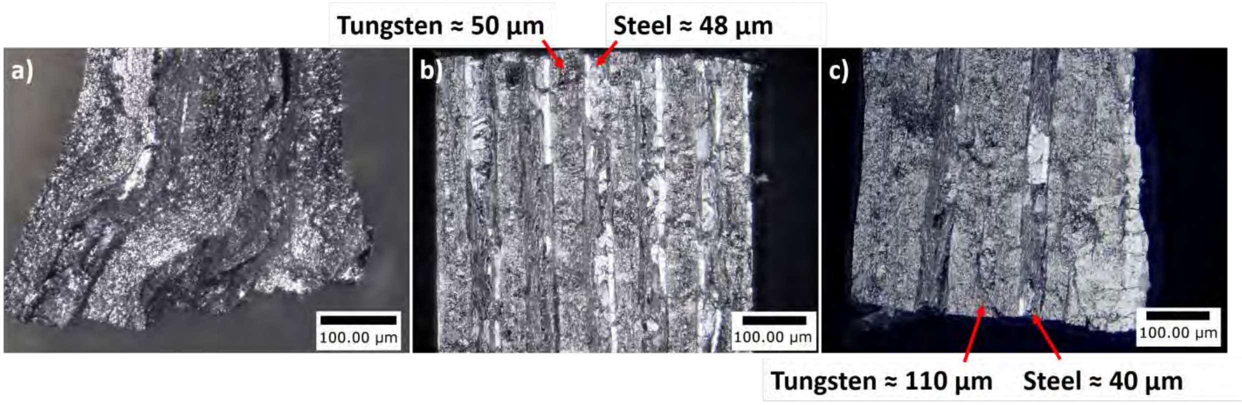

Figure 4. Fracture surfaces showing composite layers and thicknesses, a) W25-1, b) W100-2, c) W250-3.

Table 1. Summary of relevant layer parameters and room temperature tensile data for each sample. "A" denotes values for which the fracture surface was too rugged for data to be determined from the image and "B" denotes images which had too little contrast to determine the total number of layers. For samples that had brittle fracture, only the UTS is listed, which is equivalent to the fracture strength.

Sample Name	# W layers	Avg. W Thickness (µm)	# Steel Layers	Avg. Steel Thickness (µm)	YS (MPa)	UTS (MPa)	UE (%)	TE (%)
W25-1	A	A	A	A	762	879	1.0	1.9
W25-2	A	A	A	A	551	668	4.4	10.8
W25-3	A	A	A	A	742	866	3.0	3.6
W25-4	A	A	A	A	646	750	2.4	3.5
W25-5	A	A	A	A	757	847	2.2	3.1
W100-1	7	43	7	38	1072	1249	2.6	3.0
W100-2	6	50	5	48	1105	1255	3.0	3.1
W100-3	B	38	B	37	956	1280	3.8	4.9
W100-4	B	35	B	37	1090	1213	2.8	3.6
W100-5	A	A	A	A	—	477	—	—
W250-1	3	141	2	33	1340	1438	1.4	3.8
W250-2	3	146	2	35	1370	1480	1.4	1.5
W250-3	3	113	2	40	1310	1417	1.4	1.6
W250-4	3	152	2	55	—	1220	—	—
W250-5	A	A	A	A	—	743	—	—

Appendix

Fractography of Tungsten Steel Composite Materials Tensile Tested at Room Temperature

The following images show the fracture surface (left) and profile view (right) for each of the roll-bonded tungsten-steel composite samples shown in Table 1. The Keyence microscope used was an optical, digital microscope. Due to the limitations of the equipment, images of fracture surfaces with large topographical changes exhibited distortions after stitching. Such surfaces also resulted in poorer overall image quality. Further imaging with different equipment may be necessary.

Fracture Surface Profile

W25-1

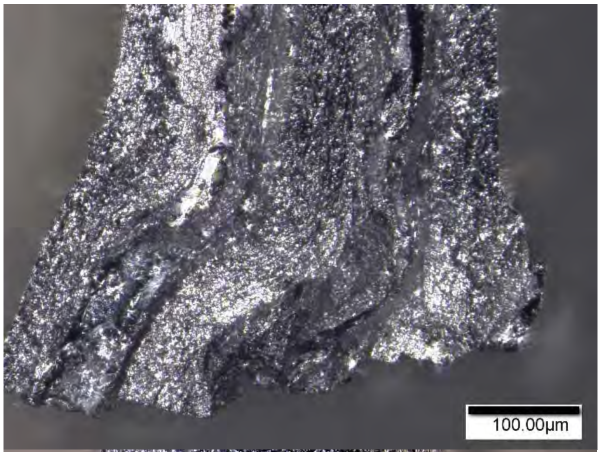

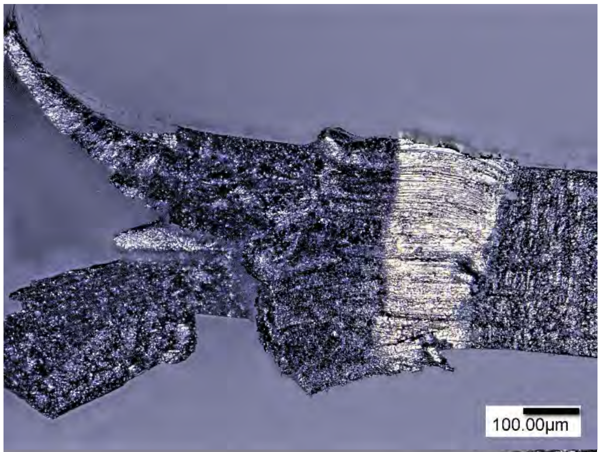

W25-2

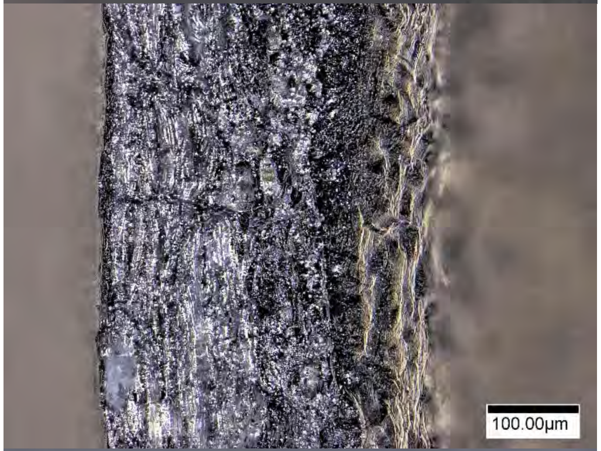

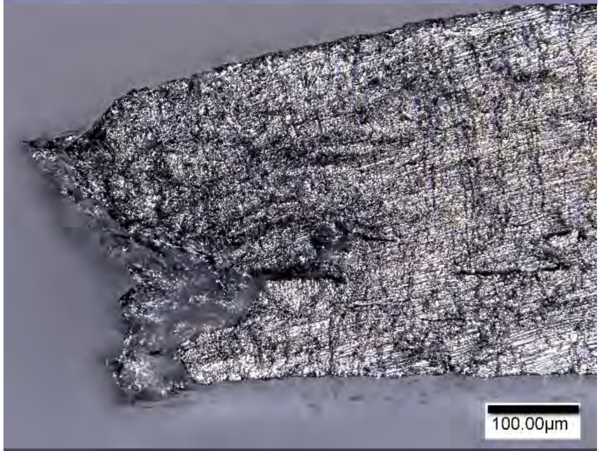

W25-3

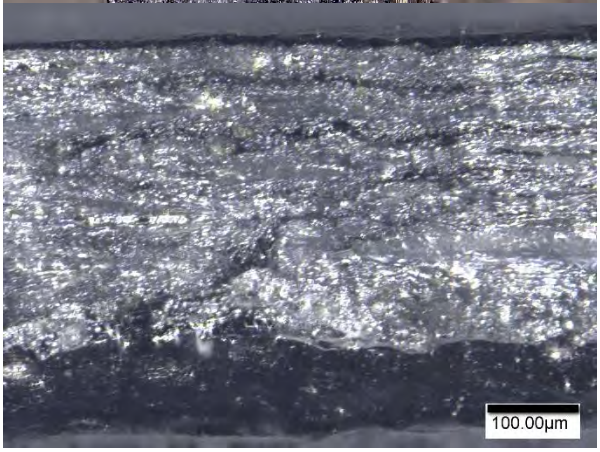

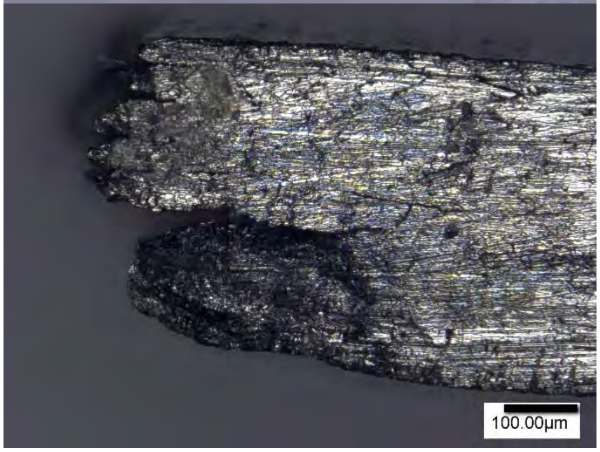

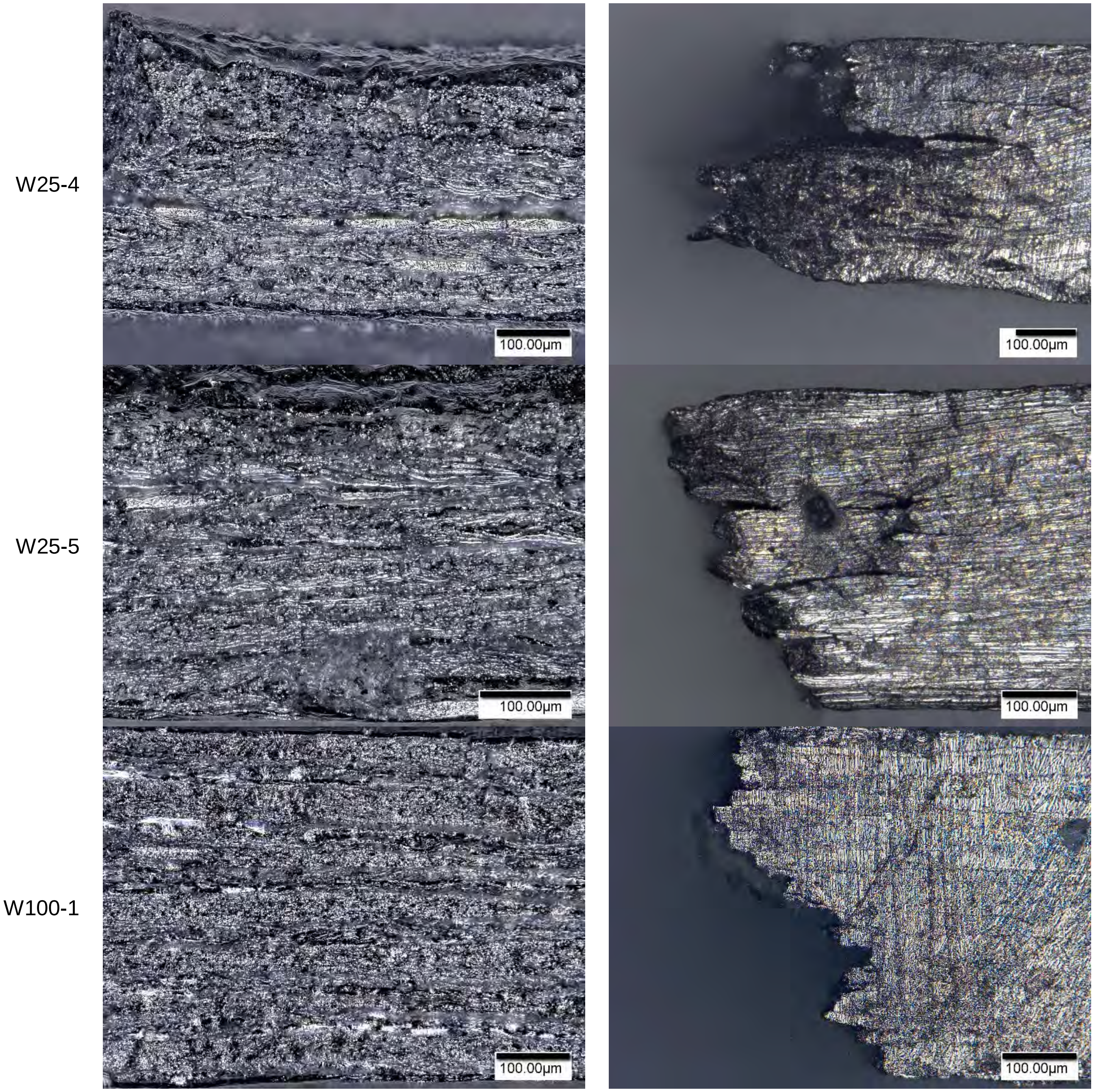
W25-4
100.00µm
100.00µm
W25-5
100.00µm
100.00µm
W100-1
100.00µm
100.00µm

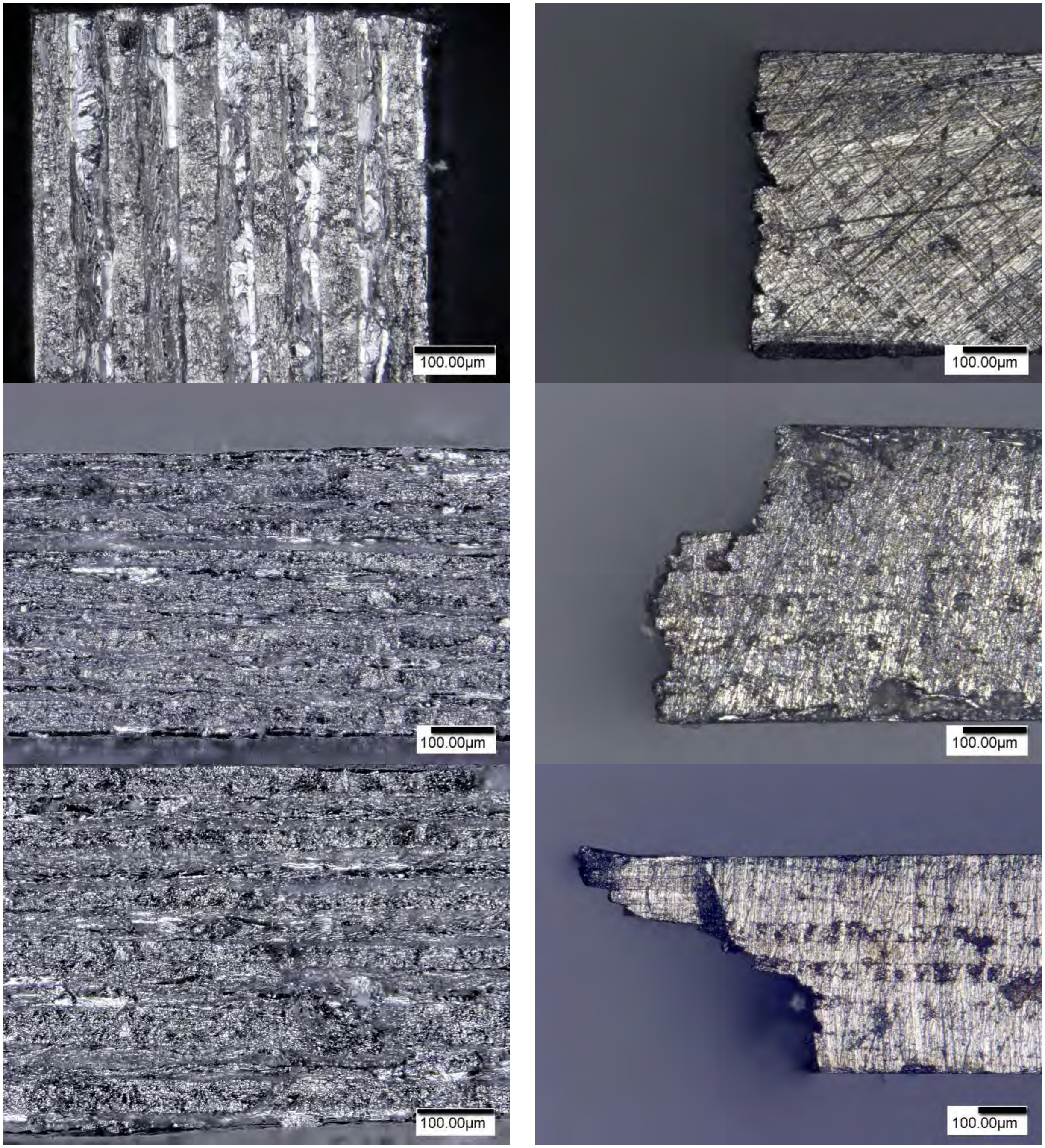
W100-2
100.00µm
100.00µm
W100-3
100.00µm
100.00µm
W100-4
100.00µm
100.00µm

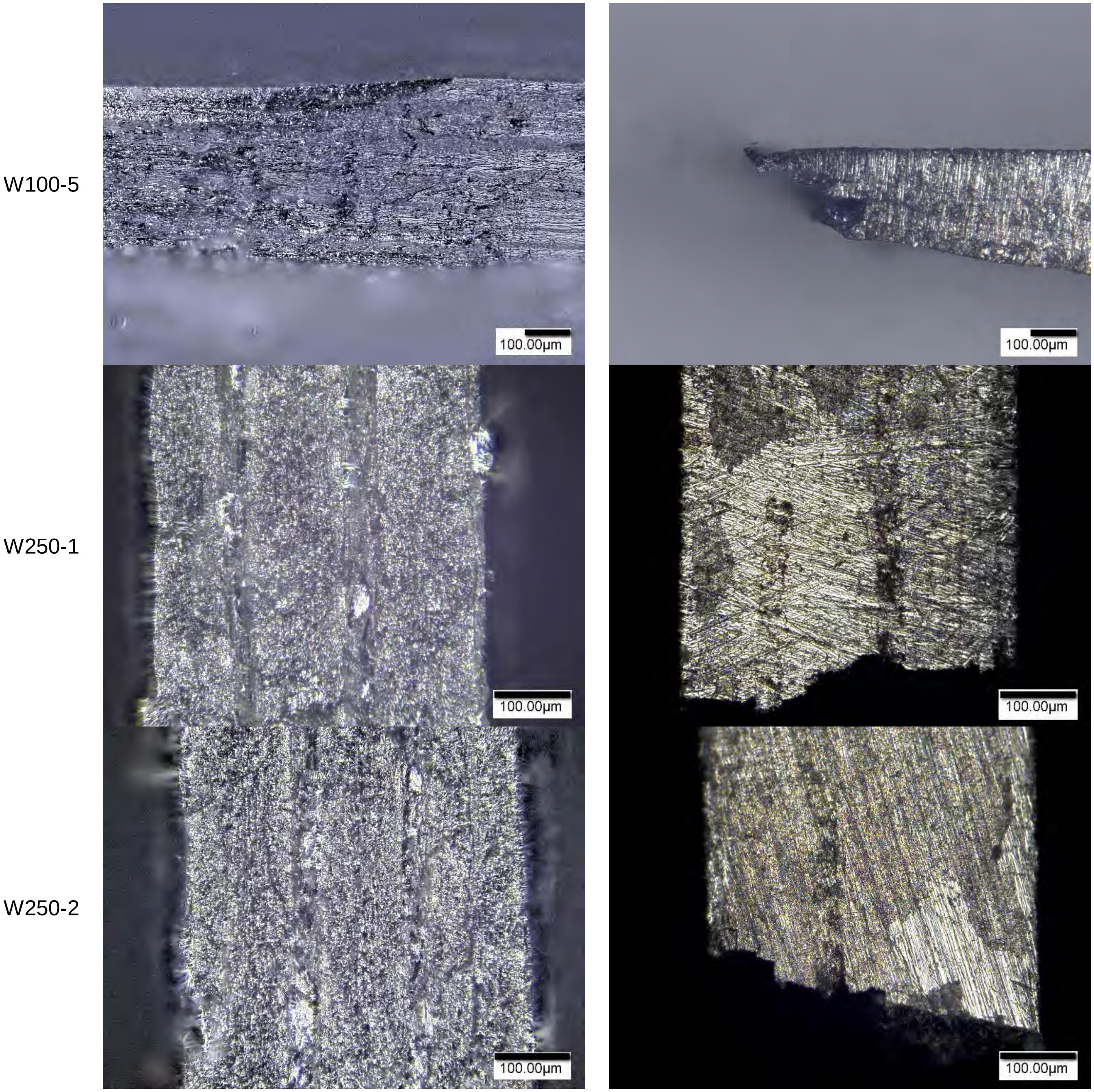
W100-5
100.00µm
100.00µm
W250-1
100.00µm
100.00µm
W250-2
100.00µm
100.00µm

W250-3

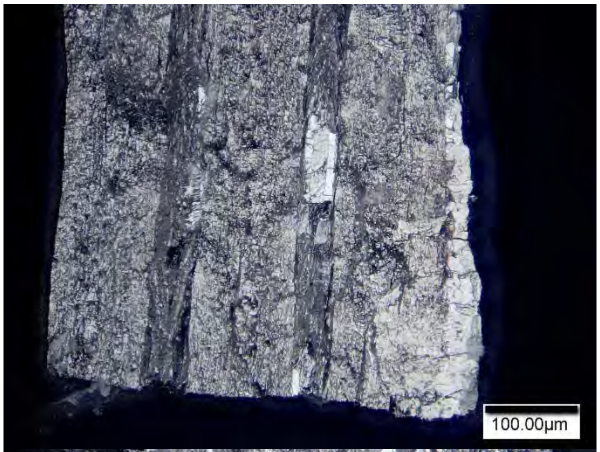

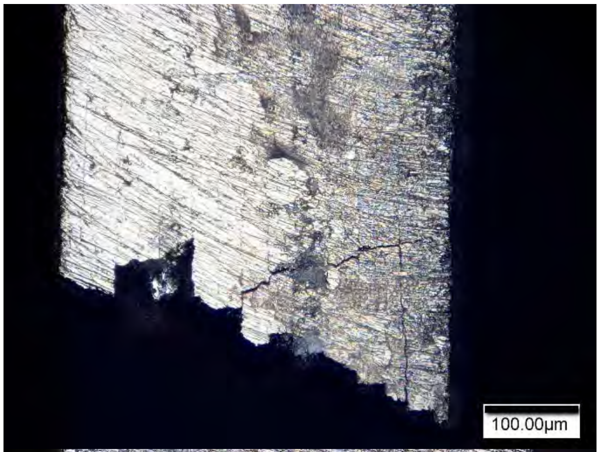

W250-4

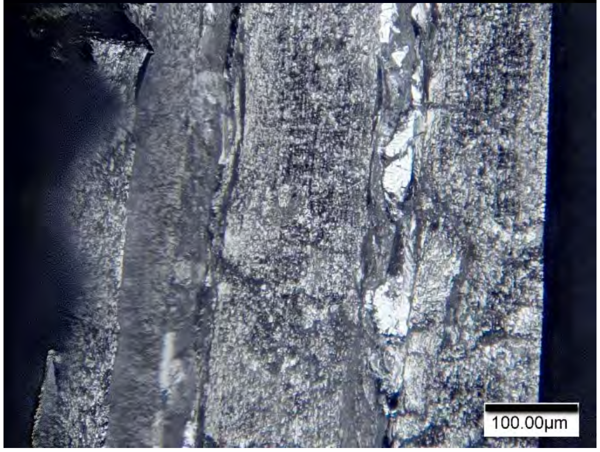

W250-5

Image not available due to high angle of fracture face

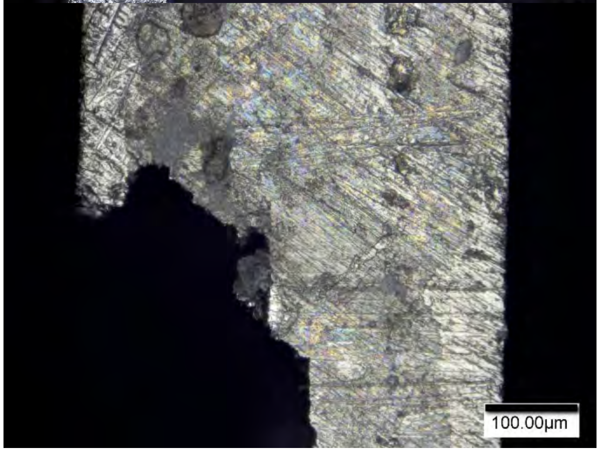

4.3 FABRICATION OF ULTRASONIC WELDED FUNCTIONALLY GRADED TUNGSTEN-STEEL LAMINATE—L. M. Garrison, D. Leonard (Oak Ridge National Laboratory) and M. Norfolk, J. Wenning (Fabrisonic LLC.)

OBJECTIVE

The objective of this project is to create functionally graded tungsten to steel laminate composite for use in plasma facing components in fusion reactors.

SUMMARY

A feasibility study for ultrasonic welding tungsten to steel was completed. The 34 trials varied the parameters of foil thickness, interlayer material, welding force, vibration amplitude, and other welding parameters. Promising results were obtained for joining tungsten directly to steel and tungsten to steel with an aluminum interlayer.

PROGRESS AND STATUS

An initial investigation of the feasibility of ultrasonic bonding was completed with the company Fabrisonic, which specializes in ultrasonic welding of dissimilar materials. This was a scoping study to evaluate the possibility of successfully welding tungsten to other candidate materials, especially steel and copper. Overall, 34 trials were completed that varied the parameters of foil thickness, interlayer material, welding force, vibration amplitude, and other welding parameters. Six of the trials that showed at least partial bonding success were selected for more in depth interface analysis (Table 1). The welding trials were completed on large stainless steel or aluminum base plates, so to prepare for interface analysis, small sub-sections of the selected trials were machined with electrical discharge machining, and then the cross sections were polished.

Table 1. Ultrasonic welding trials selected for further interface analysis

Trial number	W foil thickness	Interlayer	Substrate
23	0.025 mm	Cu	Al
28	0.10 mm	Al	Steel
29	0.10 mm	Al	Steel
31	0.10 mm	Cu	Steel
33	0.25 mm	none	Steel
34	0.25 mm	none	Steel

SEM imaging and energy dispersive X-ray spectroscopy (EDS) analysis have been completed on the trials in Table 1. For Trial 23, the W foil did not initially bond to the Cu interlayer, but after ultrasonic processing grey or silver regions were visible on the surface of the Cu. EDS analysis on Trial 23 revealed that there was W present on the surface (Figure 1). This indicates that there was partial bonding of areas of the W foil during welding but that a full layer bond was not completed.

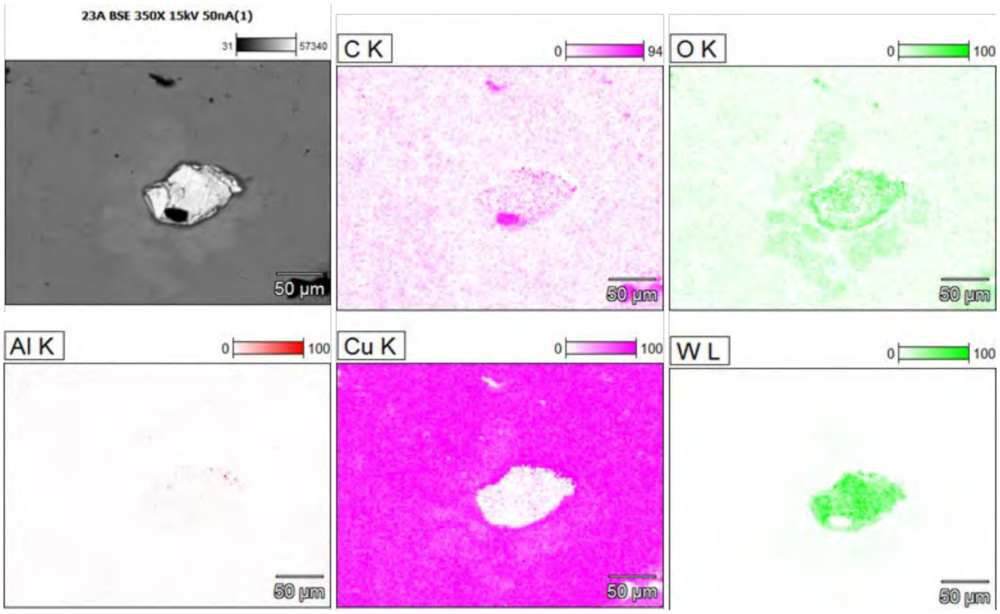

Figure 1. EDS analysis of a small W particle bonded to the Cu surface from ultrasonic weld Trial 23.

Trial 28 achieved a successful bond between all three layers, W-Al-steel (Figure 2a). The Al to steel bond had the same characteristics across the examined cross section region (Figure 2b). The W and Al also had a successful bond throughout the examined region (Figure 2c), however, many intergranular cracks developed in the W foil layer during the ultrasonic welding (Figure 2d). They were found both close to and far from the Al interlayer. As predicted, there is no noticeable mixing or intermetallic phase on the W-Al boundary (Figure 3). The phase analysis on Trial 28 identified Phase 1 to be 98.19 wt. % W and the remaining 1.81 wt. % of O, C, and Al. Phase 2 consisted of 94.31 wt. % Al, 0.63 wt. % Fe, 2.63 wt. % C, 0.75 wt. % O, and 1.67 wt. % W. Trial 29 was also a W-Al-steel weld, but used different welding parameters. This resulted in only a partial bond of the W and Al layers to the steel (Figure 4.)

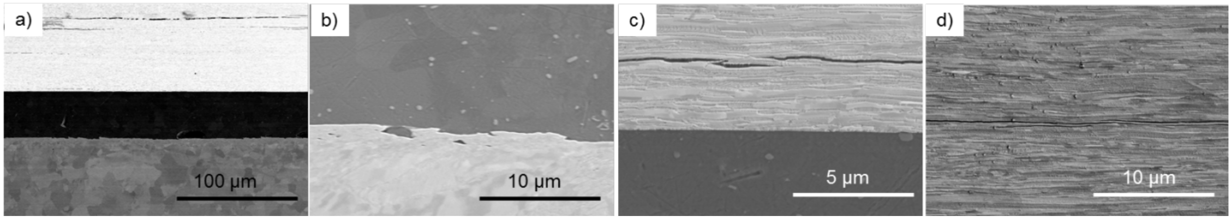

Figure 2. SEM cross section images of Trial 28. a) low magnification image of cross section, W-Al-steel top to bottom, b) Al (top) and steel (bottom) bond detail, c) W (top) and Al (bottom) bond detail, d) intergranular cracks in W layer.

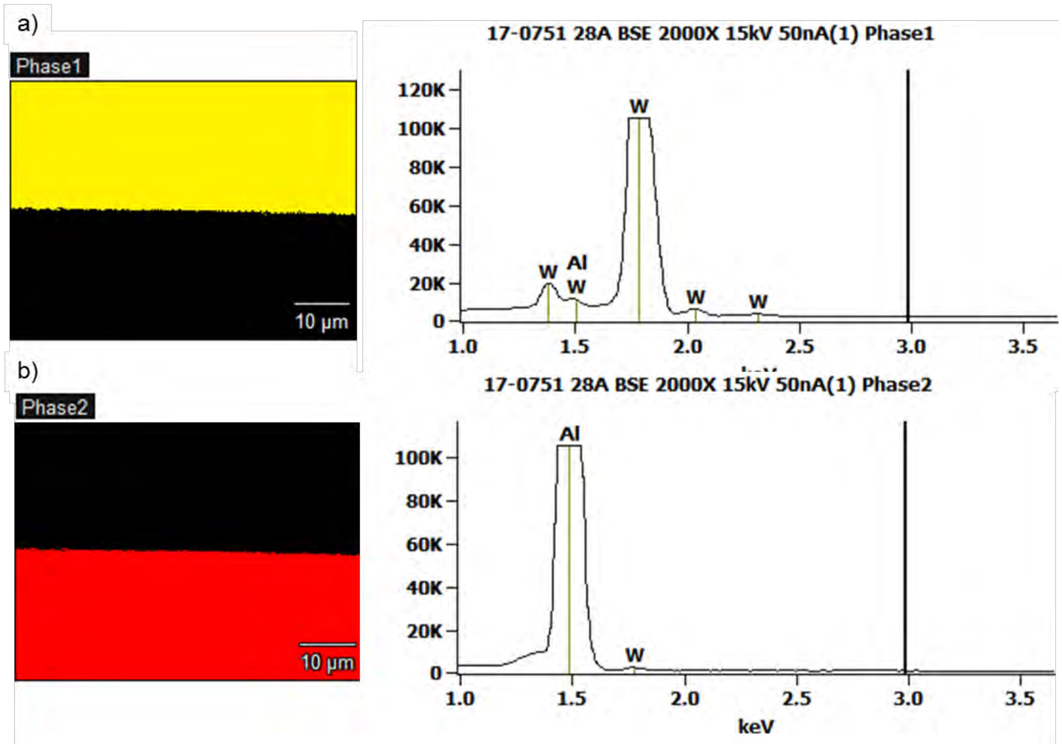

Figure 3. EDS phase analysis of the W-Al bonded region in Trial 28.

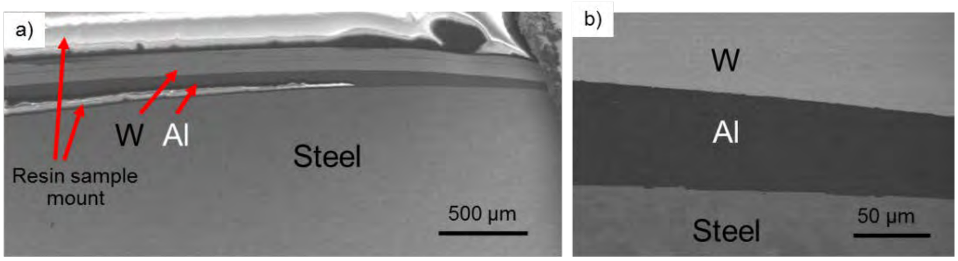

Figure 4. SEM cross section image of Trial 29.

Trial 31 used a Cu interlayer between the W foil and steel substrate. While macroscopically a bond formed and the W foil was attached to the surface, in the cross section it appears that there is a gap between the W and Cu layers (Figures 5a-b). The cross section sample was mounted in a resin material for polishing and that resin is visible in the SEM images between the layers, indicating a gap existed before polishing. Across most of the examined cross section, the Cu and steel formed a continuous bond as in Figure 5c.

Trial 33 was the second of the analyzed group that macroscopically had a bond between the W and steel, but in the cross section analysis no joint could be found (Figure 6a). This trial was the first to achieve partial success in bonding without using an interlayer between the W and steel. As with all other trials analyzed here, internal delaminations and cracks were found in the W foil after the ultrasonic welding (Figure 6b).

The final trial, number 34, achieved a successful bond between a W foil and the steel substrate without using an interlayer (Figure 7a). This ultrasonic weld required more power input than the others, and there are additional internal cracks seen in the W layer. This is likely because higher forces were used for directly bonding the tungsten to steel and the tungsten foil grains are weak against the horizontal vibrations of the sonotrode during welding. In some regions, cracks formed in the steel layer near the W-steel boundary. In the W foil, multiple internal delaminations are seen both close to and far from the steel interface.

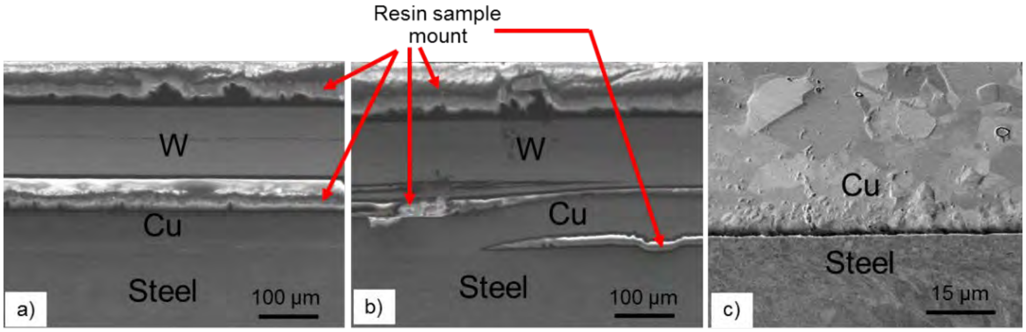

Figure 5. Trial 31with a W foil, Cu interlayer, and steel substrate. The sonotrode travel direction is left to right in the image. a) near the beginning of the sonotrode travel, the Cu is strongly bonded to the steel, b) near the end of the sonotrode travel, the end of the Cu layer is not bonded to the W but the W may be bonded to the Cu, c) detail of the Cu to steel bond.

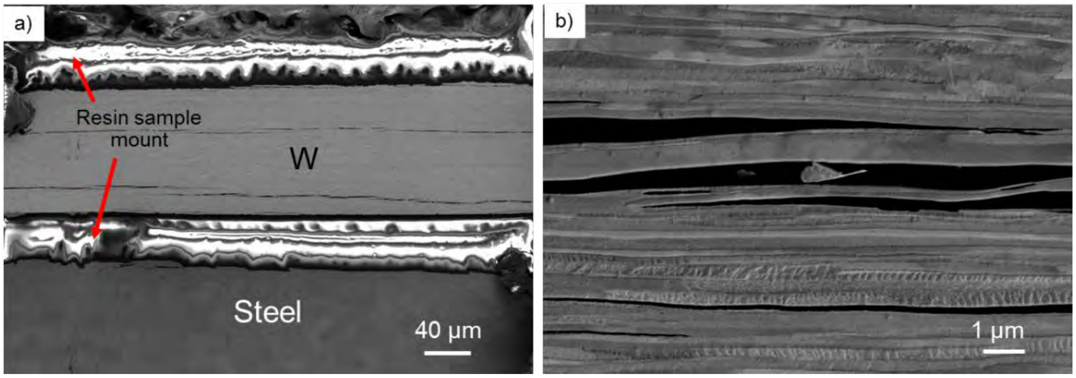

Figure 6. Trial 33 a) had no obvious bond between the W and steel layers and b) had many internal cracks in the W foil layer.

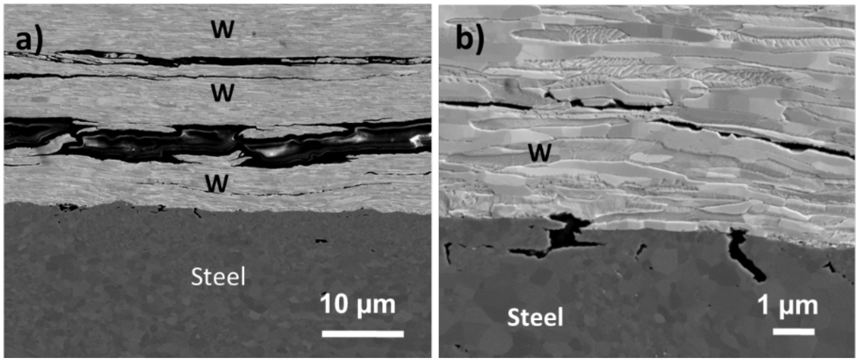

Figure 7. Cross section SEM image of ultrasonically bonded tungsten-steel composite, a) low magnification view showing multiple subdivisions in the W foil layer, b) example area with a good W to steel bond, but again with cracking in the W foil.

Again, as expected, the ultrasonic bonding does not create a mixed phase or allow for interdiffusion across the boundary as confirmed by the EDS analysis (Figure 8). Note, Figures 8 and 9 are in the opposite orientation than Figure 7, which shows the tungsten layer on top. In Figure 9, the EDS automatically calculated the likely phases in the sample. It identified three different phases. Phases 1 is the W foil, and Phases 2 and 3 are within the steel layer. The details of the identified elements are shown in Table 2. No additional phase was identified at the W-steel interface even though W and iron form several intermetallic compounds.

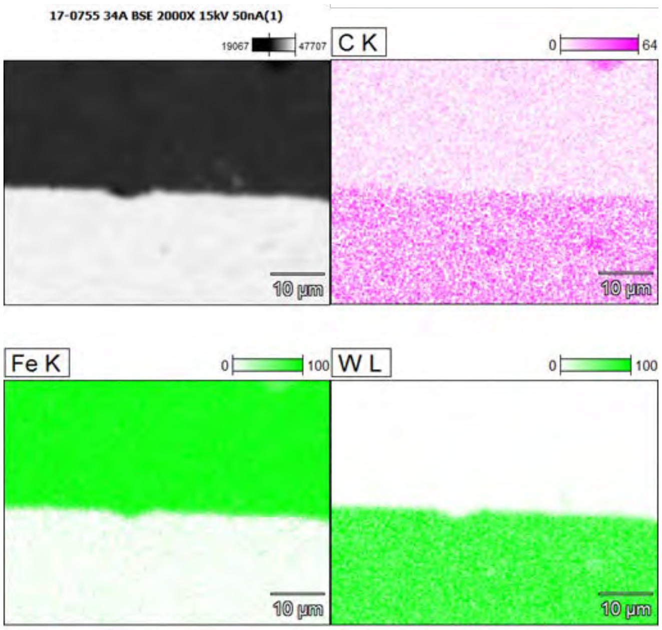

Figure 8. EDS result of Trial 34, W-steel with no interlayer.

These trials show that ultrasonic welding can be used with thin W foils with the proper selection of sonotrode force, amplitude, and frequency. Successful joints were achieved with and without an Al interlayer on a steel substrate. Partial success was achieved for a Cu interlayer with an Al or steel substrate. Even in cases where the W foil was bonded to the substrate after welding and machining of the cross section samples, cracks within the W foil were always seen. This indicates that the force necessary for creating a bond between the W and the other materials is greater than the force the W grains can withstand internally. Further analysis will determine if the internal cracking in the W layers can be reduced and if the bond strength of the layers can be measured.

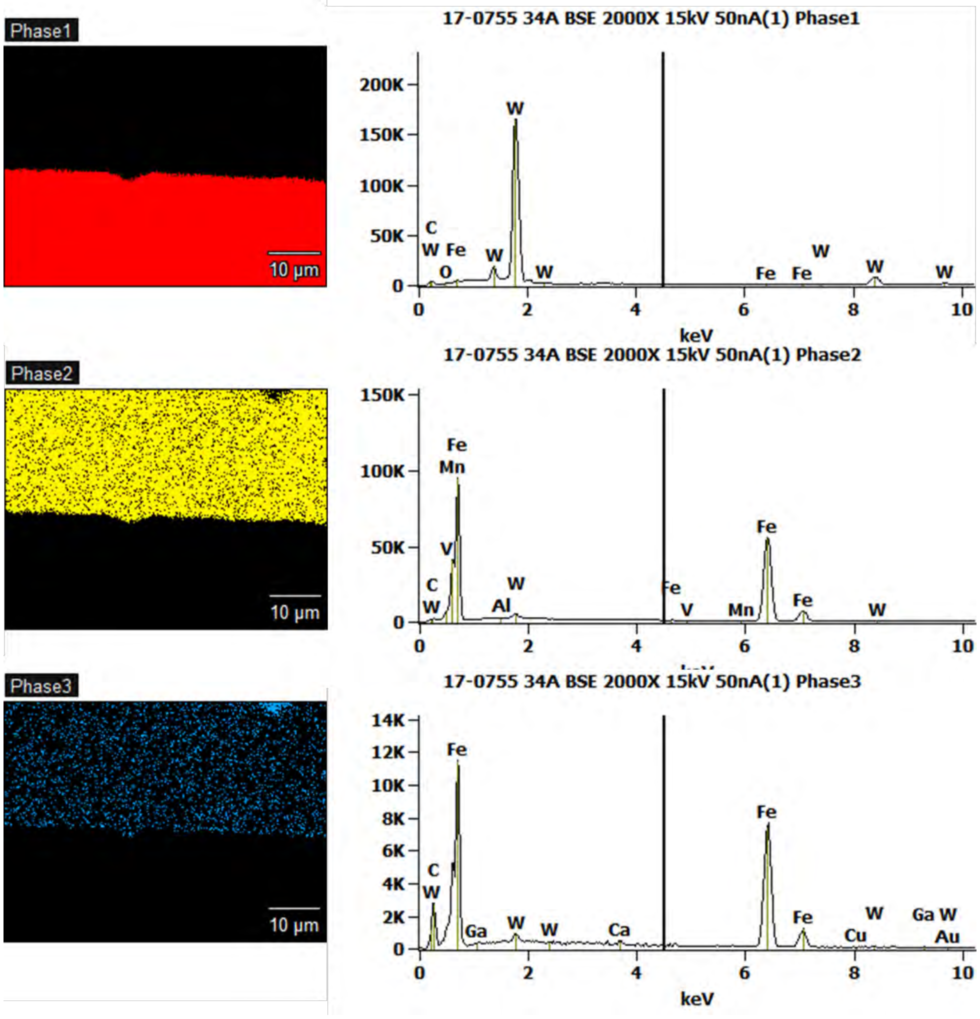

Figure 9. Phase analysis from EDS of Trial 34 W to steel direct ultrasonic bond.

Table 2. Elemental analysis of phases identified in Trial 34

Element	Phase 1	Phase 2	Phase 3
O	0.46	—	—
C	1.36	0.69	6.93
Fe	1.47	95.92	88.37
Al	—	0.28	—
V	—	0.03	—
Mn	—	0.49	—
W	96.71	2.58	3.29
Ca	—	—	0.41
Cu	—	—	0.34
Ga	—	—	0.04
Au	—	—	0.61

4.4 TUNGSTEN/SiC AND TUNGSTEN/GRAPHITE JOINING

L.M. Garrison, Y. Katoh, E. Proehl, P. Menchhofer (Oak Ridge National Laboratory)

OBJECTIVE

The objective of this project is to fabricate thin tungsten layers bonded to graphite and SiC substrates that will provide a significant reduction in neutron activated volume as compared to standard 6 mm discs for rapid screening in irradiation effects tests.

SUMMARY

Thin tungsten foils, 25 μm thick, were joined to graphite and SiC using hot pressing. Initial results showed that the W-graphite bond was weak but the W-SiC bonding was successful. Despite the good bond, SEM cross sectional analysis did not show a noticeable reaction layer between the W and SiC. Next, 6 mm disc samples will be machined to determine if the layers remain bonded after machining.

PROGRESS AND STATUS

Tungsten becomes highly activated by neutron irradiation in HFIR and takes an estimated 3 years cooling time before standard size samples can be transferred to LAMDA for post irradiation examination (PIE). Certain PIE activities such as microstructural analysis and permeation testing only require a very small volume of material. By joining a thin layer of tungsten to a substrate of graphite or SiC, the activated tungsten volume is significantly reduced, and the substrate provides the necessary structural support for handling and clamping the sample.

Graphite and SiC substrate material 2 mm thick was machined. Tungsten foils 25 μm thick were purchased from ESPI Metals. In the first joining trial, the foils and substrate material were hot pressed at 1300°C and 10 MPa in a vacuum furnace. Boron nitride was used to prevent bonding between the top of the tungsten foil and the graphite press components. The W foil was only weakly bonded to the graphite substrate, and it debonded when the material was sectioned. The W foil did bond successfully to a SiC substrate. The cross section image of the W-SiC joint is shown in Figure 1. The interface between the tungsten and SiC is relatively smooth with a few gaps or pores visible. Elemental analysis will be completed next to determine how thick the reaction layer is.

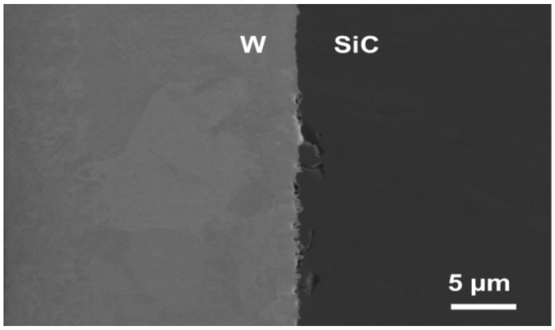

Figure 1. Hot pressed joint between tungsten and silicon carbide.

For the second joining trial, two additional samples of W-SiC were fabricated. Each joined sample consisted of a square of SiC with a 19 mm edge length and 5 mm thickness as the substrate and a W foil with 25 mm edge length and 25 μm thickness. The joining used hot pressing at 10 MPa at 1300˚C with a 30 minute ramp time and one hour hold time. A graphite foil was used to avoid the tungsten foil sticking to the ram. These second group of joined materials are being machined into 6 mm diameter disc samples. The result of the machining will determine if this joining method is suitable for large scale sample preparation or if further development is needed to prevent debonding of the W layer.

4.5 PREPARATION OF TUNGSTEN SURFACES FOR PLASMA-MATERIAL INTERACTION STUDIES

L.M. Garrison, M. Bannister, F. Meyer, D. Leonard (Oak Ridge National Laboratory)

OBJECTIVE

The objective of this project is to evaluate how surface preparation techniques change the near surface microstructure on tungsten and determine if this has an effect on plasma-material interactions.

SUMMARY

The cutting and polishing methods used on tungsten can change the characteristics of the near-surface region, which is important for the type of morphology that develops during ion implantation to simulate use as a plasma-facing component. Electrical discharge machining, slow speed sawing and water jet cutting were compared in terms of surface damage and contamination. Tungsten that has been mechanically polished has a damaged surface layer that is not representative of the bulk and can undergo further morphological changes at temperatures below tungsten's recrystallization temperature. Initial ion implantation results suggest that different polishes can result in different morphologies after ion implantation.

PROGRESS AND STATUS

Helium nanostructure formation and gas retention of tungsten have been shown to depend on factors such as grain size, grain elongation direction, crystallographic texture, and manufacturing method. Another factor that can affect the microstructure of the near surface region of tungsten is the surface polish or preparation that is used. Every step of surface preparation, starting with the machining method, introduces some artifacts to the near surface region. Figure 1 compares the surfaces of tungsten after electrical discharge machining (EDM), slow speed sawing, and water jet cutting. EDM removes material by creating a melt layer on the surface. Some of the brass EDM electrode is transferred to the surface of the tungsten. In single crystal tungsten, the stress of the localized melting and rapid re-solidification causes subsurface cracking. Slow speed sawing strains and rotates material at the surface to form a cut. In the case of the material in Figure 1b, the surface impurities deposited by the saw were copper and tin. These impurities may be from a previously cut material or from the dressing stick used with the saw blade. In water jet cutting, material is removed from the surface by creating small machining chips of strained material. The tracks of the abrasive particles can be seen in Figure 1c. Water jet cutting implanted particles of an Al-O-Mg compound in the surface.

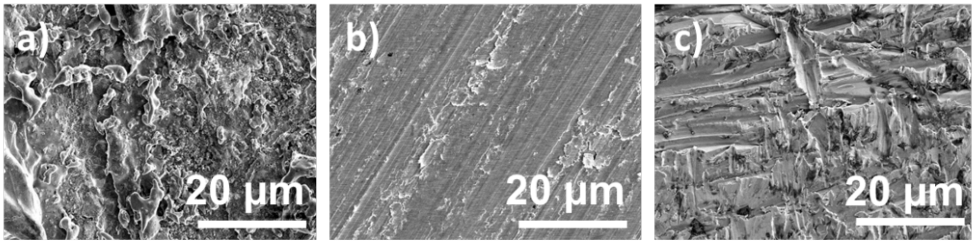

Figure 1. Tungsten surface after sectioning with a) electrical discharge machining, b) slow speed sawing, and c) water jet cutting.

After sectioning, each successive step of polishing attempts to remove the damage from the previous step. However, different artifacts are seen after each polishing step. Samples have been polished to a "mirror finish" with silicon carbide polishing pads in grades 800, 1200, and 2400; diamond suspensions of 6, 3, and 1 µm; and a 2% ammonium hydroxide, 2% hydrogen peroxide, and 96% colloidal silica solution, mixture referred to as colloidal silica. After selected polishing step, the sample surface was imaged to attempt to determine if the sample surface was representative of the bulk microstructure or if polishing artifacts could be found. Additionally, selected samples were heat treated for 30 min at 300°C or 900°C (Figure 2). The furnace vacuum was between 1×10^{-5} and 2×10^{-4} Torr. A 15°C/min ramp rate and a 20°C/min cooldown to room temperature were used.

The 800 grit sample heated to 300°C for 30 min showed little change after the heat treatment. However, the 800 grit sample heated to 900°C for 30 min showed distinct subgrain formation after the heat treatment (Figure 2). The observed apparent grains are not the true grains of the bulk polycrystalline tungsten but are a product of the polish damage plus heat treatment. The mirror finished sample does not appear significantly different than the 800 grit sample in the as-polished state. The mirror finished sample has a thinner surface layer that is damaged by the polish. After 30 min at 300°C, less polish striations and more grain texture is visible on the mirror finished sample. After 30 min at 900°C, the mirror finished sample does not show the small subgrains as seen on the 800 grit sample, but also does not show the true grains of the bulk material which are ~2-10 µm. Ion implantation or plasma exposure of tungsten is often performed at elevated temperatures such as 300 or 900°C. These heat treatment results indicate the difficultly in decoupling the polishing, temperature, and plasma effects in plasma-facing material experiments.

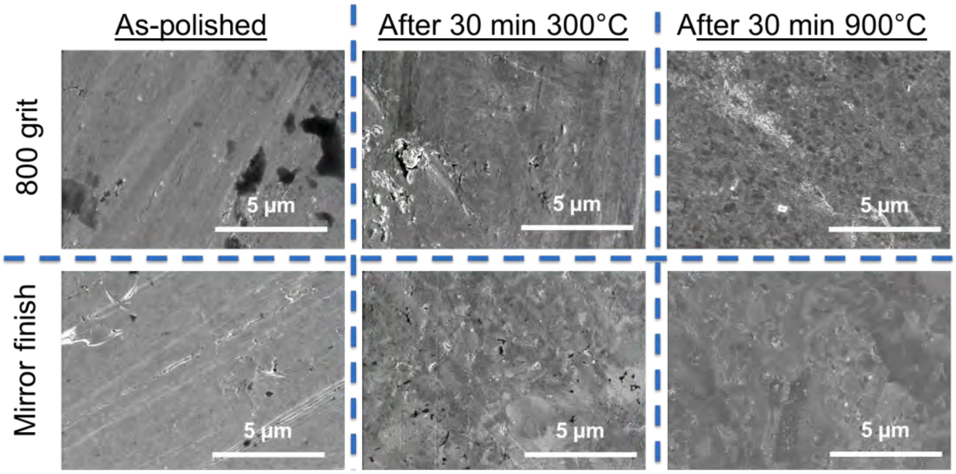

Figure 2. Polycrystalline tungsten samples prepared by either a 800 grit SiC paper or a mirror finish mechanical polish. One set was heat treated at 300°C and another at 900°C for 30 min.

Two single crystal tungsten samples (<110> normal to the surface bulk orientation) were implanted with 2 keV He^+ at 1000°C at the Multicharged Ion Research Facility (MIRF). One sample was mechanically polished to a mirror finish while the other received both the mirror finish polish and an electropolish with a KOH solution. The MIRF ion beam has a distribution of ion fluxes across the several millimeter spot size, with the highest flux at the center. For both the mechanically polished and the electropolished samples, the morphology that developed at the center of the ion beam damaged zone was similar (Figure 3). However, in the lower flux regions, the mechanically polished sample had the appearance of a polycrystalline sample because of the damage from the mechanical polish. The He-implanted morphology on the different subgrains of the mechanically polished single crystal tungsten sample was distinct. In contrast, the electropolished sample had the same morphology in all regions that experienced the same flux and the severity of the morphology change lessened as one moved from the center of the beam spot to the outer edge.

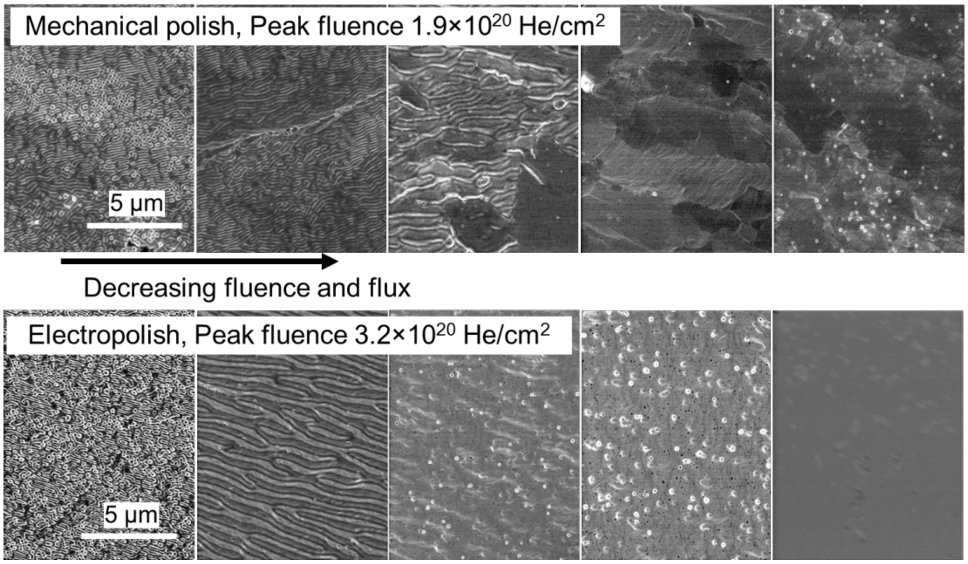

Figure 3. Single crystal tungsten that received a mechanical polish to a mirror finish and single crystal tungsten that was polished to a mirror finish and then electropolished were implanted with 2 keV He^+ at 1000°C at the MIRF.

4.6 MICROSTRUCTURE AND MECHANICAL PROPERTIES OF IRRADIATED PHENIX PROGRAM TUNGSTEN

L.M. Garrison, Y. Katoh, N. Reid, E. Proehl, (Oak Ridge National Laboratory) and M. Fukuda (Tohoku University)

OBJECTIVE

The PHENIX collaboration on tungsten irradiation aims to expand the database on neutron irradiation data for tungsten materials.

SUMMARY

Hardness tests, room temperature tensile tests, and microstructural analysis have been completed on the unirradiated control materials from the PHENIX RB*19J irradiation campaign. Almost all the varieties of polycrystalline tungsten have higher hardness and higher fracture strength than the single crystal tungsten. Grain size distributions have been calculated from SEM images of the unirradiated microstructures.

PROGRESS AND STATUS

The PHENIX US-Japan collaboration has a goal of investigating tungsten for use in future fusion reactors. For this potential use, more information is needed about the tungsten response to neutron irradiation at fusion relevant conditions. To investigate this, the PHENIX collaboration prepared over 1500 tungsten samples for the RB*19J irradiation capsule. Tests are underway to evaluate the control tungsten materials of the PHENIX irradiation campaign.

For the PHENIX US side materials, several varieties of single and polycrystalline tungsten were selected (Table 1). The materials are identified by a unique two symbol code for the RB*19J irradiation, which is also used here for tracking the many material varieties. Single crystal tungsten with orientation <100> and <110> normal to the surface will allow comparison with the previously irradiated TITAN single crystal tungsten samples.

Two varieties of commercially available tungsten, AA plate (FR, Ge, and 3E) and AA 2 mm foil (EE), were selected to compare with thick plate tungsten prepared according to the ITER specification (AT, BT, and CT). One type of thin tungsten foil (RE) was included in the irradiation because the severe plastic deformation in the fabrication of tungsten foils results in a lower ductile to brittle transition temperature. All the other polycrystalline tungsten materials were fabricated by powder sintering and rolling, but the W PIM (ZE) was fabricated with powder injection molding, which resulted in a slightly lower density.

Additionally, a set of tungsten rhenium alloys were included in the RB*19J irradiation campaign (KE, 3R, and 5E). These materials aim to further the understanding of the effect of transmutation versus other irradiation defects on the irradiated mechanical properties of tungsten. Finally a tungsten with TiC particle additions (8E) was included in the campaign to evaluate the stability and effect on irradiated behavior of the particles.

Table 1. The material codes and descriptions for the US side PHENIX RB*19J capsule materials

Material Code	Short Name	Description
FR	AA plate	Polycrystalline tungsten plate purchased from Alfa Aesar
GE	AA plate tensile A	Polycrystalline tungsten plate purchased from Alfa Aesar. Tensile bars cut in direction “A”.
3E	AA plate tensile B	Polycrystalline tungsten plate purchased from Alfa Aesar. Tensile bars cut in direction “B”.
EE	AA 2mm foil	Polycrystalline tungsten purchased from Alfa Aesar as a 2 mm thick foil
TE	SCW-100	Single crystal tungsten, produced as a cylinder with <100> as the direction along the axis by Goodfellow
UE	SCW-110	Single crystal tungsten, produced as a cylinder with <110> as the direction along the axis by Goodfellow
GW	SCW 110 GW	Single crystal tungsten produced as a cylinder with <110> as the direction along the axis by Goodfellow, different batch than “SCW-110” material
RW	SCW 100 RW	Single crystal tungsten produced as a cylinder with <100> as the direction along the axis by Goodfellow, different batch than “SCW-100” material
KE	W-0%Re	Polycrystalline tungsten reference material with no added Re fabricated by arc melting at ORNL, measured Re content is approximately 0.04%
3R	W-0.4%Re	Polycrystalline tungsten with added Re fabricated by arc melting at ORNL, measured Re content is approximately 0.4%
5E	W-2.2%Re	Polycrystalline tungsten with added Re fabricated by arc melting at ORNL, measured Re content is approximately 2.2%
RE	Rolled W foil	The foil was purchased from ESPI metals as a 0.25 mm thick sheet.
AT	Thick plate A	Thick plate W, nominally “ITER grade” polycrystalline tungsten. Samples were machined with various orientations relative to the anisotropic grains
BT	Thick plate B	Thick plate W, nominally “ITER grade” polycrystalline tungsten. Samples were machined with various orientations relative to the anisotropic grains
CT	Thick plate C	Thick plate W, nominally “ITER grade” polycrystalline tungsten. Samples were machined with various orientations relative to the anisotropic grains
ZE	W PIM	Tungsten was fabricated at Karlsruhe Institute of Technology by powder injection molding
8E	W TiC	Tungsten with TiC particle additions was fabricated at Karlsruhe Institute of Technology

The AA plate material was machined into disc samples (FR) and tensile samples with two orientations, direction “A” with material code GE and direction “B” with material code 3E. Both types of tensile samples have the same tensile axis, but the face of the tensile bar was rotated 90 degrees as shown schematically in Figure 1. Similarly, the thick plate tungsten had orientations “A” with material code AT, “B” with material code BT, and “C” with material code CT. The tensile axis of these three directions are shown in Figure 1. Materials AT and BT share a tensile direction, but different face orientation, while CT is mutually perpendicular to AT and BT.

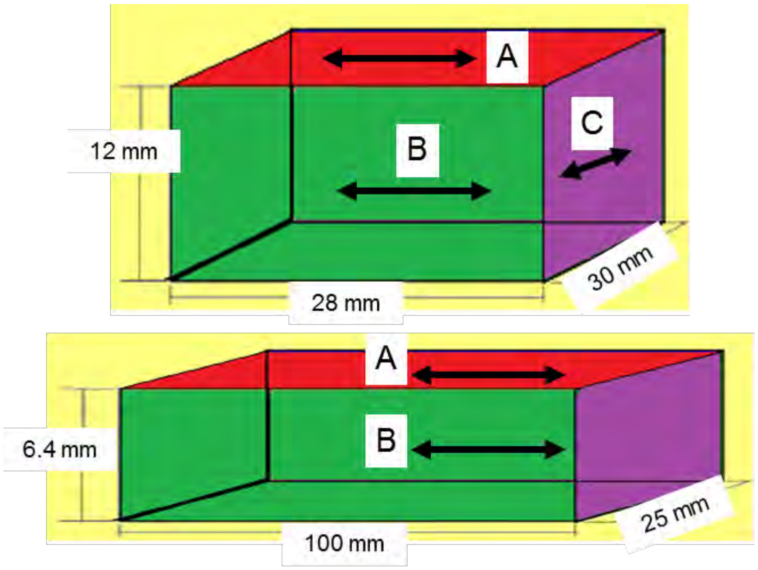

Figure 1. Top, illustration of the different tensile directions used for the thick plate tungsten material (AT, BT, and CT). Bottom, illustration of the different tensile directions used for the AA plate tungsten material (GE and 3E). Note, drawing is not to scale and dimensions of the as-received bulk material pieces are shown.

Hardness

Both single crystal and polycrystalline tungsten samples were Vickers microhardness tested using five indents, with each indent at 1000 g with a dwell time of 10 seconds. The resulting values were averaged to determine the hardness of the material (Figure 2). The error bars on Figure 2 are the standard deviation from the average of each of the five microhardness data points for each material type. The load was verified by finding maximum indent depth. The hardness indents were less than one seventh the overall thickness of the specimen to accurately measure hardness without interference of the stage material or residual stress of the specimen face opposite the surface being tested, which complies with the ASTM E384 -16 standard.

Polycrystalline tungsten (PCW) samples had higher hardness values than single crystal tungsten. The W foil had the highest microhardness of all tested materials. The hardness of the W – TiC alloy, 8E, was comparable to that of PCW without particle additions. The tungsten sample fabricated by powder injection molding, 2E, had the lowest hardness of all the PCW materials. The three ITER grade samples were all from the same block of PCW, and the three letters, A, B, and C corresponds with a different plane of cut. Within the thick plate ITER grade samples, hardness in descending order was thick plate B (BT), thick plate A (AT), thick plate C (CT), and the microstructures of the thick plate samples were analyzed using SEM. The images revealed thick plate B had slightly elongated grains with small voids, thick plate A had mostly equiaxed grains and elongated voids, and thick plate C had the most elongated grains and also elongated voids. Grain geometry and void orientation relative to the surface of indent resulted in differing hardness values.

Single crystal tungsten (SCW) had different values based on the plane of indentation on the sample. Previous published data reports hardness values about 30 HV higher for samples with the <110> directions oriented normal to the surface plane (377 HV) than samples with <100> normal to the surface plane (345 HV) due to closer packing of plane of indentation [1]. Two sets of SCW samples were tested. Within each set, one sample was cut with the <100> direction normal to the plane of indentation, and the other sample was cut with the <110> normal to the surface plane. The first set of SCW specimens fabricated by Goodfellow corroborate the literature trend that SCW with the normal in the <110> direction (UE) is harder than with the normal in the <100> direction (TE). However in the second set, the RW109 specimen, which has a normal in the <100> direction, was about 45 HV harder than the GW specimen, which has a normal in the <110> direction. The RW109 specimen's hardness was corroborated by the RW09 specimen. The inversion of the trend of hardness and plane of indentation in the GW and the RW109 samples may be the result of surface finish.

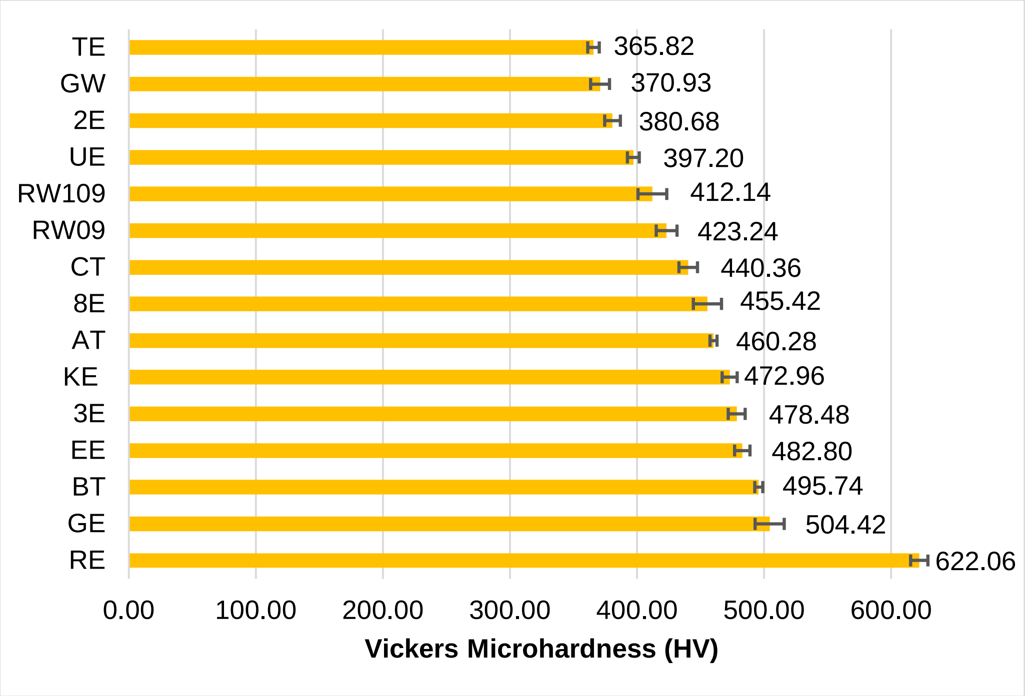

Figure 2. Vickers microhardness of single crystal and polycrystalline tungsten samples.

Tensile

Unirradiated, control tungsten SSJ2 tensile specimens were tested at room temperature (Figure 3). These were tested on the MTS load frame in LAMDA laboratory with a strain rate of 2%·min^{-1}. One sample of each material type was tested. Note, not all materials in Table 1 were fabricated in SSJ2 geometry. As expected, all breaks were brittle, with single crystal tungsten having some degree of elongation (no more than 1%).

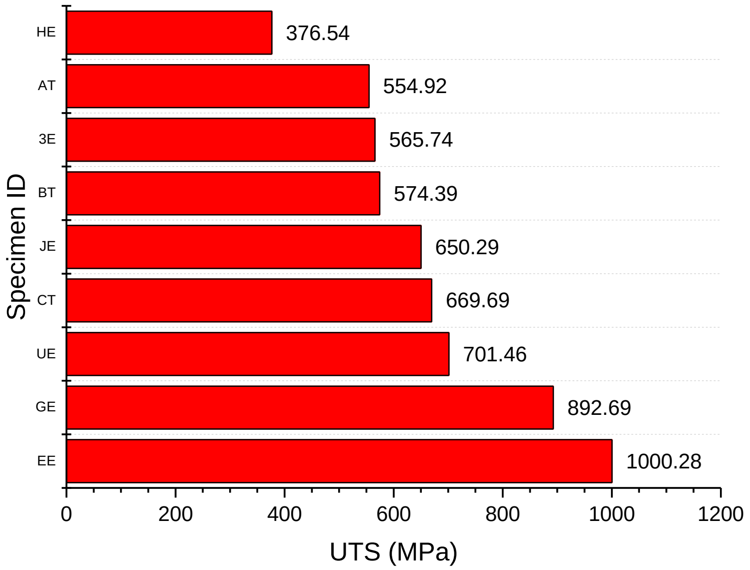

Figure 3. Ultimate tensile strength of tungsten control group at 22°C and a strain rate of 2%·min^{-1}.

The brittle fracture data shows a UTS range between 376 and 1000 MPa for the different varieties of tungsten. Single crystal tungsten specimens in the <100> plane orientation, HE and JE, were observed to have less strength than the <110> orientation, UE. This behavior has been seen in previous tests done in the TITAN campaign [2]. AA tensile plate in the “A” direction, GE, showed noticeably higher tensile strength than in the “B” direction, 3E. Because the AA plate tensile directions “A” and “B” shared the tensile direction but had a different plane orientation (Figure 1) the different tensile strength is unexpected. The difference may be due to the statistical nature of the strength of brittle tensile samples. The AA 2 mm foil specimen, EE, had the greatest tensile strength.

Microstructures were analyzed for each of the materials. The grain size and grain structure both have an influence on the strength of polycrystalline tungsten. Cracks have been known to form both intergranularly (along grain boundaries) and transgranularly (cleavage) [1]. With single crystal tungsten, the plane orientation and defect concentration have the most pronounced effect. The single crystal tungsten materials were more sensitive than the polycrystalline tungsten materials to the electrical discharge machining used to produce the tensile bars. After fabrication and polishing of the single crystal tungsten samples, some grooves remained which may have acted as crack initiation points during the tensile tests and led the bars to break prematurely.

SEM micrographs were used to relate microstructure to tensile data. Grain size distributions were determined by optical granulometry in direction of the tensile axis and transverse axis to determine a length-to-width ratio of each grain for 100 grains in each material. The summary for the grain statistics for the materials that were analyzed are shown in Figure 4. Generally, each material had a principle grain size in the range of 1-3 microns, with some dispersed larger grains (outliers) in the range of 4-6 microns. For the AA tensile plate material, GE, clusters of large grains up to 35 microns in size were present (Figure 5a). An example of the grain measurement is shown in Figure 5b. The data from the grain size analysis is shown in Table 2 and the details of the grain size analysis for each material is presented in the appendix at the end of this section. The analysis is underway for the rest of the PHENIX tungsten materials that are listed in Table 1 but not shown in Figure 4.

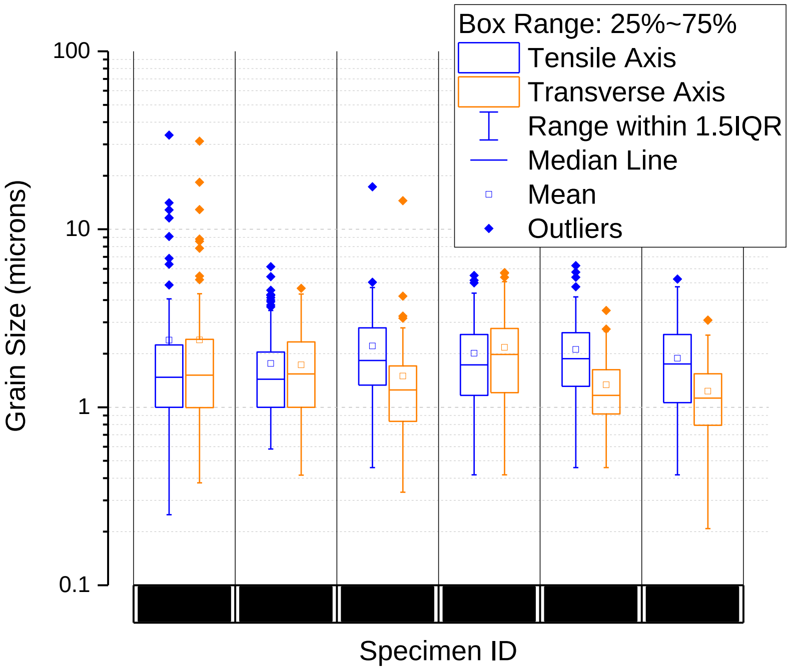

Figure 4. Box-and-whisker plot of grain size distribution statistics for a sample size of ~100 grains for each material type.

Grain elongation was seen in polycrystalline specimens 3E, BT, and CT. These had a length-to-width ratio of 1.45-1.60. Specimens GE, EE, and AT had relatively equiaxed grain structures. All specimens showed uniform grain size, with the exception of the AA tensile plate material, GE. Figure 4a shows clusters of larger grains agglomerated beside the nominal 1-3 micron equiaxed grain structure. Since the results of the statistical analysis were limited by the resolution of the micrograph SEM images, there is an upward-skewed trend in mean grain size in Figure 4.

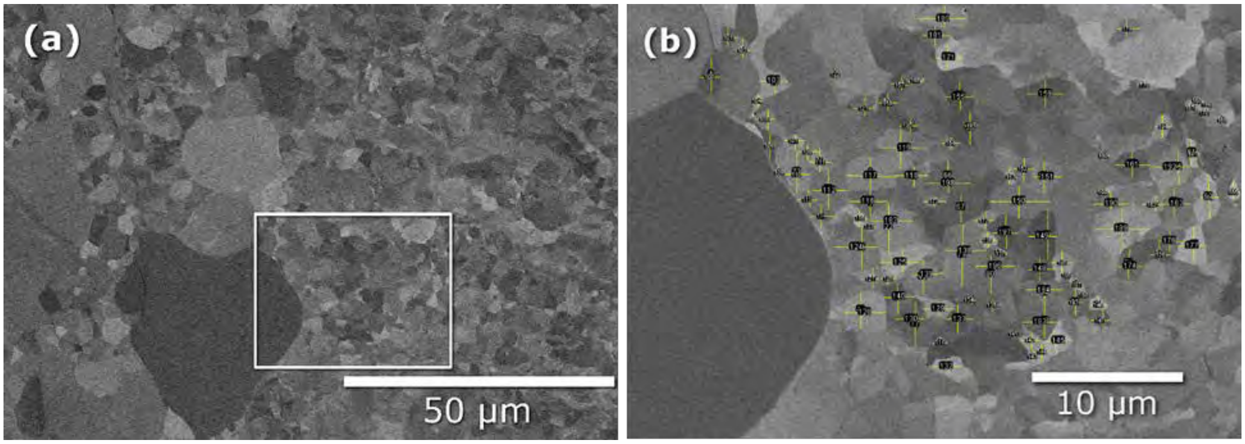

Figure 5. BSE-SEM micrograph images taken at a voltage of 10.0 kV and a probe distance of 9.1 mm for specimen GE at a) 1000 magnification b) 3000 magnification (white box in Figure 5a).

The thick plate specimens; AT, BT, and CT; were cut from a monolithic tungsten block. The face of each specimen corresponds to a different face of the block. Specimens AT and BT shared the same tensile axis, however AT is the only specimen which does not show elongated grain structure along the tensile axis. In addition, these samples appear to have pore defects in the grain structure. These have cylindrical geometry and extend in the direction of the CT tensile axis (AT transverse axis). The AA tensile plate specimens; GE and 3E; share the same tensile axis, and similarly 3E shows elongated grain structure along the tensile axis while GE is more equiaxed.

Table 2. Descriptive statistics of tungsten grains

ID	N total	Mean	Standard D	SD times 2	SD times 3	Minimum	1st Quartile	Median	3rd Quartile	Maximum	IQR	Range
GE (1)*	110**	2.38	3.86	7.73	11.59	0.24	0.99	1.47	2.24	33.79	1.24	33.54
GE (2)	110	2.39	3.66	7.33	10.99	0.37	0.99	1.51	2.4	31.26	1.41	30.89
EE (1)	100	1.76	1.1	2.2	3.3	0.58	1	1.43	2.04	6.16	1.04	5.58
EE (2)	99	1.73	0.91	1.82	2.74	0.41	0.99	1.54	2.33	4.66	1.33	4.24
3E (1)	101	2.2	1.83	3.67	5.51	0.45	1.33	1.83	2.79	17.33	1.45	16.87
3E (2)	101	1.49	1.48	2.96	4.44	0.33	0.83	1.25	1.7	14.46	0.87	14.13
AT (1)	100	2	1.09	2.18	3.27	0.41	1.16	1.72	2.56	5.5	1.39	5.08
AT (2)	100	2.17	1.17	2.34	3.52	0.41	1.2	1.97	2.77	5.7	1.56	5.29
BT (1)	100	2.11	1.09	2.18	3.27	0.45	1.31	1.87	2.62	6.25	1.31	5.79
BT (2)	100	1.33	0.59	1.18	1.77	0.45	0.91	1.16	1.62	3.5	0.7	3.04
CT (1)	100	1.88	1.02	2.04	3.06	0.41	1.06	1.75	2.56	5.25	1.5	4.83
CT (2)	100	1.23	0.6	1.21	1.81	0.2	0.79	1.12	1.54	3.08	0.75	2.87

* (1) is for the direction of tension of tensile specimens and (2) is the perpendicular direction.
** An additional 10 grains were measured at a x1.00k magnification due to their large size.

References

[1] E. Lassner and W.D. Schubert. (1999). *Tungsten: Properties, Chemistry, Technology of the Element, Alloys, and Chemical Compounds*. New York, NY: Kluwer Academic/Plenum Publishers. 20-21.
[2] L. M. Garrison, et al. 4.4 Neutron Irradiation Effects in Tungsten. Fusion Reactor Materials Program. DOE/ER-0313/61 – Volume 61 (2016).

Appendix

The SEM images and grain size analysis for the evaluated tungsten materials are shown in the following figures. Original magnification of the SEM image pairs was 400x and 3000x.

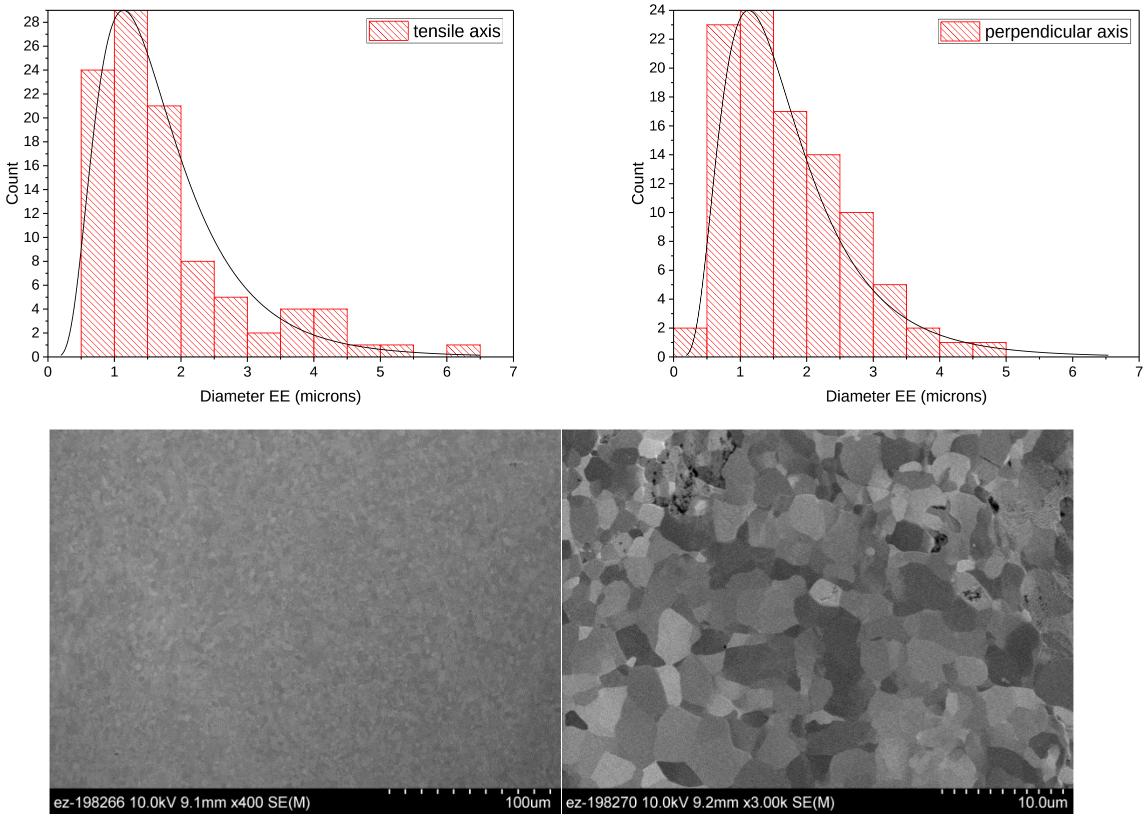

Figure A1. Material EE, AA 2 mm foil. Polycrystalline 2 mm thick tungsten foil purchased from Alfa Aesar.

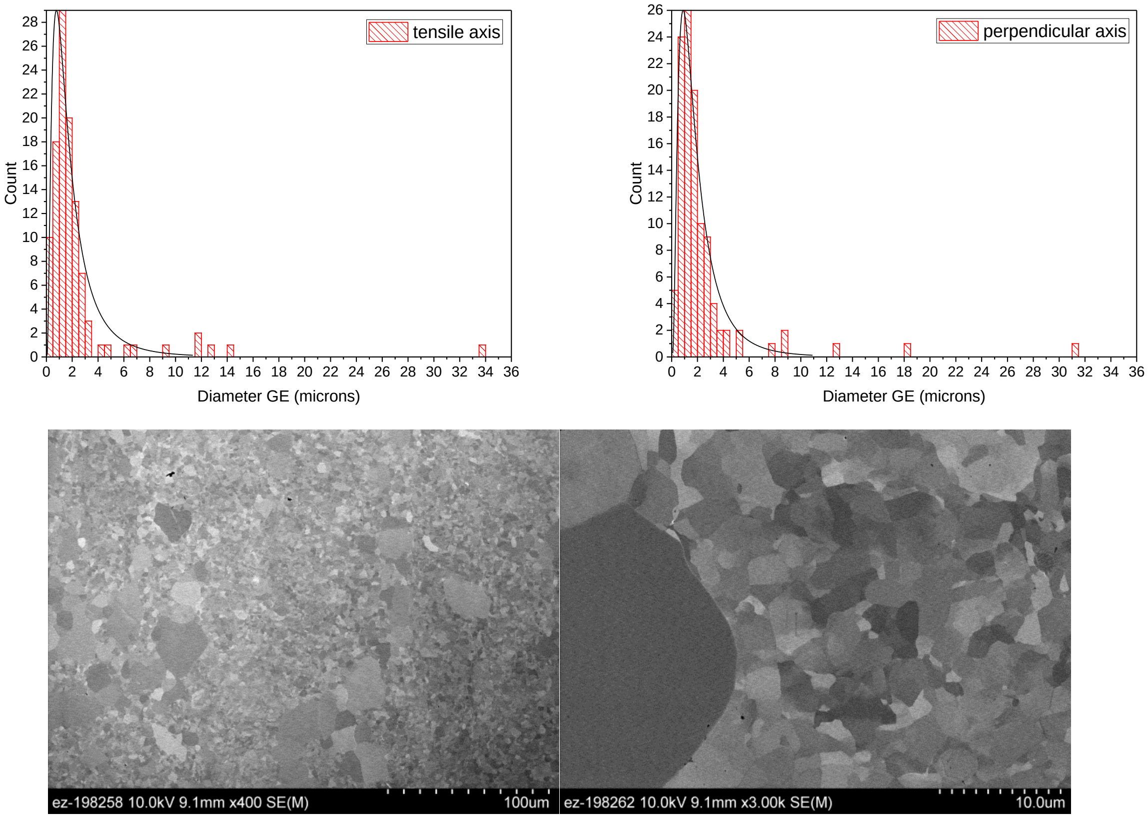

Figure A2. Material GE, AA plate tensile A. Single crystal tungsten cylinder with <110> axis direction, from Goodfellow.

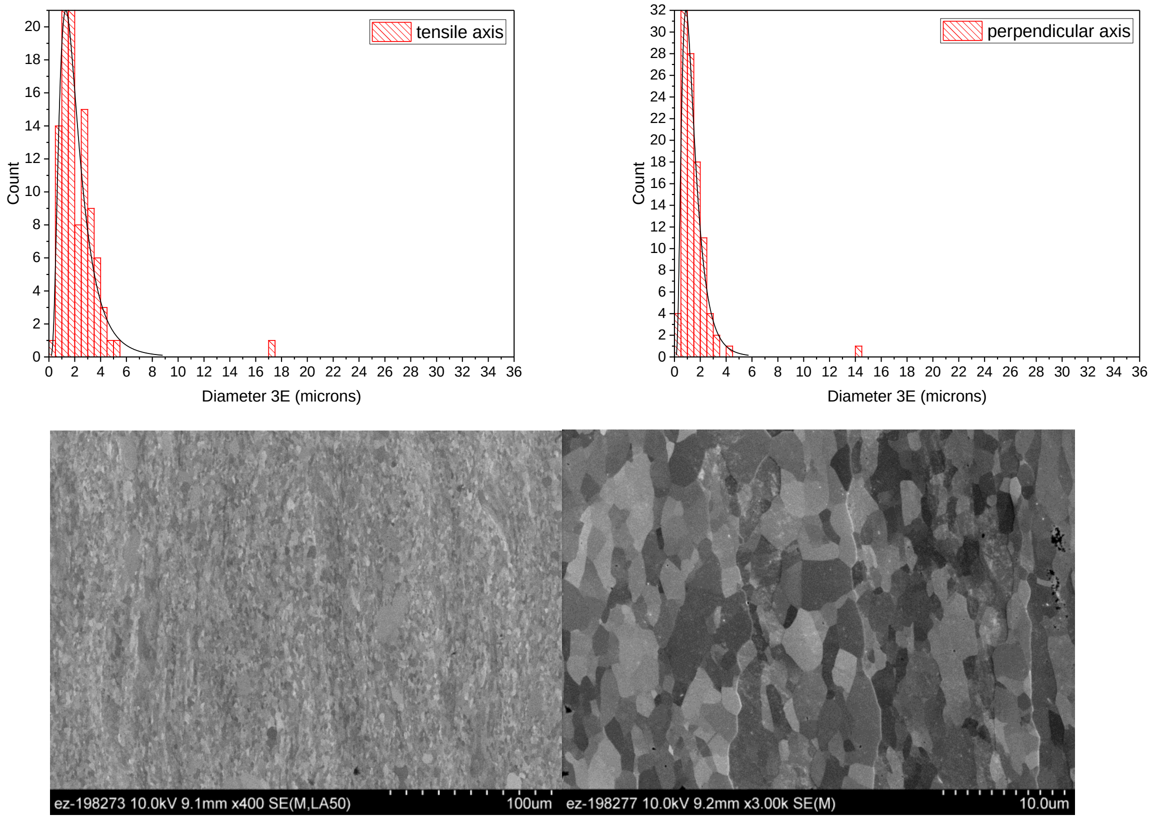

Figure A3. Material 3E, AA plate tensile B. Polycrystalline tungsten plate from Alfa Aesar.

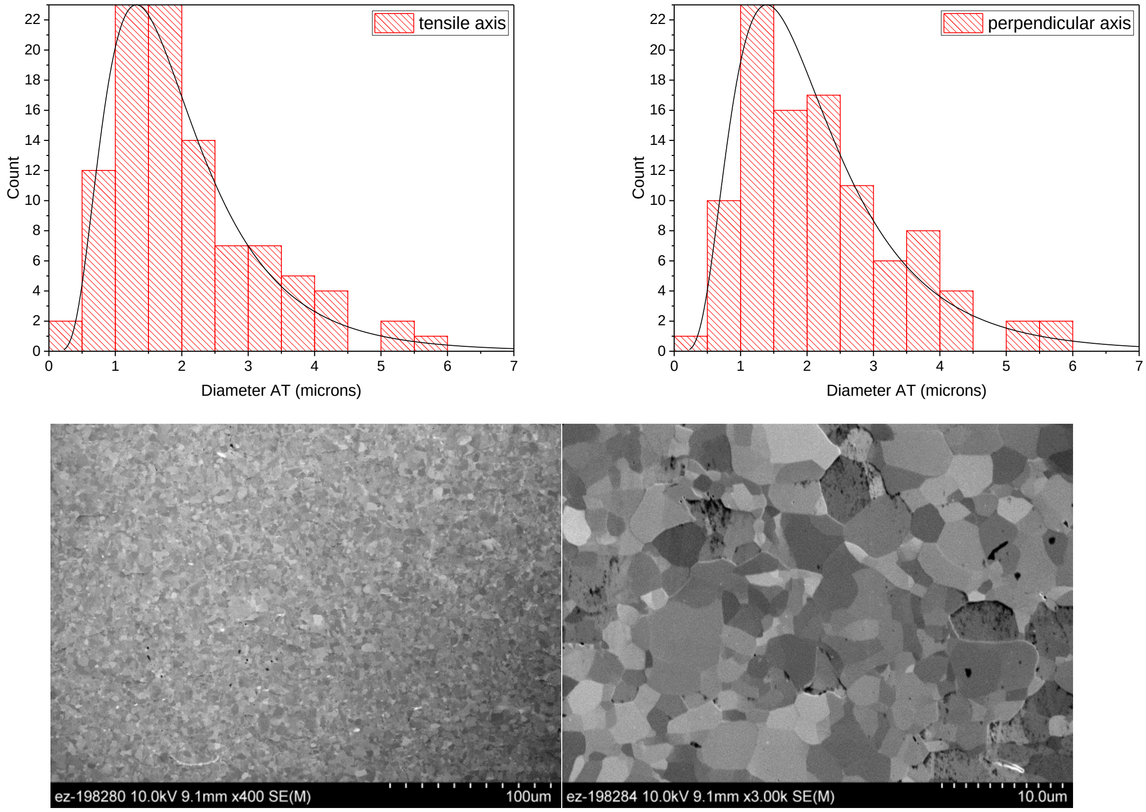

Figure A4. Material AT, thick plate orientation A. Thick plate W - “ITER grade” polycrystalline tungsten.

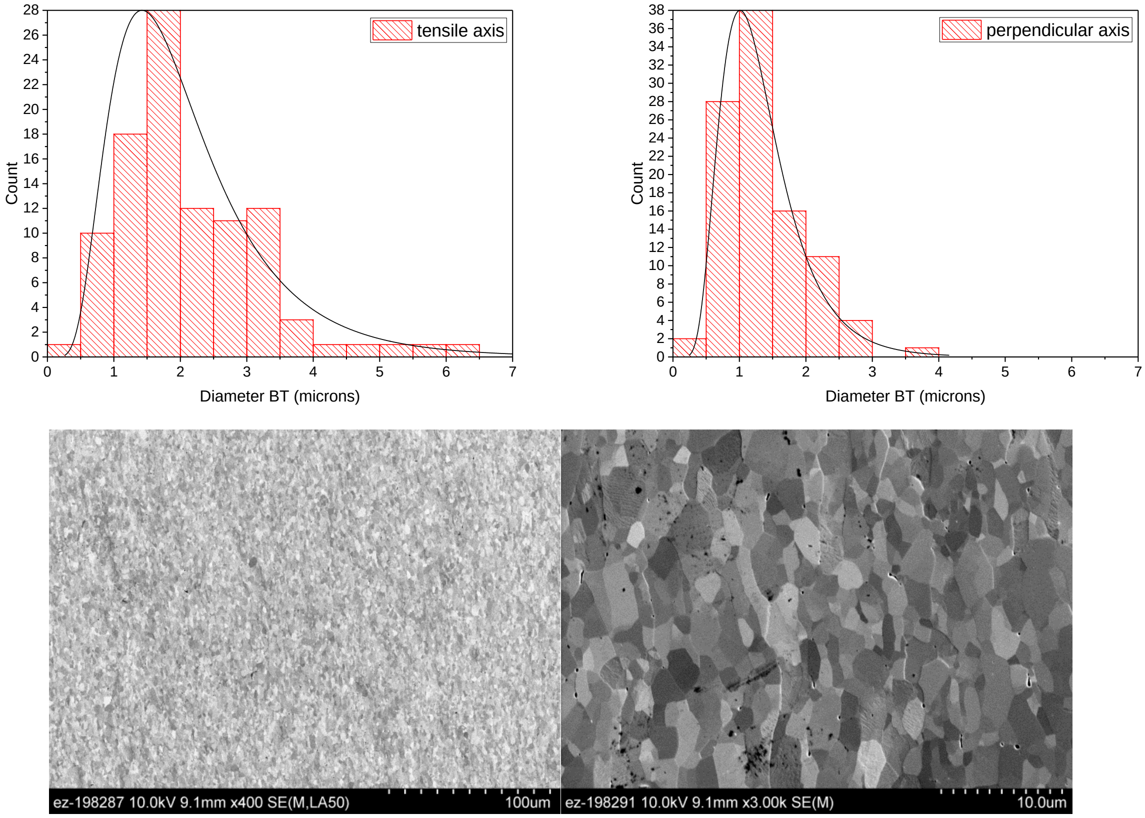

Figure A5. Material BT, thick plate orientation B. Thick plate W - “ITER grade” polycrystalline tungsten.

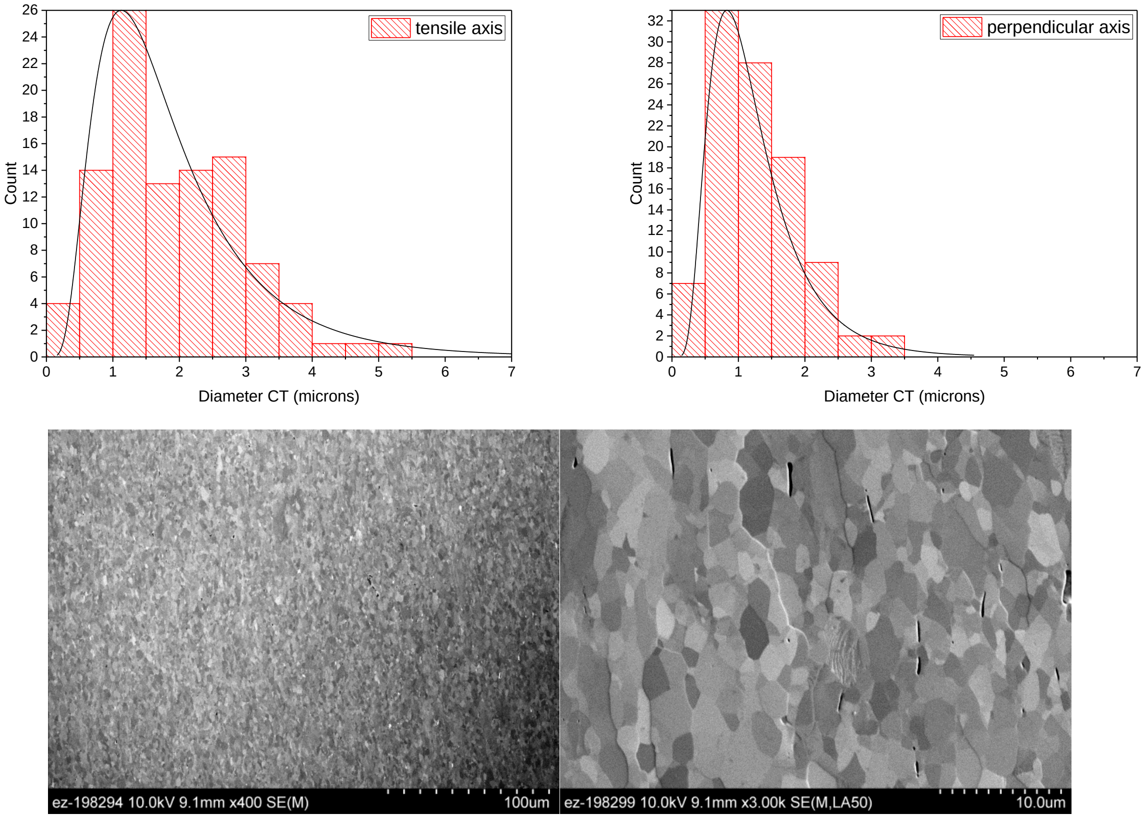

Figure A6. Material CT, thick plate orientation C. Thick plate W - “ITER grade” polycrystalline tungsten.

4.7 CHARACTERIZATION OF SELF-ION IRRADIATED TUNGSTEN

—Weilin Jiang, Danny Edwards, Giridhar Nandipati, Wahyu Setyawan, Charles H. Henager Jr., Richard J. Kurtz (Pacific Northwest National Laboratory) and Aaron French, Xuemei Wang, Lin Shao (Texas A&M University)

OBJECTIVE

The aim of this experimental work is to study defect accumulation and recovery, microstructural evolution, and transmutant precipitation in tungsten using ion irradiation, and validate modeling predictions on void lattice formation in irradiated tungsten.

SUMMARY

This progress report presents our preliminary results on self-ion irradiation in monocrystalline and polycrystalline tungsten at 300 and 900 K, characterized by in-situ Rutherford backscattering spectrometry in ion-channeling conditions (RBS/C) and ex-situ transmission electron microscopy (TEM). The RBS/C data suggest that the self-interstitials are extremely mobile during irradiation even at 300 K, leading to fast diffusion and annihilation of the interstitials probably through recombination with vacancies and surface sinks. Defect recovery is observed during 20 min isochronal annealing of 300 K irradiated tungsten. The TEM results also do not provide any evidence for formation of a damage band in irradiated tungsten, which is consistent with the RBS/C data. Edge-on ⟨100⟩{100} dislocation loops are not observed, but ½⟨111⟩{111} loops are likely present in the irradiated tungsten.

PROGRESS AND STATUS

Introduction

Recent object kinetic Monte Carlo (OKMC) simulations [1,2] predict void lattice formation in pure, polycrystalline tungsten irradiated with neutrons up to 1 dpa at 1025 K. In the simulation, grain boundary effects are taken into account, but intragranular sinks such as dislocation loops and precipitates from transmutation elements (osmium and rhenium) in neutron irradiated tungsten are not yet included. The presence of these microstructural features is known to suppress void nucleation and growth and affects microstructural evolution [3]. However, void lattice formation was observed in neutron-irradiated pure, polycrystalline tungsten in JOYO fast test reactor at 1023 K [4-6] and EBR-II reactor at 823 K [7] to high doses of 1.5 and 7 dpa, respectively. In order to validate the simulation results at lower doses in pure tungsten without precipitates of transmutation elements, self-ion irradiation and characterization of high-purity monocrystalline and polycrystalline tungsten are being performed. In addition, a comprehensive dataset [8-11] from molecular dynamics and OKMC simulations has been reported for defect production due to displacement cascades in tungsten and defect recovery during annealing at elevated temperatures. In-situ ion-channeling analysis based on Rutherford backscattering spectrometry (RBS/C) is employed in this study to investigate interstitial-type defect accumulation and recovery in monocrystalline tungsten.

Experimental Procedure

In order to estimate suitable dose rates for void lattice formation in tungsten predicted by OKMC simulations [1,2], quick Kinchin-Pease (K-P) SRIM13 (Stopping and Range of Ions in Matter, version 2013 [12]) simulations were performed for 4 MeV W ions in tungsten, where the threshold displacement energy is assumed to be 90 eV [13] and the lattice binding energy is set to 0 eV for better estimation of the atomic displacement rates [14]. The theoretical density for body-centered cubic tungsten is 19.25 g/cm^3. The results for the depth profiles of the displaced W atoms and implanted W in tungsten are shown in Figure 1(a). The peak disordering rate is 44 dpa per 10^{16} ions/cm^2 at a depth of 162 nm, which is about a half of the value from the full-damage cascade SRIM13 calculation. The profile of the implanted W is peaked at 288 nm with a maximum of 0.57 at % W per 10^{16} ions/cm^2. The recoil distribution as a function of energy from the quick K-P calculation is shown in Figure 1(b). The average recoil energy is estimated

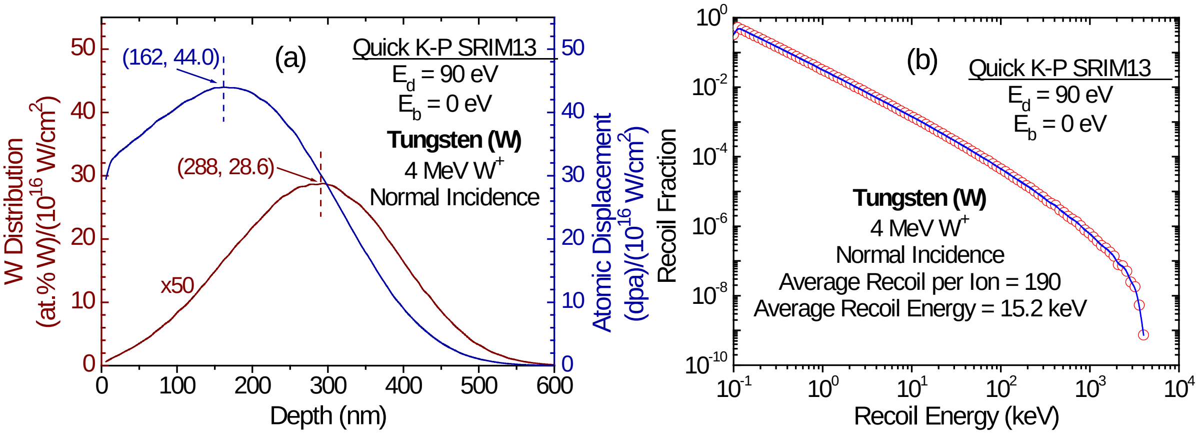

Figure 1. Quick K-P SRIM13 simulation results of 4 MeV self-ion irradiation in tungsten (a) for distributions of implants and atomic displacements and (b) for recoil distribution. E_d: threshold displacement energy; E_b: binding energy.

to be 15.2 keV with the average number of recoils per ion being 190. Based on the recoil energy, void lattice formation is likely to occur in highly pure W crystal irradiated at dose rates of 10^{-3} and 10^{-4} dpa/s to doses ranging from 0.1 to 1 dpa at 900 K.

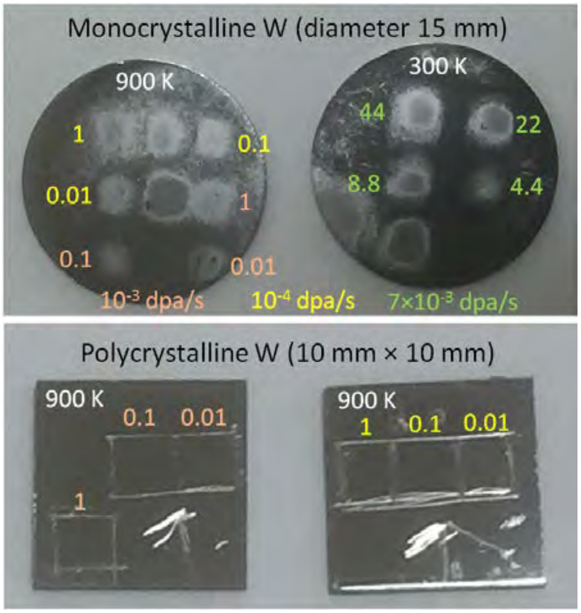

Figure 2. 4 MeV W^{2+} ion irradiation of monocrystalline and polycrystalline tungsten to the indicated peak doses in dpa at different peak dose rates (coloring) and temperatures with a defocused beam.

Monocrystalline and polycrystalline tungsten samples [15] were irradiated 7° off the surface normal with 4 MeV W^{2+} ions to peak doses of 0.01, 0.1 and 1 dpa at peak dose rates of 10^{-3} and 10^{-4} dpa/s at 900 K. The irradiation area was 2 mm × 2 mm with a defocused beam. For the monocrystalline W disk of 15 mm in diameter, self-ion irradiation started at 1 dpa and 10^{-4} dpa/s, followed by 0.1 and 0.01 dpa at the same dose rate. Additional irradiation was also performed in different areas on the sample in the sequence of 1, 0.1 and 0.01 dpa at 10^{-3} dpa/s to minimize temperature effects in the irradiated material. The two other spots in the middle column of the sample (upper panel on the left of Figure 2) are the unirradiated areas for channeling and random spectra (see below). Additional irradiation of another monocrystalline tungsten disk was performed at 300 K to higher peak doses of 4.4, 8.8, 22 and 44 dpa at a higher peak dose rate of 7×10^{-3} dpa/s. The irradiated areas on the monocrystalline W were visible immediately after irradiation, as shown in the upper panel of Figure 2, but gradually faded out over time at room temperature. Two polycrystalline samples were also used for irradiation at 10^{-3} and 10^{-4} dpa/s respectively, and the irradiation sequence was from high (1 dpa) to low (0.01 dpa) doses. Irradiated areas were hardly visible and hence marked with scratches on the surface (Figure 2, lower panel).

In-situ 2 MeV He^+ ion RBS/C along the ⟨111⟩-axial direction was performed at a scattering angle of 150° for the irradiated monocrystalline W at room temperature. The He^+ beam current was ~20 nA without applying a bias voltage to the sample, corresponding to an actual beam current of ~5 nA. A random spectrum was collected at a fixed polar angle of -7° with a rotating sample between flip angles of -3° and 3°. For the 300 K irradiated monocrystalline W, in-situ 20 min isochronal annealing at 600 and 900 K was performed. The thermal condition was achieved by adjusting the current and bias to the filament of an e-beam heater behind the grounded sample while a constant flow of liquid nitrogen was maintained. A conventional chromel-alumel thermocouple was used to measure the temperature on the sample surface. Similar in-situ RBS/C analyses of the annealed samples were also performed. Cross-sectional lamellas from polycrystalline W irradiated at 900 K to 1 dpa at 10^{-3} dpa/s were taken using an FEI Quanta dual-beam focused ion beam (FIB) microscope. Transmission electron microscopy (TEM) was performed using a JEOL JEM-ARM 200CF aberration-corrected TEM/STEM microscope operating at 200 kV. More TEM specimens are currently being prepared and analyzed.

Results

Two RBS/C spectra for a (111) oriented tungsten single crystal irradiated to a peak dose of 1 dpa (corresponding to an ion fluence of ~2.3×10^{14} W^{2+}/cm^2) at peak dose rates of 10^{-4} and 10^{-3} dpa/s at 900 K are shown in Figure 3. Also included in the figure are a RBS/C spectrum and a random spectrum from unirradiated areas (Figure 2). The depth scale, shown on the top axis, is estimated based on the SRIM database [12] with the assumption that the energy losses of both incident and backscattered ions are negligible in the near-surface region of interest (surface energy approximation) [16]. The minimum yield, χ_{min}, from the channeling spectrum for the pristine W single crystal is determined to be only ~2%, indicating that the as-received sample had high crystalline quality in the near-surface region of interest. This result is consistent with our previous report [15]. In contrast to many crystalline materials irradiated by energetic ion beams, the damage peak in the irradiated tungsten is completely invisible in the RBS/C spectra around the depth of 162 nm (channel number ~800) [Figure 1(a)]. A low concentration of atomic displacements is observed in the irradiated structure. The results indicate that self-interstitials in tungsten at 900 K are extremely mobile; most of the interstitials produced during irradiation are likely to annihilate by recombination with vacancies, diffuse out of the region and reach the surface. From Figure 3, there is a higher damage level at higher dose rate, probably due to a higher efficiency of point-defect clustering. Surface peaks located at channel number 916 grow only slightly under both irradiation conditions, indicating that the surface disordering induced by the irradiations is minimal. Since vacancies or voids are transparent to energetic ion beams, RBS/C spectra cannot identify their locations in the specimens.

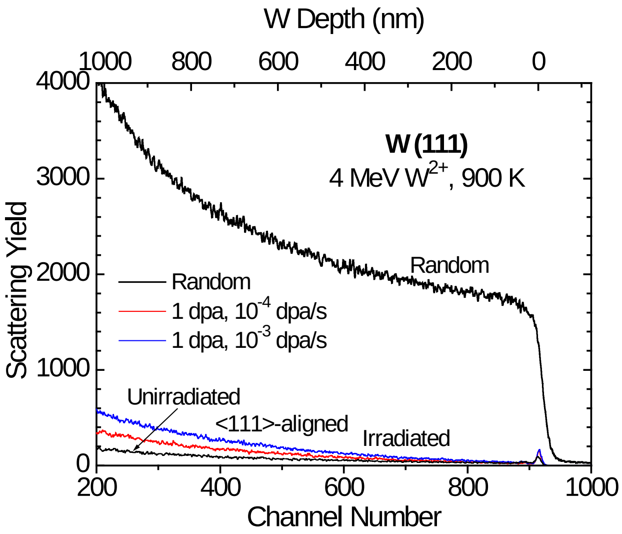

Figure 3. 2 MeV He$^+$ RBS/C spectra along the ⟨111⟩ axis in tungsten irradiated with 4 MeV W^{2+} ions at 900 K to 1 dpa at 10^{-4} and 10^{-3} dpa/s. Also included are the ⟨111⟩-aligned and random spectra from unirradiated areas.

Figure 4 shows RBS/C spectra for W irradiated to a number of higher doses at 300 K. The higher-dose irradiation is intended to produce higher levels of lattice damage for thermal annealing studies. Again, damage peaks are not observed in any of the spectra even up to 44 dpa at 300 K. This behavior is an indication of very fast migration of W interstitials in tungsten. Surface peak intensity is observed to increase with increasing dose at 300 K, due to the direct bombardment of energetic W^{2+} ions and maybe also to the incoming flux of migrating interstitials that occupied non-equilibrium sites, such as adatoms. Figure 4 also suggests that the damage levels at 8.8 and 22 dpa are nearly the same, indicating that a damage saturation stage was attained probably due to fast out-diffusion of the W interstitials. However, there is an increase in the damage level at 44 dpa. The relative disorder near the surface (depth < 50 nm) can be estimated by assuming a negligible dechanneling contribution from the very small beam angular dispersion. For an amorphous material, the level of relative disorder is 100%. From Figure 4, the irradiated sample at 44 dpa is estimated to have a relative disorder level of only 6%.

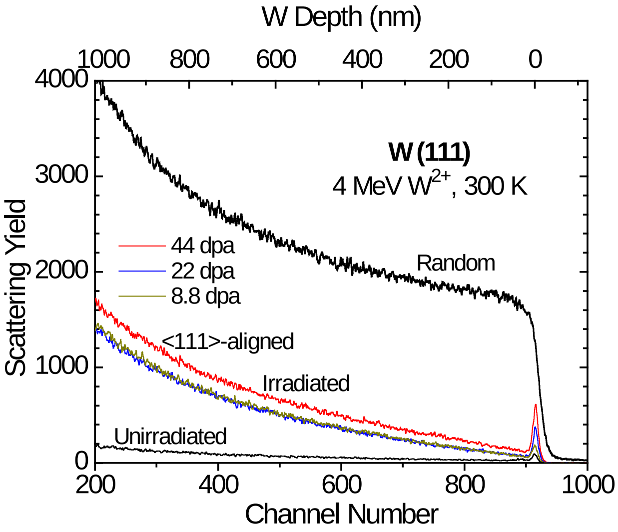

Figure 4. 2 MeV He^+ RBS/C spectra along the ⟨111⟩ axis in tungsten irradiated with 4 MeV W^{2+} ions at 300 K to 8.8, 22 and 44 dpa. Also included are the ⟨111⟩-aligned and random spectra from an unirradiated area.

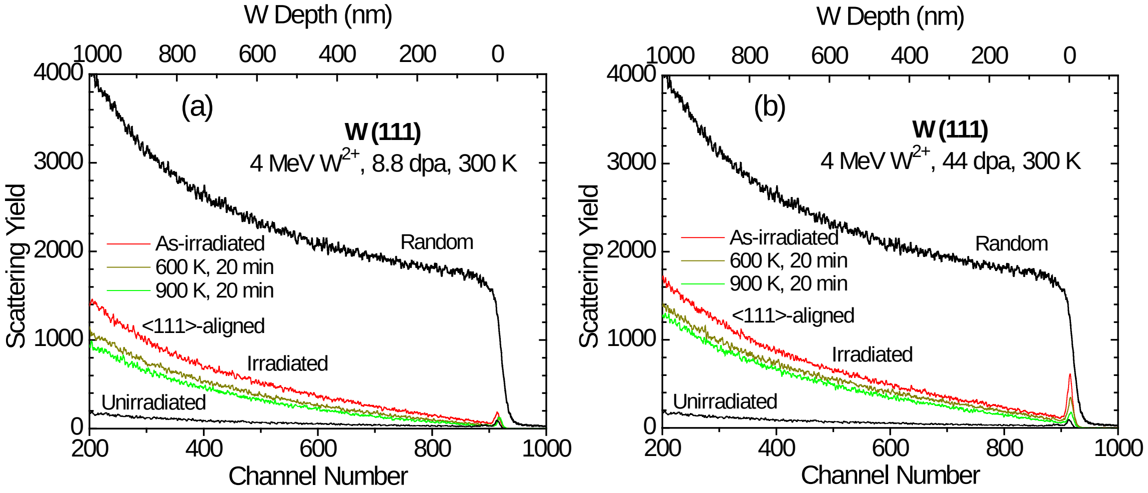

Figure 5. 2 MeV He^+ RBS/C spectra along the ⟨111⟩ axis in tungsten irradiated with 4 MeV W^{2+} ions at 300 K to (a) 8.8 dpa and (b) 44 dpa and subsequently annealed at 600 and 900 K for 20 min each. Also included are the ⟨111⟩-aligned and random spectra from an unirradiated area.

In-situ 20-min isochronal annealing at 600 and 900 K reveals recovery of defects in tungsten irradiated at 300 K, as shown in Figure 5. This recovery represents an overall reduction in the relative number of atoms displaced from the lattice sites observed along the ⟨111⟩ crystallographic axis in this study. Local lattice distortion due to the presence of dislocation loops can also contribute to the dechanneling yield. For the 8.8 dpa sample [Figure 5(a)], the surface peak was hardly changed after irradiation and recovery

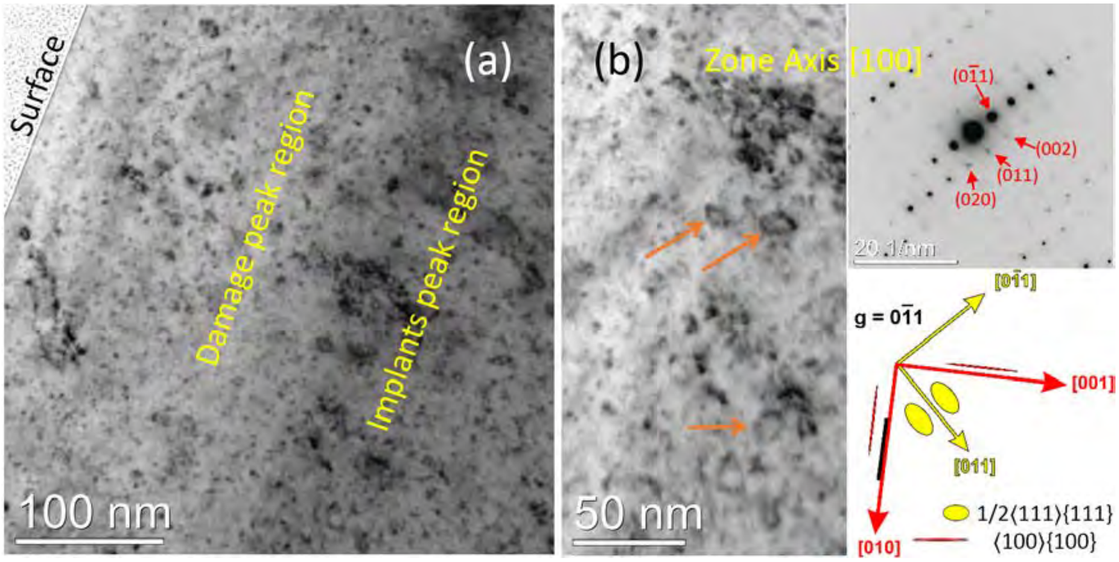

Figure 6. Bright-field TEM micrographs with zone axis W[100] (a) at a low-resolution and (b) a higher-resolution for cross-sectional view of a polycrystalline W irradiated at 900 K with 4 MeV W^{2+} ions to 1 dpa at 10^{-3} dpa/s. Insets in (b) are an electron diffraction pattern and a drawing showing the shapes of dislocation loops along different orientations.

was minimal. A rather significant recovery of lattice defects occurring at the surface of the 44 dpa sample [Figure 5(b)] is observed after annealing at 600 K and further annealing at 900 K leads to more restoration of the surface lattice order.

The microstructure of a grain in polycrystalline tungsten irradiated at 900 K to 1 dpa at 10^{-3} dpa/s is shown in Figure 6. There is no evidence of the formation of a clear damage band in the bright-field TEM image of Figure 6(a). The result is consistent with the RBS/C data in Figure 3, confirming that the self-interstitials readily recombine and quickly diffuse out of the peak region. A high density of black-spot type defects throughout the entire cross-sectional specimen is observed. Some of the surface defects likely originate from the lattice damage produced by Ga^+ ion irradiation during the FIB processing. They are indistinguishable from the defects produced by self-ion irradiation at 900 K. Removal of the surface defects by electrochemical polishing is being performed and further TEM examinations of the sample will be carried out. A previous report [17] indicates that the microstructure in a self-ion irradiated tungsten sample to 1.5 dpa at 773 K contains a large number of black spots that are dislocation loops with sizes below 2-3 nm. Figure 6(b) shows the microstructure at a higher resolution in the depth region between damage and implant peaks. Also shown in the insets of Figure 6(b) are the electron diffraction patterns and expected loop shapes projected along different orientations. The diffraction condition in this study is **g** = [1$\bar{1}$0] off the [100] zone axis. Both ½[111] and [100] type loops should be visible if present. Dislocation loops are observed in this depth region, including some of the larger ones as indicated by arrows. There is no evidence of edge-on ⟨100⟩{100} type loops; the larger loops are likely the prismatic ½⟨111⟩ type loops of vacancy character, lying on or near {111} habit planes, i.e., ½⟨111⟩{111} loops. Similar loops were reported in an earlier study of neutron-irradiated tungsten after annealing at 1373 K [18]. More recently, such loops were observed in self-ion irradiated tungsten [19]. Normally, one would expect that the isolated loops in tungsten are highly mobile and should glide to the grain boundary. The sessile nature of the loops has been attributed to their interactions with each other and with vacancy clusters in near proximity through long-range elastic fields [19]. The loop size and density increases and decreases, respectively, with increasing annealing temperature up to 1673 K, where a complete removal of the dislocation structures occurs [17]. An in-situ annealing TEM study [17] shows microstructural evolution involving an isolated loop hopping, followed by formation of loop chains, coalescence into void-like features, and finally absorption by free surfaces.

Acknowledgements

This research was supported by Office of Fusion Energy Sciences, U.S. Department of Energy (DOE) under Contract DE-AC05-76RL01830. Ion irradiation and RBS/C were performed in collaboration with Texas A&M University. TEM was carried out at PNNL.

References

[1] G. Nandipati, W. Setyawan, H. L. Heinisch, K. J. Roche, R. J. Kurtz, and B. D. Wirth, 2017; available at: https://arxiv.org/abs/1510.02732.
[2] G. Nandipati, W. Setyawan, H. L. Heinisch, K. J. Roche, R. J. Kurtz, and B. D. Wirth, 2017; available at: https://arxiv.org/abs/1606.01308.
[3] T. Tanno, A. Hasegawa, M. Fujiwara, J. C. He, S. Nogami, M. Satou, T. Shishido, K. Abe, Mater. Trans. 49 (2008) 2259.
[4] T. Tanno, A. Hasegawa, J. C. He, M. Fujiwara, S. Nogami, M. Satou, T. Shishido, K. Abe, Mater. Trans. 48 (2007) 2399.
[5] T. Tanno, A. Hasegawa, J. C. He, M. Fujiwara, M. Satou, S. Nogami, K. Abe, T. Shishido, J. Nucl. Mater. 386-388 (2009) 218.
[6] A. Hasegawa, M. Fukuda, T. Tanno, S. Nogami, Mater. Trans. 54 (2013) 466.
[7] V. K. Sikka, J. Moteff, J. Appl. Phys. 43 (1972) 4942.
[8] W. Setyawan, G. Nandipati, K. J. Roche, H. L. Heinisch, B. D. Wirth, and R. J. Kurtz, J. Nucl. Mater. 462 (2015) 329.
[9] G. Nandipati, W. Setyawan, H. L. Heinisch, K. J. Roche, R. J. Kurtz, and B. D. Wirth, J. Nucl. Mater. 462 (2015) 338.
[10] G. Nandipati, W. Setyawan, H. L. Heinisch, K. J. Roche, R. J. Kurtz, and B. D. Wirth, J. Nucl. Mater. 462 (2015) 345.
[11] W. Setyawan, G. Nandipati, and R. J. Kurtz, J. Nucl. Mater. 484 (2017) 30.
[12] J. F. Ziegler, J. P. Biearsack, U. Littmark, *The stopping and Range of Ions in Solids* (Pergamon Press, New York, 1985); available at: http://www.SRIM.org/.
[13] ASTM, ASTM Standard E521-96 (2009), *Standard Practice for Neutron Radiation Damage Simulation by Charged-Particle Irradiation,* ASTM International, West Conshohocken, PA (2009).
[14] R. E. Stoller, M. B. Toloczko, G. S. Was, A. G. Certain, S. Dwaraknath, F. A. Garner, Nucl. Instrum. Meth. Phys. Res. B 310 (2013) 75.
[15] W. Jiang, K. Kruska, C. H. Henager, Jr., and R. J. Kurtz, *Fusion Materials Semiannual Progress* Report for Period Ending December 31, 2016, DOE/ER-0313/61, U.S. Department of Energy, 115.
[16] W. K. Chu, J. W. Mayer, M. A. Nicolet, *Backscattering Spectrometry*, Academic Press, New York, CA, 1978.
[17] F. Ferroni, X. Yi, K. Arakawa, S. P. Fitzgerald, P. D. Edmondson, S. G. Roberts, Acta Mater. 90 (2015) 380.
[18] R. C. Rau, Philos. Mag. 18 (1968) 1079.
[19] D. R. Mason, X. Yi, M. A. Kirk, S. L. Dudarev, J. Phys. Condens. Matter 26 (2014) 375701.

4.8 MORPHOLOGIES OF TUNGSTEN NANOTENDRILS GROWN UNDER HELIUM EXPOSURE

—Amith Darbal, Robert Stroud (AppFive, Tempe, AZ), Kun Wang, F. W. Meyer, M. E. Bannister, Chad M. Parish (Oak Ridge National Laboratory), and R. P. Doerner, M. J. Baldwin (University of California-San Diego)

Abstract of an article in Scientific Reports 7 (2017) 42315.

Nanotendril "fuzz" will grow under He bombardment under tokamak-relevant conditions on tungsten plasma-facing materials in a magnetic fusion energy device. We have grown tungsten nanotendrils at low (50 eV) and high (12 keV) He bombardment energy, in the range 900–1000°C, and characterized them using electron microscopy. Low energy tendrils are finer (~22 nm diameter) than high-energy tendrils (~176 nm diameter), and low-energy tendrils have a smoother surface than high-energy tendrils. Cavities were omnipresent and typically ~5–10 nm in size. Oxygen was present at tendril surfaces, but tendrils were all BCC tungsten metal. Electron diffraction measured tendril growth axes and grain boundary angle/axis pairs; no preferential growth axes or angle/axis pairs were observed, and low-energy fuzz grain boundaries tended to be high angle; high energy tendril grain boundaries were not observed. We speculate that the strong tendency to high-angle grain boundaries in the low-energy tendrils implies that as the tendrils twist or bend, strain must accumulate until nucleation of a grain boundary is favorable compared to further lattice rotation. The high-energy tendrils consisted of very large (>100 nm) grains compared to the tendril size, so the nature of the high energy irradiation must enable faster growth with less lattice rotation.

4.9 PRECIPITATION OF TRANSMUTANT ELEMENTS IN NEUTRON IRRADIATED TUNGSTEN—X. Hu, C. Parish, K. Wang, Y. Katoh (Oak Ridge National Laboratory)

OBJECTIVE

The objective of this work is to characterize the W-Re-Os precipitates induced by nuclear transmutation in neutron irradiated tungsten. The goals are to determine the chemical composition, phases, and association with visible voids of precipitates within the grains and along the grain boundaries.

SUMMARY

In this study, we have used advanced electron microscope methods to explore the response of tungsten to high dose neutron irradiation in the High Flux Isotope Reactor, focusing on the detailed characterization of irradiation-induced W-Re-Os precipitates in polycrystalline tungsten through TEM, X-ray mapping in STEM, and multivariate statistical analysis data-mining of the X-ray data. The association of voids and precipitates, the chemical compositions, crystal structures and phases of precipitates along the grain boundary and within the grains were identified. The results showed that the intragranular precipitates are $(Re,Os)_2W$ Laves phase and strong association of voids and precipitates are observed. More work is needed to validate the crystalline structures of the intergranular and intragranular precipitates.

PROGRESS AND STATUS

Introduction

Tungsten (W) is perceived as the leading candidate material for plasma facing component in ITER and future fusion reactors. Its high melting temperature, high thermal conductivity, low sputtering yield, and low tritium retention rate enable its applicability in the extremely hostile fusion environment, characterized by high temperature (>500°C), and high fluxes of heat (i.e., >10MW/m^2) and particles (i.e., D, T, He, and neutrons). The combined sum of these loading conditions will impose significant challenges to W performance in service. One of the primary concerns is the significant displacement damage of lattice structure creating vacancies, interstitials, and their clusters, as well as generating significant concentrations of transmutation elements (i.e., Re, Os), induced by the 14 MeV-peak neutron irradiation. Correspondingly, the accumulation of irradiation-induced defects results in the severe microstructural evolution and thermo-mechanical property degradation.

Irradiation effects in W have drawn a great deal of attention in response to its application as plasma facing material. However, due to the lack of any fusion-relevant neutron source, the investigation of neutron irradiation effects in W have been centered on the use of fission reactors and accelerator-based ion beams serving as a surrogate for neutron irradiation. Microstructure characterization of neutron irradiated pure tungsten [1] [2] indicates that voids, dislocation loops, and transmutation-induced precipitates are the most important radiation damage features, highly dependent on irradiation temperature, dose, and neutron energy spectrum, while the transmutation precipitation behavior, the unique microstructural alteration, cannot be captured in ion irradiated pure W [3]. As one of the most significant mechanical property degradation phenomena, irradiation hardening of neutron irradiated W has been investigated intensively [4] [5] [6] [7] [8] [9], which indicates that irradiation-induced precipitation of transmutant elements is the dominant hardening source, contributing to the continuously significant increase of measured Vickers' hardness when radiation dose is greater than 0.6 dpa [9].

Although many aspects of the irradiation effects in W have been revealed, such as point defect clustering, formation of voids and dislocation loops, and the resultant macroscopic property changes, the highly interrelated phenomena of transmutant elements-defect interactions and the precipitation are not sufficiently understood. In particular, the detailed characterization of the precipitates formed in neutron irradiated W is less explored. Early studies before 2000 related to this transmutation induced precipitation phenomena used the W-Re alloys with the motivation of understanding irradiation induced solute segregation and precipitation. Sikka and Moteff [10] identified the α-Mn crystal structure (i.e., χ phase, WRe_3) of the precipitates in W-25Re alloys subjected to fast neutron irradiation to a fluence of ~1×10^{22} n/cm^2 (E > 1MeV) in the temperature range of 430~1000°C by combining the electron diffraction pattern with the W-Re phase diagram. Williams et al. [11] investigated W-based alloys containing 5, 11, and 25 pct Re irradiated in the EBR-II reactor to a fluence of 6×10^{21} n/cm^2 (E > 0.1 MeV) at 900~1500°C and found the precipitate formation in all samples. They also identified the precipitates to be cubic, Re-rich χ phase and observed the large variations in precipitate morphology and distribution. Herschitz and Seidman [12] [13] performed further investigations into W-10Re and W-25Re alloys irradiated in EBR-II at 575, 625 and 675°C to 8.6 dpa by using the atom-probe field-ion microscope. Homogeneous Re-rich χ phase precipitation was also found without association with other defects or impurity atoms. Driven by the need to develop plasma facing material for fusion reactors, the binary W-Re alloys have been proposed to increase the recrystallization temperature and ductility of W [14] in response to its embrittlement. Nemoto et al. used TEM dark field imaging to characterize the microstructure of W-26 wt% Re exposed to neutron irradiation in the FFTF reactor to a dose range of 2~11dpa at 373~800°C. Their results showed the presence and morphology of both σ and χ phase precipitates with equiaxed and lenticular morphology, respectively. A research group from Tohoku University carried out extensive microstructure characterization of W and W-alloys irradiated in various fission reactors (i.e., the fast reactor Joyo; the JMTR; and HFIR) by using TEM. He et al. found the formation of precipitates at grain boundaries without providing the phase information in W-26Re irradiated at 800°C to 0.15 dpa in JMTR. Tanno et al. [15] showed the σ and χ phase precipitates were observed in W-5Re and W-10Re alloys irradiated in Joyo at 400~750°C up to 1.54 dpa. Fukuda et al. observed large amounts of precipitates identified as σ and χ phase in all W-Re alloys irradiated in HFIR at 500 and 800°C to 1 dpa. In all abovementioned studies, the contribution of transmutation to the precipitation was not discussed, while the observed precipitates arose from the Re in the original alloys. Therefore, these studies based on neutron-irradiated W-Re alloys only provide limited insights into the transmutation induced precipitation in pure W, without capturing the mutual interactions of irradiation induced defect and the transmutant Re and Os.

Moreover, the transmutation induced precipitates were also studied in pure tungsten to some limited extent. As to the theoretical study, Cottrell [16] [17] calculated the transmutation of pure tungsten and the phase stability when exposed to fusion neutron energy spectrum and concluded that tungsten will be converted to an alloy of about 75 at% W, 13 at% Os, and 12 at% Re after five-year service in fusion reactors, which is close to the homogeneous σ field of the phase diagram. Experimental investigation of transmutation of neutron irradiated tungsten was centered on the use of available fission neutron sources. In Ref. [2], σ and χ phase precipitates were identified in the pure W irradiated at 500 and 800°C to ~1 dpa in HFIR, using the same method shown in [18]. In a recent study, Koyanagi et al. performed a more detailed characterization of two polycrystalline W samples irradiated at 650°C to 2.4 dpa and at 500°C to 4.6 dpa in HFIR. They found strong association of void-precipitate within grains and Re-Os rich precipitates along the grain boundaries without showing the detailed composition analysis and phase analysis. Although these studies specifically showed the formation of W-Re-Os precipitates in W subjected to neutron irradiation, further detailed analysis on the observed precipitates are still lacking in terms of the composition analysis, preferential precipitation sites, and correlation between transmutant elements and radiation damage. Therefore, the previous experimental studies cannot sufficiently inform the computational models predicting the performance of W in a fusion reactor environment.

The advancement of microscopy technique in recent years significantly improved the microstructural characterization of irradiated materials by revealing more details at the nanoscale. This paper describes the detailed characterization of transmutation induced precipitates in polycrystalline W following neutron irradiation in HFIR, capturing the phase determination, preferential precipitation sites, compositions, and other details.

Experimental Procedure

The polycrystalline W specimens (16×4×0.1 mm^3) used in this study were produced by PLANSEE Metall GmbH, Reutte, Austria through powder sintering and then hot and cold rolling with a purity of 99.97% (<100 ppm Mo, <30 ppm C, <30 ppm Fe, and < 20ppm O, guaranteed by the manufacturer). EBSD analysis of the W foil surface indicated that the average grain size was ~ 5 μm. The majority of the grains elongated to <101> axis, corresponding to the rolling direction and low angle grain boundaries were dominant. Neutron irradiation was in the peripheral target positions of HFIR at ORNL, USA. The two specimens studied here, OW158 and OW125, were irradiated to fast neutron fluences of 7.4×10^{25} and 14.1×10^{25} n/m^2 (E > 0.1 MeV), respectively. The corresponding irradiation temperatures (nominal values) were 650 and 500°C, respectively. In HFIR, a neutron fluence of 1×10^{25} n/m^2 (E > 0.1 MeV) corresponds to ~0.3 displacement per atom (dpa) in W with a radiation damage rate of 2.3×10^{-7} dpa/s. Therefore, the radiation damages for these two samples are 2.2 and 4.2 dpa, respectively. The calculations done by Greenwood and Garner [19] indicated that the solid transmutation products in there two samples following the neutron exposure in HFIR are 7 at% Re and 1.7 at% Os in OW158 and 9.2 at% Re and 4.6 at% Os in OW125, respectively.

Microstructural characterization of the samples was carried out in the low activation materials development and analysis lab (LAMDA) at ORNL. Electron transparent TEM foils were prepared using a focuses ion beam system (FEI Quanta 3D Dual Beam) operated at 30 kV for initial milling and at 5 kV for final thinning to minimize any FIB-induced damages. The lifted-out foils also underwent an additional 900 eV Ar ion mill using a Fischione Model 1040 NanoMill to further thin and clean the foils prior to the microstructural investigations. TEM examination was performed in an FEI Talos F200X S/TEM (200 keV, Schottky-emission, non-aberration-corrected) equipped with a SuperX four-detector X-ray energy dispersive spectroscopy (EDS) system. EDS mapping was performed using a small condenser aperture (convergence semi angle ~8 mrad) to minimize beam spread in the thin foils. X-ray EDS spectrum images were further analyzed via multivariate statistical analysis (MVSA) using the AXSIA code of Sandia National Laboratory, along with customized data file format conversion and post-processing codes written in MATLAB [20].

Results

General microstructures of as-received polycrystalline W foil

Figure 1 (a) shows the bright field TEM images of the cross section of the as-received W foil. The majority of the grains extended along the horizontal direction (rolling direction) with a typical width of 150~300 nm. Figure 1 (b) shows the TEM BF image of W foil surface (sample prepared by electro-polishing). A high number density of line dislocations is clearly visible within the grains. The EBSD analysis presented in [21] indicates that grains with <001> parallel to the surface normal and low angle grain boundaries were dominant in this material.

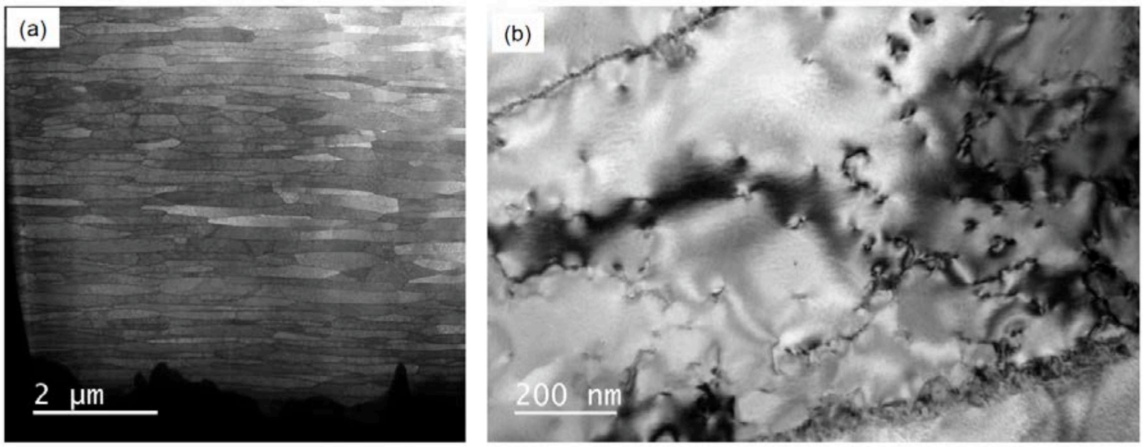

Figure 1. STEM bright field micrographs of (a) the cross section and (b) surface of the as-received W foil.

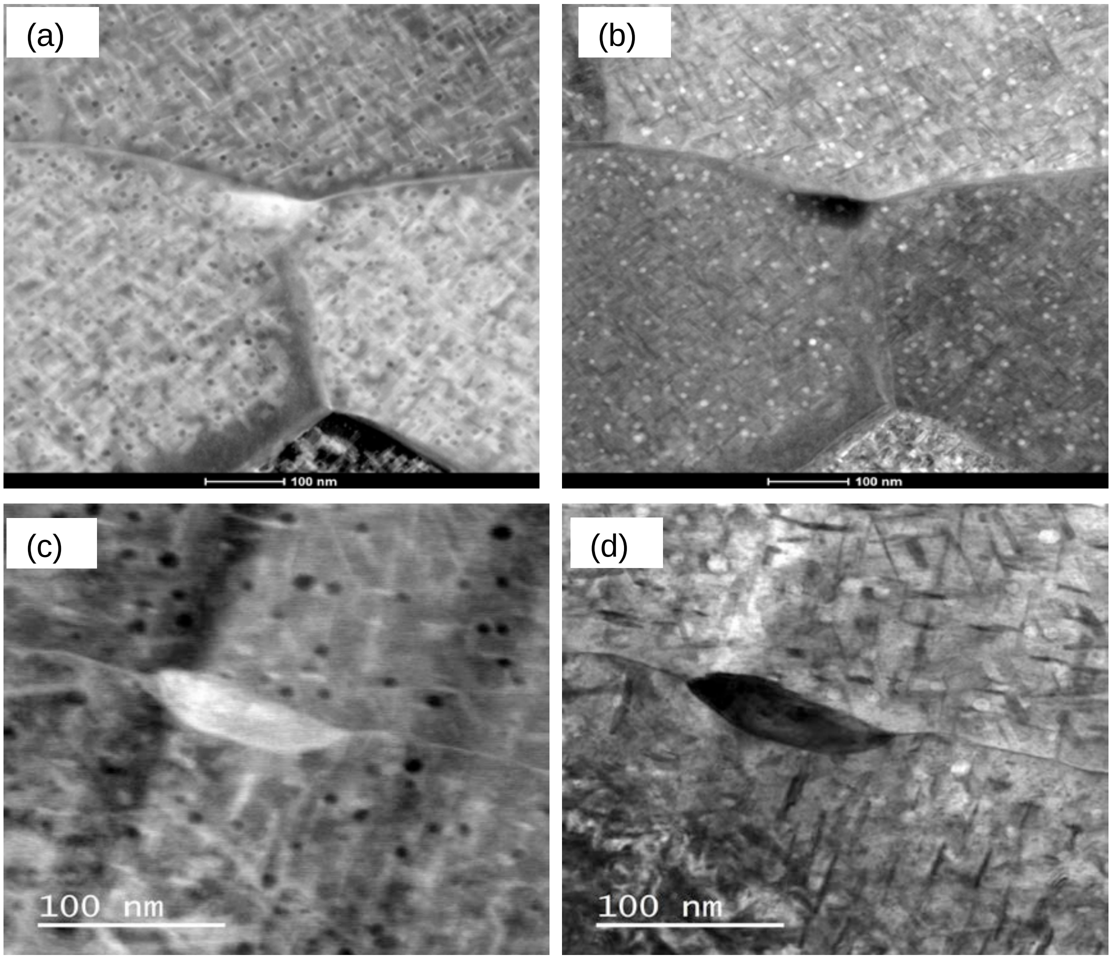

Figure 2. (a, c) HAADF and (b, d) dark field TEM images of (a, b) OW158−2.2 dpa, 650°C and (c, d) OW125−4.2 dpa, 500°C tungsten samples.

General microstructures of as-irradiated OW158 and OW125

Figure 2 shows the STEM-HAADF and DF images of the two samples following neutron irradiation in HFIR. Significant evolution of the irradiation damage and the transmutant elements occurred, giving rise to the heavily changed microstructure, as shown in Figure 2. Voids and precipitates are dominant defect features within the grains. No obvious line dislocations were observed in comparison with the as-received samples. The annihilation of the pre-existing line dislocations could be rationalized by the high mobility of these dislocation lines at the irradiation temperatures, 650°C and 500°C, resulting in the high probability of recombination with defect sinks present within the studied materials. The size and orientation of the present grains are similar to that of as-received samples. Large concentrations of voids are homogenously distributed throughout the gains in both samples. The void average sizes in OW158 (2.2 dpa, 650°C) and OW125 (4.2 dpa, 650°C) are 5.6 and 5.8 nm, respectively, while the corresponding number densities are 4×10^{21} and 6×10^{21} m^3. It is noted that no voids were observed along the grain boundaries. The significant production of transmutant elements, Re and Os, together with the concurrent radiation damage, resulted in segregation and precipitation.

The dense needle-shape precipitates were dispersed within grains while large plate-shape precipitates are found along the grain boundaries or in the intersection of grain boundaries. The average number densities of needle-shape precipitate in OW158 and OW125 are 6×10^{21} and 1.0×10^{22} m^3, respectively and the average lengths are 32.8 and 30.5 nm. In addition, strong affiliations between precipitates and voids are observed from these 2-D TEM images although further evidence is needed to confirm their associations. A narrow denudation zone with a width of 10~40 nm along grain boundaries existed in the observed areas.

Precipitates in the as-irradiated OW158 and OW125

Figure 3 shows the STEM EDS maps of the two samples to identify the chemical segregation. It is evident that all the observed precipitates within the grains or along the grain boundaries are rich in Re and Os in both samples with quite similar distributions. For the chemical composition along the grain boundaries, Os is evidently found in the big precipitates with very limited segregation along the grain boundaries while Re was not only present in the precipitates but also accumulated along the grain boundary. Considering that transmutant elements of Re and Os are continuously produced via W interacting with neutrons while Os is the secondary product, it is deduced that: (1) grain boundaries are stronger trapping sites for Re atoms; (2) the observed large precipitates along the grain boundaries mainly arose from the accumulation of Re; and (3) the majority of the present Os in these precipitates are suspected to result from the transmutation of pre-existing Re. For the precipitates dispersed within the grains, Re and Os were found in the same locations as the precipitates without showing obvious preferential nucleation sites. The Re and Os contained in these precipitates result from the local transmutation of W or the migration of Re and Os from other locations.

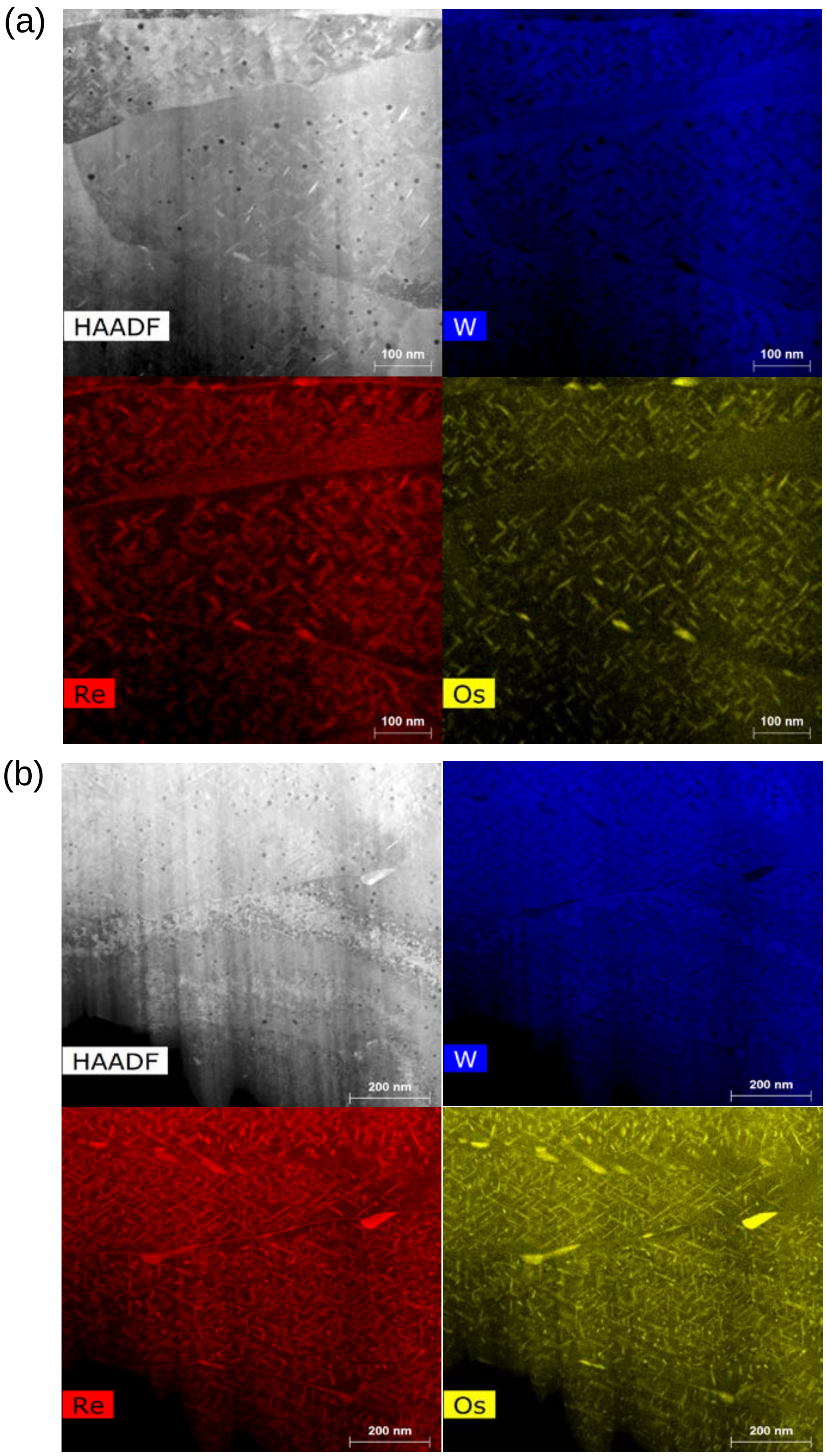

Figure 3. STEM EDS maps of tungsten samples (a) OW158 (2.2 dpa, 650°C) and (b) OW125 (4.2 dpa, 500°C).

Association of voids and precipitates within grains

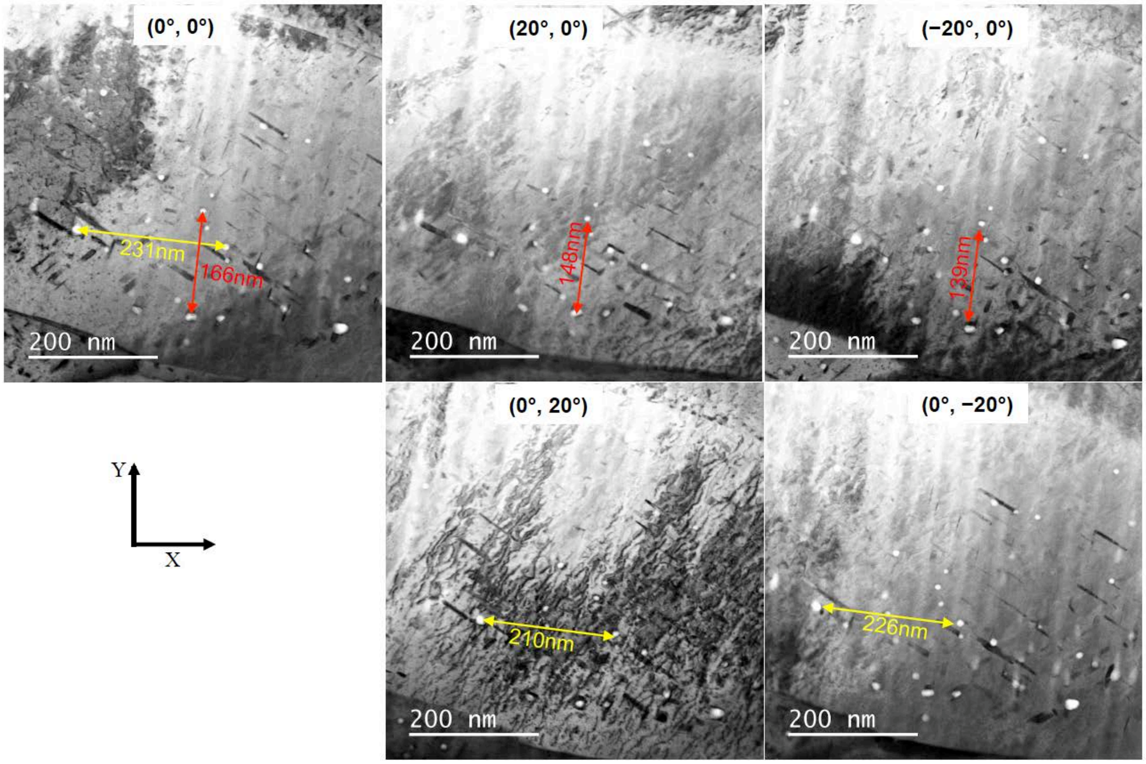

Figure 4. BF STEM images of a local area in OW158 tilted to various positions.

In Figure 2, strong association of voids and precipitates were observed within the grains. However, it is unlikely to determine whether the voids and precipitates are associated with each other or not based on the 2-D TEM images. In order to address this question, a local area with a thickness of ~ 50 nm in OW158 was tilted by ±20° with respect to X- and Y-axis. BF S/TEM images of this area at 5 different rotation positions were shown in Figure 4. The distance of two marked voids was recorded during the tilting process for each tilting direction (Red for X-axis tilting and yellow for Y-axis tilting, as shown in Figure 4). The decrease of the marked distances in the tilting process excluded the possibility that the beam alignments might lead to the same observations at various tilting positions. If the voids and precipitates are not associated with each other and the apparent association in the 2D TEM images is due to the overlap of the two defect features in the TEM foil depth direction while a gap exists between them, the relative positions of these two features will be changed when rotating the samples. Assuming the vertical distance in depth direction of one void and one precipitate is 35 nm, the maximum 40° rotation gives rise to a 24 nm separation. However, the relative positions of voids and precipitates in the observed regions barely changed, when comparing the five images shown in Figure 4. Therefore, it is concluded here that the visible voids and precipitates in the neutron-irradiated tungsten are strongly associated with each other. Intensive interactions between transmutant elements and vacancy clusters are expected during the neutron irradiation. Moreover, this tilting study also aided to the confirmation of the needle-shape precipitates, since all the visible precipitates have the similar needle shapes at various tilting positions.

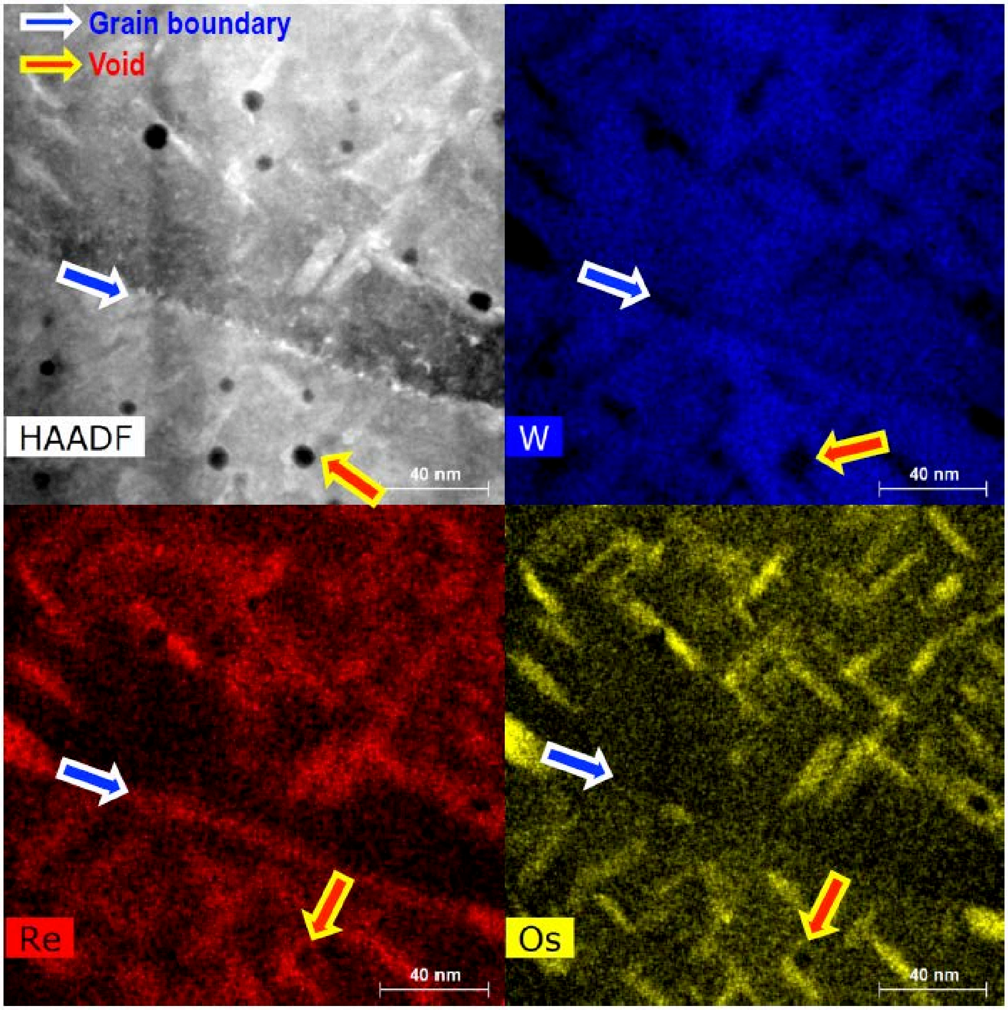

Figure 5. HAADF and EDS maps of a local area nearby a grain boundary within OW158 (2.2 dpa, 650°C).

TEM imaging at high magnification shown in Figure 5 provided more details of the interaction of the voids and precipitates in a local area near a grain boundary within OW158. It is apparent that all visible voids are embedded in the needle-shaped Re-Os rich precipitates. In contrast, not all observed precipitates were bonded to voids. Some of the visible voids were partially intersected by the associated precipitates while some are completely surrounded by the precipitates. It is noted that two preferential positions of the voids on the precipitates were observed, i.e., in the middle and near an end. Both faceted and spherical voids exist. The long axis of Re-Os rich precipitates lie along <111> directions. The precipitates were also found along the grain boundary, enriched in Re and Os as well. In addition, significant segregation of Re appeared along the grain boundary while no obvious Os were observed. Again, this is consistent with our previous conclusion that Re is preferentially trapped by the grain boundary and the Os within the large precipitates in the grain boundary is believed to arise from the transmutation of pre-accumulated Re atoms.

<u>Composition of W-Re-Os precipitates</u>

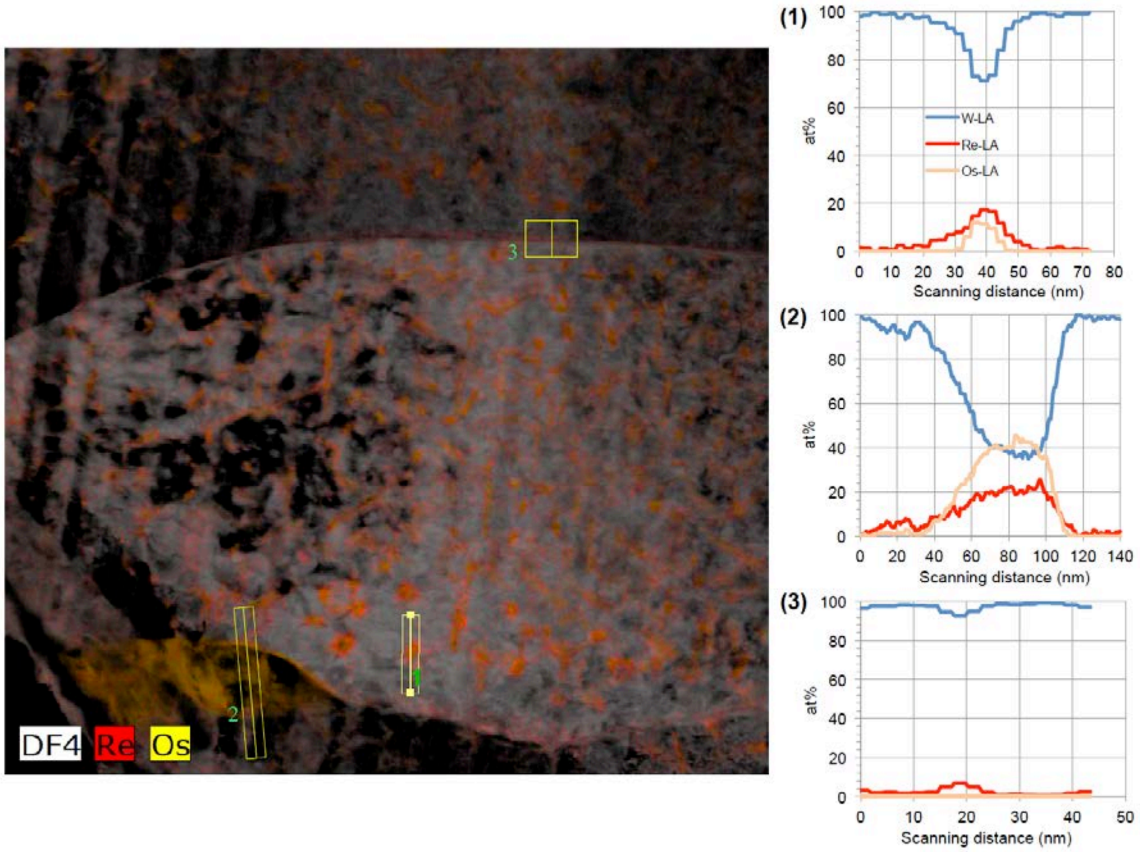

Figure 6. (Left) Overlay of TEM DF image with Re and Os distribution obtained from EDS analysis of OW158 (2.2 dpa, 650°C). (Right)W, Re, and Os compositions of the three scanned areas marked in the left TEM image.

In order to reveal the quantitative information of this complicated microstructure, OW158 was taken for further detailed analysis. A dark field TEM image incorporated with the Re and Os distribution obtained from EDS analysis was shown in Figure 6. Three areas of interest are chosen to run line scans to obtain the composition of individual element, i.e., 1. across a precipitate within the grain; 2. across a big precipitate along the grain boundary towards the interior of nearby grain; 3. across the grain boundary, as marked in Figure 6. The corresponding composition as a function of scanning distance away from the bottom line for each area is shown on the right of Figure 6. For the small needle-shape precipitate located within grains, the peak compositions of W, Re, and Os is 70%, 17%, and 13%, respectively, while the large precipitate along the grain boundary has a composition of 35% W, 21% Re, and 44% Os. Note that the measured signal arises from all the elements throughout the thickness of the scanned area. Therefore, the Re and Os contents contained inside the precipitates are expected to be bigger than these measured values unless the studied precipitates extend through the sample thickness. The determination of the composition of the precipitates enables the identification of the corresponding phases. For the scanning area 2, the large precipitate is more likely close to χ phase, considering the actual contents of Re and Os could be even higher. As to the small precipitate within the grain (scan area 1), its phase is hard to identify since the fraction of the signal contribution from the matrix tungsten atoms is unknown; therefore, the real composition of this precipitate cannot be obtained. In the scanning area 3, the W atom fraction is up to 92% together with 8% Re and negligible Os. The composition analysis verified our hypothesis that the grain boundary is a stronger sink for Re and the Os contained in the large precipitate along the grain boundary results from the transmutation of trapped Re.

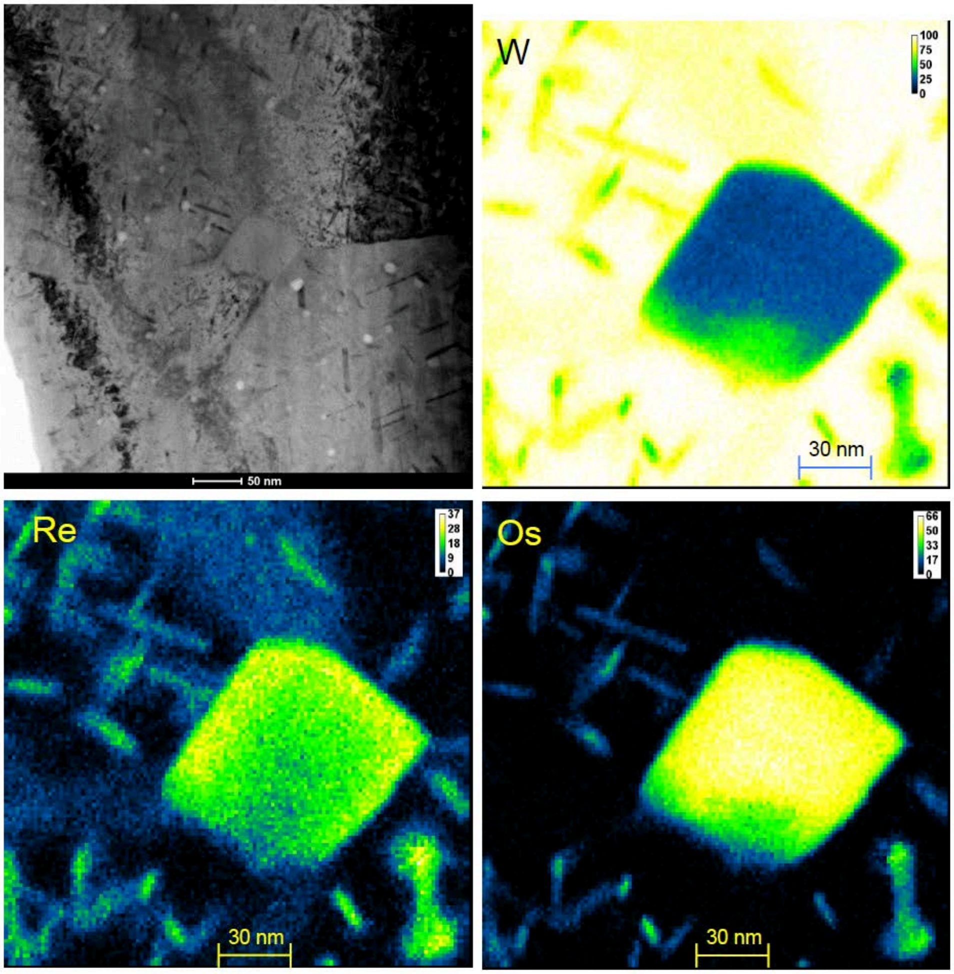

Figure 7. TEM HAADF image and the Multivariate statistical analysis decomposition of the X-ray data of a large precipitate located in the intersection of three or four grain boundaries in OW125 (4.2 dpa, 500°C).

The composition analysis of a large precipitate with a side length of 60 nm found in the intersection of four grain boundaries in the as-irradiated OW125, the higher dose sample, is shown in Figure 7. The bottom edge of this precipitate was not in full thickness and therefore was not quantitatively analyzed. The center of this particular precipitate is enriched in Os (>50%), while the atomic fraction of the transmutant Re in this area is ~24% and the remainder is W (26%). Based on this composition, it is deduced that the large precipitate located in the grain boundary is χ phase $(Re, Os)_3W$. As stated above, the large atomic fraction of Os more likely resulted from the transmutation of Re segregating in the grain boundary. As to the needle-shaped precipitates within the grains, the periphery and the center exhibit quite different compositions. More Re and Os are accumulated in the center while W still dominates the periphery. It is noted that the Re and Os in the center have almost equivalent atomic fractions. Therefore, the composition of the center obtained in this analysis is close to the σ phase field. This observation also implied that the W-Re-Os complexes formed in the early stage of the neutron irradiation serve as strong sinks for the transmutant elements as well as the irradiation induced defects, as irradiation dose is increasing. The local depletion of W and the enrichment of Re and Os could be rationalized by the Kirkendall effect and the inverse Kirkendall effect resulting from the net flux of vacancy and interstitial defects to the complexes during irradiation.

Crystal structure of precipitates

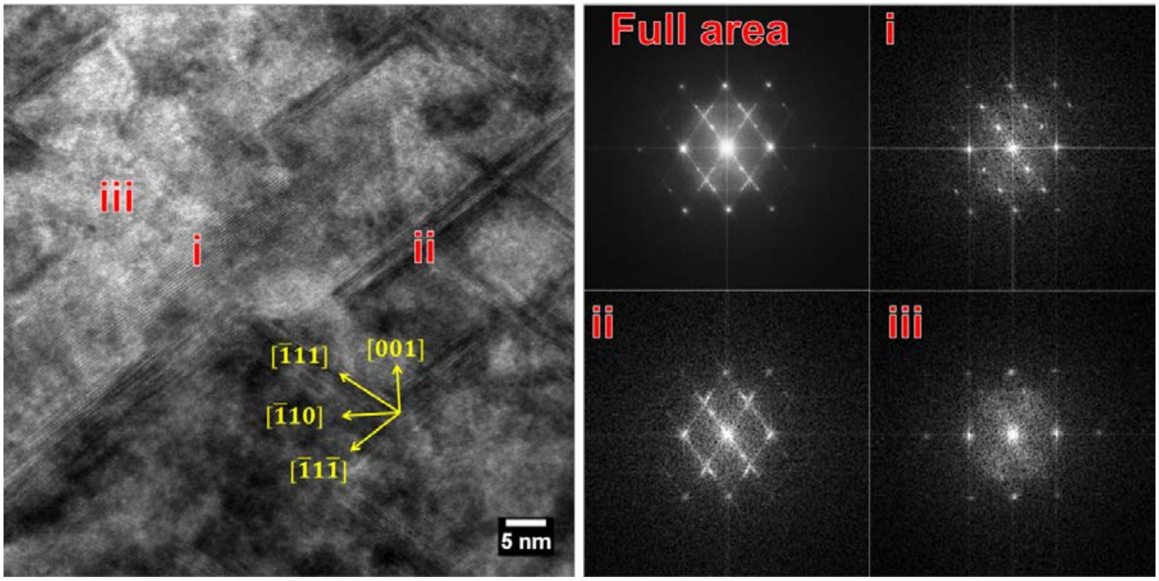

Figure 8. HREM image (left) and Fourier-transform calculated diffractograms Note that precipitates fall along <111>. 2.4 dpa, 650°C, polycrystalline sample.

Figure 8 shows a typical HREM image, tilted onto [110] W zone axis. Diffractograms calculated from Fourier transforms of the entire HREM image, and small sub-regions marked i, ii, and iii, are also given. The region i is from an unfaulted precipitate, ii from two overlapping highly faulted precipitates, and iii from the matrix. It is also important to point out that the precipitates do, indeed, fall along <111> as seen from comparison to the diffractograms. We can now analyze the unfaulted precipitate (region i) to try to find an unambiguous crystallographic identification. Figure 9a shows the diffractogram of region iii (with inverted color for clarity) indexed to W [110] to confirm the zone axis and provide a magnification calibration for the subsequent indexing of the other phases. The sigma [103] diffraction pattern was superimposed on the region I (unfaulted) diffractogram in Figure 9b. Although the bands of spots line up well with the bands in the diffractogram, the locations of the spots match very poorly. Similarly, the [112] chi in Figure 9c does not provide a good match to the locations of the spots.

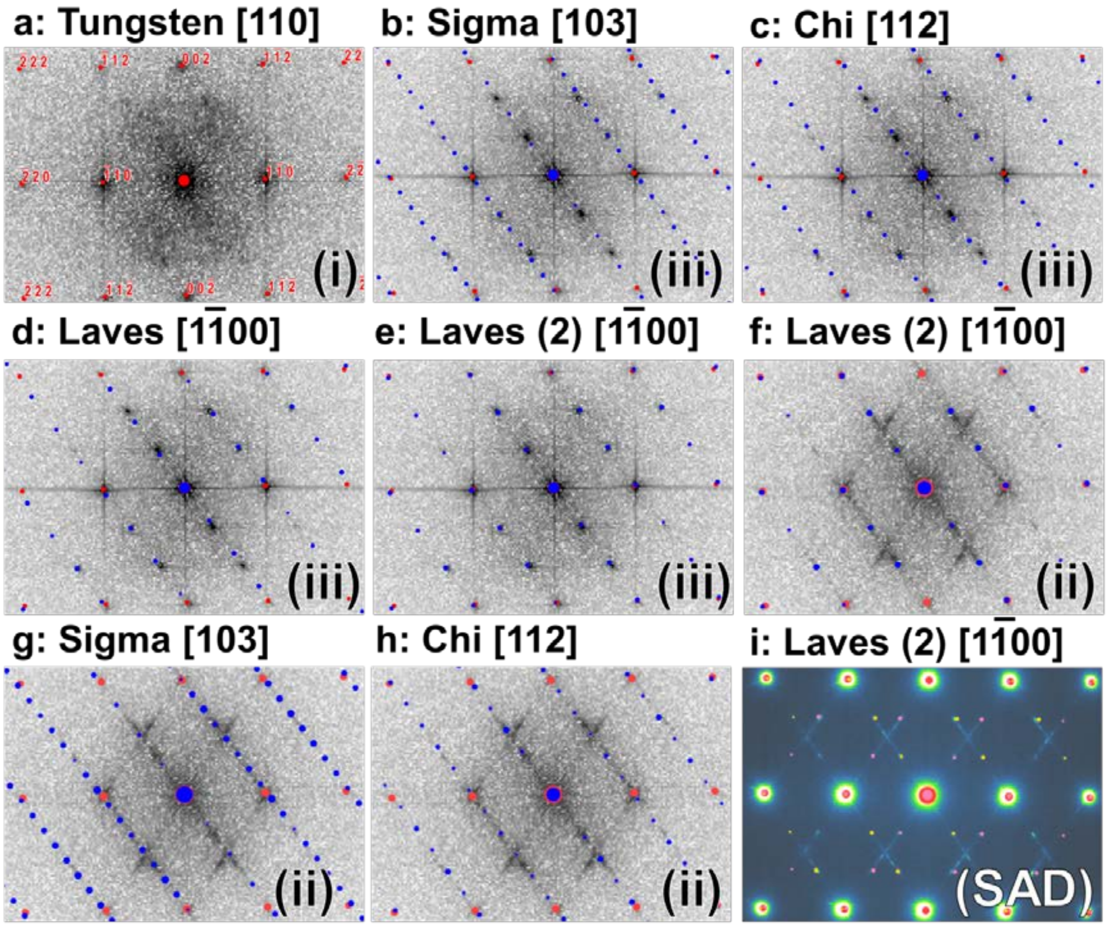

Figure 9. (a) diffractogram of the matrix, region iii, indexed to W [110]. (b-e) diffractogram of the unfaulted precipitate, region i, indexed to sigma, chi, laves, or modified laves. (f-h) diffractogram of the faulted precipitates, region ii, indexed as modified laves, sigma, and chi. (i) SAD pattern, indexed to W [110] (red), modified laves $\mathbf{1\bar{1}00}$ (yellow), and rotated modified laves $\mathbf{1\bar{1}00}$ (pink). 2.4 dpa, 650°C, polycrystalline sample.

Another Re-W intermetallic found in the ICSD data base is the Re$_2$W laves phase, collection code 650203. Superimposing a [1$\bar{1}$00] laves pattern onto the diffractogram, Figure 9d, shows a more satisfying match, although the exact locations of the simulated and experimental spots are slightly offset in the ±[0001] direction of the hexagonal pattern (which is parallel to ±[$\bar{1}$12] in the W matrix pattern.) After a slight modification of the laves crystal, from c=0.8835 nm to c=0.78 nm (Δc≈-13%), the match becomes perfect, Figure 9e. This lattice modification leads to a nearly perfect match between the interplanar distances between W112=0.129 nm and Laves0006=0.130 nm. This modified laves phase is superimposed upon the faulted precipitate diffractogram (Figure 8, region ii) in Figure 9f, which indicates that the modified laves spots fall on the bright nodes of the streaks. The sigma (Figure 9g) and chi (Figure 9h) patterns are also superimposed on this same diffractogram, and the bright spots in the simulated patterns do not particularly match with the brighter nodes in the streaks. Finally, two copies (rotated ≈70.5°) of the modified laves phase 1$\bar{1}$00 diffraction pattern are superimposed in Figure 9i, and the calculated laves diffraction spots fall very closely on the bright nodes in the SAD streaks.

Concluding remarks

Advanced electron microscope methods were used to explore the response of tungsten to high dose neutron irradiation, focusing on the detailed characterization of irradiation-induced W-Re-Os precipitates. The results showed that all precipitates present are enriched in Re and Os. The intragranular precipitates are strongly associated with the visible voids within grains. The intragranular precipitates are $(Re,Os)_2W$ Laves phase. More work is needed to validate the phase and crystalline structures of the precipitates in the neutron irradiated samples and to reveal the underlying mechanisms controlling the transmutation-induced precipitation in neutron irradiated tungsten.

References

[1] Hasegawa, A., et al., *Neutron Irradiation Behavior of Tungsten.* Materials Transactions, 2013. 54(4): p. 466-471.
[2] Fukuda, M., et al., *Microstructural development of tungsten and tungsten–rhenium alloys due to neutron irradiation in HFIR.* Journal of Nuclear Materials, 2014. 455(1-3): p. 460-463.
[3] Yi, X., et al., *Characterisation of radiation damage in W and W-based alloys from 2MeV self-ion near-bulk implantations.* Acta Materialia, 2015. 92: p. 163-177.
[4] Tanno, T., et al., *Effects of Transmutation Elements on Neutron Irradiation Hardening of Tungsten.* Materials Transactions, 2007. 48(9): p. 2399-2402.
[5] Hasegawa, A., et al., *Property change mechanism in tungsten under neutron irradiation in various reactors.* Journal of Nuclear Materials, 2011. 417(1-3): p. 491-494.
[6] Fukuda, M., et al., *Property change of advanced tungsten alloys due to neutron irradiation.* Journal of Nuclear Materials, 2013. 442(1-3): p. S273-S276.
[7] Fukuda, M., et al., *Effects of Re Content and Fabrication Process on Microstructural Changes and Hardening in Neutron Irradiated Tungsten.* Materials Transactions, 2012. 53(12): p. 2145-2150.
[8] Fukuda, M., et al., *Neutron energy spectrum influence on irradiation hardening and microstructrual development of tungsten.* Journal of Nuclear Materials, 2016: p. submitted.
[9] Hu, X., et al., *Irradiation hardening of pure tungsten exposed to neutron irradiation.* Journal of Nuclear Materials, 2016. 480: p. 235-243.
[10] Sikka, V.K. and J. Moteff, *Identification of alpha-Mn crystal structure in neutron irradiated W-Re alloy.* Metallurgical Transactions, 1974. 5(6): p. 1514-1517.
[11] Williams, R.K., et al., *Irradiation induced precipitation in tungsten based, W-Re alloys.* Metallurgical and Materials Transactions A, 1983. 14(4): p. 655-666.
[12] Herschitz, R. and D.N. Seidman, *An atomic resolution study of homogeneous radiation-induced precipitation in a neutron irradiated W-10at.% Re alloy.* Acta Metallurgica, 1984. 32(8): p. 1141-1154.
[13] Herschitz, R. and D.N. Seidman, *An atomic resolution study of radiation-induced precipitation and solute segregation effects in a neutron-irradiated W-25 at.% Re alloy.* Acta Metallurgica, 1984. 32(8): p. 1155-1171.
[14] Makarov, P. and K. Povarova, *Development of tungsten-based vacuum melted and powder structural alloys.* International Journal of Refractory Metals & Hard Materials, 2002. 20: p. 277-285.
[15] Tanno, T., et al., *Microstructure Development in Neutron Irradiated Tungsten Alloys.* Materials Transactions, 2011. 52(7): p. 1447-1451.
[16] Cottrell, G.A., *Sigma phase formation in irradiated tungsten, tantalum and molybdenum in a fusion power plant.* Journal of Nuclear Materials, 2004. 334(2-3): p. 166-168.
[17] Cottrell, G.A., R. Pampin, and N.P. Taylor, *Transmutation and Phase Stability of Tungsten Armor in Fusion Power Plants.* Fusion Science and Technology, 2006. 50: p. 89-98.
[18] Nemoto, Y., et al., *Microstructural development of neutron irradiated W–Re alloys.* Journal of Nuclear Materials, 2000. 283-287: p. 1144-1147.
[19] Greenwood, L.R. and F.A. Garner, *Transmutation of Mo, Re, W, Hf, and V in various irradiation test facilities and STARFIRE.* Journal of Nuclear Materials, 1994. 212-215: p. 635-639.
[20] Parish, C.M., *Report on the acquisition and installation of FEI Talos F200X S/TEM.* ORNL/LTR-2015/461, 2015.
[21] Koyanagi, T., et al., *Microstructural evolution of pure tungsten neutron irradiated with a mixed energy spectrum.* Journal of Nuclear Materials, 2017. 490: p. 66-74.

4.10 NEUTRON IRRADIATION EFFECTS IN TUNGSTEN—L.M. Garrison, Y. Katoh, M. McAlister, T. Koyanagi (Oak Ridge National Laboratory), L. L. Snead (Stony Brook University), T. S. Byun (Pacific Northwest National Laboratory), and T. Hwang, M. Fukuda (Tohoku University, Japan)

OBJECTIVE

The objective of this work is to evaluate the effects of neutron irradiation on the mechanical properties and microstructure of tungsten-based materials to aid in developing plasma-facing materials for fusion reactors.

SUMMARY

The aim of this work is to evaluate tungsten and tungsten-based composites for potential use as part of a plasma-facing component for future fusion reactors. Tungsten foils are considered as an option for fabricating tungsten composites, so their mechanical properties were evaluated before and after neutron irradiation in the TITAN irradiation campaign.

PROGRESS AND STATUS

Hardness, shear punch, and three point bend tests were completed on selected irradiated tungsten foils. The hardness tests focused on higher dose tungsten foils for comparison with the previously tested irradiated single crystal tungsten materials (Figure 1). In the unirradiated condition, the wrought tungsten foil has approximately 200 Hv higher than the annealed tungsten foil. The wrought tungsten foil has a high density of dislocations and smaller grains than the annealed tungsten foil, which causes the higher hardness. As neutron dose increases, the hardness difference between the two types of tungsten foil reduces. At the highest tested dose of 2.9 dpa, the hardness values are approximately the same for the wrought and annealed tungsten foils. This indicates that the irradiation induced defects, loops and voids, and irradiation induced transmutation and precipitation of Re and Os are contributing more significantly to the hardness of the material than the intrinsic material properties such as grain size.

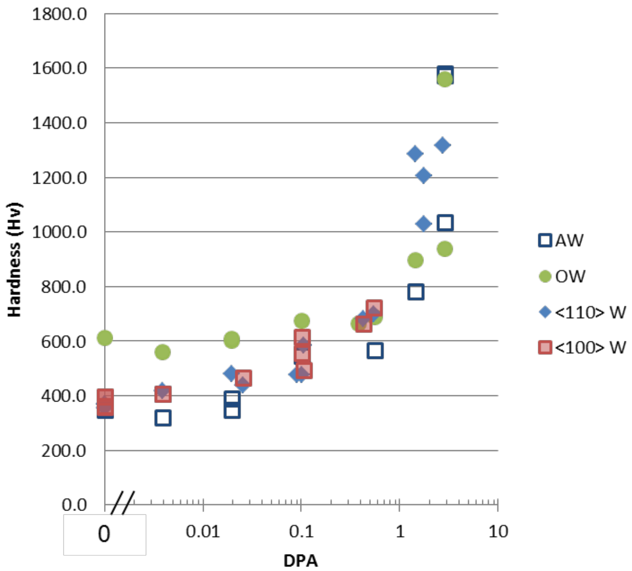

Figure 1. Vickers hardness data for annealed tungsten foils (AW), wrought tungsten foils (OW), and two orientations of single crystal tungsten (<110> W and <100> W).

Shear punch tests on unirradiated tungsten foils showed different behavior for tungsten foils with varying degrees of rolling reduction (Figure 2). In Figures 2 and 3, the elastic deformation has been removed from the data, so only the plastic deformation is shown. A vertical line is drawn from the x-axis to the shear yield stress. The x-axis of normalized displacement is the vertical displacement of the cross head divided by the original thickness of the foil. For the thickest, 0.25 mm thick, and the thinnest, 0.025 mm thick, W foils, the shear punch behavior had little elongation before failure. The medium thickness of W foil, 0.10 mm had noticeable shear elongation before failure, but the shape of the curve was different for the ESPI and the PLANSEE produced foils. The PLANSEE foil is the same manufacturer as the foil included in the TITAN irradiations. After irradiation, both the wrought foils (OW) and annealed foils (AW) were brittle in the shear punch test (Figure 3).

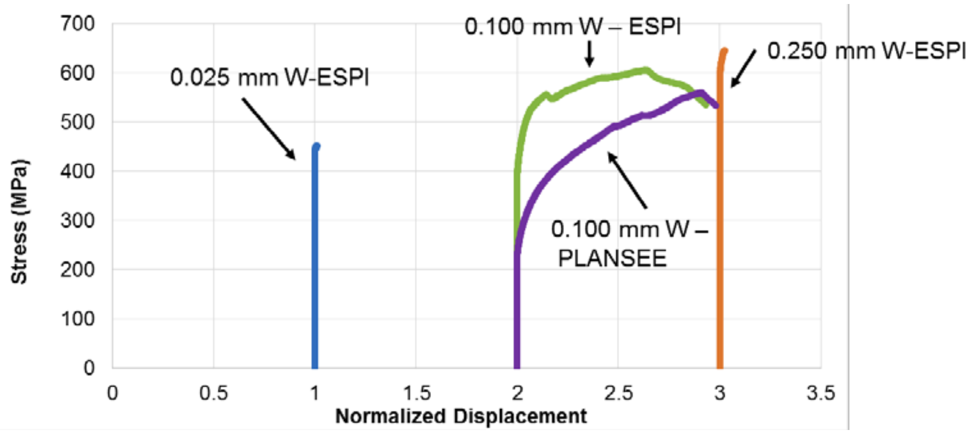

Figure 2. Retained plastic shear deformation for unirradiated, as-rolled W foils. Data is placed with an arbitrary offset on the x-axis.

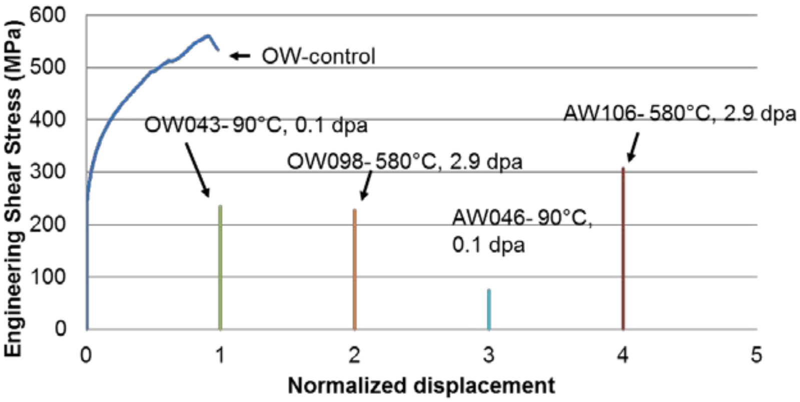

Figure 3. Retained plastic shear deformation for as-rolled W foils (OW) and annealed W foils (AW). Data is placed with an arbitrary offset on the x-axis.

Three point bend tests were performed on selected irradiated wrought and annealed tungsten foils (Figure 4). The wrought foil retains bend ductility after irradiation to 0.1 dpa at 90°C, but the annealed foil irradiated to the same conditions had a brittle failure. Both the wrought foil and annealed foil bend tested after irradiation to 2.9 dpa at 580°C had brittle failure.

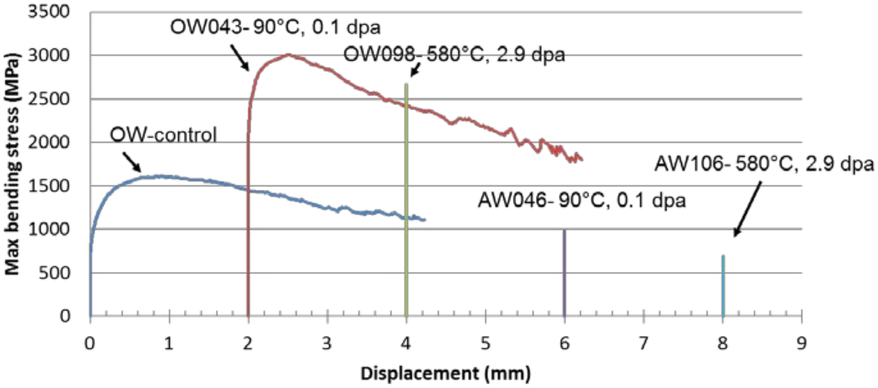

Figure 4. Three point bending test data at 22°C for selected wrought tungsten foils (OW) and annealed tungsten foils (AW). Data is placed with an arbitrary offset on the x-axis.

The wrought foil has voids and a high density of Re and Os rich precipitates after neutron irradiation at ~800°C to 1.5 dpa (Figure 5). Some but not all grain boundaries have a narrow, less than 100 nm zone denuded of precipitates. The foil that was annealed before neutron irradiation does not show voids in the imaged area of Figure 5. The shape and size of precipitates in the annealed foil is approximately the same as the wrought foil. A denuded zone is not visible near the one grain boundary that was imaged in the annealed foil, but because of the low density of grain boundaries, a representative analysis of many grain boundaries was not done. For both types of foils, wrought and annealed, the precipitates contribute significantly to the hardening and loss of shear and bend ductility after irradiation.

Wrought foil, OW158, T_{irrad} ~800°C, 1.5 dpa

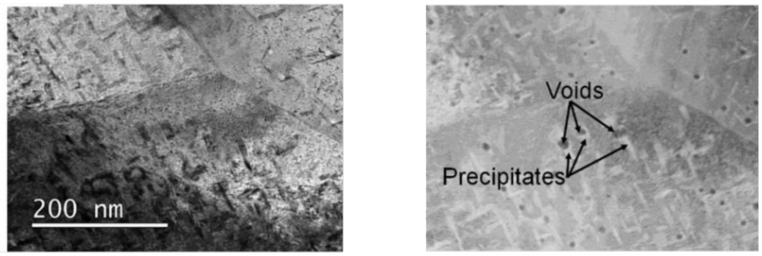

BFDF image HAADF image

Annealed foil, AW106, T_{irrad}=580°C, 2.9 dpa

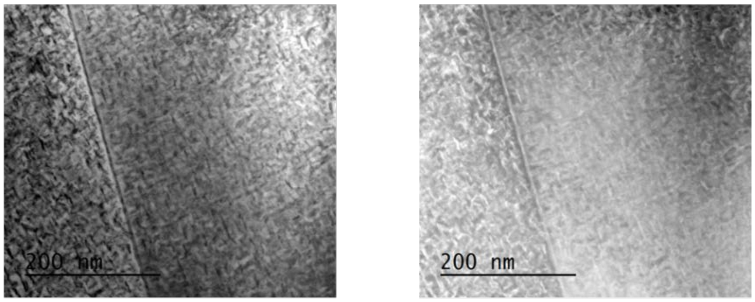

BFDF image HAADF image

Figure 5. TEM microstructure of wrought tungsten foil and annealed foils after neutron irradiation.

5. MAGNETIC AND DIAGNOSTIC SYSTEM MATERIALS

No contributions this reporting period.

6. FUSION CORROSION AND COMPATIBILITY SCIENCE

No contributions this reporting period.

7. MECHANISMS AND ANALYSIS

7.1 VIEWPOINT: NANOSCALE CHEMISTRY AND CRYSTALLOGRAPHY ARE BOTH THE OBSTACLE AND PATHWAY TO ADVANCED RADIATION-TOLERANT MATERIALS

—Chad M. Parish, Kun Wang, Philip D. Edmondson (Oak Ridge National Laboratory)

Abstract of an invited review paper, in press at Scripta Materialia.

New candidate materials for GenIV or fusion nuclear energy systems, e.g. nanostructured ferritic alloys, are distinguished from older-generation nuclear materials by much smaller feature sizes and complex local nano-chemistry and crystallography. Established and prospective nuclear materials, e.g. reactor pressure vessel steels or plasma-facing tungsten, also form small nanoscale structures under in-reactor service. Here, we discuss recent advances in materials characterization – high-efficiency X-ray mapping combined with datamining; transmission Kikuchi diffraction; and atom probe tomography – that make it possible to quantitatively characterize these nanoscale structures in unprecedented detail, which enables advances in understanding and modelling of radiation service and degradation.

7.2 EXPLORATION OF THE RADIATION RESISTANCE OF HIGH ENTROPY ALLOYS

—C. Li, S.J. Zinkle (University of Tennessee), and X. Hu, J. Qiu (Oak Ridge National Laboratory)

OBJECTIVE

The goal of this project is exploring the basic radiation resistance of high entropy alloys (HEAs) that may have the potential for very good resistance to radiation-induced property degradation.

SUMMARY

This report summarizes the experimental characterization of neutron and ion irradiated 27%Fe-27%Mn-28%Ni-18%Cr HEA. Samples have been neutron irradiated at ~70˚C from 0.1 dpa to 1 dpa. Post-irradiation isochronal annealing was conducted from 100 to 600˚C. Following each anneal, positron annihilation spectroscopy (PAS), micro-hardness and electrical resistivity were measured at room temperature. PAS indicated a major vacancy annealing process occurs at ~400˚C, and no sizable change of defects up to 600˚C. Micro-hardness measurement showed different trend in the annealing of hardness for 0.1 and 1dpa samples. A large change in electrical resistivity is observed after annealing, which may be related to the strong chemical disordering intrinsic to HEA.

PROGRESS AND STATUS

Introduction

While conventional alloys are composed of a matrix component and multiple solutes, HEAs have many elements that form a uniform medium. Many of them form single phase solid solution without formation of brittle phases that are frequently observed in conventional simple intermetallic alloys[1-6]. Due to their superior mechanical properties, HEAs have potential application as structural materials in advanced nuclear energy systems. Some preliminary ion irradiation tests suggest HEAs have good resistance to radiation degradation phenomenon such as void swelling and radiation induced segregation[7-9]**.** On the other hand, while neutron irradiation can better simulate the actual irradiation environment in a nuclear reactor, no work has been published and little is known about the behavior of HEAs after neutron irradiation. This is partly due to the fact that many HEAs contain Co, which is not desirable for neutron irradiation experiments due to high induced radioactivity.

In the current study, a novel 27%Fe-27%Mn-28%Ni-18%Cr (Co-free) single phase f.c.c HEA[10] has been characterized after neutron irradiation. The objective of this study is to investigate the evolution of irradiation induced defects and macroscopic properties through post irradiation annealing.

Experimental Procedure

Samples were irradiated at ~60˚C from 0.1 dpa to 1 dpa in the High Flux Isotope Reactor (HFIR). One SSJ3 miniature sheet tensile specimen (overall length 25 mm, thickness 0.76mm, gage length 7.6 mm and gage width 1.5 mm) and one 3 mm diameter x 0.4 mm thickness TEM disks were prepared for each irradiation condition. The samples for PAS and electrical resistivity measurement were made from the tested SS3J tensile specimen, whose geometry is shown in Figure 1. Two cuts were made (indicated by the red dash lines). The two tabs were used to make sandwich samples for PAS experiment, and the longer part of the broken tensile gage was used for electrical resistivity measurement.

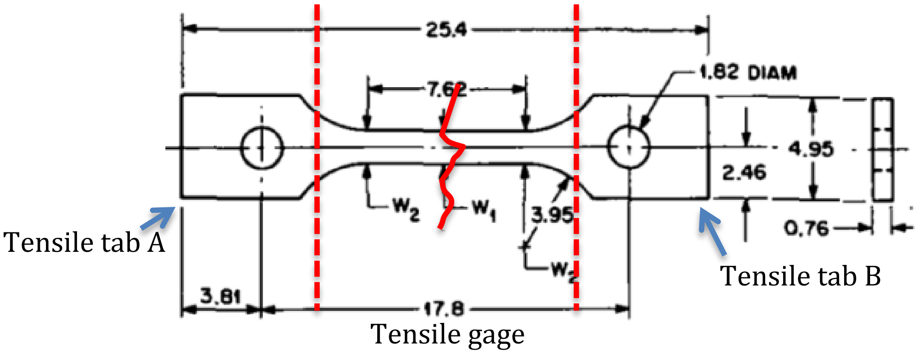

Figure 1. Sample geometry for PAS and electrical resistivity measurement.

Isochronal annealing was conducted in a high vacuum (< 5×10^{-5} torr) furnace from 100 to 600˚C, with a step size of 50˚C. Temperature was measured by a type-K thermocouple about 5 cm above the sample. During annealing, samples were wrapped in Ta foil for minimizing contamination and the ease of specimen labeling. Also, samples were placed in the same position in the furnace to make sure the experiment condition is repeatable. The sample was annealed at target temperature for 20 min, and the fluctuation in annealing temperature was smaller than 1˚C (except for at 100˚C, which was around 10˚C). Following each annealing stage, PAS, micro-hardness and electrical resistivity measurement were conducted at room temperature. Due to high residual radioactivity of the 1 dpa sample, PAS experiment was only conducted for 0.1 dpa sample.

For the PAS tests, both Positron Annihilation Lifetime Spectroscopy (PALS) and Coincidence Doppler Broadening (CDB) were measured. For PALS, 0.8 – 1 million data points are collected at each temperature to ensure good statistics and parallel comparison at different temperatures. Since no theoretical lifetime calculation has been conducted so far on this type of high entropy alloy, the iron lifetime data was used as a reference [11]. Bulk hardness was measured by a hardness indenter equipped with a Vickers indenter tip. The load and dwell time were set at 500 grams and 10 s. Calibration was done on a standard to make sure reasonable comparison between different annealing stages. 5-7 indents were made for each test condition and the standard error was calculated based on the experimental scatter of the data. Electrical resistivity was measured by four-point probe technique. 0.1 A current was applied through the outer two probes, and the voltage drop between the inner two contacts was measured. To examine the thermal emf effects, voltage with both polarities were also applied. At each annealing stage, four measurements were made first, and the sample was flipped to make another four measurements to look into the data fluctuation due to orientation and surface effects.

Results

Figure 2 shows the characteristic decay curve at each annealing temperature from raw PALS data. Since positrons are sensitive to free volume in the material, the change in the slope of the decay curves (~0-2 ps) provides information predominantly on the evolution of irradiation induced vacancy-type defects. Of all the curves, the unirradiated reference sample decays most rapidly, while the as irradiated curve decays the most slowly. This indicates the production of defects due to neutron irradiation. Also, as temperature increases the decay trend gradually approaches to the reference, suggesting the removal of defects due to annealing.

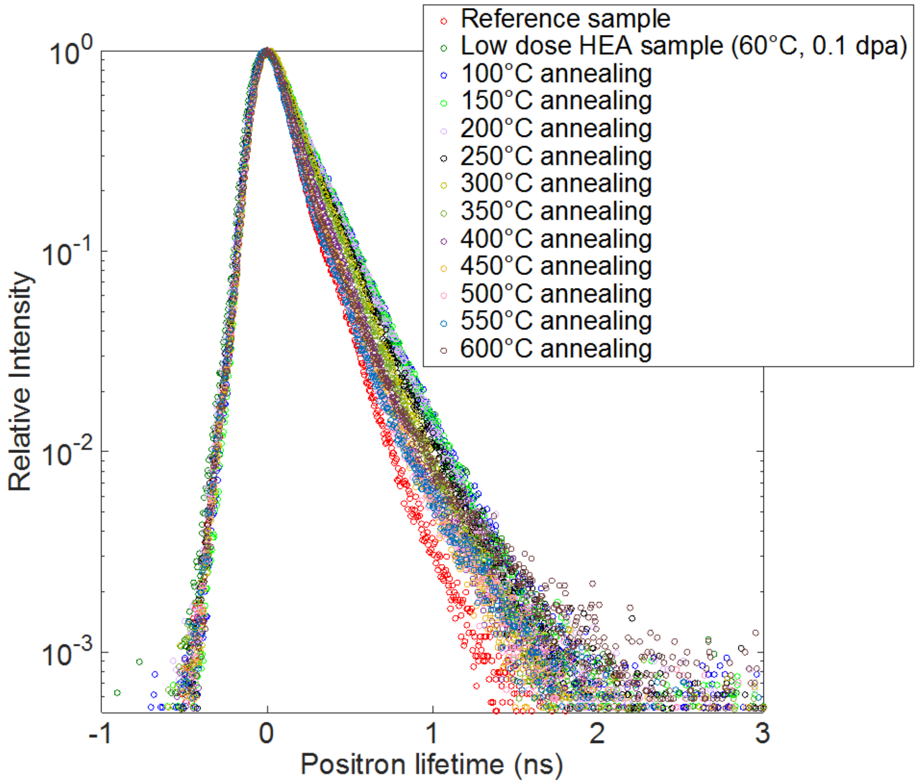

Figure 2. Raw data from PALS measurement.

Depending on the decay behavior, either two lifetime (2-tau) or three lifetime (3-tau) analysis is applied to the raw data. For typical neutron irradiated metals, 2-tau is more suitable for f.c.c crystal structure, while 3-tau is more suitable for b.c.c[12]. Since 2-tau analysis provides a good fit for our raw data, the as-irradiated microstructure resembles typical f.c.c metals. Based on 2-tau analysis, Figure 3 shows the lifetime and Figure 4 shows the trapping rate evolution as annealing temperature increases. Several observations can be made from these two curves. First, by reference to pure iron's lifetime data, tau2 should represent small vacancy clusters composing of 2 to 5 single vacancies. Second, tau2 initially slowly decreases from 200 to 400˚C, but then slowly increases from 400 to 600˚C. The transition point, 400˚C, may suggest the initialization of stage V process, which representing the thermal dissociation of vacancy clusters[13]. Third, trapping rate generally decreases as temperature increases, suggesting the continuous decreasing of defect density. It approaches that of the reference sample level at about 500˚C.

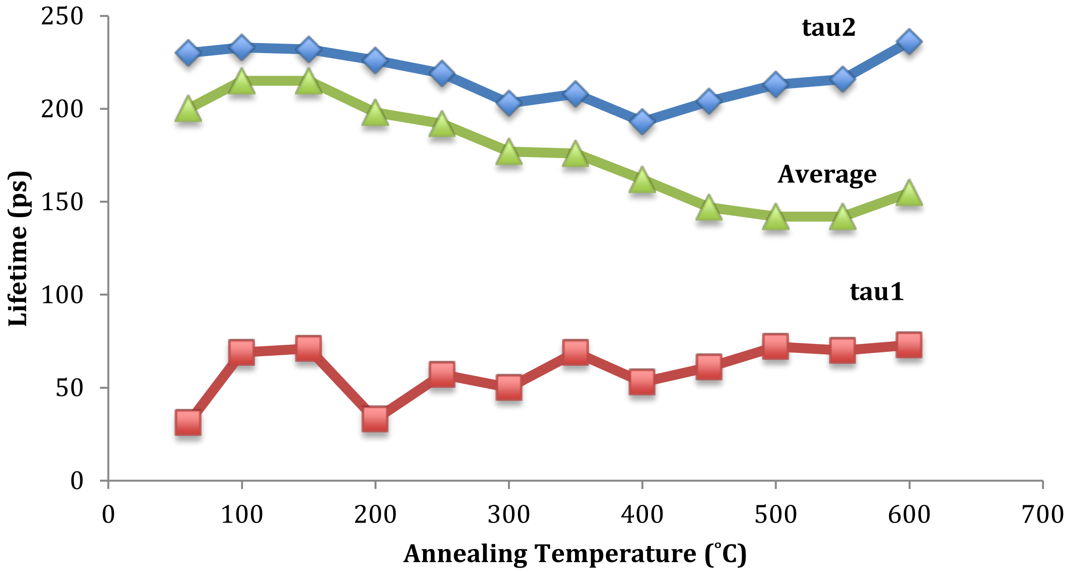

Figure 3. Lifetime evolution from 2-tau analysis.

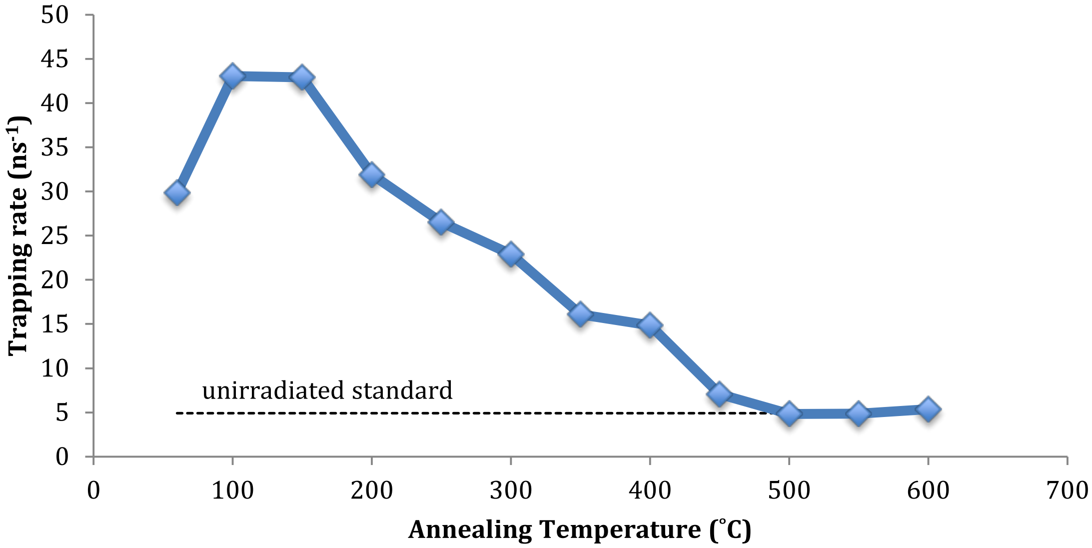

Figure 4. Trapping rate evolution from 2-tau analysis.

The CDB measurements examine the interaction probability of positrons with core or valence electrons. Figure 5 shows the raw data of electron momentum distribution from CDB measurement. The low momentum part represents interaction with valence electrons while the high momentum part represent interaction with core electrons. Compared with the irradiated sample, the reference sample exhibits lower intensity in the high momentum regime. This indicates that positrons are more likely to interact with core electrons in irradiated samples, which is consistent with the fact that radiation-induced defects increases the free volume inside the material.

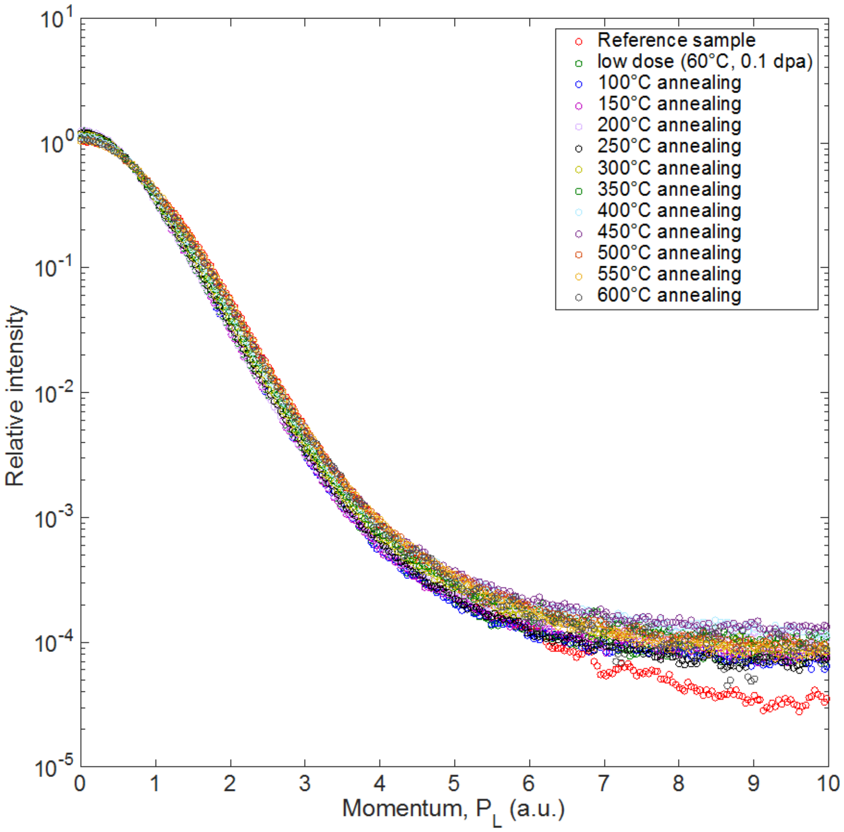

Figure 5. Raw data from CDB measurement.

Since each solute element has a different positron affinity, each element will have a characteristic momentum distribution. By plotting the ratio of high momentum region vs low momentum region, which is the S-W plot shown in Figure 6, we can obtain more information on the defects in the material. Two observations can be made from Figure 6. First, all the data points fall on the same slope suggesting that as annealing temperature increases, there is no sizable change of the chemical environment near the defects. Second, the data points move upward as temperature increases. This indicates that the overall defect density is continuously decreasing as temperature increases, which agrees with the continuous decreasing trend of trapping rate from PALS measurement.

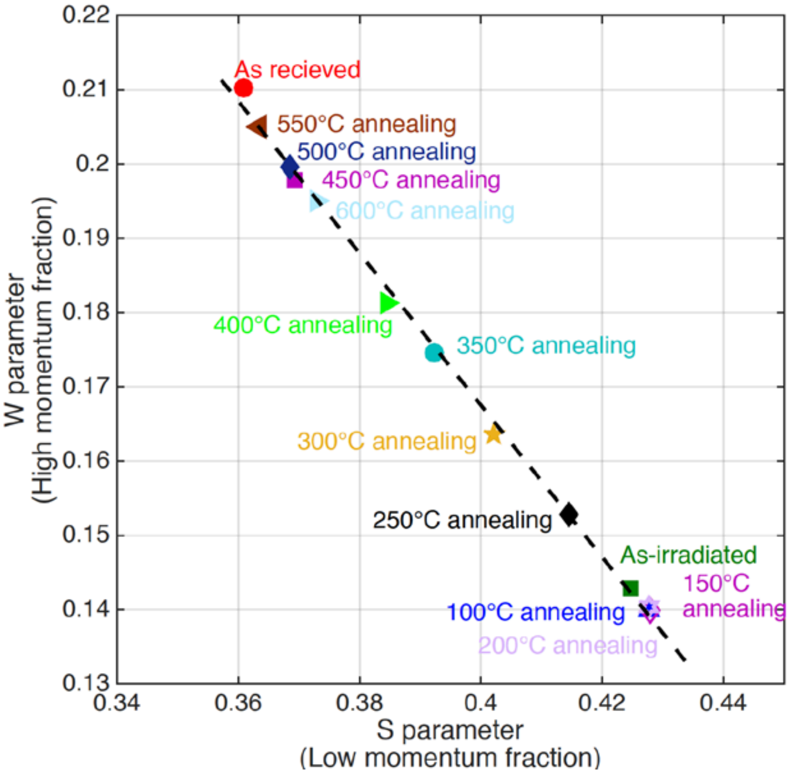

Figure 6. S-W plot from CDB measurement.

Figure 7 shows the results from micro-hardness measurement. Irradiation to 0.1 dpa produced a nearly 60% increase in hardness compared to the unirradiated sample, and the 1 dpa exhibited further increase to approximately double the unirradiated hardness. Hardness remains unchanged for both irradiated samples for annealing temperatures of 100 to 300˚C. The 0.1 dpa sample's hardness starts to decrease from 300˚C, while 1 dpa sample's hardness starts to decrease around 400˚C. The decreasing slope for the 1 dpa sample is much steeper than that of 0.1 dpa. Since annealing of hardness is related to the recovery of radiation induced defects, the different annealing trend may suggest different defect microstructures in 0.1 and 1 dpa samples[14]. Microstructure characterization, such as analytical transmission electron microscopy, will be useful to examine the defect microstructure and reveal the connection between hardness drop and defect recovery. The hardness of both samples approached the unirradiated value following the 600˚C anneal.

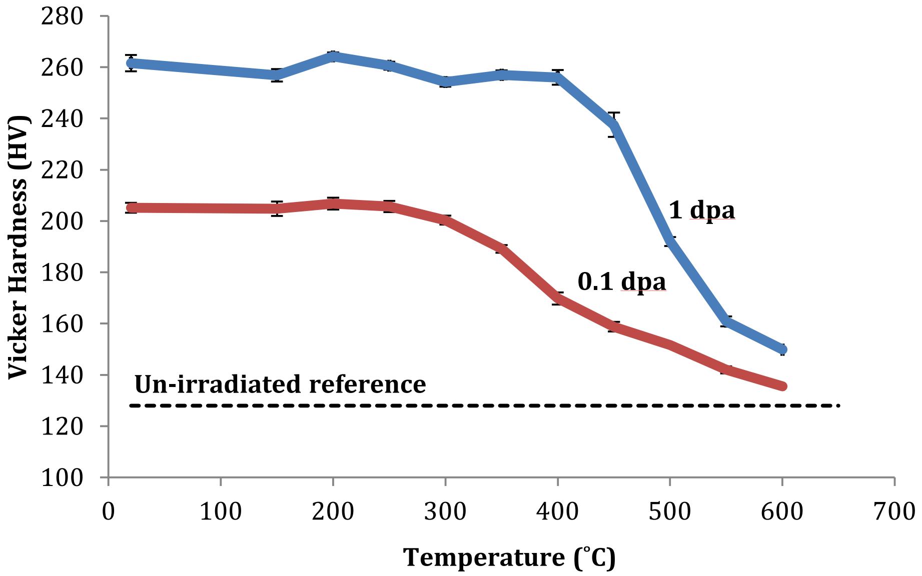

Figure 7. Micro-hardness evolution in HEA after isochronal annealing.

Results from electrical resistivity measurements are shown on Figure 8. For the as-irradiated samples, both 0.1 and 1 dpa samples shows larger than 15% increase compared to the control sample. Since radiation-produced point defects and defect clusters typically contribute only several percent of resistivity change in Fe-Cr-Ni alloys in this dose range[15, 16], other radiation-induced phenomenon may also take place. Given the unique chemical disorder of HEA, change in short range order from radiation mixing may be one possible candidate[17].

After annealing, the control sample's electrical resistivity shows a decreasing trend, which may be associated with short range rearrangement of solute atoms. Conversely, there is no consistent annealing trend for irradiated samples up to 550˚C. Since both micro-hardness and trapping rate decreases to close to reference level at 600˚C, the result suggest that this radiation-induced feature may be stable even at high annealing temperature. Although further characterization is needed to confirm the source of this behavior, the lack of an annealing effect on the electrical resistivity of the irradiated samples suggests that the resistivity increase is mainly associated with irradiation-induced changes in solute short range ordering that do not thermally anneal up to 550˚C (rather than irradiation induced defect clusters that might be the main contributor to the observed radiation induced hardness increase and changes in PALS behavior). Advanced microstructure characterization techniques, such as neutron scattering, may be able to reveal changes in the ordering of the constituent solute atoms.

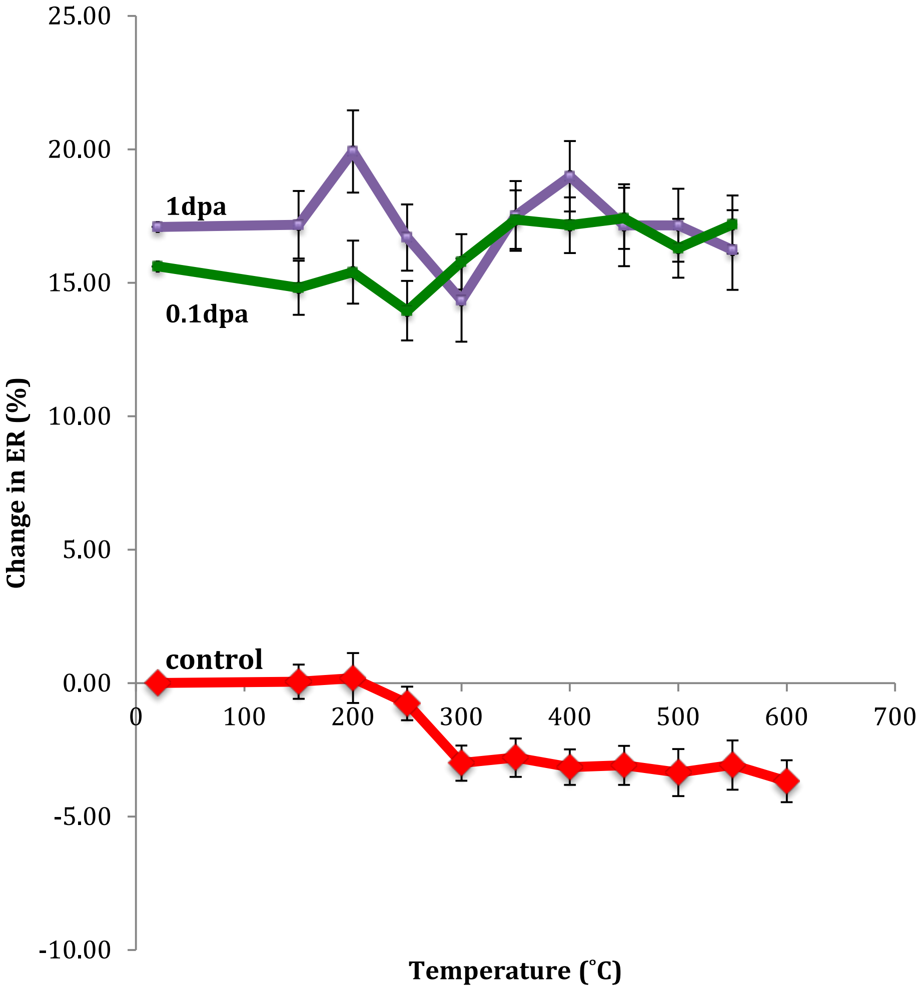

Figure 8. Change in electrical resistivity of HEA after isochronal annealing.

Future Work

More annealing will be conducted up to 700˚C to probe any possible change in material properties from PALS, micro-hardness and electrical resistivity testing. Transmission electron microscopy will be conducted to examine the defect microstructure for as-irradiated samples. Theoretical positron lifetime calculation will be performed to supplement the analysis of the PAS data.

References

[1] C. Y. Hsu, J. W. Yeh, S. K. Chen and T. T. Shun, Metallurgical and Materials Transactions a-Physical Metallurgy and Materials Science **35A** (5), 1465-1469 (2004).
[2] J. W. Yeh, S. K. Chen, J. Y. Gan, S. J. Lin, T. S. Chin, T. T. Shun, C. H. Tsau and S. Y. Chang, Metallurgical and Materials Transactions a-Physical Metallurgy and Materials Science **35A** (8), 2533-2536 (2004).
[3] C. J. Tong, Y. L. Chen, S. K. Chen, J. W. Yeh, T. T. Shun, C. H. Tsau, S. J. Lin and S. Y. Chang, Metallurgical and Materials Transactions a-Physical Metallurgy and Materials Science **36A** (4), 881-893 (2005).
[4] Y. J. Zhou, Y. Zhang, Y. L. Wang and G. L. Chen, Applied Physics Letters **90** (18), 3 (2007).
[5] C. M. Lin and H. L. Tsai, Journal of Alloys and Compounds **489** (1), 30-35 (2010).
[6] Z. Wu, Y. F. Gao and H. Bei, Scripta Materialia **109**, 108-112 (2015).

[7] N. Kumar, C. Li, K. J. Leonard, H. Bei and S. J. Zinkle, Acta Materialia **113**, 230-244 (2016).

[8] C. Lu, L. Niu, N. Chen, K. Jin, T. Yang, P. Xiu, Y. Zhang, F. Gao, H. Bei, S. Shi, M.-R. He, I. M. Robertson, W. J. Weber and L. Wang, Nature Communications **7** (2016).

[9] S. Q. Xia, X. Yang, T. F. Yang, S. Liu and Y. Zhang, Jom **67** (10), 2340-2344 (2015).

[10] Z. Wu and H. Bei, Materials Science and Engineering a-Structural Materials Properties Microstructure and Processing **640**, 217-224 (2015).

[11] A. Vehanen, P. Hautojarvi, J. Johansson, J. Ylikauppila and P. Moser, Physical Review B **25** (2), 762-780 (1982).

[12] M. Eldrup and B. N. Singh, Journal of Nuclear Materials **276**, 269-277 (2000).

[13] J. W. Corbett, *Electron radiation damage in semiconductors and metals*. (Academic Press, 1966).

[14] M. Horiki and M. Kiritani, Journal of Nuclear Materials **239** (1-3), 34-41 (1996).

[15] C. Dimitrov, M. D. C. Belo and O. Dimitrov, Journal of Physics F-Metal Physics **10** (8), 1653-1664 (1980).

[16] O. Dimitrov and C. Dimitrov, Journal of Physics F-Metal Physics **16** (8), 969-980 (1986).

[17] S. J. Zinkle, Journal of Nuclear Materials **150** (2), 140-158 (1987).

7.3 EFFECTS OF IRRADIATION AND ANNEALING ON THE MICROSTRUCTURE AND MECHANICAL PROPERTIES OF BULK METALLIC GLASS ALLOYS

L. Mora, Y. Zhang, H. Bei, J. Neuefeind, W. Dmowski, T. Egami, S. J. Zinkle (Oak Ridge National Laboratory) and J. Brechtl, M. L. Crespillo, T. Yang, H. Wang, J. Salasin, I. Gussev, M. Lang (University of Tennessee)

OBJECTIVE

The goal of this project is to study ion and neutron irradiation effects in $Zr_{52.5}Cu_{17.9}Ni_{14.6}Al_{10}Ti_5$ and $Cu_{60}Zr_{20}Hf_{10}Ti_{10}$ bulk metallic glass alloys to better understand their viability as candidates for structural applications in high-radiation fusion environments.

SUMMARY

Bulk metallic glasses (BMGs), which are advanced potentially irradiation-resistant materials, are composed of a topologically disordered structure which prohibits the creation of Frenkel pair defects. For this study, microstructural analysis and nano-indentation tests were performed on $Zr_{52.5}Cu_{17.9}Ni_{14.6}Al_{10}Ti_5$ (BAM-11) and $Cu_{60}Zr_{20}Hf_{10}Ti_{10}$ bulk metallic glass (BMG) alloys. Here samples were irradiated at 25-360^oC with 5 MeV C^+ or 9 MeV Ni^{3+} ions (midrange doses of 0.5 and 10 dpa). The BAM-11 BMG was also irradiated with fission neutrons to 0.1 dpa at ~90^oC. Neutron diffraction results indicate that the BAM-11 samples underwent disordering during neutron irradiation. At an indentation depth of ~450 nm, the alloys experienced an increase in the nano-indentation hardness of 16% and 24% respectively from the as-cast to the irradiated condition of 9 MeV Ni^{3+} 10 dpa 360^oC. At the same depth, the Young's Modulus was found to increase 10% and 24% respectively for the BAM-11 and Cu BMGs under the same irradiation conditions.

PROGRESS AND STATUS

Introduction

Although several metallic glasses have been studied for their radiation response [1-6], there are still many unanswered questions regarding how irradiation displacement damage affects their mechanical and microstructural properties. Metallic glasses are regarded as potential candidates for use in radiation environments since their amorphous structure prohibits the formation of conventional radiation defects such as vacancy-interstitial Frenkel pairs and dislocation loops that would normally occur in crystalline alloys. Originally, irradiation studies of amorphous alloys were limited to ribbon and thin film geometries. In terms of material properties, BMGs exhibit exceptional hardness, high strength, wear and corrosion resistance [7-9]. Of potential concern is that BMGs do not work harden like crystalline alloys, and exhibit deformation in the form of shear bands [10].

In addition, bulk metallic glasses are thought to have high helium permeability, due to their large free atomic volume and lack of grain boundaries which can act as helium traps [11]. The ensnaring of helium at defects is a huge issue in irradiated materials since it can result in enhanced swelling and embrittlement. Furthermore, recent studies have shown that amorphous alloys may be resistant to cavity swelling, and hence possibly tritium retention, as compared to crystalline materials, which would make them appealing for fusion energy applications [12, 13]. Finally, there have been studies which suggest that the amount of retained displacement damage can be significantly less in metallic glasses [12,14].

In our prior work, the effects of neutron irradiation at ~90°C on the material and mechanical properties of bulk metallic glass $Zr_{52.5}Cu_{17.9}Ni_{14.6}Al_{10}Ti_5$ (BAM-11) were investigated. The irradiated samples exhibited a slight increase in the Vickers hardness (roughly ~7, ~10% for 0.1, 1 dpa respectively). Using the Nix-Gao method [15], it was found that the nano-indentation hardness increased by about ~0.4% and ~66% for samples irradiated to 0.1 and 1 dpa. The dynamic Young's modulus in the sample irradiated to 0.1 dpa was ~5% less than the control sample. Furthermore, the nano-indentation Young's modulus in the sample irradiated to 0.1 and 1 dpa was approximately 1.4% and 0.9% less, respectively, as compared to the control specimen. The density of BAM-11 decreased by roughly ~0.4% for both 0.1 and 1 dpa. The results from the experiments suggest that the irradiation-induced damage begins to saturate at doses between 0.1 and 1 dpa.

For this part of the study, the effects of ion dose, temperature, and neutron bombardment on the microstructure and nano-indentation behavior of BAM-11 and $Cu_{60}Zr_{20}Hf_{10}Ti_{10}$ bulk amorphous alloys will be examined in more detail.

Experimental Procedure

Both $Zr_{52.5}Cu_{17.9}Ni_{14.6}Al_{10}Ti_5$ alloy (BAM-11) and $Cu_{60}Zr_{20}Hf_{10}Ti_{10}$ alloys were fabricated at ORNL by arc melting in an argon atmosphere using a mixture of base metals with the following purities: 99.5% Zr, 99.99% Cu, 99.99% Ni, 99.99% Al, 99.99% Hf, and 99.99% Ti. The alloys were then remelted and drop cast in a Zr-gettered helium atmosphere. Specimens were then prepared from the as-cast rods by an electrical discharge machine. The results of x-ray spectroscopy (please see paragraph below for experimental details) revealed the amorphous nature of the two alloys, and can be seen in Figure 1.

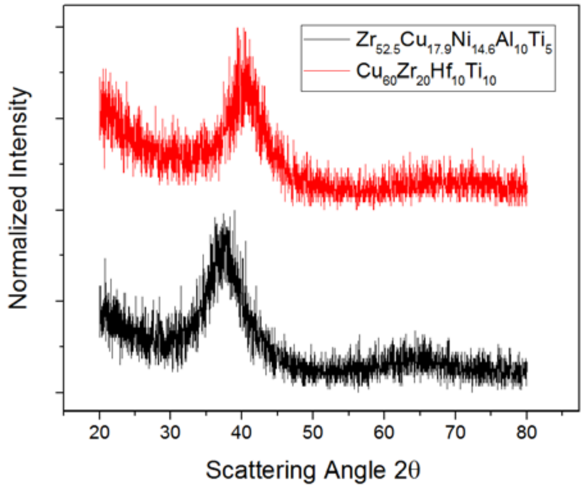

Figure 1. X-ray diffraction results of the as-fabricated BAM-11 and Cu BMGs.

After fabrication, BAM-11 samples underwent irradiation. Neutron irradiations were performed at the High Flux Isotope Reactor (HFIR). Samples were encased in a perforated rabbit capsule which allowed the coolant water to directly contact the samples. To avoid potential corrosion, the BAM-11 samples were wrapped in aluminum foil to minimize water exposure. After encapsulation, BAM-11 specimens were irradiated in HFIR in hydraulic tube 2 (HT-2). Here the samples were exposed to neutron fluences of 1.40 X 10^{20} n/cm^2 (E>0.1 MeV) (0.1 dpa) in a perforated hydraulic rabbit capsule. The specimens were wrapped in aluminum foil and the external surface of the wrapped specimens was directly exposed to the reactor coolant water at ~60^{o}C. After consideration of internal nuclear heating effects in the samples, the estimated average sample temperature is ~90^{o}C. For neutron diffraction studies, some as-cast and irradiated samples encased in quartz glass were annealed at 325^{o}C for 72 hours and 300^{o}C for two weeks. Table 1 shows the irradiation and annealing conditions for the samples.

Table 1. Sample conditions for the experiment

Condition
As-cast
Annealed 300^{o}C for two weeks
Neutron irradiated to 0.1 dpa
Neutron irradiated to 0.1 dpa and then annealed 325^{o}C for 72 hours
Neutron irradiated to 0.1 dpa and then annealed 300^{o}C for two weeks

BAM-11 and Cu BMG specimens were also ion irradiated with 9 MeV Ni^{3+} and 5.5 MeV C$^+$ ions at the University of Tennessee/ORNL Ion Beam Materials Laboratory (IBML). Before irradiation, specimens were polished to a mirror finish using colloidal silica. Samples were irradiated to midrange doses ranging from 0.5 – 10 dpa at temperatures ranging from 25-360^{o}C. To determine the necessary fluence, SRIM 2013 was performed using the quick Kinchin-Pease option, with a 40 eV displacement threshold and ~0 eV binding energy [16]. To increase the statistical accuracy of the analysis, 5 x 10^5 ions were used. After the simulation finished, the irradiation fluence and corresponding dpa were calculated using the vacancy.txt, E2recoils.txt and ioniz.txt output files. At the given energies, the ions had a projected range of approximately 3 µm.

A plot of the irradiation damage verses depth profiles can be seen in Figure 2. The calculated displacement damage for the C$^+$ ion irradiation varies by over one order of magnitude between the surface and peak damage region, and varies by about a factor of five for the Ni^{3+} ion irradiation. As can be seen, the peak for the C$^+$ was much narrower than that for the Ni^{3+}. To minimize problems associated with surface effects and diffusional broadening, an intermediate depth (~1.5 µm) was selected for reporting the damage level in this report although it is recognized that the damage level varies with depth. Table 2 lists the ion specie, midrange damage, ion fluence, irradiation temperature, and irradiation time for the experiments.

Table 2. Ion Irradiation Matrix for BMG Materials

Ion Species	Midrange damage (dpa)	Fluence (ions/cm^2)	Temp (°C)	Irr. Time (h)
9 MeV Ni^{3+}	0.5	1.2 E+15	25	0.3
	10	2.4 E+16		7
	0.5	1.2 E+15	290	0.3
	10	2.4 E+16		7
	0.5	1.2 E+15	360	0.3
	10	2.4 E+16		7
5.5 MeV C$^+$	0.5	4.0 E+16	25	7
			290	
			360	

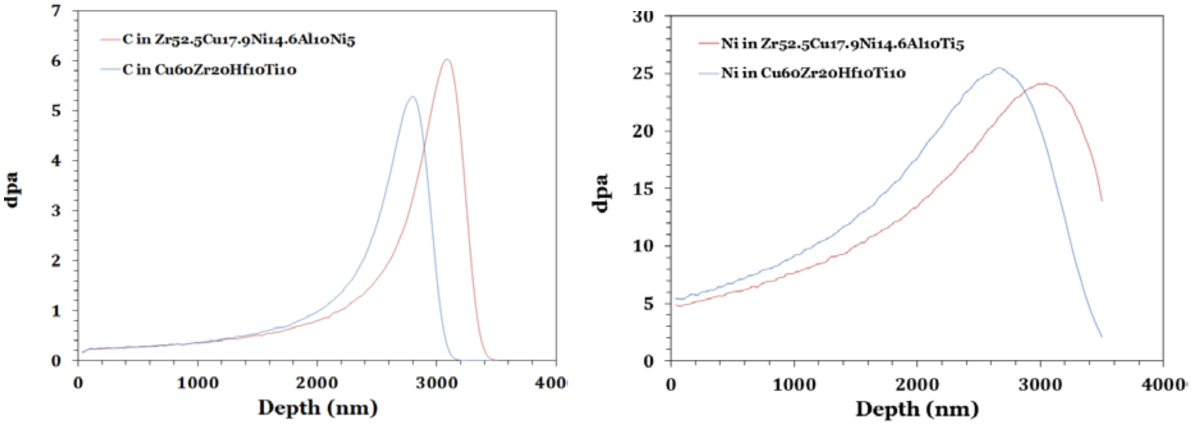

Figure 2. Ni^{3+} and C$^+$ Ion damage vs. depth profiles for the Zr and Cu based BMGs.

Microstructural characterizations of the irradiated and annealed bulk metallic glass specimens were performed via transmission electron microscopy (TEM), neutron diffraction (bulk neutron irradiated BAM-11 only), x-ray diffraction and Raman spectroscopy. The microstructural characterizations have not been performed on the samples exposed to Ni^{3+} ions to a dose of 0.5 dpa or C$^+$ ions at temperatures below 360^{o}C, but will done in future studies. The TEM study was performed in the Low Activation Materials Development and Analysis (LAMDA) laboratory at ORNL while the x-ray diffraction and Raman spectroscopy were performed at the Science and Engineering Research Facility at the University of Tennessee. The neutron diffraction experiment was performed in the Spallation Neutron Source at Oak Ridge National Laboratory.

TEM foils were fabricated using an FEI Quanta Dual-beam focused ion beam (FIB)/SEM with a final thinning step of 2kV Ga$^+$ ions at a glancing angle of about 4° to minimize ion beam milling damage. The samples were then examined and analyzed in a JEOL JEM-2100F TEM/STEM at 200 kV using the techniques of bright field (BF) imaging, selected area electron diffraction (SAED), and high resolution TEM (HRTEM).

For the neutron diffraction experiments, samples were carefully suspended in 6 mm diameter vanadium cups in which glass wool was centered on top of the canister. Samples were positioned such that their cross-sectional area was perpendicular to the neutron beam. Here samples with a mass of ~0.5 g were exposed to a neutron flux of ~10^8 /cm^2s and environmental temperature of 25^{o}C for three hours. After data was collected, PDFgetN software was utilized to determine the radial distribution function.

X-ray diffraction on the as-fabricated and ion irradiated samples was performed using a Panalytical Empyrean diffractometer equipped with a Xe proportional detector. The x-ray consisted of a Cu beam with a K-alpha wavelength of 1.54 Å, and the diffraction angle 2θ ranged between 20-80 degrees. Glancing angles ranging from 0.5-1 degree were used to examine whether any crystallization occurred in the irradiated region. The glancing angles were calculated using the method described in [17]. In addition, the Powder Bragg-Brentano method was used to better examine samples which had crystallized.

Raman spectrometry was done using a LabRam HR Evolution from Horiba Scientific. To acquire the spectra, a Mplan N 100x objective lens was used in conjunction with a laser beam consisting of a wavelength of 785 nm, (at 50 % power). A 10-minute acquisition time was used to collect high resolution spectra in which the accumulation correction was enabled for each sample.

Nano-indentation hardness and Young's modulus measurements were performed at room temperature using a Keysight Technologies G200 Nano-indenter with a Berkovich diamond (3-sided pyramidal tip) in continuous stiffness measurement mode with a constant loading rate of 400 μNs^{-1}. For statistical accuracy, ~20 indents were made where hardness was measured as a function of depth from the point of contact of the nano-indenter with the surface to a depth of ~2500 nm. The hardness data below a depth of ~100 nm from the specimen surface was omitted due to large data scatter associated with surface roughness. Hardness was calculated using the Oliver and Pharr method [18, 19]. The area function of the tip in addition to the machine stiffness for the nano-indenter was calibrated by indenting on a standard fused silica sample [20].

Microstructural Characterization

Figure 3 shows the x-ray diffraction patterns for the as-cast and Ni^{3+} and C^+ irradiated BAM-11 and $Cu_{60}Zr_{20}Hf_{10}Ti_{10}$ BMGs. In most cases, the original amorphous structure was retained following irradiation. As can be seen, the only sample which appears to have partially crystallized under irradiation is the Cu BMG irradiated by Ni^{3+} at 360^{o}C. Interestingly, samples irradiated by 5.5 MeV C^+ ions to a dose of 0.5 dpa at the same temperature (same amount of irradiation time as Ni^{3+} 10 dpa), did not crystallize. It should also be mentioned that a second amorphous hump and a sharp peak at 54.3^o emerged in the BAM-11 sample at the same condition. Line scan experiments found that the peak at ~54.3^o was most likely due to surface impurities, and not crystallization in the alloy.

The fact that the Cu alloy crystallized, while the BAM-11 did not during irradiation at 360^{o}C, was surprising. Especially since the crystallization temperature T_x = 509^{o}C [21] of $Cu_{60}Zr_{20}Hf_{10}Ti_{10}$ BMG is significantly higher than that of BAM-11, which is 393^{o}C [22]. Subsequent x-ray diffraction, which was conducted on the unirradiated side of the sample, revealed similar crystal structure (see Figure 4), which means that the heating may have been caused the specimen to crystallize, and not the irradiation.

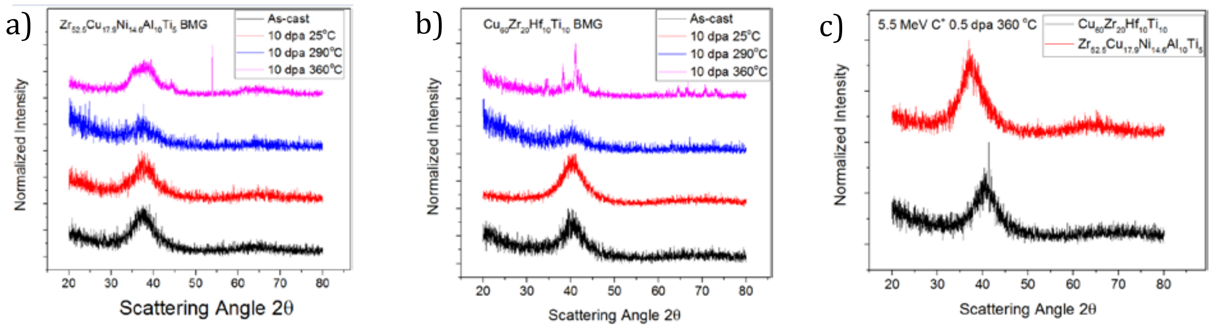

Figure 3. X-ray diffraction patterns for samples a) BAM-11 BMG irradiated by 9 MeV Ni^{3+} ions, b) $Cu_{60}Zr_{20}Hf_{10}Ti_{10}$ BMG irradiated by 9 MeV Ni^{3+} ions c) BAM-11 and Cu BMG irradiated by 5.5 MeV C^{+} ions.

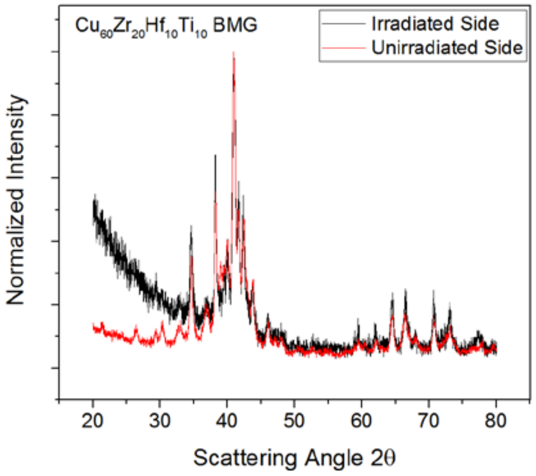

Figure 4. Glancing x-ray diffraction results on both the irradiated and unirradiated side of the Cu BMG sample irradiated by 9 MeV Ni^{3+} ions at 360^{o}C.

Subsequent power diffraction in conjunction with qualitative and quantitative phase analysis was performed to analyze the crystal phases in the alloy. Here qualitative phase ID was determined in Highscore using the PDF4+ database while quantitative phase analysis was performed via Rietveld refinement in GSAS II [23]. It was revealed that the crystallites were most likely composed of tetragonal CuTi (space group P4/mmm) [24] and hexagonal CuTiZr (space group P63/mmc) [25]. In addition, the analysis also showed that Hf did not combine to form any compounds, and therefore most likely remained in the matrix. The results of the Rietveld refinement analysis can be seen in Figure 5 and Table 3. The analysis revealed that the crystalline phases are dominated by some form of CuZrTi solid solution phase at 81.7 wt. % with the secondary phase being CuTi at 18.3 wt. %. The background of the pattern suggests a large amorphous content, and due to the sample morphology, this amount of amorphous content count could not be quantified. This amorphous background leads to a tricky refinement, especially when it comes to characterizing the peak shapes, and thus leads to a high figure of merit, χ^2.

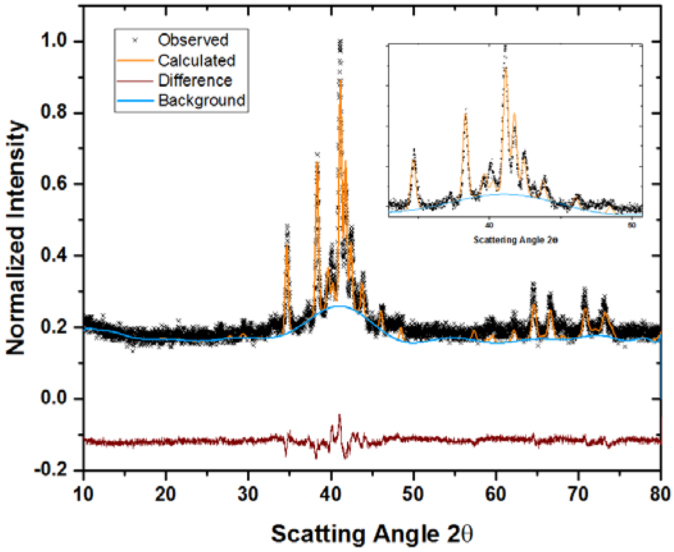

Figure 5. Rietveld refinement analysis of x-ray diffraction pattern for partially crystallized $Cu_{60}Zr_{20}Hf_{10}Ti_{10}$ BMG.

Table 3. Results of the Rietveld refinement which list the experimental parameters, crystal data, and refinement for multi-phase $Cu_{60}Zr_{20}Hf_{10}Ti_{10}$ BMG

	CuZrTi	**CuTi**
Refinement:		
Goodness of fit, [χ^2]	4.66	
wRp	11.08 %	
Rexp	5.16 %	
Software	GSAS II [23]	
Variables		
Background	Chebyschev-Background	
Lattice parameter	*a, c*	*a, c*
Sample Displacement [Å]	89.3 µm	
Gaussian shape parameters	U, V, W	
Crystal Data:		
Crystal system	Hexagonal	Tetragonal
Space group	(194) $P6_3/mmc$	(123) $P4/mmm$
*a=b** [Å]	5.167 (2)	3.182 (3)
*C**, [Å]	8.265 (2)	2.853 (3)
Volume, [Å^3]	191.12 (2)	28.904 (9)
Weight Percent	81.7 (7) %	18.3 (5) %

*Estimated standard deviations are 3σ

The results of the TEM bright field imaging of the Cu BMG sample irradiated to 10 dpa at 360°C can be seen in Figure 6a. The crystallites that can be seen here were observed throughout the entire lift-out specimen (irradiation and unirradiated regions), supporting the results of the x-ray diffraction experiments that the crystallization may be thermally induced rather than irradiation-induced. The corresponding diffraction pattern can be seen in Figure 6b, which shows a very complex crystallographic structure. Additional analysis is planned to further study the crystalline structure in this alloy to increase our fundamental understanding of crystal formation in amorphous alloys.

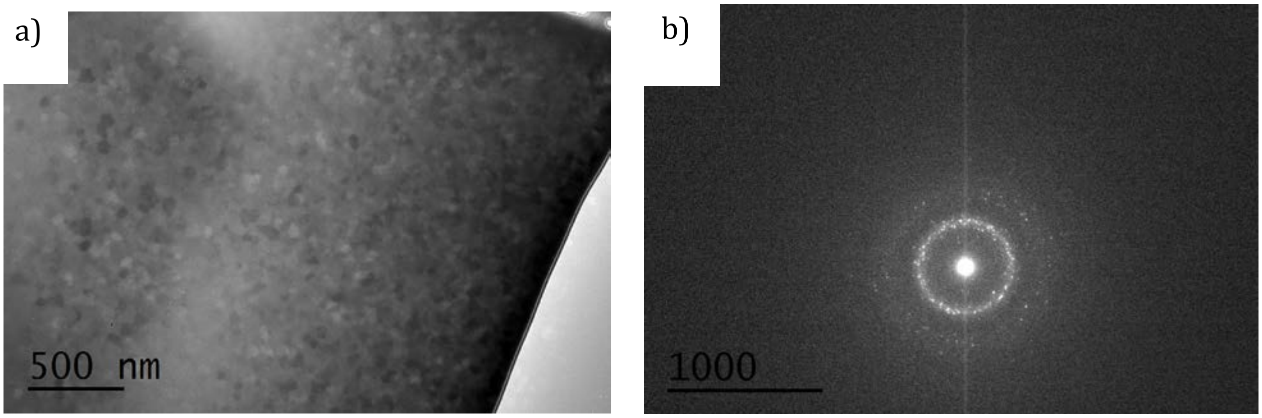

Figure 6. a) Bright Field Image revealing the crystallites that formed in the $Cu_{60}Zr_{20}Hf_{10}Ti_{10}$ BMG during irradiation to 10 dpa at 360°C. 6b) The corresponding diffraction pattern.

Figure 7 shows the result of Raman spectral analysis on the as-cast and 10 dpa 360°C crystallized Cu BMG. As can be seen, a peak emerges at ~825 cm^{-1}, which indicates the formation of a new bonding structure, or phase, in the alloy. In addition, there appears to be a broadening of the peak at ~1275 cm^{-1} as well, further supporting the idea of emerging structure in the glass. Raman analysis will be performed on the other irradiated samples in the future to confirm that there was no change compared to the as-cast samples.

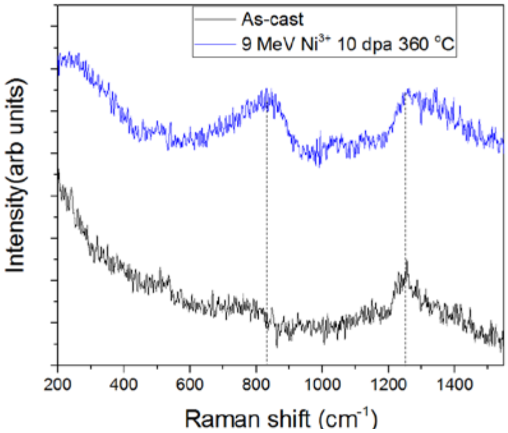

Figure 7. The Raman spectra of the as-cast and partially crystallized $Cu_{60}Zr_{60}Hf_{10}Ti_{10}$ BMG.

Figure 8 shows the radial distribution function (RDF) of annealed and 0.1 dpa neutron irradiated BAM-11; the inset highlights the upper half of the first peak. Overall, only slight differences in atomic spacing occurred due to irradiation and/or thermal annealing. The changes in the 1st nearest neighbor distances are summarized in Table 4. As can be seen in the table, the sample irradiated to 0.1 dpa exhibited a decrease in the 1st nearest neighbor distance while the sample that was annealed to 300°C for two weeks saw an increase. Additionally, the samples which were annealed after irradiation exhibited an increase in their 1st nearest neighbor distances as compared to the as-cast condition.

Furthermore, the curve for the sample irradiated to 0.1 dpa had a slightly lower and broader peak, suggesting that neutron collision cascades led to slight structural disordering (rejuvenation) in the alloy. On the other hand, annealing BAM-11 at 300°C for 2 weeks resulted in a taller and narrower peak, which is evidence for structural ordering (relaxation). Thus, it can be surmised from the above results that irradiating BAM-11 with neutrons leads to slight structural rejuvenation that is characterized by an increase in free volume content and greater atomic disordering. It also appears that annealing the sample after neutron irradiation partially reverses the effects of the irradiation induced disordering**,** as exhibited by its broader and increased peak height that approaches the curve for the unirradiated BAM-11. Furthermore, the annealing done under the condition of 325°C for 72 hours appears to have a greater reversing effect as compared to the 300°C for 2 weeks as illustrated by a higher peak. Further analysis will be performed to better understand how irradiation and annealing affect the microstructure of the alloy.

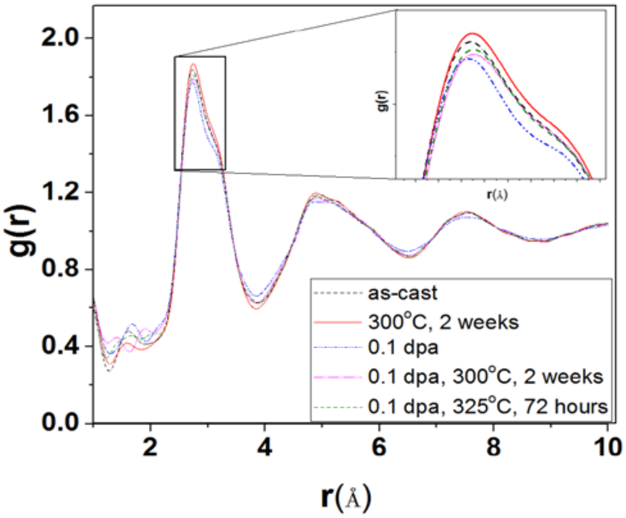

Figure 8. Radial distribution function for the neutron irradiated and annealed BAM-11 BMG.

Table 4. Sample conditions and first radial distance as evaluated from neutron diffraction data

Condition	**R_1(Å)**
As-cast	2.74
Annealed 300°C for two weeks	2.75
Neutron irradiated to 0.1 dpa	2.73
Neutron irradiated to 0.1 dpa and then annealed 325°C for 72 hours	2.75
Neutron irradiated to 0.1 dpa and then annealed 300°C for two weeks	2.75

Nano-indentation Properties

Nano-indentation hardness was measured as a function of depth from the point of contact of the nano-indenter with the surface to a depth of about ~2500 nm. The hardness data for a depth of less than ~100 nm from the specimen surface was discarded due to large data scatter associated with surface roughness. The depth-dependence hardness values of the as-cast and Ni^{3+} irradiated Zr and Cu BMG specimens can be seen in Figures 9a and b, respectively. As can be seen in the figures, the hardness decreased with respect to indentation depth for both the as-cast and ion irradiated samples, indicating a significant indentation size effect in addition to potential ion irradiation effects. The BAM-11 BMG exhibited a slight increase in hardening after 10 dpa at 25-290^{o}C in the irradiated region. However, the sample irradiated to 10 dpa at 360^{o}C exhibited significant hardening at all depths. The BAM-11 sample irradiated at the same dose condition at 290^{o}C experienced hardening, in general, as compared to the as-received condition. The general behavior for the Cu BMG seems to be minor radiation effects at 25^{o}C and 290^{o}C and major changes at 360^{o}C in both the irradiated and unirradiated regions. The Cu sample irradiated at 25^{o}C also exhibits increasing hardness for depths >750 nm, which appears to be an anomaly since this region of the sample should be weakly affected by irradiation damage due to long range strain fields beneath the indenter (irradiation region should be ≤450 nm indent depths). As discussed in [26], the discrepancy between the hardness tests could be a result of surface effects due to machining or mechanical polishing effects, or a near-surface composition gradient due to chemical inhomogeneity or near-surface radiation induced solute segregation. Further tests will try to resolve these issues.

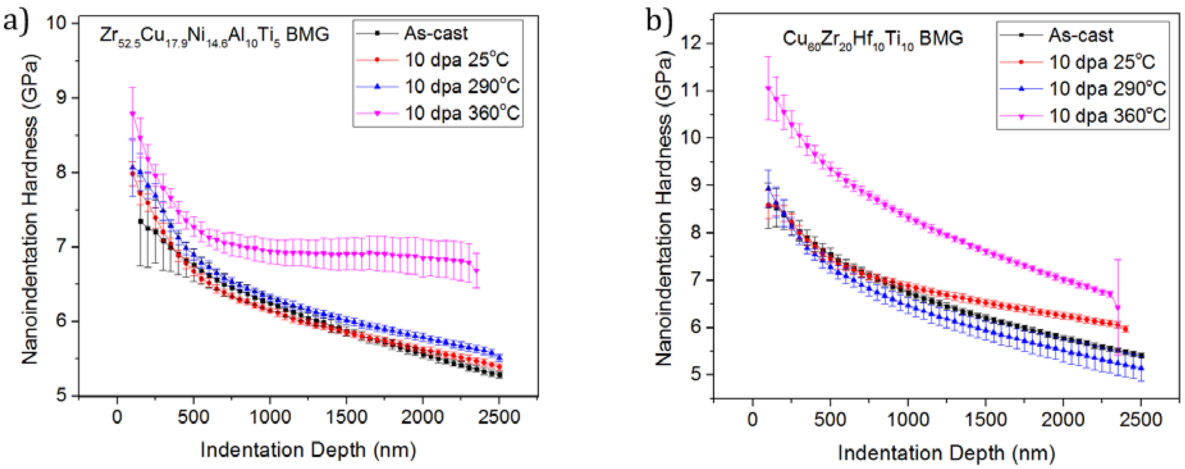

Figure 9. Nano-indentation hardness vs. indentation depth for a) BAM-11 and b) Cu BMG as-cast and irradiated samples. Here the irradiation condition is 9 MeV Ni^{3+} to 10 dpa at temperatures ranging from ambient to 360^{o}C

As discussed above, the hardness values for both alloys irradiated at 10 dpa 360^{o}C had significantly higher nano-indentation hardness in the irradiated and unirradiated regions as compared to the other conditions, with the greatest increase in the $Cu_{60}Zr_{20}Hf_{10}Ti_{10}$ metallic glass. In the Cu alloy, this was most likely due to crystallization of the structure. On the other hand, it is not entirely clear at this point why there was such an increase in the hardness of the BAM-11 at the same condition. Perhaps there is crystallization that has occurred on a scale that cannot be detected by x-ray diffraction. The second amorphous hump in the corresponding x-ray diffraction pattern hints that there is indeed significant structural rearrangement occurring.

Figures 10a and b show the nano-indentation Young's modulus vs. nano-indentation depth for the unirradiated and irradiated BMG alloys. Like the hardness data, the modulus also decreased with respect to indentation depth. However, the modulus exhibited anomalous behavior for both alloys which cannot be explained by irradiation effects. For example, the modulus in both alloys was significantly higher in the irradiated samples at depths beyond the irradiated region. For BAM-11, there appears an increase of the material stiffness with respect to the irradiation temperature. The same was true for the Cu BMG indented to depths <1000 nm. After 1000 nm, the modulus values for the Cu BMG sample irradiated at 360°C drop below the values of the sample irradiated at 290°C. Additional experiments are planned to see if the above results are anomalous or not.

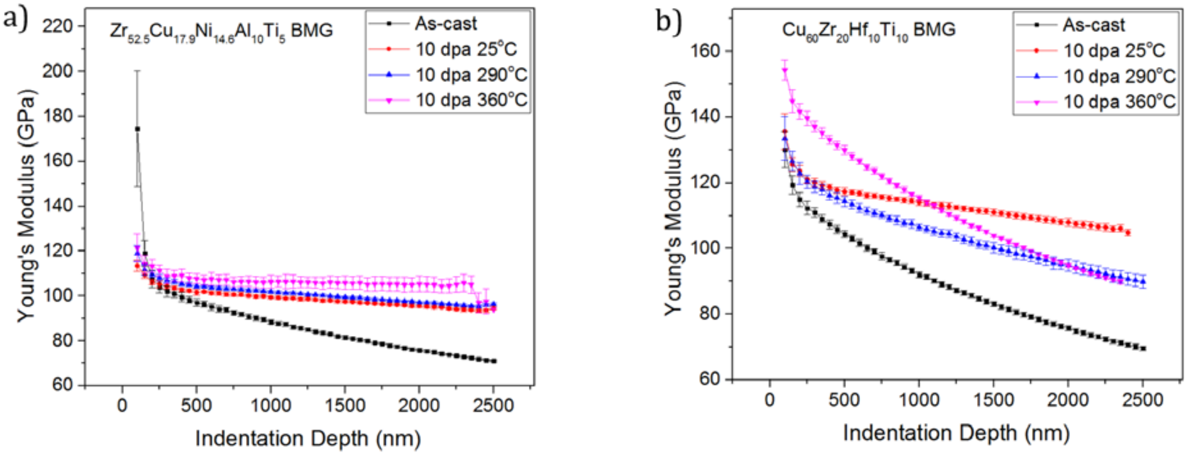

Figure 10. Nano-indentation Young's Modulus vs. indentation depth for a) BAM-11 and b) Cu BMG as-cast and irradiated samples. Here the irradiation condition is 9 MeV Ni^{3+} to 10 dpa at temperatures ranging from ambient to 360°C.

As was discussed in [20], nano-indentation data was examined at 200 nm for an ion range of ~1.36 µm since the nano-indenter tip is sensitive to material properties 5-10 times beyond its penetration depth. Using this proportion of indentation depth/ion range, the nano-indentation hardness and modulus was examined at ~450 nm which is displayed in Table 5. As can be seen in the table, there was no significant change in the hardness of both alloys after the room temperature and 290°C irradiations. The hardness of both BMGs increased after irradiation at 360°C. Furthermore, the Young's modulus was found to gradually increase with respect to irradiation temperature. It was observed that there was an increase in the hardness, from the as-cast to the maximum temperature of 16% for BAM-11 and 24% for the Cu BMG. In terms of the modulus, there was a 10% increase for the BAM-11 and a 24% increase for the Cu BMG. Based on the changes in nano-indentation properties, it appears that $Cu_{60}Zr_{20}Hf_{10}Ti_{10}$ BMG is less resistant to irradiation displacement cascades as compared to the $Zr_{52.5}Cu_{17.9}Ni_{14.6}Al_{10}Ti_5$ BMG. Table 6 compares the average nano-indentation and Young's hardness values for BAM-11 BMG from this and previous studies. Further analysis will be performed on the samples to determine potential causes of the quantitative differences in the two studies.

Table 5. Summary of nano-indentation results on virgin and irradiated BMG samples at a depth of 450 nm

	Alloy	As-cast	10 dpa 25 °C	10 dpa 290 °C	10 dpa 360 °C
Average Hardness^a (GPa)	**$Zr_{52.5}Cu_{17.9}Ni_{14.6}Al_{10}Ti_5$**	**6.83 +/- 0.21**	**6.78 +/- 0.70**	**6.99 +/- 0.07**	**7.36 +/- 0.12**
	$Cu_{60}Zr_{20}Hf_{10}Ti_{10}$	**7.64 +/ 0.14**	**7.56 +/- 0.11**	**7.42 +/- 0.16**	**9.50 +/- 0.15**
Average Young's Modulus^a (GPa)	**$Zr_{52.5}Cu_{17.9}Ni_{14.6}Al_{10}Ti_5$**	**98.27 +/- 1.40**	**102.28 +/- 0.78**	**105.07 +/- 0.91**	**107.89 +/- 2.40**
	$Cu_{60}Zr_{20}Hf_{10}Ti_{10}$	**105.88 +/- 1.24**	**117.70 +/- 1.00**	**115.33 +/- 1.71**	**131.43 +/- 1.28**

Table 6. Comparison of average nano-indentation hardness and Young's modulus on BAM-11 BMG. R.T.: room temperature, H.T.: high temperature, *: current study

	As-cast	10 dpa R.T.	10 dpa H.T.
Average Hardness (GPa)	6.8* 6.9 [20]	6.8* 5.7 [27]	7.0* (290°C) 6.0 (300°C) [27]
% diff between * and ref.	1.0	17.6	15.4
Average Young's Modulus (GPa)	98.3* 102.2 [20]	102.3* 93.5 [27]	105.1* 98.1 [27]
% diff between * and ref.	3.9	9.0	6.9

To examine whether thermal or irradiation effects played the largest role in affecting the nano-indentation properties in the crystallized Cu BMG alloy, the nano-indentation hardness was measured in the irradiated region and unirradiated (polished front surface shielded from the ion beam) regions of the alloy. Figure 11 compares the nano-indentation hardness of the two regions in which there is a negligible difference in the hardness values. This provides evidence that at this irradiation condition thermal effects play a greater role than primary knock-on events in changing the material properties of the alloy. However, more investigation will be needed to gain a better understanding on this issue.

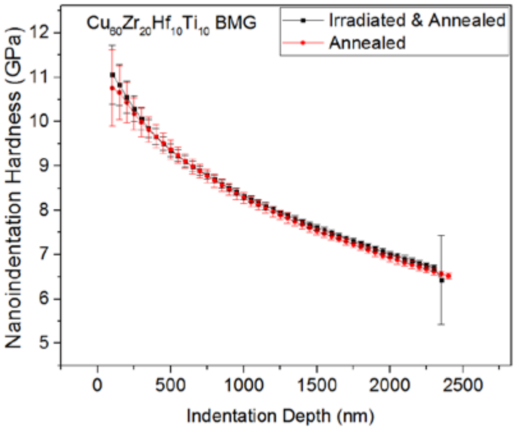

Figure 11. A comparison of the nano-indentation hardness in both the irradiated and annealed and annealed only regions in the Cu BMG alloy after irradiation by 9 MeV Ni^{3+} to 10 dpa at 360°C.

To compare the effects of dose on the nano-indentation properties, the hardness was plotted for both alloys exposed to room temperature Ni^{3+} irradiations to a damage level of 0.5 and 10 dpa, and is illustrated in Figures 12a and b). The data appears anomalous, and will therefore be further examined in the future. In the BAM-11 sample, the hardness was larger for the irradiated samples. However, beyond the irradiation region, the sample irradiated to 0.5 dpa became significantly lower. In the Cu alloy, the hardness did not significantly change in the irradiated region. However, beyond a depth of ~700 nm, the sample irradiated to 0.5 dpa exhibited larger hardness as compared to the other conditions. The reasons for the above discrepancies may be due to structural inhomogeneities in the host material that led to significant differences in mechanical properties of the samples that were produced from it.

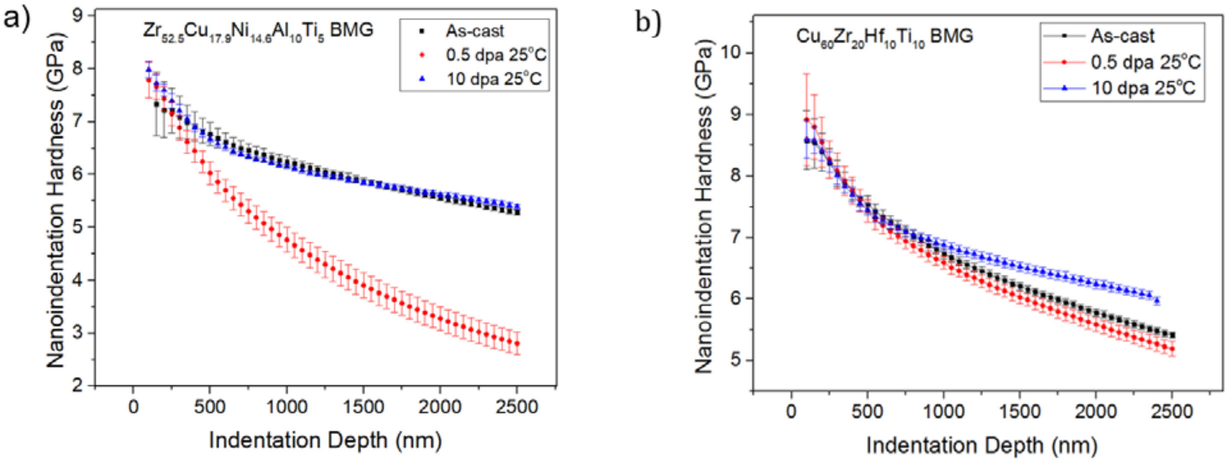

Figure 12. Nano-indentation hardness vs. indenter depth plots for a) BAM-11 and b) Cu BMG for different Ni^{3+} ion irradiation dose.

Next, the effects of primary knock-on energy on the nano-indentation hardness in both alloys were analyzed. Here the hardness vs. indentation depth was plotted for the as-cast, the sample irradiated by 5.5 MeV C^+, and 9 MeV Ni^{3+} to 0.5 dpa (see Figures 13a and b). In the BAM-11, the sample irradiated by the 9 MeV Ni^{3+} exhibited larger hardness values as compared to the other conditions until an indentation depth of approximately 250 nm. On the other hand, the BAM-11 sample irradiated by 5.5 MeV C^+ exhibited the lowest hardness until an indentation depth of 450 nm. Beyond 450 nm, the sample irradiated by 9 MeV Ni^{3+} ions had the lowest hardness values. In the Cu BMG, a similar trend was observed for hardness values up until 250 nm. However, unlike the BAM-11 sample, the hardness values for the sample irradiated by C^+ ions were the lowest until a depth of 1450 nm. As of now, the reasons for this behavior are unclear, and will require further experimentation and analysis to help identify possible mechanisms.

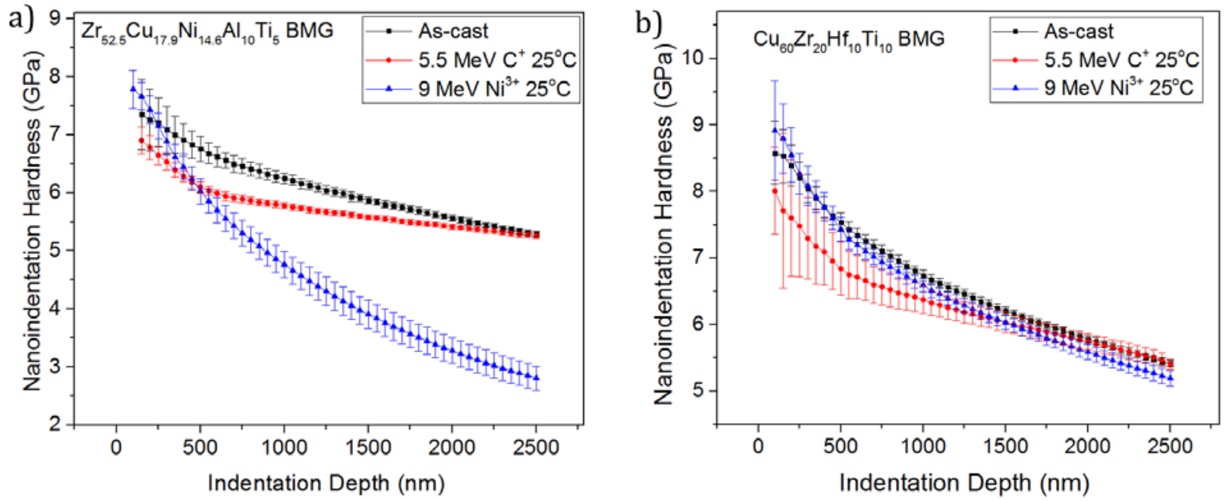

Figure 13. Nanoindentation hardness as a function of depth for a) $Zr_{52.5}Cu_{17.9}Ni_{14.6}Al_{10}Ti_5$ and b) $Cu_{60}Zr_{20}Hf_{10}Ti_{10}$ BMGs irradiated by 5.5 MeV C^+ and 9 MeV Ni^{3+} ions at room temperature to 0.5 dpa.

Nano-indentation tests were performed on the as-cast and heat-treated BAM-11 (300°C, 2 weeks). As can be seen in Figure 14, the nano-indentation hardness was significantly higher. The increase in hardness is most likely due to the thermally induced structural relaxation occurring in the alloy. This idea is supported in [28], where they theorized that a decrease in free volume, which accompanies structural relaxation, results in a higher resistance to plastic deformation.

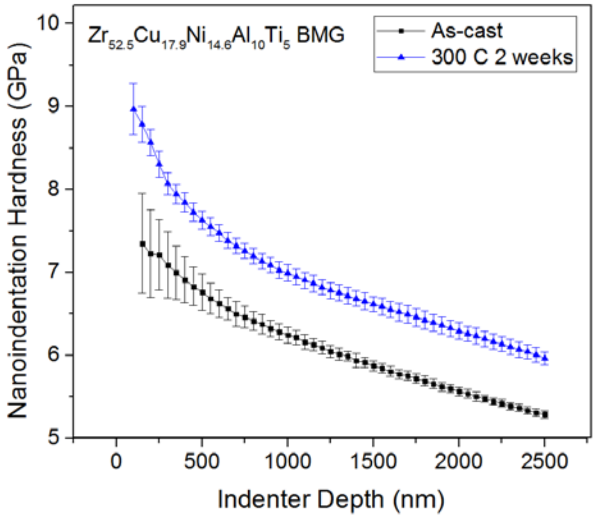

Figure 14. Nanoindentation hardness vs. indenter depth for as-cast and heat-treated BAM-11 BMG. The annealing condition was 300°C for 2 weeks.

The Nix-Gao model [15] was used to analyze the data to avoid discrepancies associated with surface defects and underlying substrate effects. For this method, the square of the nano-indentation hardness was plotted vs. the reciprocal of the indentation depth. Samples with uniform hardness should exhibit a linear relationship in this type of plot, whereas near-surface regions with a different indentation property behavior can be identified by a shift in the slope of the curve. To determine the extrapolated bulk hardness H_0, a line is fit to the data and extrapolated towards the ordinate axis. The hardness H_0 occurs where the abscissa equals zero and corresponds to the hardness at an arbitrarily large depth in the material.

The plots for H^2 vs. 1/h along with its corresponding extrapolated hardness values can be seen in Figures 15-20. The vertical line in the plot corresponds to an indenter depth of 450 nm, which is near the expected transition between hardness dominated by unirradiated and ion-irradiated regions. The hardness was extrapolated in different regions, namely the data within and beyond the irradiated region. The data, for the most part, observed non-linear behavior. In addition, the slope of the data points in the irradiated region was different than the slope for the points outside the irradiated region (also true for the as-cast material, which was somewhat surprising). This difference in the gradients led to different values for the extrapolated hardness.

This deviation from the law proposed by Nix & Gao may be due to a few factors. Firstly, the proposed law, which models the strain-gradient plasticity in crystalline materials, depends on dislocations contained in the matrix. Since the deformation in metallic glasses involves an entirely different mechanism, namely shear transformation zones, the hardness may behave in a different way with respect to the indentation depth. This is supported by the observation that the near-surface hardness behavior of the as-cast material is different for the deeper extrapolated hardness (6.65 GPa vs. 5.07 GPa for BAM-11). Secondly, the slope of H^2 is dependent on the shear modulus of the material [15], which is assumed constant in the model. However, atomic rearrangements caused by primary knock-on effects may change the modulus, and consequently, the slope. The above ideas support the idea that the dislocation-based deformation model may not be relevant for BMGs.

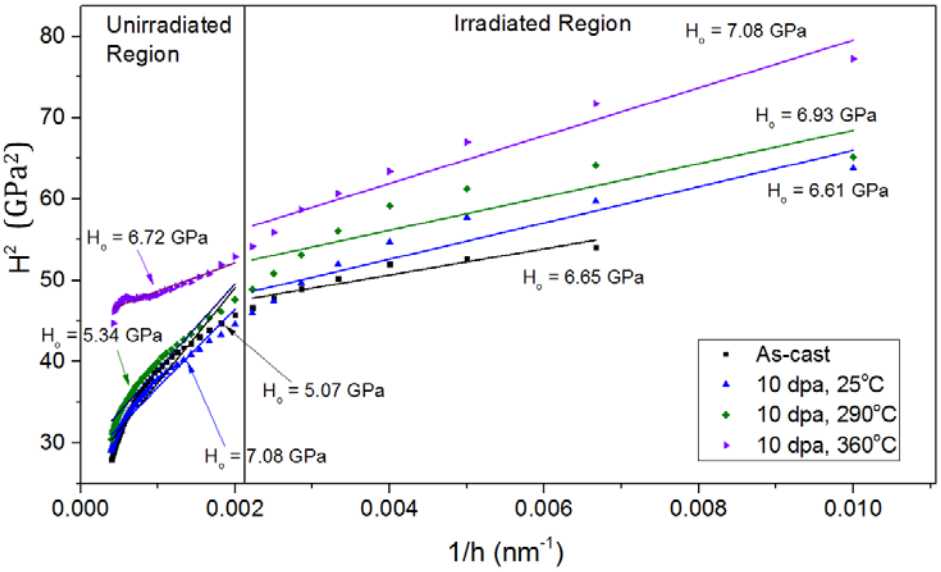

Figure 15. H^2 vs. 1/h (with extrapolated hardness H_o) for BAM-11 BMG in the as-cast vs. irradiation conditions.

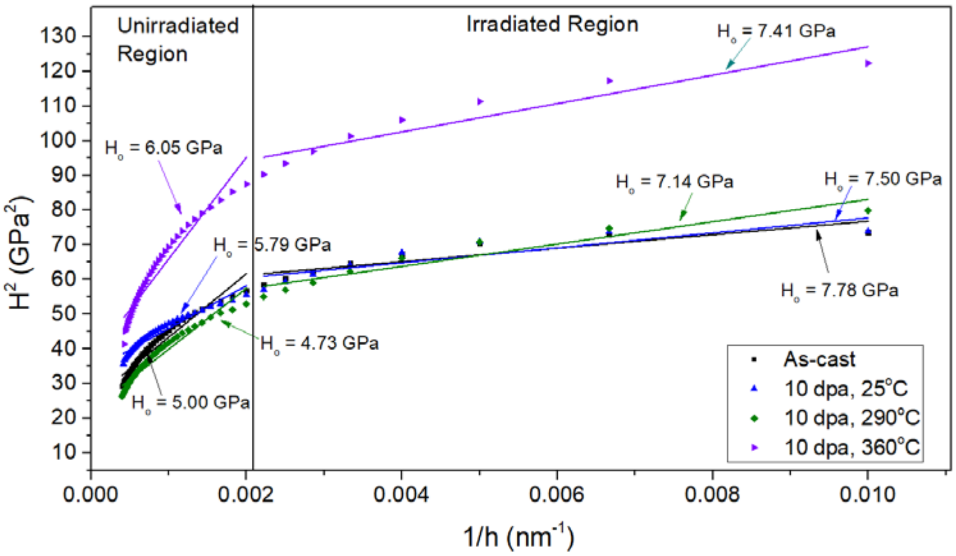

Figure 16. H^2 vs. 1/h (with extrapolated hardness H_o) for Cu BMG in the as-cast vs. 9 MeV Ni^{3+} irradiation conditions.

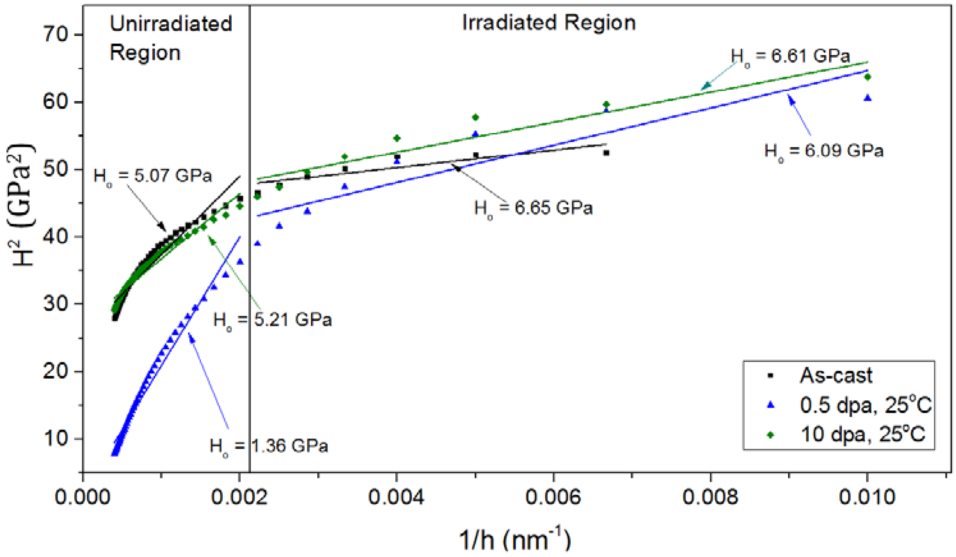

Figure 17. H^2 vs. 1/h (with extrapolated hardness H_o) for BAM-11 BMG in the as-cast vs. 9 MeV Ni^{3+}irradiation conditions.

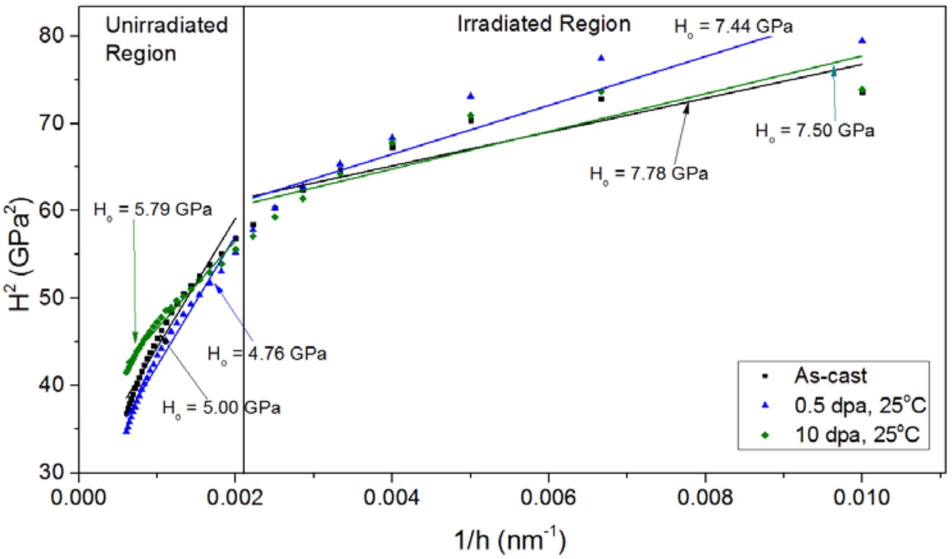

Figure 18. H^2 vs. 1/h (with extrapolated hardness H_o) for Cu BMG in the as-cast vs. 9 MeV Ni^{3+}irradiation conditions.

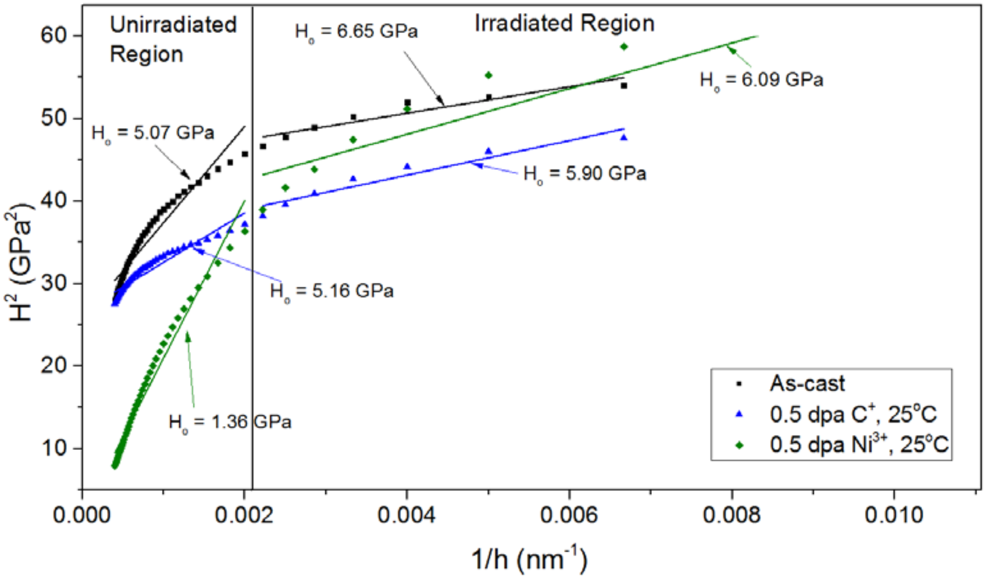

Figure 19. Effects of ion species (9 MeV Ni^{3+}/5.5 MeV C^+) on H^2 vs. 1/h behavior (with extrapolated hardness H_o) for BAM-11 BMG.

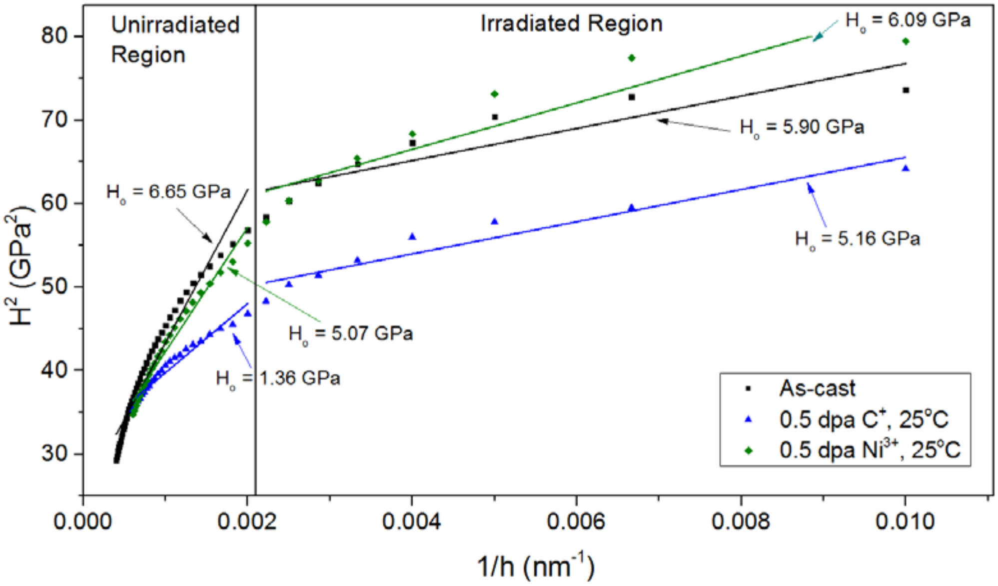

Figure 20. Effects of ion species (9 MeV Ni^{3+}/5.5 MeV C$^+$) on H^2 vs. 1/h behavior (with extrapolated hardness H$_o$) for Cu BMG.

Tables 7 and 8 summarize the extrapolated hardness H$_o$ in the irradiated and unirradiated conditions. H$_o$ was found to be significantly higher in the near-surface (irradiated) region under all conditions, including the as-cast unirradiated material. The extrapolated hardness in both alloys also decreased after irradiation by 9 MeV Ni^{3+} to a dose of 0.5 dpa at ambient condition. Furthermore, both alloys exposed to Ni^{3+} at 10 dpa, exhibited a general increase in H$_o$ with respect to irradiation temperature. Samples irradiated by 5.5 MeV C$^+$ to a dose of 0.5 dpa at room temperature also exhibited an increase in the extrapolated hardness. Except for the as-cast and sample irradiated by 9 MeV Ni^{3+} at ambient, the Cu BMG exhibited a larger increase in the extrapolated hardness as compared to BAM-11 BMG. These results signify that the Cu BMG may have less radiation resistance as compared to the Zr based BMG. In addition, BAM-11 sample irradiated by 9 MeV Ni^{3+} at room temperature had a significantly lower H$_o$ value as compared to other samples. This discrepancy may have been the result of an inherently different microstructure in the sample due to inhomogeneities in the bar that it was produced from rather than irradiation effects. These results provide further evidence that the $Cu_{60}Zr_{20}Hf_{10}Ti_{10}$ BMG has less resistance to irradiation displacement damage as compared to BAM-11 BMG.

Table 7. Nix-Gao extrapolated hardness for BAM-11 BMG. The first row is for the as-cast condition.

Ion Species	Ion Energy (MeV)	Irradiation Dose (dpa)	Irradiation Temperature (^{o}C)	Extrapolated Hardness (GPa^{2})		
				Unirradiated Region	Irradiated Region	Percent Change
-	-	-	-	5.07	6.65	31.2
Ni^{3+}	9	0.5	25	1.36	6.09	348
Ni^{3+}	9	10	25	5.21	6.61	26.9
Ni^{3+}	9	10	290	5.34	6.93	29.8
Ni^{3+}	9	10	360	6.72	7.08	5.36
C^{+}	5.5	0.5	25	5.16	5.9	14.3

Table 8. Nix-Gao extrapolated hardness for Cu BMG. The first row is for the as-cast condition.

Ion Species	Ion Energy (MeV)	Irradiation Dose (dpa)	Irradiation Temperature (^{o}C)	Extrapolated Hardness (GPa^{2})		
				Unirradiated Region	Irradiated Region	Percent Change
-	-	-	-	5.00	7.78	55.6
Ni^{3+}	9	0.5	25	4.76	7.44	56.3
Ni^{3+}	9	10	25	5.79	7.50	29.5
Ni^{3+}	9	10	290	4.73	7.14	51.0
Ni^{3+}	9	10	360	6.05	7.41	22.5
C^{+}	5.5	0.5	25	5.28	6.8	28.8

Results

After BMG samples were irradiated with 5-9 MeV C^{+} or Ni^{3+} ions (midrange doses of 0.5 and 10 dpa) and fission neutrons to 0.1 dpa at ~90^{o}C they, for the most part, remained amorphous. However, the Cu BMG irradiated to a dose of 10 dpa at 360^{o}C experienced crystallization in both the irradiated and unirradiated regions. Neutron diffraction results indicated that the BAM-11 samples underwent minor disordering during neutron irradiation up to a dose of 0.1 dpa. Furthermore, annealing the as-cast alloy at 300^{o}C for 2 weeks results in slight structural relaxation, which was accompanied by a significant increase in the nano-indentation hardness and concomitant decrease in the free volume content. In terms of the nano-indentation behavior, there were no significant changes in the nano-indentation hardness of the alloy except for the samples irradiated by 9 MeV Ni^{3+} ions at 360^{o}C to 10 dpa. For instance, at an indentation depth of ~450 nm, BAM-11 and Cu BMG experience an increase in the nano-indentation hardness of 16% and 24% respectively, from the as-cast to the irradiation condition of 9 MeV Ni^{3+} 10 dpa 360^{o}C. At the same depth, the Young's Modulus was found increase 10% and 24% to respectively for the BAM-11 and Cu BMGs under the same irradiation conditions. In addition, the Young's Modulus, as a function of indenter depth, was found to increase with respect to irradiation temperature for the 9 MeV Ni^{3+} irradiations. Nix-Gao analysis revealed that the H^{2} vs. 1/h did not observe linear behavior for either as-cast or ion irradiated BMGs, which may be due to inherent depth-dependent deformation behavior in BMGs along with effects of irradiation displacement damage on the microstructure and mechanical property of the alloys. The extrapolated hardness was found, in general, to increase with respect to irradiation temperature when irradiated by 9 MeV Ni^{3+} ions to a dose of 10 dpa. Additionally, the BAM-11 alloy exhibited an increase in the extrapolated hardness of 11% from the as-cast condition after irradiation by 9 MeV Ni^{3+} ions to a dose of 10 dpa at room temperature. The Cu BMG exhibited an increase of 28% in the Nix-Gao hardness over the same range of conditions. With respect to the 5.5 MeV C^+ irradiation, there was only a slight increase in extrapolated hardness. The above results indicate that BAM-11 may be better suited for a nuclear fusion environment as compared to $Cu_{60}Zr_{20}Hf_{10}Ti_{10}$ BMG, but further experiments and analysis are required to test the validity of this assertion.

In summary, the material response of BAM-11 and Cu BMG exhibit noticeable radiation resistance at lower temperature. However, further studies of these bulk metallic glass alloys are needed to fully understand the effects of temperature and irradiation on the material. Future planned studies include energy dispersive electron diffraction studies using TEM, analysis of in situ compression experiments conducted at Argonne National Laboratory, nano-indentation and in situ bend tests on the neutron irradiated samples, and helium diffusion studies. It is hoped through the above studies that a much greater understanding of the behavior of bulk metallic glasses in extreme environments will be obtained.

References

[1] A. Gupta, S. Habibi, & G. Principi, Materials Science and Engineering, A134 (1991) 992-995.

[2] R. Gerling, F.P. Schimansky & R. Wagner, Scr. Metall., 17 (1983) 203.

[3] R. Gerling & R. Wagner, Journal of Nuclear Materials, 107 (1982) 311-317.

[4] M. Jaouen, J. Mimault, P. Chartier, T. Girardeau & G. Tourillon, Nuclear Instruments and Methods in Physics Research B69 (1992) 287-292.

[5] J. Carter, E.G. Fu, G. Bassiri, B.M. Dvorak, N.D. Theodore, G. Xie, D.A. Lucca, M. Martin, M. Hollander, X. Zhang & L. Shao, Nuclear Instrument and Methods in Phys. Research B, 267 (2009) 1519-1521.

[6] J. Carter, E.G. Fu, G. Bassiri, B.M. Dvorak, N.D. Theodore, G. Xie, D.A. Lucca, M. Martin, M. Hollander, X. Zhang & L. Shao, Material Science Forums Vols. 561-565, (2007) 1737-1740.

[7] Y. Fukumoto, A. Ishii, A. Iwase. Y Yokoyama, F. Hori, Journal of Physics 225 (2010) 1-5.

[8] A. L. Greer, K. L. Rutherford, & I. M. Hutchings, Int. Mater. Rev. 2002, 47, 87-112.

[9] S. V. Madge, A. Caron, R. Gralla, G. Wilde & S. K. Mishra, Intermetallics 2014, 47, 6-10.

[10] S. V. Madge, Metals 2015, 5, 1279-1305.

[11] W.J. Weber, R.C. Ewing, C.A. Angell, G.W. Arnold, A.N.Cormack, J.M. Delaye, D.L. Griscom, L.W. Hobbs, A.Navrotsky, D.L. Price, A.M. Stoneham, and M.C. Weinberg, J. Mater. Res. 12 (1997) 1946-1978.

[12] A. G. Perez-Bergquist, H. Bei, Y. Zhang, and S.J. Zinkle, Fusion Materials Semiannual Progress Report for Period Ending December 31, 2013, DOE/ER-0313/55, U. S. Department of Energy, 55.

[13] X. Mei, B. Wang, C. Dong, F. Gong, Y. Wang, and Z. Wang, Nucl. Instrum. Methods Phys. Res. B 307(2013) 11-15.

[14] W.J. Weber, R.C. Ewing, C.A. Angell, G.W. Arnold, A.N. Cormack, J.M. Delaye, D.L. Griscom, L.W. Hobbs, A. Navrotsky, D.L. Price, A.M. Stoneham, and M.C. Weinberg, J. Mater. Res.12 (1997) 1946-1978.

[15] W.D. Nix and H. Gao, J. Mech. Phys. Solids, 46, (1998) 411-425.

[16] R.E. Stoller, M.B. Toloczko, G.S. Was, A.G. Certain, S. Dwaraknath and F.A. Garner, Nuclear Instruments and Methods in Physics Research B 310 (2013) 75–80.

[17] M. F. Toneya, T. C. Huang, S. Brennan and Zophia Rek, J. Mater. Res., Vol. 3, No. 2, Mar/Apr 1988.

[18] W.C. Oliver and G.M. Pharr, J. Mater. Res. 7 (1992) 1564-1583.

[19] W.C. Oliver and G.M. Pharr, J. Mater. Res. 19 (2004) 3-20.

[20] A. G. Perez-Bergquist, H. Bei, K. J. Leonard, Y. Zhang, S. J. Zinkle, Intermetallics 53 (2014) 62-66.

[21] Z. Xin Wang, D. Q. Zhao, M. X. Pan, W. H. Wang, T. Okada and W Utsumi, J. Phys.: Condens. Matter 15 (2003) 5923–5932.

[22] C.T. Liu, L. Heatherly, D. S. Easton, C. A. Carmichael, J. H. Schneibel, C. H. Chen, et al.

[23] Toby, B. H., & Von Dreele, R. B. (2013). "GSAS-II: the genesis of a modern open-source all-purpose crystallography software package". *Journal of Applied Crystallography*, **46**(2), 544-549.
[24] R.J. Furlan, G. Bambakidis, J.S. Cantrell, R.C. Bowman Jr., A.J. Maeland, J. Less-Common Met., 116, 375, (1986).
[25] Y. Xinlin, X.-Q. Chen, A.V. Grytsiv, A.V., P. Rogl, R. Podloucky, V. Pomjakushin, H. Schmidt, G. Giester, Intermetallics, 16, 651, (2008).
[26] J. Brechtl, N.A.P. Kiran Kumar, H. Bei, Y., and S. J. Zinkle, Fusion Materials Semiannual Progress Report for Period Ending June 30, 2015, DOE/ER- 0313/58, U.S. Department of Energy, 223.
[27] A. G. Perez-Bergquist, J. Brechtl, H. Bei, Y. Zhang and S. J. Zinkle, Fusion Reactor Materials Program, Volume 56 Semiannual Progress Report, Fusion Materials Semiannual Progress Report for Period Ending June 30, 2014, DOE/ER-0313/56, U. S. Department of Energy, 184.
[28] W. H. Jiang, F. X. Liu, H. Choo, and P. K. Liaw, Materials Transactions, Vol. 48, No. 7 (2007) pp. 1781 to 1784.

7.4 MICROSTRUCTURE-BASED VISCOPLASTICITY MODEL OF TUNGSTEN IN PLASMA TRANSIENTS

—David Rivera, Giacomo Po, Yue Haung, Nasr M. Ghoniem (University of California, Los Angeles)

SUMMARY

Materials developed with special surface architecture are shown here to be more resilient to the transient thermomechanical environments imposed by intermittent exposures to high heat flux thermal loading typical of long-pulse plasma transients. In Part 1 of this article, we present experimental results that show the relaxation of residual thermal stresses in micro-engineered W surfaces. A dislocation-based model is extended within the framework of large deformation crystal plasticity. The model is applied to the deformation of single crystals, polycrystals, and micro-engineered surfaces composed of a uniform density of micro-pillars. The model is utilized to design tapered surface micro-pillar architecture, composed of a Re core and W coatings. Residual stresses generated by cyclic thermomechanical loading of these architectures show that the surface can be in a compressive stress state, following a short shakedown plasma exposure, thus mitigating surface fracture.

PROGRESS AND STATUS

Introduction

Plasma-facing materials (PFM) are required for a great number of technological applications, encompassing space electric propulsion devices, micro-electronics fabrication, fusion energy conversion, and pulsed power devices, just to name a few. Continued development of these systems relies on fundamental advances in our understanding of material performance and survival in extreme environments. The demand of higher performance materials is even greater in future technologies that will require materials to operate in substantially more aggressive scenarios. In such applications, PFM encounter unprecedented severe thermomechanical environments, as plasma ions and electrons slam onto the surface. Many physical degradation phenomena ensue, including material loss by ablation, blistering, sputtering and evaporation, as well as traditional thermomechanical damage in the form of extensive plastic deformation and complex surface cracking. The environment severity is correlated with two main parameters. The first is the total amount of absorbed energy density that passes through the surface, Γt (kWh/cm^2); a measure of the material lifetime. The second load-related parameter is the instantaneous heat flux, Γ (MW/m^2). While Γt is indicative of the duration through which the material will have to survive successive amounts of energy, delivered to its surface either continuously or intermittently, Γ is associated with the response time scale of the material itself to instantaneous pulses of energy. Generally, if Γ is high, the material lifetime is low, and vice-versa.

To understand thermomechanical damage induced by intermittent high heat flux, one has to consider the main driver of damage accumulation, namely plastic deformation of some material regions that are constrained from expansion by cooler regions, or by external boundary conditions. Transient high heat flux induces a temperature gradient across PFM, which can result in thermal stresses that exceed the yield point of the material. Considerations of cooling would require that a mechanical force, generated by the fluid pressure on the cold side, would also act on the PFM simultaneously with the thermal stress. While the mechanical force is generally constant, the thermal stress will fluctuate with each cycle, as the plasma heat source is turned on and off. Several interacting phenomena and manifestations of thermomechanical damage may take place under these specialized loading conditions; encompassing purely elastic response, shakedown behavior, reverse plasticity with ratcheting, viscoplastic deformation, and surface fracture. Considerations of the possibility of these outcomes, and finding solutions to mitigate the accumulation of thermomechanical damage through materials design are desirable pursuits in the development of resilient PFM for many demanding applications. We review briefly here related research on these phenomena as motivating background for the present work. We will first discuss classical approaches of elasto-plasticity employed for the solution of this problem. Since these approaches will be shown to have serious limitations and approximations, we will then review more fundamental modeling strategies that are based on including microstructure information. A discussion of experimental testing methods will be given, followed by engineering design approaches that are used to mitigate thermomechanical damage effects.

Despite the success of classical elasto-plasticity methods in design applications (e.g. the adoption of the Bree diagram by the ASME design code for high temperature components [7, 8, 9]), they are limited in describing severe plasma transient effects on PFM. For example, Bree's original analysis was based on an elastic perfectly plastic, one-dimensional stress model of residual stresses, where material properties are assumed not to change from cycle-to-cycle. However, high temperature deformation entails a variety of physical phenomena such as dislocation climb, recovery, recrystallization, and subgrain growth, in addition to traditional dislocation glide mechanisms accompanying plastic deformation. All of these mechanisms become active to varying degrees by the presence of an elevated temperature (typically $>$ 0.4T $_m$), and lead to gradual changes in the constitutive behavior of the material as severe thermal cycles are applied to it. The lack of any physical input into the thermomechanics of high heat flux components casts doubt on the predictive qualities of classical models. For these reasons, physically-based approaches, where dislocations are modeled as the basic carriers of plastic deformation, can lead to greater insight into the nature of thermomechanical damage accumulation.

The primary aim of the visco-plastic formulation presented here is to describe the thermomechanical response of PFM on a physical basis, where the microstructure (dislocations and grains) is represented. Among the earliest of microstructure-based plasticity models is a formulation by Kocks and Mecking (KM - model) [10, 11, 12]. The KM - model assumes that the strain rate, temperature, and internal parameters such as dislocation density (ρ), all play a role in determining the flow stress. This, in turn, follows the well-known Taylor hardening relation, namely that $\sigma = s(\dot{\varepsilon},T)\hat{\alpha}\mu b\sqrt{\rho}$, where $s(\dot{\varepsilon},T)$ is a rate sensitive function, $\hat{\alpha}$ is a constant on the order of unity, and μ is the shear modulus. This flow stress depends only on the resistance to deformation offered by the presence of dislocations. Since hardening or softening can occur as a result of dislocation-dislocation interactions, both the hardening and recovery rates have to be modeled. The Taylor hardening relationship in the KM model is written as: $\sigma d\sigma/d\varepsilon = (\alpha\mu b)^2/2 \times d\rho/d\varepsilon$, where the dislocation density is assumed to be a function of the strain via a rate equation that balances dislocation production with further straining and its rate of recovery, as: $d\rho/d\varepsilon = (\Lambda b)^{-1} - L_r N_r \nu_r/\dot{\varepsilon}$. The first term in the equation describes the rate of dislocation storage; while the second is the dynamic recovery rate. Λ is the mean free path a dislocation travels before it is annihilated or ceases to contribute to the plastic flow of the material, it is assumed to be proportional to the dislocation spacing $1/\sqrt{\rho}$, L_r is the length of dislocation segments, N_r is the dislocation density, and ν_r is the rate at which the dislocations are rearranged. The glide kinetics of the model can be described with an Arrhenius equation of the form: $\dot{\varepsilon} = \dot{\varepsilon}_o \exp - \dfrac{\Delta G(s_A)}{kT}$. The activation energy for dislocation glide $\Delta G(s_A)$ is dependent on stress and is given by: $s \equiv \dfrac{\sigma}{\overset{\square}{\sigma}} = \left(\dfrac{\dot{\varepsilon}}{\dot{\varepsilon}_o}\right)^{1/m}$, where $\overset{\square}{\sigma}$ is the flow stress at 0 K, and m is the strain rate sensitivity.

Following similar lines to the KM approach, dislocation density based plasticity models have been advanced. Estrin et.al. [13] developed a model, which takes into account the cellular nature of the dislocation microstructure, and adequately described stages III, IV, and V of the stress-strain curve. Prinz and Argon similarly developed a framework by which stages III and IV of the stress-strain curve were accurately predicted [14]. Temporal dynamical behavior and spatial patterning have been analyzed with dislocation density models. Kubin and Estrin described the critical conditions for the Portevin-Le Chatelier effect [15], while the collective dynamical behavior of dislocations was investigated by Ananthakrishna [16], and by Kubin, Fressengeas, and Ananthakrishna [17] . Spatial patterning of dislocations in ordered structures, such as dislocation cells and Persistent Slip Bands (PSB) has been modeled with dislocation density equations by Walgraef and Aifantis [18, 19, 20], and extensively by Aifantis [21]. On the other hand, Kamada and Zikry developed a 3-D dislocation-based model, and applied the model to the deformation of intermetallics [22], and the effects of grain boundaries on large-strain deformation was also studied [23]. Several applications of the model were extended to other material systems [24, 25]. Arsenlis and Parks developed a dislocation-density based model to study the crystallographic aspects of geometrically-necessary and statistically-stored dislocation densities [26], and the evolution of crystallographic dislocation density in crystal plasticity [27].

It is interesting to note that despite the wide variety of dislocation-based models of plasticity[28], there have been relatively few formulations which explicitly incorporate high temperature effects, such as creep and creep-fatigue interactions [29]. At elevated temperatures ($T > 0.5T_m$), additional elements must be included in a micro-structure-based model. The subgrain microstructure becomes the rate controlling mechanism, and details of subgrain boundaries (e.g. the dislocation spacing inside the subgrain boundary, misorientation angles, etc.) take on a more urgent importance. In fact, subgrain boundaries are considered the main source of the long-range internal backstress [30, 31]. Additionally, plastic deformation is no longer controlled by dislocation glide, but is often described as *climb-controlled-glide*, where the effective slip rates are much slower glide rate at low-temperature thanks to the sluggish climb of dislocation cores in vacancy supersaturations.

In Section 2, we present details of the GMA model, where it is formulated within the large deformation framework of the Finite Element Method (FEM) in Subsection 2.1, and extended to modeling bcc polycrystals in Subsection 2.2. Section 3 presents the results of FEM simulations based on the present GMA-poly model. First, the model is calibrated with a suitable set of parameters for the creep deformation of tungsten in Subsection 3.1. This is followed by presenting results of simulations in a representative polycrystal in Subsection 3.2. Since the experimental results were made on micro pillars that have a composite structure, with a rhenium core and a thin tungsten coating, results of simulations of the experimental conditions presented in a previous publication will be shown in Subsection 3.3 for homogeneous plastic deformation of the W shell. Based on the insight gained from the microstructure-based crystal viscoelasticity model, we then present ideas on how to design a plasma-resilient surface with controlled micro-pillar architecture in Subsection 3.4. Finally, conclusions of this study are given in Section 4.

Dislocation-Based Crystal Viscoplasticty

We have formulated a microstructure-based model that contains these critical elements necessary to describe high-temperature deformation [32]. In its original form, the Ghoniem-Matthews-Amodeo (GMA) model assumes that the material is homogeneous, and does not account for large-deformation kinematics that would be associated with creep-type deformation. Moreover, it does not explicitly account for the slip systems in each grain so as to model spatially non-homogeneous deformation. In this work, we will extend the GMA model within the framework of large-deformation crystal plasticity. The current extension of the model will be termed GMA-poly for brevity. The GMA model captures key high temperature deformation phenomena, such as recrystallization, subgrain nucleation and growth, static and dynamic recovery, in addition to the basic ingredients of dislocation storage and annihilation inherent in the KM model and all other variants [32]. The formulation is based on many developments in creep theory, such as the work by Nabarro [33], Gittus [34], Bullough *et al.* [35, 36], Heald *et al.* [37], and Kassner [38]. Under these conditions, dislocation cells form and evolve into subgrains. The inclusion of the subgrain microstructure evolution is a key aspect of this model as reviewed in references [39, 40]. The GMA model is based on earlier developments and experimental observations by a number of investigators (Takeuchi *et al.* [41], Langdon [42], Challenger *et al.* [43], Michel *et al.* [44], and Cuddy [45])).

Large-Deformation FEM Crystal Plasticity Framework

The purpose of the GMA model is to compute shear strain rates in slip systems from knowledge of dislocation densities, as will be presented in subsection 2.2. It is incorporated into a crystal plasticity framework with large deformation by recognizing the key connection between physics (shear rates from dislocation densities) and mechanics (displacements and stresses). First, the plastic velocity gradient tensor, $\mathbf{L}^p$, is computed by summing up the shear strain rates ($\dot{\gamma}_\alpha$) on all slip systems (α), described by the slip vector (s^α) and the plane normal (n^α). Thus,

$$\mathbf{L}^p = \sum_{\alpha=1}^{m} \dot{\gamma}_\alpha s^{(\alpha)} \otimes n^{(\alpha)} \tag{1}$$

The increment of deformation in a crystal is assumed to take place by a multiplicative decomposition of the total deformation gradient tensor into an elastic and a plastic component: $\mathbf{F} = \mathbf{F}^e \cdot \mathbf{F}^p$. The total deformation gradient is determined from the displacement vector field, as: $\mathbf{F} = \nabla \mathbf{u} + \mathbf{I}$, where $\mathbf{u}$ is the displacement vector, and $\mathbf{I}$ is the identity matrix. The deformation mapping is assumed to start from a reference state to an intermediate state by simple shear deformation on slip systems. This is followed by elastic lattice deformation from the intermediate to current current configuration.

The shear strain rate $\dot{\gamma}$ is calculated by solving a system of ODEs representing various dislocation densities, as well as an evolution equation for the subgrain radius, as will be described in the next subsection. By distributing the ODE’s constituting the structure of the GMA model over a computational grid provided by an FE mesh, the shear strain rate $\dot{\gamma}$ can be computed in every element. Upon finding the shear strain rate from GMA model, the components of the velocity gradient can in turn be found by a similar process in which the system of ODE’s is solved point-wise over an FE mesh. For rate-dependent plastic deformation gradient tensor, $\mathbf{F}^p$ is updated with the following space-dependent equation, once the components of the velocity gradient are known: $\dot{\mathbf{F}}^{\mathbf{p}} = \mathbf{L}^p \cdot \mathbf{F}^p$. The assumption of multiplicative decomposition of the elastic and plastic deformation gradient tensors is then utilized to calculate $\mathbf{F}^e$, which is necessary to determine the stress state. A potential energy functional, Π can be expressed as:

$$\Pi = \int_{B_0} \tilde{w}(\mathbf{E}^{\mathbf{e}}) J^p d\Omega_0 - \oint_{\partial B_0} t_i u_i dS_0 \tag{2}$$

where $\tilde{w}$ is the strain energy density per unit intermediate volume and J^p is the determinant of $\mathbf{F}^p$. The relationship between volumes in the intermediate and reference configurations: $J^p d\Omega_0 = d\tilde{\Omega}$ has been used. Based on the minimum total potential energy principle, the displacement field minimizes the potential energy with a given $\mathbf{F}^p$. The first variation of Π with respect to an arbitrary change in $\mathbf{u}$ vanishes, which gives the following weak form of the equilibrium equation:

$$\delta\Pi = \int_{B_0} P_{iJ} \delta u_{i,J} d\Omega_0 - \oint_{\partial B_0} t_i \delta u_i dS_0 = 0 \quad \forall \delta\mathbf{u} \tag{3}$$

where the first Piola stress **P** is given in terms of the second intermediate stress **W** and can be expressed as $P_{iJ} = W_{\alpha\beta} F^{e}_{i\alpha} G^{p}_{J\beta} J^{p}$. Assuming that the strain energy density is quadratic in the elastic strain, **W** can be expressed as $W_{\alpha\beta} = \frac{\partial W}{\partial E^{e}_{\alpha\beta}} = \lambda E^{e}_{\gamma\gamma}\delta_{\alpha\beta} + 2\mu E^{e}_{\alpha\beta}$. Equation 3 is the weak formulation of the large deformation problem, which can be implemented within the FEM framework.

Polycrystalline GMA Viscoplasticity Model

In low-temperature plasticity models, the flow stress is generally dictated by the dislocation density, with additional contributions from the grain size (the Hall-Petch effect). Hence, efforts to develop strong materials are focused on grain refinement and nano-crystalline materials. However, at elevated temperatures, grain growth takes place, and individual grains subjected to an applied stress for prolonged periods start to subdivide themselves naturally into sub grains of a size that is inversely proportional to the applied stress [40]. This behavior is so unusual, and when modeling high temperature deformation, one must then account for the nucleation and growth of such sub grains. This is because the role of the original grain boundaries in controlling the creep resistance is replaced with that of subboundaries. The various dislocation processes that take place at elevated temperatures are discussed by Gittus [46], Li [47], and Sandström [48, 49], and can be summarized as: multiplication of dislocations within the subgrains., annihilation of mobile dislocations within the subgrains, annihilation of dislocations at the subgrain walls, absorption of dislocations by the subgrain walls, emission of dislocations by the subgrain walls, nucleation of new subgrains, and growth of subgrains by coalescence.

In this polycrystalline development of the GMA model, we consider each grain to have a number of slip systems, each of which (α) is described by a vector diad, **s** and **n** for the slip direction and normal, respectively. Each grain has a grain diameter, d_g, and is further subdivided into sub grains. Thus, on average, only a set of slip systems is considered for each grain because misorientations between sub grains are small, as can be seen schematically in Figure 2. The average sub grain radius is R_{sb}, which can grow to reduce the stored elastic energy, or shrink due to nucleation of fresh sub grains during deformation. The dislocation population is divided into three interaction groups, distinguished by their average speed. Mobile dislocations have a density of ρ_m and those can glide causing plastic deformation. Forest or *static* dislocations do not move and they obstruct the motion of mobile dislocations resulting in hardening. Finally, near sub boundaries, dislocations align to enter or leave the sub boundary; they move slowly by climb, and their density is ρ_b. The sketch in Figure 1 shows the elements of the conceptual model, originally presented in reference [32].

While the original presentation of the GMA model can be found in Reference [32], we further expand this model here, incorporating a number of novel features. These are: (1) extension to multi-slip crystals; (2) an update of the dislocation mobility law with a more comprehensive formulation for bcc metals [50]; (3) incorporation of the model into a large-deformation FEM framework, as discussed in the previous subsection; and (4) applications in the design of high heat flux resistant materials. We give here a concise description of the original model, and then extend it to the large-deformation of polycrystals.

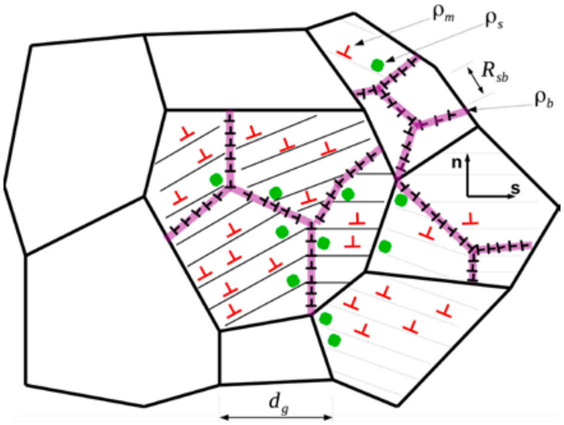

Figure 1. Sketch of the main features of the GMA model. Each grain has a diameter d_g, is subdivided into sub grains, each of which has a radius R_{sb}. Within each grain, three dislocation groups are present: forest with density ρ_s, mobile with density ρ_m, and boundary dislocations of density ρ_b.

The GMA model develops conservation equations using rate processes for the three main dislocation populations on each slip system, $\rho_m^{(\alpha)}, \rho_s^{(\alpha)}, \rho_b^{(\alpha)}$, for mobile, static, and boundary dislocations, respectively. The rates are assumed to change by frequencies that are determined by basic glide, climb, or annihilation rates. Subgrains provide a source of mobile dislocations, and also act as barriers for mobile dislocations. The rate of mobile dislocation production within subgrains is the frequency of source operation times the source density. The frequency of source operation is $(\rho_m^{(\alpha)})^{1/2} v_g$, where $(\rho_m^{(\alpha)})^{1/2}$ is the reciprocal of the mean free path of mobile dislocations in slip system α. Thus, the rate of change of the mobile dislocation density as a result of mobile source operation is $(\rho_m^{(\alpha)})^{3/2} v_g$. Another dislocation source is the activation of links within the static dislocation population, which contributes to the growth of mobile dislocation line length. The frequency of static source activation is $v_g^{(\alpha)}/h$, where h is the dislocation spacing within the subgrains, and each time a source is activated, its length expands from h to R_{sb}, where R_{sb} is the subgrain radius. Thus, the frequency of line length production is $(v_g^{(\alpha)}/h)\times\frac{R_{sb}}{h}$, and the rate of change of the mobile dislocation density from this source is $\beta\rho_s^{(\alpha)} R_{sb} v_g/h^2$, where β is a geometry fitting factor. The dislocation spacing within the wall, h can be written as: $h=\frac{1}{(\rho_s+\rho_b)R_{sb}}$. On the other hand, the frequency of immobilization is $v_g^{(\alpha)}/(2R_{sb})$, since dislocations travel across the sub grain diameter before they are immobilized. Thus, the rate of immobilization is $\rho_m^{(\alpha)} v_g/(2R_{sb})$. Other rates have been derived in reference [32]. The rate of mobile dislocation recovery by climb is $8v_{cm}\rho_m^{(\alpha)}$, and the rate of dynamic recovery is $\delta v_g^{(\alpha)}\rho_m^{(\alpha)}(\rho_m^{(\alpha)}+\rho_s^{(\alpha)})$, where v_{cm} is the mobile dislocation climb velocity, and δ is the average distance between annihilating dislocations.

These glide-controlled rates are complemented by static and dynamic recovery rates. The phenomenon of dislocation climb contributes to the static recovery rate, and proceeds by the climb of dislocation dipoles into the subgrains. The effective stress the dislocation dipoles exert on each other can be expressed as: $\sigma_c = \mu b/2\pi(1-\nu)s$, where s is the separation distance between the dipoles. The climb-to-mutual annihilation of a dipole with initial separation s_0 is shown to be $\tau; \frac{s_0}{4v_c}$ [32], where the initial dipole separation is $s_0 = \rho_m^{-1/2}$. Thus, the recovery rate of mobile dislocations is $-\frac{2\rho_m}{\tau} = -8\rho_m^{3/2} v_{cm}$.

Likewise, the forest dislocation recovery rate can be expressed as $-\frac{2\rho_s}{\tau} = -8\rho_s \frac{v_{cs}}{h}$, where the initial dipole separation is $s_0 = h$. The flux of vacancies along the dislocation core can be expressed as [51].

$$j_p = 2D_p \sigma_c^{(\alpha)} \Omega / L_p kT \tag{4}$$

where D_p is the core diffusion coefficient, and L_p is the path length for diffusion along core, Ω the atomic volume, and $\sigma_c^{(\alpha)}$ is the climb component of the stress tensor in slip system α. The climb velocity is then

$$v_c^{(\alpha)} = 2\pi b D_p \sigma_c^{(\alpha)} \Omega / L_p^2 kT \tag{5}$$

Dynamic recovery explains the saturation of strain hardening [52], because it assumes that mobile dislocations of opposite sign would annihilate each other over time. This was first recognized by Johnson and Gilman [53], and Webster [54], and can be expressed by the following recovery rate: $-\delta\rho_m^{(\alpha)}(\rho_m^{(\alpha)} + \rho_s^{(\alpha)})v_g$, where δ is an average distance between dislocations characterizing annihilations [36, 55]. The grain boundary evolution can be modeled as the product of driving pressure and mobility [32].

The sub-boundary energy per unit area, γ_{sb} for low-angle subgrain boundary can be expressed as: $\gamma_{sb} ; \frac{2\mu b^2}{3} \rho_b^{(\alpha)} R_{sb}$. Since, the subgrain grows by boundary coalescing of collapsing small subgrains, the total force acting on a boundary for a collapsing subgrain (the Gibb's Thompson driving force, $\frac{2\gamma_{sb}}{R_{sb}}$) can be written as: $P_{sb} ; (4/3)\mu b^2 \rho_b$, and the growth rate of a sugrain is simply the product of the sub grain mobility and the driving force, $\partial R_{sb}/\partial t = M_{sb}(P_{sb} - 2\pi r_p^2 N_p \gamma_{sb})$, where the effects of any precipitates (density N_p and radius r_p) is taken to oppose the driving Gibbs-Thompson force. Sugrains are assumed to nucleate when the total density exceeds a critical value. It is assumed that the driving force for nucleation has the form $\mu b(\rho_\alpha^{1/2} - K_c/2R_{sb})$, where ρ_α is the sum of the mobile and forest dislocation densities in slip system α. K_c is a constant on the order of 10 [56, 57]. The time to nucleate a new subgrain configuration is expressed as : $\tau = (kT/\mu\eta_v K_c \rho^{1/2} D_s)[\rho^{1/2} - (K_c/2R_{sb})]\Omega$. The above expressions can be combined to obtain the following rate equation for subgrain radius.

$$\frac{dR_{sb}}{dt} = -\mu\eta_v K_c R_{sb}[\rho^{1/2} - (K_c/2R_{sb})]^2 \Omega D_s / kT \tag{6}$$

Equation (6) is only applicable when there is a driving force for nucleation, i.e. $\rho^{1/2} > K_c/2R_{sb}$. The total dislocation density in the grain is $\rho = \sum_{\alpha=1}^{N}(\rho_m^{(\alpha)} + \rho_s^{(\alpha)})$.

The summary presented above requires knowledge of the glide velocity, which is one of the most significant ingredients in the the GMA formalism. Because the model is an effective phenomenological procedure, the resolved shear stress on a glide plane is assumed to be resisted by a friction stress that takes into account the effects of solute atoms on dislocation motion. The internal stress must thus be be analyzed, since the effective stress, which is a function of internal stress, will be incorporated in the formulation of dislocation velocity. The internal stress is caused by any opposition to dislocation motions, and this opposition can be characterized into three sources. The first source is any precipitates and other dislocations that oppose dislocation motions. The internal stress that mobile dislocations must overcome is $\mu b/2\pi\lambda$, where λ is the effective obstacle spacing, and μ is the shear modulus. In the case where both precipitate and dislocation obstacles are present, the effective obstacle spacing λ is given as

$$\lambda = 1/(1/\lambda_d + 1/\lambda_p) \tag{7}$$

λ_d is the inter-dislocation spacing, and is given as $\lambda_d = 1/\rho_m^{1/2}$. λ_p is the inter-precipitate spacing, and is given as $\lambda_p = 1/(N_p r_p)^{1/2}$, where N_p is the volume concentration of precipitates, and r_p is the mean radius. The second source of opposition are the dislocations that have not yet neutralized their long-range stress fields. Essentially these dislocations have not moved into their low-energy configuration. The mobile dislocations could be accelerated or retarded depending on the nature of these un-neutralized stress fields. These unstable dislocations are forest dislocations within the subgrains. The boundary dislocations themselves do not contribute to the internal stress beyond a distance greater than the average dislocation distance within the subgrains [58]. Combining the effects of precipitates and unstable forest dislocations, the long-range internal stress can be expressed as

$$\tau_i^{(\alpha)} = \mu b/2\pi\lambda + \zeta\mu b(\rho_s^{(\alpha)})^{1/2} \tag{8}$$

The third source of opposition is the friction resistance to glide from over-sized solutes. These typically are solute particles used to strengthen metals. For well-annealed materials without hardening precipitates and heat treatment, this stress can be identified as the initial flow stress, τ_0. Therefore, the resolved effective stress, τ_e can be represented as the following, where $\tau_{a,\alpha}$ is the applied shear stress component on slip system α.

$$\tau_e^{(\alpha)} = \tau_a^{(\alpha)} - \tau_i^{(\alpha)} - \tau_0^{(\alpha)} \tag{9}$$

A comprehensive phenomenological dislocation mobility law for the glide velocity in bcc metals has been recently developed by us [50]. The mobility law is based on fundamental theory of kink-pair controlled motion in the low temperature regime, and on phonon drag limited motion at high temperatures. The general form of the dislocation velocity (edge or screw) is given as[50]:

$$v_g^{(\alpha)}(\sigma,T) = \begin{cases} \dfrac{\tau_{e,\alpha} b}{B(\sigma,T)} \exp\left(-\dfrac{\Delta G_{kp}(\sigma,T)}{2k_B T}\right) & \text{if} \Delta G_{kp}(\sigma,T) > 0 \\ \dfrac{\tau b}{B(\sigma,T)} & \text{if} \Delta G_{kp}(\sigma,T) \le 0 \end{cases} \tag{10}$$

In Eq. (10), the free energy of kink-pair nucleation is ΔG_{kp}, such that $\Delta G_{kp} > 0$ defines the regime of active kink-pair mechanism. The function $B(\sigma, T)$ is a phonon drag coefficient, determined from atomistic simulations [50], and is a function of the temperature and the entire stress tensor, σ. The kink-pair nucleation energy ΔG_{kp} is also a function of temperature and the stress tensor, and allows manifestations of key aspects of plastic deformation in bcc metals (e.g. W), such as the tension-compression asymmetry, and the twinning-anti-twinning asymmetry [50]. $\tau_{e,\alpha}$ is the resolved shear stress on slip system α in terms of the Mandel stress:

$$\tau_e^{(\alpha)} = M_{\delta\gamma} s_\gamma^{(\alpha)} n_\delta^{(\alpha)} = W_{\delta\beta} F_{i\beta}^e F_{i\gamma}^e s_\gamma^{(\alpha)} n_\delta^{(\alpha)} \tag{11}$$

For the purposes of the present studies of creep deformation of tungsten at high temperature, we adopt a simplified version of the mobility law, given by:

$$v_g^{(\alpha)} = \frac{a_1 \tau_e^{(\alpha)} \Omega}{kT} \exp\left(\frac{-\Delta G_g}{kT} \right) \tag{12}$$

where a_1 and ΔG_g are fitting parameters.

The overall model is comprised of three conservation equations for the dislocation densities, and one rate equation for the average size (radius) of the subgrain. These are given by:

$$\frac{d\rho_m^{(\alpha)}}{dt} = v_{g,\alpha} (\rho_m^{(\alpha)})^{3/2} + v_{g,\alpha} \beta R_{sb} \rho_s^{(\alpha)} / h^2 - v_{g,\alpha} \rho_m^{(\alpha)} / (2R_{sb}) \tag{13}$$

$$-8(\rho_m^{(\alpha)})^{3/2} v_{cm} - \delta \rho_m (\rho_m^{(\alpha)} + \rho_s^{(\alpha)}) v_{g,\alpha} \tag{14}$$

$$\frac{d\rho_s^{(\alpha)}}{dt} = v_{g,\alpha} \rho_m^{(\alpha)} / (2R_{sb}) - 8\rho_s^{(\alpha)} v_{cs} / h - \delta v_{g,\alpha} \rho_m^{(\alpha)} \rho_s^{(\alpha)} \tag{15}$$

$$\frac{d\rho_b^{(\alpha)}}{dt} = 8(1 - 2\zeta) \rho_s^{(\alpha)} \frac{v_c}{h} - \left(\frac{\rho_b^{(\alpha)}}{R_{sb}}\right) M_{sb} (p_s - 2\pi r_p^2 N_p \gamma_{sb}) \tag{16}$$

$$\frac{dR_{sb}}{dt} = M_{sb} (p_s - 2\pi r_p^2 N_p \gamma_{sb}) - \mu \eta_v K_c R_{sb} [\rho^{1/2} - \frac{K_c}{2R_{sb}}] \frac{\Omega D_s}{kT} \tag{17}$$

The shear strain rate in slip system α is finally given by the Orowan–Baily relationship, which is needed to solve Equation 1 within the FE framework described in the previous subsection.

$$\frac{d\gamma_\alpha}{dt} = b \rho_m^{(\alpha)} v_g^{(\alpha)} \tag{18}$$

The first three conservation equations balance production (source) and annihilation rates. For $\rho_m^{(\alpha)}$, the first and second terms are the production rates from the mobile population and sub grain walls, respectively, the third is for annihilation at sub grain walls, the fourth is for climb recovery, and the last is for dynamic recovery. For $\rho_s^{(\alpha)}$, the first term is for immobilization at sub grain walls, the second is for climb recovery, and the last is for dynamic recovery. For $\rho_b^{(\alpha)}$, the first term is the production rate from static dislocations incoming into the boundary, the second is for annihilation of boundary dislocations by the creation of new sub grain surface. Finally, the rate equation for the sub grain radius is a balance between the growth rate by reduction of surface area, and the second is the rate of annihilation by creation of new sub grain surface.

Results

Model Calibration

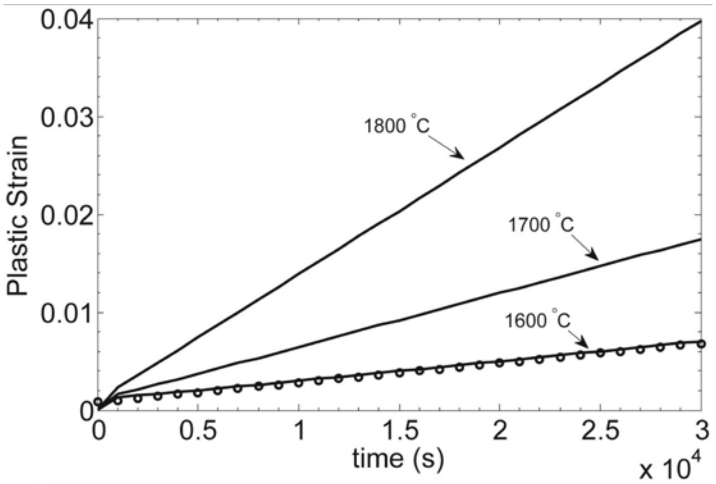

Figure 2. Model calibration results using fitting parameters given in table 1, experimental data (open circles) at 1600 °C taken from Robinson and Sherby [59].

The extended GMA model was first calibrated to obtain the best possible fitting parameters for the creep response of tungsten at high temperature. The results of the fitting procedure are shown in Figure 2 , together with experimental data at 1600 °C taken from reference [59]. The optimized set of fitting parameters are listed in table 1. The values of the atomic volume and magnitude of the Burgers vector were taken as $\Omega = 1.58\times10^{-29}\,\mathrm{m}^3$, and 0.274 nm, respectively. The current set of parameters listed in Table 1 reproduce the experimental data for the transient and steady state regime of tungsten creep at 1600 °C, and show that as the temperature is increased further, the creep rate increases significantly, as observed experimentally [59]. It is worth mentioning that a more extensive fitting procedure for creep strain as a function of temperature and stress has been previously achieved for the ferritic steel HT-9 in reference [32].

Table 1. Fitting parameters used in the viscoplasticity model for W

Parameter	Value	Unit	Description
β	1×10^{4}	-	Source density parameter
a_1	170	$m\ s^{-1}$	phonon drag parameter
ζ	0.2	-	static-to-boundary fraction
X_{jog}	0.0455	-	Jog fraction
D_0	1×10^{-11}	$m^2\ s^{-1}$ [59]	Diffusion pre-exponential
E_{self}	5.95	eV [59]	Self-diffusion energy
Q	18.2	Ω [60]	Activation Volume
ΔG_g	3.18	eV	Glide activation energy

Modeling Polycrystalline Materials

To demonstrate the feasibility of the computational algorithm discussed in Section 2, a simplified polycrystal model will be presented as an example. A five-grain tungsten polycrystal disc of diameter 0.6 um and height of 0.16 um, as shown in Figure 2, is subjected to a tensile strain rate of 0.02 s^{-1}. The top surface was allowed to move only in the z-direction, while the bottom surface was constrained to move only in x and y directions. For simplicity, only one slip system in each grain was considered, as shown in Figure 3. Detailed slip directions and slip plane normals are listed in Table 2.

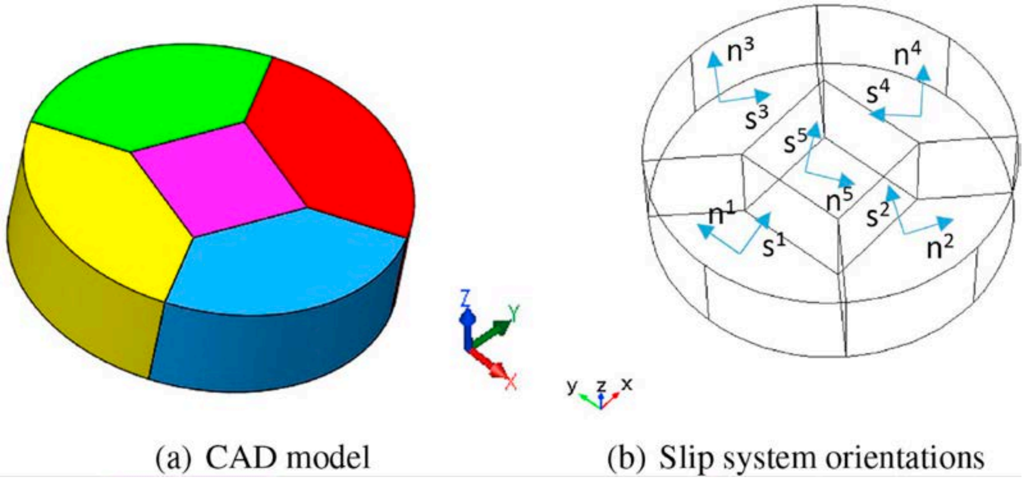

(a) CAD model (b) Slip system orientations

Figure 3. Five-grain tungsten polycrystal model.

Table 2. Slip system orientations

Slip system No.	Slip directions	Slip plane
1	[111]	$[\bar{1}01]$
2	$[\bar{1}11]$	$[0\bar{1}1]$
3	$[\bar{1}\bar{1}1]$	[011]
4	$[\bar{1}11]$	[101]
5	[111]	$[0\bar{1}1]$

The simulations were carried out at 1600 °C, with the GMA fitting parameters obtained in Subsection 2.2. All equations, including the ODEs in the GMA model and the weak form of the equilibrium Equation 3 were solved in the commercial COMSOL software.

The spatial distribution of the Cauchy stress in z-direction (σ_{zz}) in the deformed configuration is shown in Figure 4. Stress concentrations can be observed near the grain boundaries of different grains. This observation matches well with expectations, based on the orientations of assigned slip systems in the five grains. The stress-strain curves are plotted at one representative point inside each grain, as shown in Figure 5. It is interesting to note in this illustrative example that the stress field is quite inhomogeneous, and that stresses vary from grain to grain by almost a factor of 2 at a strain of ≈ 4%.

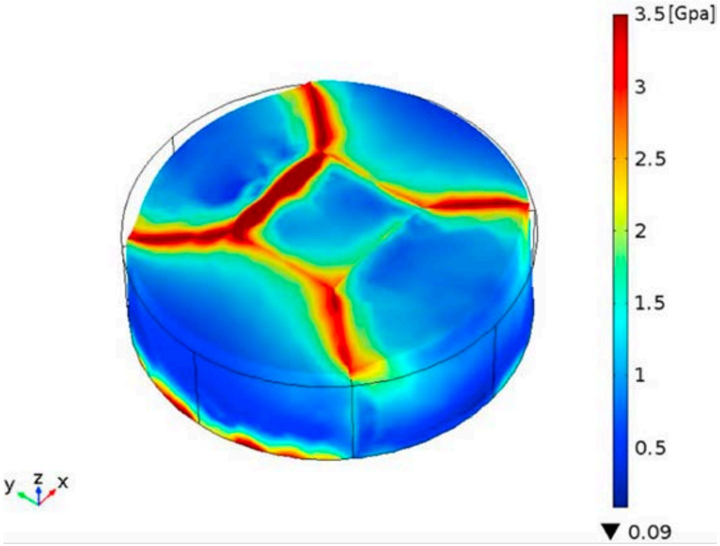

Figure 4. Von-mises stress distributions in 5 W grains. Note the severe stress concentrations at grain boundaries.

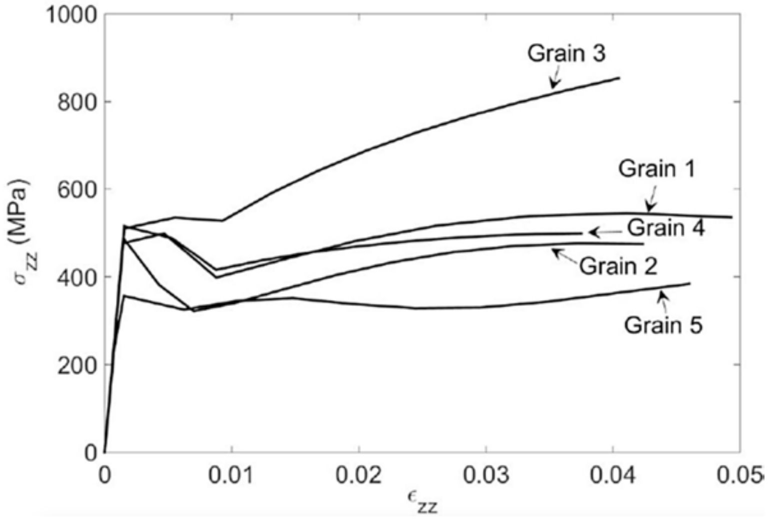

Figure 5. Stress-strain curves in the five tungsten grains. Note the strong variation of the stress-strain response, with the stress in grain 3 being more than twice the stress in other grains.

Viscoplastic Response to Cyclic Thermal Loading

The developed model has been further integrated into a multi-physics framework, where a transient heat conduction problem is coupled with the GMA-poly elastic-viscoplastic model. In this section, we present results of the multi physics model, assuming that tungsten behaves as a homogeneous elasto-viscoplastic material, ignoring the grain structure in the thin W coating around the rhenium core. We also assume that the rhenium core of the pillars behaves elastically. The thin tungsten layer did not exhibit a clear polycrystalline structure, while the stress range of the rhenium core in micropillars did not exceed its yield point. First, simulations were carried out for flat samples with a smooth W surface, which is exposed to repeated heating/ cooling plasma cycles. To contrast the mechanical behavior, additional simulations were carried out for just one micro-pillar, with all the details of coupling transient heat conduction with elasticity in the interior core of the pillar (Re) and elasto-viscoplasticity for the W coating.

The plasma-exposed samples are 2" diameter substrates made of molybdenum upon which W armor can be deposited. The flange is chosen to be made of this material as well in order to minimize the thermal stresses associated with testing at high temperatures. The samples must also be machined to allow for six taped (10-32) holes in order to secure the samples to the flange without leaking. The samples themselves have a cup-like structure in order to thin the layer being impacted with the heat flux sufficiently to generate a temperature gradient across the thickness of the sample. A three dimensional, rear, and cross sectional view of the sample geometry can be seen in Figure 6-(a), (b), and (c) respectively. The sample is 1" thick and the pocket or cup is machined to be offset 3 mm from the surface, in essence the heat flux is impinging upon a 3 mm thick surface being cooled on the back end.

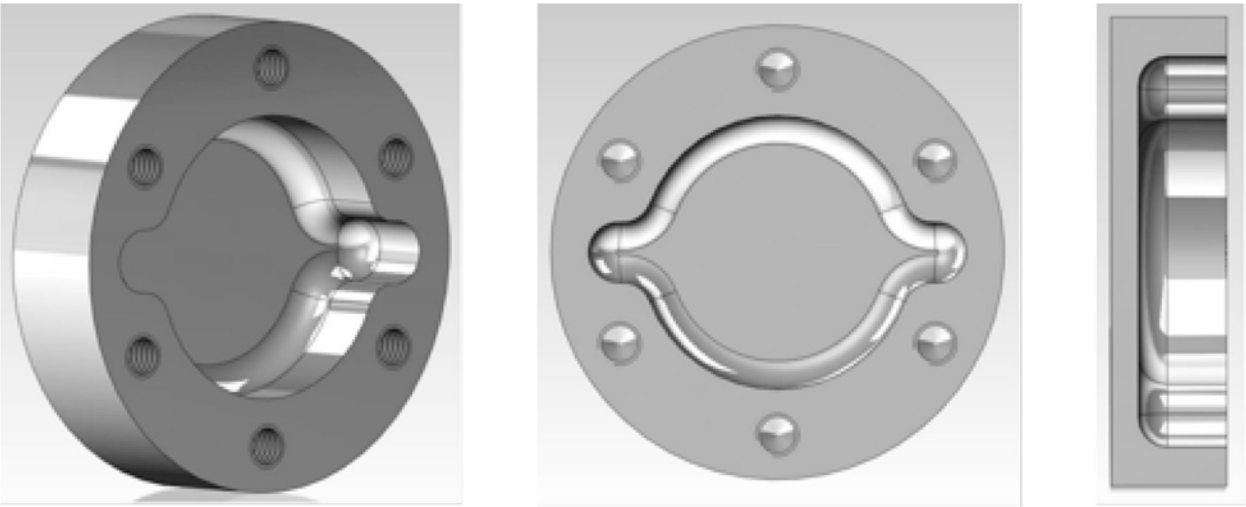

(a) (b)

Figure 6. Sample geometry (a) 3D view of sample showing back pocket (b) Rear view of sample, the six small holes on the perimeter are threaded in order to attach the sample to the flange, samples are 2" in diameter (c) Cross sectional view of sample, thickness is 0.5" and 0.118" at the thinnest point.

The back side of the sample is water cooled, and the cooling rate is controlled through the coolant velocity. The back side boundary condition has been set to simulate convective cooling, with the heat transfer coefficient being the control parameter. Typical simulation results for the surface stress (h=3 kW $m^{-2} K^{-1}$) are shown in Figure 8, where the color map is for the hoop stress at different times during a plasma exposure thermal cycle. It is seen that the hoop stress reverses from compressive to tensile, and by the end of the cool-down phase of the plasma cycle, it stays around 2 GPa. Such high tensile stress can explain our experimental findings reported in Part 1 that, for low rates of cooling, the sample fractures after only a few cycles of plasma exposure. The fracture toughness of polycrystalline W is high at temperatures above 800 $^{\circ}$C (around 100 MPa$\sqrt{m}$), but falls sharply to less that 20 MPa$\sqrt{m}$ as the temperature decreases below 400 $^{\circ}$C [61]. The dependence of the maximum surface hoop stress on the water cooling rate is shown in Figure 9. As the water cooling rate is increased, the maximum compressive hoop stress is delayed during the cycle on-time, and its value decreases. It is clear that as the sample is cooled more vigorously, the residual plastic strain becomes small, and that the sample does not have significant locked-in residual stresses at the end of the plasma cycle. The critical value of the heat transfer coefficient is found to be around 6 kW $m^{-2} K^{-1}$. Below this value, tensile stresses develop during the cool-down cycle, resulting in surface fracture.

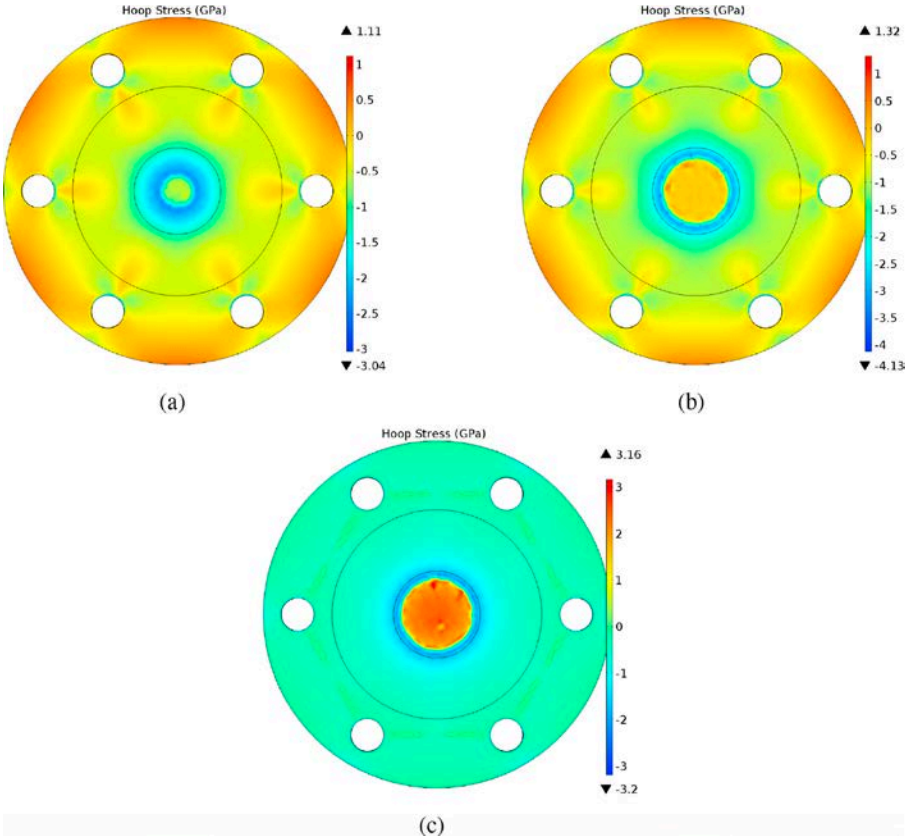

(a) (b)

(c)

Figure 7. Hoop stress distribution during a plasma exposure cycle (T_{on} =5 s, T_{off} =5 s), for h=3 kW m^{-2} K^{-1} . 2s Stress distribution at 2 s 4s at 6 s, 9s residual stress at 9 s.

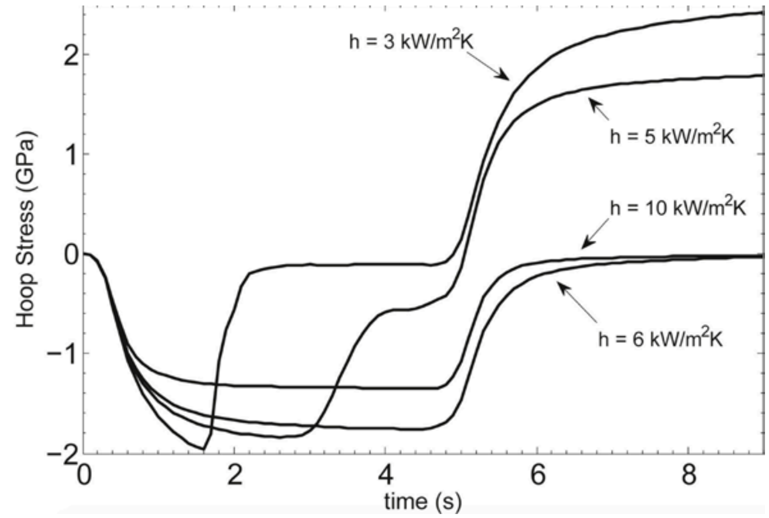

Figure 8. The influence of cooling on the development of residual stresses at the end of a plasma heat cycle. The maximum hoop stress is shown as a function of time for various values of the heat transfer coefficient, h.

The next set of simulations were conducted for micro-pillars that form the protective layer on top of the sample substrate. The micro-pillars were modeled as a 2 μm radius Re cylindrical core covered with a tapered W coat ranging in thickness from 0.5 μm at the thinnest point to 3 μm at the thickest point (base of the column), the pillar is 35 μm in height. An illustration of the pillars can be seen in Figure 10, where the residual stress distribution at 43 s (radial stress in Figure 8 , and tangential in Figure 9) is displayed as a color map. An incoming heat flux boundary condition was applied to the top of the pillar, while the bottom is modeled as connected to a semi-infinite solid. Adiabatic surfaces are assumed for the remaining boundaries as the vast majority of heat flow will enter and exit through the top and bottom of the micropillar, respectively. The micropillar is subjected to 6 pulses at a heat flux of 27 MW m^{-2} (T$_{\mathrm{on}}$=5 s, T$_{\mathrm{off}}$=2 s). The residual tangential and radial stresses are on the order of 1.3 GPa at the thinnest point of the W coating (towards the top of the pillar). Such a stress state could still be survivable without fracture given the small scale of the coating, however thermal fatigue would likely lead to fracture of the W coating in an extended thermal cycling environment, as was experimentally observed in Part 1.

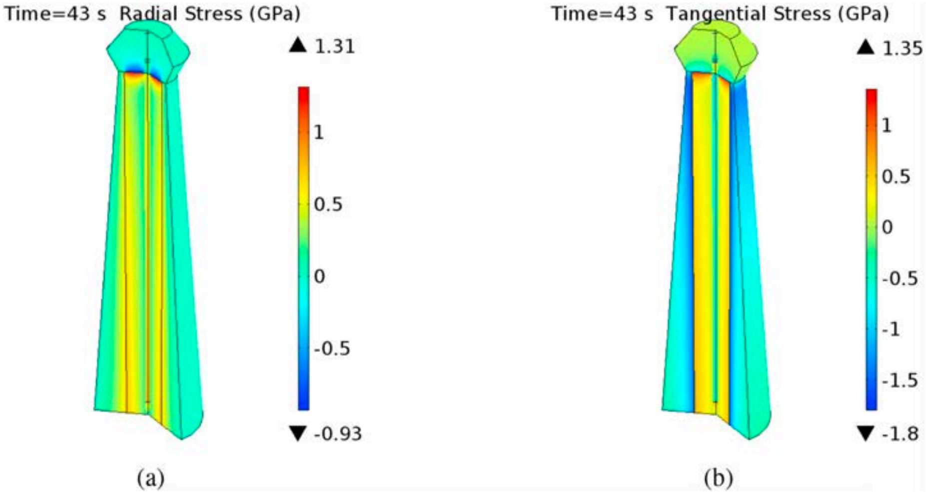

(a) (b)

Figure 9. Color maps of the radial and tangential stresses in a micropillar at the end of 6 plasma cycles. The heat flux is 27 MW m^{-2} (T$_{\mathrm{on}}$=5 s, T$_{\mathrm{off}}$=2 s). Note that the pillar is constructed of a Re pillar core with a W coating.

The contrast in the stress response of a micro-pillar relative to a conventional (planar) surface can be observed in Figure 9 for a 27 MW m^{-2} heat flux of 5 s duration. It is interesting to see that while the confinement of the cooler parts of the smooth surface sample causes high compressive stresses during the heat up phase, followed by high tensile residual stresses during cool-down, the micro-pillar behavior is quite the opposite. The rhenium core expansion during the heating part of the cycle puts the outer tungsten shell into tension, and residual stresses are relieved during the cool-down phase.The plastic strain plotted in Figure 9 shows that, while larger plastic strains accumulate at higher heat flux levels, samples with flat smooth surfaces clearly retain higher levels of plastic strain, as compared to micropillars. Tapering of the pillars appears to be helpful in that residual plastic strain is reduced even further. This can be understood on geometric grounds, since thicker tapered W shells distribute the tensile stress caused by the expansion of the inner Re core.

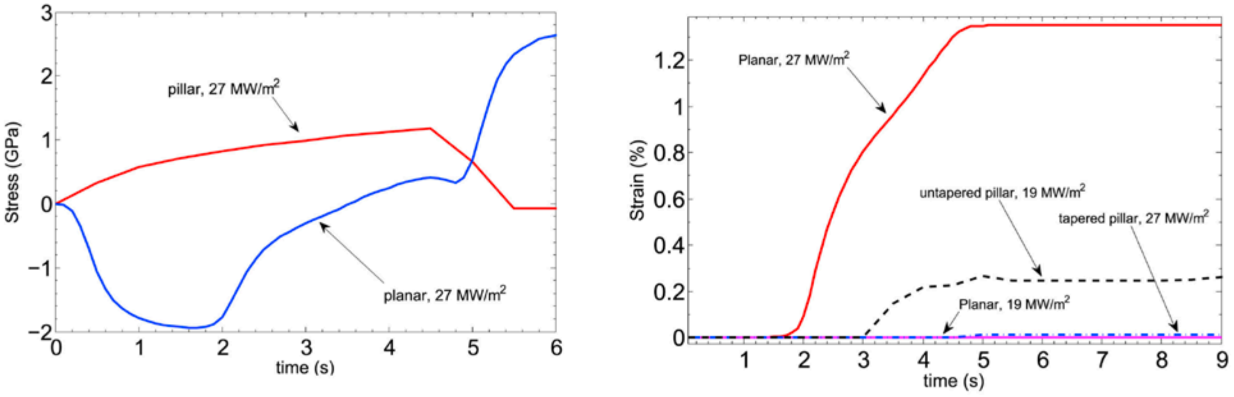

(a) (b)

Figure 10. (a) Tangential stress in a sample with a smooth planar surface compared to a sample with a W-Re pillar during a 5 s pulse at a heat flux of 27 MW m^{-2} . (b) Plastic strain in a smooth planar sample, tapered, and non-tapered W-Re micro-pillars, respectively, after one 5 s pulse.

Further changes in the geometry of the pillar can be shown to impact the stress response of the feature. The stress profile during a thermal pulse for a tapered and non-tapered micro-pillar is presented in Figure 10. The stress evolution for these slightly different geometries is similar but for the fact that the non-tapered variant was exposed to a much smaller heat flux of 19 MW/m^2 relative to the tapered counterpart in which a 27 MW/m^2 pulse was applied. Both pillar varieties experience tensile tangential stresses at the onset of the heat trial as would be expected from the larger expansion of the Re core, subsequent pulses however indicate that the W coat falls into a state of compressive residual stress. This compression stems from the contraction of the Re core upon cool-down of the pillar. The W coat is plastically deformed (expanded) under the aggressive Re pillar expansion during the first two thermal cycles, as the pillar cools the Re core attempts to contract back to its original dimension, in doing so it places the permanently enlarged W coat surrounding it into a state of compression. This thermomechanical condition amounts to placing the W coating under a state of pre-stress, all ensuing thermal pulses will have the effect of unloading the micro-feature from this residual stress. This demonstrates that a minor change in geometry can reduce the stress state and suggests an avenue for design optimization.

Because the plastic strain in the model is derived from the Orowan relation ($\dot{\varepsilon} = b v_g \rho_m$) the glide velocity ($v_g$) is a key variable controlling the deformation of a body. Corresponding glide velocities for a planar high heat flux sample (HHFS), tapered micro-pillar (TMP), and non-tapered micro-pillar (NTMP) are compared in Figure 10 for a given thermal loading scenario. The v_g for the tapered pillar is again shown to be markedly reduced compared to a flat W surface, and is a principal reason behind the resultant reduction of plastic strain in tapered pillars. This simple geometric change, allows more of the volume to distribute the body force generated due to plastic strain within the dendrite during a thermal transient event, and alleviates excessive plastic distortion. This reduces the chance of thermal cracking under repeated plasma loading.

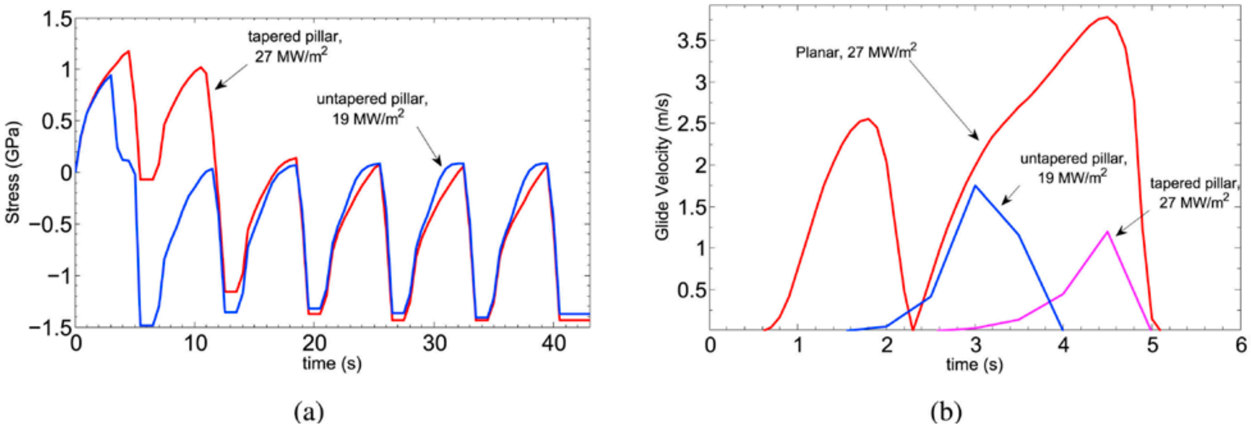

Figure 11. Applied heat flux of 27 MW/m^2 Tangential stress in the W-Re pillar during a series of six 5 s pulses, note the material is pre-stressed during the initial pulse glide velocity in both high heat flux (HHF) sample and W-Re pillar during a 5 s pulse.

Design of Resilient Surfaces

The stark difference in thermomechanical behavior between architectures suggested by Figure 10 for the tapered and non-tapered variants of the pillars implies that surface features can be designed to accommodate a given thermal loading scenario. In light of this, surface geometry which promotes heat dissipation will be a favorable candidate for surface architectures in thermally aggressive environments. Figure 12 demonstrates how changes in geometry such as taper vs. no-taper can impact the load seen by the pillar. For comparison, the figure shows the temperature rise experienced by a thin (1.5 mm) plate with a conventional surface undergoing a 27 MW/m^2 heat pulse on one face, and actively cooled on the opposing face (h = 10 kW/m^2). Mitigation of the temperature rise in tapered pillars even for a significant heat flux of 27 MW/m^2 demonstrates the potential that surface micro-engineering may have in the development of new thermal shielding.

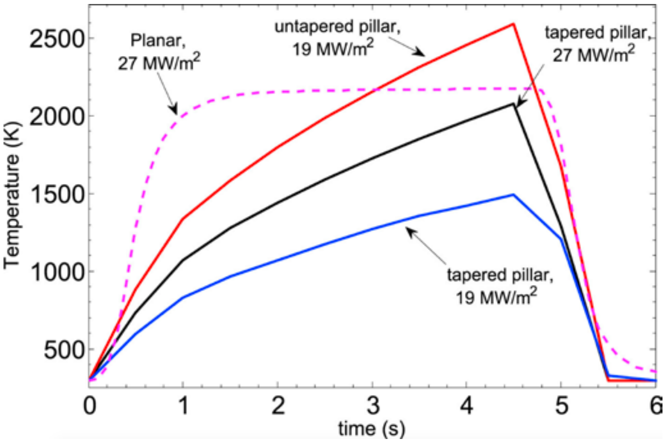

Figure 12. Comparison of the temperature profile at the surface of an actively cooled (h = 10 kW/m^2) planar high heat flux sample (HHFS) and micro-pillars for a single 5 s pulse, note how the tapered micro-pillar maintains a lower temperature for a pulse of the same magnitude (27 MW/m^2).

A snapshot of the stress profiles across the W coating of a pillar undergoing a 27 MW/m ^{2} heat pulse is shown in Figure 12. The stress is clearly concentrated at the Re-W interface, and decays towards the surface. Figure 12 displays the residual stress along the thickness of the W coating after 6 pulses of 27 MW/m ^{2} intensity. The surface of the pillar can be seen to remain in a state of compressive stress, and can differ significantly in magnitude depending on the shape. It should be noted that the tapered pillar experiences a reduced residual stress even across the thinnest span of the coating (0.5 μm) relative to the un-tapered variant with W-coating that is twice as thick (1 μm). Factors such as the diameter of the Re core and W coating thickness will determine whether the surface stress present after the loading cycle will be tensile or compressive. From Figure 12 it can be observed that thinner coatings will tend to remain in a state of residual compressive stress while thicker variants will tend towards a tensile surface stress. This result denotes a range of pre-stress conditions an architected surface may be placed under for operation in a given environment. The pre-stress can be designated during the design phase of the material and modified to best conform to the needs of the application by a simple modification of geometric parameters such as coating thickness and core pillar diameter.

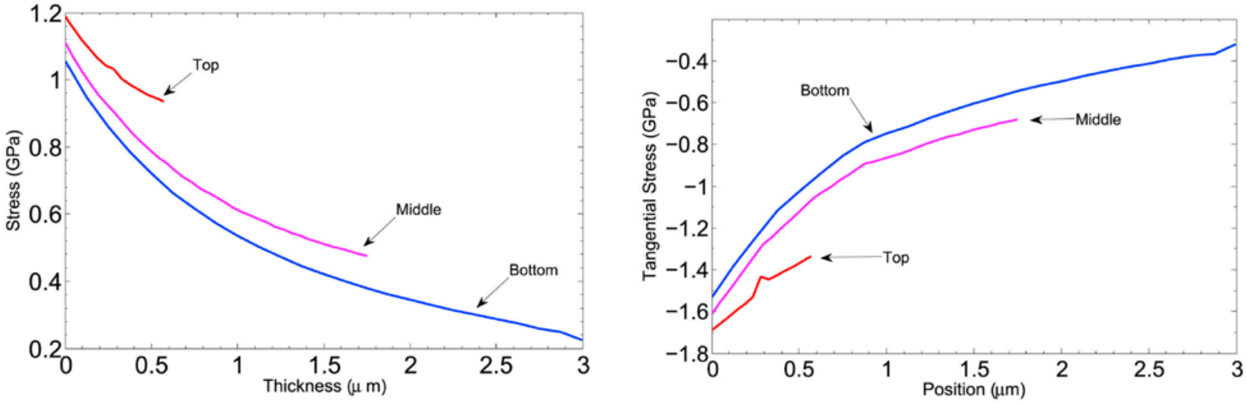

(a) (b)

Figure 13. Residual tangential stress profiles across the thickness of a tapered pillar at 3 s of a 5 s pulse, 27 MW/m ^{2} intensity, at different locations along the height, from the topmost region (T) where the thickness is the smallest (∶ 0.5 μm) to the base of the pillar where the thickness is greatest (B) (∶ 3 μm) residual stress in the W-coating. Broken lines represent straight W-Re dendrite, no taper, Re pillar (rod) radius = 2 μm, W-coating thickness is 1 μm, vs tapered pillar (solid lines), the tapered pillar profiles are taken at the end of 6 pulses or 43 s time, the 6 s snapshot for the non-tapered dendrite is the residual stress remaining after the initial pulse and illustrates ratcheting during the thermal cycle.

Due to the expansion constraints arising between W and Re, the maximum stress condition within the micro-pillar always arises at the interface between the two materials, in light of this, damage is in terms of plastic flow or cracking is most likely to originate at this location. Because this interfacial stress is the maximum stress seen by the pillar, minimization of this quantity will lead to residual stress reduction. In fact, the interface condition between the Re core and the W coating is not as sharp as assumed in the present calculations. During plasma transients, inter-diffusion will take place between Re and W, thus giving gradual changes in their elastic properties across the interface. Based on available inter-diffusion data, we estimate that the Re-W interface will extend well into the W coating after only a few plasma transients. Thus, the interface stresses determined here are to be taken as upper bounds.

Conclusions and Future Work

In this work, we presented a significant extension of the GMA viscoplasticity model, for simulations of plastic stress/strain distributions in materials undergoing cyclic thermal loading. The resulting plastic damage from the model is associated with fatigue-creep damage accumulation in materials exposed to cyclic high heat flux. The main motivation is to replace design rules of damage accumulation in mechanical components, where creep and fatigue phenomena are coupled and are hard to separate. Moreover, the model gives a desired link to the material's microstructure, where grain size, dislocation density and subgrains are described. Dislocation densities and subgrain evolution during thermomechanical cycles are well-described. Hence, the time dependence of microstructural features of plasma-facing components can be described in a way that is useful in assessing component reliability. Extension of the GMA model to polycrystalline materials within the framework of large deformation crystal plasticity has been demonstrated. The example studied here clearly shows large residual stresses at grain boundaries, which may result in grain boundary fracture or even grain ejection into the plasma.

Through direct comparison of the GMA viscoelasticity model and experimental results, we demonstrated the existence of a critical cooling rate, above which residual thermal stresses do not reverse and become tensile during the cooling part of the plasma cycle. It is shown experimentally and through modeling that if the effective heat transfer coefficient is less than 6 kW $m^{-2}K^{-1}$, large residual stresses build up on the surface, potentially leading to surface fracture. On the other hand, more aggressive cooling of plasma-facing surfaces results in the elimination of most of the tensile residual stress during the off-time of the plasma cycle.

A specific micro-engineered surface architecture that is composed on micro-pillars, each possessing an elastic Re core, and surrounded by a W shell has been designed, using CVD techniques. Unlike flat W surfaces that undergo tremendous compression during high heat flux plasma cycles, followed by stress several and potential surface fracture during the cooling cycle, the developed micro-engineered surfaces are shown to be quite resilient. Careful control of the W shell thickness and the Re core size of each micro-pillar through the CVD manufacturing process is shown to result in exactly the opposite behavior, as compared to flat W surfaces. The Re core first pushes on the W coating, putting it in tension during the heating phase, and when followed by contraction during the cooling phase of the plasma, the W-coating is put under compression. This would prevent surface fracture; which is a feature commonly observed in plasma-facing flat W samples. Subsequent plasma cycles are shown to result in the W coating mostly under compression, which is primarily caused by the pre-stress induced during the first few cycles.

The potential for development of materials with tailorable properties exists for plasma-facing components that are operating at extreme heat flux. Through modifications in surface geometry, it has been shown that materials can be made to perform beyond their apparent intrinsic limits. The model presented here reveals that small changes in the geometry of micro-features making up the surface of W armor can markedly alter their residual stress state. This opens a pathway for optimization of armor concepts based on the design of constituent micron-scale entities comprising the surface. In the thermal loading scenario studied here, the temperature rise was the sole contributor to the generation of stress. Consequently, ideal geometric configurations that exhibit large surface areas for quick heat dissipation are expected to offer greater performance margins.

Acknowledgements

This work is partially supported by the Air Force Office of Scientific Research (AFOSR), Award No: FA9550-11-1-0282 with UCLA, and by the US Department of Energy, Award Number DE-FG02-03ER54708 with UCLA. The technical assistance of Edward Gao with programming aspects of the GMA model is acknowledged.

References

[1] EW Parkes. Structural effects of repeated thermal loading. *Thermal Stress*, 1964.

[2] W Jiang and FA Leckie. A direct method for the shakedown analysis of structures under sustained and cyclic loads. *Journal of applied mechanics*, 59(2):251–260, 1992.

[3] J Bree. Elastic-plastic behaviour of thin tubes subjected to internal pressure and intermittent high-heat fluxes with application to fast-nuclear-reactor fuel elements. *The Journal of Strain Analysis for Engineering Design*, 2(3):226–238, 1967.

[4] TM Mulcahy. Thermal ratcheting of a beam element having an idealized bauschinger effect. *Journal of Engineering Materials and Technology*, 98(3):264–271, 1976.

[5] Hany F Abdalla, Mohammad M Megahed, and Maher YA Younan. A simplified technique for shakedown limit load determination. *Nuclear Engineering and Design*, 237(12):1231–1240, 2007.

[6] J Zarka, FC Arnaudeau, J Casier, and G Baylac. A practical method to determine elastic or plastic shakedown of structures. *Simplified methods in pressure vessel analysis*, 1978.

[7] George Webster and Robert A Ainsworth. *High temperature component life assessment*. Springer Science & Business Media, 2013.

[8] ASME Boiler and Pressure Vessel Code. section iii, 1998.

[9] ARS Ponter and S Karadeniz. An extended shakedown theory for structures that suffer cyclic thermal loading, part 1: Theory. *Journal of applied mechanics*, 52(4):877–882, 1985.

[10] H Mecking and K Lücke. Quantitative analyse der bereich iii-verfestigung von silber-einkristallen. *Acta Metallurgica*, 17(3):279–289, 1969.

[11] Thomas H Alden. Theory of plastic flow in strain-hardened metals. *Philosophical Magazine*, 25(4):785–811, 1972.

[12] H Mecking and UF Kocks. Kinetics of flow and strain-hardening. *Acta Metallurgica*, 29(11):1865–1875, 1981.

[13] Yu Estrin, LS Toth, A Molinari, and Y Bréchet. A dislocation-based model for all hardening stages in large strain deformation. *Acta materialia*, 46(15):5509–5522, 1998.

[14] FB Prinz and AS Argon. The evolution of plastic resistance in large strain plastic flow of single phase subgrain forming metals. *Acta Metallurgica*, 32(7):1021–1028, 1984.

[15] LP Kubin and Yu Estrin. Evolution of dislocation densities and the critical conditions for the portevin-le chatelier effect. *Acta metallurgica et materialia*, 38(5):697–708, 1990.

[16] Garani Ananthakrishna. Current theoretical approaches to collective behavior of dislocations. *Physics Reports*, 440(4):113–259, 2007.

[17] LP Kubin, C Fressengeas, and G Ananthakrishna. Collective behaviour of dislocations in plasticity. *Dislocations in solids*, 11:101–192, 2002.

[18] Daniel Walgraef and Elias C Aifantis. On the formation and stability of dislocation patterns?i: one-dimensional considerations. *International journal of engineering science*, 23(12):1351–1358, 1985.

[19] Daniel Walgraef and Elias C Aifantis. On the formation and stability of dislocation patterns?ii: two-dimensional considerations. *International journal of engineering science*, 23(12):1359–1364, 1985.

[20] Daniel Walgraef and Elias C Aifantis. Dislocation patterning in fatigued metals as a result of dynamical instabilities. *Journal of applied physics*, 58(2):688–691, 1985.

[21] Elias C Aifantis. The physics of plastic deformation. *International Journal of Plasticity*, 3(3):211–247, 1987.

[22] T Kameda and MA Zikry. Three dimensional dislocation-based crystalline constitutive formulation for ordered intermetallics. *Scripta materialia*, 38(4):631–636, 1998.

[23] WM Ashmawi and MA Zikry. Effects of grain boundaries and dislocation density evolution on large strain deformation modes in fcc crystalline materials. *Journal of computer-aided materials design*, 7(1):55–62, 2000.

[24] P Shanthraj and MA Zikry. Dislocation density evolution and interactions in crystalline materials. *Acta Materialia*, 59(20):7695–7702, 2011.

[25] P Shanthraj and MA Zikry. Dislocation-density mechanisms for void interactions in crystalline materials. *International Journal of Plasticity*, 34:154–163, 2012.

[26] A Arsenlis and DM Parks. Crystallographic aspects of geometrically-necessary and statistically-stored dislocation density. *Acta materialia*, 47(5):1597–1611, 1999.
[27] Athanasios Arsenlis and David M Parks. Modeling the evolution of crystallographic dislocation density in crystal plasticity. *Journal of the Mechanics and Physics of Solids*, 50(9):1979–2009, 2002.
[28] UF Kocks and H Mecking. Physics and phenomenology of strain hardening: the fcc case. *Progress in materials science*, 48(3):171–273, 2003.
[29] Franz Roters, Philip Eisenlohr, Luc Hantcherli, Denny Dharmawan Tjahjanto, Thomas R Bieler, and Dierk Raabe. Overview of constitutive laws, kinematics, homogenization and multiscale methods in crystal plasticity finite-element modeling: Theory, experiments, applications. *Acta Materialia*, 58(4):1152–1211, 2010.
[30] ME Kassner, MT Perez-Prado, M Long, and KS Vecchio. Dislocation microstructure and internal-stress measurements by convergent-beam electron diffraction on creep-deformed cu and al. *Metallurgical and Materials Transactions A*, 33(2):311–317, 2002.
[31] ME Kassner, P Geantil, and LE Levine. Long range internal stresses in single-phase crystalline materials. *International Journal of Plasticity*, 45:44–60, 2013.
[32] Nasr M. Ghoniem, JR Matthews, and Robert John Amodeo. A dislocation model for creep in engineering materials. *Res Mechanica*, 29:197–219, 1990.
[33] F.R.N. Nabarro. *Theory of Crystal Dislocations*. Oxford at the Clarendon Press, Oxford, England, 1967.
[34] J. Gittus. The mechanical equation of states: Dislocation creep due to stresses varying in magnitude and direction. *Philosophical Magazine*, pages 1423–1440, 1971.
[35] R. Bullough and J. R. Willis. Stress-induced point defect-dislocation interaction and its relevance to irradiation creep. *Philosophical Magazine*, 31:855, 1975.
[36] R. Bullough, M. W. Finnis, and M. H. Wood. A theory of irradiation and thermal creep by dislocation climb. *Journal of Nuclear Materials*, 104:1263, 1981.
[37] P. T. Heald and M. V. Speight. Steady-state irradiation creep. *Philosophical Magazine*, 29:1075, 1974.
[38] ME Kassner. Recent developments in understanding the mechanism of five-power-law creep. *Materials Science and Engineering: A*, 410:20–23, 2005.
[39] Robert J Amodeo and Nasr M Ghoniem. A review of experimental observations and theoretical models of dislocation cells and subgrains. *Res mechanica*, 23(2-3):137–160, 1988.
[40] D. Holt. Dislocation cell formation in metals. *Journal of Applied Physics*, 41:3197, 1970.
[41] A. S. Argon S. Takeuchi. Steady-state creep of single-phase crystalline matter at high temperature. *Journal of Applied Materials Science*, 11:1542–1566, 1976.
[42] T. G. Langdon. Dislocations and creep. *Proc. Conf. on Dislocations and the Properties of Real Materials, Royal Society of London*, page 221, 1984.
[43] K. D. Challenger and J. Moteff. Quantitative characterization of substructure of aisi-316 stainless-steel resulting from creep. *Metall Trans*, 4:749, 1973.
[44] D. J. Michel, J. Moteff, and A. J. Lovell. Substructure of type 316 stainless-steel deformed in slow tension atdegrees C. *Acta Metallurgica*, 21:1269, 1973.
[45] I. J. Cuddy. Internal stresses and structures developed during creep. *Metall Trans*, 1:395, 1970.
[46] J. H. Gittus. Multiaxial mechanical equation of states for a work-hardening/recovery model of dislocation creep. *Philosophical Magazine*, 25:1233, 1972.
[47] J. C. M. Li. Possibility of subgrain rotation during recrystallization. *Journal of Applied Physics*, 33(10), 1962.
[48] Rolf Sandstrom. Subgrain growth occurring by boundary migration. *Acta Metallurgica*, 25:905–911, 1977.
[49] Rolf Sandstrom. On recovery of dislocations in subgrains and subgrain coalescence. *Acta Metallurgica*, 25:897–904, 1977.
[50] Giacomo Po, Yinan Cui, and Cereceda David Rivera, David, Tom D. Swinburne, Jaime Marian, and Nasr Ghoniem. A phenomenological dislocation mobility law for bcc metals. *Acta Materialia* 119 (2016): 123-135.

[51] H. E. Evans and G. Knowles. Model of creep in pure materials. *Acta Metallurgica*, 25:963, 1977.

[52] E. Voce. The relationship between stress and strain for homogeneous deformation. *Inst Metals*, 74:537, 1948.

[53] W. G. Johnson and J. J. Gilman. Dislocation velocities, dislocation densities, and plastic flow in lithium fluoride crystals. *Journal of Applied Physics*, 30:129, 1950.

[54] G. A. Webster. In support of a model of creep based on dislocation dynamics. *Philosophical Magazine*, 14:775, 1966.

[55] U. Essmann and H. Mughrabi. Annihilation of dislocations during tensile and cyclic deformation and limits of dislocation densities. *Philosophical Magazine*, 40(6), 1979.

[56] J. H. Gittus. Theoretical value of ratio (K) of cell diameter to dislocation spacing for a material undergoing dislocation-creep. *Philosophical Magazine*, 35:293, 1977.

[57] J. H. Gittus. Theoretical relationship between free-energy and dislocation cell diameter during creep. *Philosophical Magazine A*, 39:829, 1979.

[58] J. Friedel. *Dislocations*. Addison-Wesley Publishing Company, Inc., 1964.

[59] SL Robinson and OD Sherby. Mechanical behavior of polycrystalline tungsten at elevated temperature. *Acta Metallurgica*, 17(2):109–125, 1969.

[60] Peter L Raffo. Yielding and fracture in tungsten and tungsten-rhenium alloys. *Journal of the Less Common Metals*, 17(2):133–149, 1969.

[61] B Gludovatz, S Wurster, A Hoffmann, and R Pippan. Fracture toughness of polycrystalline tungsten alloys. *International Journal of Refractory Metals and Hard Materials*, 28(6):674–678, 2010.

7.5 CONTROLLING STRAIN BURSTS AND AVALANCHES AT THE NANO-TO-MICRO SCALE—Y.N. Cui, G. Po, N.M. Ghoniem (University of California, Los Angeles)

OBJECTIVE

The purpose of this work is to gain a fundamental understanding of the underlying physics and statistical laws of intermittent crystal plasticity. This knowledge is needed to direct innovative approaches to overcome the deformation uncontrollability and catastrophic collapse issues for nano- and micro-scale materials, especially under irradiation.

SUMMARY

We demonstrate, through 3-dimensional discrete dislocation dynamics simulations, that the complex dynamical response of nano and micro crystals to external constraints can be tuned. Under load rate control, strain bursts are shown to exhibit scale-free avalanche statistics, similar to critical phenomena in many physical systems. For the other extreme of displacement rate control, strain burst response transitions to quasi-periodic oscillations, similar to stick-slip earthquakes. External load mode control is shown to enable a qualitative transition in the complex collective dynamics of dislocations from self-organized criticality to quasi-periodic oscillations. It opens new possibilities for novel experiments with a faster response rate than currently obtainable, which can be designed to explore this regime.

PROGRESS AND STATUS

Introduction

The realization that the release of plastic strain by intermittent bursts exhibits ubiquitous power law scaling avalanche behavior have stimulated recent interest in understanding whether complex dislocation dynamics can be described similar to self-organized critical (SOC) nonequilibrium natural systems (such as earthquakes, sand pile sliding). In a SOC system, the dynamics has an attractor characterized by infinite correlation time and length, hence displaying scale-free scaling. A key hypothesis behind this abstraction is that the driving force varying rate is much slower than the internal relaxation rate [1] of a system undergoing SOC. Nevertheless, since this condition may not always hold, one wonders if the qualitative aspects of a system's dynamical behavior change when the driving force changing rate is comparable to its internal relaxation rate? Our objective here is to investigate the relationship between the external driving force and relaxation dynamics associated with strain bursts during nano- and micro-scale plastic deformation of crystals.

Simple model estimation

At the smallest of physical scales (e.g. nano-to-micro scale), the release of plastic strain by intermittent “bursts" has been found to belong to this power-law scaling behavior [2, 3].One additionally unique aspect of plasticity is that the driving force varying rate can be experimentally tailored. Considering a simple but illustrative case, a pillar is subjected to uniaxial compression in Figure 1a. The force actuator, typically a voice coil, can exert an open-loop stress rate $\dot{\sigma}_0$ and/or be controlled to impose a strain rate $\dot{\varepsilon}_0$. For a proportional controller with stiffness Kp, the internal stress rate in the pillar is,

$$\dot{\sigma} = \frac{\alpha E}{1+\alpha}\left(\dot{\varepsilon}_0 - \dot{\varepsilon}^p\right) + \frac{\dot{\sigma}_0}{1+\alpha} \tag{1}$$

where $\alpha = K_p / K$ is the relative stiffness ratio, $K=EA/H$ is the pillar stiffness, E, A and H are the Young module, cross section area and height of the pillar, respectively. $\dot{\varepsilon}^p$ is the plastic strain rate due to all internal dislocation dynamical activities. Once the stiffness ratio α is infinitely large, or $\dot{\sigma}_0$ and $\dot{\varepsilon}_0$ are very low, $\dot{\sigma}$ becomes very sensitive to $\dot{\varepsilon}^p$, implying that the driving force changing rate ($\dot{\sigma}$) is dominated by and comparable to its internal relaxation rate ($\dot{\varepsilon}^p$). This indicates that the corresponding slip statistics are expected to violate SOC.

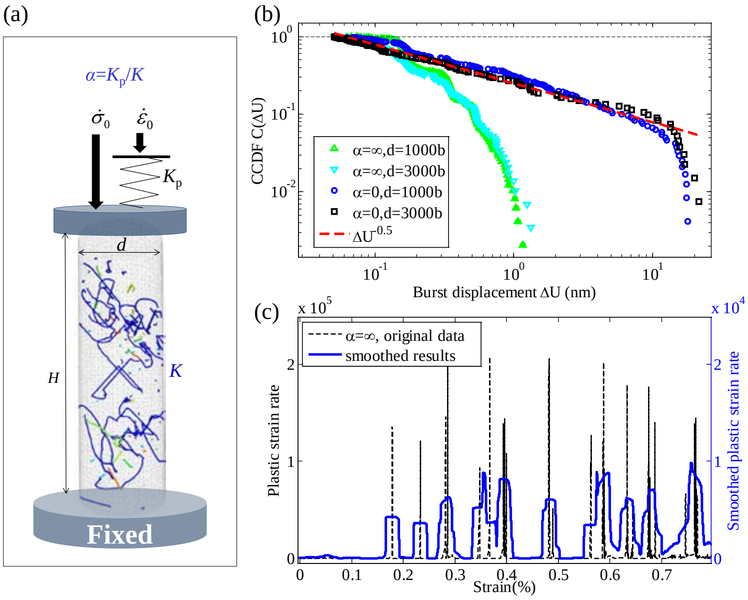

Figure 1. (a) Simplified sketch of pillar compression with an open-loop and closed-loop control. (b) Complementary cumulative distribution function of burst displacement under pure strain control ($\alpha=\infty$) and pure stress control ($\alpha=0$) for pillars of different diameters d. (c) Typical results of the evolution of plastic strain rate and its averaged value in 0.24 μs windows, showing quasi-periodic strain bursts under pure strain control.

Dislocation Dynamics Simulation results

The vast majority of existing submicron mechanical testing experiments can only cover a narrow range of machine stiffness. In addition, the current experimental controller response rate is much slower than sample plastic relaxation rate by about 4 orders of magnitude. Therefore, most previous experimental conditions correspond to the regime where SOC is observed. Discrete dislocation dynamics (DDD) studies, as a computer simulation tool, make it possible to supplement experimental testing and explore regimes that are currently difficult to access experimentally [4]. The current research presents the first systematic 3D-DDD investigation on the slip statistics at submicron scale, accounting for the effects of the interaction of an external loading mode. Compared with most of existing two dimensional (2D) DDD studies, the key approximations inherent in 2D techniques are resolved. Specifically, dislocation junction formation and destruction, and the occurrence of cross slip are all accounted for with minimal ad hoc assumptions.

The simulation setup is shown in Figure 1a. We conducted simulations of compression tests on Cu pillars of different diameters, ranging from 1000-3000 b (~300 nm- 1 μm), where b is the burgers vector magnitude. Two extreme machine stiffness cases are first considered, corresponding to "pure strain control" ($\alpha=\infty$) and "pure stress control" ($\alpha=0$). Fifty and twenty separate simulations with different initial dislocation configurations are carried out under each loading mode for d=1000 b and d=3000 b, respectively.

Figure 2a shows some typical stress-strain curves under different loading modes. Figure 1b presents the results of statistical analysis of the burst displacement magnitude ΔU. To obtain maximum resolution of the limited simulation data set, the complementary cumulative distribution function (CCDF) is used. Figure 1b clearly illustrates that ΔU, under pure stress control, exhibits a well-defined power law distribution spanning several orders of magnitude. The power law exponent for the corresponding probability density is found to be 1.5, agreeing well with the generally accepted range of 1.35 ~ 1.67 [2, 3]. In contrast, the CCDF of ΔU under pure strain control seems not to exhibit power-law scaling behavior for both small and large system sizes. Meanwhile, most of the data concentrate within one order of magnitude. When discussing the temporal statistics of earthquakes, distinct dynamical behaviors are distinguished by the coefficient of variation $C=S_x/m_x$ [5], where S_x and m_x are the standard deviation and mean value, respectively. For the cases of $C>1$ and $C<1$, the distribution is referred to as "clustered" and "quasi-periodic", respectively. Taking the results of ΔU here, C is calculated as 1.9 and 0.9 under pure stress and pure strain control, respectively. This suggests that the dynamical behaviors under pure strain control become quasi-periodic. Similar to previous studies [6], quasi-periodicity here is found to be stochastic, due to the intrinsic scatter induced by random cross slip or different dislocation configurations. Quasi-periodic strain bursts under pure strain control are manifested through the smoothed plastic strain rate, as clearly shown in Figure 1c.

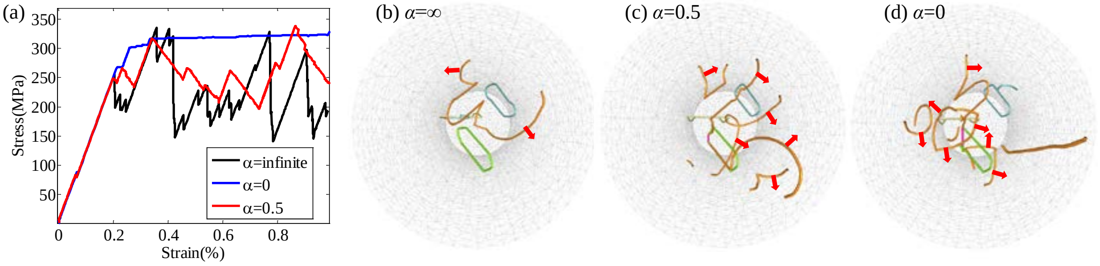

Figure 2. Typical simulation results under different loading modes for pillar with d=1000 b. (a) Stress-strain curves; (b-d) Snapshots of dislocation configurations (from top view) at a strain value of 0.4%, arrows indicate the bowing out directions of activated sources

Close examination of dislocation configuration evolution reveals that the mechanisms that control avalanche versus quasi-periodic burst behavior are significantly different. Under pure strain control, each strain burst is found to be dominated by sequential activation and deactivation of single arm dislocation sources in the submicron regime (see Figure 2b). Even if a weaker source is formed during one burst event, sometimes it also cannot operate due to the lower prevailing stress after relaxation. This makes it difficult to trigger simultaneous operation of multiple dislocation sources. By contrast, dislocation avalanche under pure stress control is clearly associated with correlated dislocation motion. If one activated source leads to the formation of a weaker one, it can be immediately activated. All correlated sources contribute then to an increasing magnitude of the strain burst, turning it into an "avalanche" (see Figure 2d).

Dislocation based branching model

To further elucidate the statistical difference between avalanches versus quasi-periodic dynamics, a simple dislocation based branching model is proposed. It is inspired by the present 3D-DDD simulations, and motivated by Zapperi's sand-pile branching model [7], in which we translate the branching idea into dislocation language. The discrete plastic deformation is assumed to mainly proceed through the intermittent activation of dislocation sources. One activated source may lead to the stochastic generation/activation of other sources, similar to a branching process shown in Figure 3a. Figure 3b presents predicted typical stress-strain curves under different loading modes, which agree well with our simulation results in Figure 2a, including the stress level and the stepped or serrated burst features. In addition, the power law scaling of burst displacement ΔU is also well reproduced under pure stress control in Figure 3c. It clearly indicates that as the machine stiffness increases, the power law tails gradually become too wide to recognize proper scale-free power law statistics.

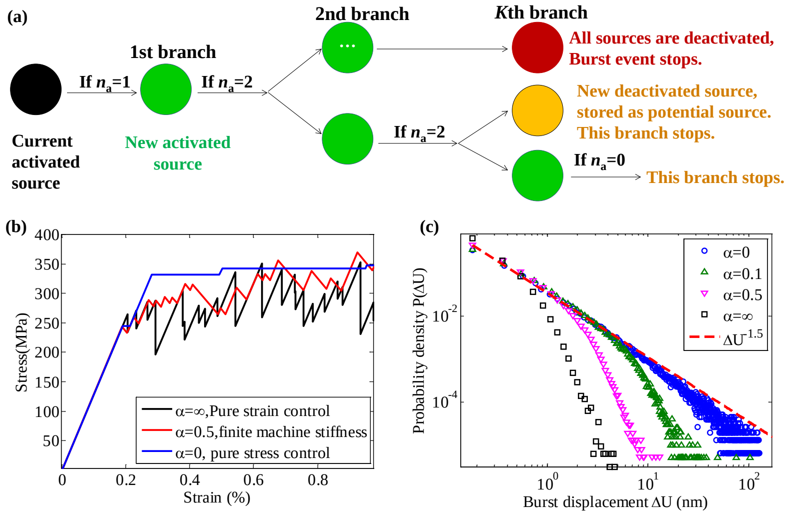

Figure 3. (a) Schematic showing the random branching dislocation source generation and activation process, n_a is the number of newly generated dislocation sources, green filled circles represent that new source is activated, only activated source may trigger further branching process; (b) Typical predicted stress-strain curve for pillar with *d*=1000 b, (c) Predicated probability density function of burst displacement for different machine stiffness.

Acknowledgements

This work is supported by the U.S. Department of Energy, Office of Fusion Energy Sciences, Grant number DE-FG02-03ER54708 with UCLA.

References

[1] P. Bak. How nature works: the science of self-organized criticality, New York, NY: Copernicus Press, (1996).
[2] F.F. Csikor, C. Motz, D. Weygand, M. Zaiser, S. Zapperi. Dislocation avalanches, strain bursts, and the problem of plastic forming at the micrometer scale, Science 318 (2007) 251.
[3] D.M. Dimiduk, C. Woodward, R. LeSar, M.D. Uchic. Scale-Free Intermittent Flow in Crystal Plasticity, Science 312 (2006) 1188-1190.
[4] G. Po, M. Mohamed, T. Crosby, C. Erel, A. El-Azab, N. Ghoniem. Recent Progress in Discrete Dislocation Dynamics and Its Applications to Micro Plasticity, JOM 66 (2014) 2108-2120.
[5] Y. Ben-Zion. Collective behavior of earthquakes and faults: Continuum-discrete transitions, progressive evolutionary changes, and different dynamic regimes, Reviews of Geophysics 46 (2008).
[6] S. Papanikolaou, D.M. Dimiduk, W. Choi, J.P. Sethna, M.D. Uchic, C.F. Woodward, S. Zapperi. Quasi-periodic events in crystal plasticity and the self-organized avalanche oscillator, Nature 490 (2012) 517-521.
[7] S. Zapperi, K.B. Lauritsen, H.E. Stanley. Self-Organized Branching Processes: Mean-Field Theory for Avalanches, Physical Review Letters 75 (1995) 4071-4074.

8. MODELING PROCESSES IN FUSION SYSTEM MATERIALS

8.1 DEVELOPMENT OF INTERATOMIC POTENTIALS IN TUNGSTEN-RHENIUM SYSTEMS

—W. Setyawan and R. J. Kurtz (Pacific Northwest National Laboratory), and N. Gao (Institute of Modern Physics, Chinese Academy of Science, China)

OBJECTIVE

The objective of this research is to develop interatomic potentials for exploring radiation damage in W in the presence of solid trans-mutant Re and radiation-induced precipitation of W-Re intermetallics.

SUMMARY

New reference data are generated using ab initio methods corresponding to interstitial configurations in bcc W and hcp Re. Initial fits of EAM potentials for pure W and Re systems are presented. Several parametrizations are explored. For W, the order of stability among bcc, fcc, and hcp can be reproduced. However, the potentials typically predict the <100> dumbbell to be the most stable interstitial configuration. For Re, the order of stability among hcp, fcc, and bcc is also reproduced. Notably, the Re potential labeled as Re_eam_1/set22 predicts the correct ground state for the interstitial configuration, namely configuration C, consistent with DFT, however its formation energy is 8.07 eV compared to DFT value of 6.52 eV.

PROGRESS AND STATUS

Update on Tungsten

In the previous report, a preliminary fitting of the W potential was presented where the potential reproduced the equation of state adequately. In this report, this potential is labeled as W_eam_1. Ab initio forces, energies, and stresses of reference structures were used in the fit. The reference structures were single phases of bcc, fcc, hcp, and simple cubic, bcc with hydrostatic strains from -0.2 to 0.2, nine melt structures (three melts, each with hydrostatic strains of -0.05, 0, and 0.2), bcc 54-atom structures with various numbers of vacancy, slab systems of {100}, {110}, and {111} surfaces (each with two different thicknesses). For this potential, an EAM formulation with the following parametrization was used:

$$E = \frac{1}{2}\sum_{i,j(j\neq i)} \phi_{s_i s_j}(r_{ij}) + \sum_i F_{s_i}(\rho_i) \tag{1}$$

$\phi_{s_i s_j}$ is the pair interaction that depends on the type s_i of atom-*i* and type s_j of atom-*i* and the distance between the atoms r_{ij}. The functional F_{s_i} is the embedding energy, which is a function of the electron density ρ_i at the location of atom-*i* induced by all other atoms. The electron density ρ_i is given by

$$\rho_i = \sum_{j\neq i} \rho_{s_j}(r_{ij}) \tag{2}$$

where ρ_{s_j} is the atomic electron density function of atom-*j*. The pair interaction is parameterized with a polynomial and a smoothing cutoff function as follows:

$$\phi(r) = \psi\left(\frac{r - r_c}{h_1}\right)\sum_{n=0}^{5} a_n (r - r_0)^n \tag{3}$$

where the cutoff function ψ is given by

$$\psi(x) = \frac{x^4}{1 + x^4} \tag{4}$$

The embedding energy is parameterized with the following polynomial that ensures it is zero when the electron density vanishes. The atomic electron density is parameterized with a screened Coulomb function multiplied with a smoothing cutoff function:

$$\rho(r) = \psi\left(\frac{r - r_c}{h_2}\right)\frac{b_1}{r}e^{-b_2 r} \tag{5}$$

$$F(\rho) = \sum_{n=1}^{5} c_n \rho^n \tag{6}$$

Table 1. Fitted parameters of the W_eam_1 and W_eam_1b. Energies are in eV and distances are in Å. The cutoff distance of the potential is set at r_c = 6.6 Å which represents the midpoint between the 6th and 7th nearest-neighbor distances in bcc.

Parameters	W_eam_1	W_eam_1b
r_c	6.6	6.6
a_0	-23.68505	-15.51469
a_1	-1.18950	7.14636
a_2	8.56144	-0.13522
a_3	7.98912	-21.37304
a_4	-4.49762	-23.31562
a_5	-10.39484	-8.73693
r_0	3.50644	3.97355
h_1	8.11175	8.16291
b_1	6.61199	6.11802
b_2	1.03695	0.97053
h_2	0.10532	0.00544
c_1	-5.09856	-8.38035
c_2	4.54812	7.08477
c_3	-1.47838	-1.72095
c_4	0.27400	-0.35073
c_5	-0.01957	0.15538

In this report, the melting behavior and defect formation energies are evaluated. The melting point is determined by increasing the temperature in which at each temperature, MD relaxation is performed for 200,000 steps under the *NPT* ensemble. The time step is 1 fs. The radial distribution function (RDF) is calculated at each temperature after a full relaxation. The RDFs at different temperatures are shown in Figure 1. The corresponding configurations are shown in Figure 2. The results indicate that W becomes locally disordered at 3500 K and completely disordered at 5400 K. The experimental melting temperature is 3,695 K. Future simulations are needed to determine the melting temperature more accurately by monitoring a solid/liquid interface as a function of temperature. Table 2 summarizes the cohesive energies, lattice constants, and defect formation energies. Starting from W_eam_1, another fit is performed by adding <111>, <110>, and <100> dumbbell structures in the reference, and labeled as W_eam_1b. Table 1 shows the fitted parameters for W_eam_1b. Table 2 summarizes the defect formation energies. Compared to W_eam_1, W_eam_1b yields stable configurations of db111, db110, db100, O (interstitial atom at an octahedral site), and T (interstitial atom at a tetrahedral site). Nevertheless, W_eam_1 and W_eam_1b fail to yield db111 as the ground state configuration for an interstitial atom, and further improvement is needed. Additional DFT calculations are performed to obtain the interstitial configurations at O and T sites, which will be added to the reference structure for future fitting. Different parametrizations may also be explored in the future to improve the fit.

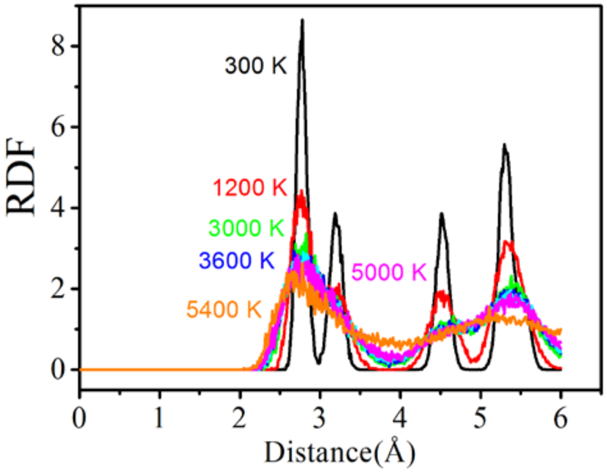

Figure 1. Radial distribution function of W at various temperatures.

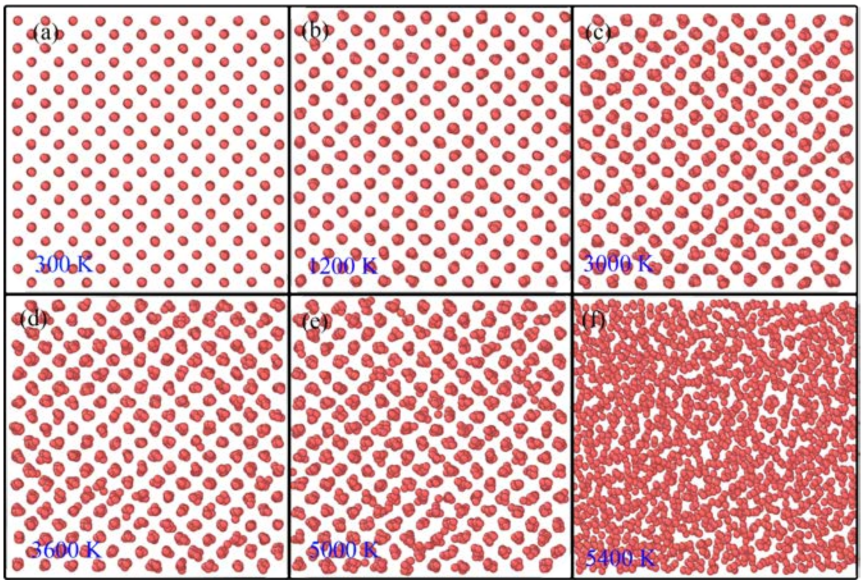

Figure 2. Snapshot of atomic structure of W at various temperatures.

Table 2. Evaluation of W_eam_1 and W_eam1b compared to DFT. Cohesive energies (E_c) and defect formation energies are in eV and lattice constants are in Å. The DFT cohesive energies have been shifted such that the bcc matches the experimental value. When an initial interstitial configuration is unstable after relaxation, the final configuration is presented in place of the formation energy.

Property	DFT (4x4x4 cell)	W_eam_1	W_eam_1b
a (bcc)	3.1856	3.1962	3.1861
E_c bcc	8.90	8.90	8.89
E_c hcp	8.41	8.71	8.75
E_c fcc	8.42	8.47	8.54
vac	3.15	4.06	4.24
db111	10.07	6.26	7.32
db110	10.89	6.09	7.27
db100	12.01	5.41	7.14
O	12.06	db100	7.14
T	11.54	db100	7.10

Update on Rhenium

DFT calculations are performed for interstitial configurations in hcp Re. The interstitial locations are shown in Figure 3. Defect configurations are created using an orthorhombic cell containing 180 atoms (i.e. the undefected cell contains 180 atoms). Following a convergence test of defect formation energies with respect to **k**-points, a Γ-centered grid of 4x4x4 is sufficient to converge the defect formation energies to within 10 meV. Table 3 summarizes the formation energies.

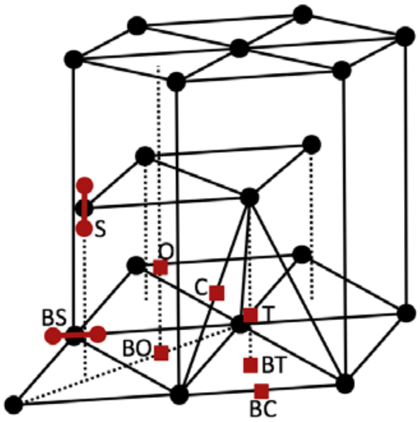

Figure 3. Schematic drawing showing interstitial locations in hcp.

For Re, the first EAM parametrization is as follows:

$$\phi(r) = \psi\left(\frac{r - r_c}{h_1}\right) D[(1 - \exp(-\alpha r))^2 - 1] \tag{7}$$

where the cutoff function ψ is previously given in Equation (4). The atomic electron density follows Equation (5). The embedding energy is:

$$F(\rho) = c_1\sqrt{\rho} + c_2\rho^2 \tag{8}$$

The reference structures for fitting include those reported in the previous report [1] as well as the defect configurations that are presented in this report. At the beginning, the pair interaction is set to zero, the atomic density is set with b_1 = 7 (corresponding to the valence of Re), h_2 = 0.01 (i.e. with minimal cutoff smoothing), and b_2 is solved to give electron density of 1 at the reference hcp structure, b_2 is found to be 1.29175. Then the embedding function is fit. In the next stage, the embedding energy is divided by two aiming at an equal partition with the pair interaction, and the pair interaction is fit keeping the atomic density and embedding energy fixed. Fifty trial sets of parameter values are generated randomly. The best set is taken for the next stage. In the next stage, the pair interaction, atomic density, and embedding energy are optimized at the same time. Again, fifty trial sets are generated randomly. While most sets correctly predict hcp to be the ground state, they predict fcc to be less stable than hcp by only about 2 meV/atom, except set22 (labeled as Re_eam_1/set22) where the difference is > 10 meV/atom. Evaluation of set22 is presented in Table 3 and its fitted parameters are given in Table 4. Set22 correctly gives interstitial configuration C to be the most stable; however, configurations O, S, and T are not stable and relax to C.

The second EAM parametrization that is explored is the following. Sum functions of cubic polynomials are added to the POTFIT code. The pair interaction is:

$$\phi(r) = \sum_{i=1}^{15} f_i(a_i - r)^3\theta(a_i - r) \tag{9}$$

where θ is a Heaviside step function. The atomic density is:

$$\begin{gathered} \rho(r) = \textstyle\sum_{i=1}^{4} g_i(b_i - r)^3\theta(b_i - r), \text{ for } r \geq r_{min} \\ r = r_{min}, \text{ for } r < r_{min} \end{gathered} \tag{10}$$

The embedding energy follows Equation (8). The potentials from this second parametrization are labeled with Re_eam_2. The starting atomic density is taken from that of tungsten EAM [2] multiplied by 7/6 (ratio of the electronic valence of Re and W). Then the fit proceeds with a similar procedure as previously described. With this parametrization, most sets predict hcp to be the ground state and a good number of them also predict fcc to be less stable than hcp by at least 60 meV/atom (the DFT difference between hcp and fcc is 60 meV/atom). However, none of the sets predicts interstitial configurations C, S, or T to be the most stable (DFT data shows that C, S, and T are the most stable configurations within 10 meV). Typically, the sets from this fit give BC or distorted O to be the most stable. Evaluation of set49 (Re_eam_2/49) is presented in Table 3 with its fitted parameters given in Table 5. Future work will include parametrization using piecewise splines for more flexibility. The first parametrization, which uses simple analytical functions (Equations 7-8), is intended to provide a reasonable starting point for the splines through curve fitting, e.g. using Re_eam_1/set22. Different numbers and positions of the spline knots will be explored.

Table 3. Evaluation of Re_eam_1 and Re_eam_2 compared to DFT. Cohesive energies (E_c) and defect formation energies are in eV and lattice constants are in Å. The DFT cohesive energies have been shifted such that the hcp matches the experimental value. The experimental lattice constants for hcp is a = 2.76 Å and c/a = 1.615. When an initial interstitial configuration is unstable after relaxation, the final configuration is presented in place of the formation energy.

Property	DFT (180-atom cell)	Re_eam_1/set22	Re_eam_2/set49
a (hcp)	2.7766	2.7554	2.8017
c/a (hcp)	1.6155	1.6478	1.5855
E_c hcp	8.03	8.02	8.04
E_c fcc	7.97	8.01	7.96
E_c bcc	7.72	7.95	7.84
vac	3.08	2.70	2.99
C	6.52	8.07	distorted O
O	8.13	C	7.93
S	6.53	C	BC
T	6.52	C	BC
BO	7.41	8.29	8.07
BS	8.09	8.27	BC
BT	BO	BO	BC
BC	BO	BS	7.91

Table 4. Fitted parameters for Re_eam_1/set22. Energies are in eV and distances are in Å. The cutoff distance of the potential is set at r_c = 5.4 Å which represents the midpoint between the 5th and 6th nearest-neighbor distances in hcp.

Parameters	Re_eam_1/set22
r_c	5.4
D	1.47090
α	1.25872
h_1	2.71771
b_1	11.02242
b_2	1.34338
h_2	0.14918
c_1	-5.31949
c_2	1.35412

Table 5. Fitted parameters for Re_eam_2/set49. Energies are in eV and distances are in Å. The cutoff distance of the potential is set at r_c = 5.4 Å which represents the midpoint between the 5th and 6th nearest-neighbor distances in hcp.

Parameters	Re_eam_1/set22
r_c	5.4
a_1, a_2, a_3, a_4, a_5	2.43990, 2.55679, 2.70906, 2.83302, 2.94811
a_6, a_7, a_8, a_9, a_{10}	3.20526, 3.57743, 3.67419, 4.27970, 4.69975
a_{11}, a_{12}, a_{13}, a_{14}, a_{15}	4.770169, 4.94784, 5.31315, 5.34538, 5.4
f_1, f_2, f_3, f_4, f_5	20.27067, -3.06785, -2.57277, -2.75760, 4.64598
f_6, f_7, f_8, f_9, f_{10}	0.40940, 1.40067, -1.73973, 0.28612, 1.28437
f_{11}, f_{12}, f_{13}, f_{14}, f_{15}	-0.93819, -0.46948, 2.38722, -4.48160, 2.13542
r_{min}	1.15557
b_1, b_2, b_3, b_4	2.55110, 3.09120, 3.30598, 4.82922
g_1, g_2, g_3, g_4	-2.53543, 1.58551, -0.61493, 0.05764
c_1	-2.02150
c_2	0.08529

Acknowledgement

This research has been supported by the U.S. Department of Energy, Office of Science, Office of Fusion Energy Sciences (DE-AC06-76RL0-1830). NG acknowledges the support by National Natural Science Foundation of China (11375242, 11675230) and by the Youth Innovation Promotion Association CAS.

References

[1] Setyawan, W and R. J. Kurtz, in *Fusion Reactor Materials Program Semiannual Progress Reports*, Vol. 61, 2016, ORNL, p. 151-158.
[2] Marinica, M.C, et al., *Journal of Physics Condensed Matter* 25 (2013) 395502.

8.2 CONFIGURATIONAL MULTIPLICITY OF GRAIN BOUNDARY PHASES IN BCC METALS—Timofey Frolov, R. E. Rudd (Lawrence Livermore National Laboratory), W. Setyawan, R. J. Kurtz (Pacific Northwest National Laboratory), J. Marian (University of California Los Angeles), A. R. Oganov (Stony Brook University), and Q. Zhu (University of Nevada Las Vegas)

Extended abstract of a paper submitted to Physical Review Letters.

The objective of this study is to develop a computational methodology to predict structure and energies of tungsten grain boundaries, especially the high-temperature grain boundary phases. Grain boundary properties are needed for thermomechanical model of recrystallization of tungsten for magnetic fusion applications being developed by the Marian Group at UCLA.

While conventional grain boundary (GB) structures created as a union of two perfect half crystals have been studied extensively, other configurations with different atomic density may exist that cannot be predicted by standard methods. There is evidence that these GBs significantly affect material properties in fcc metals, but their existence and impact on properties in bcc metals remains largely unexplored. Here, we use a newly developed computational tool, based on evolutionary algorithms, to perform a grand-canonical search of high-angle symmetric tilt GBs in bcc tungsten, and we find new ground states that cannot be described using the conventional structural unit model. Our predictions are confirmed by first-principles calculations.

8.3 EFFECT OF SIA TRAPPING AND DETRAPPING ON DEFECT ACCUMULATION IN TUNGSTEN DUE TO RADIATION CORRESPONDING TO 14-MeV-NEUTRON AND HFIR PKA SPECTRA

—Giridhar Nandipati, Wahyu Setyawan, Kenneth J. Roche, Richard J. Kurtz (Pacific Northwest National Laboratory), Brian D. Wirth (University of Tennessee)

This is an Extended Abstract for a paper in preparation for journal submission.

Object kinetic Monte Carlo (OKMC) simulations using KSOME (kinetic simulation of microstructure evolution, an OKMC code) [1, 2] were performed at a temperature of 1025 K to study the effect of trapping and detrapping of self-interstitial atom (SIA) clusters by impurities on defect accumulation in bulk polycrystalline tungsten subjected to a radiation corresponding to 14-MeV-neutron and the High Flux Isotope Reactor (HFIR) primary knock-on atom (PKA) spectra. The evolution of point defect properties was studied as a function of dose (up to 1.0 dpa), dose rate (~ $10^{-4} - 10^{-8}$ dpa/s), detrapping activation barrier (∞, 0.5, 1.9 eV), impurity concentration (100 – 250 appm), and grain size (2, 4, 10 μm). Impurities were considered permanent traps for vacancies, while SIA clusters can detrap as a whole with a detrapping barrier. For both PKA spectra, point defect accumulation with dose and dose rate is qualitatively similar, however quantitatively, differences are seen due to differences in displacement cascade production rates of various defect cluster sizes. Defect accumulation is always lower in the case of HFIR due to higher production of small defect clusters. Regardless of the occurrence of SIA detrapping processes, defect and defect cluster densities decreased with decreasing dose rate for both PKA spectra. Furthermore, for the grain sizes no influence of grain size on defect accumulation was observed. A detrapped SIA cluster diffuses in a random one-dimensional direction, thus trapping and detrapping forces it to diffuse three-dimensionally. Hence, as expected, defect accumulation is lower. Interestingly, with SIA detrapping, the defect accumulation rate increases at first and then decreases with increasing impurity concentration. Implying that an optimum impurity concentration is required before defect accumulation starts to decrease with increasing impurity concentration. However, without SIA detrapping, defect accumulation always increases with impurity concentration. Furthermore, the sensitivity of defect accumulation to changes in the value of the detrapping barrier seem to depend strongly on the cascade insertion rate, which in turn depends on the PKA spectrum and dose rate. A detailed comparison of defect accumulation between the two PKA spectra in relation to differences in defect production rates and impurity concentration is discussed.

Acknowledgements

The work was performed at Pacific Northwest National Laboratory (PNNL), which is operated by Battelle for the United States Department of Energy (US DOE) under Contract DE-AC06-76RL0-1830. The US DOE, Office of Fusion Energy Sciences (FES) and Office of Advanced Scientific Computing Research (ASCR) supported this study through the SciDAC-3 program. All computations were performed on HOPPER at the National Energy Research Scientific Computing Center (NERSC) and PNNL's Institutional Resources (PIC). The authors would like to thank Larry Greenwood of PNNL for providing the PKA spectra for 14 MeV neutrons and HFIR.

References

[1] G. Nandipati, W. Setyawan, H. L. Heinisch, K. J. Roche, R. J. Kurtz, B. D. Wirth, *J. Nucl. Mater*. (2015) 462 338–344.

[2] G. Nandipati, W. Setyawan, H. L. Heinisch, K. J. Roche, R. J. Kurtz, B. D. Wirth *Semi-annual Progress Report* DOE/ER-0313/54 (June2013) 179–183.

8.4 SIMULATING IRRADIATION HARDENING IN TUNGSTEN UNDER FAST NEUTRON IRRADIATION INCLUDING TRANSMUTATION RHENIUM PRODUCTION

—Chen-Hsi Huang, Jaime Marian (Department of Materials Science and Engineering, University of California Los Angeles), and Mark R. Gilbert (Culham Science Centre, Abingdon, UK)

OBJECTIVE

The main aim of this work is to use state-of-the-art modeling of irradiation damage production and accumulation to predict the potential hardening in tungsten under conditions of DEMO reactor. To test whether our calculations can reliably provide such predictions, we first simulate irradiation experiments in JOYO and HFIR and compare our predictions with the experimental measurements.

SUMMARY

Simulations of neutron damage under fusion energy conditions must capture the effects of transmutation, both in terms of accurate chemical inventory calculations as well as the physics of the interactions between transmutation elements and irradiation defect clusters. In this work, we integrate neutronics, primary damage calculations, molecular dynamics results, rhenium transmutation calculations, and stochastic cluster dynamics simulations in order to study neutron damage in single-crystal tungsten to mimic divertor materials. We use established correlations to translate damage accumulation into hardening increases and compare our results to the experimental measurements. We find hardening increases in excess of 5000 MPa in all cases, which casts doubts about the integrity of W-based materials under long-term fusion exposure.

PROGRESS AND STATUS

Introduction

Tungsten is being considered as a candidate structural material in magnetic fusion energy devices due to its high strength and excellent high temperature properties [1-4]. Upon fast neutron irradiation in the 600-1000^{o}C temperature range, W transmutes into Re via either neutron multiplication (n,2n) or neutron capture (n,γ) reactions, followed by β-decay, at rates that depend on the shape and magnitude of the neutron flux spectrum[5], which varies with position in the reactor. For the DEMO (*DEMOnstration fusion power plant*) reactor concept, calculations show that the transmutation rate is 2000 and 7000 atomic parts per million (appm) per displacement per atom (dpa) in the divertor and the equatorial plane of the first wall, respectively (in each case, damage accumulates at rates of 3.4 and 4.4 dpa/year) [6,7]. The irradiated microstructure initially evolves by accumulating a high density of prismatic dislocation loops and vacancy clusters, approximately up to 0.15 dpa [8-11]. Subsequently, a void lattice emerges and fully develops at fluences of around 1 dpa. After a critical dose that ranges between 5 dpa for fast (>1 MeV) neutron irradiation [10] and 2.2 dpa in modified target rabbits in the HFIR [11,12], W and W-Re alloys develop a high density of nanometric precipitates with acicular shape at Re concentrations well below the solubility limit [10,11]. The structure of these precipitates is consistent with σ (W_7Re_6) and χ (WRe_3) intermetallic phases, which under equilibrium conditions only occur at temperatures and Re concentrations substantially higher than those found in neutron irradiation studies [13]. A principal signature of the formation of these intermetallic structures in body-centered cubic (bcc) W is the sharp increase in hardness and embrittlement [9-11]. Qualitatively similar observations have been recently made in W-2Re and W-1Re-1Os alloys subjected to heavy ion irradiation [14,15], clearly establishing a link between primary damage production and Re precipitation.

Several works using density functional theory (DFT) calculations have revealed the importance of mixed interstitial dumbbells in solute transport in W alloyed with Re [16-19] and Os [16,17,19], Ta [19], as well as Ti and V [18,20]. Mixed dumbbells overcome the mixing tendency of vacancy-mediated transport, leading to solute clustering and incipient precipitate growth. We have calculated the nucleation times and growth rates by implementing these mechanisms in lattice kinetic Monte Carlo simulations of bcc W-Re alloys [21]. However, these simulations are insufficient to provide statistically-meaningful precipitate number densities and size distributions in a more global sense. This information is essential in order to establish a link between irradiation damage and mechanical behavior, as will be discussed below.

In this work we carry out mean-field simulations (using the *stochastic cluster dynamics* method, discussed below) to study the long term evolution of W under neutron irradiation. While recent works have attempted to couple transmutation with irradiation damage calculations [22,23], here we consider the effects of transmutation on microstructural evolution and mechanical property degradation as the isotope inventory builds up with dose and Re atoms increase in number. Our simulations provide the number densities and size distributions of defect clusters with irradiation dose, which are subsequently used to estimate the amount of hardening brought about under neutron exposure in reactor conditions. Our study is motivated by the work of Hasegawa and co-workers [9,10] and Hu et al. [11], who measured hardening of W single crystals under nominal irradiation conditions in JOYO and HFIR respectively. We consider both of these scenarios for our simulations, as well as that of a hypothetical DEMO reactor as an estimator of potential divertor performance. These three different reactor scenarios are modeled by way of their respective neutron spectra and primary recoil energy distributions, which are obtained via neutronics calculations and post-processing of the corresponding data.

Next we provide a brief description of the methods used, as well as the parameterization and physical data analysis. This is followed by the results and a critical discussion of our main findings.

Theory and methods

Stochastic cluster dynamics method

Stochastic cluster dynamics (SCD) is a stochastic variant of the mean-field rate theory technique, alternative to the standard ordinary differential equation (ODE) based implementations, that eliminates the need to solve exceedingly large sets of PDEs and relies instead on sparse stochastic sampling from the underlying kinetic master equation [24,25]. Rather than dealing with continuously varying defect concentrations in a nominally infinite volume, SCD evolves an integer-valued defect population N_i in a finite material volume V, thus avoiding combinatorial explosion in the number of ODEs. This makes SCD ideal to treat problems where the dimensionality of the cluster size space is high, e.g., when multi-species simulations are of interest. SCD recasts the standard ODE system into stochastic equations of the form:

$$\frac{dN_i}{dt} = \overbrace{g}_i - \sum_i \overbrace{s}_{ij} N_i + \sum_j \overbrace{s}_{ji} N_j - \sum_{i,j} \overbrace{k}_{ij} N_i N_j + \sum_{j,k} \overbrace{k}_{jk} N_j N_k \qquad (1)$$

where the set $\{\overbrace{g}, \overbrace{s}, \overbrace{k}\}$ represents the reaction rates of 0^{th} (insertion), 1^{st} (thermal dissociation, annihilation at sinks), and 2^{nd} (binary reactions) order kinetic processes occurring inside V. Here we are concerned with material point simulations --akin to *bulk* irradiation experiments-- and we thus ignore spatial effects and the Fickian term of the full partial differential equation system. SCD uses a modified version of the *residence time* or *kinetic Monte Carlo* (kMC) algorithm to select from among the event rate set and evolves the system in time. The detailed description of the SCD method can be found in ref. [24]. In this work, system volume is fixed at 10^{-20} m^3 and it is ensured that at all times $V^{\frac{1}{3}} > l$, where l is the maximum of the diffusion lengths l_i of all species i in the system, defined as:

$$l = \max\{li\}$$

$$l_i = \sqrt{\frac{D_i}{R_i}}$$

Here, D_i and R_i^{-1} are the diffusivity and the lifetime of a mobile cluster within V. From Eq. (1), $R_i = \overbrace{s} + \sum_i \overbrace{k}_{ij} N_i$. In other words, we ensure that the characteristic diffusion length of any defect species is contained within the simulation volume at any given time.

We consider the binary system W-Re with time-dependent Re concentrations as given by the transmutation rates in three distinct neutron environments. As such, the cluster species considered in this work are combinations of the three elementary species: vacancies, self-interstitials atoms, and Re atoms. As mentioned above, the important role of mixed dumbbells in Re-cluster nucleation in irradiated W-Re alloys has been well established in our earlier studies [21] and so in this work mixed-dumbbells are included as an additional species.

Method parameterization

SCD simulations require characterizing the complete $\{\overbrace{g}, \overbrace{s}, \overbrace{k}\}$ parameter set. The g set is defined by the irradiation conditions and primary knock-on atom (PKA) distributions. The s requires knowledge of cluster binding energies and defect diffusivities, as do the k rates. Many of these values have been calculated in previous works [21,26], and in the following we simply discuss the calculation of those needed to complete the parameter set.

Damage insertion rates

The calculation of damage insertion rates is a two-step process involving (i) the determination of PKA energy distributions from neutron energy spectra, and (ii) conversion of PKA energies into point defect numbers and size distributions obtained from molecular dynamics (MD) simulations of displacement cascades (see, e.g., Reference [25]). The resulting rate gives the number of PKA inserted in the simulation volume per unit time.

For the first step, SCD uses *cumulative probability distribution functions* (cpdfs) generated from the corresponding neutron energy spectra (DEMO, HFIR, or JOYO) using the SPECTRA-PKA code [27,28]. This code folds a neutron irradiation spectrum with cross section (reaction probability) matrices (defining the cross section for each neutron energy E_i to create a recoil at each energy E_j for the complete set of possible nuclear reactions on each isotope in the input material, including elastic and inelastic scattering, and non-elastic reactions such as neutron capture or neutron multiplication. The group-to-group recoil probability matrices were derived from the latest version of the TENDL nuclear data libraries [29]. SPECTRA-PKA sums the resulting vector recoil spectra across all reactions on each target isotope, and then across all isotopes (according to appropriate isotopic ratios in the material) to produce the total and cumulative PKA distributions. For the case of W the isotopic composition used was that of the natural abundance. The distributions obtained from SPECTRA-PKA for the three neutron spectra considered are shown in Figure 1.

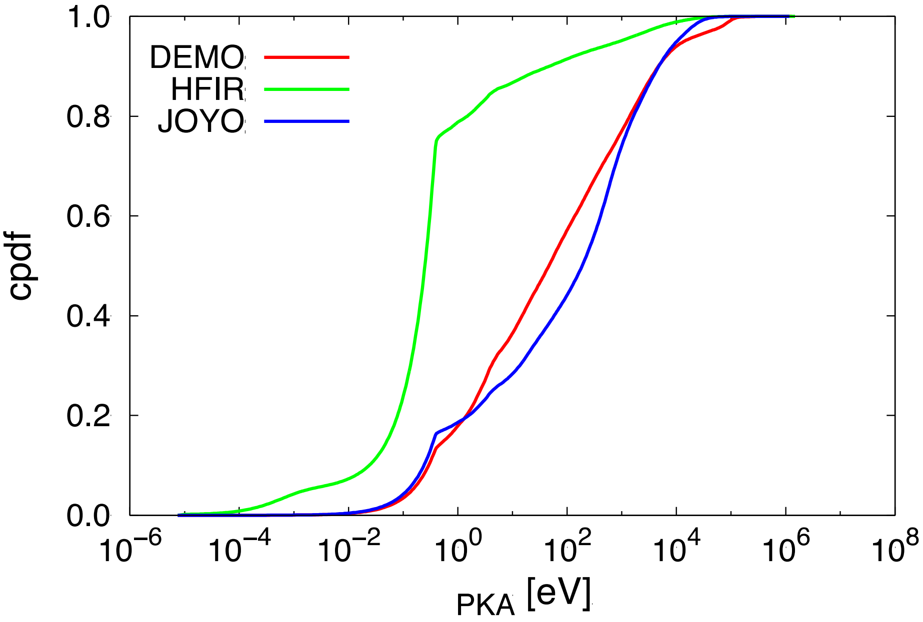

Figure 1. PKA cumulative probability distribution function (cpdf) in W for DEMO, HFIR, and JOYO reactors.

Each PKA creates defects containing vacancies and interstitials, with the number, size, and distribution of such defects strongly determined by the energy of the original PKA, E_{PKA}. Defects are then inserted into the system according to the relations of defect distribution to PKA energy, which are typically obtained from atomistic simulations of displacement cascades for a number of PKA energies and temperatures [30,31]. Recent studies have revealed good agreement between experimental measurements of defects number densities and sizes and MD simulations [32]. Here we use the correlations obtained by Setyawan et al. [31] linking numbers and fractions of clustered SIAs and vacancies with E_{PKA}. The dependence of the number of Frenkel pairs N_F E_{PKA} was seen to display two distinct regimes, each characterized by a power law of the type $N_F=aE^b_{PKA}$:

$$\Delta E_{ij} = \begin{cases} N_F = 0.4172\,\left(\frac{E_{PKA}}{E_d}\right)^{0.74}, if\ \frac{E_{PKA}}{E_d} < 341{,}42 \\ N_F = 0.0126\,\left(\frac{E_{PKA}}{E_d}\right)^{1.34},\ otherwise \end{cases} \qquad (2)$$

where E_d= 128 eV was the average displacement threshold energy for W using the interatomic potential of Juslin et al. [33]. The dependency of N_F with temperature was seen to be weak and is not considered in this study. We set the minimum value of E_{PKA} to produce a stable Frenkel pair inside the material to be 620 eV [25]. For their part, the fractions of clustered SIAs and vacancies f_c^{SIA}, f_c^V depend strongly on PKA energy and temperature, respectively, according to:

$$f_c^{SIA} = 0.09021\left(\frac{E_{PKA}}{E_d}\right)^{0.326} \qquad (3)$$

$$f_c^V = 0.625 - 1.750 \times 10^{-4} T(4) \qquad (4)$$

where T is absolute temperature. In simulations, when a damage insertion event is selected within the kMC algorithm, the corresponding cpdf function (DEMO, JOYO, or HFIR) is sampled to get E_{PKA}, and then the above correlations are applied to insert the appropriate number and arrangement of defect clusters.

As well, the transmutation rate of W into Re was calculated using the inventory code FISPACT-II [34] for the same three neutron spectra used for the calculation of PKA distributions (using TENDL [29] data, as before). FISPACT-II also calculates instantaneous dpa rates using total NRT [35] dpa cross sections derived from the full nuclear reaction data, and in this case assuming a displacement threshold energy E_d based on experimental data for W of 55 [36]. For each reactor this profile of dpa rates was integrated in time and used to approximate the irradiation time taken to reach a dose of F≈2 dpa. The data in Table 1, showing the dpa rate and Re production (in atomic parts per million, appm) per dpa, were obtained by finding the gradient of the FISPACT-II data over these calculated irradiation times (assuming a linear response). It can be seen that Re production is extremely high in HFIR (although eventually Os production is even greater) with a value much larger than the other two reactors. The transmutation of Re as a function of irradiation dose is shown in Figure 2.

Table 1. DPA rates and Re production rates due to W transmutation for DEMO, HFIR, and JOYO

Reactor	PKA rate[$s^{-1}cm^{-3}$]	Dpa rate[s^{-1}]	Re production rate [appm dpa^{-1}]
DEMO	$5.61x10^{15}$	$1.887x10^{-7}$	522+182F
HFIR	$8.41x10^{15}$	$3.249x10^{-7}$	34267-16886F
JOYO	$3.00x10^{15}$	$5.331x10^{-7}$	1057+247F

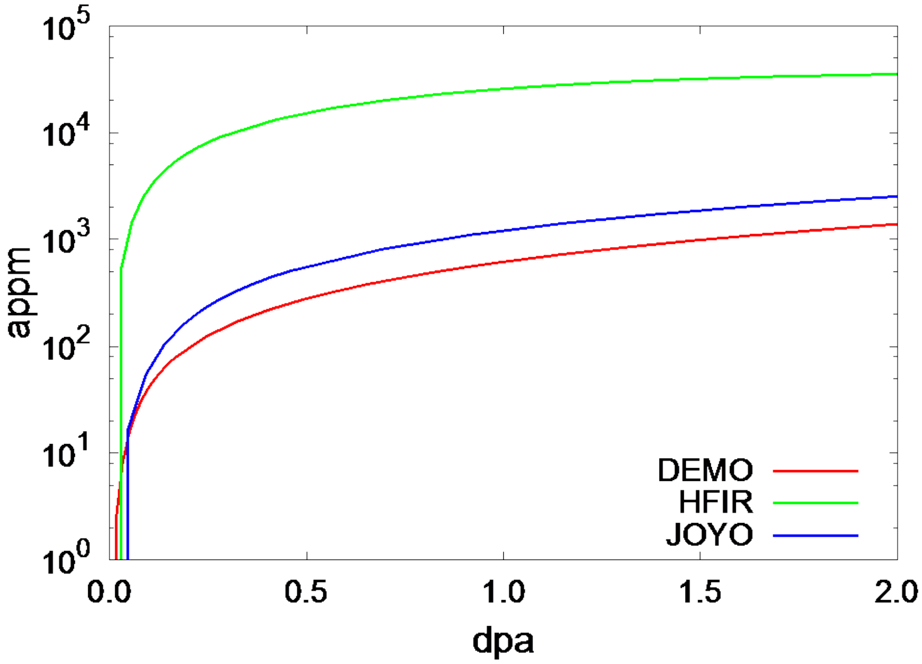

Figure 2. Calculated transmutation of Re as function of dose for DEMO, HFIR, and JOYO reactors.

Diffusion coefficients

The mobile species in the present SCD simulations are: single and pure SIA clusters, single and pure vacancy clusters up to a size of three vacancies, as well as single Re atoms and single mixed-dumbbells. Tracer diffusion coefficients (*i.e.*, in the absence of a concentration gradient) for an object diffusing in 3D is assumed to follow an Arrhenius temperature dependence of $D(T)= D_0 \exp(-E_a/kT)$, where E_a is the activation energy, and D_0 is a diffusion pre-factor. The parameters for SIA and vacancy clusters have been published by Marian and Hoang [25]. The diffusivities of Re solute atoms and mixed dumbbells have been characterized in our previous kMC simulations [21], and are used in rate theory/SCD simulations for the first time. The results are given in Table 2.

Table 2. Diffusivity parameters for mobile defect species involving Re

Species	D_0 [cm^2 s^{-1}]	E_a [eV]
Mixed dumbbell	1.498×10^{-3}	0.12
Re atom	2.709×10^{-2}	4.79

Binding energies

Within classical nucleation theory, the binding energy is defined as the energy required to detach a monomer from its parent cluster. This is achieved by calculating the energies of cluster configurations with N elements, and comparing them with energies of N-1 clusters and a monomer placed at infinity. Defined in this way, binding energies are positive when clusters are energetically favored over a collection of disjoint monomers. The binding energies for pure SIA and vacancy clusters in W employed in this work have been provided in previous studies [25], and here we focus on species containing Re atoms.

- *Re clusters*: For lack of a better model, here we consider Re clusters with a bcc structure, and we calculate the binding energies using a lattice Hamiltonian for the W-Re system developed by the authors [21, 26]. For consistency with our findings in Reference 21, we construct the cluster structures assuming a solute concentration roughly equal to 50 at.%. To calculate the binding energy, Re atoms are removed one by one from the surface of the parent cluster and placed as far from the cluster surface as permitted by the computational cell size. The Re atoms in the cluster are extracted in the order of their distance to the center of mass of the cluster. The resulting data points are then fitted to a linear relation of the type: $e_b^{Re}=aN_{Re}+b$, where a and b is fitting constants. Results are shown in Figure 3, along with the least-squares fit of:

$$e_b^{Re} = 4.736 \times 10^{-6} N_{Re} - 0.0258\ [eV] \tag{5}$$

  The above expression yields negative values for $N_{Re}<5448$, indicating that Re cluster below that size are energetically unstable. This is consistent with the thermodynamics of W-Re alloys, which are seen to prefer a solid solution state up to large Re concentrations.

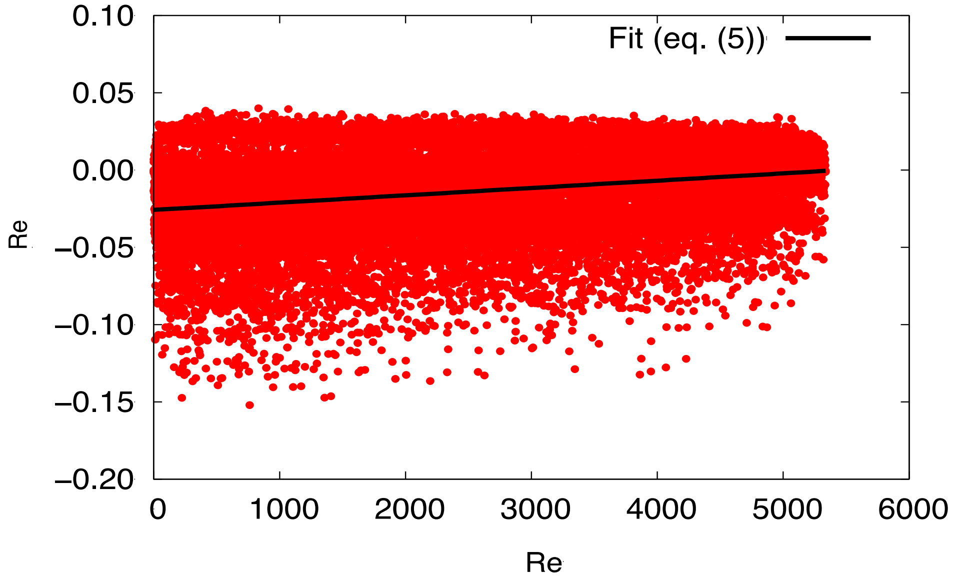

Figure 3. Binding energy of a Re atom to a pure Re cluster as a function of the cluster size. The binding energy is negative, indicating unstable clusters.

- *Vacancy-Re clusters*: The thermodynamics of W-Re systems suggests that V-Re clusters are energetically stable up to relatively large sizes [21,37]. To compute the binding energy of V_m-Re_n complexes, the structure of clusters with m vacancies and n Re atoms was first optimized via simulated annealing using Metropolis Monte Carlo. We considered clusters with up to eight vacancies (m<=8), and for each value of m the number of Re atoms was increased one by one up to a maximum Re/vacancy ratio of 8. A bi-variate fitting was then performed to extract correlations relating the binding energy to m and n. The results of the calculations are given in Figure 4. The fitted correlations are given as:

$$e_b^{V_m \boldsymbol{Re}_n} = 0.079 + 0.154(\frac{m}{n}) \tag{6}$$

$$e_b^{\boldsymbol{V}_m Re_n} = 0.273(\frac{n^{0.59}}{m^{0.31}}) \tag{7}$$

with both energies in electron volts.

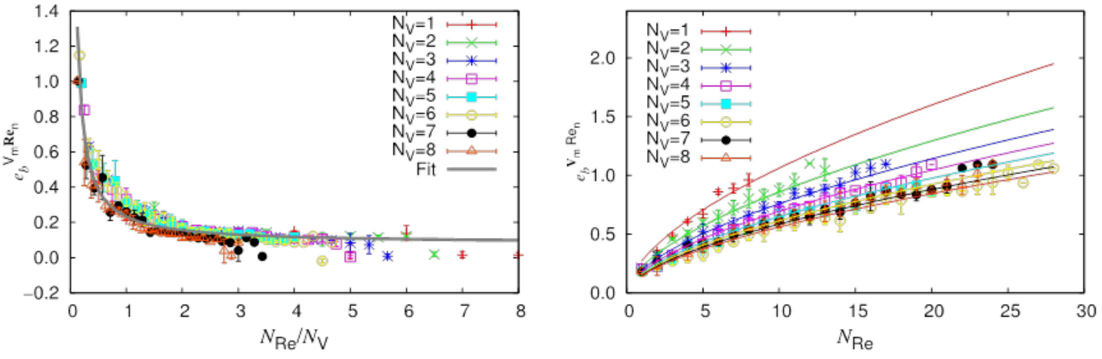

(a) (b)

Figure 4. Binding energies of (a) Re atoms and (b) vacancies to a V-Re cluster in terms of the numbers of each species, N_{Re} and N_V, in the cluster.

- *SIA-Re clusters and mixed-dumbbell clusters*: The physics of the interaction between self-interstitial atoms and Re atoms the most complex of all species involving Re atoms. There are several scenarios to be considered. (i) First, pure SIA clusters moving one-dimensionally may interact with Re solute atoms that slow down their migration. We assume that, in this case, both species maintain their separate status (they do not form a mixed SIA-Re complex) but they are bound with an energy of 0.8 eV. (ii) Second, mixed dumbbells diffusing three-dimensionally may aggregate into clusters that are oriented along <111> directions. These clusters are thermally stable and immobile. There is evidence for this mechanism from DFT calculations [18]. (iii) Third, if a SIA cluster interacts with a Re cluster, they form a bound complex with binding energy also equal to 0.8 eV when the interstitial cluster is larger than three. Otherwise, the bound complex is treated as in (ii) and does not dissociate. All these mechanisms are implemented in our SCD calculations.

Results

We perform simulations for the DEMO, HFIR, and JOYO reactors, each at five different temperatures: 673, 773, 873, 973, and 1073 K. As described earlier, the dpa rates for each reactor were obtained from the same FISPACT-II simulations used to evaluate Re production, shown in Table 1. The population and sizes all the cluster species discussed above are tracked with time for each temperature and the results are post-processed for estimating the amount of irradiation induced hardening. For consistency with the measurements by Hu *et al.* [11], the simulations are run up to a dose of 2 dpa in single-crystal W targets. In all cases, a dislocation density of $10^{14}m^{-2}$ was assumed, in line with what would be expected in well-annealed W specimens.

Cluster size distributions and number densities

Next, we provide cluster size histograms for all reactor scenarios and temperatures. We subdivide all cluster species as *loops*, *voids*, or *precipitates*[1]. Since there might be some ambiguity in these definitions the following rules are adopted: a cluster is classified as an SIA loop if it contains more SIAs than solute atoms; a void is defined as a cluster that contains more vacancies than solute atoms; else, the cluster is considered as a solute precipitate. The diameter of the cluster is calculated by assuming spherical shapes for voids and precipitates, and a disc with a thickness of one Burgers vector for SIA loops. The size distributions of all species at 0.5, 1.0, and 2.0 dpa for DEMO, HFIR, and JOYO are shown in Figures 5, 6, and 7, respectively. The distributions are different for different reactor spectra. In general, at elevated temperatures, defect concentrations tend to decrease, Re precipitates tend to have larger size, voids are seen to increase in size in DEMO, and the size of precipitates appears to be quite insensitive to temperature and dose in HFIR.

To plot the number densities, for consistency with experimental measurement techniques, we apply a TEM visibility size limit of 1.0 nm to all clusters. Visible clusters at 673 K for all three reactor cases as a function of dose are shown in Figure 8. Figures 9, 10, and 11 show the evolution of the cluster densities with dose as a function of temperature for each reactor environment. As shown, SIA loops are not visible or barely above the visibility threshold. Voids are nonexistent in HFIR and accumulate only at very low levels in JOYO. In all three cases, Re clusters are the dominant damage feature, building up at similar rates in all three reactor cases.

Irradiation hardening calculations

Irradiation hardening is caused by the formation of a high number density of nanoscale features that act as obstacles to dislocation motion. The increase in hardness ΔH_y due to the presence of irradiation obstacles can be obtained from a simple *dispersed barrier hardening* model as [38,39]:

$$\Delta H_y = 3.2 M\alpha\mu b(Nd)^{\frac{1}{2}} \qquad (8)$$

---

[1] These are simply names to broadly categorize damage species. We do not mean for these definitions to be interpreted in their strictest physical meaning, e.g. we may refer to a 15-atom Re cluster as a *precipitate* even though it may physically not fit the definition of one.

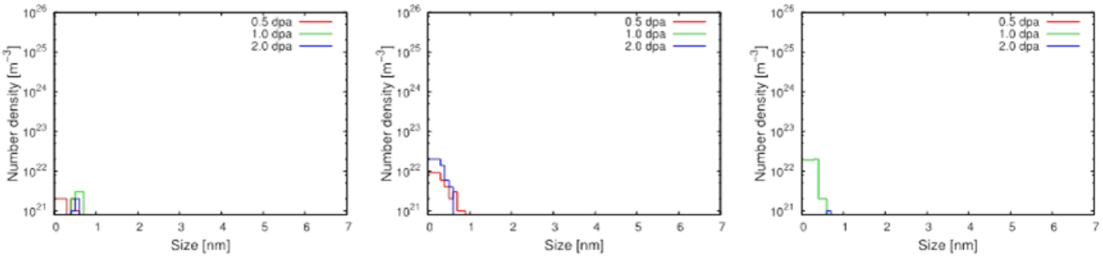

(a) SIA loops at 673 K. (b) SIA loops at 873 K. (c) SIA loops at 1073 K.

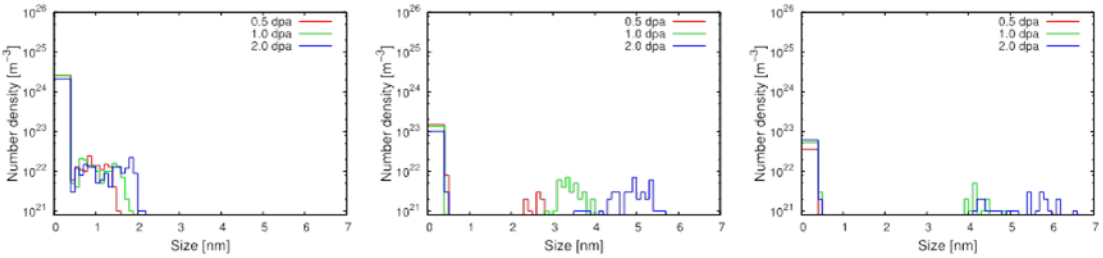

(d) Voids at 673 K. (e) Voids at 873 K. (f) Voids at 1073 K.

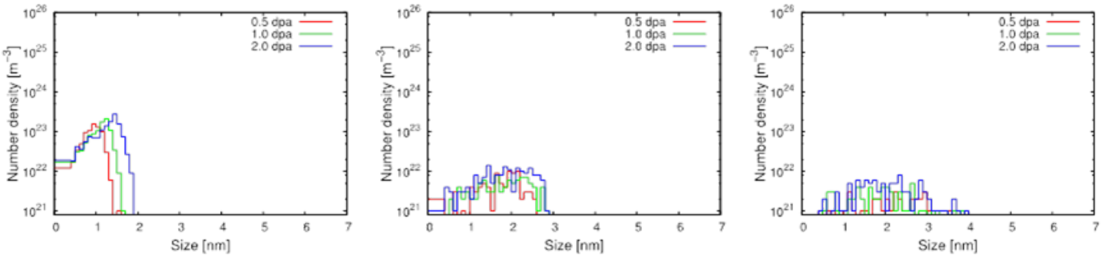

(g) Re precipitates at 673 K. (h) Re precipitates at 873 K. (i) Re precipitates at 1073 K.

Figure 5. Cluster size histograms of SIA loops, voids, and Re precipitates for DEMO irradiation conditions. All the plots are shown in the same scale for cross-comparison.

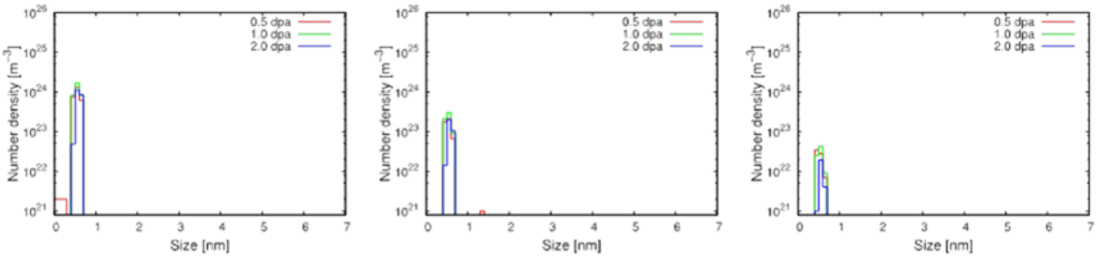

(a) SIA loops at 673 K. (b) SIA loops at 873 K. (c) SIA loops at 1073 K.

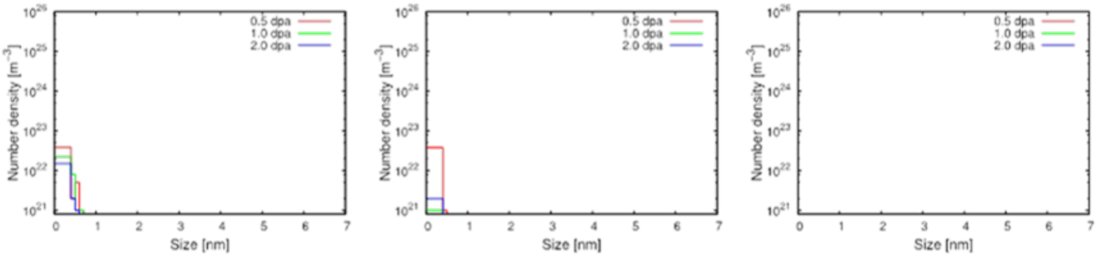

(d) Voids at 673 K. (e) Voids at 873 K. (f) Voids at 1073 K.

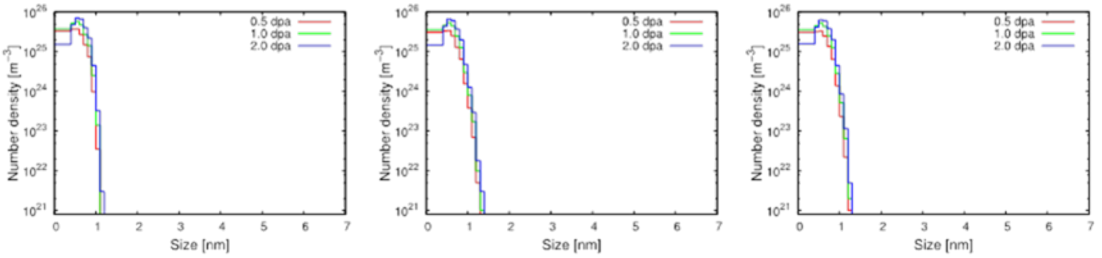

(g) Re precipitates at 673 K. (h) Re precipitates at 873 K. (i) Re precipitates at 1073 K.

Figure 6. Cluster size histograms of SIA loops, voids, and Re precipitates for HFIR irradiation conditions. All the plots are shown in the same scale for cross-comparison.

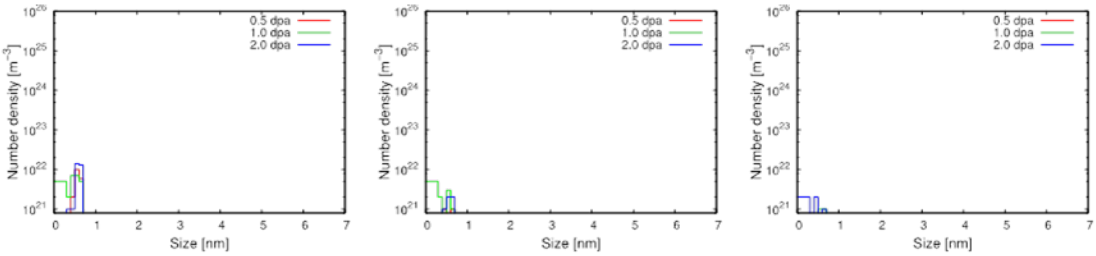

(a) SIA loops at 673 K. (b) SIA loops at 873 K. (c) SIA loops at 1073 K.

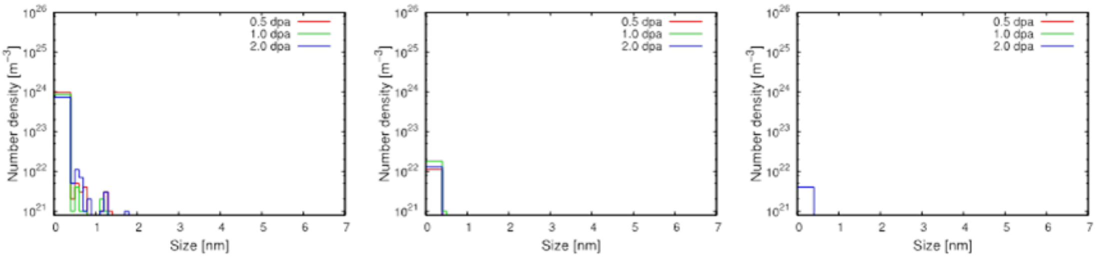

(d) Voids at 673 K. (e) Voids at 873 K. (f) Voids at 1073 K.

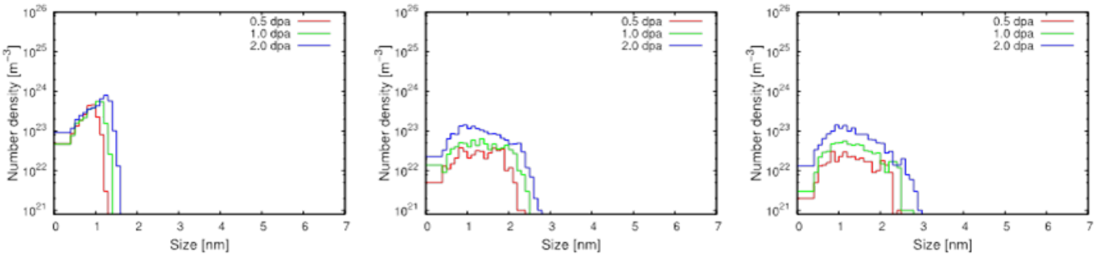

Figure 7. Cluster size histograms of SIA loops, voids, and Re precipitates for JOYO irradiation conditions. All the plots are shown in the same scale for cross-comparison.

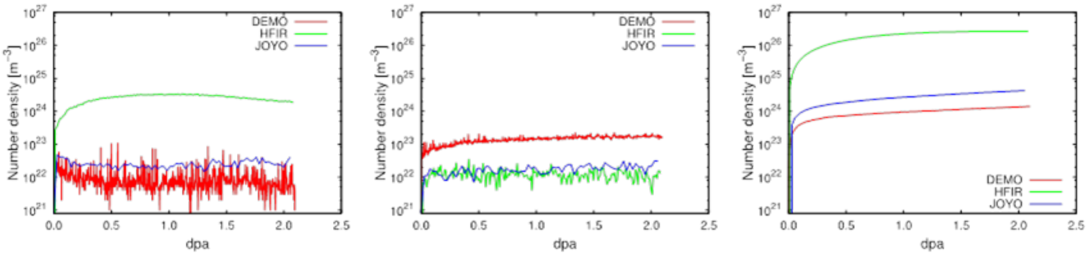

(a) SIA loops. (b) Voids. (c) Re precipitates.

Figure 8. Accumulation of all SIA loops, voids, and Re precipitates clusters as a function of dose at 673 K for DEMO, HFIR, and JOYO irradiation conditions.

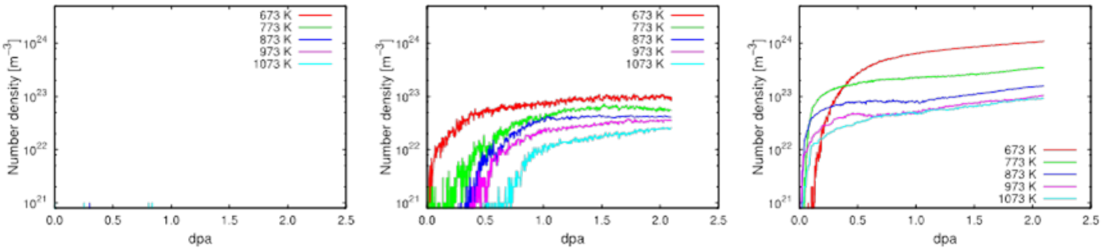

(a) SIA loops. (b) Voids. (c) Re precipitates.

Figure 9. Accumulation of visible SIA loops, voids, and Re precipitates as a function of dose at different temperatures for DEMO irradiation conditions.

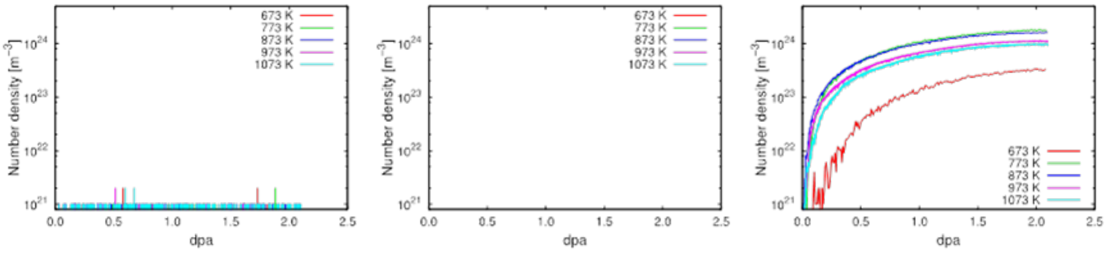

(a) SIA loops. (b) Voids. (c) Re precipitates.

Figure 10. Accumulation of visible SIA loops, voids, and Re precipitates as a function of dose at different temperatures for HFIR irradiation conditions.

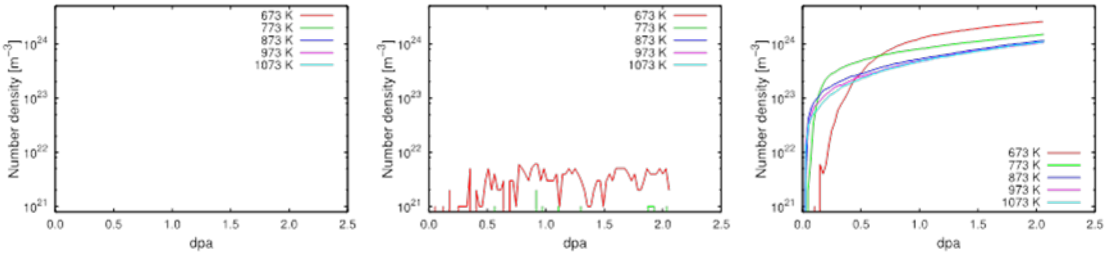

(a) SIA loops. (b) Voids. (c) Re precipitates.

Figure 11. Accumulation of visible (>1.0 nm) SIA loops, voids, and Re precipitates as a function of dose at different temperatures for JOYO irradiation conditions.

where M is the Taylor factor, α is the defect strength coefficient, μ is the shear modulus, b is the magnitude of the Burgers vector, and N and d are the number density of clusters and their size, respectively. In a recent study, Hu et al. have shown that for values of M=3.06, μ=161 GPa, and b=0.42 nm, the above expression provides a good agreement between measured (Vickers) hardness increases and the measured number and size of defect clusters for a set of α parameters listed in Table 3 [11]. When combining size histograms with integer-valued cluster populations, the factor inside the square root $(Nd)^{0.5}$ in eq. (8) must be replaced with:

$$Nd = \int \rho(n)d(n)dn$$

where ρ(n) is the number density of a cluster of n defects and d(n) is the corresponding cluster diameter. This integral can be approximated by a sum of discrete bins describing the histogram of cluster sizes such as those provided in Figures 5 to 7. Next, we apply this discrete version of eq. (8) using the above cluster size distributions and number densities to calculate ΔH_y according to our modeling results.

Table 3. The defect cluster barrier strength α for different types and diameter of clusters. All values from Reference [11].

Defects	Size	Barrier strength factor (α)
Dislocation loops	>1.0 nm	0.15
Voids	1-2 nm	0.25
Voids	2-3 nm	0.30
Voids	3-4 nm	0.35
Voids	>4 nm	0.40
Precipitates	>1.0 nm	0.60

Figure 12 shows our results for ΔH_y separated by contributions from the three different types of clusters considered here, as a function of temperature and dose. Generally speaking, the trends observed can be summarized as:

1. Irradiation hardening is more pronounced under JOYO conditions, followed by HFIR, followed by DEMO.
2. Hardening increases with irradiation dose, and is in the level of several thousands of MPa.
3. Hardening is weakly dependent on temperature, following generally a softening trend except at the lowest temperature for HFIR.
4. Re precipitates unquestionably represent the largest contribution to hardening of all irradiation clusters considered here. In DEMO, the contribution from voids is also predicted to be substantial. In all cases, hardening by irradiation loops is negligible compared to the other two.

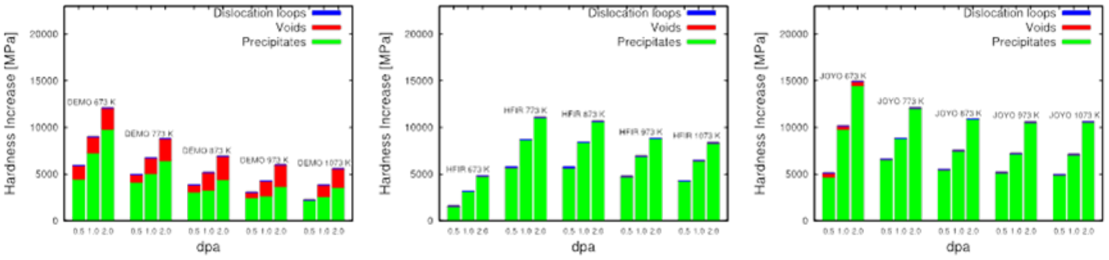

(a) DEMO. (b) HFIR. (c) JOYO.

Figure 12. Radiation-induced hardening contributions from different cluster types calculated using eq. (8) for (a) DEMO (b) HFIR, and (c) JOYO irradiation conditions.

These calculations were performed under the assumption that interactions between SIA loops and Re clusters result in a complex formed by both reactants that can only dissociate as the original products (as opposed to one by one as according to classical nucleation theory). Next we explore variations from this assumption to study the sensitivity of the results to two different physical scenarios that represent extreme cases in terms of defect accumulation.

Hardening calculations without dissociation of Re-SIA clusters

To examine the effect of the mechanism of precipitate-loop reaction on global hardening, here we run simulations assuming that Re-SIA cluster complexes are thermally stable and thus cannot dissociate. This is an extreme case, intended to provide an upper bound on the number of clusters and thus on the final hardening levels. Figure 13 shows the corresponding calculations for all three reactor scenarios. It can be seen that ΔH_y increases by approximately 50% compared to the prior cases, a direct consequence of a larger accumulation of clusters in the simulation volume. As well, the relative contribution of SIA loops to the total hardening increases. The contribution due to voids also noticeably increases because the immobilization of SIA clusters at Re-loop complexes results in reduced recombination rates and vacancy/void accumulation.

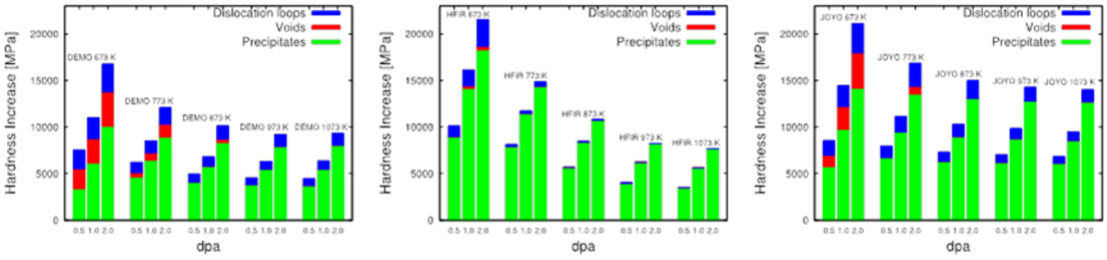

(a) DEMO. (b) HFIR. (c) JOYO.

Figure 13. Radiation-induced hardening assuming thermally-stable (non-dissociative) Re-SI cluster complexes for (a) DEMO, (b) HFIR and (c) JOYO irradiation conditions.

Hardening calculations with no sinks

We have also performed simulations in a system with no sinks. When sinks are removed defects can only disappear via recombination, which removes the imbalance between vacancies and interstitials. The presence of Re, which renders interstitials mobile in 3D via the formation of mixed dumbbells, increases recombination rates relative to pure W. As Figure 14 shows, this reduces the accumulation of defects in the volume and, with it, the associated hardening levels. Another interesting finding is that the temperature trend in the HFIR case is reversed with respect to the other two cases.

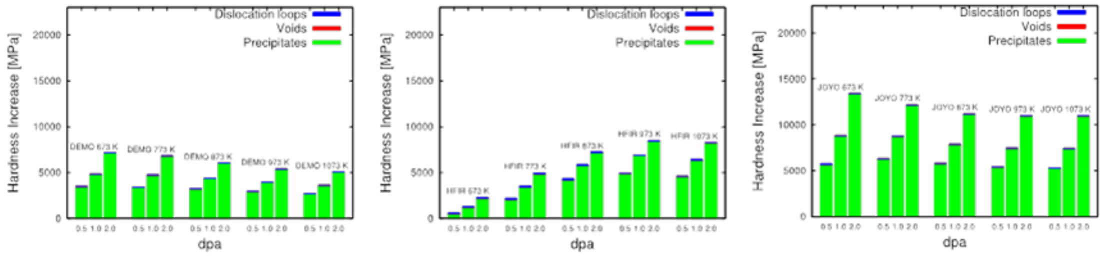

(a) DEMO. (b) HFIR. (c) JOYO.

Figure 14. Radiation-induced hardening in a volume without sinks for (a) DEMO, (b) HFIR and (c) JOYO irradiation conditions.

Discussions

The main aim of this work is to use state-of-the-art modeling of irradiation damage production and accumulation to predict the potential hardening in tungsten under DEMO conditions. To gauge whether our calculations can reliably provide such predictions, we simulate irradiation experiments in JOYO and HFIR and compare our predictions with the experimental measurements. Despite the tremendous progress achieved in the understanding of irradiation damage over the last several decades, several key challenges remain in terms of fusion energy conditions. The physics describing the interactions between irradiation defects and transmutation elements is insufficient (or, at least, for the W-Re system considered here). These interactions are critical because they give rise to defect-solute complexes and other clusters that contribute substantially to hardening in irradiated materials. Our approach has been to describe these interactions based on atomistic modeling results and common sense, and to check them against the measurements of hardening in JOYO and HFIR.

There are also numerical challenges inherent to modeling transmutation and damage in fusion conditions. It is well known that to achieve meaningful doses, methods based on the mean-field approximation (MFA) must be used. At the same time, the number of equations required to deal with multiple species interacting with each other is prohibitively high. Direct atomistic or Monte Carlo methods cannot yet provide sufficiently-long time scales to approach the necessary doses. Our method of stochastic cluster dynamics can trivially treat multispecies scenarios and is thus well suited to study processes where transmutation plays a role. At the same time, its underlying physics is based on MFA, which makes it efficient enough to capture the long-term evolution of irradiated systems. Although transmutation has been considered in irradiation damage studies, we believe that this is the first work where damage and transmutation element production have been considered in unison from the start. Yet, even if one accepts these simulations as the state of the art, many unknowns remain, as evidenced by the uncertainty in the results vis a vis the experimental measurements. For example, analysis of the results in HFIR shows that voids are the main contributors to hardening at low doses. However, in the simulations we see no such predominance under any of the three scenarios considered here (Figures 12, 13, and 14). This probably points to the existence of other mechanisms of vacancy immobilization and/or SIA escape not considered here. We do capture hardening by voids in DEMO in all cases except when there are no sinks present (Figure 14), but still not dominant compared to Re precipitates.

What is clear is that the contribution to hardening from these precipitates is absolutely dominant and a factor that cannot be ignored when looking at the evolution of W-based alloys under fusion irradiation conditions. From a quantitative point of view, the experiments in the HFIR show that hardening ranges between 5000 and 8000 MPa at doses above 1 dpa with a weak temperature dependence in the 500~800^{o}C interval. The simulation scenario closest to those measurements is that discussed in Section 3.4, which considers single crystals with no sinks (Figure 14). As well, the standard case, discussed in Section 3.2, furnishes results not far from the experimental measurements. This probably allows us to discard the remaining case, characterized by thermally-stable complexes involving SIAs and Re atoms. Our conclusion is that the most likely scenario based on our results is the standard one of Setion. 3.2, with a low sink density and a moderate binding between SIA clusters and Re atoms. If so, this would indicate hardening levels on the order of five to ten thousand MPa for DEMO, which would likely lead to intolerable embrittlement amounts in W. Of course, these calculations include only a simple picture of the total chemical complexity associated with full transmutation inventory situations (e.g. Os, Ta, Pt, etc.), but they give an idea of the degradation of W-based alloys subjected to first wall conditions.

References

[1] S. J. Zinkle, N. M. Ghoniem, Operating temperature windows for fusion reactor structural materials, Fusion Engineering and Design 51–52 (2000) 55–71.

[2] M. Rieth, S. L. Dudarev, S. M. Gonzalez de Vicente, J. Aktaa, T. Ahlgren, S. Antusch, D. E. J. Armstrong, M. Balden, N. Baluc, M. F. Barthe, W. W. Basuki, M. Battabyal, C. S. Becquart, D. Blagoeva, H. Boldyryeva, J. Brinkmann, M. Celino, L. Ciupinski, J. B. Correia, A. De Backer, C. Domain, E. Gaganidze, C. Garc ́ıa-Rosales, J. Gibson, M. R. Gilbert, S. Giusepponi, B. Gludovatz, H. Greuner, K. Heinola, T. Ho ̈schen, A. Hoffmann, N. Holstein, F. Koch, W. Krauss, H. Li, S. Lindig, J. Linke, C. Linsmeier, P. Lo ́pez-Ruiz, H. Maier, J. Matejicek, T. P. Mishra, M. Muhammed, A. Mun ̃oz, M. Muzyk, K. Nordlund, D. Nguyen-Manh, J. Opschoor, N. Orda ́s, T. Palacios, G. Pintsuk, R. Pippan, J. Reiser, J. Riesch, S. G. Roberts, L. Romaner, M. Rosin ̃ski, M. Sanchez, W. Schulmeyer, H. Traxler, A. Uren ̃a, J. G. van der Laan, L. Veleva, S. Wahlberg, M. Walter, T. Weber, T. Weitkamp, S. Wurster, M. A. Yar, J. H. You, A. Zivelonghi, Recent progress in research on tungsten materials for nuclear fusion applications in Europe, J. Nucl. Mater. 432 (1-3) (2013) 482–500.

[3] S.P.Fitzgerald, D.Nguyen-Manh, Peierls potential for crowdions in the bcc transition metals, Phys. Rev. Lett. 101 (2008) 115504.

[4] C. S. Becquart, C. Domain, An object Kinetic Monte Carlo Simulation of the dynamics of helium and point defects in tungsten, J. Nucl. Mater. 385 (2) (2009) 223–227.

[5] M. R. Gilbert, J. -Ch. Sublet, S. L. Dudarev, Spatial heterogeneity of tungsten transmutation in a fusion device, Nucl. Fusion 57 (2017) 044002.

[6] M. R. Gilbert, J.-C. Sublet, Neutron-induced transmutation effects in W and W-alloys in a fusion environment, Nuclear Fusion 51 (4) (2011) 043005.

[7] M. R. Gilbert, S. L. Dudarev, S. Zheng, L. W. Packer, J.-C. Sublet, An integrated model for materials in a fusion power plant: transmutation, gas production, and helium embrittlement under neutron irradiation, Nuclear Fusion 52 (8) (2012) 083019.

[8] J. He, G. Tang, A. Hasegawa, K. Abe, Microstructural development and irradiation hardening of w and w–(3–26) wt% re alloys after high- temperature neutron irradiation to 0.15 dpa, Nuclear fusion 46 (11) (2006) 877.

[9] T. Tanno, A. Hasegawa, J. C. He, M. Fujiwara, M. Satou, S. Nogami, K. Abe, T. Shishido, Effects of transmutation elements on the microstructural evolution and electrical resistivity of neutron-irradiated tungsten, J. Nucl. Mater. 386–388 (2009) 218–221.

[10] A. Hasegawa, T. Tanno, S. Nogami, M. Satou, Property change mechanism in tungsten under neutron irradiation in various reactors, J. Nucl. Mater. 417 (1–3) (2011) 491–494.

[11] X. Hu, T. Koyanagi, M. Fukuda, N. K. Kumar, L. L. Snead, B. D. Wirth, Y. Katoh, Irradiation hardening of pure tungsten exposed to neutron irradiation, Journal of Nuclear Materials 480 (2016) 235 – 243.

[12] X. Hu, T. Koyanagi, Y. Katoh, M. Fukuda, B. D. Wirth, L. L. Snead, Defect evolution in neutron-irradiated single crystalline tungsten, DOE/ER-0313/58-Semiannual Progress Report, June 30, 2015 (2015).

[13] G. Cottrell, Sigma phase formation in irradiated tungsten, tantalum and molybdenum in a fusion power plant, Journal of nuclear materials 334 (2) (2004) 166–168.

[14] A. Xu, C. Beck, D. E. Armstrong, K. Rajan, G. D. Smith, P. A. Bagot, S. G. Roberts, Ion-irradiation-induced clustering in w-re and w-re- os alloys: A comparative study using atom probe tomography and nano-indentation measurements, Acta Materialia 87 (2015) 121 – 127.

[15] A.Xu,D.E.Armstrong,C.Beck,M.P.Moody,G.D.Smith,P.A.Bagot,S.G.Roberts, Ion-irradiation induced clustering in w-re-ta, w-re and w-ta alloys: An atom probe tomography and nanoindentation study, Acta Materialia 124 (2017) 71 – 78.

[16] T. Suzudo, M. Yamaguchi, A. Hasegawa, Stability and mobility of rhenium and osmium in tungsten: first principles study, Modelling Simul. Mater. Sci. Eng. 22 (7) (2014) 075006.

[17] T. Suzudo, M. Yamaguchi, A. Hasegawa, Migration of rhenium and osmium interstitials in tungsten, Journal of Nuclear Materials 467, Part 1 (2015) 418–423.

[18] L. Gharaee, J. Marian, P. Erhart, The role of interstitial binding in radiation induced segregation in w-re alloys, Journal of Applied Physics 120 (2).

[19] W. Setyawan, G. Nandipati, R. J. Kurtz, Interaction of interstitial clusters with rhenium, osmium, and tantalum in tungsten, Tech. Rep. DOE/ER-0313/60 (June 2016).

[20] L. Gharaee, P. Erhart, A first-principles investigation of interstitial defects in dilute tungsten alloys, Journal of Nuclear Materials 467, Part1 (2015) 448–456.

[21] C.-H. Huang, L. Gharaee, Y. Zhao, P. Erhart, J. Marian, Mechanism of Re precipitation in irradiated W-Re alloys from kinetic Monte Carlo simulations, ArXiv e-prints arXiv:1702.03019.

[22] P. Vladimirov, S. Bouffard, Displacement damage and transmutations in metals under neutron and proton irradiation, Comptes Rendus Physique 9 (3) (2008) 303 – 322, materials subjected to fast neutron irradiation.

[23] R. Rayaprolu, S. Mller, C. Linsmeier, S. Spellerberg, Simulation of neutron irradiation damage in tungsten using higher energy protons, Nuclear Materials and Energy 9 (2016) 29 – 35.

[24] J. Marian, V. V. Bulatov, Stochastic cluster dynamics method for simulations of multispecies irradiation damage accumulation, Journal of Nuclear Materials 415 (1) (2011) 84 – 95.

[25] J. Marian, T. L. Hoang, Modeling fast neutron irradiation damage accumulation in tungsten, Journal of Nuclear Materials 429 (1–3) (2012) 293 – 297.

[26] C.-H. Huang, J. Marian, A generalized ising model for studying alloy evolution under irradiation and its use in kinetic monte carlo simulations, Journal of Physics: Condensed Matter 28 (42) (2016) 425201.

[27] M. Gilbert, J. Marian, J.-Ch. Sublet, Energy spectra of primary knock-on at oms under neutron irradiation, J. Nucl. Mater. 467 (2015) 121–134. 15

[28] M. R. Gilbert, J.-Ch. Sublet, PKA distributions: Contributions from transmutation products and from radioactive decay, Nucl. Mater. Energy 9 (2016) 576–580.

[29] A. J. Koning, D. Rochman, J. Kopecky, J-Ch. Sublet, M. Fleming, E. Bauge, S. Hilaire, P. Romain, B. Morillon, H. Duarte, S. vander Marck, S. Pomp, H. Sjostrand, R. Forrest, H. Henriksson, O. Cabellos, S. Goriely, J. Leppanen, H. Leeb, A. Plompen, R. Mills, TENDL-2015, release Date: January 18, 2016.

[30] A. E. S and, S. L. Dudarev, K. Nordlund, High-energy collision cascades in tungsten: Dislocation loops structure and clustering scaling laws, EPL (Europhysics Letters) 103 (4) (2013) 46003.

[31] W. Setyawan, G. Nandipati, K. J. Roche, H. L. Heinisch, B. D. Wirth, R. J. Kurtz, Displacement cascades and defects annealing in tungsten, part i: Defect database from molecular dynamics simulations, Journal of Nuclear Materials 462 (2015) 329 – 337.

[32] X. Yi, A. E. Sand, D. R. Mason, M. A. Kirk, S. G. Roberts, K. Nordlund, S. L. Dudarev, Direct observation of size scaling and elastic interaction between nano-scale defects in collision cascades, EPL (Europhysics Letters) 110 (3) (2015) 36001.

[33] N. Juslin, B. Wirth, Interatomic potentials for simulation of he bubble formation in w, Journal of Nuclear Materials 432 (1) (2013) 61–66.

[34] J-Ch. Sublet, J. W. Eastwood, J. G. Morgan, M. R. Gilbert, M. Fleming, W. Arter, FISPACT-II: an advanced simulation system for activation, transmutation and material modelling, Nucl. Data Sheets 139 (2017) 77–137.

[35] M. J. Norgett, M. T. Robinson, I. M. Torrens, A proposed method of calculating displacement dose rates., Nucl. Eng. Des. 33 (1975) 50–54.

[36] D. R. Mason, X. Yi, M. A. Kirk, S. L. Dudarev, Elastic trapping of dislocation loops in cascades in ion-irradiated tungsten foils, J. Phys.: Condens. Matter 26 (2014) 375701.

[37] J. S. Wro´bel, D. Nguyen-Manh, K. J. Kurzydłowski, S. L. Dudarev, A first-principles model for anomalous segregation in dilute ternary tungsten-rhenium-vacancy alloys, Journal of Physics: Condensed Matter 29 (14) (2017) 145403.

[38] F. Kroupa, P. Hirsch, Elastic interaction between prismatic dislocation loops and straight dislocations, Discussions of the Faraday Society 38 (1964) 49 – 55.

[39] S. Zinkle, Y. Matsukawa, Observation and analysis of defect cluster production and interactions with dislocations, Journal of Nuclear Materials 329–333, Part A (2004) 88 – 96, proceedings of the 11th International Conference on Fusion Reactor Materials (ICFRM-11).

8.5 MODELING DUCTILE-PHASE TOUGHENED TUNGSTEN FOR PLASMA-FACING MATERIALS: PROGRESS IN DAMAGE FINITE ELEMENT ANALYSIS OF TUNGSTEN-COPPER BEND TESTS

—B. N. Nguyen, C. H. Henager, Jr., R. J. Kurtz (Pacific Northwest National Laboratory)

OBJECTIVE

The objective of this study is to investigate the deformation behavior of ductile phase toughened W-composites such as W-Cu and W-Ni-Fe using a multiscale finite element model that involves a microstructural dual-phase model where the constituent phases (i.e., W, Cu, Ni-Fe) are finely discretized and are described by a continuum damage model. Such a model is suitable for modeling deformation, cracking, and crack bridging for W-Cu, W-Ni-Fe, and other ductile phase toughened W-composites, or more generally, any multi-phase composite structure where two or more phases undergo cooperative deformation in a composite system. Our current work focuses on validating the dual-phase microstructural approach by simulating the response and damage development of W-Cu specimens subjected to three-point bending and comparing the predictions to the experimental results to validate the model.

SUMMARY

A promising approach to increasing fracture toughness and decreasing the ductile-brittle transition temperature (DBTT) of a W-alloy is by ductile-phase toughening (DPT) [1-3]. In this method, a ductile phase is included in a brittle matrix to prevent fracture propagation by crack bridging or crack deflection. Liquid-phase sintered W-Ni-Fe alloys and hot-pressed and sintered W-Cu composites are two examples of such materials that PNNL and the University of California at Santa Barbara are investigating. However, there is a need for improved mechanical property models of such composite systems in order to begin to optimize these structural materials with regard to strength and fracture toughness. This report describes a dual-phase microstructural model that has recently been developed at PNNL. The model predictions have been validated against the experimental results for W-Cu bend bar tests.

PROGRESS AND STATUS

Introduction

Tungsten (W) and W-alloys are the solid materials of choice for plasma-facing components (PFCs) of future fusion reactors, such as the International Thermonuclear Experimental Reactor (ITER) and Demonstration Power Plant (DEMO), due to their high melting point, strength at high temperatures, high thermal conductivity, low coefficient of thermal expansion, and low sputtering yield [4-6]. However, W and most W-alloys exhibit low fracture toughness and a high DBTT that would render them as brittle materials during reactor operations [4, 6, 7]. The DBTT for unirradiated W-alloys typically ranges from 573K to 1273K (300 to 1000˚C), and in a reactor environment radiation hardening would further elevate this range [6, 8, 9]. W-alloys toughened by engineered reinforcement architectures, such as ductile-phase toughening (DPT), are strong candidates for PFCs. In DPT, a ductile phase is included in a brittle matrix to prevent catastrophic fracture propagation. The principles of DPT are illustrated in Figure 1, which shows an actual and schematic illustration of ductile bridging ligaments stretching across an open crack in a brittle matrix material, such as W [10]. W-Cu is a model DPT composite for our purposes.

Model Development

The approach developed to build the finite element (FE) model for a W-Cu single-edge-notched bend (SENB) bar was presented in our previous semiannual report [11]. This approach generates homogenized, meshed regions alongside the dual-phase meshed region shown in Figure 2a to create a fully meshed model of a bend bar that corresponds to the physical dimensions of our 3-point or 4-point bend samples. The as-created FE mesh shown in Figure 2a for the bending specimen possesses three regions: the dual phase W-Cu microstructural region containing the notch, and two adjacent continuum homogenized Cu-W regions. During the past report period, this approach was applied to a significantly larger microstructure domain than the domain used previously to more accurately capture damage and large plastic deformations in the region of interest containing the notch.

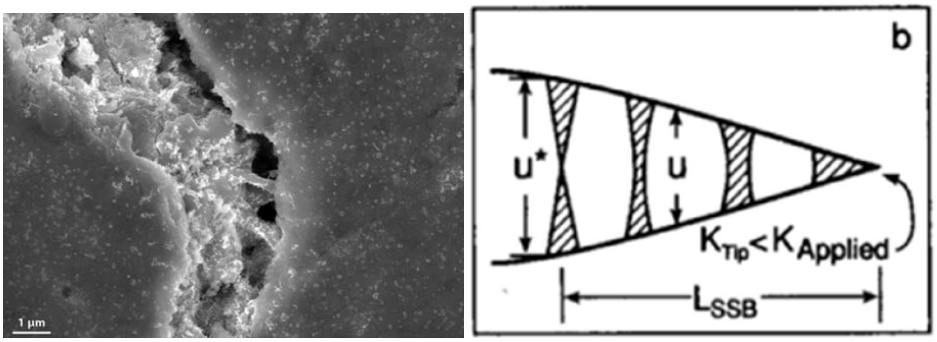

Figure 1. a) SEM image of a crack in a W-Cu test specimen where the ductile phase (Cu) is effectively bridging the crack. b) A steady-state bridging zone shown schematically in 2D [10].

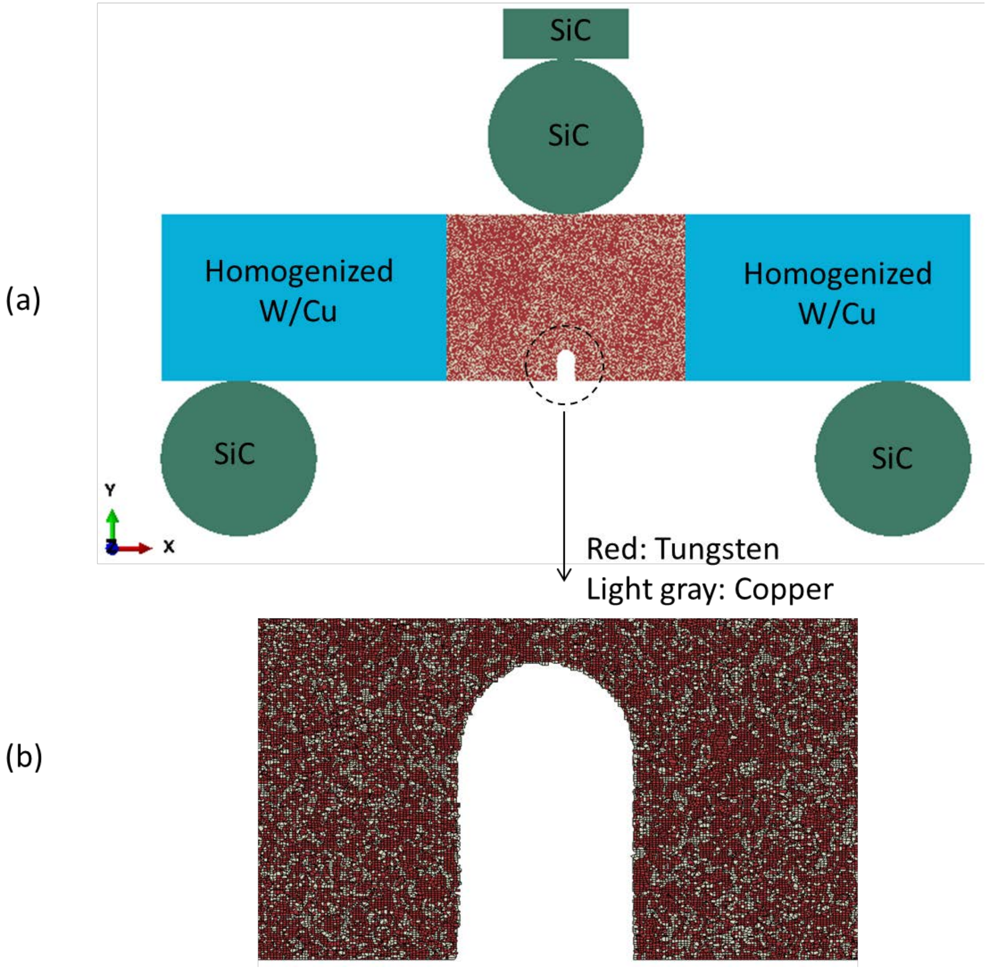

Figure 2. (a) The FE mesh of the W-Cu SENB bar that is 3.3 x 1.6 x 16 mm in size. This mesh contains 639327 2D plane-strain elements including 578486 elements in the microstructural zone. (b) A magnified view of the notch region with the constituent phases identified by color.

First, the microstructural region is created from a digital image of an actual microstructure using the public domain software OOF2[1] that creates multiple mesh domains with high-resolution elements at phase boundaries. Figure 2b shows a magnified view of the microstructural meshed region where the Cu elements (colored in light gray) are embedded in the W elements (colored in dark red). In the model illustrated in Figure 2, the volume fractions of W and of Cu were determined to be 67.5% and 32.5%, respectively. The OOF2 software allows the user to specify mechanical properties for each meshed domain and generates an input file containing FE mesh information and material assignments for ABAQUS®. Plastic deformation and damage are allowed only in the microstructural dual phase region.

Next, a FORTRAN script was written and used to mesh the homogenized Cu-W elastic regions that are connected to the microstructural region to achieve the meshing for the whole specimen. The elastic properties of the homogenized Cu-W regions were computed using EMTA [12] considering the same volume fractions of W and Cu as for the microstructural region. Finally, to complete the FE model for the W-Cu SENB bar, meshing for the supports and loading pin in silicon carbide (SiC) was performed

---

[1] OOF2 was developed at the National Institute of Standards and Technology (NIST). See http://www.ctcms.nist.gov/oof/oof2/.

considering their actual dimension (diameter = 3.1 mm) and support span (*L*=13 mm). The loading bar in SiC that applied the displacements to the loading pin was also modeled.

The constitutive behaviors of W and of Cu considered in the analyses are described by an elastic-plastic damage model implemented in PNNL's EMTA-NLA [13] that acts as a user-subroutine module of ABAQUS®. The model considers the different behaviors in tension and compression by only computing the damage evolution for a tensile stress state. While the stress/strain behaviors of the *macroscale* Cu (e.g., [14]) and *macroscale* W (e.g., [15]) are rather well-known, the same kinds of elastic-plastic responses of these metals at the micron-scale of the microstructure (~grain size) are not known and constitute a challenge in this research. This problem is known as the size effect on the material strength that has been reported for various materials including metals and ceramics. In this work, starting from the reported stress/strain data for Cu and W [14-15] considered as lower bounds, adjustments of the constitutive model parameters for W and Cu were conducted through FE analyses of the SENB test until the predicted load-displacement response and crack propagation pattern match the experimental results.

Results

The FE model for the Cu-W SENB specimen subjected to three-point bending was analyzed by ABAQUS®. Figure 3 shows the predicted damage distribution and crack pattern in the dual phase region at 0.18-mm applied displacement. Damage is quantified by a damage indicator that varies from 0 to 1. If the failure indicator is equal to 1, total failure (or fracture) occurs and is captured by a vanishing element method. Cracks are predicted to initiate and meanderingly propagate away from the notch. Figure 3 clearly shows the linking-up of cracks to form a main crack at this advanced stage of fracture. Figure 4 shows the cracked region observed in new experiments (performed at room temperature) that validate the model predictions for crack pattern and propagation. Comparing Figure 4 to Figure 3 shows a very good agreement between the predicted and experimental crack propagation directions. The predicted load-displacement response reported in Figure 5 also agrees well with the experimental data.

Conclusions

During this report period, important progress has been made in both modeling and experimental efforts to develop ductile phase-toughened tungsten for plasma-facing applications. We have developed and experimentally validated a dual-phase microstructural approach to simulate W-Cu SENB tests. The current model predictions show very good agreement with our recent experimental data with respect to load-displacement curves and crack pattern as well as propagation direction in the W-Cu composite. The model can effectively capture the bridging mechanism responsible for retarding crack propagation. The developed approach appears to be robust and can be further enhanced to tailor the mechanical properties of DPT composites provided the constitutive properties are known.

Future Work

We will present our recent work at the 18th International Conference on Fusion Reactor Materials (IFRM18). The developed approach will be applied to study W-Ni-Fe composites through similar analyses.

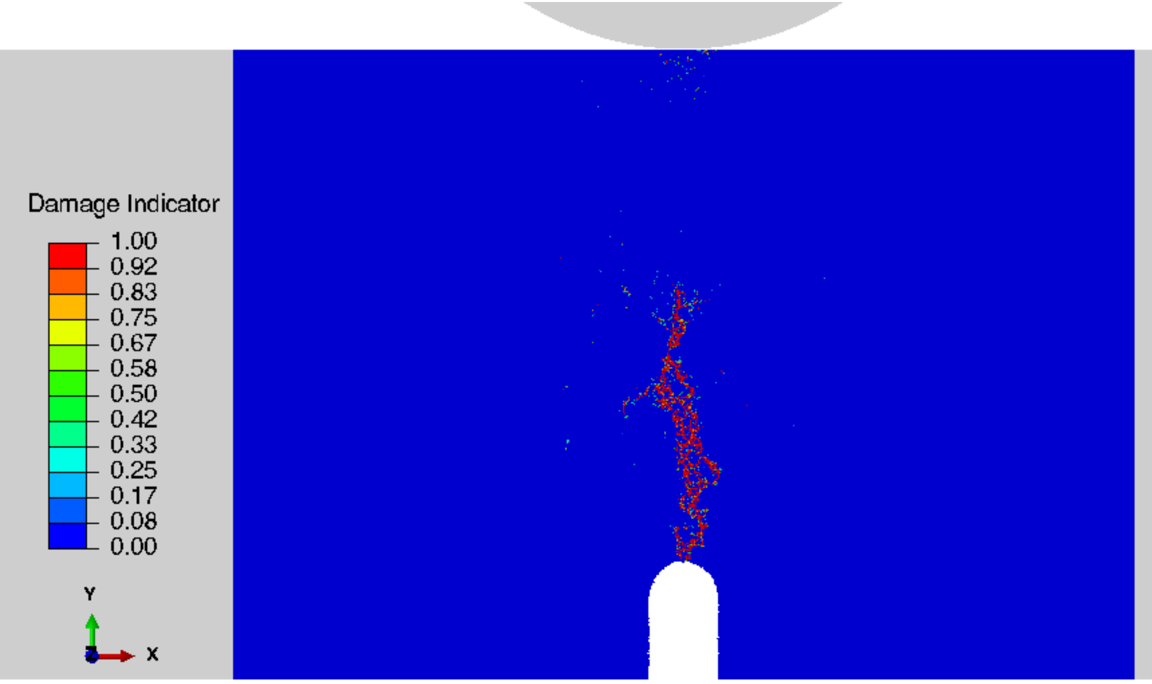

Figure 3. Predicted damage distribution and crack pattern in the microstructural dual-phase region of the W-Cu SENB specimen for 0.18-mm applied displacement.

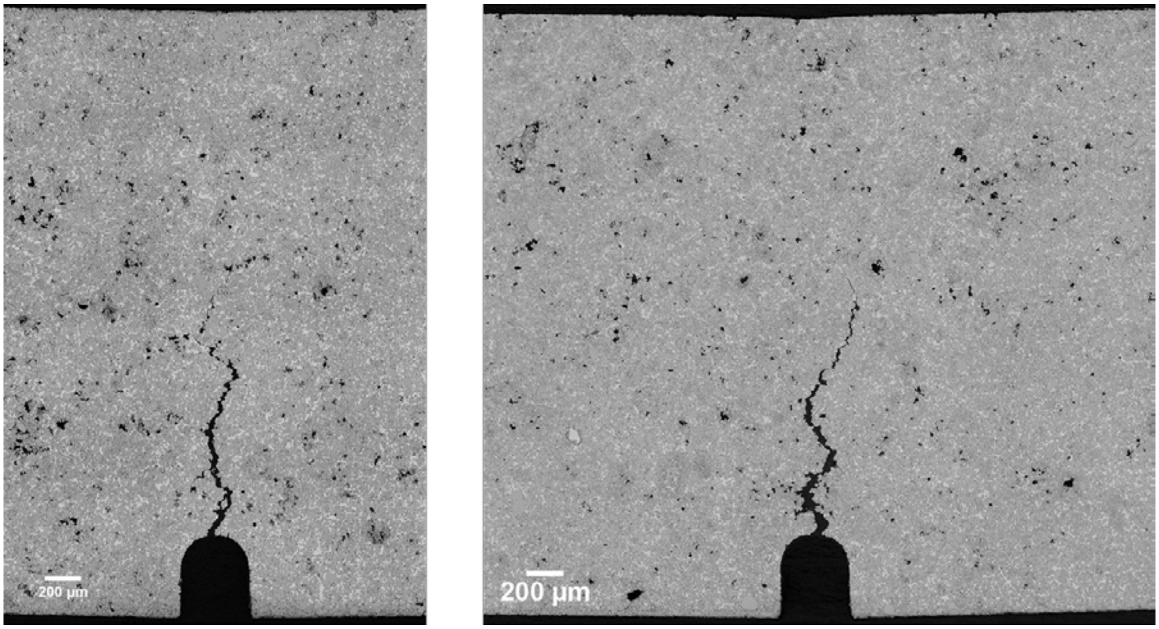

Figure 4. Experimental crack patterns obtained after room temperature bend tests of W-Cu specimens.

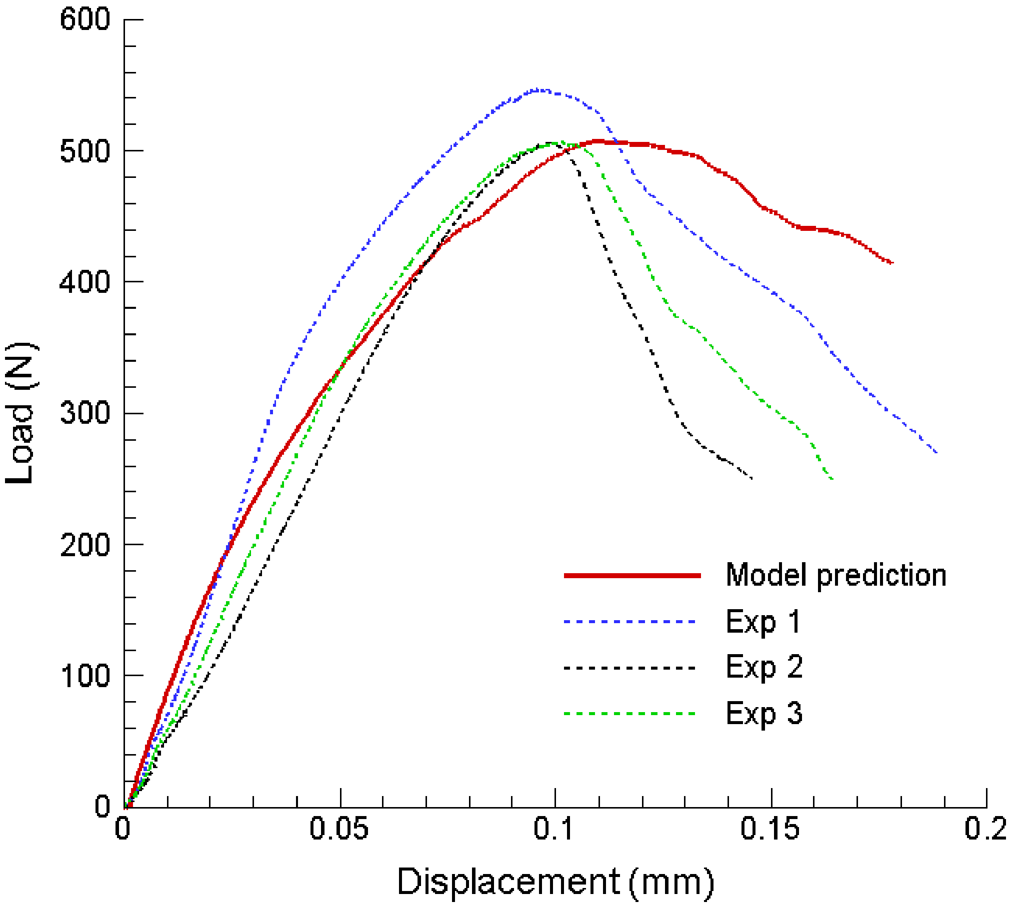

Figure 5. Predicted load-displacement response compared to experimental results for W-Cu SENB specimens.

References

[1] Deve, H.E., A.G. Evans, G.R. Odette, R. Mehrabian, M.L. Emiliani, and R.J. Hecht, Acta metallurgica et materialia, 1990. 38(8): p. 1491-502.

[2] Erdogan, F. and P.F. Joseph, J. Am. Ceram. Soc., 1989. 72(2): p. 262-270.

[3] Sigl, L.S., P.A. Mataga, B.J. Dalgleish, R.M. McMeeking, and A.G. Evans, Acta Metall., 1988. 36(4): p. 945-953.

[4] Rieth, M., J.L. Boutard, S.L. Dudarev, T. Ahlgren, S. Antusch, N. Baluc, M.F. Barthe, C.S. Becquart, L. Ciupinski, J.B. Correia, C. Domain, J. Fikar, E. Fortuna, C.C. Fu, E. Gaganidze, T.L. Galan, C. Garcia-Rosales, B. Gludovatz, H. Greuner, K. Heinola, N. Holstein, N. Juslin, F. Koch, W. Krauss, K.J. Kurzydlowski, J. Linke, C. Linsmeier, N. Luzginova, H. Maier, M.S. Martinez, J.M. Missiaen, M. Muhammed, A. Munoz, M. Muzyk, K. Nordlund, D. Nguyen-Manh, P. Norajitra, J. Opschoor, G. Pintsuk, R. Pippan, G. Ritz, L. Romaner, D. Rupp, R. Schaublin, J. Schlosser, I. Uytdenhouwen, J.G. Van Der Laan, L. Veleva, L. Ventelon, S. Wahlberg, F. Willaime, S. Wurster, and M.A. Yar, J. Nucl. Mater., 2011. 417: p. 463-467.

[5] Pitts, R.A., A. Kukushkin, A. Loarte, A. Martin, M. Merola, C.E. Kessel, V. Komarov, and M. Shimada, Physica Scripta Volume T, 2009. 2009(T138): p. 014001 (10 pp.).

[6] Mertens, P., T. Hirai, M. Knaup, O. Neubauer, V. Philipps, J. Rapp, V. Riccardo, S. Sadakov, B. Schweer, A. Terra, I. Uytdenhouwen, and U. Samm, Fusion Eng. Des., 2009. 84(7-11): p. 1289-93.

[7] Mertens, P., V. Philipps, G. Pintsuk, V. Riccardo, U. Samm, V. Thompson, and I. Uytdenhouwen, Physica Scripta Volume T, 2009. 2009(T138): p. 014032 (5 pp.).

[8] Gludovatz, B., S. Wurster, A. Hoffmann, and R. Pippan, Int. J. Refract. Met. Hard Mater., 2010. 28(6): p. 674-8.

[9] Zinkle, S.J. and N.M. Ghoniem, Fusion Eng. Des., 2000. 51-52: p. 55-71.

[10] Odette, G.R., B.L. Chao, J.W. Sheckherd, and G.E. Lucas, Acta Metallurgica et Materialia, 1992. 40(9): p. 2381-9.

[11] Nguyen BN, CH Henager, Jr, and RJ Kurtz. 2017. "Modeling Ductile-Phase Toughened Tungsten for Plasma-Facing Materials: Progress in Damage Finite Element Analysis of the Tungsten-Copper Bend Bar Tests." Chapter 8.4 in Fusion Materials Semiannual Progress Report For the Period Ending December 31, 2016, vol. 61; DOE/ER-0313/61, ed. FW Wiffen and S Melton, pp. 171-177, Oak Ridge National Laboratory, Oak Ridge, TN.

[12] Nguyen, B.N., EMTA User's Guide. Pacific Northwest National Laboratory, Richland, WA, 2010, PNNL-19997.

[13] Nguyen, B.N., EMTA-NLA User's Guide. Pacific Northwest National Laboratory, Richland, WA, 2010, PNNL-20013.

[14] Sandstrom, R. and Hallgren, Stress strain flow curves for Cu-OFP, Royal Institute of Technology, Swedish Nuclear Fuel and Waste Management Co, 2009, R-09-14.

[15] Dummer T, JC Lasalvia, G Ravichadran, and MA Meyers. Acta Materialia, 1998, 146(17): p. 6267-90.

9. FUSION SYSTEM DESIGN

No contributions this reporting period.

10. IRRADIATION METHODS, EXPERIMENTS AND SCHEDULES

10.1 MINIATURE MECHANICAL TEST DEVELOPMENT FOR TUNGSTEN-BASED MATERIALS—L. M. Garrison, Emily Proehl, Frank Chen (Oak Ridge National Laboratory)

OBJECTIVE

The aim of this work is to develop miniature mechanical test methods that can be used to evaluate neutron-irradiated tungsten and tungsten composite samples in LAMDA.

SUMMARY

Because of activation concerns after irradiation, miniaturized, non-standard tungsten sample geometries are often used. Additionally, many tungsten based composites employ tungsten foils or tungsten fibers which also cannot use standard size mechanical test fixtures. A miniaturized, non-standard fracture toughness test is being developed for tungsten samples with dimensions 10×4×2 mm^3. This geometry of fracture toughness tungsten samples was included in the PHENIX RB*19J irradiation capsule. Initial tests on the unirradiated control samples from the RB*19J materials are underway in preparation for future tests with the irradiated tungsten samples.

PROGRESS AND STATUS

Fracture toughness testing will be conducted on several types of tungsten materials from the PHENIX RB*19J irradiation campaign to collect comparative fracture toughness data. The PHENIX sample size, 10×4×2 mm^3, is nonstandard and does not comply with the ASTM 399 or ASTM 1820-16 standards for fracture toughness testing. Therefore, a fixture with a span of 6.1 mm will be used to accommodate the 10 mm length of the PHENIX three-point bend specimens (Figure 1). A load was successfully applied to the tungsten specimens using the fixture in Figure 1b, so pre-cracking can be performed.

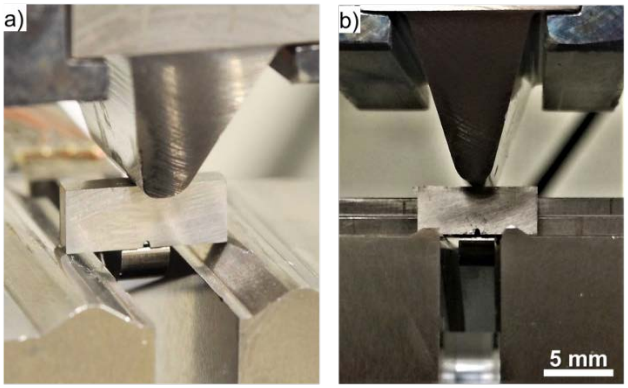

Figure 1. a) PHENIX specimen size (10 mm long) does not span distance between support radii on standard fixture. b) The fixture that will be used with the miniature W samples has a span of 6.1 mm.

During the applied test load cycle, the crack length was not measured accurately on the three-point bend software using the standard compliance equation. Therefore, the compliance coefficients must be altered in the fracture toughness software to match the nonstandard three-point bend specimen geometry. The load-line displacement and compliance is heavily dependent on the span to width ratio (S/W) of the specimen; the standard S/W ratio is 4 per ASTM E399–12, whereas the PHENIX samples have a S/W ratio of 1.525. Equation (1) shows load-line displacement, which is dependent on span, width, and load [1]:

$$EB\delta/P \cdot \left(\frac{1-a/W}{S/W}\right) = 1.193 - 1.980 \cdot a/W + 4.478 \cdot (a/W)^2 - 4.443 \cdot (a/W)^3 + 1.739 \cdot (a/W)^4 \qquad (1)$$

Where , E is Young's modulus, B is sample thickness, δ is load-line displacement, P is applied load, a is crack length, W is the width of the sample, and S is the span between the two points of contact between the supports and the sample.

Equation (1) must be manipulated using polynomial curve fitting to an inverse compliance expression format equal to a/W, an input determined by the three-point bend software program to measure stress intensity. Once Equation (1) is modified, allowing the crack length to be accurately measured by the clip gauge, fatigue pre-cracking will begin, followed by three-point bend testing to attain critical stress intensity, or fracture toughness, K_{IC}.

References

[1] F. Haggag and J. Underwood, "Compliance of three-point bend specimen at the load line," International Journal of Fracture. 26-2 (1984) R63-R65.

10.2 **HFIR IRRADIATION EXPERIMENTS**—J.P. Robertson (Oak Ridge National Laboratory)

Status of the Reactor

HFIR completed 3.7 cycles during the first half of 2017. Cycle 470 began on January 3, 2017 and ended on January 28, 2017, accumulating 2160.04 MWD, Cycle 471 began on February 14, 2017 and ended on March 11, 2017 (2180.37 MWD), Cycle 472 began on May 3, 2017 and ended on May 27, 2017 (2074.94 MWD), and Cycle 473 began on June 13 and is expected to end on July 8.

Summary of Recent, Current and Planned Fusion Materials Program Experiments

Experiment Designation	Primary Materials	Specimen Types*	Irradiation Temperature (°C)	Max Exposure (dpa)	Number of Reactor Cycles	Irradiation Period (month/year)		
Beryllium reflector (RB) irradiation capsules								
RB-15J	F82H	T, F, FT	300, 400	6	10	6/08	–	12/09
RB-19J	W alloys and F82H	various	250/300C, 500C, 800C, 1200C	1.5	6	6/16		12/16
Target zone full-length capsules								
JP-25	F82H	T, FT	300, 500	20	10	2/99	–	1/01
JP-26	F82H	T, FT	300,400,500	9	5	12/03	–	11/04
JP-27	F82H	T, FT	300, 400	21	13	12/03	–	1/08
JP-28	F82H	T, FT	300,400,500	80	46	4/05	–	7/13
JP-29	F82H	T, FT	300,400,500	80	46	1/05	–	7/13
12-DCT	F82H	DCT	50	1.6	1	8/11	–	8/11
JP-30	F82H	T, FT	300,400,650	20	~10	11/11	–	8/13
JP-31	F82H	T, FT	300,400,650	20	~10	11/11	–	8/13
Target zone rabbit capsules (DOE-JAEA)								
F8A1	F82H	T, FT	300	50	29	2/09	–	7/13
F8A2	“	“	“	“	“	“	–	“
F8B1	“	“	“	“	“	“	–	“
F8B2	“	“	“	“	“	“	–	“
JCR-1	SiC/SiC	Bend bars	800	30	15	10/04	–	1/09
JCR-2	“	“	“	“	“	“	–	“
JCR-3	“	“	“	“	“	“	–	“
JCR-4	“	“	“	“	“	“	–	“
JCR-5	“	“	“	>50	>25	10/04	–	2/11
JCR-6	“	“	“	“	“	“	–	“
JCR-7	“	“	“	“	“	“	–	“
JCR-8	“	“	“	“	“	“	–	“
JCR-9	“	“	500	30	15	10/04	–	1/09
JCR-10	“	“	“	“	“	“	–	“
JCR-11	“	“	“	“	“	“	–	“

Experiment Designation	Primary Materials	Specimen Types*	Irradiation Temperature (°C)	Max Exposure (dpa)	Number of Reactor Cycles	Irradiation Period (month/year)		
Target zone rabbit capsules (DOE-JAEA) Continued								
JCR-12	"	"	"	"	"	"	–	"
F11A3	F82H	T, FT	300	20	12	5/11	–	2/13
F11A4	"	"	"	"	"	"	–	"
F11B3	"	"	"	"	"	"	–	"
M4-TEN	F82H	DCT	50	1.6	1	8/11	–	8/11
JCR11-01	SiC/SiC	Bend bars	950	50	25	11/12	–	3/16
JCR11-02	SiC/SiC	Bend bars	950	10	5	10/12	–	8/13
JCR11-03	SiC/SiC	Bend bars	950	30	15	5/13	–	8/15
JCR11-04	SiC/SiC	Bend bars	950	30	15	5/13	–	8/15
JCR11-05	SiC/SiC	Bend bars	950	50	25	10/12	–	3/16
JCR11-06	SiC/SiC	Bend bars	950	10	5	10/12	–	7/13
JCR11-07	SiC/SiC	Bend bars	950	100	50	10/12	–	
JCR11-08	SiC/SiC	Bend bars	950	100	50	10/12	–	
JCR11-09	SiC/SiC	UDMC	950	4	2	6/13	–	11/13
JCR11-10	SiC/SiC	UDMC	950	10	8	6/13	–	8/14
JCR11-11	SiC/SiC	UDMC	950	30	15	6/13	–	8/15
JCR11-12	SiC/SiC	UDMC	950	100	50	6/13	–	3/16
F13A5	F82H	T, FT	300	10	9	1/14	–	3/15
F13A6	F82H	T, FT	300	50	28	1/14	–	
F13B4	F82H	T, FT	300	10	9	1/14	–	3/15
F13B5	F82H	T, FT	300	20	18	1/14	–	3/16
SCF6	SiC/SiC	Bend bars	600	10	6	11/14	–	10/15
SCF7	SiC/SiC	Bend bars	600	30	14	11/14	–	1/17
SCF8	SiC/SiC	Bend bars	600	100	45	11/14	–	
SCF9	SiC/SiC	Bend bars	600	200	90	11/14	–	5/17
SCF10	SiC/SiC	Bend bars	950	10	5	1/15	–	10/15
SCF11	SiC/SiC	Bend bars	950	30	14	1/15	–	
SCF12	SiC/SiC	Bend bars	950	100	45	1/15	–	3/16
Target zone rabbit capsules (DOE-NIFS)								
T8A1	SiC	BSR	300	0.01	HT**	10/09	–	10/09
T8A2	SiC	BSR	300	0.1	HT	10/09	–	10/09
T8B1	SiC	BSR	500	0.01	HT	10/09	–	10/09
T8B2	SiC	BSR	500	0.1	HT	10/09	–	10/09
T8C1	SiC	BSR	500	~1	1	5/09	–	6/09
T8D1	SiC	BSR	800	0.1	HT	3/11	–	10/09
T8E1	SiC	BSR	800	~1	1	8/09	–	8/09
T8F1	SiC	BSR	1200	~1	1	8/09	–	8/09
T9A1	W, Ni	Discs	90	0.1	HT	1/09	–	10/09
T9A2	W, Ni	Discs	90	1.2	1	1/09	–	1/09
T9C1	Steels	T, MC	500	5.5	3	11/09	–	2/10
T9C2	Steels	T, MC	500	9.6	5	11/09	–	6/10
T9G1	Steels	T, MC	300	1.2	1	6/09	–	8/09
T9G2	Steels	T, MC	300	9.6	8	6/09	–	8/11

Experiment Designation	Primary Materials	Specimen Types*	Irradiation Temperature (°C)	Max Exposure (dpa)	Number of Reactor Cycles	Irradiation Period (month/year)		
Target zone rabbit capsules (DOE-NIFS) Continued								
MTTN01	Steels	T, MC	300	4.8	4	1/12	–	8/11
300-LD-1	Steels	SSJ, MC	300	2	1	5/12	–	6/12
300-HD-1	Steels	SSJ, MC	300	12	6	5/12	–	2/13
500-LD-1	Steels	SSJ, MC	500	2	1	5/12	–	6/12
500-HD-1	Steels	SSJ, MC	500	12	6	5/12	–	2/13
500-HD-2	Steels	SSJ, MC	500	12	6	5/12	–	2/13
500-HD-3	Steels	SSJ, MC	500	12	6	5/12	–	2/13
650-LD-1	Steels	SSJ, MC	650	2	1	5/12	–	6/12
650-LD-2	Steels	SSJ, MC	650	2	1	5/12	–	6/12
650-HD-1	Steels	SSJ, MC	650	12	6	5/12	–	2/13
650-HD-2	Steels	SSJ, MC	650	12	6	5/12	–	2/13
300-LD-2	Steels, W	SSJ, MC	300	2	2	7/12	–	8/12
300-MD-1	Steels, W	SSJ, MC	300	7	4	7/12	–	2/13
500-LD-2	Steels, W	SSJ, MC	500	2	2	1/13	–	7/13
300-LD-3	Steels, W	SSJ, MC	300	2	2	7/12	–	11/12
300-HD-2	Steels, W	SSJ, MC	300	12	8	7/12	–	2/14
500-LD-3	Steels, W	SSJ, MC	500	2	1	7/12	–	8/12
500-HD-4	Steels, W	SSJ, MC	500	12	6	7/12	–	7/13
650-LD-3	Steels, W	SSJ, MC	650	2	2	10/12	–	7/13
650-HD-3	Steels, W	SSJ, MC	650	12	8	7/12	–	11/13
PC1	Various	SSJ, MC	80/100	0.02	HT	6/12	–	6/12
PC1A	Various	SSJ, MC	80/100	0.02	HT	6/12	–	6/12
PC2	Various	SSJ, MC	80/100	0.1	HT	6/12	–	6/12
PC2A	Various	SSJ, MC	80/100	0.1	HT	6/12	–	6/12
PC3	Various	SSJ, MC	80/100	0.5	HT	6/12	–	7/12
PC3A	Various	SSJ, MC	80/100	0.5	HT	6/12	–	7/12
PC4	Various	SSJ, MC	80/100	2	1	6/12	–	7/12
PC4A	Various	SSJ, MC	80/100	2	1	6/12	–	7/12
PC5	Various	SSJ, MC	80/100	20	9	6/12	–	11/13
TB-300-1	Steels, W	SSJ, MC	300	0.02	HT	8/12	–	8/12
TB-300-2	Steels, W	SSJ, MC	300	0.1	HT	8/12	–	8/12
TB-300-3	Steels, W	SSJ, MC	300	0.5	HT	8/12	–	8/12
TB-300-4	Steels, W	SSJ, MC	300	7	5	7/12	–	6/13
TB-500-1	Steels, W	SSJ, MC	500	0.1	HT	8/12	–	8/12
TB-500-2	Steels, W	SSJ, MC	500	0.5	HT	8/12	–	8/12
TB-500-3	Steels, W	SSJ, MC	500	7	4	7/12	–	2/13
TB-650-1	Steels, W	SSJ, MC	650	0.1	HT	8/12	–	8/12
TB-650-2	Steels, W	SSJ, MC	650	0.5	HT	8/12	–	8/12
TB-650-3	Steels, W	SSJ, MC	650	7	5	7/12	–	6/13
TB-650-4	Steels, W	SSJ, MC	650	20	11	7/12	–	7/14
TTN09	SiC	Joint	500	3.4	2	8/11	–	11/11
TTN10	SiC	Joint	500	4.1	2	8/11	–	11/11
TTN11	SiC	Joint	800	4	2	3/12	–	5/12
TTN01	SiC	BSR	300	1	1	2/11	–	3/11
TTN02	SiC	BSR	300	10	6	2/11	–	12/11

Experiment Designation	Primary Materials	Specimen Types*	Irradiation Temperature (°C)	Max Exposure (dpa)	Number of Reactor Cycles	Irradiation Period (month/year)		
Target zone rabbit capsules (DOE-NIFS) Continued								
TTN03	SiC	BSR	300	20	11	2/11	–	8/13
TTN04	SiC	BSR	500	10	6	5/11	–	4/12
TTN05	SiC	BSR	500	20	11	5/11	–	8/13
TTN06	SiC	BSR	800	10	6	5/11	–	4/12
TTN07	SiC	BSR	800	20	11	5/11	–	8/13
TTN08	SiC	BSR	1200	10	6	5/11	–	8/12
TTN16	SiC	Fiber BSR	500	1	1	11/11	–	12/11
TTN17	SiC	Fiber BSR	500	10	6	8/11	–	6/12
TTN18	SiC	Fiber BSR	500	20	11	8/11	–	8/13
TTN19	SiC	Fiber BSR	1200	1	1	3/12	–	4/12
TTN20	SiC	Fiber BSR	1200	10	6	3/12	–	11/12
PXW1	W	Discs	800	2	1		–	
PXW2	W	Discs	800	2	1	1/15	–	2/15
PXW3	W	Discs	800	6	3		–	
PXW4	W	Discs	1100	2	1		–	
PXW5	W	Discs	1100	2	1	1/15	–	2/15
PXW8	W	Discs	1100	6	3		–	
Target zone rabbit capsules (US-NIFS-JAEA)								
T11-01J	V-4Cr-4Ti	BTC	425	2	1	11/12	–	12/12
T11-02J	V-4Cr-4Ti	BTC	425	6	3	1/13	–	7/13
T11-03J	V-4Cr-4Ti	BTC	425	2	1	11/12	–	12/12
T11-04J	V-4Cr-4Ti	BTC	425	6	3	1/13	–	7/13
T11-05J	SiC	BTC	600	2	1	11/12	–	12/12
T11-06J	SiC	BTC	600	6	3	1/13	–	7/13
T11-08J	SiC	BTC	600	6	3	1/13	–	7/13
T11-09J	SiC	BTC	600	2	1	11/12	–	12/12
T11-11J	SiC	BTC	600	2	1	11/12	–	12/12
T11-13J	Graphite	BTC	600	2	1	11/12	–	12/12
T11-14J	Graphite	BTC	600	6	3	1/13	–	7/13
J12-01	F82H	BTC	300	1.5	1	1/13	–	2/13
J12-02	F82H	BTC	300	6	3	5/13	–	7/13
J12-03	F82H	BTC	300	1.5	1	5/13	–	2/13
J12-04	F82H	BTC	300	6	3	1/13	–	6/13
J12-05	F82H	BTC	300	1.5	1	1/13	–	2/13
J12-06	F82H	BTC	300	6	3	5/13	–	6/13
Target zone rabbit capsules (US-IMR)								
MX-1	Ceramics	Various	400	2	1	7/13	–	8/13
MX-2	Ceramics	Various	400	6	3	7/13	–	3/14
MX-3	Ceramics	Various	400	10	6	7/13	–	7/14
MX-4	Ceramics	Various	700	2	1	7/13	–	8/13
MX-5	Ceramics	Various	700	6	3	7/13	–	2/14

Experiment Designation	Primary Materials	Specimen Types*	Irradiation Temperature (°C)	Max Exposure (dpa)	Number of Reactor Cycles	Irradiation Period (month/year)		
Target zone rabbit capsules (US-IMR) Continued								
MX-6	Ceramics	Various	700	10	5	7/13	–	5/14
MX-7	Ceramics	Various	1000	2	1	7/13	–	8/13
MX-8	Ceramics	Various	1000	6	3	7/13	–	3/14
MX-9	Ceramics	Various	1000	10	5	7/13	–	5/14
IMR2	Various	Various	200	2	1	6/15	–	7/15
IMR3	Various	Various	200	2	1	6/15	–	7/15
IMR4	Various	Various	200	2	1	6/16	–	7/16
IMR5	Various	Various	200	4	2	12/15	–	2/16
IMR6	Various	Various	600	2	1	6/16	–	7/16
IMR7	Various	Various	600	6	3	6/16	–	9/30
IMR8	Various	Various	600	10	5	6/16	–	3/17
IMR9	Various	Various	1000	2	1	6/16	–	7/16
IMR10	Various	Various	1000	10	5	6/16	–	1/17
IMR11	Various	Various	1000	10	5	6/16	–	1/17
Target zone rabbit capsules (US)								
SCJ2-10	Ceramics	Joint	500	3	2	5/14	–	7/14
SCJ2-11	Ceramics	Joint	500	>10	12	5/14	–	3/16
SCJ2-12	Ceramics	Joint	500	3	2	5/14	–	7/14
SCJ2-16	Ceramics	Joint	1000	3	2	6/14	–	8/14
SCJ2-17	Ceramics	Joint	1000	3	2	6/14	–	8/14

*T = Tensile, F = Fatigue, FT = Fracture Toughness, MC = Multipurpose Coupon, BSR = Bend Stress Relaxation Creep, DCT = Disc Compact Tension, BTC: Bellows-loaded Tensile Creep, UDMC: Uni-directional Mini-composite. Most experiments also contain TEM disks, other special purpose specimens, and monitors occupying small spaces.
**Hydraulic tube – fractional cycle exposures.